9-4-2013

A selection of biomechanical research problems : from modeling to experimentation

Cyrus Abbasi

Cyrus Omid Abbasi
Candidate

Mechanical Engineering
Department

This dissertation is approved, and it is acceptable in quality and form for publication:

Approved by the Dissertation Committee:

Tariq A. Khraishi, PhD, Chairperson

Yu-Lin Shen, PhD

Bret R. Baack, MD

Thomas J. Harrison, MD

A SELECTION OF BIOMECHANICAL RESEARCH PROBLEMS: FROM MODELING TO EXPERIMENTATION

BY

CYRUS OMID ABBASI

B.S., Civil Engineering, California State University, Fresno, 2009

DISSERTATION

Submitted in Partial Fulfillment of the
Requirements for the Degree of
Doctor of Philosophy

Engineering

The University of New Mexico
Albuquerque, New Mexico

July, 2013

DEDICATION

I Cyrus Omid Abbasi, dedicate this work to my Father, Mother, Brother and Sister.

Specifically, this work is dedicated to my Father, who has protected and supported me throughout all stages of my life. Without doubt, I would have not been the person who I am today, without the guidance and encouragements of my lovely father.

Dear father, thank you and I love you.

Your Son: Cyrus Omid Abbasi

A SELECTION OF BIOMECHANICAL RESEARCH PROBLEMS: FROM MODELING TO EXPERIMENTATION

BY

Cyrus Omid Abbasi

B.S., CIVIL ENGINEERING, CALIFORNIA STATE UNIVERSITY, FRESNO, 2009

PHD, ENGINEERING, UNIVERSITY OF NEW MEXICO, 2013

ABSTRACT

The research undertakings within this manuscript illustrate the importance of biomechanics in today's science. Without doubt, biomechanics can be utilized to obtain a better understanding of many unsolved mysteries involved in the field of medicine. Moreover, biomechanics can be used to develop better prosthetic or surgical devices as well.

Chapter 2 represents a medical problem, which has not been solved for more than a century. With the use of fundamental principles of biomechanics', a better insight of this problem and its possible causes were obtained. Chapter 3 investigates the mechanical interaction between the human teeth and some processed food products during mastication, which is a routine but crucial daily activity of a human being. Chapter 4 looks at a problem within the field of surgery. In this chapter the stability and reliability of two different Suturing-Techniques are explored. Chapters 5 and 6 represent new patent

designs as a result of the investigations made in Chapter 4. Chapter 7 studies the impact and load transfer patterns during the collision between a child's head and the ground.

All of the above mentioned chapters show the significance of biomechanics in solving a range of different medical problems that involve physical and or mechanical characters.

TABLE OF CONTENTS

LIST OF FIGURES

LIST OF CHARTS

LIST OF TABLES

CHAPTER 1

1-1 Introduction

The terminology “biomechanics” integrates the prefix “bio”, which means “life,” and the field of “mechanics” [1]. Mechanics is a subfield of engineering, which studies the motion or equilibrium/rest of matter and the forces that instigate matter’s motion or equilibrium/rest [2]. Mechanics relies on the concepts of time, space, force, energy, and matter [2]. The terminology biomechanics was adopted by the international community of scientists during the early 1970s in order to portray the science relating the study of the mechanical aspects of living organisms [3].

Despite being a relatively young field, biomechanics is quickly becoming a widely studied and utilized scientific field by the scientists affiliated with various other fields. These scientists or professionals may be associated with the fields of physical therapy, kinesiology, orthopedics, cardiology, sports medicine and biomedical science amongst many more [3]. Within all these fields, biomechanics is mostly used to study the structural behavior of living things.

Biomechanists use the principals of mechanics to study the anatomical and functional aspects of living organisms during motion or at rest [4]. Within the field of biomechanics, kinesiology, which is the study of human movement [5] as well as the field of human exercise science, are the most widely studied subfields of biomechanics [1].

The study of human biomechanics shines light on the engineering aspects of the human body. Specifically, the mechanical engineering aspects of the human body are studied. Simple daily tasks such as walking, gripping a soda can, changing clothes or

even special cases of human behavior such as walking on the moon or the blood flow within the arteries during a space shuttle takeoff can be investigated via the utility of biomechanics. To be more precise, human biomechanics studies the response of the organs, extremities, blood flow, the skeleton and other parts of the body to external or internal loadings or trigger mechanisms. Running, climbing and kicking a football are some examples of external loads imposed on the body. Hiccups, sneezing, bloated bladder or a swollen ankle can cause internal loads on the body. An electrical shock or an increase in hormonal levels is an example of external or internal trigger mechanisms that can put the body under stress [1].

By knowing the response of the body to these loading conditions physicians can better understand the physical aspects of certain disease per say and with that can make a better diagnosis or heal the patient in a more effective and accelerated way. Engineers can design more suitable products that account for certain physical behaviors of the body, which were not accounted for before. For instance a more comfortable shoe can be designed, which can optimize the walking pattern of an individual to decrease any potential back pain for instance.

This manuscript makes use of the principles of biomechanics to investigate the mechanical aspects of some interesting medical features/issues with regards to the human body. Every chapter is concerned with a different biomechanical study or development.

The following paragraphs present short introductions to the Chapters 2 through 8.

1-2 Chapter 2

Chapter 2 presents an alternative etiology regarding a retinal disease called "*Purtscher retinopathy*". Purtscher retinopathy is a retinal disease affecting the posterior pole of the retina. The effects include hemorrhages and exudates in the human retina. Although this disease has been discovered a century ago, no concrete etiology has been established for this disease. This chapter aims to find a possible etiology through literature review and computational fluid dynamics (CFD). CFD is utilized to compare the blood flow pattern within a 45.0° and a 90.0° retinal micro vessel bifurcation. The wall shear stresses at the interior vessel walls of these two different bifurcations were investigated and compared to each other. The parametric investigations showed different flow patterns and wall shear stress values for bifurcations with a 90.0 degree angle than for bifurcations with a 45.0 degree angle.

1-3 Chapter 3

Chapter 3 represents the interaction between human teeth and processed food products. For this work cereal was the chosen food. In this chapter fracturing of two different cereal products during mastication is investigated. A main aim of this study was to determine the fragmentation potential of the two cereal products into smaller fragments suitable for swallowing. The process of mastication was simulated via the utility of finite element method. The obtained results illustrated that in the case of both cereal products, the fracturing into small pieces tends to occur prior to the completion of the first mastication cycle.

1-4 Chapter 4

Chapter 4 compares the reliability and stability of two different surgical Suturing-Techniques. The Suturing-Techniques are utilized to securely anchor surgical drains to a patient's skin or inner organs. Surgical drain are often utilized to draw excess or unwanted bodily fluids such as blood form a specific location within the body of a patient.

After a surgical procedure it is very common that at the location, where the surgery was conducted, excessive bleeding or collection of any other bodily fluids would occur. The presence of such fluids can be the cause of infections and or prolonged healing processes. Surgical drains prove to be very effective in drawing out such fluids.

A surgical drain is a long tube. One of its ends is placed inside the body at the spot, where the surgical procedure has been performed. The other end either exits the body through the skin of the patient or is connected to other organs such as the large intestine, which can serve as a natural exit route. In either case, the drain needs to be attached to patient's skin or an organ. This will ensure that the drain does not dislodge from its designated placement.

The anchoring is usually done with sutures, which are run through the skin or other underlying organ in the vicinity of the drain and then wrapped around the drain to hold it tightly in place. The wrapping of the sutures around the drain is called a Suturing-Technique. The Suturing-Techniques can vary.

The most common Suturing-Technique is called the Roman Sandal, which is actually taught to medical students/residents as the standard Suturing-Technique. Within this

chapter another Suturing-Technique has been developed called the Modified Roman Sandal. The main purpose of the work within this chapter is to compare the reliability and stability of these two Suturing-Techniques. It is hoped that the medical, specifically the surgical community, can benefit from the findings of this chapter.

1-5 Chapter 5

Chapter 5 represents a patent work, which came about as an alternative drain design inspired by the investigation of the drain and suturing systems within Chapter 4. The patent herein actually includes several designs, where the utility of surgical sutures as a direct method of anchoring is avoided. Several anchoring systems are introduced, which are integrated in the design of a surgical drain. The systems developed here can be integrated to a wide range of existing surgical drain designs currently available on the market.

1-6 Chapter 6

Chapter 6 represents a patent work, which also came about as result of observations made during the work detailed in chapter 4. Unlike the patent laid out in chapter 5, the designs herein utilize sutures as a direct means of anchoring. The designs within this section incorporate a *Flexible Section*. The *Flexible Section* provides two major advancements to a drain/catheter.

The first advancement is the super flexibility of the drain/catheter. The second advancement is a secure and reliable anchorage capability of the drain/catheter, which can be achieved by utilizing surgical sutures. The *Flexible Section* can be used as an anchoring-location. The sutures can securely be wrapped around the *Flexible Section* and then connect the drain/catheter to the skin/tissue. The *Flexible Section* guarantees a slip-less suture-to-drain connection. Moreover, the systems developed here can be integrated to a wide range of surgical drain/catheter designs that are currently available on the market.

1-7 Chapter 7

Chapter 7 investigates the *Fall-Patterns* involved during twelve different shortfalls of a six months old child. Shortfalls initiate from simple home furniture items that have a height of 0.5 ft, 1.0 ft, 1.5 ft, 2.0 ft, 2.5 ft or 3.0 ft. For ethical purposes, no human subjects were involved. Rather, a digital model of the child is developed and with it, the shortfalls of the child are simulated within a Rigid Body Dynamics code. Moreover, the forces/accelerations experienced by the child's head throughout each shortfall simulation are recorded. Specifically, this chapter focused on the forces/accelerations involved during the impact of the child's head and ground. Very high and possibly fatal impact accelerations are found in this chapter.

Chapter 7 also includes a *Future Work* section, which suggest additional future research based on the finding of this chapter. The suggested future research is intended to investigate the movement-patterns of the unfused bones composing the skull of a six months old child, if they are subjected to the forces/accelerations obtained in this chapter.

CHAPTER 2

2-1 Authors

1. Thomas J. Harrison MD., Santa Fe, NM.
2. Cyrus O. Abbasi B.S., University of New Mexico, Mechanical Engineering Department.
3. Tariq A. Khraishi PhD., University of New Mexico, Mechanical Engineering Department.

2-2 Title

Purtscher Retinopathy: An Alternative Etiology Supported by Computer Fluid Dynamic Simulations.

2-3 Abstract

2-3-1 Purpose

To explore an alternative etiology for Purtscher retinopathy by literature review and fluid dynamics computational simulations of wall shear stress (WSS) profiles.

2-3-2 Methods

Computer simulations were developed, incorporating posterior pole retinal microvascular flow parameters, to demonstrate WSS profiles at 90° and 45° angle artery/arteriolar branching.

2-3-3 Results

Computer simulations reveal WSS profiles dependent on artery/arteriolar branching angles. At high flow rates an area of changed WSS and flow swirling and reversal was noted at the proximal fillet of the 90° arteriolar branching. These changes did not appear at the 45° arteriolar branching until the flow rate was increased an additional 30%.

2-3-4 Conclusions

Computer simulation data, as well as review of the history and clinical findings of Purtscher and Purtscher-like retinopathy, present evidence that an additional etiology for Purtscher retinopathy may be a rheological event at a retinal posterior pole foci of vascular endothelial dysregulation, followed by downstream endothelin-induced vasculopathy. (Invest Ophthalmol Vis Sci. 2011;52:8102–8107) DOI:10.1167/iovs.11-7734.

2-4 Introduction

Purtscher retinopathy is a well known, but seldom observed, member of the traumatic retinopathies that has defied an exact etiology since it was first described by Othmar Purtscher a century ago [6]. Purtscher observed a delayed posterior pole retinopathy with hemorrhages and exudates in several men who had sustained head injuries. Shortly after Purtscher's original description, a similar constellation of findings were described in individuals with compressive chest injuries [7]. In the ensuing years Purtscher retinopathy has been associated with a confusing number of seemingly disparate traumatic and non-traumatic diseases (Table 1).

Clinical findings of Purtscher retinopathy and Purtscher-like retinopathy have been described in numerous articles, reviews and textbooks [8 to 11]. They consist of delayed involvement of the retinal posterior pole inner layers with ischemic lesions of the superficial nerve-fiber layer (cotton wool spots), infarcts of the retinal capillary bed (Purtscher Flecken), flame hemorrhages (superficial retinal layers), and dot/blot hemorrhages (deeper layers of the inner retina). Optic nerve edema and hemorrhage are common. Involvement of the choroid, retinal pigment epithelium and macula, although reported, are not typically a part of Purtscher retinopathy.

It is important to differentiate between Purtscher retinopathy and Purtscher-like retinopathy. The clinical appearance of Purtscher-like retinopathy varies from a complete clinical picture to a few cotton wool spots as noted in connective tissue diseases. Clinical presentations of Purtscher retinopathy and Purtscher-like retinopathy blend in a gradient which has made the search for a common etiology difficult.

Various etiologies for Purtscher retinopathy and Purtscher-like retinopathy have been described; however, none have completely explained the clinical presentation or the entire spectrum of associated diseases. The etiology of Purtscher and Purtscher-like retinopathy has been investigated chiefly by focus on a specific disease or set of diseases in which Purtscher retinopathy has been observed. Review of these associated diseases suggests they fall into three categories: toxic and/or obstructive emboli, intravascular volume surges and intracephalic shock waves.

Currently, retinal arteriolar and capillary embolism with microinfarction is considered the most acceptable etiology for Purtscher retinopathy and there is pathological and experimental evidence to support this hypothesis. Behrens-Bauman and others have shown that injected particles such as leucocytes, glass beads or platelet aggregates would occasionally produce Purtscher-like retinopathy in experimental animals [12 to 15]. There is no question that many types of emboli have been associated with Purtscher retinopathy. However, the multiple varieties of emboli, and the varied diseases that create these emboli, as well as the rarity with which Purtscher retinopathy occurs, suggests that there is more to the syndrome than just arteriolar and/or capillary embolization.

Intravascular volume surge from chest trauma such as seat hole chest compression [16], valsalva maneuvers [17] and weight lifting [18] has been reported to produce Purtscher and Purtscher-like retinopathy. The pathophysiology of these cases is suspected to involve sudden intravascular volume surges resulting in endothelial damage [18]. However, Burton proposed air emboli as a possible etiology for Purtscher retinopathy in chest compression injuries [19].

Historically, Purtscher retinopathy has been associated with head injuries and of special interest to this discussion are the unilateral contrecoup cases of Purtscher retinopathy described by Burton and others [19 to 21]. One of us (TJH) has seen two cases of left sided head trauma with orbital fractures, lid lacerations and subconjunctival hemorrhages, but with normal fundi examinations and 20/20 vision on the injured side. However, the contralateral fundi in these cases were found to have classic Purtscher retinopathy, optic nerve involvement and persistent 20/200 vision.

In these cases an embolic or intravascular volume surge was deemed unlikely as was toxic cellular aggregation. That the injury provided protection from Purtscher retinopathy in the ipsilateral eye was also thought to be doubtful. The most likely scenario was an intracephalic, extravascular shock wave, generated by the head injury, transmitted to the opposite fundus resulting in unilateral contralateral Purtscher retinopathy.

A serious argument against end organ capillary embolization as the comprehensive etiology for Purtscher retinopathy is the occurrence of Purtscher retinopathy and Purtscher-like retinopathy in non-embolic syndromes, head trauma and chest compression injuries. In addition the delayed occurrence of clinical signs of Purtscher retinopathy is not typical of embolic vascular obstructive disease but perhaps rather a nonembolic toxic ischemia.

The fact that Purtscher retinopathy occurs rarely, bilaterally, unilaterally, and associated with many disparate diseases suggests an unusual and complex interaction of anatomical and physiological events. In addition, it can be assumed that the unique and

specific retinal appearance of Purtscher retinopathy could have a single anatomical focus of tissue damage.

A new approach would be to look upstream from capillary occlusion in the retinal posterior pole vascular system for a susceptible focus of vasculopathy where Purtscher retinopathy clinical presentations converge.

2-5 Methods and Results

Computer simulations of retinal blood flow were developed using a sophisticated computational fluids dynamics (CFD) code (Academic ANSYS-CFD, Release 12.1; ANSYS Inc., Cannonsburg, PA). The name of the utilized code herein is ANSYS-CFX. In the last 25 years, CFD codes have been used to evaluate the dynamics of both Newtonian and non-Newtonian fluids within a simple or highly complicated environment such as a piston of a combustion engine or, in this case, in the human retinal blood flow system [10 to 14]. The code has proved to be a reliable and repeatable tool in studying three-dimensional hemodynamics in complex arterial geometries [15 & 16].

CFD works on the basis of finite element methods, which incorporates the fundamental partial differential Navier–Stokes (NS) equations describing the patterns of blood flow. After constructing a representative model of a complex arterial geometry within the CFD code, the code discretizes the model into many smaller volumes called elements (note that these elements are three dimensional). These elements (usually cubes, tetrahedral, hexahedral, or prisms) are interconnected to each other at their corner points (called nodes).

By using the divergence theorem, the code converts the volume integrals (NS equations) of the elements into surface integrals. The surface integrals are used to evaluate the flux of blood through all the surfaces of an element. The flux exiting from one element is equal to the flux entering into the adjacent element. Thus, mass is conserved and the laws of conservation of mass are observed. From the numerical solution of the NS equations for all the elements, hemodynamic quantities such as WSS

are obtained by the CFD code. Contrary to experimental flow studies, various parameters of the flow model such as blood viscosity, density, and wall roughness can be modified within the code. These convenient capabilities of CFD make it attractive to hemodynamic research groups.

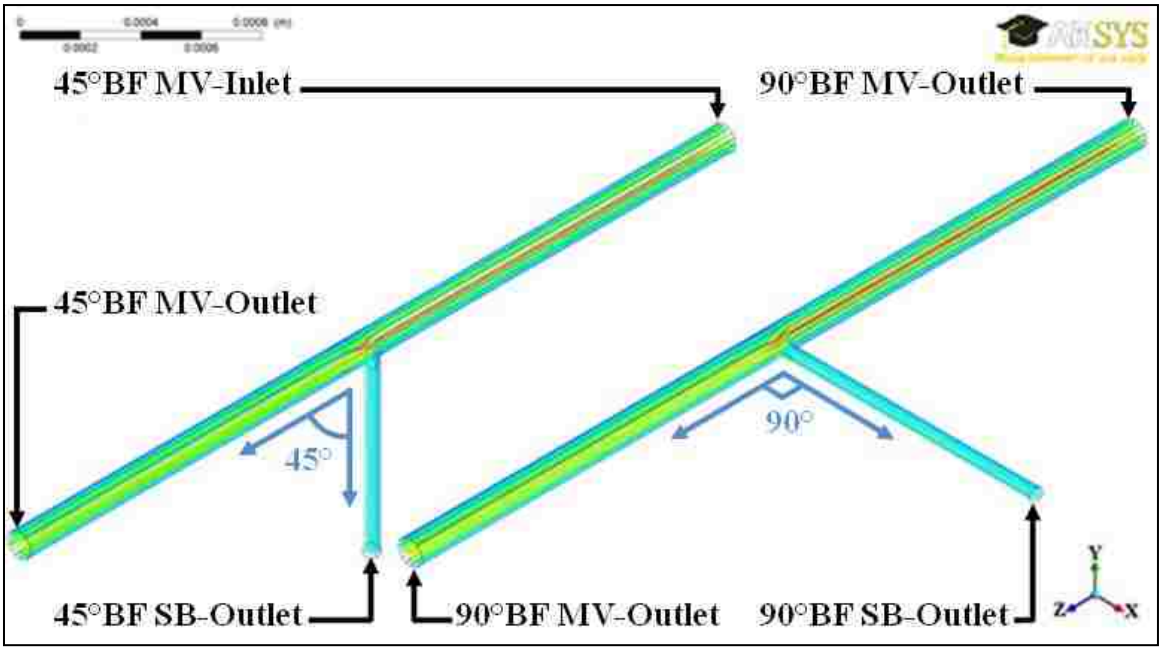

Figure 1: Three-dimensional computer/CFD models of both the 90°and 45° retinal bifurcations. BF: Bifurcation. MV: Main Vessel. SB: Side Branch.

Figure 1 demonstrates the three-dimensional nature of computer studies from which two-dimensional figures are later derived. Computer results as depicted by Figures 1 though 13. Specifically Figs. 6 to 13 reveal WSS calculations as a function of blood flow rate and bifurcation angle. Blood properties and flow data are provided in Table 1.

Table 1: Dimensions of the 90° & 45° Bifurcation Models				
Member			Diameter μm [16]	Length μm
90°	Main Vessel (MV)	[*]	110	3300
	Side Branch (SB)	[12]	65	1040
45°	MV	[*]	110	3300
	SB	[12]	65	1040
*: Nagaoka T, et al. IOVS 2003;44:ARVO E-Abstract 340.				
Retinal Blood Flow (RBF) & the Inlet Velocity at the MVs [13]				
RBF into MVs		= 6.667E-10 m^3/sec		
Area of MVs		= 9.503E-09 m^2		
MV Inlet Velocity		= 0.0702 m/sec		
Density and "Dynamic" Viscosity				
Density		[14] = 1060 kg/m^3		
Dynamic Viscosity		[15 & 16] = 1.05 cP		
Maximum Dynamic Viscosity		[15 & 16] = 5.70 cP		
Reynolds Number & Entrance Length (Le)				
Reynolds Number		[17] = 7.790		
Le within the MVs		[18] = 5.141 μm		

Table 1: Utilized Dimensions of the 90° and 45° Bifurcations; Natural Retinal Blood Flow/Velocity, Density, and Dynamic Viscosity; and Calculated Reynolds Number and Entrance Length within the Main Vessels of the 90° and 45° Bifurcations.

Figures 2 to 5 represent composite pictures with points of interest (labeled A through E, X, Y, and A´ through E´]. These points lie along the S1, S2, or S3 line paths. In later figures, WSS values at these points were important to discuss. S1 is a line path along the main artery base that extends beyond the arteriolar branch above it. S2 is a line path that passes through the proximal fillet, which links the main artery with the branch artery. S3 is a line path that passes through the distal fillet. WSS values were plotted along these three line paths. Note that the line sense of S3 goes opposite to the blood flow direction in the arteriolar and along the blood flow direction in the main artery. In WSS figures (Figs. 6–11), findings for 90° and 45° branching are superimposed for direct comparison.

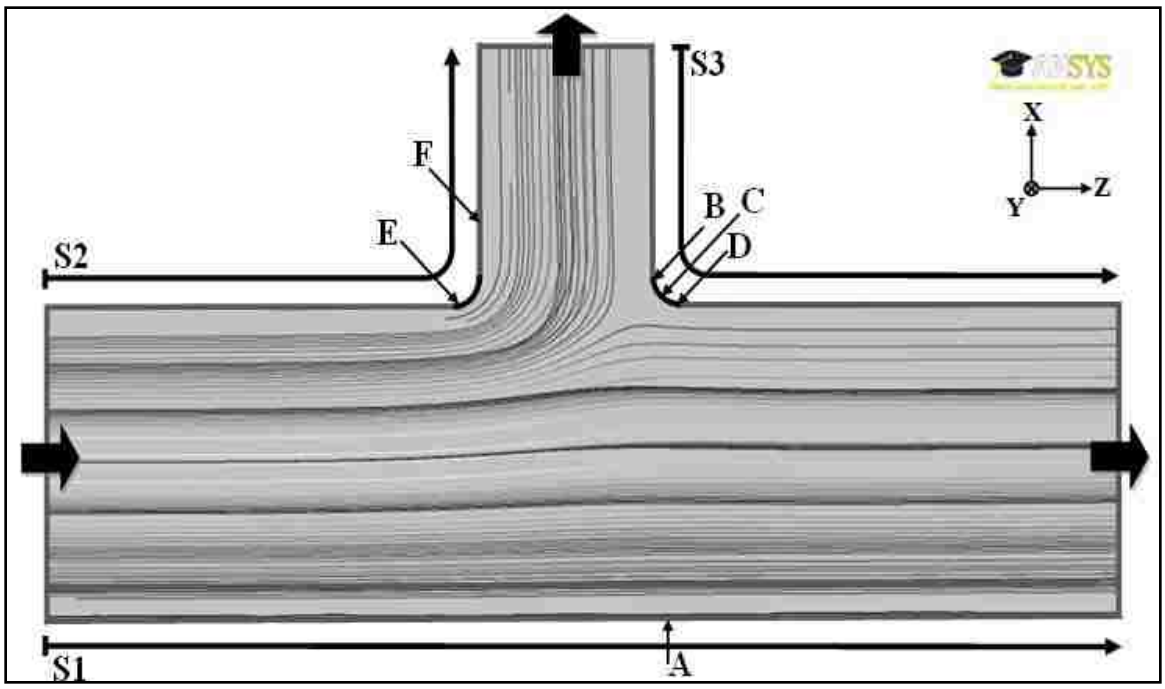

Figure 2: Side view of the 90° retinal bifurcation showing the fluid/blood stream lines at the normal retinal blood flow.

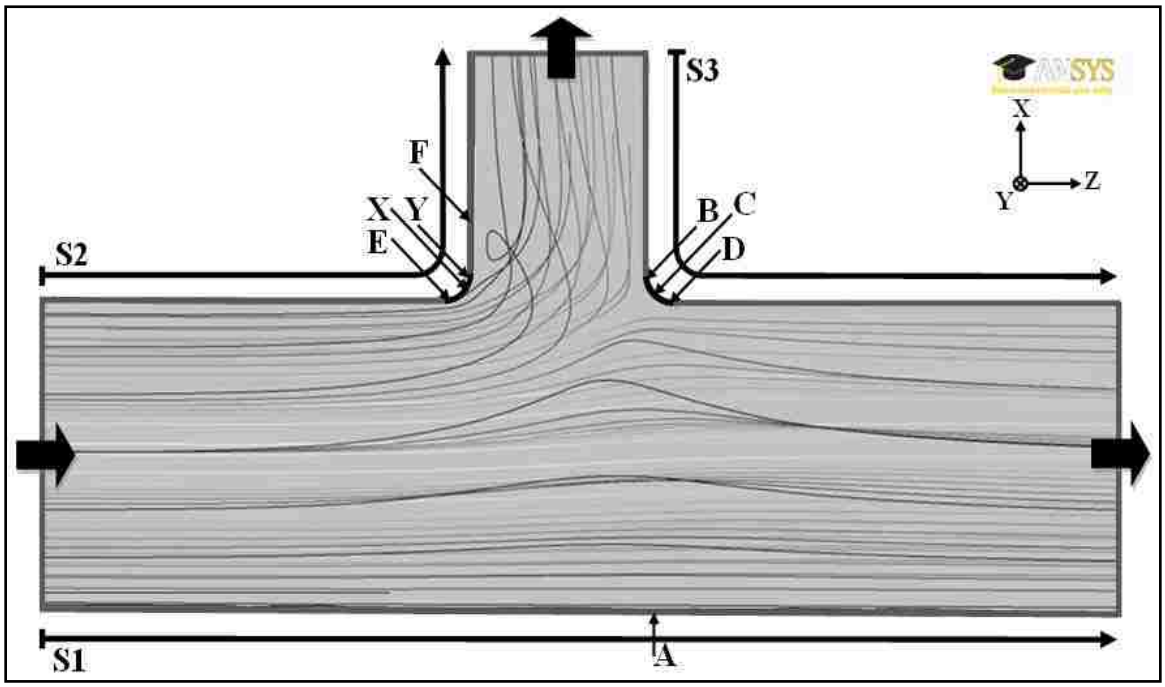

Figure 3: Side view of the 90° retinal bifurcation showing the fluid/blood stream lines at 25 times the normal retinal blood flow. Note the blood flow swirling beneath point F.

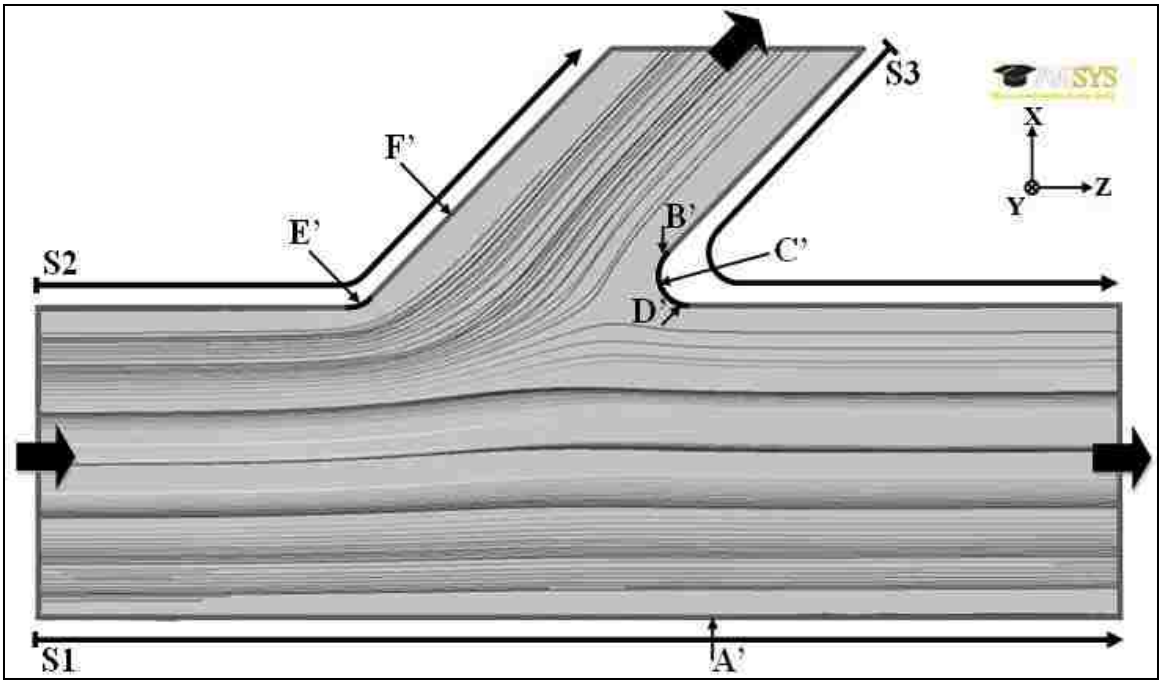

Figure 4: Side view of the 45° retinal bifurcation showing the fluid/blood stream lines at the normal retinal blood flow.

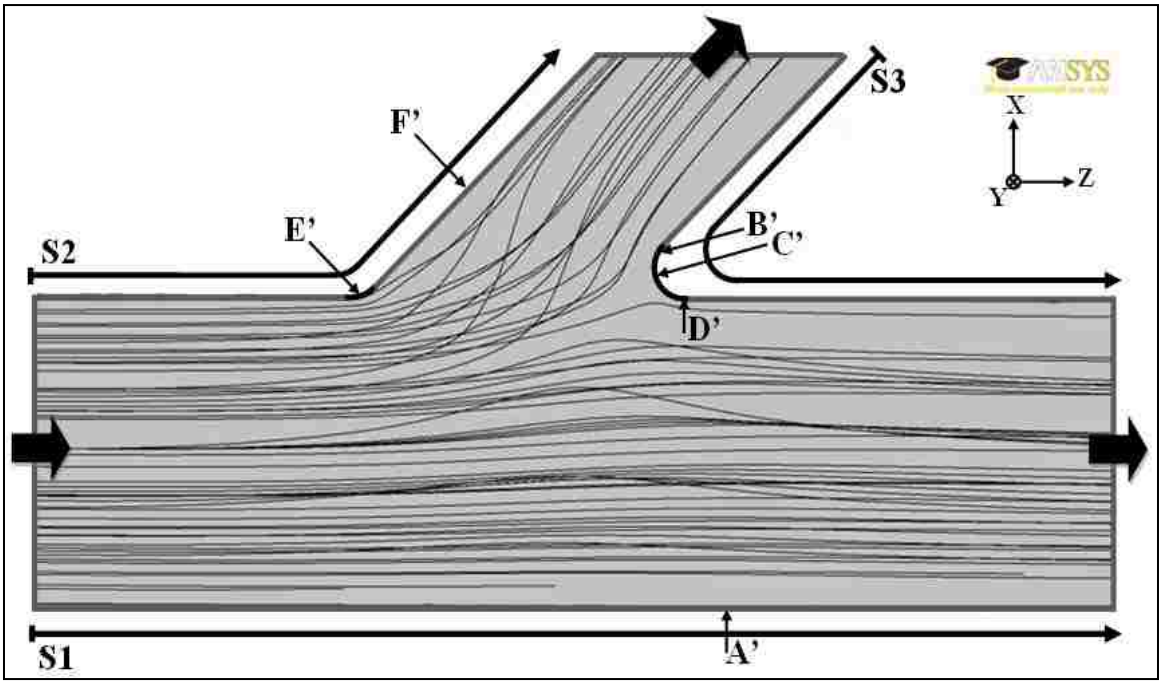

Figure 5: Side view of the 45° retinal bifurcation showing the fluid/blood stream lines at 25 times the normal retinal blood flow.

2-5-1 Normal Blood Flow

Along S1 (Chart 1), with normal blood flow conditions (Table 1), there are no significant WSS profile differences between ninety and forty-five degree arteriolar bifurcation angles.

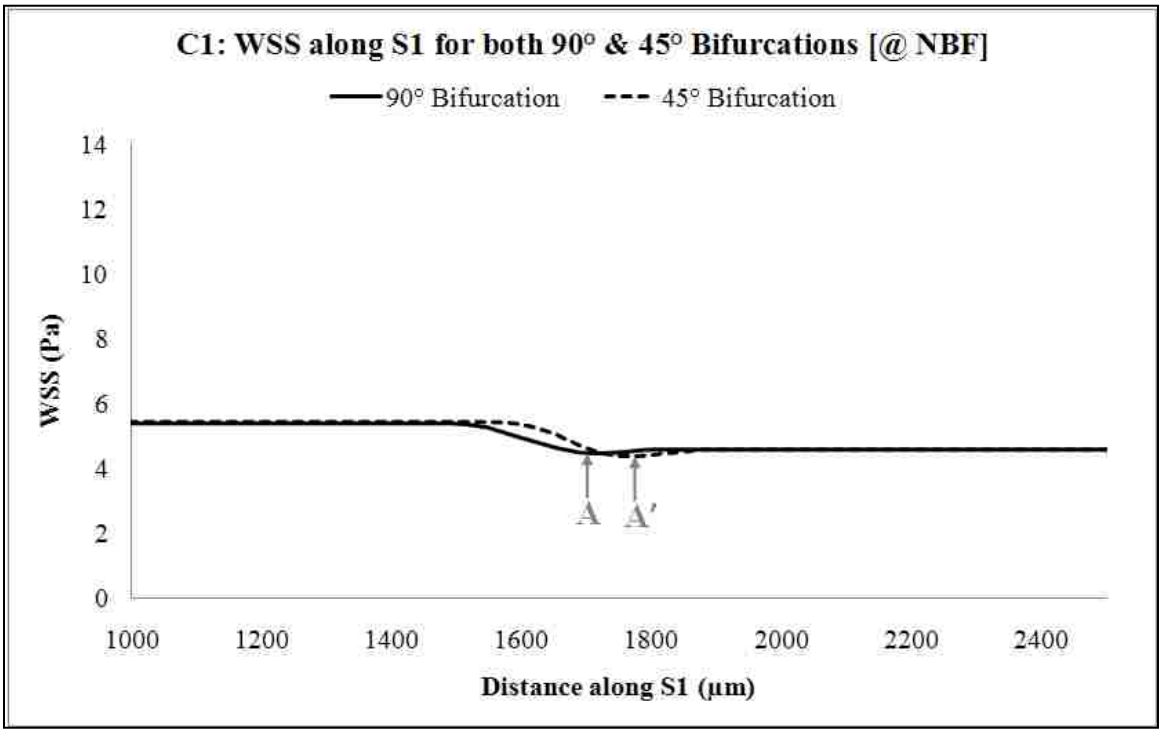

Chart 1: WSS versus distance along S1 for both the 90° and 45° bifurcations measured at the normal retinal blood flow.

Along S2 (Chart 2), with normal blood flow, both forty-five and ninety degree branch angle profiles, show a sharp increase in WSS at the upstream fillet. For the ninety degree angle branching, the WSS increase initiates from the main artery shortly before the proximal fillet and reaches a maximum at point E. This maximum value is followed by a sharp WSS decrease that reaches a minimum at point F. Again along S2 (Chart 2) and for the forty-five degree WSS profile, the sharp WSS increase initiates at the artery somewhat before the fillet region and reaches maximum at point E' followed by a minimum at point F'. The maximum ninety degree angle WSS is 14.5% higher than the maximum WSS of the forty-five degree angle branch. The minimum ninety degree branch WSS (at point F) is 34.5% higher than the minimum WSS of the forty-five degree branch (at point F'].

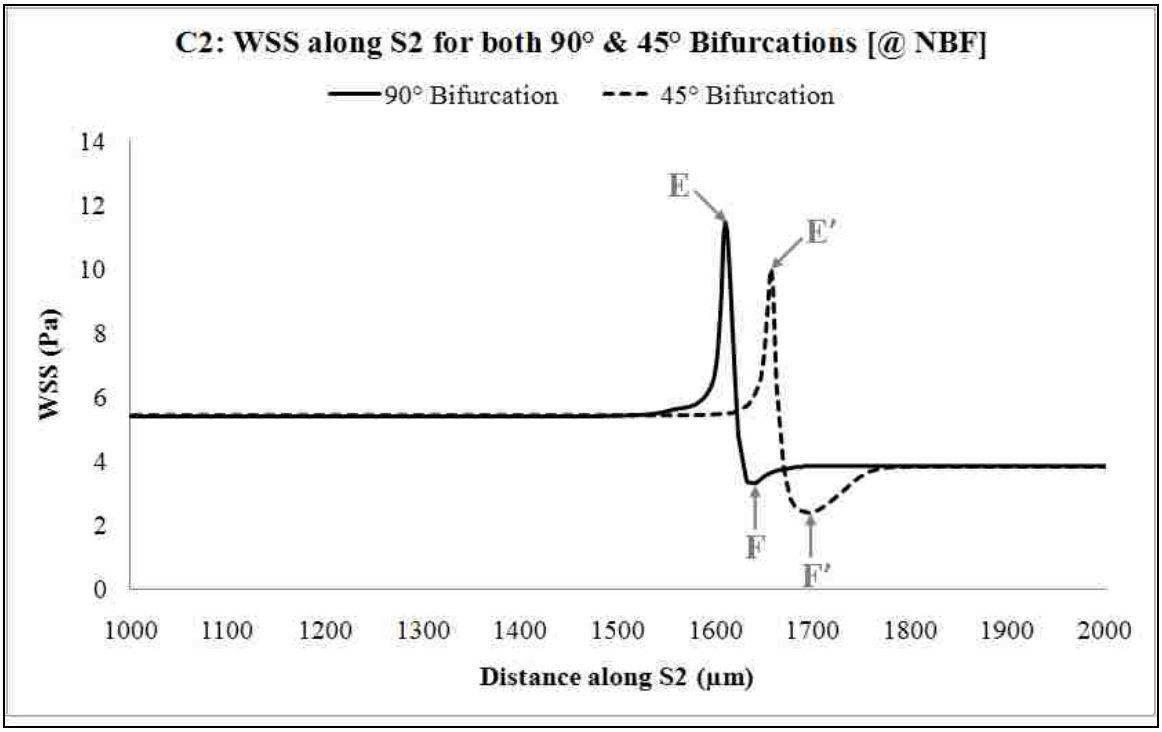

Chart 2: WSS versus distance along S2 for both the 90° and 45° bifurcations measured at the normal retinal blood flow.

For S3, with normal blood flow conditions (Table 1), both ninety and forty-five degree WSS profiles behave similarly (Chart 3). Of interest is that the WSS value at point B' of the forty-five degree angle branch is 25.3% higher than the corresponding value of the ninety degree branching (point B). Wall shear stress value at point D' of the forty-five degree branching is 2.87% higher than the corresponding value of the ninety degree branching (point D]. The first maximum WSS, for the forty-five degree branching at B', is 11.9% lower than the second (global) maximum occurring at D'. In addition, for the ninety degree branching first maximum WSS occurring at B is 27.7% lower than the second (global) maximum occurring at D. Note that the shear stress at points C and C’ are zero since these are bifurcation points for the flow streamlines.

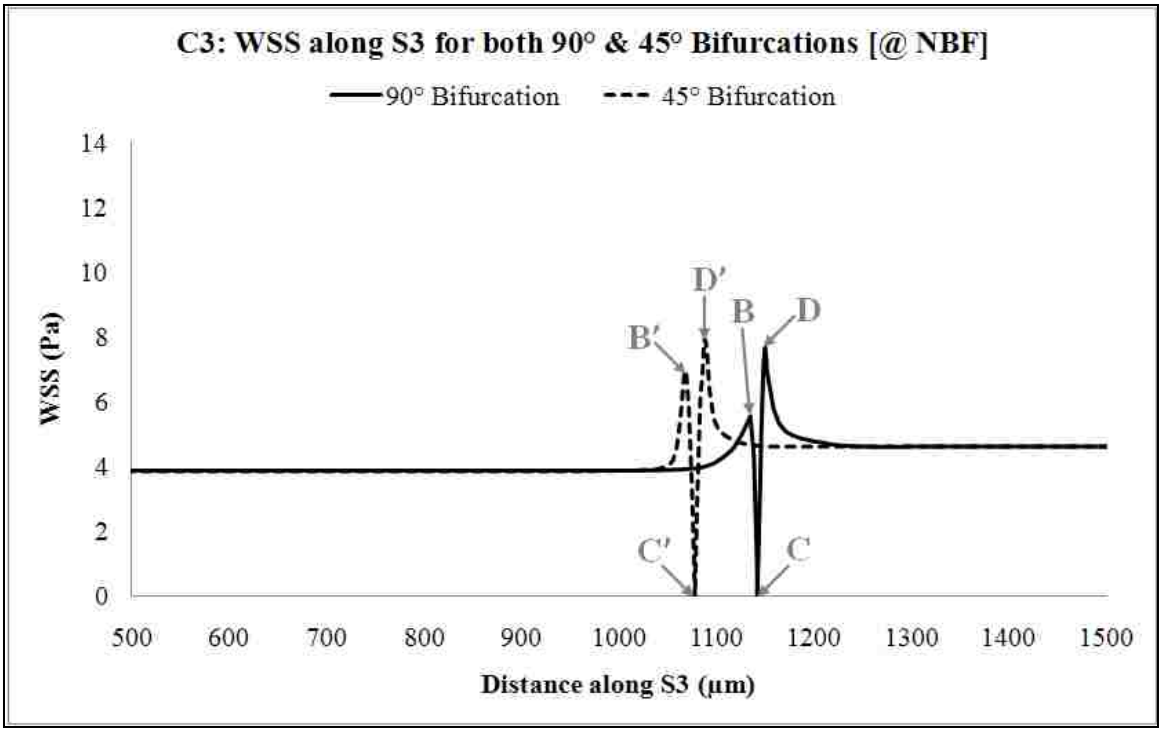

Chart 3: WSS versus distance along S3 for both the 90° and 45° bifurcations measured at the normal retinal blood flow.

2-5-2 Twenty Five times Normal Blood Flow

Along S1, for twenty-five times the normal blood flow rate (Chart 4), the WSS drop pattern, noted at normal blood flow, reverses. The WSS drop of the ninety degree branching (point A) is steeper compared to the smoother WSS drop of the forty-five degree branching (point A').

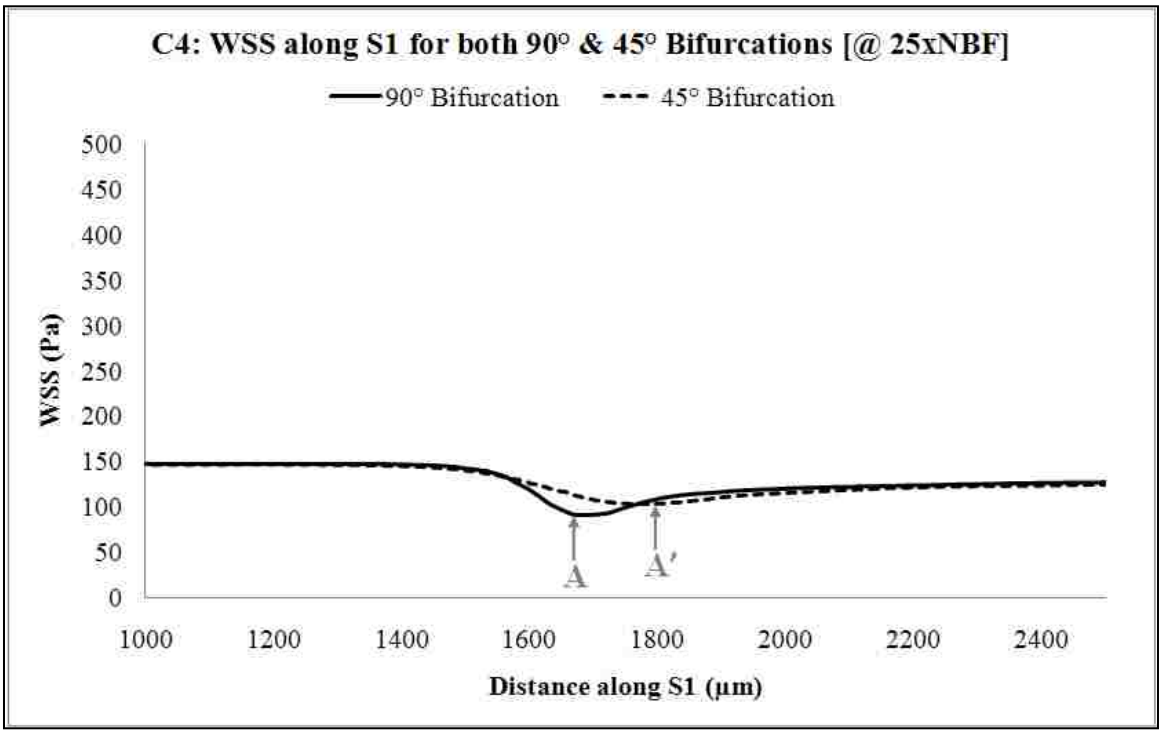

Chart 4: WSS versus distance along S1 for both the 90° and 45° bifurcations measured at 25 times the normal retinal blood flow.

Along S2, for twenty-five times the normal blood flow rate (Chart 5), similar WSS patterns to those occurring with normal blood flow conditions are noted. However, for the ninety degree branching, after reaching a maximum WSS value at point E, the WSS does not directly drop to a minimum value as seen with normal blood flow. Rather, it drops to a minimum at point X followed by a small WSS increase to point Y and then decreases to a second (global) minimum at point F. The

occurrence of this WSS behavior is due to swirling blood flow observed in the ninety degree branching angle at high flow levels (Figure 3), which is not observed at normal blood flow (Figure 2). This swirling pattern is not seen in the forty-five degree branching unless the blood flow is increased an additional 30%.

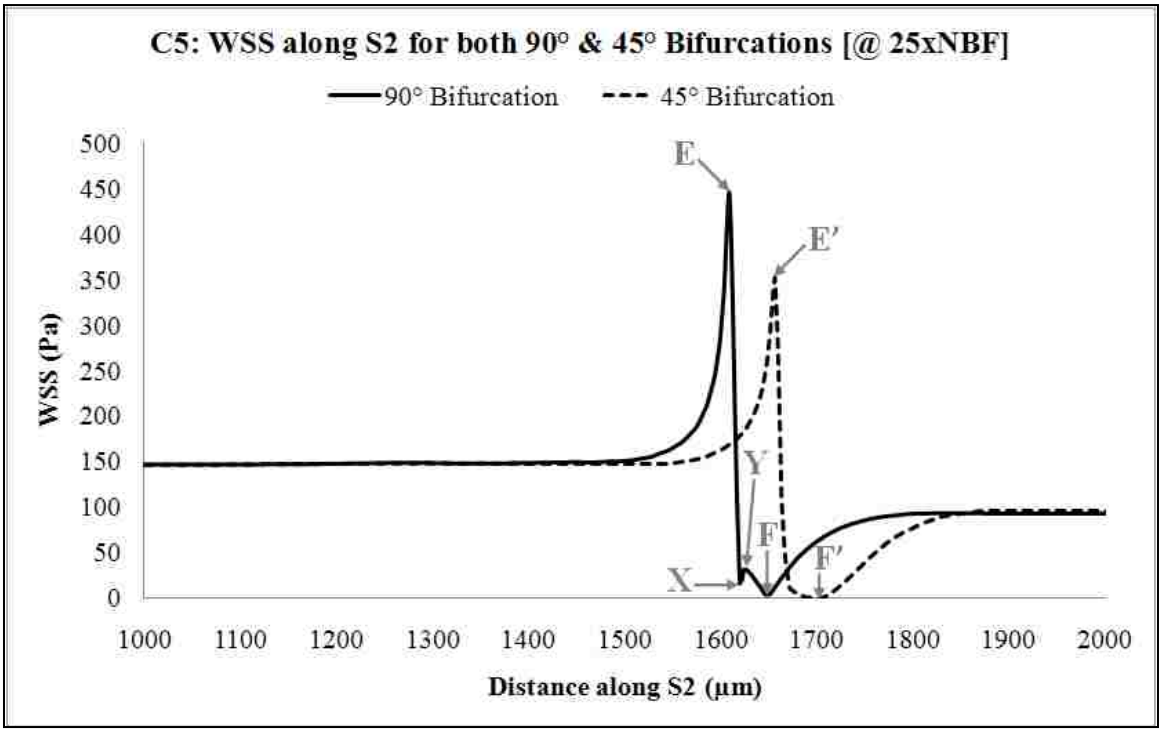

Chart 5: WSS versus distance along S2 for both the 90° and 45° bifurcations measured at 25 times the normal retinal blood flow.

Along S3, for twenty-five times the normal blood flow rate (Chart 6) and for both forty-five and ninety degree angle branching, a sharp increase in WSS values is noted at B' and B. Point B' of the forty-five degree branching is 43.9% higher than the corresponding value for the ninety degree branching at point B. After the two lines drop to zero at the distal fillet points C' and C, the WSS sharply increases and reaches a second (local) WSS maximum at points D' and D.

At this point the forty-five degree branching is 6.36% higher that the ninety degree branching. Further, for the forty-five degree branching, the first (global) maximum WSS occurring at B' is 35.1% higher than the second (local) maximum occurring at D'. Note that under normal blood flow conditions (Chart 3), the WSS at B' is 11.9% lower than that of point D'. Hence, the WSS pattern has reversed. For the ninety degree branching the first maximum WSS occurring at B is only slightly (0.19%) lower than the second maximum occurring at D. Under normal blood flow conditions (Chart 3), the WSS value at point B is 27.7% lower than at point D, whereas at twenty-five times normal blood flow both values (for points B and D, Chart 6) are almost equal.

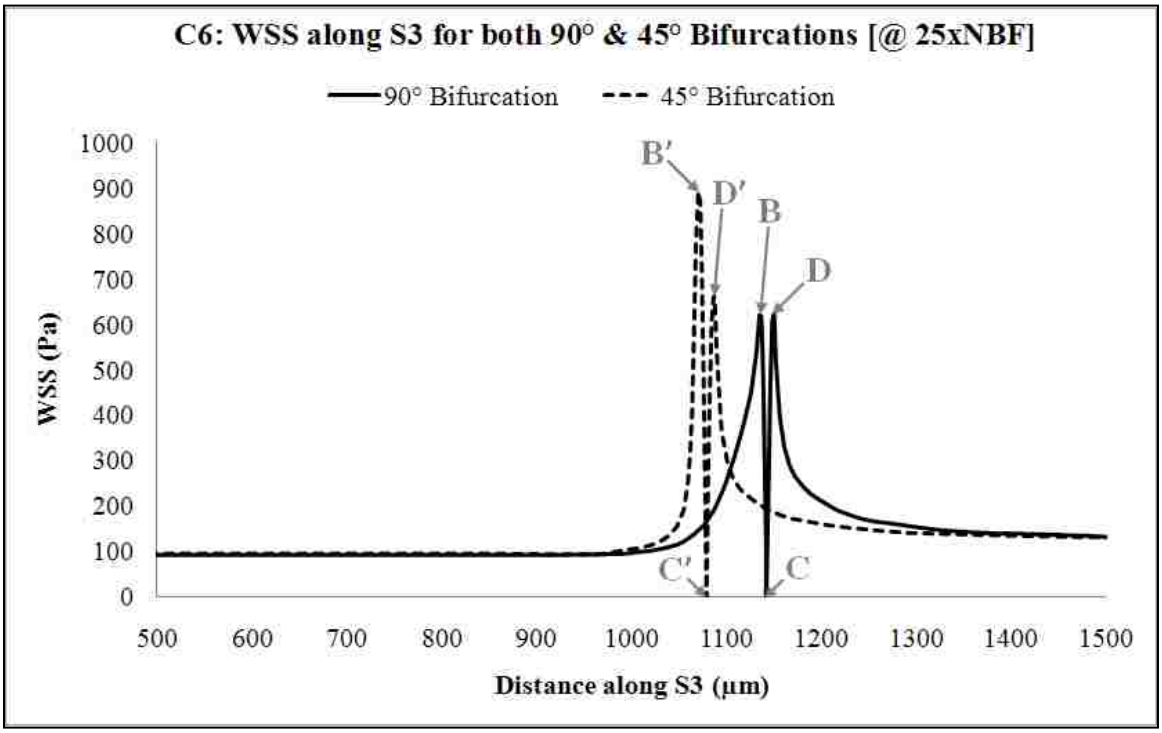

Chart 6: WSS versus distance along S3 for both the 90° and 45° bifurcations measured at 25 times the normal retinal blood flow.

2-6 Discussion

The etiology of Purtscher and Purtscher-like retinopathy has been investigated chiefly by focus on a specific disease or set of diseases in which Purtscher retinopathy has been observed. Review of these diseases suggests they fall into three categories: toxic and/or obstructive emboli, intravascular volume surges and intracephalic shock waves.

Currently, retinal arteriolar and capillary embolism with microinfarction is considered the most acceptable etiology for Purtscher retinopathy and there is pathological and experimental evidence to support this hypothesis [25 to 28].

A serious argument against end organ capillary embolization as the only etiology for Purtscher retinopathy is the occurrence of Purtscher retinopathy in non-embolic syndromes, head trauma and chest compression injuries. In addition the delayed clinical signs of Purtscher retinopathy would be more typical of non-embolic toxic ischemia rather than embolic vascular obstructive disease.

The fact that Purtscher retinopathy occurs rarely, bilaterally, unilaterally, and associated with many disparate diseases suggests an unusual and complex interaction of vascular anatomical and physiological events.

2-6-1 Retinal Microvascular System

The inner retinal microvascular system has three aspects, which makes it uniquely vulnerable to endothelial dysregulation. It is, unlike the choriocapillaris, a terminal vascular complex, unfenestrated and autoregulated. The microvascular system of the inner retinal is derived from the central retinal artery and is a terminal system with no anastomoses outside the retina. Branches from the central retinal artery form two capillary plexi, one within the ganglion cell layer and the other in the inner nuclear layer. Rarely do capillaries from these plexi extend into the outer plexiform layer. At the fovea, the layers of the inner retinal thin to form the foveal pit. At this point there are no inner retinal vessels.

Inner retinal vascular endothelia respond to mechanical, hormonal and chemical flow stimuli by the production of auto-regulators among which are nitric oxide, prostacyclin and endothelin peptides to achieve downstream vascular balance [29 & 30].

2-6-2 Wall Shear Stress

Vascular equilibrium, in a closed autoregulated system such as the inner retinal microvascular system, depends on being able to sense local blood flow dynamics. This signal transduction process is mediated through vascular endothelial cells [32]. Endothelial cells respond to spatiotemporal gradients of flow effecting downstream vascular utoregulation [33 & 34]. Wall shear stress, as the relation between force (pressure) and the longitudinal/axial force, becomes the key mechano-signal transducer of information between the blood and the vessel wall [32].

2-6-3 Retinal Microcirculation Geometry

Microcirculation system bifurcation angles have been shown to begin with obtuse branching and then develop to acute angles as the system progresses into capillaries [35]. The retinal microcirculation is no exception. Paul Henkind's India ink preparations reveal the artery/arteriole branchings in the retinal posterior pole to be predominantly at right or obtuse angles, as opposed to the periphery where there is a broad capillary network of acute angle dichotomous branchings [35 & 36]. Apple and Rabb describe the retinal posterior pole vascular system to bend sharply and vertically into the retina [37].

Variable wall shear stress throughout the vascular system, especially at vessel branching, results in complex chains of rheological events that can produce areas of disease predilection. Data from studies of cardiac lesions [38 & 39], intracranial aneurysms [40], abdominal aneurysms [41], and atherosclerotic plaques [42] show the effect of vascular culprit areas, vulnerable to rupture, atherosclerosis and trauma.

2-6-4 Retinal Vascular Endothelium

Vascular endothelial dysregulation with endothelin production as part of Purtscher and Purtscher-like retinopathy has been suggested by some authors [34]. Blood, in disease situations, to which retinal endothelial cells are exposed, contains potential endothelial dysregulatory substances that have been known to be associated with Purtscher-like retinopathy. These toxic aggregations do not necessarily need to be embolic at terminal capillaries, but can cause upstream endothelial dysregulation by way of WSS alterations, augmenting cellular aggregation and cellular adherence to retinal vascular endothelium.

Endothelin peptides are powerful vaso-constricting that are normally produced by vascular endothelium. In disease states, dysregulated endothelium overproduces these vasoconstrictive substances. Endothelin-1 is found systemically elevated in septic and endotoxic shock syndromes, such as renal failure [43], hemolysis, elevated liver enzymes and low platelet of "HELLP" syndrome [44] and adult Still disease [45]. It is with these systemic diseases, associated with abnormal systemic endothelin, that Purtscher retinopathy is associated.

2-6-5 Optic Nerve

One of the more universal aspects of Purtscher and Purtscher-like retinopathy is optic nerve involvement. Hayreh has demonstrated that the vascular supply of the optic nerve is variable and individualistic [46]. It is logical to assume that the branching angles of optic nerve vascular supply would follow the usual obtuse to acute angle configuration of vascular microsystems [8 & 9]. Studies have shown that the optic nerve head is autoregulated; thereby, susceptible to endothelial direction [47]. Optic nerve vascular homeostasis follows the same vascular homeostasis of retinal vessels, that is, a balance dependent on factors emerging from upstream endothelium.

Flammer and others have made the observation that vascular endothelial dysregulation syndrome with diffusion of endothelin to the optic nerve head results in vasoconstriction and increases the risk for venous occlusion as well as weakening the blood brain barrier [48 & 49]. They suggest that the pathogenesis of glaucomatous optic neuropathy is due, in part, to vascular endothelial dysregulation.

Literature suggests that endothelial dysregulation with an outpouring of vasoconstrictive endothelins, with or without embolization, may produce Purtscher retinopathy. Clinical characteristics of Purtscher retinopathy point to a posterior pole focus of dysregulation where blood flow patterns allow damage at critical endothelial areas, i.e. the ninety degree angle branching as noted in the above computer simulations. Irregular blood flow with flow separation and retrograde flow, under traumatic circumstances, may result in endothelial dysregulation.

2-6-6 Limitations

Involvement of choroid, retinal pigment epithelium, and macula have been reported in a cases of Purtscher retinopathy. Often these findings are associated with head injury where ancillary trauma can be incriminated. However, there are cases of non-traumatic disease such as toxic embolization, cellular aggregation and adhesion, as well as vaso-constrictive and vasoocclusive events, where choroid, and macular disease have been described [50]. Although vision recovery is not uncommon in cases of Purtscher retinopathy, chronic vision loss secondary to macular and retinal pigment epithelium damage does occur. More commonly permanent visual loss is secondary to optic atrophy. These unusual findings should not detract from the aboveproposed hypothesis, but rather be considered as pathology that has occurred in association with classic Purtscher retinopathy, but not necessarily related to the pathophysiology of endothelial dysregulation.

The effect of intracephalic shock wave is affected by many variables, such as media density, shock vector direction, magnitude of trauma, and others. These complex variables, as related to Purtscher retinopathy, attest to the rarity and multiple clinical presentations following head trauma. The above computer programs were not developed to demonstrate a profile for intracephalic shock waves as they encounter a perpendicular arteriolar branch as opposed to a profile for an encounter with a dichotomous acute angle branch. Further computer simulation studies are planned to investigate extravascular shock wave effect on endothelial dysregulation.

In order to elicit wall shear stress flow disruptions within our computer models, flow rates were increased twenty five times above normal flow rate. Our purpose was

to demonstrate that at extremes of flow, ninety degree angle branchings, common to the retinal posterior pole, are more susceptible to flow disturbances and subsequent endothelial dysregulation than forty-five degree angle branchings. By keeping flow rates constant, although high, we were able to more accurately compare, as a single variable, branching angles.

There is thought that the retinal vascular Reynolds number is too low to reach disturbed flow conditions. However, our study shows that although the retinal Reynolds number is linear with retinal blood flow rate (from the definition of Reynolds number), WSS rise with Reynolds number (or alternatively flow rate) is non-linear. In fact, it rises more rapidly at the rate of a 3^{rd} order polynomial (Figures 12 and 13). This suggests that WSS values, especially at bifurcation regions as shown here, are very sensitive to changes in the blood flow rate; these changes may be responsible for Purtscher retinopathy.

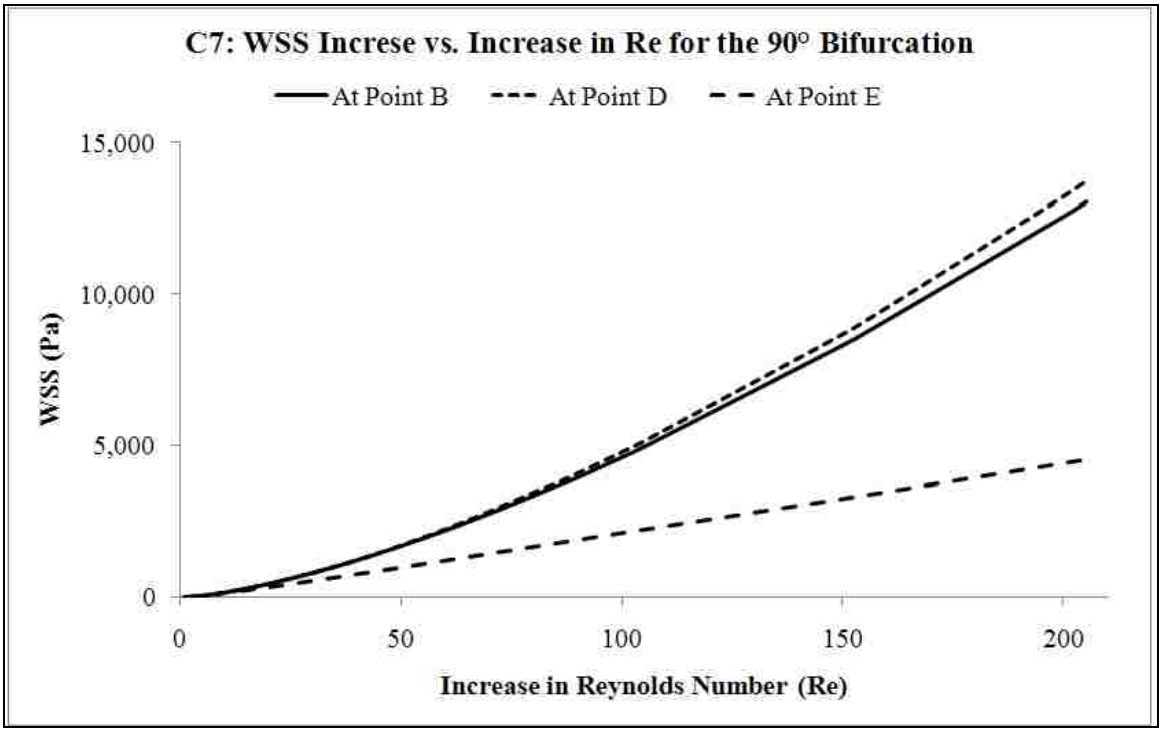

Chart 7: WSS at Points B and D along the S3 and Point E along the S2 of the 90° bifurcation versus increase in Reynolds number.

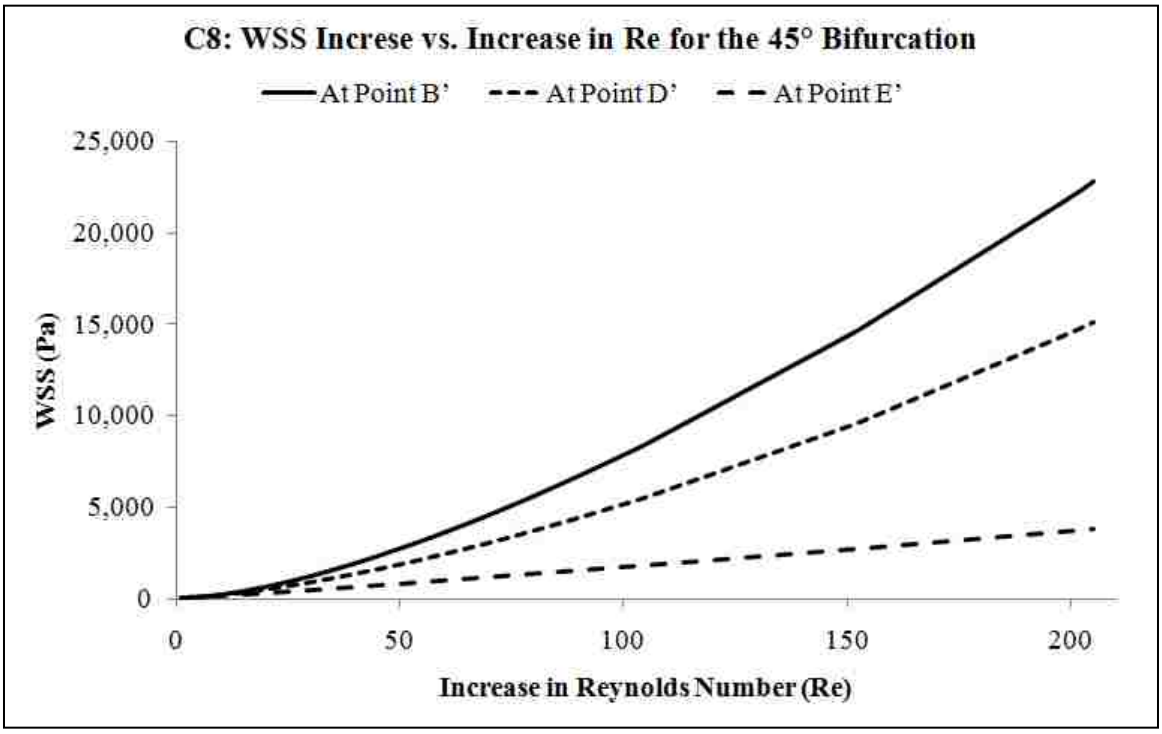

Chart 8: WSS at Points B´ and D´ along the S3 and Point E´ along the S2 of the 45° bifurcation versus increase in Reynolds number.

2-6-7 Treatment Avenues

The above hypothesis provides evidence for research into an avenue of treatment for Purtscher retinopathy. Endothelin receptor antagonists are now being tested for treatment of a variety of conditions including pulmonary hypertension, congestive heart failure, renal failure, cancer, cerebro-vascular disease, hypertensive retinopathy and glaucoma. A productive avenue of research may be to evaluate endothelin receptor antagonists in the management of Purtscher and Purtscher-like retinopathy.

2-7 Conclusions

It is difficult not to incriminate capillary embolic occlusion in the etiology of Purtscher retinopathy, and indeed the syndrome does involve occlusive end organ vasculopathy as noted by fluorescein, experimental and pathologic evidence. These studies cannot be ignored. However, limiting our perspective to capillary emboli ignores a number of perplexing contradictions associated with this rare disease and suggests a comprehensive etiology has been incompletely described.

The above computer simulation studies of wall shear stress profiles comparing ninety degree angle versus forty-five degree arteriolar branching reveal an area, at the ninety degree angle artery/arteriolar branching, where the margin between physiological and disruptive flow is narrow. It is at this culprit junction where endothelial dysregulation, under stressful conditions, is more likely to occur. Computer dynamic flow simulations, in addition to literature review, suggests that a possible additional pathophysiology that initiates Purtscher retinopathy, within a milieu of embolization, volume surges and extravascular shock waves, may be an inner layer retinal posterior pole rheological event that results in vascular endothelial dysregulation. This endothelial dysregulation with pathogenic release of endothelins may contribute to downstream occlusive vasculopathy of Purtscher retinopathy.

CHAPTER 3

3-1 Authors

1. Lotfi Hedjazi B.S., Biopolymères, Interactions & Assemblages, Nantes, France.
2. Sofiane Guessasma B.S., Biopolymères, Interactions & Assemblages, Nantes, France.
3. Cyrus O. Abbasi B.S., University of New Mexico, Mechanical Engineering Department.
4. Guy Della Valle, B.S., Biopolymères, Interactions & Assemblages, Nantes, France.
5. Tariq A. Khraishi PhD., University of New Mexico, Mechanical Engineering Department.

3-2 Title

Realistic Simulation of Cereal Food Breakdown Using Finite Element Methods.

3-3 Abstract

Human mastication is a complex oral process that leads to food breakdown. The understanding of the mechanics of mastication requires the knowledge of food item properties and geometry, chewing force amplitude and frequency, mandibular trajectory as well as a precise information about food-teeth contact. In this work, all these oral aspects are handled numerically using a finite element (FE) model. First, experimental procedures are used to determine molar geometry and internal structure of two breakfast cereals. Second, a FE model is developed accounting for the exact geometry of both food items and teeth to simulate food breakdown. The loading conditions including normal and sliding motions of the teeth system are reproduced for each product. Teeth-food item contact is optimized to avoid significant material overlapping. The model is able, at least for the first bites, to determine strain and stress distributions that develop upon mastication loading. It also highlights the shearing effect associated to food compression during mastication. Simple considerations about failure strain of the solid material allow the conversion of the strain distributions to food fragments. The major finding is that fragmentation occurs earlier before complete occlusion and tends to produce a large number of fragments.

3-4 Introduction

The main function of mastication is reducing the size of the food item to ease swallowing and contributes to food chemical and physical degradation [51]. The complex nature of the forces involved during mastication and food complexity makes it difficult to follow experimentally the stress and strain states that develop in the food item during mastication stage. These states would be very informative about sequencing of rupture events and in turn, the formation of the food bolus [52].

Our interest in cereal products arises by considering that cereals are major members amongst many processed foods consumed by humans. Moreover, for some individuals, it is difficult to maintain regular consumption of cereals because of age, dental problems and/or inadequate formulations. It is thus an exciting challenge to be able to adjust the formulation and design process of transformed products to match some mastication criteria. But, before addressing this challenge, one has to know how the structure and texture of a cereal food item affects the human mastication.

In such a way, this work is a first attempt to consider realistic simulation of food degradation using FE computation. Our approach is rendered realistic as much as possible by adhering to relevant characteristics of human mastication. The ideas detailed in this work focus on the implementation of the mechanical model, typically on how oral parameters are handled. The paper shows also the product structural effects involved during the simulation of the human mastication.

3-5 Methods

3-5-1 Acquiring the Mold of the Upper and Lower Human Teeth

An upper and a lower mold of the human teeth were created from the imprints of a volunteer. The molds were prepared at a local dental office as illustrated in Fig. 6.

Figure 6: On the left the mold of the lower human teeth is shown. On the right the mold of the upper human teeth is shown.

3-5-2 CMM Mapping of the Molds

CMM refers to *coordinate measuring machine*. During a CMM mapping process the outer surface of a 3D object is probed and with that the special coordinates of many points on the surface of the object are recoded. These coordinates are then postprocessed resulting in a digital map of the object's surface. For this project the CMM measurements were split in two different sets of measurements; first the mold of the lower teeth and then the mold of the upper teeth were measured.

3-5-2-1 Lower Teeth

The mold of the lower teeth was fixated on the "DCC Gage Brown & Sharpe" coordinate measuring machine (Hexagon Metrology, Inc. 250 Circuit Drive North Kingstown, RI 02852, USA). A 1.5 mm radius "Renishaw" touch probe was mounted at the tip of the CMM (Renishaw Inc. 5277 Trillium Blvd. Hoffman Estates, IL 60192, USA). Via the manual CMM controller, approximately 1000 3D measurements of the teeth were taken and recorded. These thousand measurements consisted of hundred parallel lines, each with ten measurements.

Each of the lines initiated from the interior portion of the mold (i.e. next to the tongue) and stretched over the teeth to the exterior portion of the mold (i.e. next to the inner portions of the cheeks/lips). The recorded XYZ (i.e. three dimensional coordinates of the measured points) measurements were extracted in Microsoft Excel Word format and converted to Microsoft Excel format for subsequent digital 3D modeling.

3-5-2-2 Upper Teeth

The mold of the lower teeth was fixated on the “DCC Gage Brown & Sharpe” coordinate measuring machine. A 1.5 mm radius “Renishaw” touch probe was mounted at the tip of the CMM. Via the manual CMM controller, approximately 1000 3D measurements of the teeth were taken and recorded. These thousand measurements consisted of hundred parallel lines, each with ten measurements. Each of the lines initiated from the interior portion of the mold (i.e. space above the tongue) and stretched over the teeth to the exterior portion of the mold (i.e. next to the inner portions of the cheeks/lips).

The recorded XYZ (i.e. three dimensional coordinates of the measured points) measurements were extracted in Microsoft Excel Word format and converted to Microsoft Excel format for subsequent digital 3D modeling.

3-5-3 Three Dimensional Laser Scanning

The digital measurements obtained from the CMM process resulted in non-satisfactory resolutions. For that reason a second more precise method of scanning was used, namely 3D laser (3DL) scanning. About one million XYZ coordinates points corresponding to the surface of the 3D scanned model were obtained. This number of points is 1000 times more than the CMM surface mapping. The point density reaches typical values of 100 points mm^{-2}. With this areal point density the obtained model possessed the adequate resolution. A high resolution of the outer surface of the generated 3D models is crucial for purposes of FE meshing.

FE meshing refers to breakup of any digital model in very small continuous pieces such as cubes, triangles and more. These small pieces or building blocks of the bulk model are connected to each other at their corners. Upon the application of stress of displacement loadings, these small building blocks deform and thereby the distance between their corners stretch. The stretch is then used to calculate the present stress and strain levels in the bulk object. The details of the mesh are explained in Sec. 3-54.

For this project the 3DL scans were split in two different sets; first the mold of the lower teeth and then the mold of the upper teeth scanned. The generated upper 3D teeth digital model was brought to the correct relation with the lower teeth model within a program called SolidWorks, which is introduced in section 3-531 as illustrated in Fig. 7.

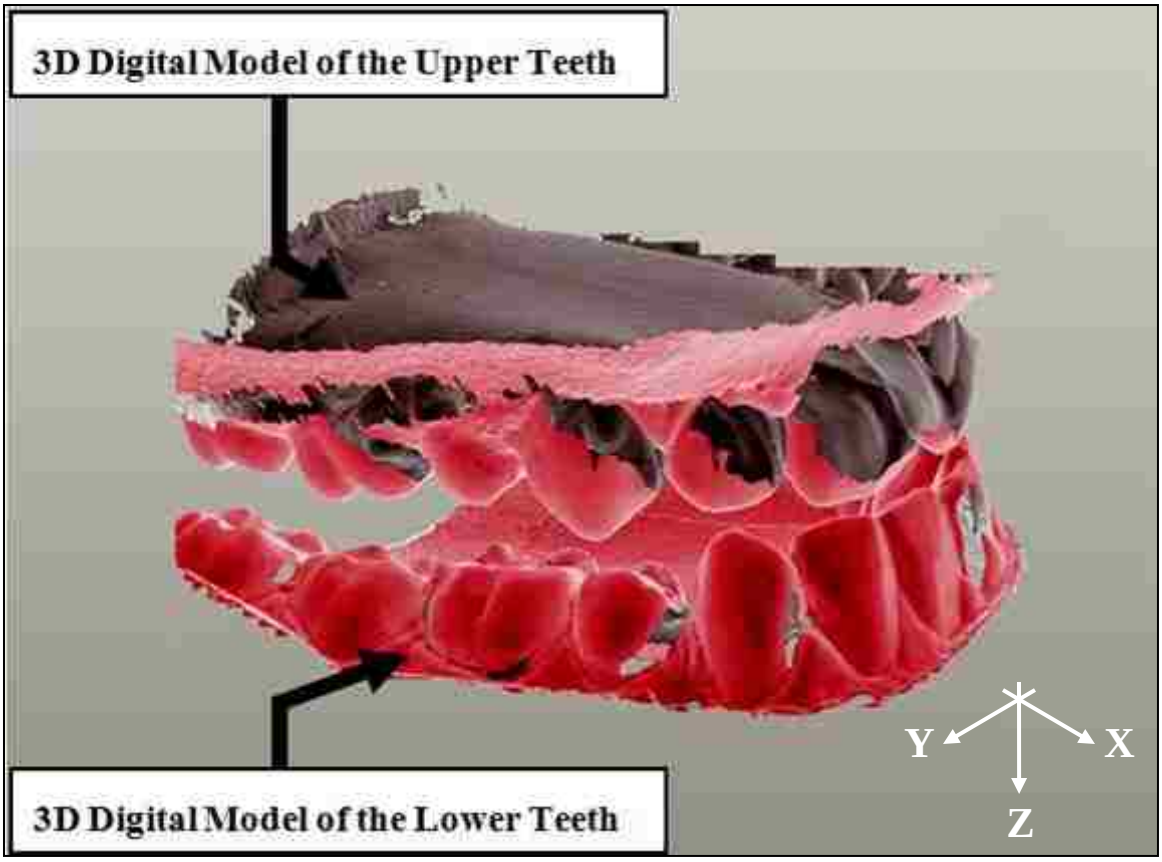

Figure 7: The Upper and Lower teeth models put on top of each other with the correct sense of relation.

3-5-3-1 Lower Teeth

The mold of the lower teeth was placed in the *NextEngine 3D Scanner* (NextEngine, Inc. 401 Wilshire Blvd., Ninth Floor, Santa Monica, CA 90401, USA). The scanner was set on a Bracket mode, 12 divisions and a 0.16 inch precision. The subsequent scan resulted in a high quality 3D digital copy of the mold of the lower teeth. The generated 3D model was then transformed to a 3D SolidWorks CAD model (Dassault Systemes SolidWorks Corp. 300 Baker Avenue, Concord, MA 01742, USA).

3-5-3-2 Upper Teeth

The mold of the upper teeth was on the *NextEngine 3D Scanner*. The scanner was set on a Bracket mode, 12 divisions and a 0.16 inch precision. The subsequent scan resulted in a high quality 3D digital copy of mold of the upper teeth. The generated 3D model was then transformed to a 3D SolidWorks CAD model.

3-5-4 Finite Element Methods and Meshing

The 3D digital models are converted to triangular irregular meshing using plane elements as illustrated in Fig. 8 and Fig. 9.

Figure 8: Rough view of surface meshing.

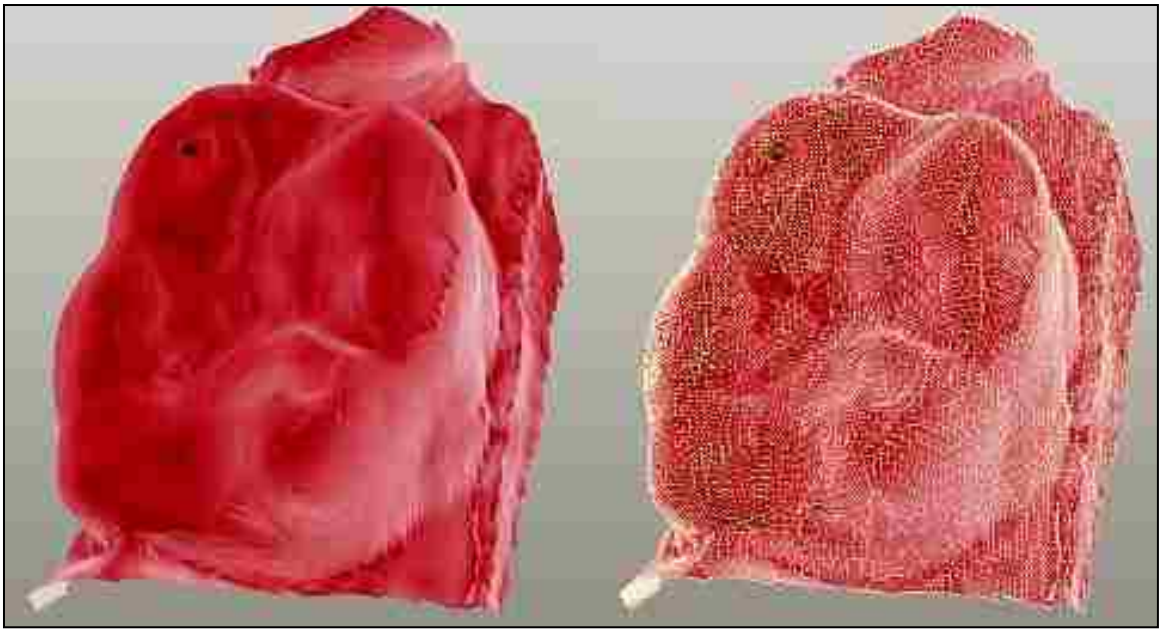

Figure 9: Close up views on surface topography and meshing of one molar.

Each element is described by two nodes capable of displacements in the relative *x-y* plane. In order to allow 3D displacement of the mandible, surface meshes are extruded into volume meshing using prism elements in Z direction.

3-5-5 Chosen Cereals, their 3D Digital Shapes and Mesh Patterns

Two commercial breakfast cereal foods, Miel Pops (M) and Golden Grahams (G), are selected as a case study as shown in Fig. 10.

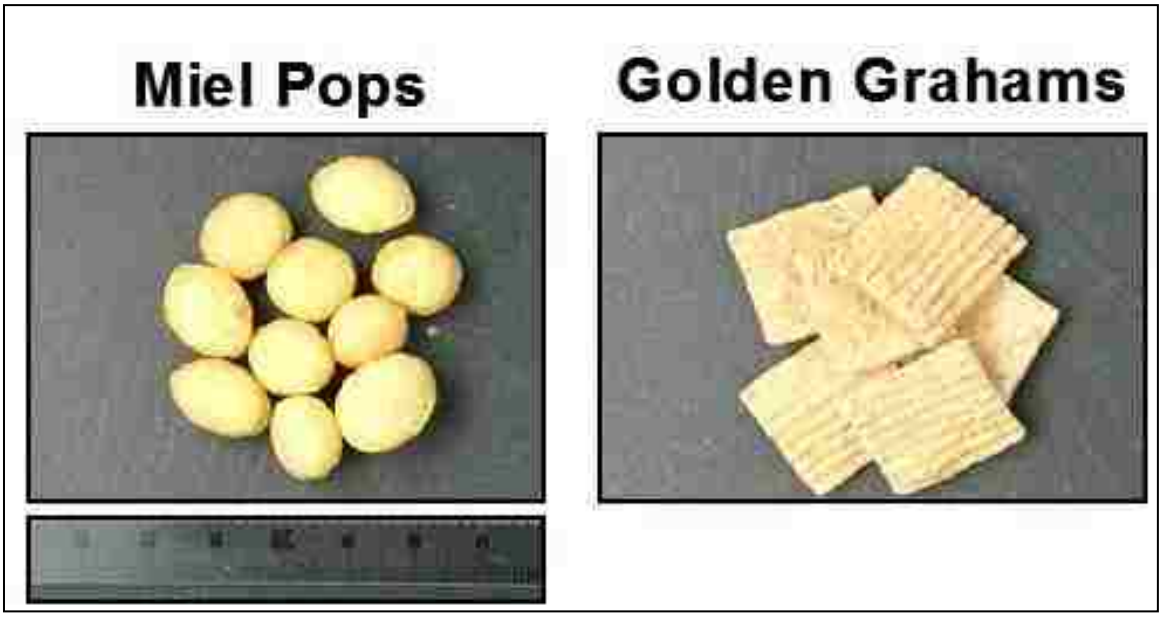

Figure 10: Selected breakfast cereals M and G.

The two cereal products are characterized by their different formulations, geometry and texture. Table 1 shows the composition and fracture energy data of the chosen cereal products [53]. Note that failure energy is derived from Kramer cell experiments as detailed in the same work.

Table 2: Composition of both Cereal Types				
Cereal Type	**Moisture (Wet Basis)**	**Sugar Content (g/100g)**	**Starch Content**	**Failure Energy**
M	3.60	33.00	55.00	13.20
G	3.70	31.80	49.20	15.10

Table 2: Moisture, Sugar Content, Starch Content and Failure Energy of both Cereal Types.

The 3D structure of a piece of cereal is acquired using synchrotron radiation at the ID19 beam line from ESRF facility in Grenoble (France) using a two-dimensional detector as well as a CCD camera for computerized X-ray micro-tomography (XRT) experiments.

The number of radiographic images needed for 3D feature reconstruction ranges from 1200 to 1500 depending on samples. The pixel size is fixed to 6.47 µm but the whole acquisition of the samples requires several stacks to be built and gathered. The process leads to crop volumes in the range 4.2 to 8.6 x 109 voxels. Separation between the solid and the voids is clearly established thanks to the good contrast. A thresholding operator is then performed to process towards binary images.

Because of computation resources limitation, the full resolution of the images could not be used for finite element computation. Sub-resolutions are then recomputed and the subsequent effect on the internal structure is evaluated. Cell size and wall cell size distributions are determined using granulometry technique. Octahedral structuring elements are grown numerically and the distribution of each size class is recorded.

In addition to size distributions, the relative density of each sample is computed as well. This quantity expresses the density for the internal material over that of the solid phase. The density values are normalized and then categorized within the range of 0.0 to 1.0.

By considering the density of the solid phase as the measurement unit, the relative density is expressed by Eqn. 1.

$$\rho = \sum_{x \to 1}^{V} \left\{ \frac{\delta_x}{V} \right\} \quad \& \quad Porosity = 1 - \rho \qquad \text{(Eqn. 1)}$$

At x = 0.0, δ_x = 0.0, and at x = 225.0, δ_x = 1.0.

ρ = Relative density

V = Volume of the internal material (voxel)

δ_x = Threshold function of the gray level

x = Grey level of the images coded at 8 bits

In order to compute the relative density, we have to provide, in Eqn. 1, an evaluation of the internal volume which is clearly lower than the cereal volume. For that reason, a contour of the internal material has to be found. Different approaches can be attempted such as the *Fill-hole approach*, the *manual boundary detection* and the *Wrap-technique*.

The Wrap-technique was chosen because the Fill-hole approach fails in detecting the open void structure and the manual boundary detection is a time consuming method. The basic idea of Wrap-technique is to roll a hard sphere of radius r = 10.0 voxels along the surface of the solid phase. Wrap-technique proved to be powerful in determining the closed contours of the studied cereal items as well as their relative density.

Fig. 11 and Fig. 12 show the actual cross-section and the closed contours of the G cereal item obtained via the use of the Wrap-technique.

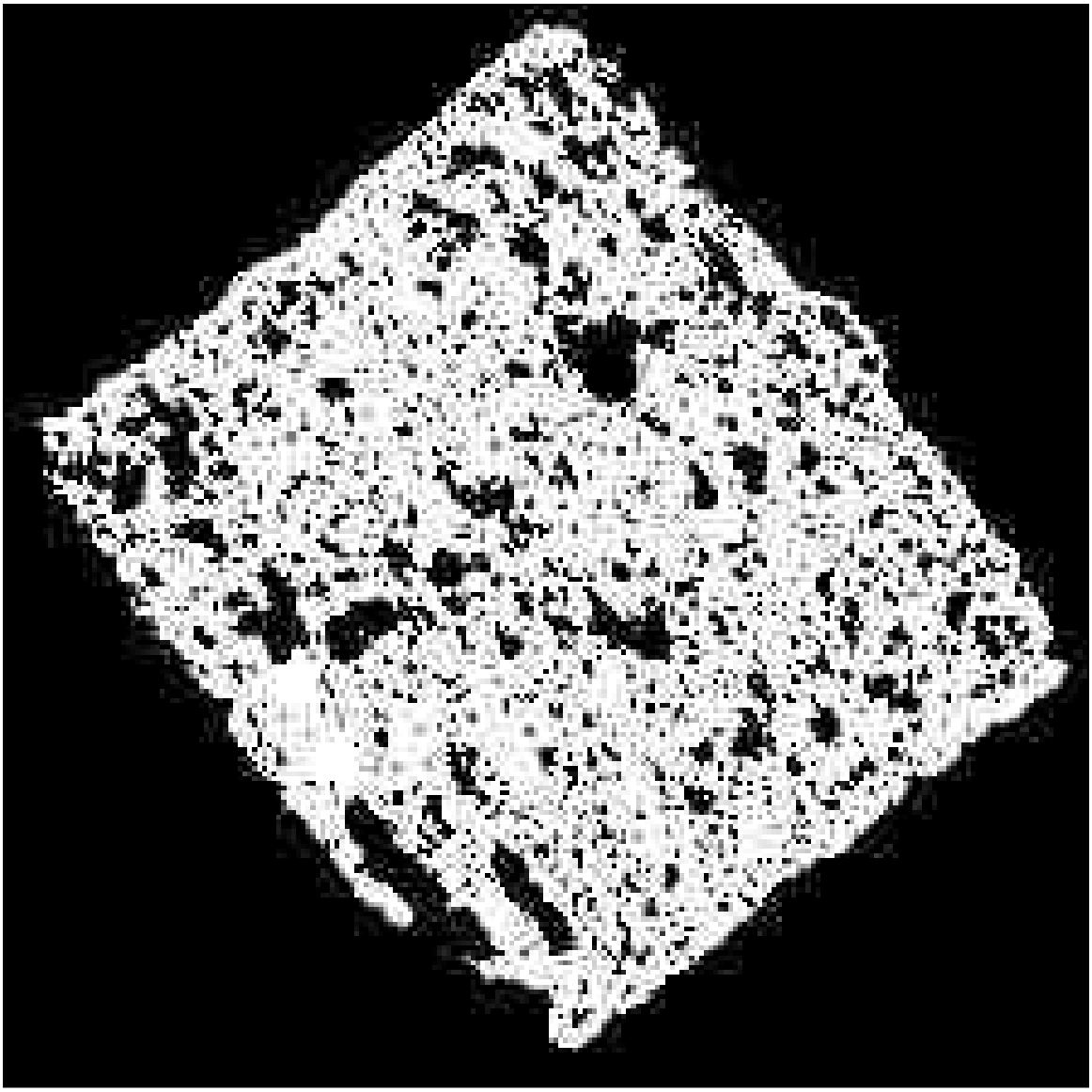

Figure 11: Cross-sectional insight of the G cereal item obtained via the Wrap-technique.

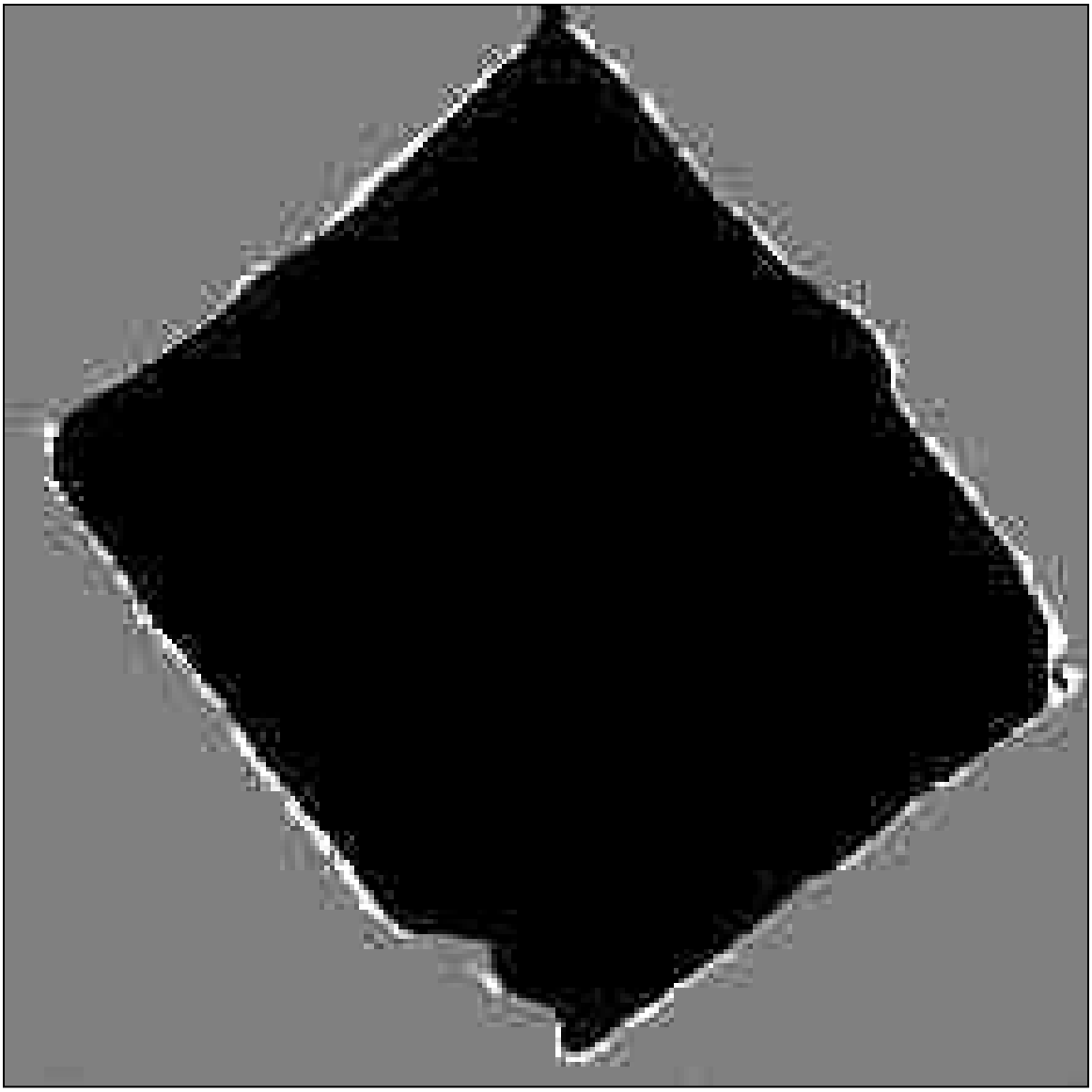

Figure 12: Closed contours of the G cereal item obtained via the Wrap-technique.

Fig. 13 and Fig. 14 show the actual cross-section and the closed contours of the G cereal item obtained via the use of the Wrap-technique.

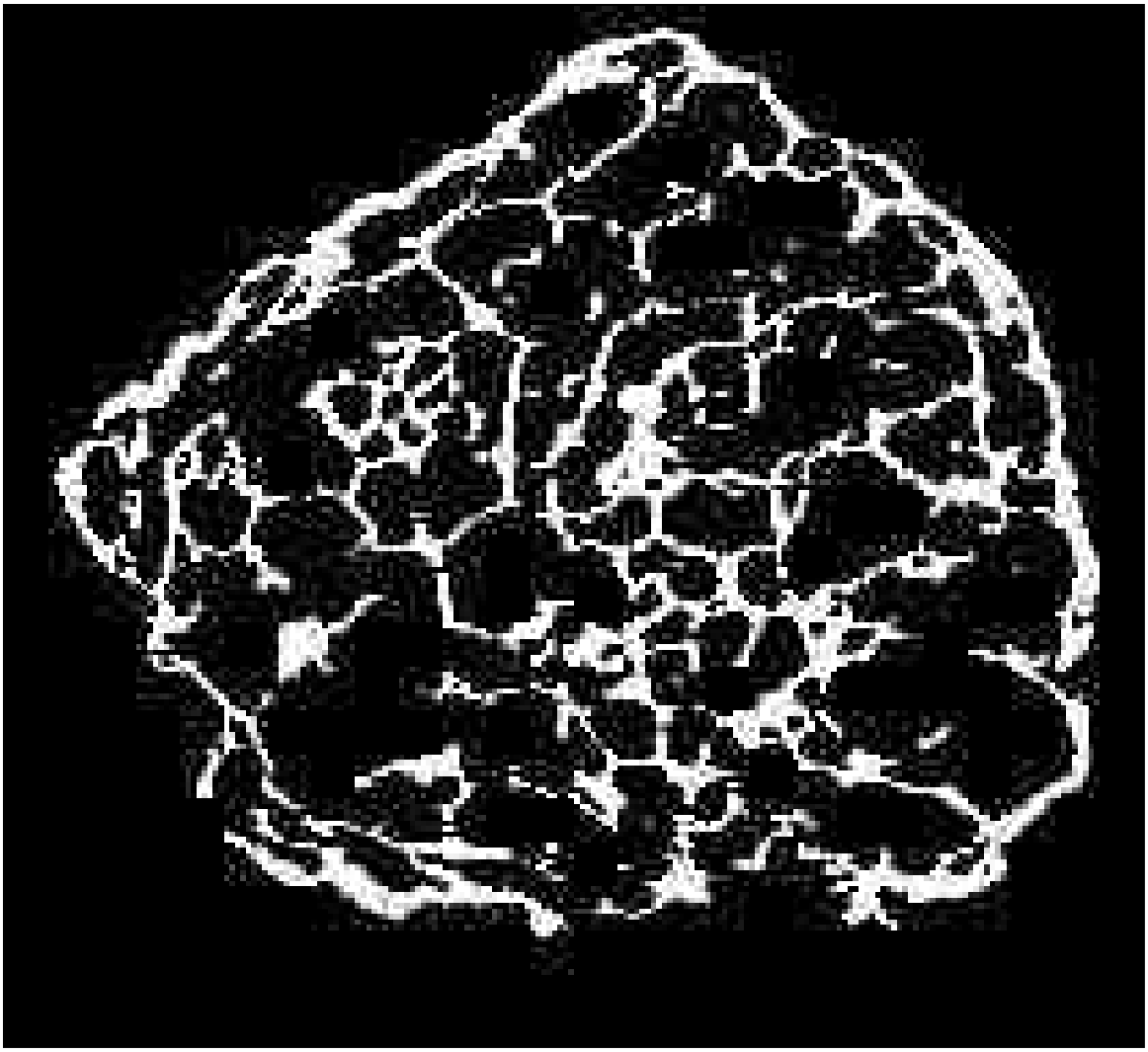

Figure 13: Cross-sectional insight of the M cereal item obtained via the Wrap-technique.

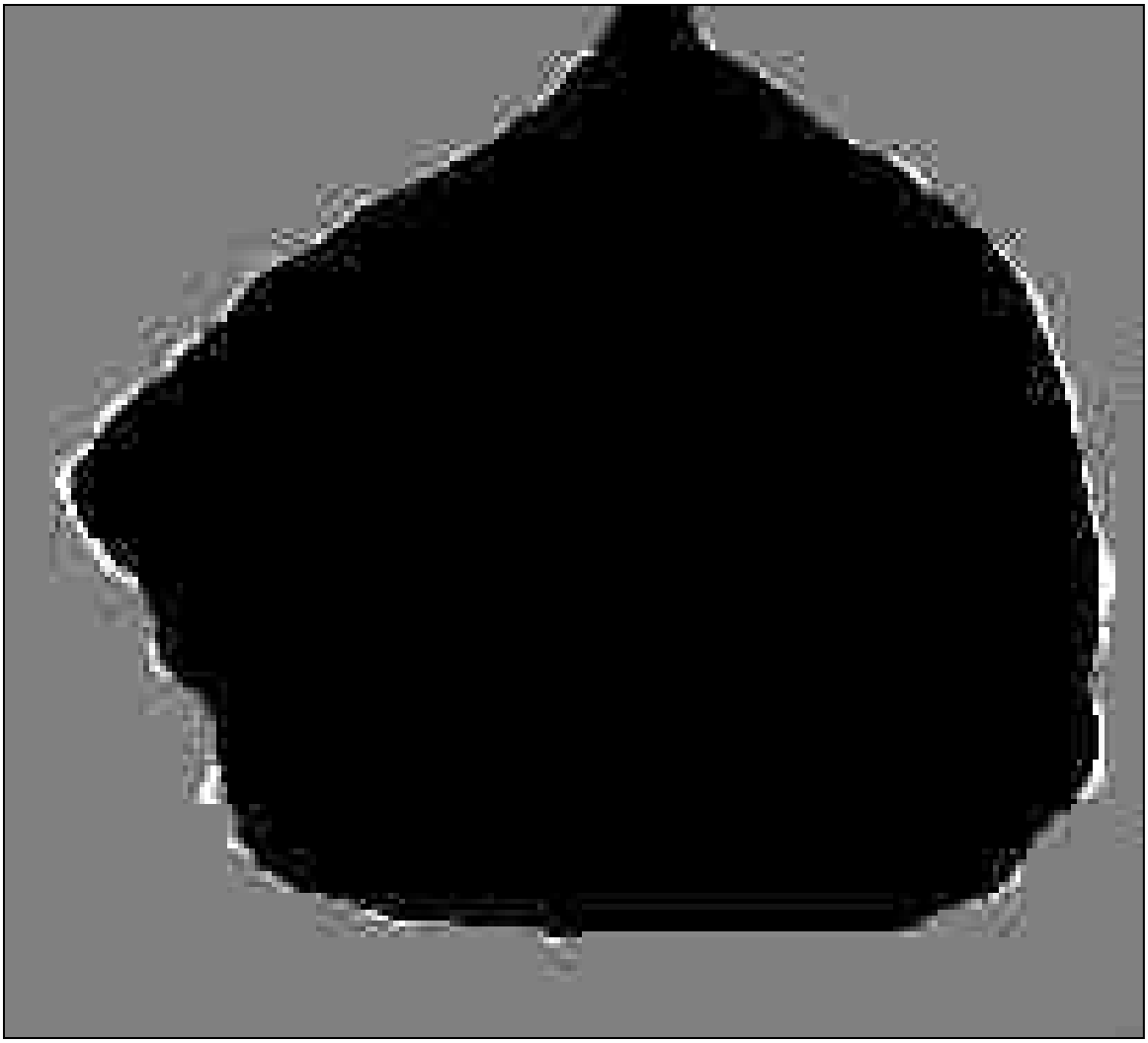

Figure 14: Closed contours of the M cereal item obtained via the Wrap-technique.

The void contents, as computed using Eqn. 1, are approximately 46.0 % and 74.0 % for G and M cereal items respectively.

After the outer surface (Fig. 15 & Fig. 16) and the structure of the cereal products have been obtained, the cereal volumes were meshed.

Figure 15: Outer surface of the M cereal piece.

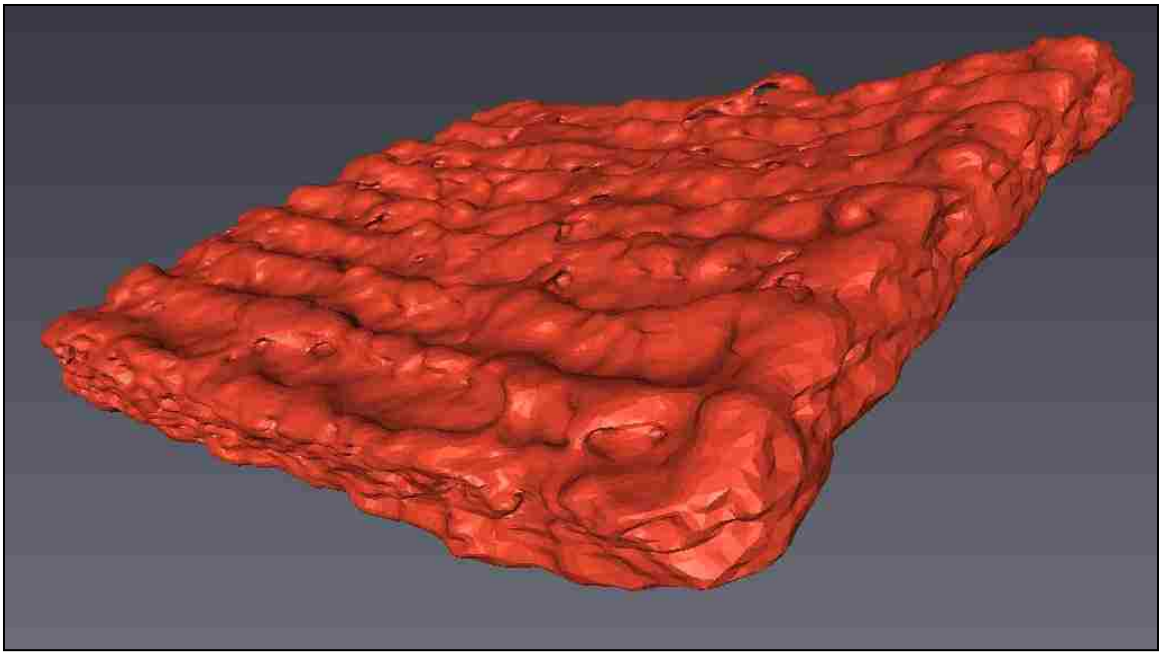

Figure 16: Outer surface of the G cereal piece.

Meshing of the food item is irregular. For this matter tetrahedral elements, where each element is described by four nodes are utilized. An element can be visualized as a triangle. A node is a corner of the element. Three degrees of freedom are associated to each node corresponding to 3D structural displacements. Irregular meshing allows, in this study, a substantial node saving because the element size is adjusted depending on the local solid curvature.

Despite the assistance of the irregular meshing technique in keeping the number of nodes at a minimum, on average, each cereal product still utilizes about 127,000 elements in its mesh. Contact between the teeth and a cereal item is established via the use of contact elements. The contact elements are located on the outer surfaces of the sliding rigid upper and lower teeth systems as well as on the outer surface of the deformable cereal item. The point-to-point contact is managed using the penalty method where normal and tangential stiffness are implemented when surface overlap

is detected. Fig. 17 shows the geometry and meshing of the whole system. The whole model stands with less than 38,000 elements for each tooth, 127,000 elements involved in the cereal item. Around 26,000 elements are contact elements. Note that in this study the virtual human mastication with two molars and a cereal piece requires less than 200,000 elements.

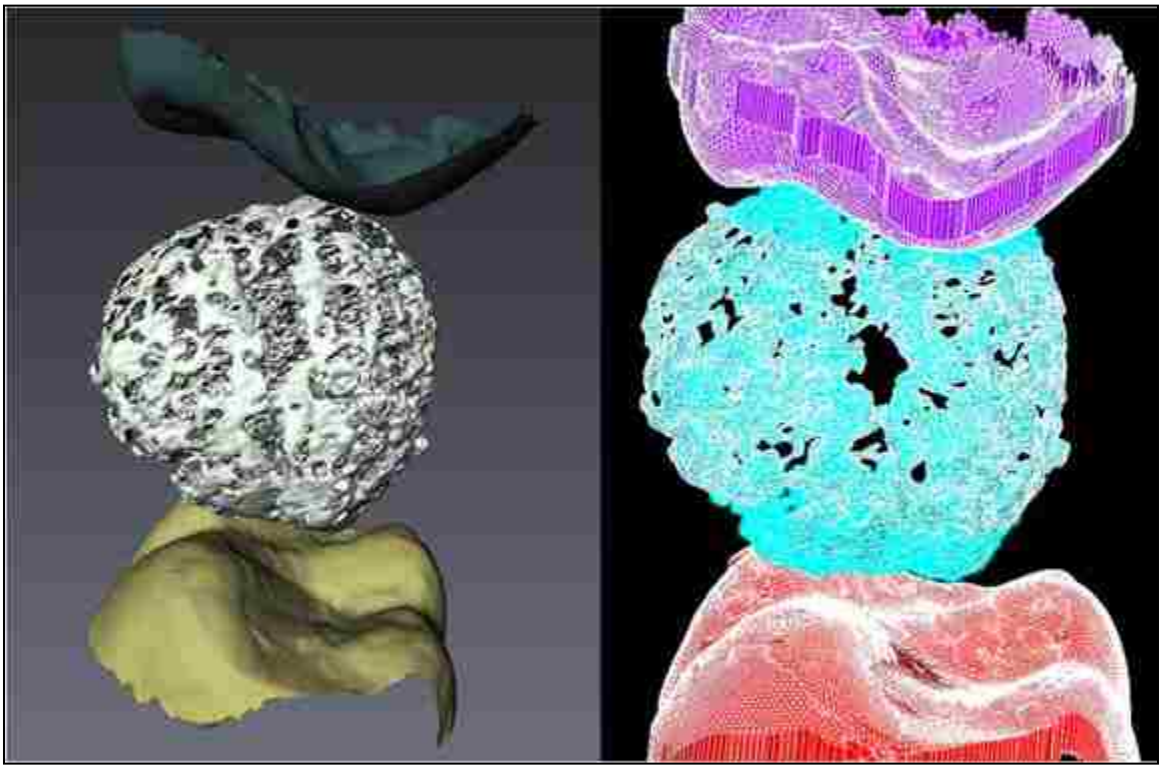

Figure 17: On the left the geometries of the teeth and a M cereal piece is illustrated. On the right the mesh patterns of the teeth and a M cereal piece are illustrate. Note that the teeth contain one layer of rigid contact elements.

3-5-6 Material Properties

Isotropic elastic properties for both cereal items are utilized as follows. The cereal items possess the following properties:

- E_c = 0.231 GPa, where E_c is defined as the cereal item's *Modulus of Elasticity*
- ν_c = 0.30, where ν_c is defined as the cereal item's *Poison's Ratio*

To avoid strain development in *teeth*, i.e. make the teeth rigid, the following material properties are utilized for the *teeth*:

- $E_t/E_c > 2{,}000$, where E_t is defined as the teeth's *Modulus of Elasticity*
- ν_t = 0.23, where ν_t is defined as the teeth's *Poison's Ratio*

3-5-7 Boundary Conditions and Shearing Angle

The upper tooth is fixed in space to simulate the fixed relation of the upper teeth to any food item during the process of mastication. For this study the lower tooth is allowed to move in the vertical direction, i.e. along the Z direction as well as in the transverse direction, i.e. along the X direction as illustrated by the coordinates in Fig. 18.

The lower tooth then presses up on the cereal, which in turn is pressed against the rigid and stationary upper tooth. By doing so the mastication of the cereal product is simulated. During this simulation the cereal item at one node, is inhibited to move along the X and Y directions. This ensures that the cereal item does not undergo any rigid body motion or rotation.

The simulation also accounts for the shearing angle within the cereal item, which is the actual cause of cereal fracture. The shearing angle is defined as follows:

$$\theta = \left|\frac{U_x}{U_z}\right| \qquad \text{(Eqn. 2)}$$

θ = Shearing angle

U_x = Displacements imposed on the nodes of the lower tooth along the X direction

U_z = Displacements imposed on the nodes of the lower tooth along the Z direction

3-6 Results and Discussions

The effect of resolution roughening is studied through the pore (void) and solid phase (wall) size distributions. Table 2 summarizes the numerical results for three sub-resolutions A, B and C. The pixel size in each sub-resolution is defined as *d*X, where X is substituted with the letters A, B and C. With this definition the pixel size ratios amongst the three sub-resolutions can be established as follows:

- $dA = 2 \times dB = 8 \times dC = 16 \times dD$
- $dD = 6.47\mu m$, which is the original pixel size

Table 3:
Some Characteristics of both Cereal Types

	Average Void Size (µm)			Average Solid Size (µm)			Relative Density (ρ)
Resolution →	A	B	C	A	B	C	
M Cereal →	219	267	304	89	80	77	0.26
G Cereal →	198	209	272	301	182	161	0.54

Table 3: Numerical results compilation for the studied products.

Distributions are processed in a cumulative referential. The obtained numerical size distributions of all preceding size distribution results for a given size class are added to each other. By doing so, the highest size class contains the whole distribution count. All classes are then scaled with regards to the total size distributions. Our results indicate that size distributions are similar in shape regardless of the resolution. However, they have different lower bounds.

The finest resolution (C) incorporates thin walls as small as 15 µm instead of 60 µm for resolution (A). All distributions end up to about 970 µm, which represents the largest pore size in the structure. The evaluation of the largest pore size is more precise with the fine resolution because of narrower size classes. 8.0 % of small walls with resolution-A are lost in the case of the M cereal item, whereas only 3.0 % of small walls are lost with the resolution-B. 60.0 % of small walls with resolution-A are lost in the case of the G cereal item, whereas only 27.0 % of small walls are lost with the resolution-B.

In a similar way, the study of resolution effects on cell wall size distributions reveals a lower size cut-off for resolution-A. The effects on missing walls seem to be stronger in this case. Up to 55.0 % and 47.0 % of small cell walls (< 45 µm for the M cereal item & <134 µm for the G cereal item) disappear for resolution-A in the case of the M cereal item and G cereal item, respectively. As illustrated in Table 3, these percentages decrease to about 23.0 % and 20.0 % in the case of resolution-B for the M cereal item and the G cereal item, respectively.

The effect of the shear angle was also studied in this work. Fig. 18 & Fig. 19 show typical nodal solutions for a compression of about 1.6 mm without shearing effect. Despite local contact, strain is transmitted to the whole internal structure and with that no sign of strain localization is observed near the contact region as illustrated in Fig. 19. Note that no strain is observed anywhere in the upper of lower teeth. This is satisfying, since the upper and the lower teeth were modeled to be rigid.

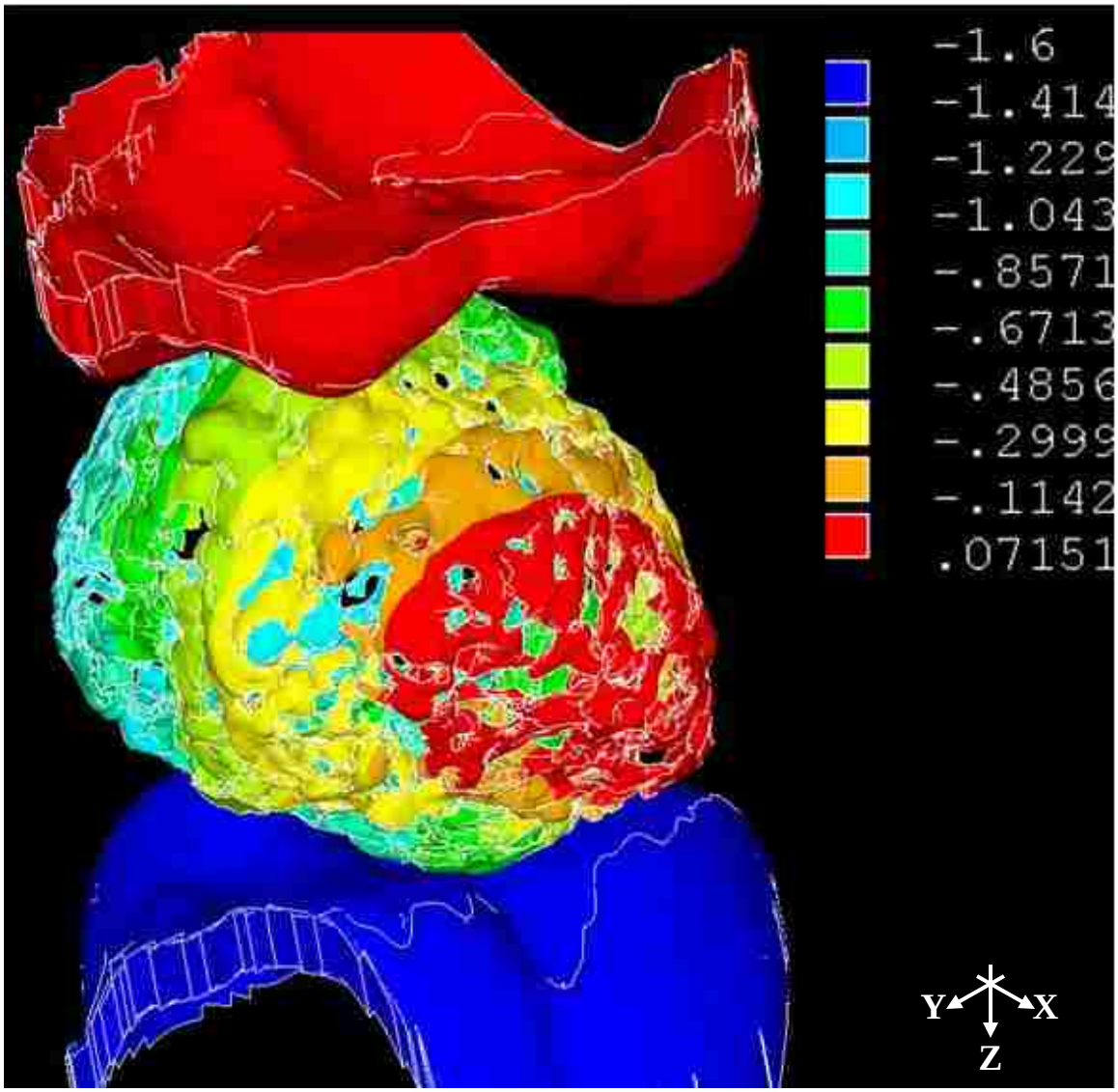

Figure 18: Displacement (U_z) along the Z-direction (mm).

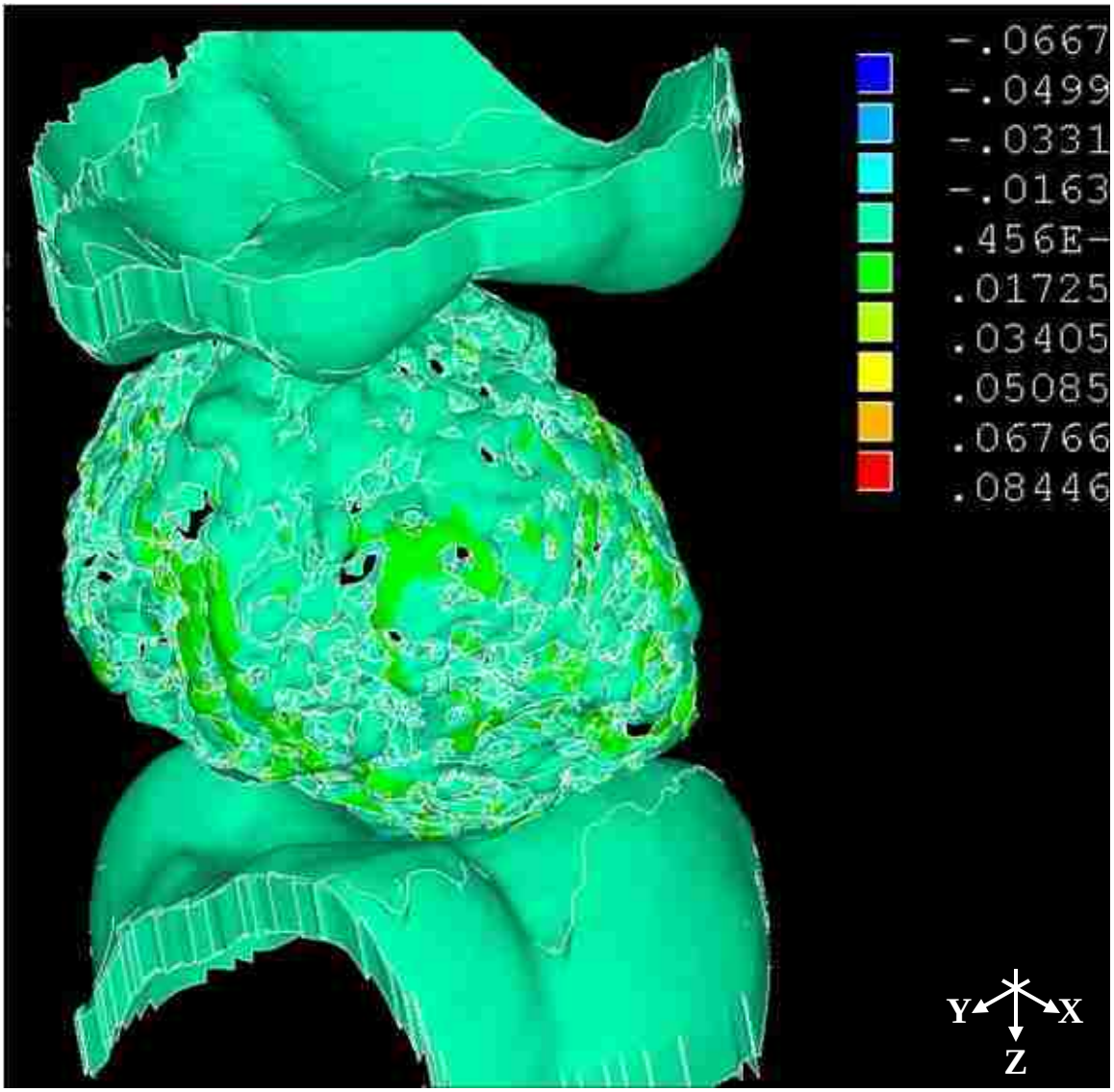

Figure 19: Strain (ε_{ZZ}) along the Z-direction.

To determine whether only one mastication cycle results in the fracture of the cereal items, it is necessary to compare the strain data illustrated within Fig. 19 with the results obtained by Guessasma et al. In their work, they have determined the necessary strain values that lead to the failure/breakage of starch [54]. They have discovered that strain values at or below 2.0 % are sufficient for the fragmentation of starch. The range of Z-strains seen in Fig. 19 spans between 6.7 % and 8.5 %. By comparing the data obtained

herein with the data obtained by Guessasma et al., it becomes clear that the fragmentation of the M cereal item occurs within the early stages of the applied displacement loading. A similar conclusion can be made for the G cereal item, since it has very similar starch content compared to the M cereal item.

Fig. 20 underlines the effect of the shearing angle to the X-displacements within the mastication simulations.

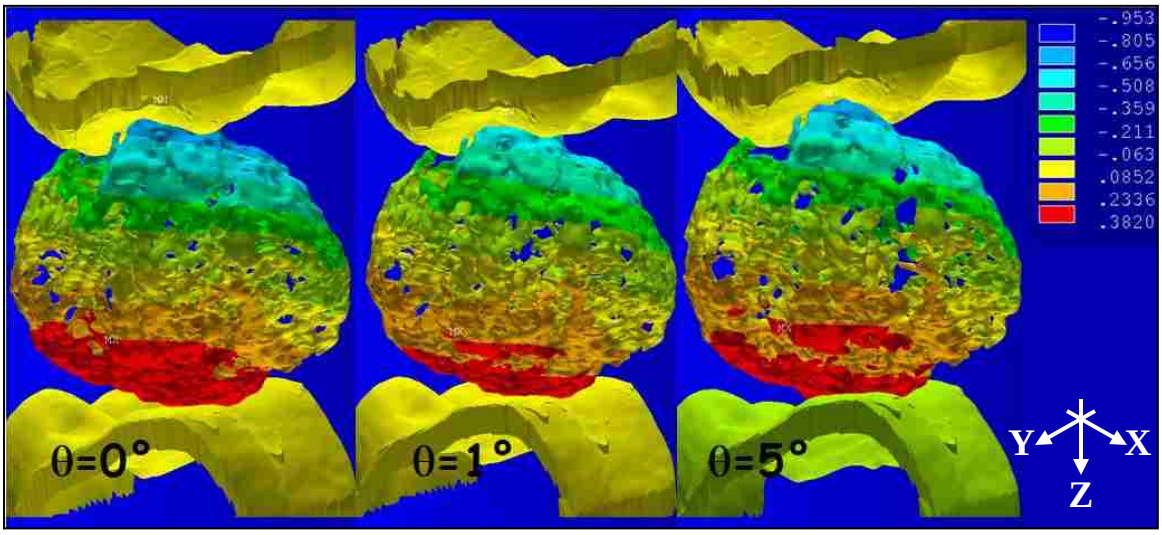

Figure 20: U_x-Cereal distribution as a function of shearing angle θ.

From Fig. 20, it can be concluded that an increase in the shearing angle θ slightly modifies the cereal's X-displacement distribution. Therefore, it is expected that the strain distributions along the Z-direction, namely ε_{ZZ} also are affected as a result of this θ variation. It should also be mentioned that the different shapes of the cereal items influence the fate of the ε_{ZZ} as well. By comparing the ε_{ZZ} strain distributions for both cereal items at the same shearing angle θ, a ε_{ZZ} strain distribution of about 0.08 and 0.02 for the M cereal item and the G cereal item was observed, respectively. Hence, the ε_{ZZ} within the M cereal item is higher than the ε_{ZZ} developed in the G cereal item.

Moreover, the relative density of a cereal product determines its resistance to fragmentation as well. A higher density and with that a lower void volume results in higher resistance to the applied mastication load. The G cereal has an approximate relative density of 107.69 % higher than the M cereal product.

Based the differences between the G and the M cereal products as mentioned above, failure probability is likely to be higher in the case of M. This is confirmed by the lower fracture energy observed experimentally for this cereal item.

3-7 Conclusion

The main finding in this work is the fact that fragmentation is likely to occur during the initial deformation stages of a mastication cycle. This leads to the conclusion that before the completion of the first occlusion, the cereal items are already fragmented. Our computation also shows that, despite having very similar material properties, the two cereal items display different strain distributions during mastication. This result particularly highlights the role of shape of a cereal product as well as its internal structure during the fragmentation process. Further processing, in near future, is needed to convert strain solutions into fragments distribution. By doing so, it will be possible to compare experimental and numerical fragment size distributions, at least for the first mastication cycles.

CHAPTER 4

4-1 Authors

1. Cyrus O. Abbasi B.S., University of New Mexico, Mechanical Engineering Department.
2. Amorette Maestas B.S., University of New Mexico, School of Medicine.
3. Tariq A. Khraishi PhD., University of New Mexico, Mechanical Engineering Department.
4. Bret Baack MD., University of New Mexico, Department of Plastic Surgery.

4-2 Title

Modified Roman Sandal: A Drain Anchorage Technique, More Effective and Reliable than the Conventional Roman Sandal.

4-3 Abstract

Displacement or movement of surgical drains from their intended placement location of attachment can lead to postoperative complications. The location of attachment can be on a patient's skin or on his/her internal organs. After such displacements, which can either occur over long periods of time through normal oscillatory breathing motion or on accidental basis, the patients usually undergoes a secondary operation so that a new drain can be placed at the correct location. The usual drain anchoring mechanisms involve the use of a common Suturing-Technique, namely the Roman Sandal (RS) Suturing-Technique.

This manuscript directly investigates the mechanical properties of the RS to determine the reliability and effectiveness of this Suturing-Technique. Furthermore, a second Suturing-Technique, namely a modified Roman Sandal (MRS) technique has been developed and investigated in this manuscript as well. To determine the fixation offered by these two Suturing-Techniques, the failure of the techniques under identical experimental conditions was investigated. The results obtained show that on average, the RS would fail right after one testing oscillation, whereas the MRS would fail above hundred testing oscillations. These results showed that the RS Suturing-Technique is not very effective in securing a drain. On the other hand the MRS Suturing-Technique proved to be more effective and reliable when it comes to securing a drain at its designated location.

4-4 Background and Rationale

Surgical tubes are efficient and reliable means to extract or relocate unwanted bodily fluids from or within the body of patient after a surgery. For instant, after the removal of a cancerous tumor, the remaining cavity is usually filled with bodily fluids, such as blood, that can cause infections and delay the healing process of the affected area. After employing the drains fully within the body, or partially within and partially extending out of the body, they are held in place by suture-threads that are knotted around the surgical tube and then sutured to the skin or the surrounding healthy area.

It is common practice that surgeons use the "RS technique" to attach drains to the skin or to an internal organ. In case of drains attached to the skin of a patient, although not referenced in the literature, it has been reported by nurses at the University of New Mexico Hospital, that due to the natural respiratory oscillatory motion of the patient's body as well as his/her movements such as turning in bed, the knots loosen up within a period of 1 to 3 weeks. Based on this loosening, the drain can move and be displaced from its intended position. This proves that although the RS Suturing-Technique is a commonly practiced method of drain anchorage, this technique often allows the drain to become mobile. Furthermore, the nurses have also reported that upon accidental events such as the drain getting stuck to a doorknob etc., the entire drain can be pulled out due to the rupture of the sutures or the patient's skin or internal tissue. Accidental dislodgement increases morbidity [55]. Hence, a second surgery will be needed to place a new drain, which adds to the growing cost and complications of a hospital stay.

Despite the importance of the proper anchorage of a surgical drain to the skin or to an internal organ, few studies have addressed it. Some of the solutions [56 & 57] require the suture to be passed through the drain itself, which interrupts the closed drainage system and increases the risk of infection [58].

Within this experiment it is hypothesized that in the case of natural, not accidental, knot failure, the inherent structural nature of the RS Suturing-Technique is the main cause of knot loosening and with that the dislodgment of the drain. In this experiment, we will concentrate on drains that are attached to the skin. We will mechanically mimic the in and out movement of the drain into the skin caused by the natural oscillatory movements involved in respiration. By doing so, we will investigate the reliability and the effectiveness of the RS and MRS, which we have developed herein. The reliability and effectiveness of both techniques are based both on the amount of oscillations it took for them to fail as well as the distance they slipped along the drain.

4-5 Materials/Equipment Utilized

1. Jackson-Pratt (JP) drains with an external diameter of 7.0 mm and an internal diameter of 4.0 mm.
2. "*3-0 (2.0 metric)*", Silk Black Braided suture-threads made by "Ethicon" as illustrated in Fig. 21.
3. 4.0" Sanding Sponge made by "Tool Choice" as illustrated in Fig. 21.
4. Two Mechanical Spring Scales made by "OHAUS" as illustrated in Fig. 21.
5. An Instron tensile testing machine, model 1101 as illustrated in Fig. 21.
6. A hole-puncher as illustrated in Fig. 21.
7. Custom-made Fixture/Grip System designed for the Instron machine. See Figs. 22 & Fig. 23.

Figure 21: 4.0" Sponge, hole-puncher, OHAUS Scales and the Suture.

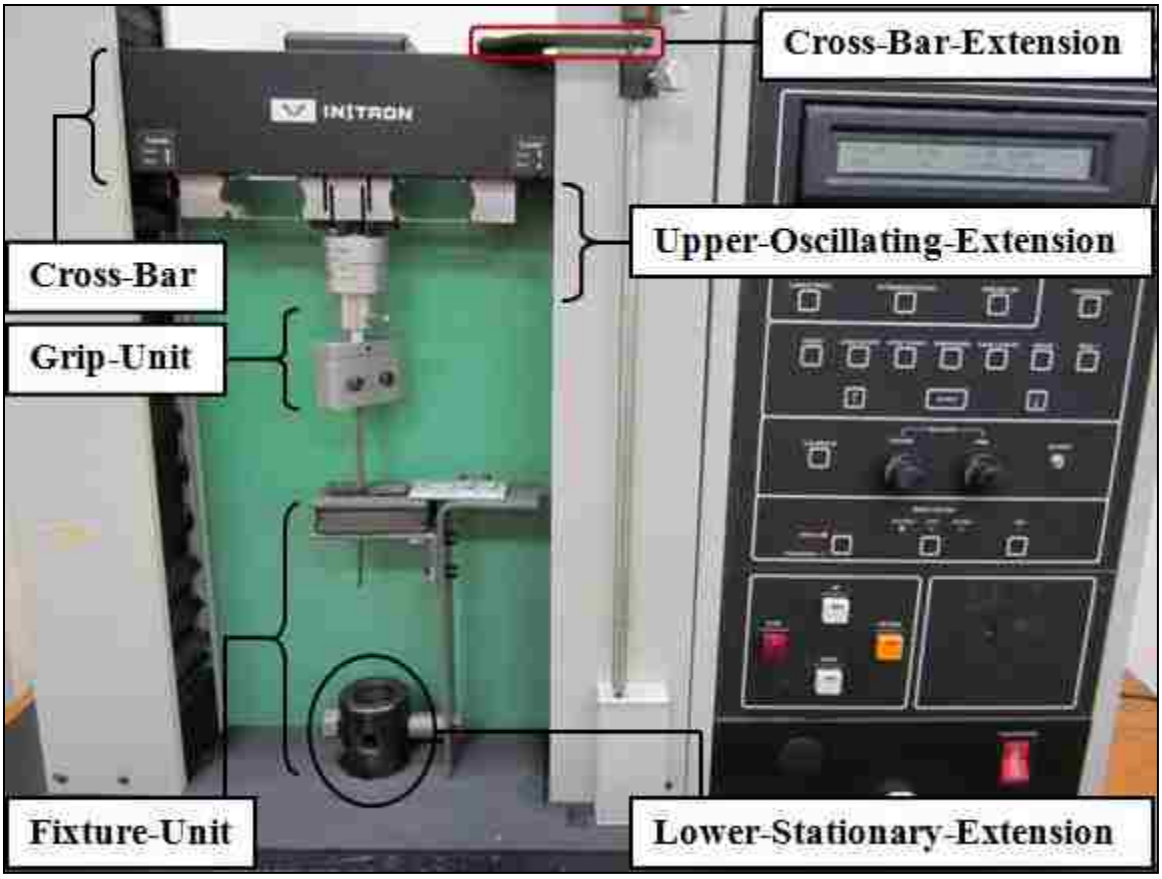

Figure 22: Instron tensile testing machine & the Fixture/Grip system.

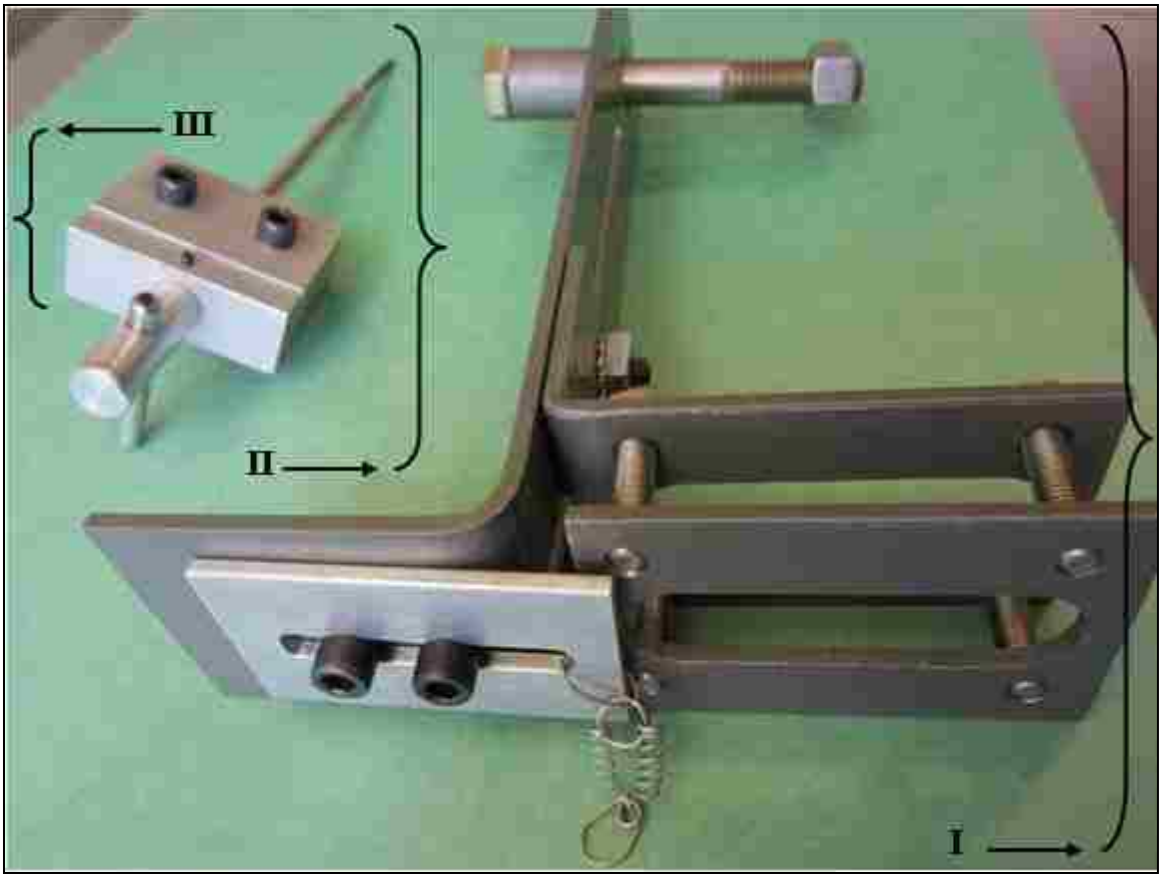

Figure 23: *Fixture-Unit* (I), *Grip-Unit* (II) & DGM: Drain Gripping Mechanism (III).

4-6 Methods

The mechanical reliability of both the RS and the MRS Suturing-Techniques are tested via the use of the Instron tensile testing machine. The Instron machine (IM) is normally used to test the tensile or compressive strength of a material specimen by pulling or pushing on it. The IM has a stationary arm to which one end of the sample is attached. The IM has also a mobile arm to which the other end of the sample is attached. The mobile arm can move up and down and with that it exerts tensile or compressive loads to the sample. The IM is also used to simulate fatigue testing of a specimen. During fatigue testing, the moving cross bar of the IM, which is attached to one end of the sample, moves up and down about a datum plane in an oscillatory vertical fashion. The oscillatory motion continues until the sample brakes, or in engineering terms fatigues.

Since the loosening of the suture knots in a natural setting also initiates after long periods of cycling of a patient's skin or drain, the latter testing feature of the IM, namely fatigue testing capability is utilized for this experiment. It should be noted that either the skin or the drain is usually the stationary item whereas the other one undergoes the oscillatory motion. We took the skin to be stationary and the drain to be mobile.

To simulate such oscillatory behavior, a custom-made *Fixture-Unit* and a *Grip-Unit* were designed and constructed (see Fig. 22). This *Fixture-Unit* was attached to the Lower-Stationary-Extension of the IM (see Fig. 22). The *Fixture-Unit*'s main tasks were to house a skin mimicking sponge as well as provide a location where the sutures could be attached. The stationary sponge mimics the skin of a patient through which the drain runs through and oscillates.

As far as the point of suturing attachment, two different options were experimented with. The first option was a totally stationary and rigid metallic ring, which was attached directly on top of the sponge and flush with it (Fig. 24). However, the rigidity of this ring caused the frequent tearing of the sutures. Based on that, a second and more flexible point of suture attachment was utilized.

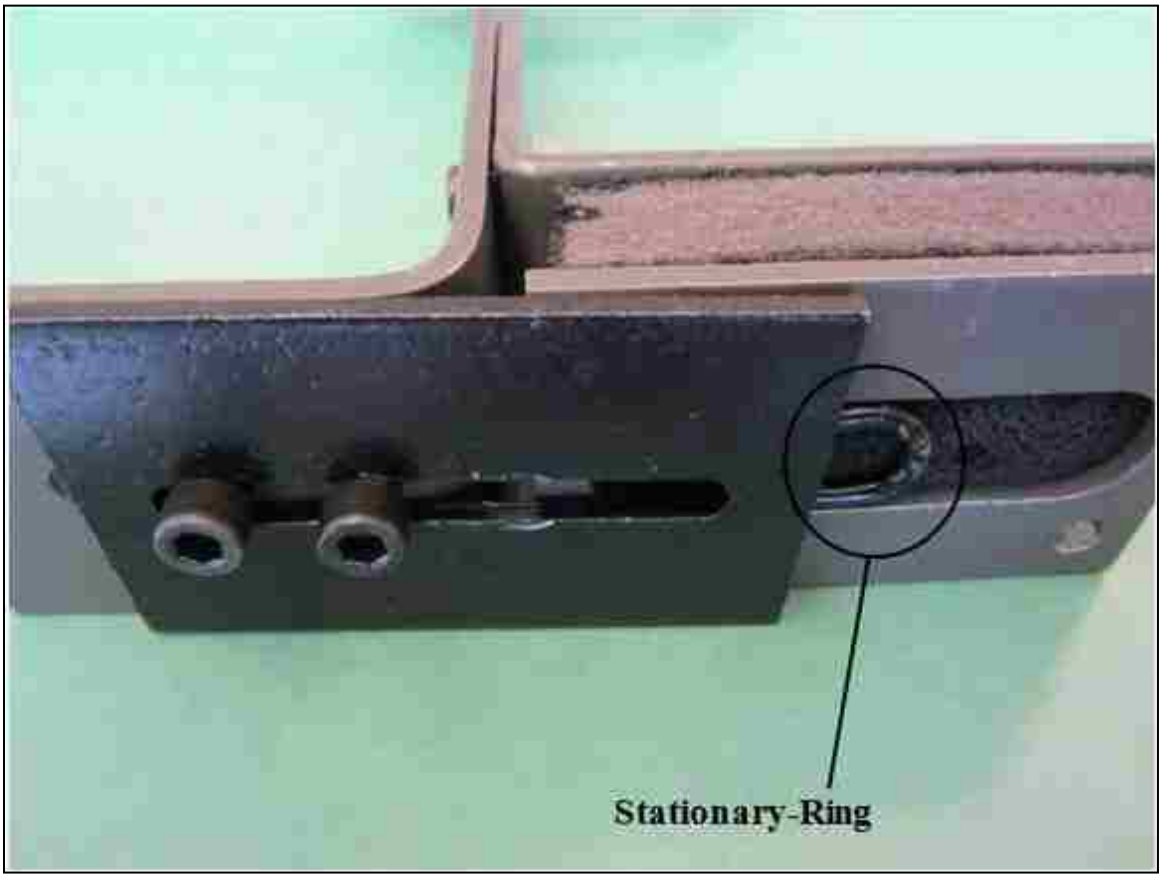

Figure 24: Stationary-Ring utilized as the point of Suture Attachment.

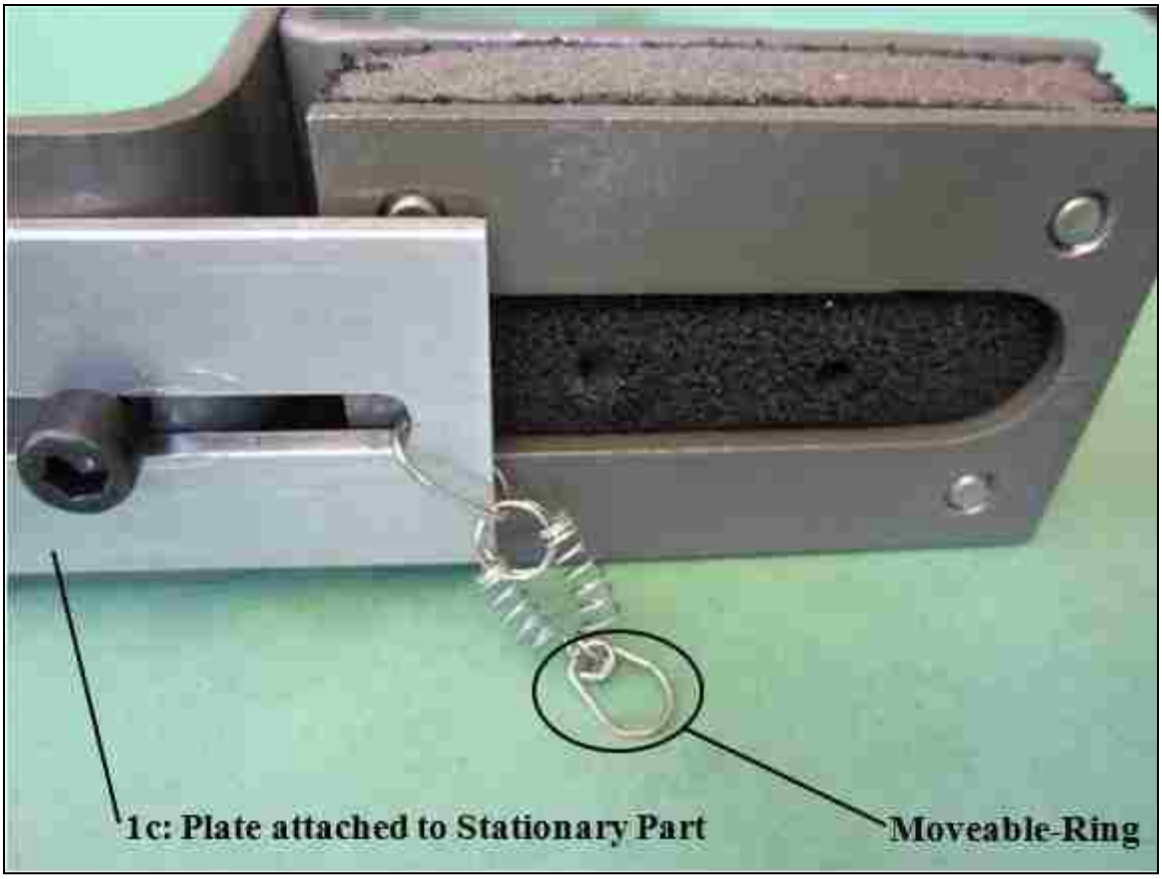

Figure 25: Moveable-Ring utilized as the moveable point of Suture Attachment.

As shown in Fig. 25 the second point of suture attachment was a metallic ring that was attached to a spring. The ring was the actual point of suture attachment. The spring was an intermediate connecting member between the ring and a plate (i.e. Part 1c shown in Fig. 26) attached to the stationary *Fixture-Unit*. By using the spring, the rigid ring becomes moveable. Upon the vertical movement of the drain and along with that the sutures, the sutures pulled on an elastic point of attachment. The elasticity of the spring was chosen to fall as close as possible to the elasticity of the human skin as reported by Scandola et al [59]. With that, not only the sutures didn't rupture but also the natural elasticity of the human skin was accounted for. The drain was attached to a *Grip-Unit*,

which was in turn attached to the Upper-Oscillating-Extension of the IM (see Fig. 22). A detailed description of all the members of the Fixture/*Grip-Unit* is stated below.

4-6-1 Detailed Description of the *Fixture-Unit* and the *Grip-Unit*

A *Fixture/Grip* (FG) system consisting of a *Fixture-Unit* and a *Grip-Unit* (Fig. 22) has been designed for this research project. The FG system is indented to serve as an attachment base for the drain and the sutures that wrap tightly around the drain. To be more precise, the *Fixture-Unit* mimics the skin of a patient through which the drain passes and to which the sutures get attached to. The *Grip-Unit* tightly holds on to the drain and is the oscillating part of the FG system.

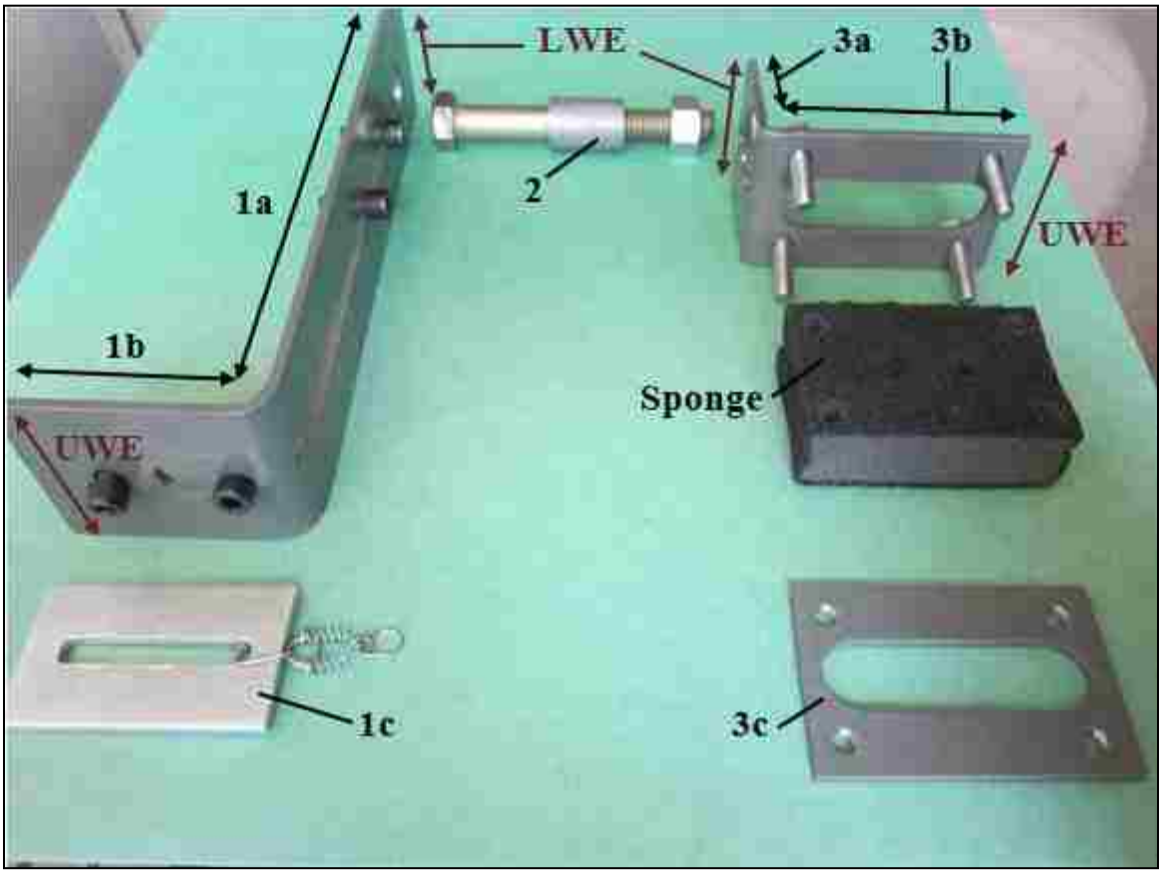

Figure 26: Disassembled *Fixture-Unit*.

As seen in Fig. 26, the *Fixture-Unit* consists of three parts. Part one is composed of a vertical portion (1a) and a horizontal portion (1b). It serves as the backbone of the fixture to which other parts are directly attached. Segment 1a has a length (L) of 8.0″, a width (W) of 2.0″ and a thickness (T) of ¼″. Along the mid-width of segment 1a, a circular hole with a diameter of ½″, serves as an opening through which a ½″-diameter bolt passes. The distance between the center of the hole and the Lower-Width-Edge (LWE) of segment 1a is 1¼″. The bolt then passes through part 2, which is a metallic cylinder of 1.0″ length, ¾″ outer diameter and ½″ inner diameter. Lastly, the bolt passes through the Lower-Stationary-Extension of the IM and reaches its nut as shown in Fig. 22. The nut is then tightened providing a firm connection between the fixture and the IM.

The cylinder, i.e. part 2 can be exchanged with another cylinder that has a different length. This gives a second horizontal degree of freedom (DOF) to the fixture. Two inches away from the LWE of segment 1a another opening, i.e. a slit, has been situated along the mid-width of segment 1a as well. The slit has an L of 5½″ and a W of ¼″. Through this opening two ¼″ screws pass, which connect part 1 to part 3. To be precise the connection occurs between segment 1a and segment 3a, which is the vertical segment of part 3. Segment 3a has an L of 1½″, a W of 2.0″ and a T of ¼″. One-eighth inches away from the LWE of segment 3a an opening, i.e. a slit, has been situated along the mid-width of segment 3a. The slit has an L of 1⅛″ and a W of ¼″. The openings of parts 1a and 3a provide a 6.0″ vertical DOF to part 3.

Segment 1c is a plate that serves as a base to which the spring is attached via a metallic ring. Segment 1c connects to segment 1b and with that is fixed in the vertical

direction. To establish this connection, which is enabled via two ½″ long, ¼″-diameter screws, three ¼″-diameter holes has been placed at mid-width of segment 1b. The first hole is ⅝″ away from the Upper-Width-Edge (UWE) of segment 1b. The second hole has a ⅝″ center-to-center-distance to the first hole. The 3rd hole has a ⅝″ center to center distance to the second hole. Only the second and 3rd holes are used for connection purposes of segment 1c.

Segment 1c has an L of 2.5″, a W of 1.5″ and a T of ¼″. At mid-width of segment 1c and ¼″ away from both of its width-edges a 2.0″ long and ¼″ wide slot has been placed. At one end of the opening two interlocking links connect segment 1c to a spring of ¼″ length and 333 N/m stiffness. At the other end of the spring, a second ring is attached. Since this ring is attached to the moveable end of the spring, it is called the *Movable-Ring*. The Movable-Ring serves as the connection point of sutures to the *Fixture-Unit*. The utility of the spring is to mimic the human skin's natural stiffness of 331N/m [59] as well as to prevent the sutures from tearing. The tearing can be caused by the oscillating tension forces exerted on the sutures during the experiments.

Part 3 also consists of a horizontal segment that is denoted as 3b. Segment 3b has an L of 3.0″, a W of 2.0″ and a T of ¼″. Along the mid-width of this segment, an opening, i.e. a slit, with an L of 2½″ and a W of ¾″ has been situated. This opening starts 1/4″ away from the UWE of segment 3b and ends 1/4″ away from the intersection of segments 3a & 3b. Close to each corner of segment 3b is a hole with a diameter slightly larger than ¼″. Four ¼″-diameter screws, each 1.0″-long, pass

through the holes and a sponge and then reach the ¼″ threaded holes of segment 3c. Segment 3c has the same dimensions and characteristics as segment 3b.

Segments 3b & 3c serve as a unit, which sandwiches the skin-mimicking sponge. The four bolts connecting these two segments can be replaced by bolts of lengths other than 1.0″. This provides a DOF regarding the thickness of the sponge as well as the level of compressing of the sponge. The sponge has an L of 2¾″, a W of 2.0″ and a T of 1.0″. For this research project a gap of ¾″ between segments 3b & 3c has been chosen. Under this circumstance the sponge is compressed by ¼″, which causes it to slightly contact the drain from all directions, i.e. 360°. The slight squeezing ensures a perfect contact between the drain and the sponge throughout the ¾″ sponge's final thickness. A 5.0 mm-diameter (very close to ¼"-diameter) hole is punched at each corner of the sponge to allow passage for the four bolts connecting segments 3b & 3c.

One inch away from both sponge's width-edges, along the mid-width of the sponge, a total of two 5.0 mm-diameter holes are punched as well. These holes provide a snug passage for the drain that is attached to the vertically oscillating *Grip-Unit*. It should be noted that only one of the holes is used for a single set of experimental trial(s). The sponge is rotated to provide an unused hole for the next set of experimental trial(s). The holes are punched with a hole-puncher (see Fig. 21) to preserve consistency.

The *Grip-Unit* is attached to the Upper-Oscillating-Extension of the IM, i.e. a 10.0 lbs load-cell as seen in Fig. 22. The *Grip-Unit* consists of a drain-gripping-mechanism (DGM) shown in Fig. 23, a ½″-diameter cylindrical extrusion as well as a

2.0 mm-diameter, 15.0 cm-long, solid copper rod. As illustrated in Fig. 27 the DGM is composed of two aluminum blocks each having a semi-cylindrical groove with a diameter slightly less that 7.0 mm, i.e. the outer diameter of the JP-drain. The two blocks are connected to each other via two ¼″-diameter screws. The copper rod is easily inserted in a 10.0 cm-long piece of JP-drain, which has an inner diameter of 3.0 mm. Then they are placed within the grooves of the DGM as it is tightened.

The copper rod is utilized to prevent the drain from crumbling under the forces exerted by the DGM's gripping-blocks as well as any potential buckling caused by the oscillating motions during the experimental trials. The cylindrical extrusion serves as the connecting part between the DGM and the Upper-Oscillating-Extension of the IM (see Fig. 22). A secure connection between the DGM and the Upper-Oscillating-Extension is guaranteed by a ¼″-diameter dowel that passes through both of them as shown in Fig. 22.

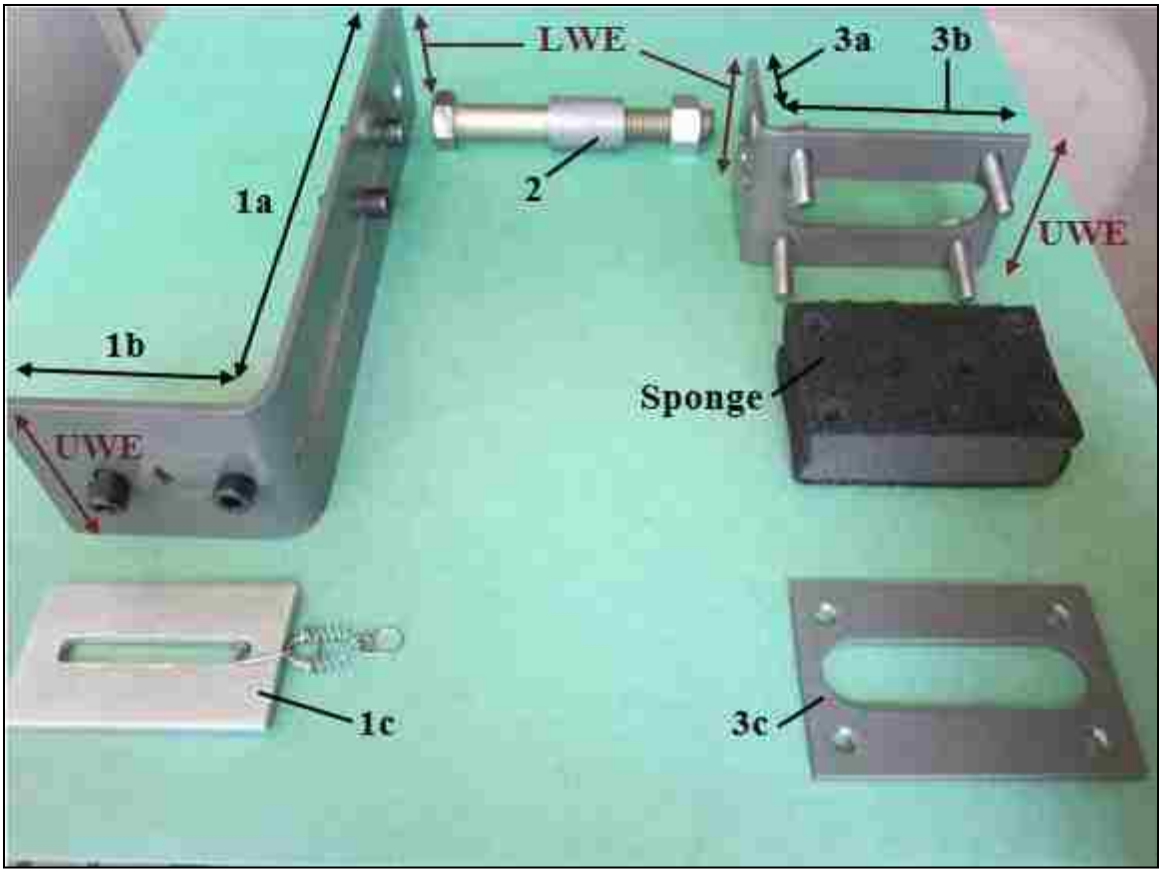

Figure 27: Disassembled *Grip-Unit*.

With the use of this fixture/grip system, the system closely replicates the typical orientation of the drain and suture on the body, where the drain moves in a perpendicular direction relative to the suture [60].

4-6-2 Step-by-Step Wrapping of RS and MRS Suturing-Techniques

4-6-2-1 RS Suturing-Technique

Fig. 28 shows one of the RS test-trails that were experimented with in the laboratory. The RS Suturing-Technique involves two Knot-Units. Each Knot-Unit consists of 4 surgeon's knots as shown in Fig. 28 to Fig. 30. Note that each Knot-Unit, consisting of four surgeon's knots, is 1.5 mm-long as illustrated in Fig. 30. At the point of attachment, the suture is wrapped and tightened around the moveable-ring.

During surgeries, Dr. Baack anchors the sutures to a patient's skin about 0.2 mm to 0.5 mm away from the drains outer surface. For this reason a 3.0 mm separation between the point of suture attachment and the outer surface of the drain was chosen for this study See Fig. 30. This distance was measured and held consistent for all the RS experimental trials.

Figure 28: RS Suturing-Technique with 1.0 cm initial separation between the LB and the second Knot-Unit used in the research setting.

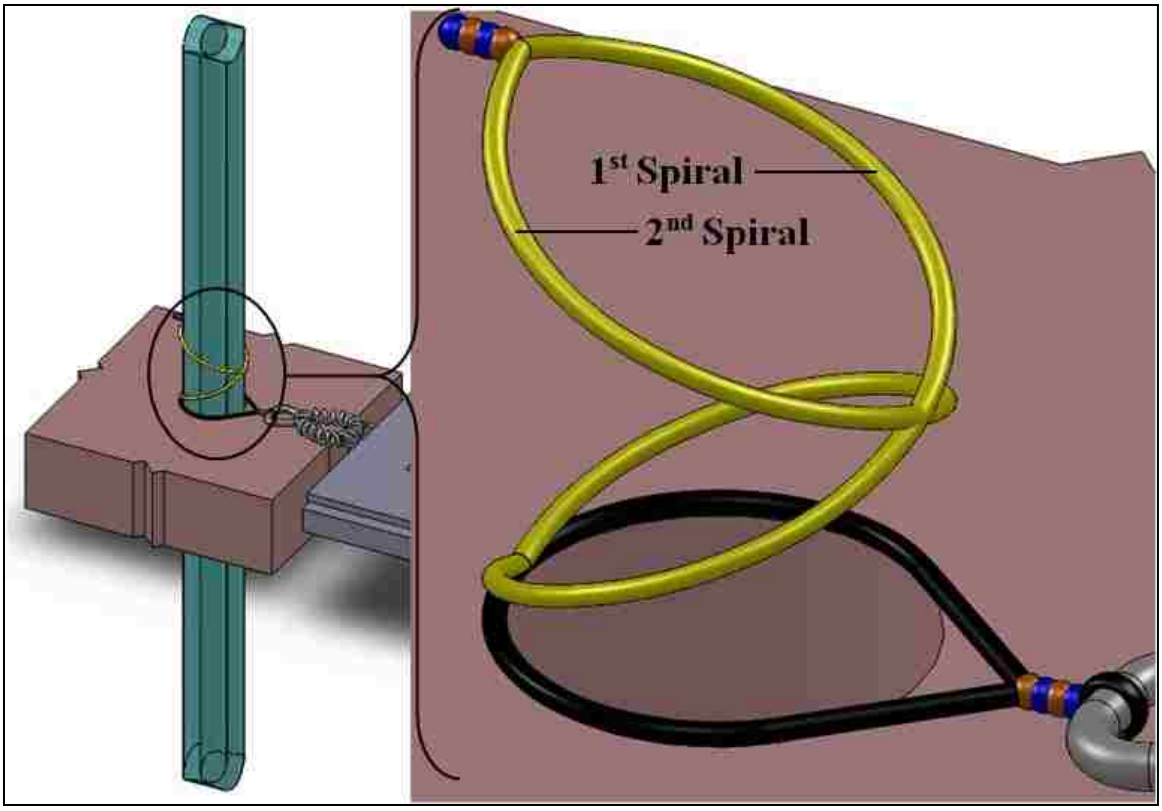

Figure 29: Isometric View. The RS Suturing-Technique. On the left the RS is employed around the JP-Drain, which passes through the skin. On the right, a zoomed view of the RS Suturing-Technique. Note that the drain is not shown on the right side.

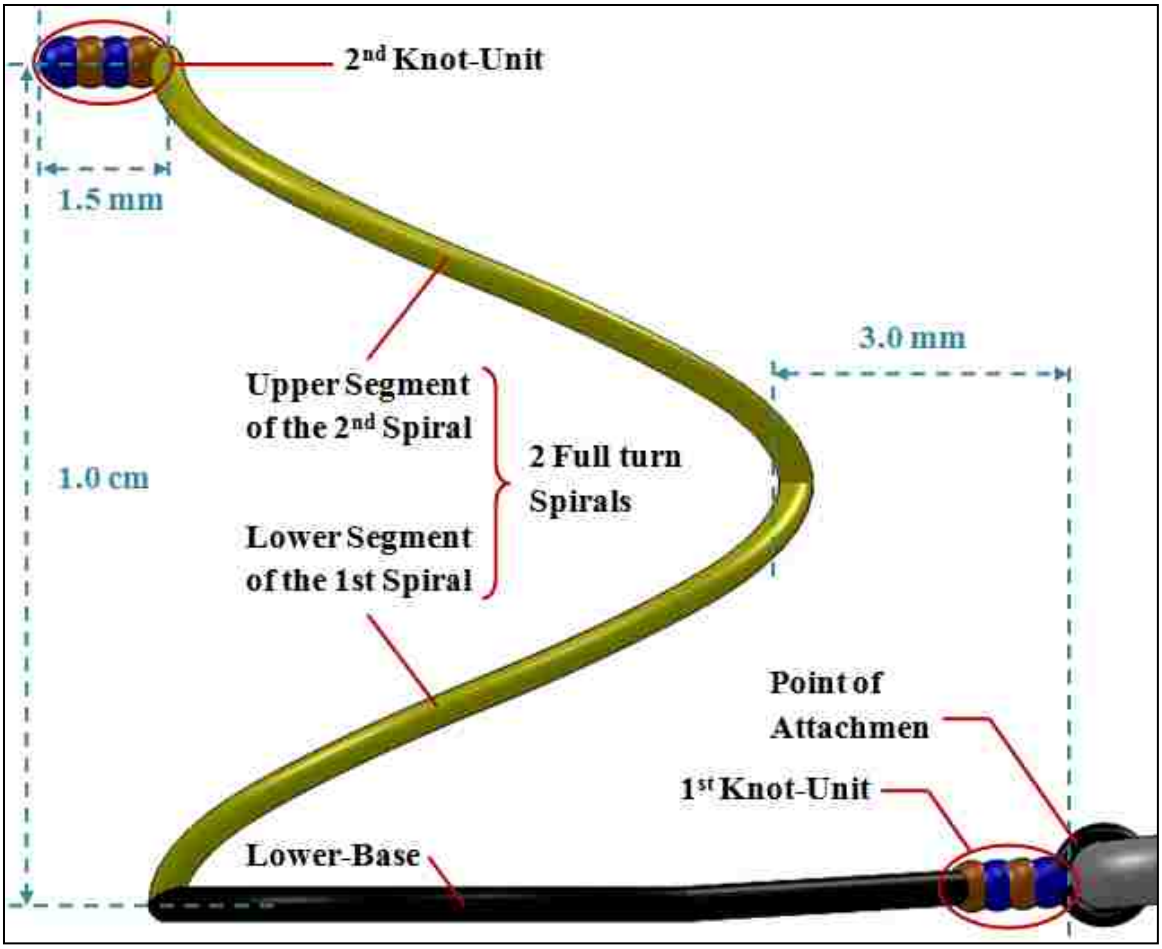

Figure 30: Side View. The RS Suturing-Technique. The two Knot-Units, the LB, the two yellow full-turn spiral segments as well as the mode of attachment to the Movable-Ring are shown. Note that the drain is not shown.

Starting from the first Knot-Unit, the both suture ends are wrapped around the drain in a half circular fashion, resulting in a circle around the drain. This circle is shown in black color Fig. 30. It should be noted that the circle is wrapped around the drain in a horizontal fashion, i.e. flush with the sponge's top surface. This circle is taken to be the Lower-Base (LB) of the RS Suture-Unit. From there the sutures made another full spiral turn around the drain. The heights of the spirals are 1.0 cm measured with respect to the LB.

Note that in Fig. 30 the lower segment of the second spiral is behind the visible lower segment of the first spiral and hence not visible. Also, the upper segment of the first spiral is behind the visible upper segment of the second spiral and hence not visible. These spiral suture segments are shown in yellow as illustrated in Fig. 30. The 1.0 cm spiral height is consistent with the spiral height commonly applied during surgeries according to Dr. Baack. At this point a second Knot-Unit was knotted.

While fastening all the knots involved in the RS Suture-Unit, both participating suture ends where pulled with two mechanical spring scales until a tension of 2.0 N was reached in the sutures. Fig. 21 illustrates how the scales are attached to both ends of the suture. By doing so, a consistency in the knotting procedures was established to target a unified strength within all the knots.

The applied force of 2.0 N was established while Dr. Baack was pulling on the sutures of a test-surgeon's-knot. After Dr. Baack felt that he had reached the right tensions, tensions around 2.0 N were read from both mechanical spring scales.

4-6-2-2 MRS Suturing-Technique

Fig. 31 shows one of the MRS test-trials that were conducted for this work. The MRS Suturing-Technique involves three Knot-Units. Each Knot-Unit consists of 4 surgeon's knots as shown in Fig. 32 & Fig. 33. Note that each Knot-Unit consisting of four surgeon's knots is 1.5 mm long as previously illustrated in Fig. 30. At the point of attachment, the suture is wrapped and tightened to the moveable-ring. The ring to which the Knot-Unit is anchored to is approximately 3.0 mm away from the face of the drain as shown in Fig. 33.

Figure 31: MRS Suturing-Technique with 2.5 mm initial separation between the LB and the UB used in the research setting.

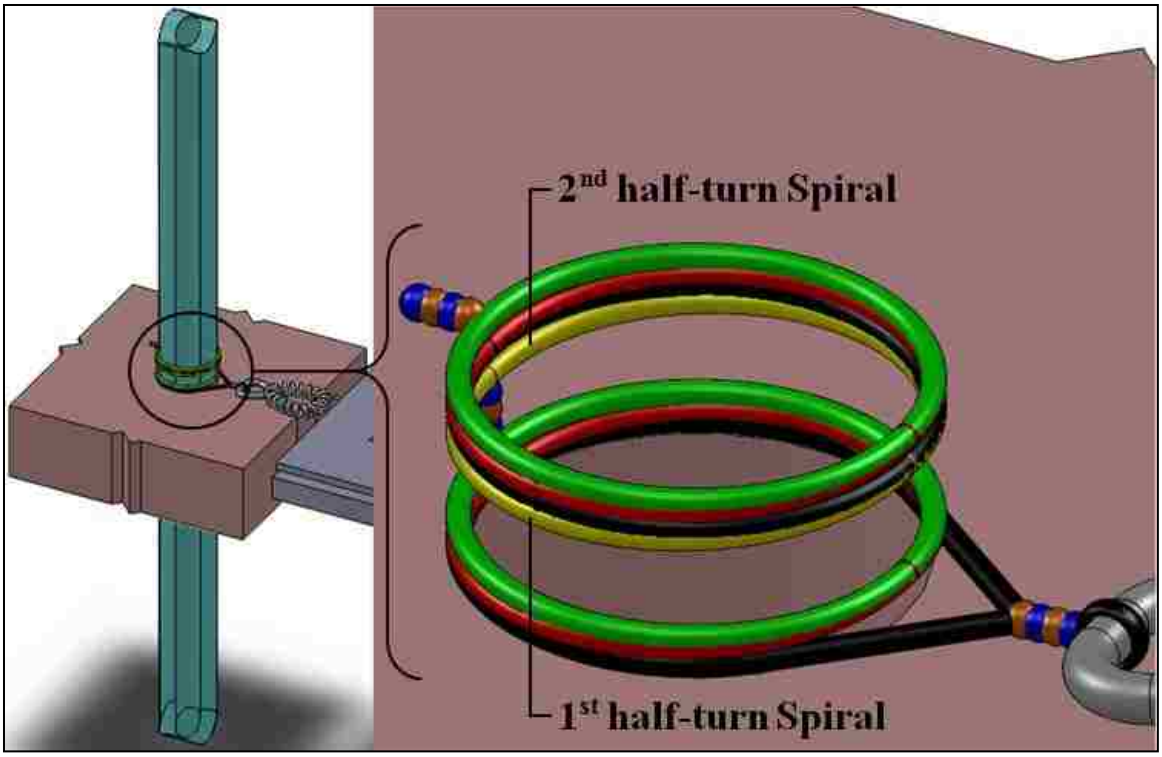

Figure 32: Isometric View. The MRS Suturing-Technique. On the left the MRS is employed around the JP-Drain, which passes through the skin. On the right, a zoomed view of the MRS Suturing-Technique, the three Knot-Units as well as the mode of attachment to the Movable-Ring are shown. Note that the drain is not shown on the right side.

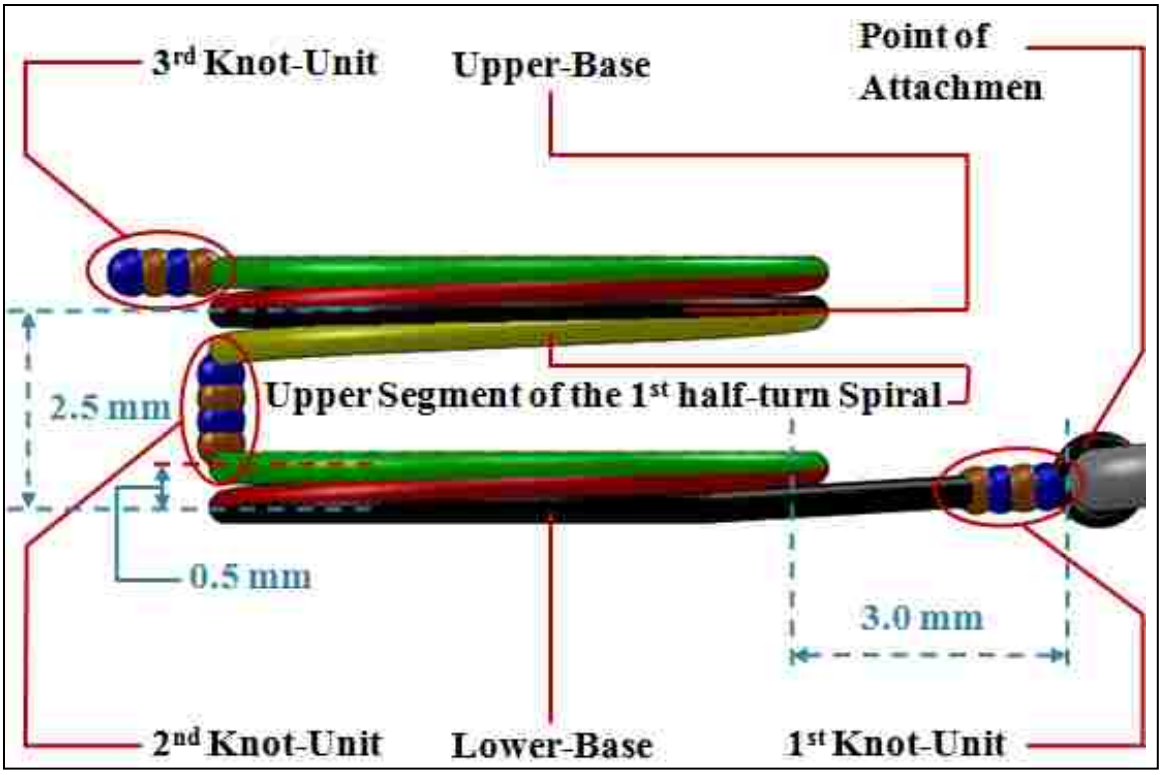

Figure 33: Side View. The MRS Suturing-Technique. The three Knot-Units, the LB and UB, the red and green segments, the two yellow half-turn spiral segments as well as the mode of attachment to the Movable-Ring are shown. Note that the drain is not shown.

Starting from the first Knot-Unit the both suture ends are wrapped around the drain in a half circular fashion, resulting in a circle around the drain. This circle is shown in black color Fig. 33. It should be noted that the circle is wrapped around the drain in a horizontal fashion, i.e. flush with the sponge's top surface. This circle is taken to be the LB of the MRS Suture-Unit. From there the sutures made another half-turn around the drain directly above and touching the LB. This segment of the sutures is shown in red. Then another half-turn is made by both sutures shown in green. At this point the second Knot-Unit is placed. A half-turn spiral was then made by both suture-threads, resulting in the yellow Suture-Unit segments.

As shown in Fig. 33, while wrapping the half-spirals around the drain, the second Knot-Unit is held against the outer surface of the drain in a vertical fashion to ensure that the sutures are tightly wrapped around the drain. At this point, a vertical half-turn is made around the drain by both suture-thread-ends resulting in the Upper-Base (UB) shown in black. The red and green segments, which followed on top of the LB, are also repeated on top of the UB. The placement of the 3rd Knot-Unit completes the MRS Suturing-Technique.

Note that the height of the half-turn spirals are 0.5 mm measured from the end of the second Knot-Unit. Also, note that the separation between the LB and the starting point of the second Knot-Unit is about 0.5 mm as shown in Fig. 33.

The addition of the second Knot-Unit's 1.5 mm length with the 0.5 mm height of the spirals as well as a 0.5 mm separation between the LB and the starting point of the second Knot-Unit, results in a total vertical displacement of 2.5 mm between the LB and the UB as shown in Fig. 33.

While fastening all the knots involved in the RS Suture-Unit, both participating suture-thread-ends where pulled with two mechanical spring scales until a tension force of 2.0 N was reached in the suture-threads.

4-6-3 Failure Criteria used in Comparing both Suturing-Techniques

4-6-3-1 *Suture-Unit-Displacement*

The *Suture-Unit-Displacement* was considered the first failure within this work. It occurs along the drain's outer surface. The *Suture-Unit-Displacement* or *slippage* is defined as the dislodgment-distance of the Suture-Unit's LB from a previously specified datum as illustrated in Fig. 34 and Fig. 35. The datum is taken to be an imaginary surface parallel and coincident with the upper surface of the sponge. The location directly below the LB was marked with a black marker all around the drain. The black markings are shown in Fig. 34 and Fig. 35 for the RS and the MRS Suturing-Techniques, respectively. This was done to determine the deviation of the LB, involved in either the RS or the MRS experimental trials from their datum. The location of marking is indicated by the white dashed lines in Fig. 28 and Fig. 31. Note that the white dashed lines refer to a location directly beneath the upper surface of sponge, which cannot be seen unless the drain is exiting the sponge.

We defined the maximum amount of dislodgment to be 5.0 mm. In real life, a 5.0 mm slippage of the Suture-Unit, i.e. *Suture-Unit-Displacement,* would be enough to expose the drainage holes/canals of a surgical drain. Therefore, a 5.0 mm *Suture-Unit-Displacement* could lead to undesirable infections. Hence, if a Suture-Unit experienced a *Suture-Unit-Displacement* of 5.0 mm or more during the experimental trials, it was classified as a failed unit. During each oscillatory experiment, the separation between the datum and the LB of the involved Suture-

Unit was measured. The experiment was terminated once the datum and the LB were separated by a distance of 5.0 mm.

4-6-3-2 *Suture-Unit-Collapse*

The *Suture-Unit-collapse* was the second failure criterion. It is defined by the difference between the initial and the final distance between the LB and the second Knot-Unit in the case of the RS Suturing-Technique. With regards to the MRS, the *Suture-Unit-collapse* is defined by the difference between the final and the initial distance between the LB and the UB as illustrated in Fig. 34 and Fig. 35. Note that the *Suture-Unit-collapse* is measured once the Knot-Unit has slipped 5.0 mm or more. This criterion underlines how well a Suturing-Technique maintained its shape, i.e. its structural integrity during the experiment.

Figure 34: The RS Suturing-Technique reaching a Suture-Unit-Displacement of 9.0 mm.

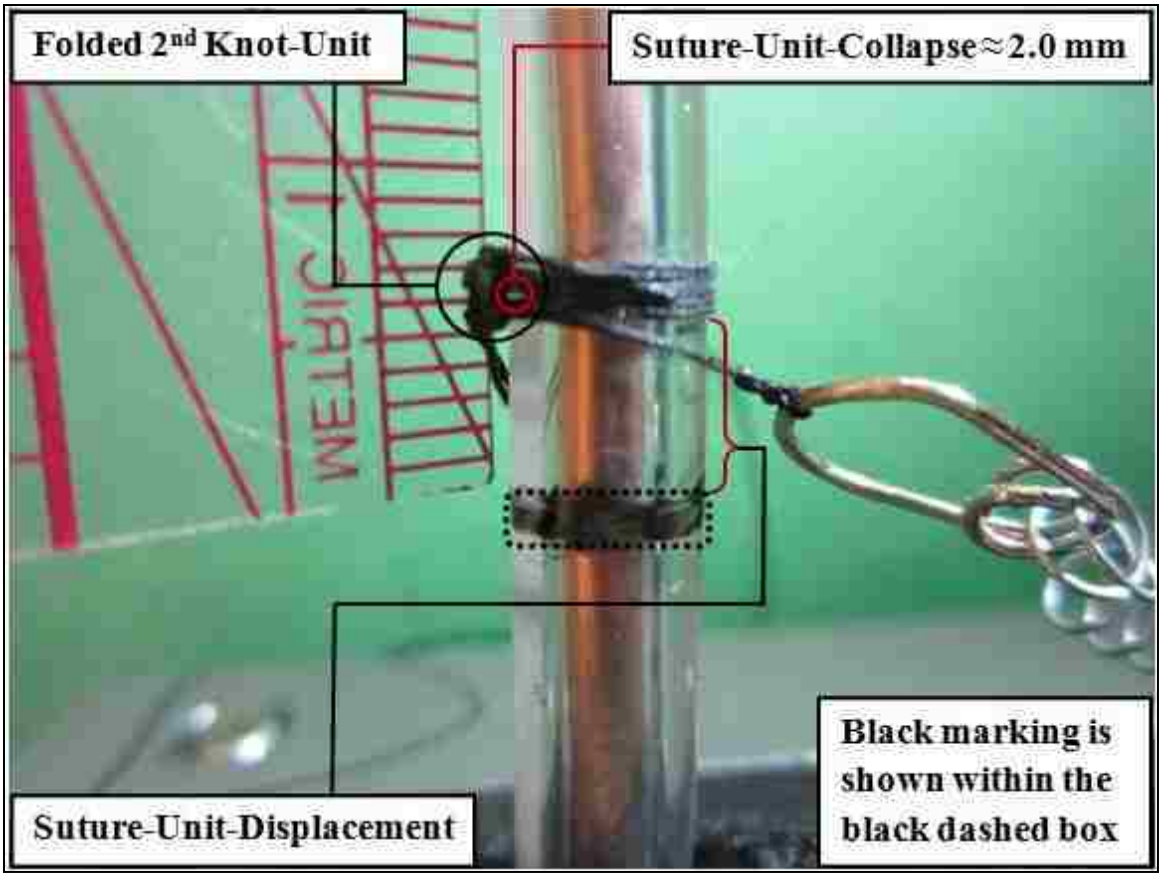

Figure 35: The MRS Suturing-Technique reaching a Suture-Unit-Displacement of 5.0 mm.

4-6-3-3 Number-of-Oscillations Needed to Achieve Suture-Failure

The *Number-of-Oscillations* needed to achieve suture-failure, was the third failure criterion tracked during all the experimental settings. To be specific, this failure criterion tracks the *Number-of-Oscillations* needed to achieve *Suture-Unit-Displacement and/or Suture-Unit-collapse*. Hence, during each experimental run, the *Number-of-Oscillations* needed to achieve *Suture-Unit-Displacement and/or Suture-Unit-collapse* was recorded.

4-6-4 Parameters Utilized for the IM's Settings

The IM, model 1101 is a displacement-controlled IM. This means that the amplitude of oscillation, i.e. the distance oscillated up and down, is controlled via two stationary Displacement-Controlling-Knobs (called stops) that can be fastened at a certain distance away from each other (see Fig. 36). The moving Cross-Bar of the IM has an extension that is situated between these two stationary Displacement-Controlling-Knobs as shown in Fig. 22 and Fig. 36.

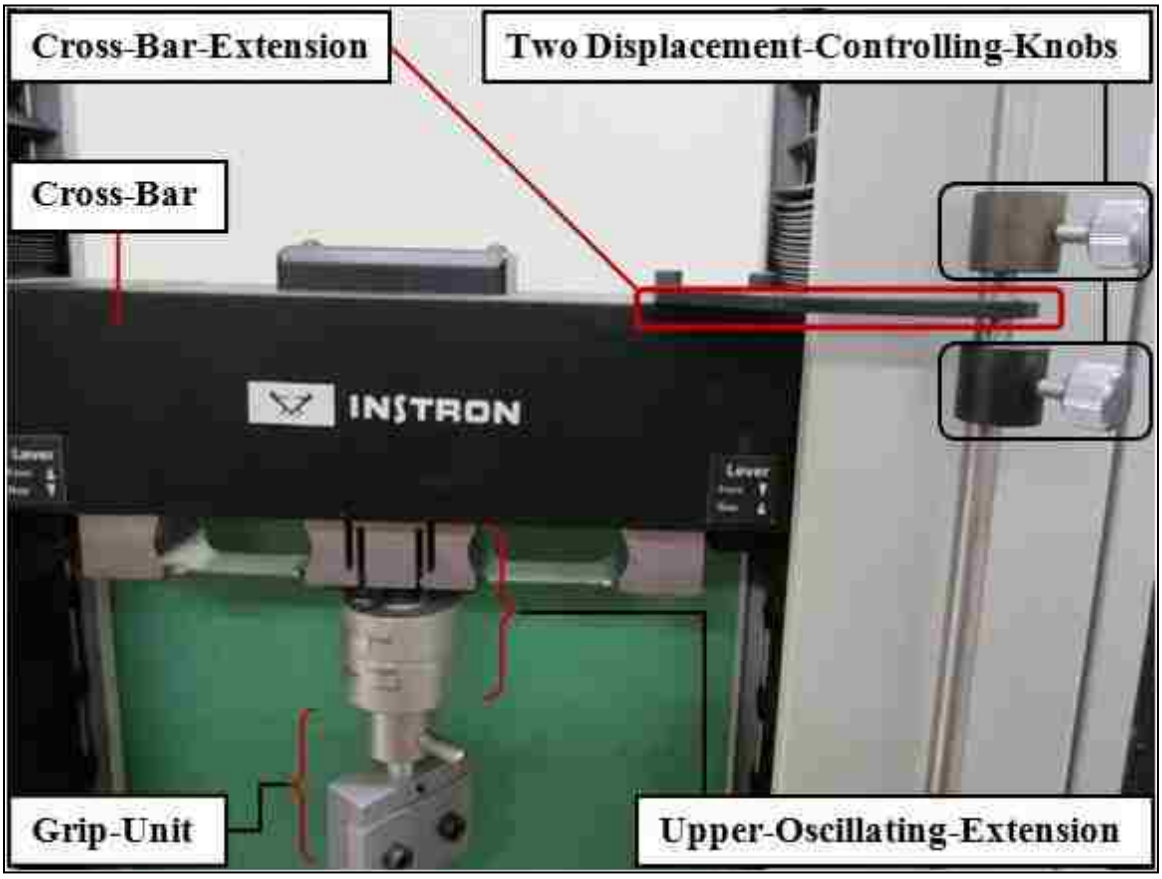

Figure 36: The Cross-Bar, Cross-Bar-Extension, Two Displacement-Controlling-Knobs, Grip-Unit as well as the Upper-Oscillating-Extension of the IM.

Once the Cross-Bar-Extension touches any of the two Displacement-Controlling-Knobs, the direction of the oscillation changes. Hence, the Cross-Bar and with it, the drain is moves in the opposite direction. Therefore, the direction of the oscillatory motion can be controlled via this displacement-controlled mechanism. Note that the datum's movement mimics the movement of the Cross-Bar.

The natural oscillatory respiratory motion of the body is taken to be the main cause of Suture-Unit failure. Therefore, the natural average frequency of the chest's oscillatory movement was needed to correctly set the oscillatory motion of the IM. The average respiratory frequency for adults over 18 years old is 12-20 breaths per minute [61]. We took 15 breathes per minute as our target respiratory oscillation frequency. Based on that, an oscillation speed of 30.0 cm/min was calculated. We chose a close value of 12.0 inches/min for the vertical oscillatory motion of the IM. This is because, 12.0 inches/min, was already a preset oscillation speed of the IM.

For the initiation of the experiments, the right combination between the following experimental parameters was needed:

1) The distance between the two knobs.

2) The location where the extension of the mobile arm needed to be at.

3) The right sponge firmness.

The following are the different experimental conditions, which lead to choosing the best combination.

4-6-4-1 First Combination

A combination of a soft sponge and a 1.0 cm distance between the two controlling knobs was used. The extension of the mobile arm was set to touch the lower knob at the start of the experiment, which meant that the LB of the sutures would not penetrate the sponge. It would only travel 1.0 cm above the sponge's surface and then come back to the surface of the sponge.

Note that any upwards or deviation of the LB of the suture from the datum results in a pulling action of the Suture-Unit. This pulling action is caused due to the fact that the Suture-Unit is tightened to the stationary point of attachment. The presence of the spring only provides some additional room before the suture is ruptured if the distance of up and down movement is too large.

With that said, the Suture-Unit still experiences tension upon departure from the datum, even in the presence of the spring. However, this setting resulted in very inconsistent failure results of both Suturing-Techniques. This was due to the softness of the sponge and the insufficient amount of drain penetration, i.e. 5.0 mm into the sponge.

4-6-4-2 Second Combination

A combination of a soft sponge and a 1.0 cm distance between the two controlling knobs was used. The extension of the mobile arm was located in between the two controlling knobs, which meant that the LB of the sutures would penetrate the sponge for a distance of 5.0 mm. Then it would travel 5.0 mm above the sponge's surface. The Suture-Unit would then oscillate between these two locations.

4-6-4-3 Third Combination

A combination of a coarse sponge and a 2.0 cm distance between the two controlling knobs was used. The extension of the mobile arm was located in between the two controlling knobs, which meant that the LB would penetrate the sponge for a distance of 1.0 cm. Then it would travel 1.0 cm above the sponge's surface. The Suture-Unit would then oscillate between these two locations.

4-6-4-4 Chosen Combination

The third combination was the one chosen to conduct the experimental trials of this research project.

During the use of the first combination it was determined that the without penetration of both Suture-Units the structural integrity of the Suture-Units would not alter despite the pulling action of the spring on the Suture-Unit. In fact, the pulling action of the spring, which occurred during the upward motion of the Suture-Unit, made the spiral segment of the RS Suture-Unit as well as the UB of the MRS Suture-Unit to develop a harder and harder grip with every oscillation. Based on this finding, it was determined that in order for both Suturing-Techniques to fail, the penetration of the LB into the sponge is necessary.

The second combination resulted in occasional and inconsistent failures of both Suture-Units. The reason for this inconsistency was the short amount of sponge penetration as well as the loose grip of the sponge on the surface of the drain. The role of sponge stiffness turned out to be very crucial. The sponge directly contacts the drain, which passes through it at a 90° angle. The LB of the Suture-Unit needed to be dislocated by the sponge in order to dislodge the Suture-Unit. If the sponge was not firm enough the LB of the Suture-Unit would easily penetrate into the internal portion of the sponge without being disrupted at all. However, it was determined that with sponge that has a rough surface as well as firm internal mass, the LB of the Suture-Unit would be dislocated upon touching the surface of the sponge. Moreover, the internal firmness of the sponge

guaranteed a well distributed and continuous interfacial contact between the surface of the drain and the surface of the hole punched into the sponge.

Besides utilizing a sponge with at rough surface as well as a firm internal mass, the penetration distance of the Suture-Unit into the sponge proved to be crucial also. Once the Suture-Unit penetrates into the sponge, the frictional force applied by the surface of the hole onto the Suture-Unit, exerts a major pulling force on the Suture-Unit. This pulling action acts on the Suture-Unit while it is penetrating the sponge and while it is retracting from the sponge. The importance of this fractional force can be analogous to the frictional force that anchors the foundational pillars of a bridge that runs over a river. With that said, this frictional force along with a rough sponge surface work perfectly together to disrupt the structural configuration of a Suture-Unit and ultimately make it dislodge from its intended position. The longer the penetration distance the further the dislodgment of the Suture-Unit. Therefore, a 1.0 cm sponge penetration was chosen.

In order to further enhance the consistency of the well distributed and continuous contact of the drain with the sponge material, the largest puncher of the hole-puncher was used. This puncher had a diameter of 5.0 mm, which results in a hole, 2.0 mm smaller in diameter than the used drain. The smaller diameter of the hole also ensures that the drain experiences some amount of frictional force while going in and out of the sponge as opposed to no frictional force in case of a hole with the same diameter as the outer diameter of the drain.

Based on these reasons the third combination proved to be best combination of the three and was selected for conducting the research.

It should be noted that a sponge with a rough surface as well as a firm internal mass does not necessarily possess the same mechanical properties of the skin such as the skin's elasticity, hardness and roughness. However, the point of this research project was to compare the reliability and effectiveness of two different Suture-Units, namely the RS and the MRS, under the same exact conditions. More importantly, we needed to observe consistent failure behavior of both the RS and the MRS Suturing-Techniques. Only a firm sponge could satisfy all these requirements and that's why it was chosen.

4-6-5 Parameters Utilized to Maintain Consistent Experimental Settings

The JP-Drain was cut into 10.0 cm-long pieces and attached to the *Grip-Unit*. For the experiments involving the RS Suturing-Technique, a new drain piece was used for every ten experimental trials. Since the Knot-Units of every Suture-Unit would leave a minute impression on the surface of the drain, the drain was rotated about 30.0 ° before the next RS Suture-Unit was wrapped around the same drain. By doing so, it was ensured that a fresh and untouched portion of the drain's surface was used for all the ten individual trials. Also, for the experiments involving the RS Suturing-Technique, a new sponge was utilized after the tenth experimental trial.

For the experiments involving the MRS Suturing-Technique, a new drain piece was utilized. This was due to the high *Number-of-Oscillations* required to achieve failure for this Suturing-Technique. Also, a new sponge was used for each experimental trial involving the MRS Suturing-Technique.

For every experimental trial, a new set of 18" suture-threads were utilized. A loop was knotted at both ends of the suture-threads as illustrated in Fig. 21. The loops provided secure locations at which, mechanical spring scales could be attached to the suture-threads. With the scales, the required tension force of 2.0 N was applied at both ends of the sutures as the surgeon's knots were tied.

4-7 Results and Discussions

4-7-1 RS Suture-Units

A total of 42 experimental trials were conducted while investigating the reliability and effectiveness of the RS Suturing-Techniques. This number exceeds the necessary 40 number of trials, required for obtaining statistically viable results. 36 RS trials failed during the first oscillation of each experimental run. Six of them failed during the second oscillation. Therefore, the results obtained for the trials involving the RS suturing-technique, were sorted in two different categories:

1. The 36 RS Suture-Units Failed after “One” Oscillation
2. The 6 RS Suture-Units Failed after “Two” Oscillations

Charts 9 & 10 show these the results obtained for these two categories.

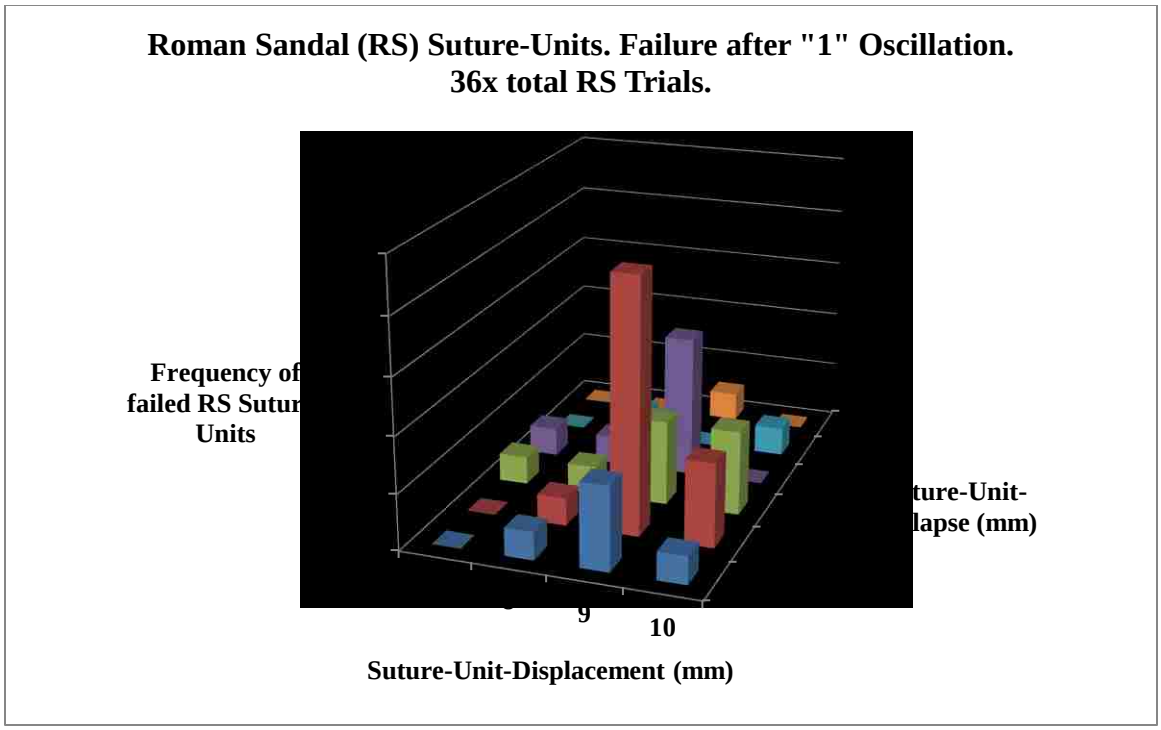

Chart 9: 36 total of RS experimental trials all failed after “1” oscillation.

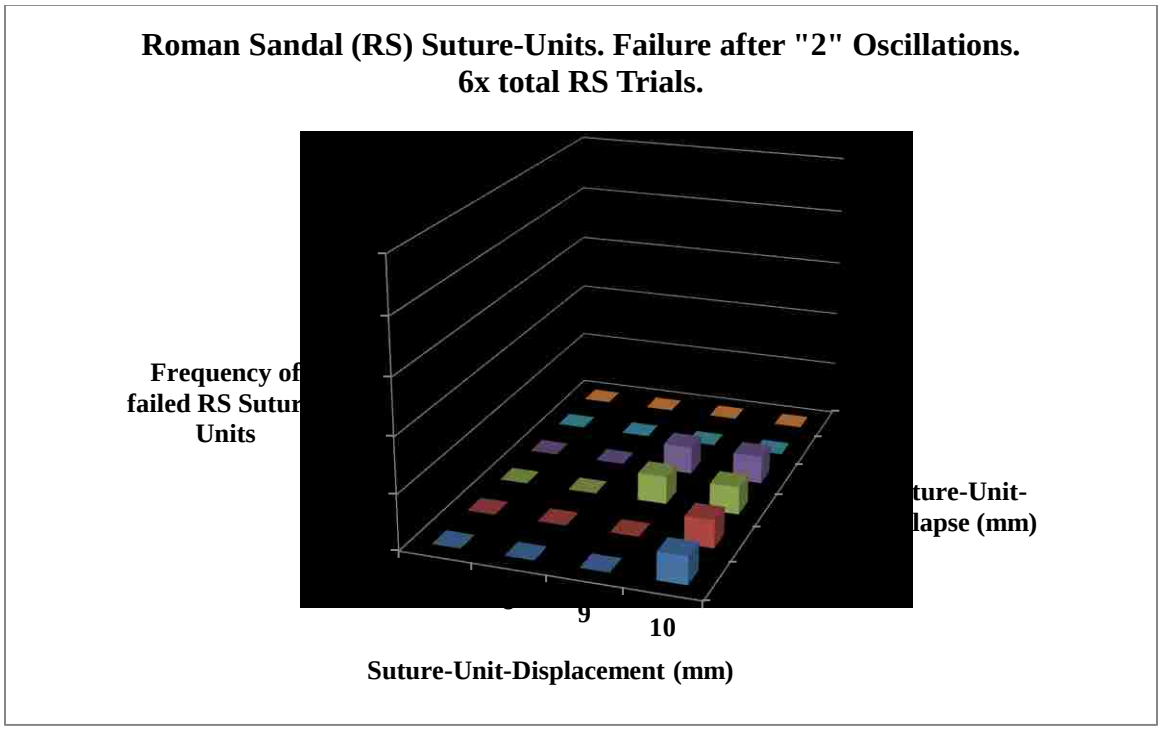

Chart 10: 6 RS experimental trials all failed after “2” oscillations.

4-7-1-1 First Category: The 36 RS Suture-Units Failed after "1" Oscillation

Chart 9 illustrates the results obtained of this category. The results are graphed with the following criterion in mind.

The "*Suture-Unit-Displacement*" axis represents the displacement of the LB with respect to the black circle marked on the drain. The *Suture-Unit-Displacement* was measured right after the termination of the first oscillation. The "*Suture-Unit-collapse*" axis represents the final separation between the LB and the second Knot-Unit.

The "Frequency of failed RS Suture-Units" axis represents the number of RS Suture-Units failed under the same circumstances described by the two horizontal axes.

Notice that for all experimental trials within the first category, the magnitude of the *Suture-Unit-Displacement* at the point of failure, i.e. after the termination of the first oscillation, was equal or higher than 7.0 mm. This shows that all 36 RS Suture-Units dislodged more than the previously defined failure criterion of 5.0 mm. Eight of the RS Suture-Units were displaced by 1.0 cm followed by 21 trials, which were displaced by 9.0 mm. Five of them were displaced by 8.0 mm and the remaining two trails were displaced by 7.0 mm.

During these experimental trials, it was observed that in all of the 36 trials, the LBs of the RS Suture-Units did not penetrate the sponge at all. While the drain penetrated the sponge, at some point the LB of the RS Suture-Unit touched the surface of the sponge. After touching the sponge, the LB just sat on the sponge's

surface. As the drain penetrated more and more into the sponge, the distance between the LB and second Knot-Unit reduced more and more. Finally, the LB and the second Knot-Unit came in contact. At the end of the 1.0 cm penetration, the drain would stop and then go back up. On the way back up, the second Knot-Unit and the LB would separate again. At the end of the 2.0 cm upward motion, the experiment was terminated. The resulting *Suture-Unit-collapse*s ranged between 3.0 mm to 8.0 mm. However, the majority of the measured *Suture-Unit-collapse*s were 4.0 mm.

From the obtained results, three distinct behavioral patterns for the RS Suture-Units can be seen:

1) The dislodgment of the RS Suture-Unit is directly dependent on the amount of drain's penetration into the sponge. Meaning, if the amount of penetrations was higher, let's say 2.0 cm, the Suture-Units would also be displaced in the vicinity of 2.0 cm.

   The following parallel between this behavior seen in a laboratory setting and reality, i.e. where the patient's skin is involved, can be seen. As the patient's rate of respiratory motion increases, his/her the rate of drain oscillation, with respect to his/her skin increases as well. An increased amplitude of drain's oscillation, could lead to deeper penetrations of the Suture-Unit into the patient's skin. This could directly increase the risk of a Suture-Unit's failure.

2) The LB is the most vulnerable segment of the entire RS Suture-Unit. This is because it shows an almost negligible amount of resistance to the forces exerted on it by the sponge's surface as the drain is lowered into the sponge.

   To overcome the vulnerability of the RS's LB, the area where the LB of the Suture-Unit is located, needs to be guarded by bandage or tape.

3) The frictional forces existing between all segments of the RS Suture-Unit (the LB and the spiral segments) and the drain's surface are only effective during the upward motion of the drain. These frictional forces exist

between the outer surface of the drain and the suture-threads, which are in direct contact with it. The more suture material wrapped around the drain, the more frictional force is expected [62]. The existence of these frictional forces is contingent upon the contact between the suture-threads and the drain's outer surface. If there is no contact, there will be no frictional force.

During the upward motion of the drain, the spring pulls on the Suture-Unit making it tighter and tighter. As the Suture-Unit gets tighter, a significant amount of frictional forces are developed between the drain's outer surface and the sutures. These frictional forces are good, because they prevent the Suture-Unit from slippage.

During the downward motion of the spring, the existence of such frictional forces should also be expected. This is because the spring will always pull on the Suture-Unit whenever its LB deviates from the datum. However, the rough surface of the sponge does not allow the LB of the Suture-Unit to deviate from the datum. Rather, the LB sits on the sponge's surface, i.e. the datum. Therefore, during the downwards drain motion, the second Knot-Unit approaches the LB, which is located right at the datum. With that, the spiral segments of the suture collapse. However, the lengths of the spiral segments do not change during the collapse. This causes the spiral segments to lose contact with the drain's outer surface and expand into the open space around the drain. This behavior is similar to the

Chinese Finger Trap, which shrinks when the fingers move away from each other and opens when the fingers move closer to each other.

4-7-1-2 Second Category: The 6 RS Suture-Units Failed after "2" Oscillations

Looking at Chart 10, it can be observed that four of the trials failed with a *Suture-Unit-Displacement* of 1.0 cm and the remaining two failed with a *Suture-Unit-Displacement* of 9.0 mm. The *Suture-Unit-collapses* ranged from 3.0 mm to 6.0 mm with the highest concentration around 5.0 mm and 6.0 mm.

During the conduction of these six experiments, it was observed that the LB of the Suture-Unit, indeed penetrated into the inner portions of the sponge. This behavior goes against the patterns we observed during the 36 trials discussed above.

The entire RS trials were divided in five groups. The first four groups contained 10 RS experimental trials. The fifth group contained two RS experimental trials. As mentioned before, a new sponge was used for every group. The experimental trials discussed in this section were the last trials within each group. They were either the tenth or the ninth trial within each group. For that reason, the surface of the sponge that was used for each group, was somewhat worn out by the time the ninth or the tenth trials within a group were conducted.

The worn out sponge's surface, resulted in a weaker grip around the drain. Hence, unlike the 36 trials discussed above, the LBs involved in these six trials, did not experience the same amount of force during their first encounter with the sponge's surface. However, during the second oscillation, the LB of each of these six RS trials behaved in the same fashion as the LBs involved in the other 36

trials. Meaning, they sat on the surface of the sponge while the drain was getting lowered into the sponge.

From this behavior, in addition to the three behavioral patterns stated previously (see Sec. 4-7-1-1), an additional behavioral pattern with regards to the RS Suture-Units has been concluded:

4) Although the LB of the RS suture shows negligible amount of resistance to external agitations, a looser surface area of the sponge, prevented the Suture-Unit to fail during the first oscillation.

    Hence, the looser the skin of patient, the lesser is the probability of the RS Suture-Unit's LB failure. Therefore, the performance of the RS Suture-Unit is related to the skin roughness of a patient as well.

4-7-2 MRS Suture-Units

A total of five experimental MRS trials were conducted. This is due to fact that each run needed more than 100 oscillations to result in the failure of the MRS Suture-Units. This positive jump in the effectiveness of the MRS Suture-Unit performance was so overwhelming that, five trials were sufficient to contrast the difference between the reliability of the RS and MRS Suturing-Techniques.

Chart 11 through Chart 16 show the results obtained for the experimental trials involving the MRS Suture-Units.

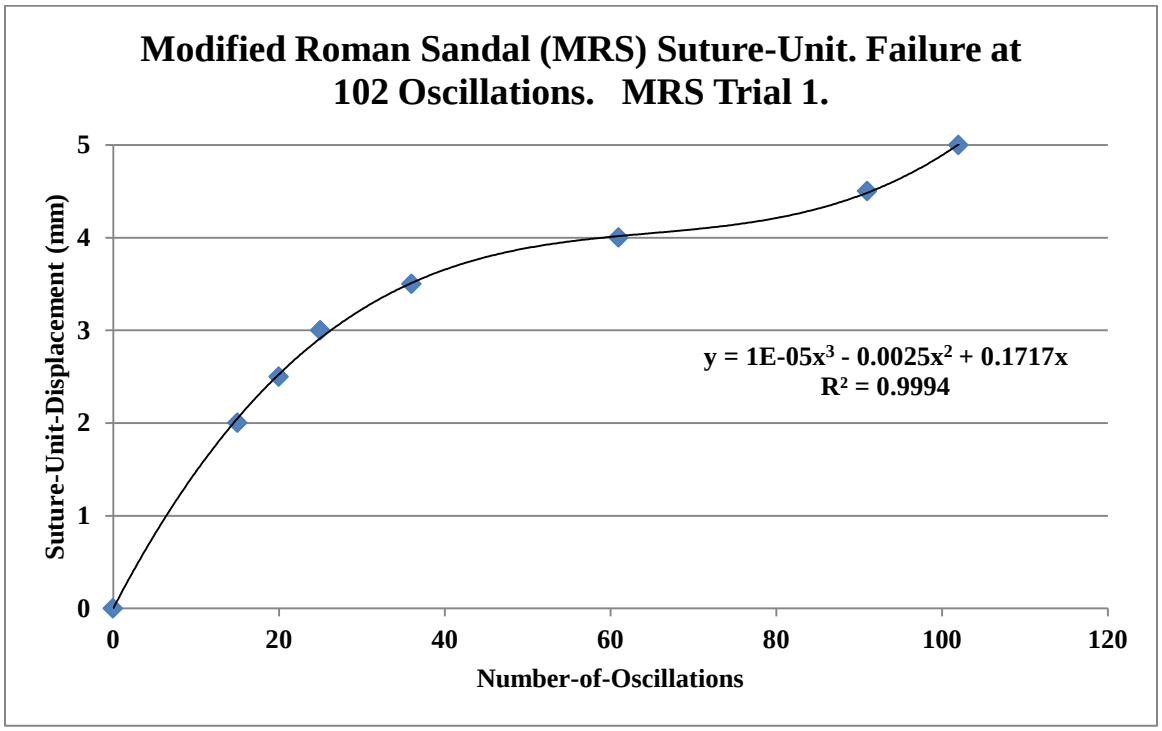

Chart 11: 1st MRS Experimental Trial. Failure occurred after 102 oscillations.

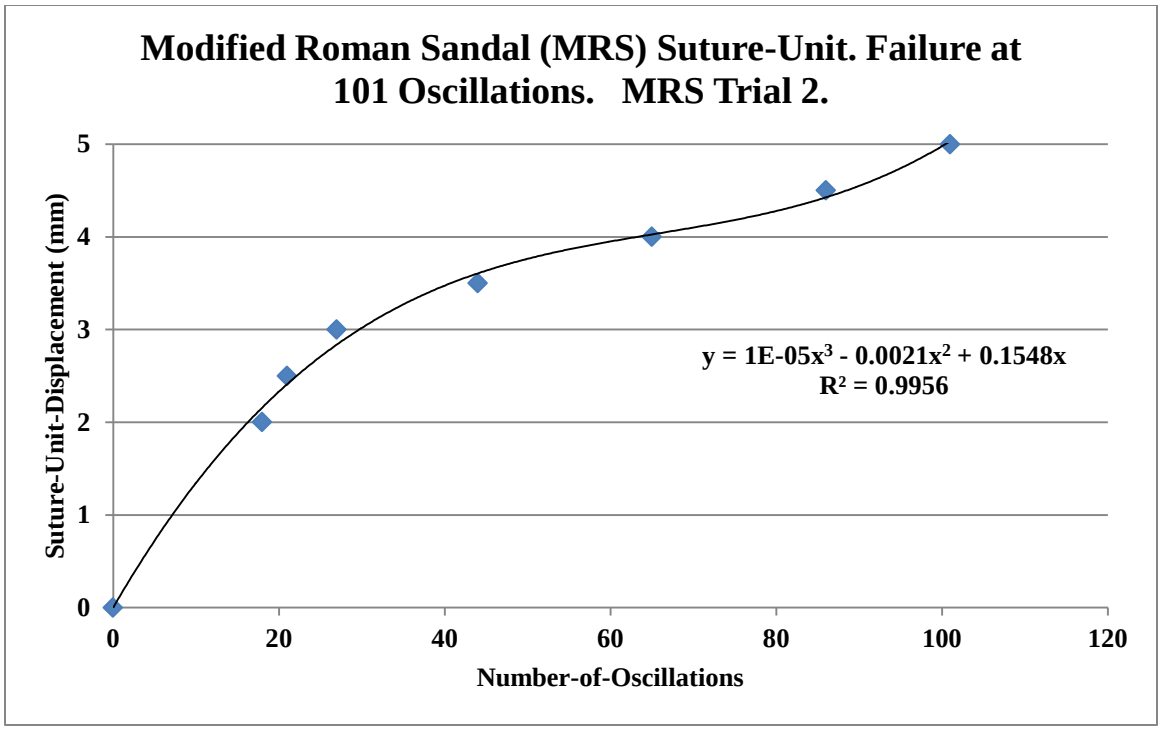

Chart 12: 2nd MRS Experimental Trial. Failure occurred after 101 oscillations.

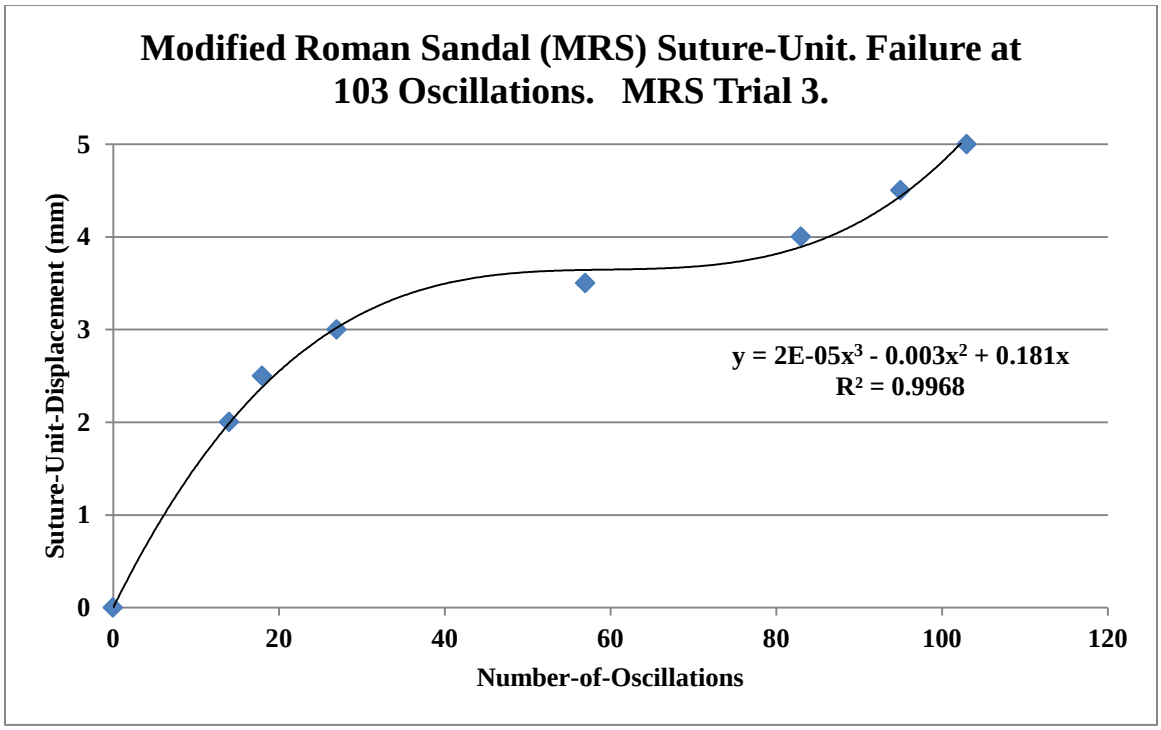

Chart 13: 3rd MRS Experimental Trial. Failure occurred after 103 oscillations.

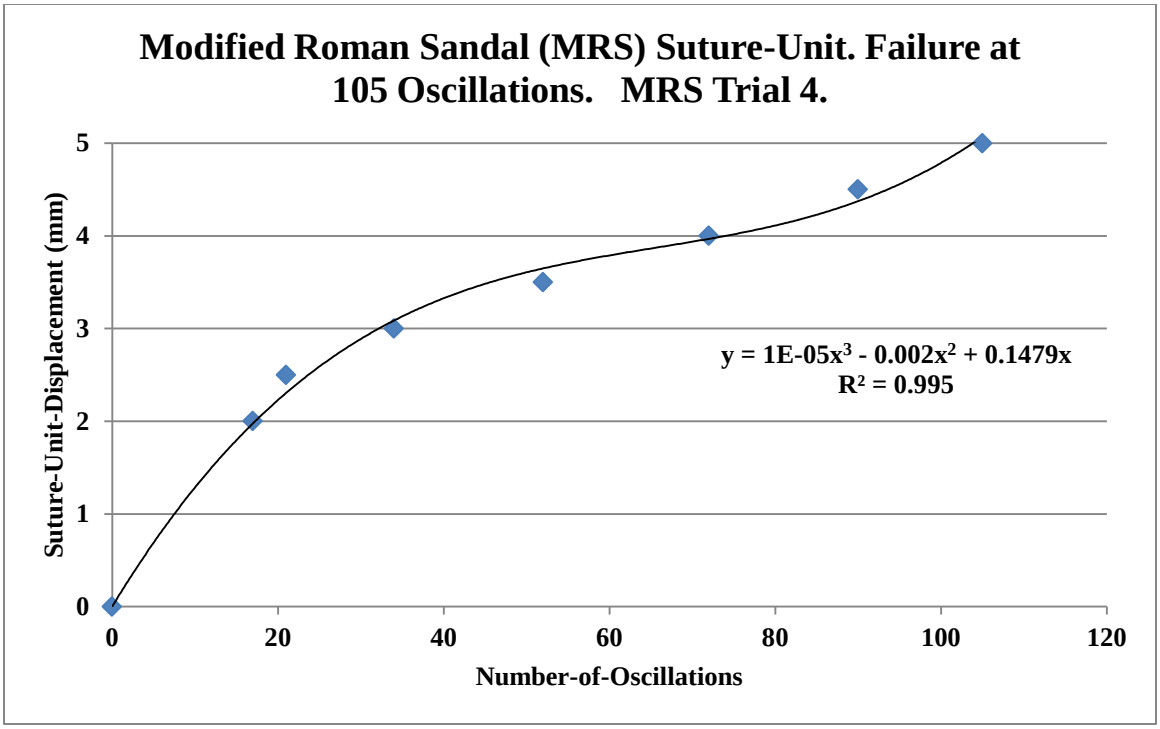

Chart 14: 4th MRS Experimental Trial. Failure occurred after 105 oscillations.

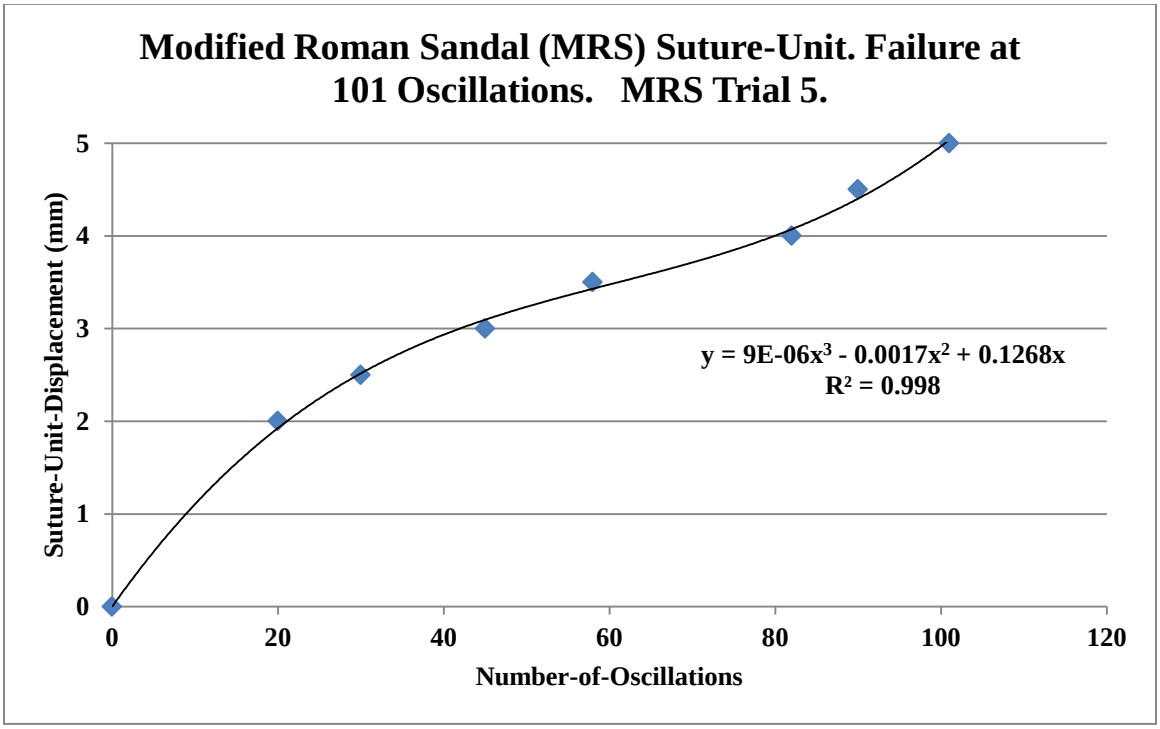

Chart 15: 5th MRS Experimental Trial. Failure occurred after 101 oscillations.

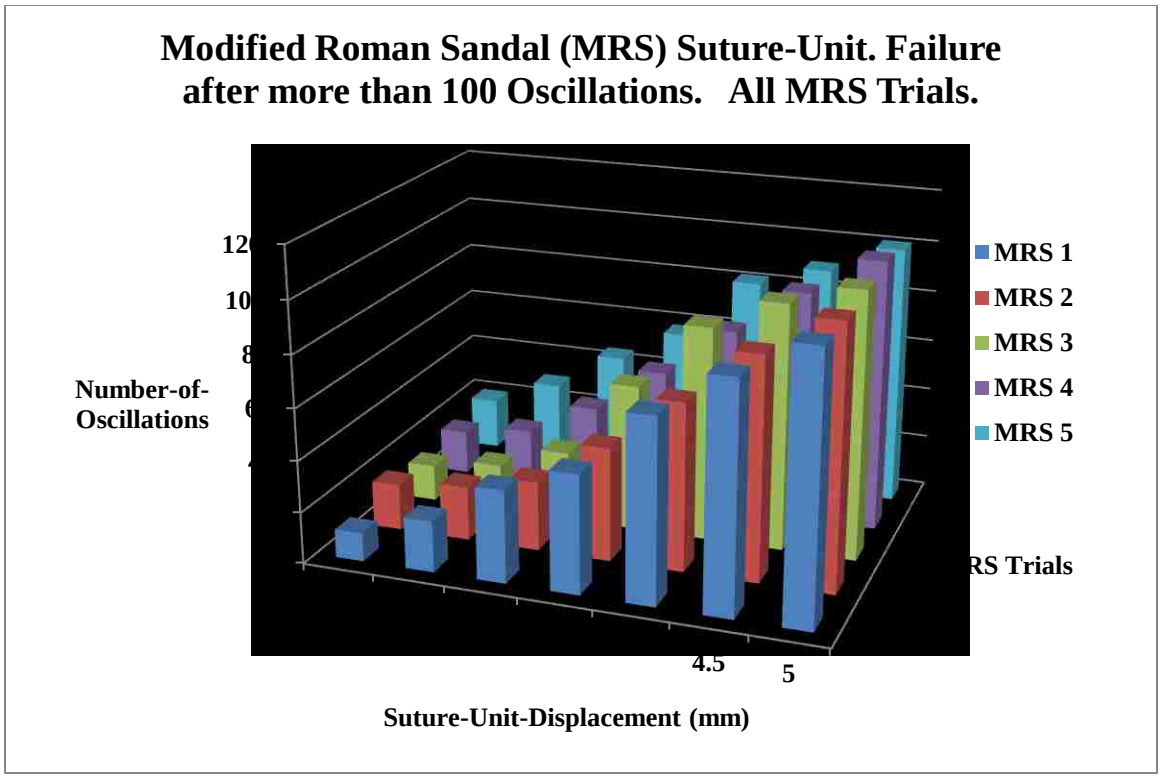

Chart 16: All MRS Experimental Trials.

During the initial displacements of the LB, only 16.8 oscillations on average were needed to reach a displacement of 2.0 mm. However, as the numbers of oscillations increased, it got more and more difficult for the MRS Suture-Units to slip along the drain. Looking at Chart 11 through Chart 15, one can see a general pattern. Up to circa 80 oscillations, the displacement of the Suture-Unit becomes harder and harder. Between 80 to 100 oscillations, the displacement of the Suture-Unit becomes slightly easier.

The following conclusions can be made in regards to the mechanical behavior of the MRS Suture-Units:

1) After fitting appropriate trend lines in each of these charts, it became clear that all of the samples behaved in a non-linear pattern. To be precise, they all followed the pattern of a third degree polynomial for the span covering the displacement of 0.0 mm to 5.0 mm. The Suture-Units reach the 2.0 mm displacement mark within 16.8 oscillations on average. However, the 4.0 mm displacement is reached around 72.6 oscillations. This shows that the Suture-Unit required approximately 3.3 times the Number-of-Oscillations to reach twice the first displacement. During the initial oscillation range, the second knot system loses its vertical position and folds back onto itself. This results in a *Suture-Unit-collapse* of about 2.0 mm as shown in Fig. 35. Moreover, in Fig. 35 one can see that the 0.5 mm spiral suture segments are no more visible and that they have collapsed.

   The collapse of the spiral segments were also observed during the initial oscillation range for each MRS experimental trial. Hence, the 2.0 mm mark is reached very quickly. It should be noted that the 2.0 mm displacement only applies to the LB up to this point with the UB not being displaced at all. The UB starts to become displaced once the LB and the red and green colored suture segments right above it, are in continuous contact with the UB.

2) During the experiments involving the MRS Suture-Units, it was observed that the segments below the Suture-Unit's second Knot-Unit became in permanent

contact with the segments above the second Knot-Unit. Judging from the results shown in Charts 11 through 15, as well as the behavior of the MRS Suture-Units during the experimental trials, the MRS Suture-Unit settles after the folding of the second Knot-Unit as well as the collapse of the spiral segments.

In other words, the collapsed configuration of the MRS holds a better grip onto the drain when compared to the original non-collapsed confirmation. This is because the lower and the upper suture segments, located beneath and above the second Knot-Unit, work as a unified unit once both of them touch the second Knot-Unit. Moreover, the upper suture segments act as a barrier to the movements of the lower suture segments and vice versa.

3) There are five additional horizontal circular suture segments involved in a MRS Suture-Unit when compared to the RS Suturing-Technique. Two of these segments are perfectly horizontal and are colored in green. The other two are also almost horizontal and are colored in red. The fifth segment is the UB. Together with the LB and the two half-turn spirals involved, these segments exert a frictional force on the drain that is 2.48 times (6.7/2.7, see the two bullets below) more than the frictional force that the drain experiences from the suture segments of the RS Suturing-Technique.

This is because the frictional forces between the suture segments and the drain's outer surface are dependent on the length of the suture segments, which are in direct contact with the drain's outer surface. Note that the length

of the suture segments, consecutively depends on the total number of turns that the suture-threads make around the drain. The more turns are made, the more suture-thread-length comes in contact with the drain. Careful accounting of the total number of turns involved in both techniques reveals the following:

- The suture segments involved in the RS make 2.7 turns around the drain.
- The suture segments involved in the MRS make 6.7 turns around the drain.

Note that the LBs of both Suture-Units make a 255.0° contact with the drain's outer surface. This results in a total of 0.7 turns, which is common to the LBs of both Suture-Units. Moreover, the two full-turn spiral segments of the RS Suture-Unit, collectively result in two complete turns around the drain's outer surface. Whereas the two half-turn spirals of the MRS Suture-Unit, collectively result in one complete turnaround the drain's outer surface.

4) The additional second Knot-Unit involved in the MRS Suture-Unit serves a special purpose. Together with the first Knot-Unit, it locks the thread-lengths of the LB and the lower red and green segments. By doing so the collapse of the spiral portion does not alter the initial tightness of these three segments of the MRS Suture-Unit.

However, the collapse of the spiral suture segments of the RS Suture-Unit results in the widening of the LB as well as the spiral segments incorporated within the RS Suture-Unit. This explains the extreme vulnerability of the RS Suturing-Technique's LB, which is only effective if the spiral segments of the

RS Suture-Unit preserve their original 3D configuration. Moreover, the thread-lengths of the UB, the upper red and green segments as well as the spiral segments of the MRS, are also fixed between the second and the third Knot-Units.

Since the spiral segments of the MRS Suture-Unit are not that lengthy, unlike the spiral segments of the RS Suture-Unit, their collapse, only minimally alters the lengths of the UB, and the upper red and green segments. With only a minimal change in length, only a very small loosening at the upper segments of the MRS Suture-Unit occurs. Therefore, a tight grip along these segments of the drain is still maintained. Note that a tight grip correlates to higher frictional forces between the drain's outer surface and the suture-threads.

The small loosening in the upper segments occurs gradually and reaches its peak around 80 oscillations. The *Suture-Unit-Displacement* becomes easier after this loosening-peak is reached. This is because the upper suture segments have a minutely looser grip around the drain's outer surface. With that, they exert a lower frictional force compared to the frictional force that they exerted on the drain's outer surface during the beginning stages of each experimental trial. This explains the easier *Suture-Unit-Displacement* patterns that are observable after circa 80 oscillations. See Charts 11 through 15.

Chart 16 is a superposition of the entire five MRS Suture-Unit experimental trials. This chart directly underlines the similarity of the mechanical behavior of all the five MRS Suture-Units under experimental conditions.

4-8 Conclusion

Displacement of surgical drains from their intended location of attachment can lead to postoperative complications. The location of attachment can be on a patient's skin or on his/her internal organs. After such displacements, which can either occur over long periods of time through normal oscillatory breathing motion or on accidental basis, the patients usually undergo a secondary operation so that a new drain can be placed at the correct location. The usual drain anchoring mechanisms involve the use of a common Suturing-Technique, namely the RS Suturing-Technique. This manuscript directly investigated the mechanical properties of the RS to determine the reliability and effectiveness of this Suturing-Technique. Furthermore, a second Suturing-Technique, namely a MRS Suturing-Technique was developed and investigated in this manuscript as well.

Under similar mechanical oscillatory loading conditions, on average, the RS Suture-Units failed only after one oscillation. However, the MRS Suture-Units failed after more than 100 oscillations. Furthermore, the average RS *Suture-Unit-Displacement/slippage* along the drain's outer surface was 9.0 mm, whereas the average MRS *Suture-Unit-Displacement/slippage* along the drain's outer surface was 5.0 mm.

The hypothesis of this work was to prove that the MRS Suturing-Technique is a more reliable and effective anchoring technique compared to the RS Suturing-Technique. Based on the above findings, the hypothesis of this manuscript has been validated.

CHAPTER 5

5-1 Inventors

1. Cyrus O. Abbasi B.S., University of New Mexico, Mechanical Engineering Department.
2. Tariq A. Khraishi PhD., University of New Mexico, Mechanical Engineering Department.
3. Bret Baack MD., University of New Mexico, Department of Plastic Surgery.

5-2 Title

Bi- or Quad Cantilevered Surgical Drain/Cantilever Systems.

5-3 Abstract

A new anchoring system is developed to securely attach surgical drains inside and/or outside of the human/animal body. The new anchoring system will make the herein designs superior to the existing designs [P1-P20]. The developed securing mechanisms are categorized in two different types. The first type is a bi-cantilevered and the second quad-cantilevered drain/cantilever system.

5-4 Background of the Invention

Surgical tubes are efficient and reliable means to extract or relocate unwanted bodily fluids from or within the body of patient after a surgery. For instant, after the removal of a cancerous tumor the remaining cavity is usually filled with bodily fluids such as blood that can cause infections and delay the healing process of the affected area. After employing the drains within or extending out of the body, they are held in place by suture-threads that are knotted around the surgical tube and then sutured to the skin or the surrounding health area.

Upon the constant respiration of the patient, the knots might loosen up and the drain can move and be displaced from its intended configuration. In case of drains attached to the skin of a patient, it has been reported that upon the natural respiratory motion of the patient's body the knots will loosen up within a period of 2 to 3 weeks. Furthermore, it has also been reported that upon accidental events (e.g. such as the drain getting stuck to a doorknob) the entire drain can be pulled out due to the rupture of the sutures or the anchoring skin/tissue. Hence, a second surgery will be needed to place a new drain.

The herein developed new drain/cantilever systems intend to address these natural and /or accidental securing complications. They will ensure a safer and more reliable placement and attachment of a surgical drain within or outside of a patient's body. The invention also includes its own specific packaging technique, which enables the surgeon to place the drain/cantilever system through a small skin/tissue incisions or natural body openings. It should be noted that the herein described drain/cantilever systems are applicable to most of the surgical drains and catheters available on the market.

5-5 Summary of the Invention

This document includes two types of the drain/cantilever systems that can be employed on surgical drains with either a circular or a rectangular cross-sectioned drain, namely a bi-cantilevered or a quad-cantilevered drain/cantilever system. Examples of these the bi-cantilevered and the quad-cantilevered drain/cantilever types are shown in Figs. 37 & 40 respectively.

The drain/cantilever systems are intended to be manufactured from biocompatible and flexible polymer material. Both drain/cantilever types can be utilized completely within the patient's body or extending from the body's interior and passing through the skin into its exterior surroundings or vice versa.

In the case of extension from the interior to the exterior of the body, both types can be inserted through the skin into the body from the outside environment or pulled out through the skin after being placed within the interior of the patient's body. The drains usually can -pass through the natural openings of the body or through the skin/tissue-incisions performed by the operating surgeon.

Naturally for large drain/cantilevers spans (see Figs. 37 & 40), the surgeon is restricted to larger natural openings or skin/tissue incisions. In order to address this restriction, a specific packaging technique for both the bi- or quad-cantilevers will be laid out. The packaged drain/cantilever systems will then reduce the span of the drain/cantilever system and enable the surgeon to insert the drain system through a small natural opening or skin/tissue incision. Specific design details about both drain/cantilever systems and their packaging are explained as follows.

5-5-1 'Bi-Cantilevered' Drain/Cantilever System, 'Circular-Shaped' Drain

As illustrated in Fig. 37, this design is composed of a circular surgical drainage tube (divided in Sections 1 & 2) and two extruding rectangular-shaped cantilevers. Sections 1 & 2 have an external diameter of 7.0 mm and a uniform thickness of 2.0 mm. Section 1 depicts the top-end (usually external to the body) of the drain which serves as an outlet for the drained fluid. An illustrative representative extension of section 1 is shown in Fig. 43. Section 2 is the low-end (usually internal to the body) of the drain which serves as an inlet for the drained fluid. An illustrative representative extension of section 2 is shown in Fig. 44. Note that sections 1 & 2 can be of any arbitrary length. Section 2 contains a series of holes that are each 1.0 cm apart (see Fig. 44). Each extruded rectangular-shaped cantilever is 5.0 cm-long and composed of a proximal short segment and a distal long segment (see Fig. 45).

As illustrated in Fig. 45 the inherent angles between the drain and the cantilevers are 90 °. However, the drain/cantilever system can be attached to skin/tissue surfaces that are not necessarily perpendicular to the longitudinal axis of the drain. The purpose of the shorter proximal segment is to provide the drain/cantilever system the necessary degree of flexibility, which allows it to be attached to non-perpendicular supporting surfaces. The proximal segments give the cantilevers rotational flexibility about their longitudinal axes as well. It has a length, width and depth of 3.0 mm, 4.0 mm and 3.0 mm respectively. The longer distal segment contains five 2.0 mm-diameter holes, which serve as a passage for sutures that anchor the drain/cantilever system to the skin/tissue. The distal segment has a length, width and depth of 4.7 cm, 6.0 mm and 3.0 mm respectively. The five holes embedded in the proximal cantilever

segment are spaced 1 cm away from each other. The surgeon can also use them as a convenient location for trimming the length of the cantilevers if necessarily. Based on the flexible nature of the cantilevers, they can easily be stitched to a planar and non-planar underlying skin/tissue surface.

In order to minimize the span of the drain/cantilever system (see Fig. 37), the cantilevers can be wrapped up around the drain and held in place via a thin plastic wrap (See Fig. 46). This packing technique allows the drain/cantilever system to be placed through the skin/tissue incisions or natural body openings with diameters/lengths several times shorter than the fully extended span of the two cantilevers. After the placement of the drain/cantilever system, the plastic wrap can be easily cut through and removed by the surgeon. The cantilevers can then be opened and stitched to the underlying skin/tissue surface.

Two other alternative bi-cantilevered designs have also been developed for a drain/cantilever system with a circular drain. Alternative one (See Fig. 49) possesses cantilevers that have the shape of a quarter-circle. Alternative two (See Fig. 52) possesses cantilevers with a semicircular shape. Also note that other alternatives can be achieved by utilizing a combination of a rectangular, quarter-circular, semicircular cantilevers and/or cantilevers having a shape anywhere from a rectangle to a in the design of a bi-cantilevered drain/cantilever system with a circular drain. All of these alternative designs also possess the rotational flexibility of their cantilevers, which arises due to the proximal sections of the cantilevers. Analogous to the petals of a blossom that are wrapped around each other, all non-rectangular cantilevers of these

alternative designs can also be wrapped around the drain and packaged within a plastic wrap as well.

All the holes have a diameter of 2.0 mm. Holes around the perimeter of the cantilevers are 4.0 mm away from the perimeter of the cantilever measured from their centers (see Figs. 49 & 52). They are also 1.0 cm apart from each other measured from their centers. Only two holes are 0.5 cm apart measured from their centers, which are placed in the middle of the quad-circular or semicircular cantilevers. These two holes sweep through the entire radial span of the quad-circular or semicircular cantilevers (see Figs. 49 & 52).

5-5-2 'Bi-Cantilevered' Drain/Cantilever System, 'Rectangular-Shaped' Drain

All the three previously described bi-cantilevered designs can also be applied to a drain/cantilever system with a rectangular-shaped drain. Fig 55 illustrates a bi-cantilevered drain/cantilever system with two rectangular-shaped cantilevers extruding from the rectangular drain. The exterior base and the width of the rectangular surgical tube are 1.0 cm and 7.0 mm reactively. It has a uniform thickness of 2.0 mm all around. The rectangular drain is also composed of two sections. Similar to the bi-cantilevered system demonstrated above, section 1 depicts the top-end (usually external to the body) of the drain which serves as an outlet for the drained fluid. Section 2 is the low-end (usually internal to the body) of the drain which serves as an inlet for the drained fluid. The dimensions of the cantilevers and their proximal and distal segments are the same as the bi-cantilevered system outlined above. Fig 58 illustrates a fully packaged bi-cantilevered drain/cantilever.

Two alternative bi-cantilevered designs have been developed for the rectangular drain/cantilever system as well. Alternative one (See Fig. 61) shows cantilevers that have the shape of a quarter-circle. Alternative two (See Fig. 64) possesses cantilevers with a semicircular shape. Other alternatives can also be employed where a mixed combination of rectangular, quarter-circular, semicircular cantilevers or cantilevers having a shape anywhere from a rectangle to a semicircle are attached to the base, width of rectangular-shaped drain. All of the designs also possess the rotational flexibility, which arises due to the proximal sections of the cantilevers. Similar to the petal of a flower, all non-rectangular cantilevers of these alternative designs can be wrapped around the drain and packaged within a plastic wrap as well. Note that the

above described cantilevers within this section have been extruded from the base of the rectangular drain (see Figs. 55 to 66). Alternatively the cantilevers can be extruded from the width of the rectangular drain (see Figs. 67 to 75).

Similar to the previous designs, the holes have a diameter of 2.0 mm. Holes around the perimeter of the cantilevers are 4.0 mm away from the perimeter of the cantilever measured from their centers. They are also 1.0 cm apart from each other measured from their centers. Only two holes are 0.5 cm apart measured from their centers, which are placed in the middle of the quad-circular or semicircular cantilevers. These two holes sweep through the entire radial span of the quad-circular or semicircular cantilevers.

5-5-3 'Quad-Cantilevered' Drain/Cantilever System, 'Circular-Shaped' Drain

As illustrated in Fig. 76 (identical to Fig. 40 and inserted here again for convenience), this design is composed of a circular surgical drainage tube and four rectangular-shaped extruding cantilevers. Each of the cantilevers possesses the same dimensions and components as discussed for the bi-cantilevered drain/cantilever systems. Similar to a bi-cantilevered drain/cantilever system, the quad-cantilevered drain/cantilever system can also be packaged as shown in Fig. 76.

One alternative quad-cantilevered design has been developed herein as well. Fig. 80 shows cantilevers that have the shape of a quarter-circle. Also note that other alternatives can be achieved by utilizing a combination of a rectangular, quarter-circular and/or cantilevers having a shape anywhere from a rectangle to a quarter-circle in the design of a quad-cantilevered drain/cantilever system with a circular drain. This design also possesses the rotational flexibility, which arises due to the rectangular beginning-section of the cantilevers. Similar to the petal of a flower, all cantilevers of the alternative designs can be wrapped around the drain and packaged within a plastic wrap as well.

All the holes have a diameter of 2.0 mm. Holes around the perimeter of the cantilevers are 4.0 mm away from the perimeter of the cantilever measured from their centers. They are also 1.0 cm apart from each other measured from their centers. Only two holes are 0.5 cm apart measured from their centers, which are placed in the middle of the quad-circular or semicircular cantilevers. These two holes sweep through the entire radial span of the quad-circular or semicircular cantilevers.

5-5-4 'Quad-Cantilevered' Drain/Cantilever System, 'Rectangular-Shaped' Drain

As illustrated in Fig. 83, this design is composed of a rectangular surgical drainage tube and four rectangular-shaped extruding cantilevers. Each of the cantilevers possesses the same dimensions and components as discussed for the bi-cantilevered drain/cantilever systems.

One alternative quad-cantilevered design has been developed herein as well. Fig. 86 shows cantilevers that have the shape of a quarter-circle. Also note that other alternatives can be achieved by utilizing a combination of a rectangular, quarter-circular and/or cantilevers having a shape anywhere from a rectangle to a quarter-circle in the design of a quad-cantilevered drain/cantilever system with a rectangular drain. This design also possesses the rotational flexibility, which arises due to the rectangular beginning-section of the cantilevers. Similar to the petal of a flower, both cantilevers of the alternative designs can be wrapped around the drain and packaged within a plastic wrap as well.

All the holes have a diameter of 2.0 mm. Holes around the perimeter of the cantilevers are 4.0 mm away from the perimeter of the cantilever measured from their centers. They are also 1.0 cm apart from each other measured from their centers. Only two holes are 0.5 cm apart measured from their centers, which are placed in the middle of the quad-circular or semicircular cantilevers. These two holes sweep through the entire radial span of the quad-circular or semicircular cantilevers.

5-5-5 Additional Details about the Designs

Fillets: All of the fillets at corners of the cantilevers of all shapes have a radius of 3.0 mm. All of the fillets at the intersections of the drains (circular and square) and the proximal segments of the cantilevers (all shapes) are 1.0 mm in radius. All the fillets at the transition zones between the proximal and the distal sections of the cantilevers have a radius of 1.0 mm.

Design Dimensions: It should be noted that all the above mentioned dimensions are for illustrative purposes only and can be changed according to the different utilities of the drain/cantilever systems, i.e. different types of surgeries, locations of attachment, drainage volume and the properties of its polymer material, etc.

5-6 Claims

5-6-1 First Claim

A bi-cantilevered surgical drain/cantilever system with a circular drain and two flexible cantilevers is designed. It can be utilized for the drainage of unwanted bodily fluids or the insertion of medication into the body. The two cantilevers can be of a rectangular, quarter-circular, semicircular shape or of a shape that is swept around the longitudinal axis of the drain anywhere from the shape a rectangle to the shape of a semicircle. The cantilevers are extruded out of the circular drain and thence one part with the drain. The cantilevers are utilized as a secure means of attachment of the drain to the patient's skin or tissue. This drain/cantilever system can be utilized interior or exterior to the patient’s body. Due to the specific packaging technique of the drain/cantilever system, it can be placed through skin/tissue incisions or natural openings several times smaller than the fully spanned drain/cantilever system. Excessive strain on natural openings and the introduction of large incisions of the skin/tissue are minimized or prevented on this way. The bi-cantilevered surgical drain/cantilever system with a circular drain and two flexible cantilevers can be applied to most types of currently available circular drains in order to provide a more reliable anchoring mechanism.

5-6-2 Second Claim

A bi-cantilevered surgical drain/cantilever system with a rectangular drain and two flexible cantilevers is designed. It can be utilized for the drainage of unwanted bodily fluids or the insertion of medication into the body. The two cantilevers can be of a rectangular, quarter-circular, semicircular shape or of a shape that is swept around the longitudinal axis of the drain anywhere from the shape a rectangle to the shape of a semicircle. The cantilevers are extruded out of the circular drain and thence one part with the drain. The cantilevers are utilized as a secure means of attachment of the drain to the patient's skin or tissue. This drain/cantilever system can be utilized interior or exterior to the patient’s body. Due to the specific packaging technique of the drain/cantilever system, it can be placed through skin/tissue incisions or natural openings several times smaller than the fully spanned drain/cantilever system. Excessive strain on natural openings and the introduction of large incisions of the skin/tissue are minimized or prevented on this way. The bi-cantilevered surgical drain/cantilever system with a rectangular drain and two flexible cantilevers can be applied to most types of currently available rectangular drains in order to provide a more reliable anchoring mechanism.

5-6-3 Third Claim

A quad-cantilevered surgical drain/cantilever system with a circular drain and four flexible cantilevers is designed. It can be utilized for the drainage of unwanted bodily fluids or the insertion of medication into the body. The four cantilevers can be of a rectangular, quarter-circular or of a shape that is swept around the longitudinal axis of the drain anywhere from the shape a rectangle to the shape of a quarter-circle. The cantilevers are extruded out of the circular drain and thence one part with the drain. The cantilevers are utilized as a secure means of attachment of the drain to the patient's skin or tissue. This drain/cantilever system can be utilized interior or exterior to the patient’s body. Due to the specific packaging technique of the drain/cantilever system, it can be placed through skin/tissue incisions or natural openings several times smaller than the fully spanned drain/cantilever system. Excessive strain on natural openings and the introduction of large incisions of the skin/tissue are minimized or prevented on this way. The quad-cantilevered surgical drain/cantilever system with a circular drain and four flexible cantilevers can be applied to most types of currently available circular drains in order to provide a more reliable anchoring mechanism.

5-6-4 Forth Claim

A quad-cantilevered surgical drain/cantilever system with a rectangular drain and four flexible cantilevers is designed. It can be utilized for the drainage of unwanted bodily fluids or the insertion of medication into the body. The four cantilevers can be of a rectangular, quarter-circular or of a shape that is swept around the longitudinal axis of the drain anywhere from the shape a rectangle to the shape of a quarter-circle. The cantilevers are extruded out of the rectangular drain and thence one piece with the drain. The cantilevers are utilized as a secure means of attachment of the drain to the patient's skin or tissue. This drain/cantilever system can be utilized interior or exterior to the patient’s body. Due to the specific packaging technique of the drain/cantilever system, it can be placed through skin/tissue incisions or natural openings several times smaller than the fully spanned drain/cantilever system. Excessive strain on natural openings and the introduction of large incisions of the skin/tissue are minimized or prevented on this way. The quad-cantilevered surgical drain/cantilever system with a rectangular drain and four flexible cantilevers can be applied to most types of currently available circular drains in order to provide a more reliable anchoring mechanism.

5-7 Figures

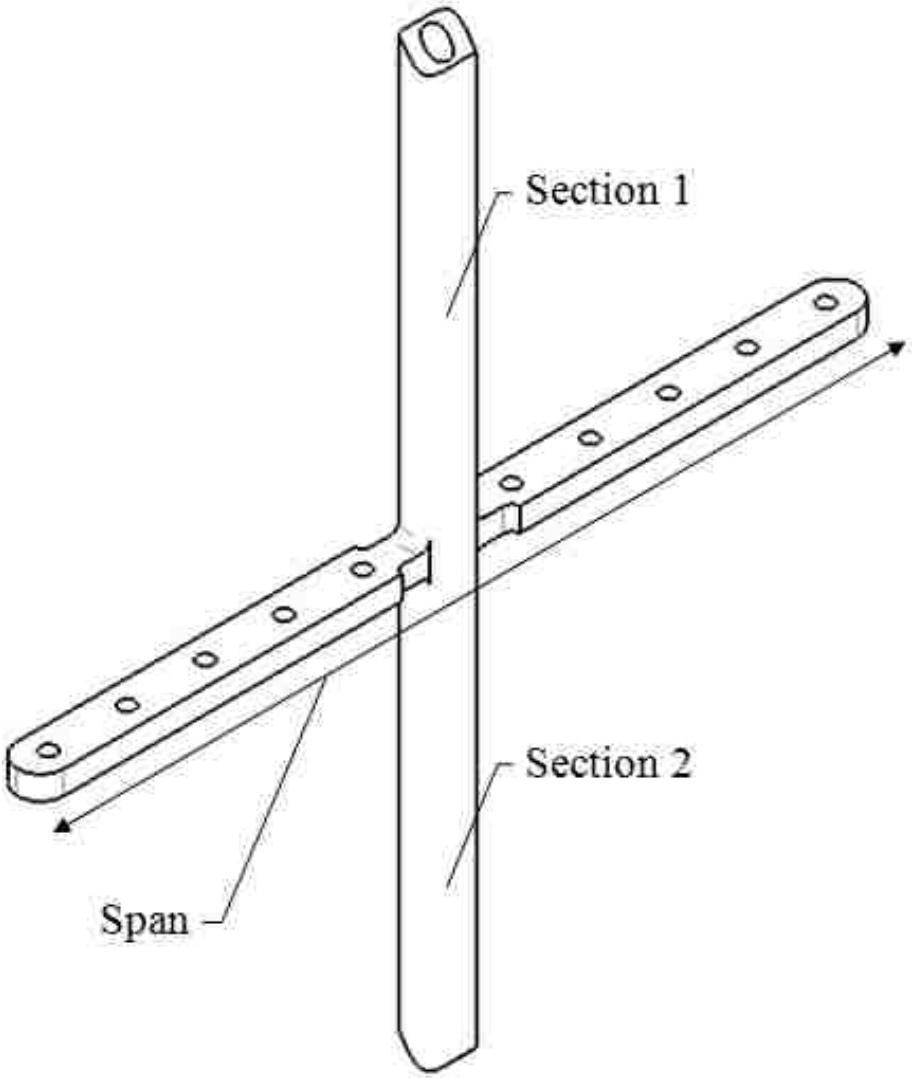

Figure 37: Isometric View. Bi-Cantilevered Drain/Cantilever System composed of a Circular Drain and two Rectangular-shaped Cantilevers. An Example of the First Drain/Cantilever System Type.

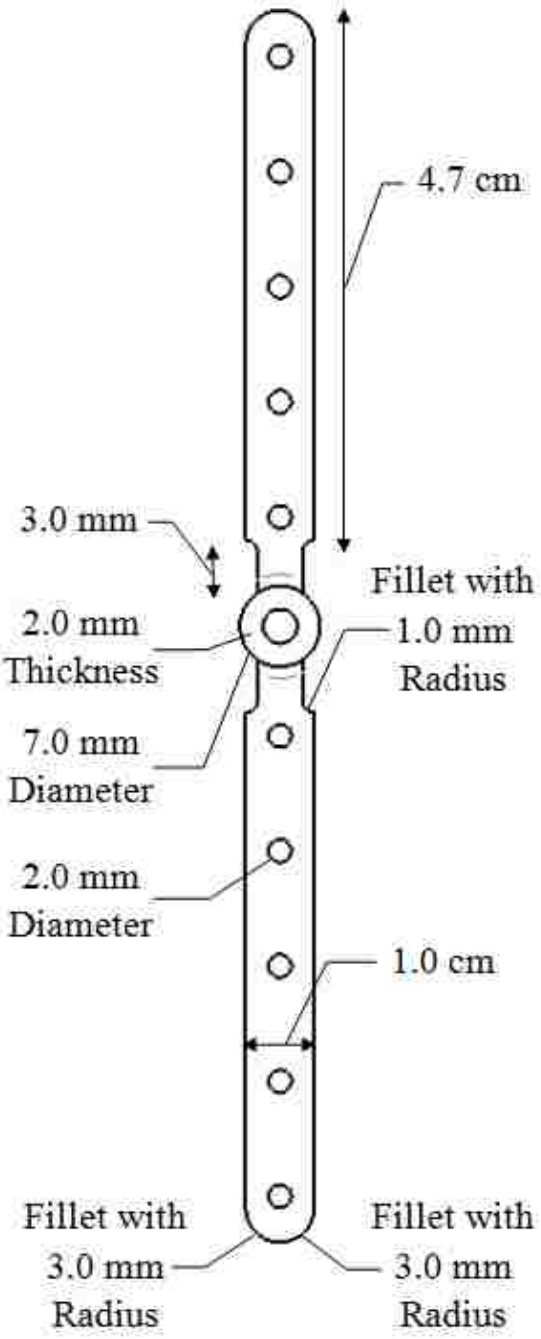

Figure 38: Top View. Bi-Cantilevered Drain/Cantilever System composed of a Circular Drain and two Rectangular-shaped Cantilevers.

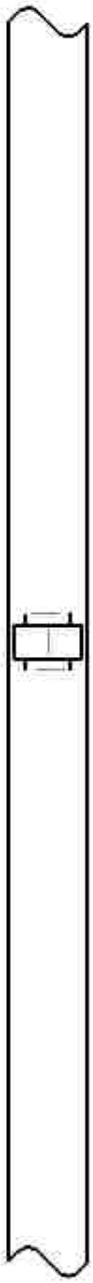

Figure 39: Side View. Bi-Cantilevered Drain/Cantilever System composed of a Circular Drain and two Rectangular-shaped Cantilevers.

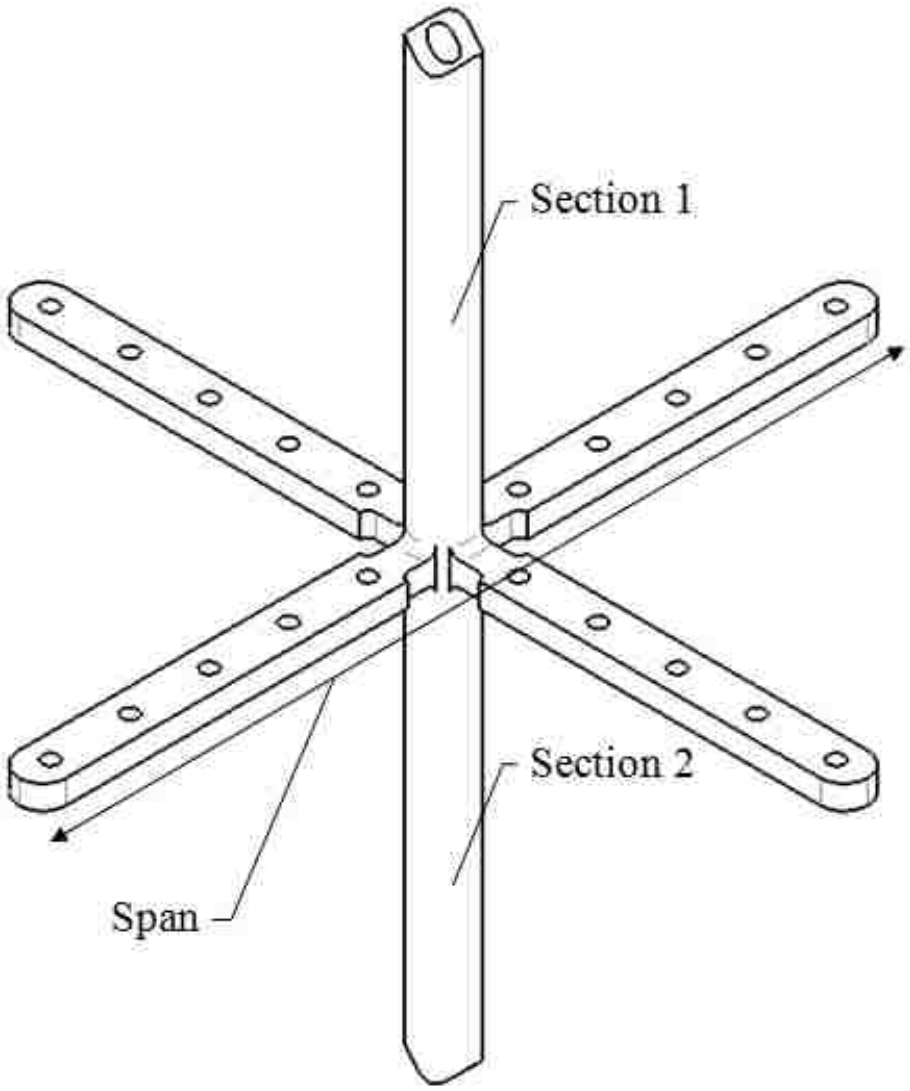

Figure 40: Isometric View. Example of Quad-Cantilevered Drain/Cantilever System composed of a Circular Drain and four Rectangular-shaped Cantilevers. An Example of the Second Drain/Cantilever System Type.

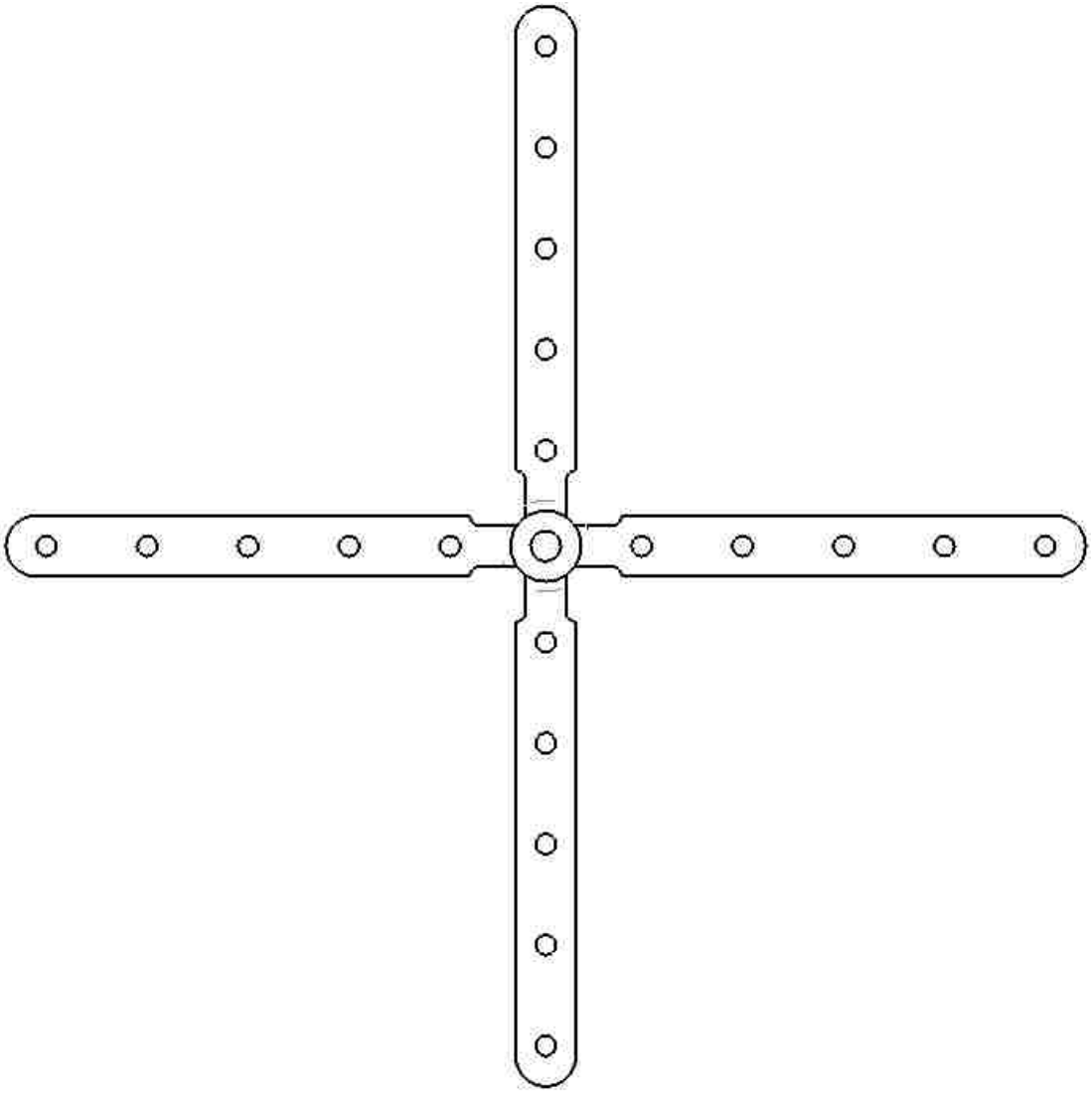

Figure 41: Top View. Quad-Cantilevered Drain/Cantilever System composed of a Circular Drain and four Rectangular-shaped Cantilevers.

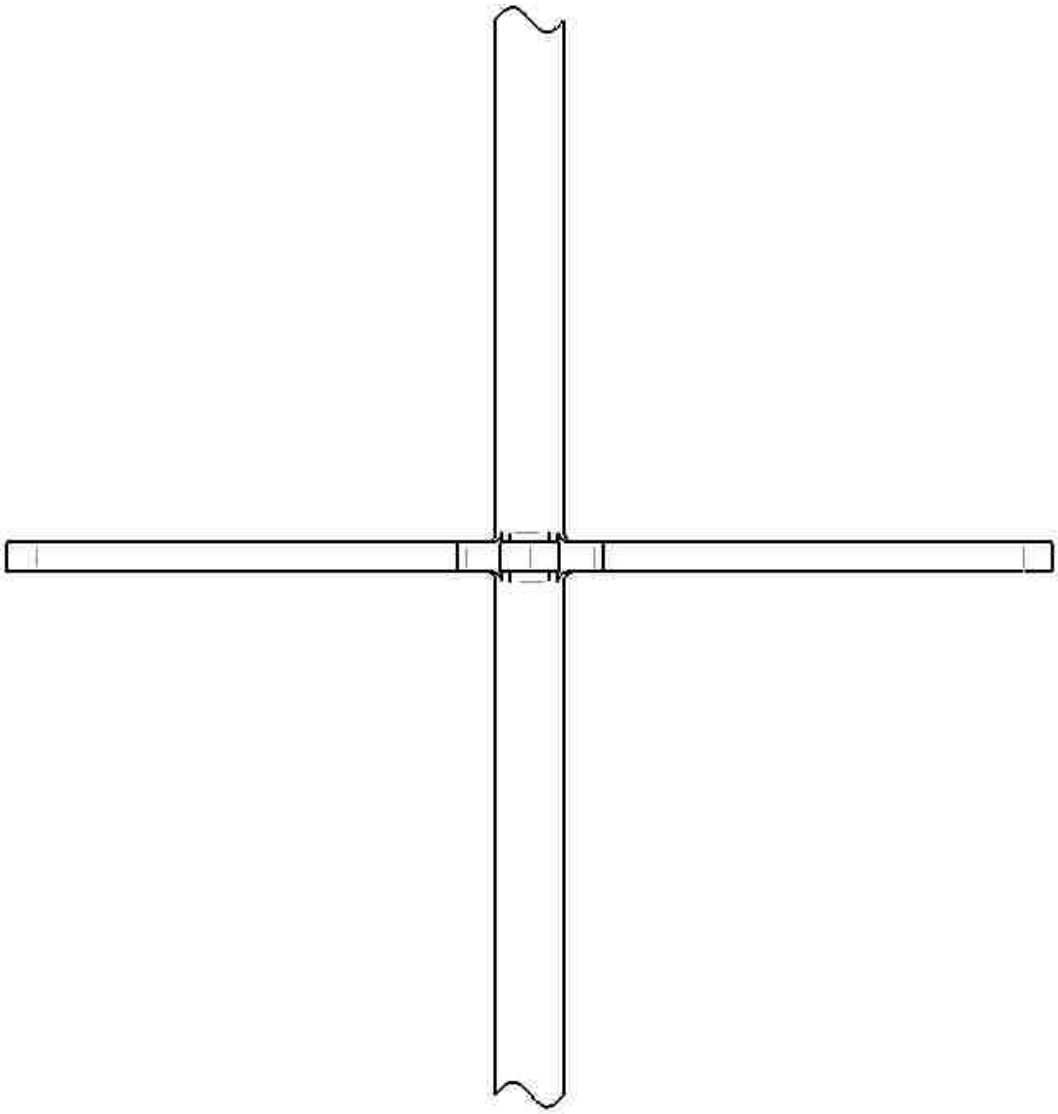

Figure 42: Side View. Quad-Cantilevered Drain/Cantilever System composed of a Circular Drain and four Rectangular-shaped Cantilevers.

Figure 43: Isometric View. Illustrative representative of the extension of Section 1.

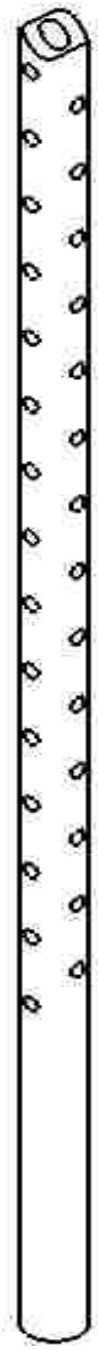

Figure 44: Isometric View. Illustrative representative of the extension of Section 2.

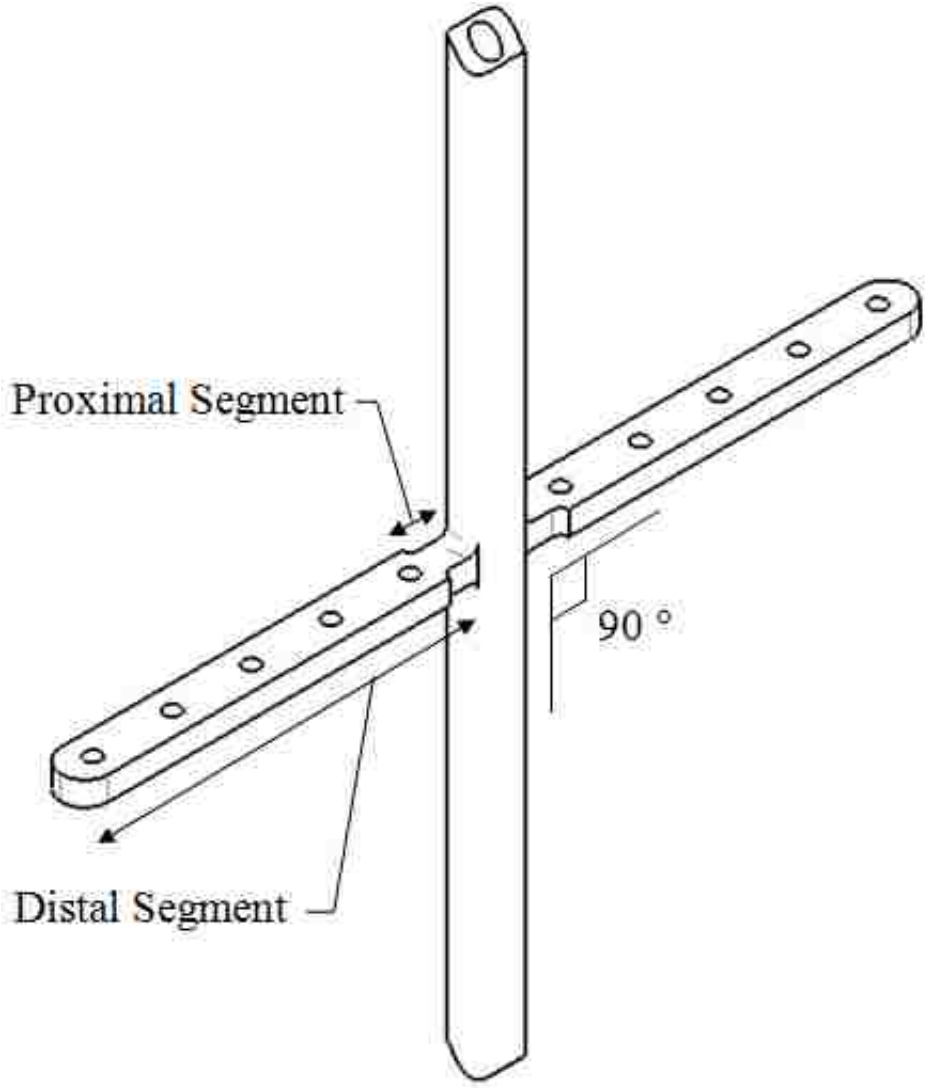

Figure 45: Isometric View. Bi-Cantilevered Drain/Cantilever System with a Circular Drain, showing the Proximal and Distal segments of the Rectangular-shaped Cantilevers.

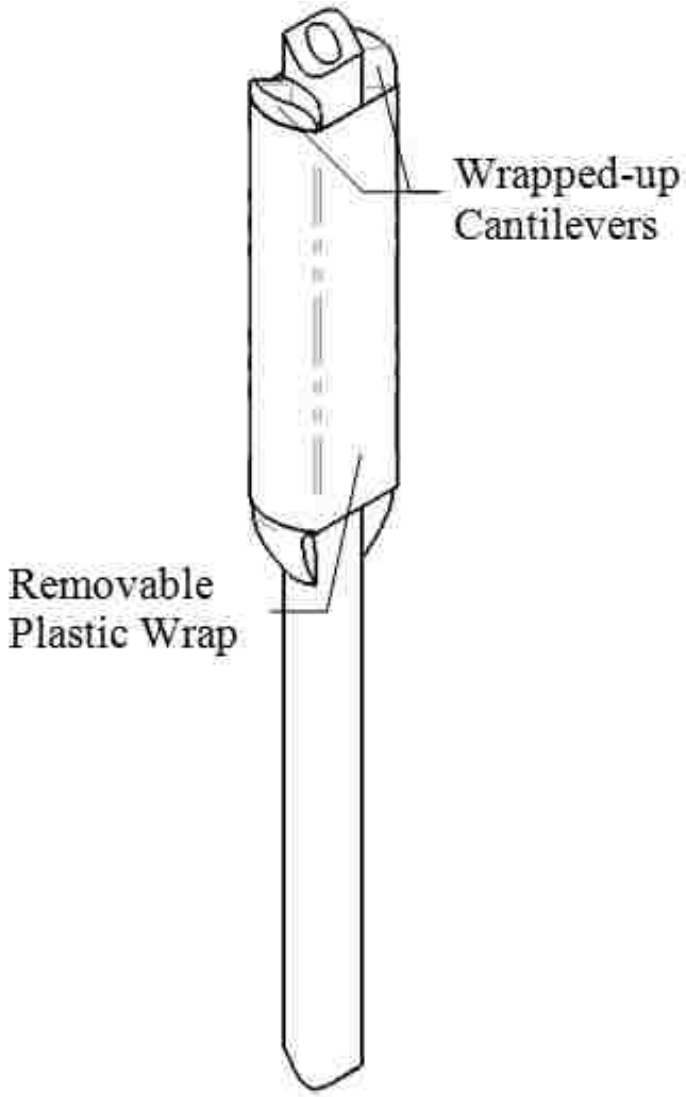

Figure 46: Isometric View. Packaging of the Bi-Cantilevered Drain/Cantilever System with a Circular Drain, via a Removable Plastic Wrap.

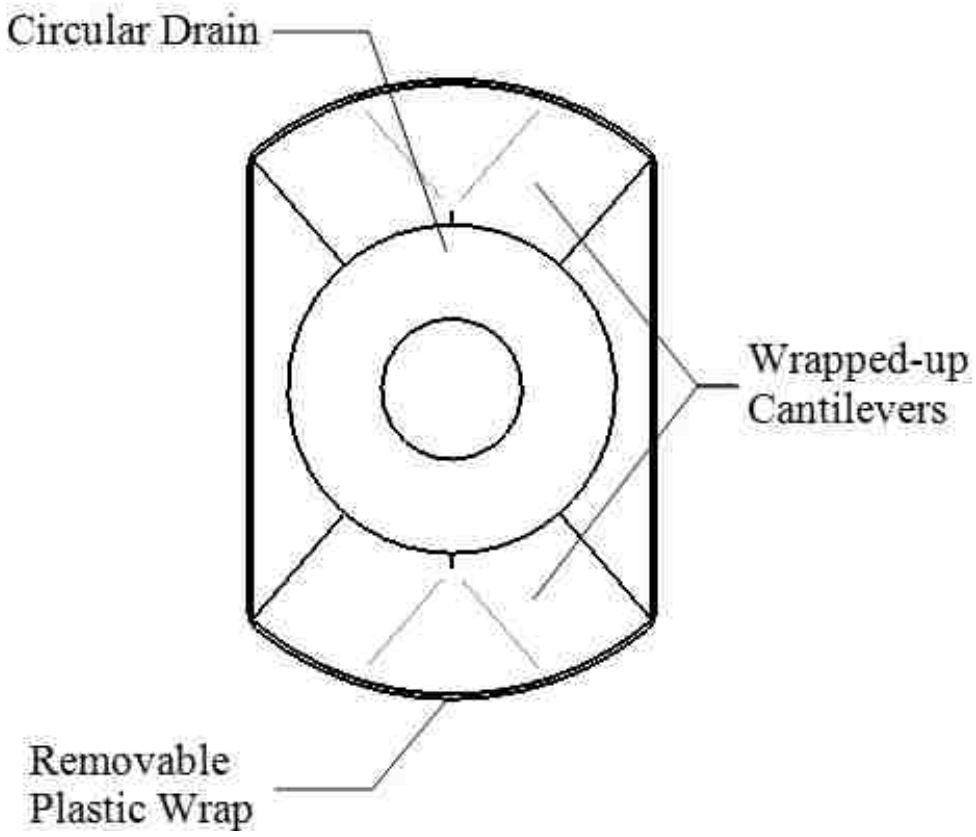

Figure 47: Enlarged Top View. Packaging of the Bi-Cantilevered Drain/Cantilever System with a Circular Drain, via a Removable Plastic Wrap.

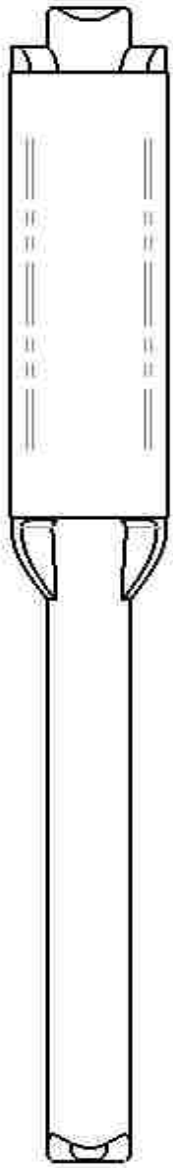

Figure 48: Side View. Packaging of the Bi-Cantilevered Drain/Cantilever System with a Circular Drain, via a Removable Plastic Wrap.

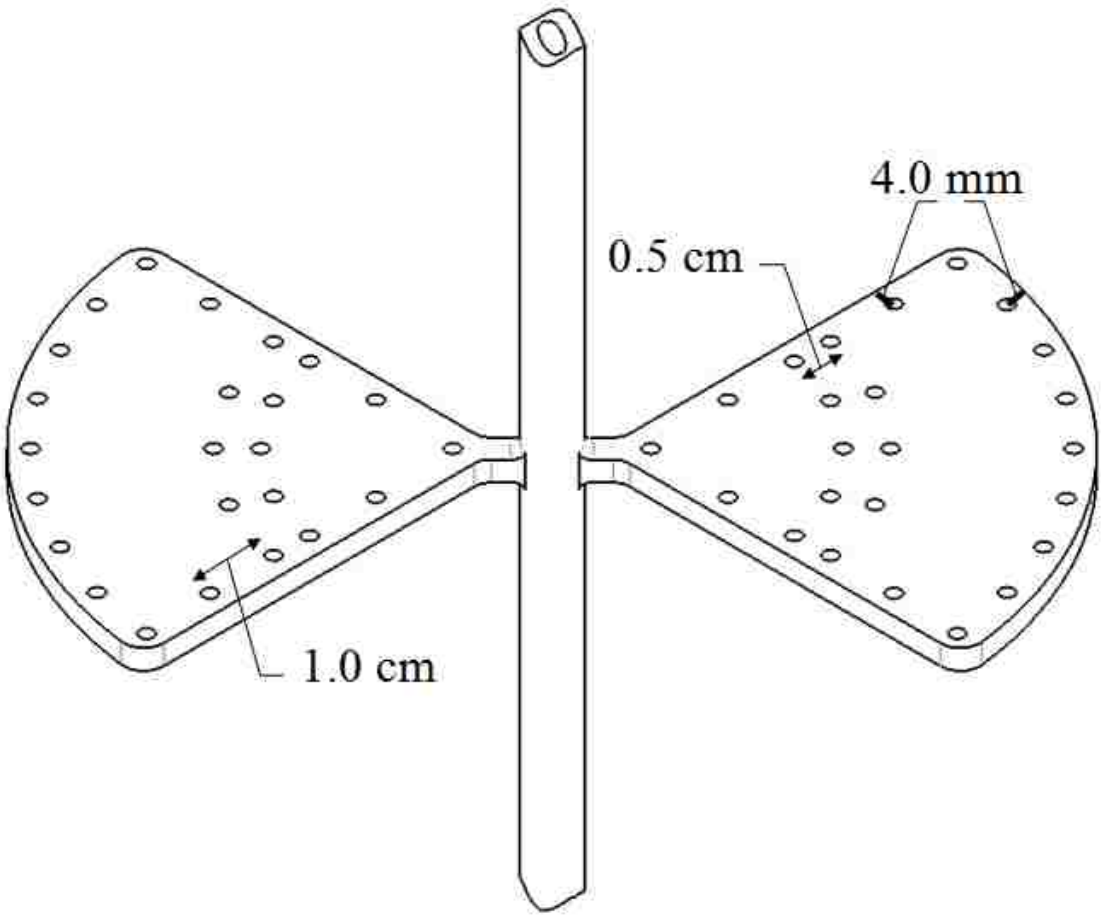

Figure 49: Isometric View. Bi-Cantilevered Drain/Cantilever System composed of a Circular Drain and two Quarter-Circular-shaped Cantilevers.

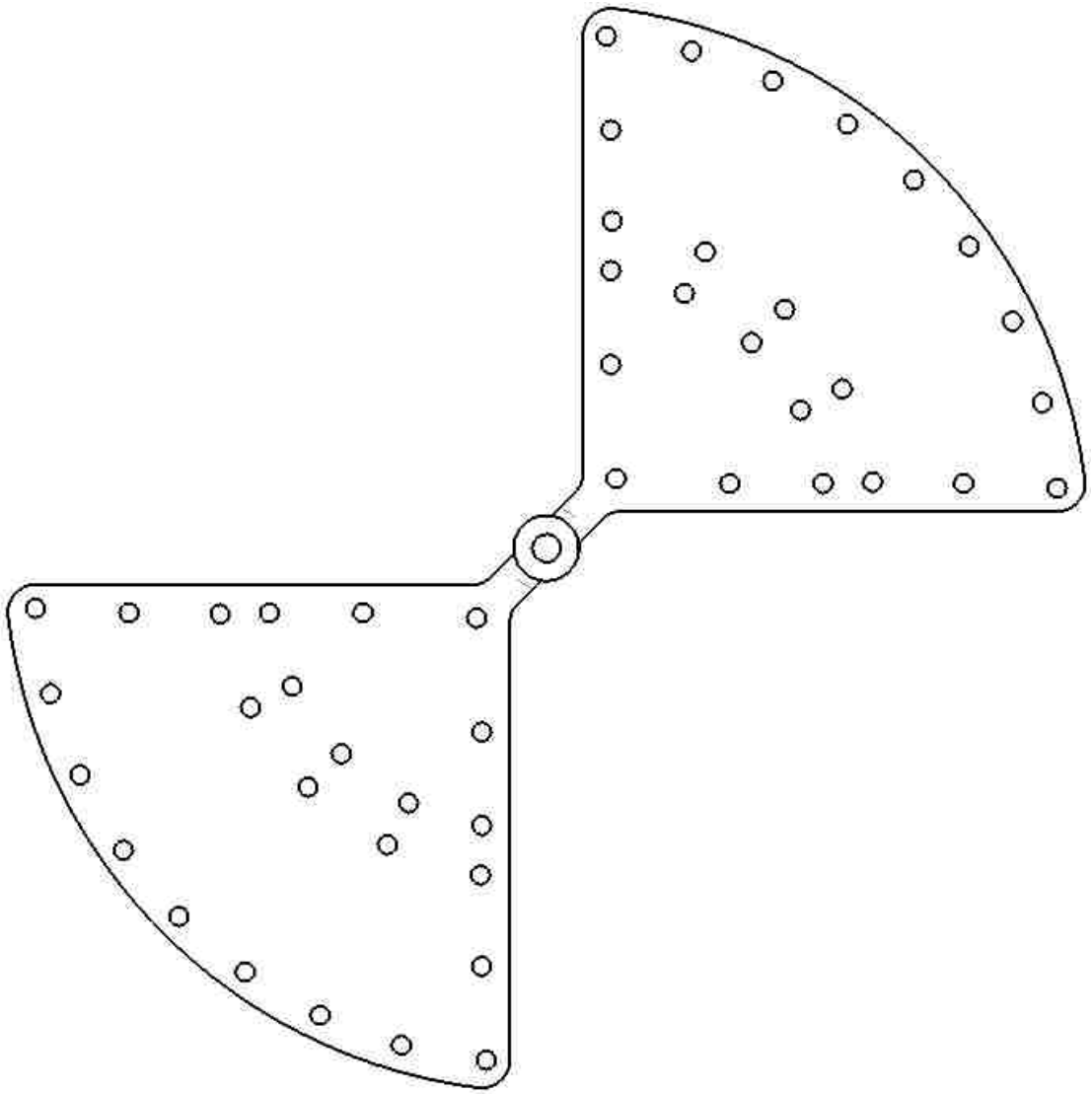

Figure 50: Top View. Bi-Cantilevered Drain/Cantilever System composed of a Circular Drain and two Quarter-Circular-shaped Cantilevers.

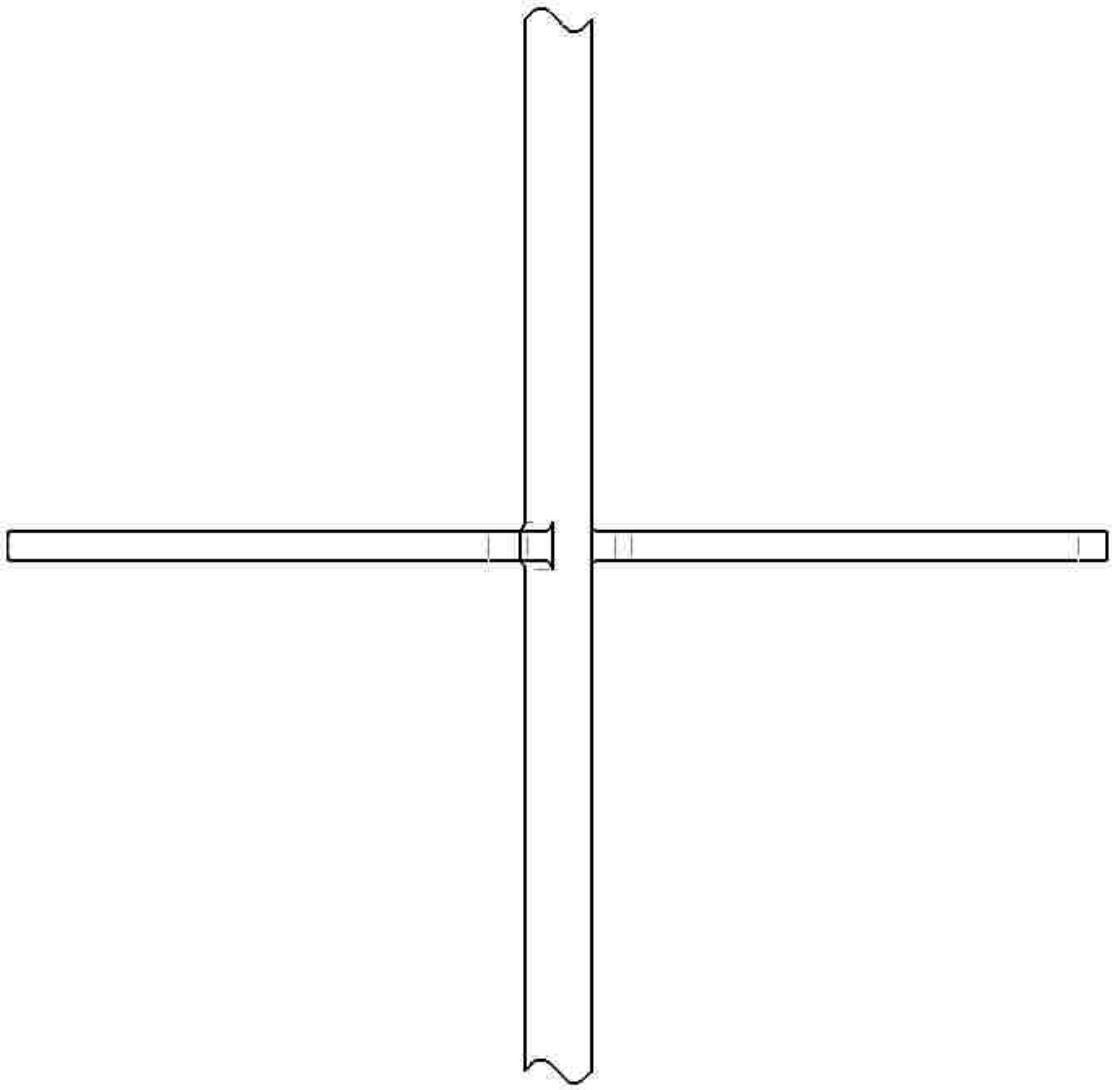

Figure 51: Side View. Bi-Cantilevered Drain/Cantilever System composed of a Circular Drain and two Quarter-Circular-shaped Cantilevers.

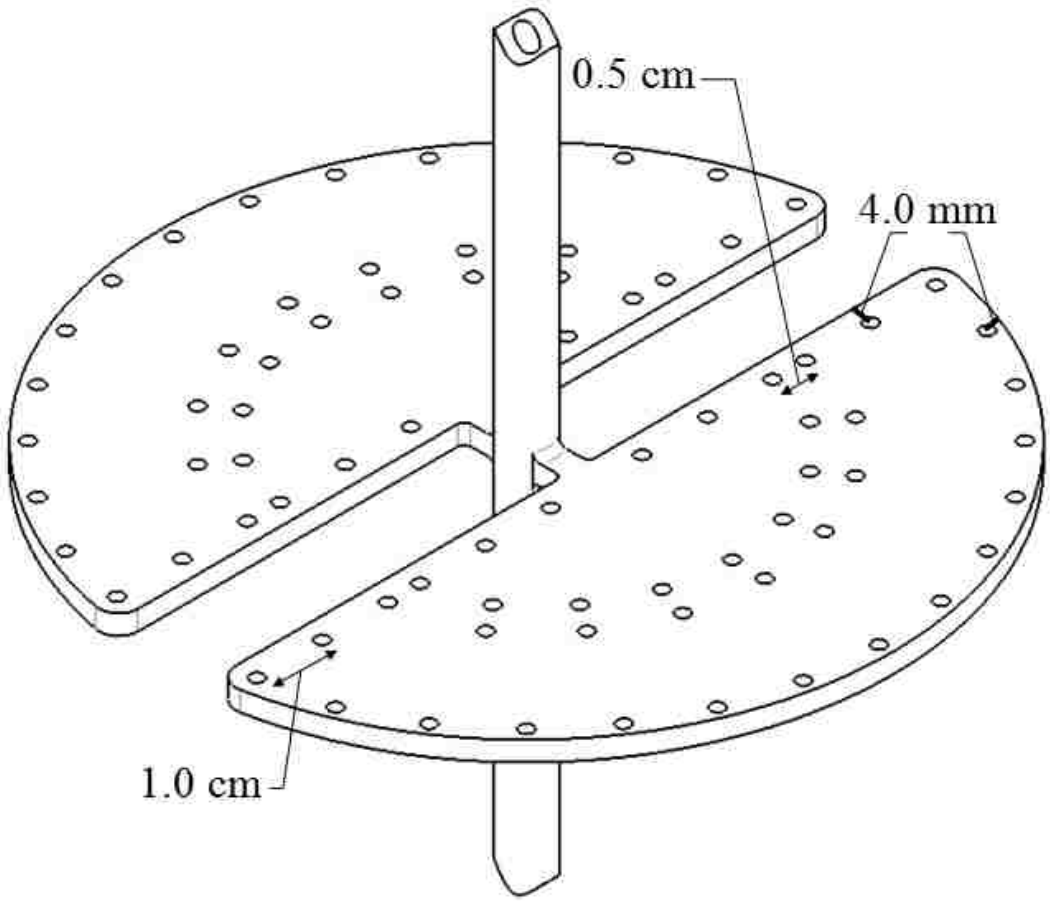

Figure 52: Isometric View. Bi-Cantilevered Drain/Cantilever System composed of a Circular Drain and two Quarter-Circular-shaped Cantilevers.

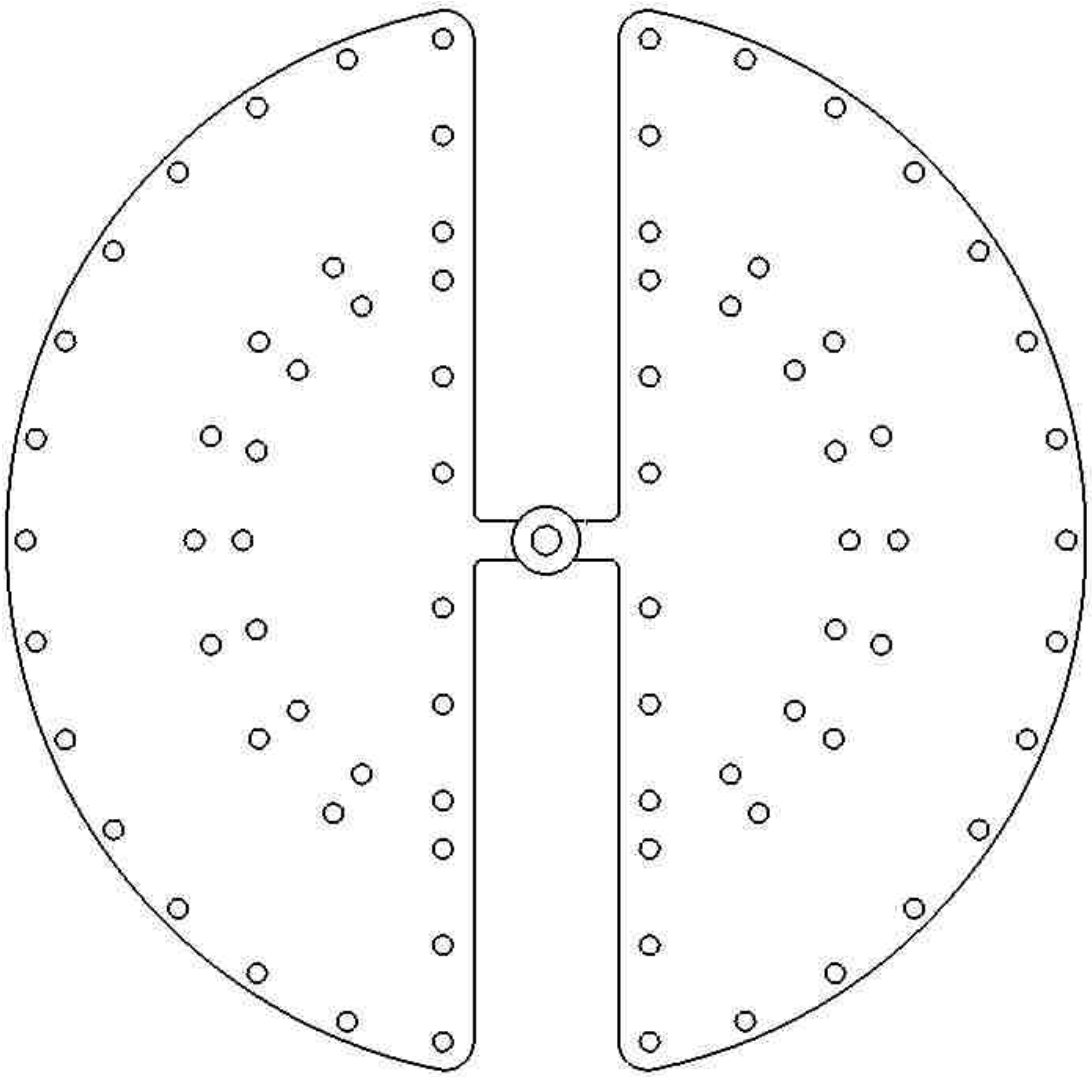

Figure 53: Top View. Bi-Cantilevered Drain/Cantilever System composed of a Circular Drain and two Quarter-Circular-shaped Cantilevers.

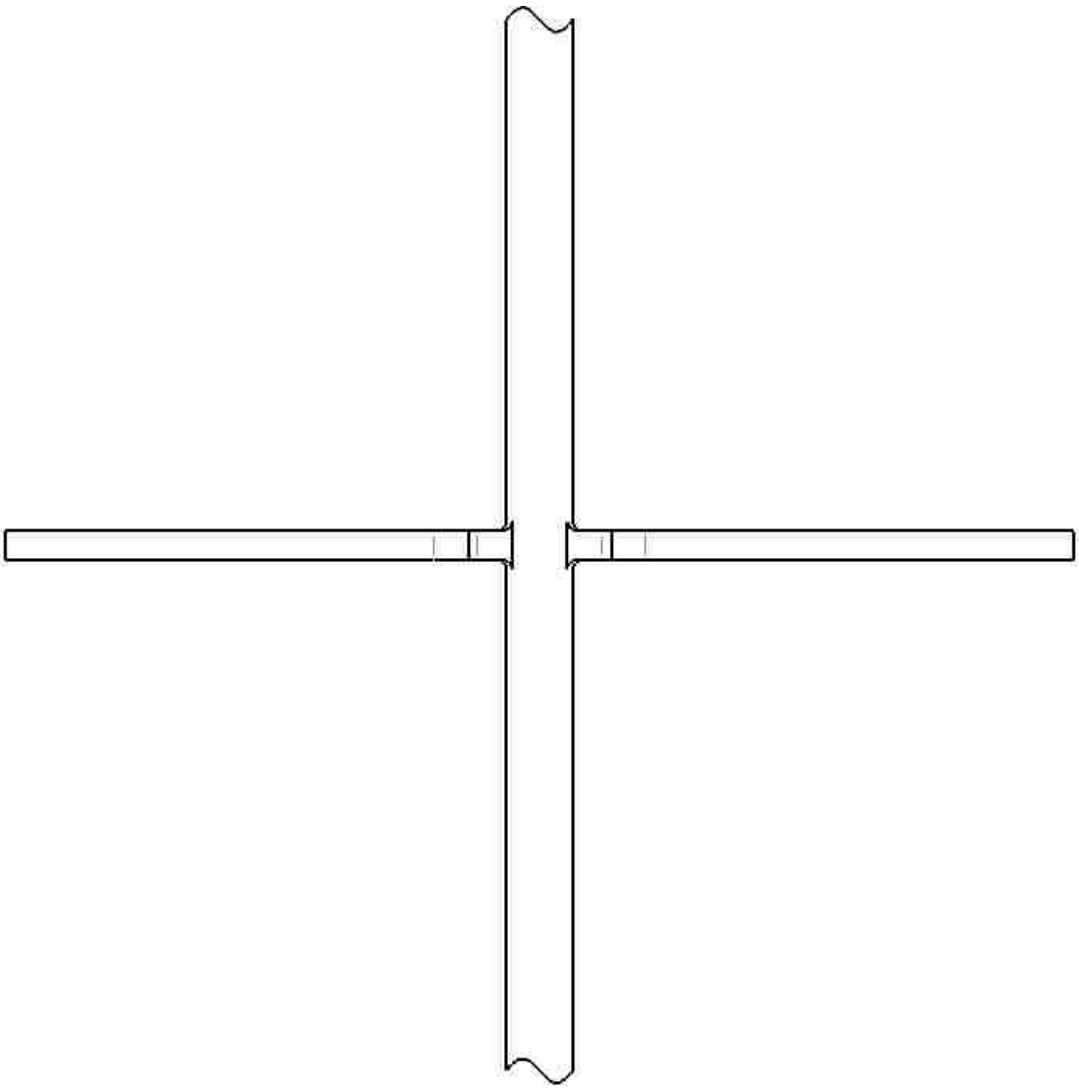

Figure 54: Side View. Bi-Cantilevered Drain/Cantilever System composed of a Circular Drain and two Quarter-Circular-shaped Cantilevers.

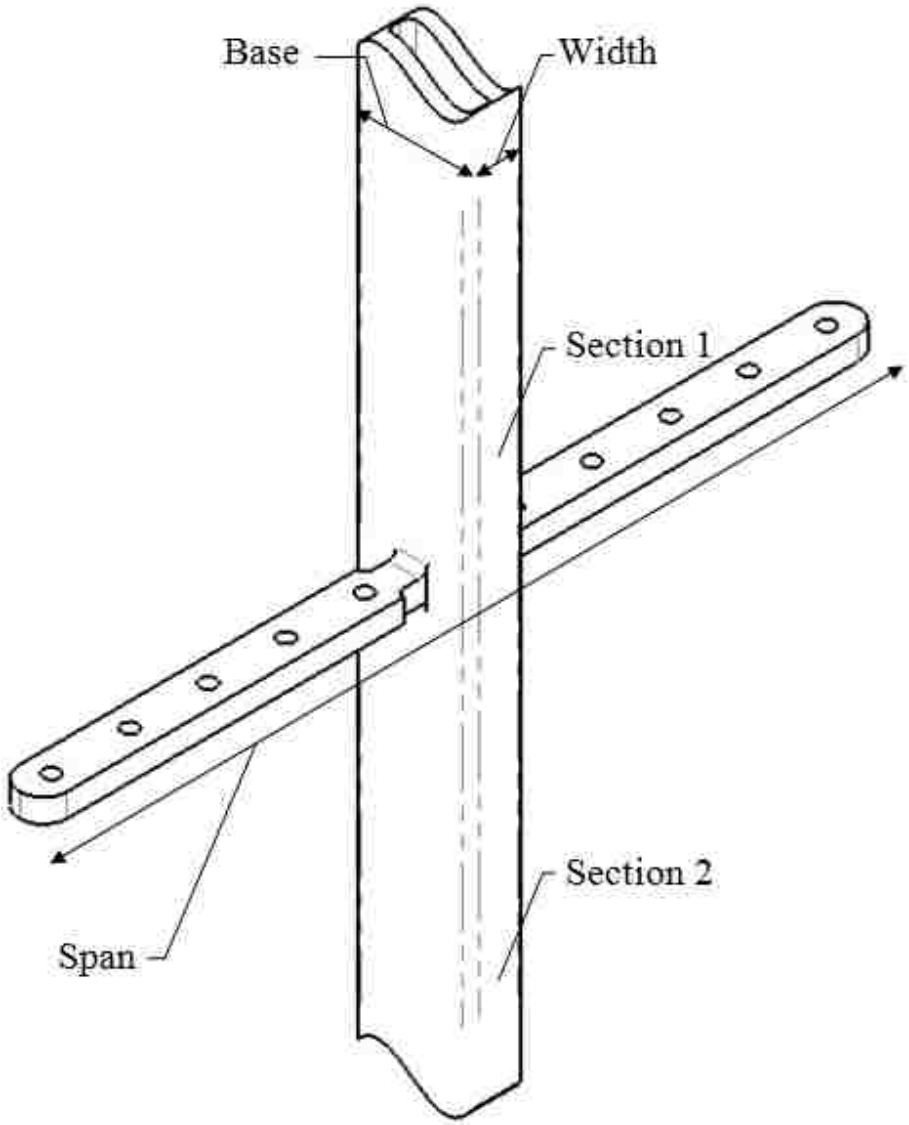

Figure 55: Isometric View. Bi-Cantilevered Drain/Cantilever composed of a Rectangular Drain and two Rectangular-shaped Cantilevers attached to the Base.

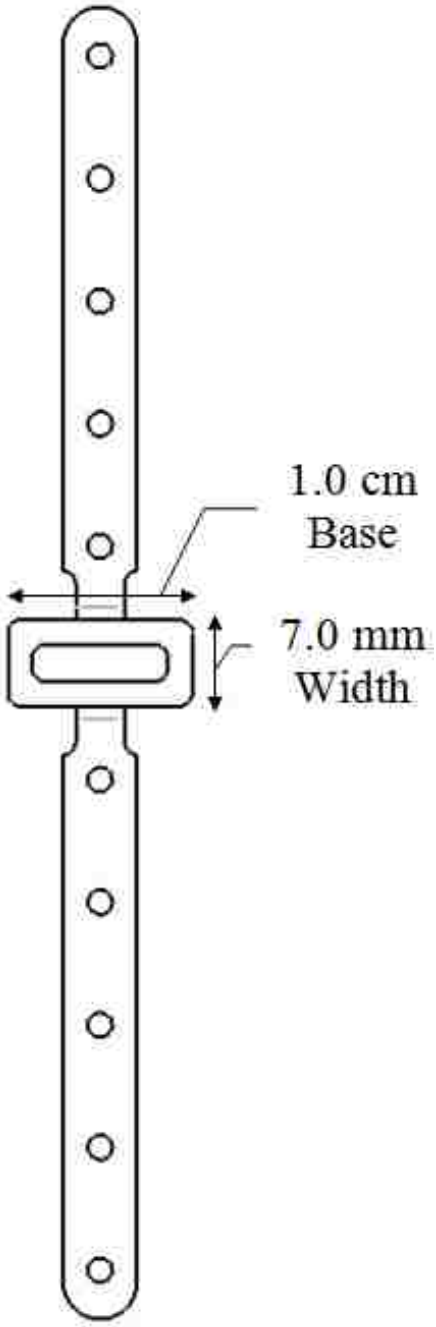

Figure 56: Top View. Bi-Cantilevered Drain/Cantilever composed of a Rectangular Drain and two Rectangular-shaped Cantilevers attached to the Base.

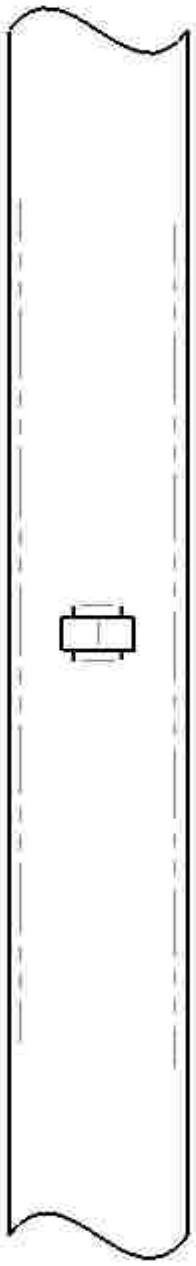

Figure 57: Side View. Bi-Cantilevered Drain/Cantilever composed of a Rectangular Drain and two Rectangular-shaped Cantilevers attached to the Base.

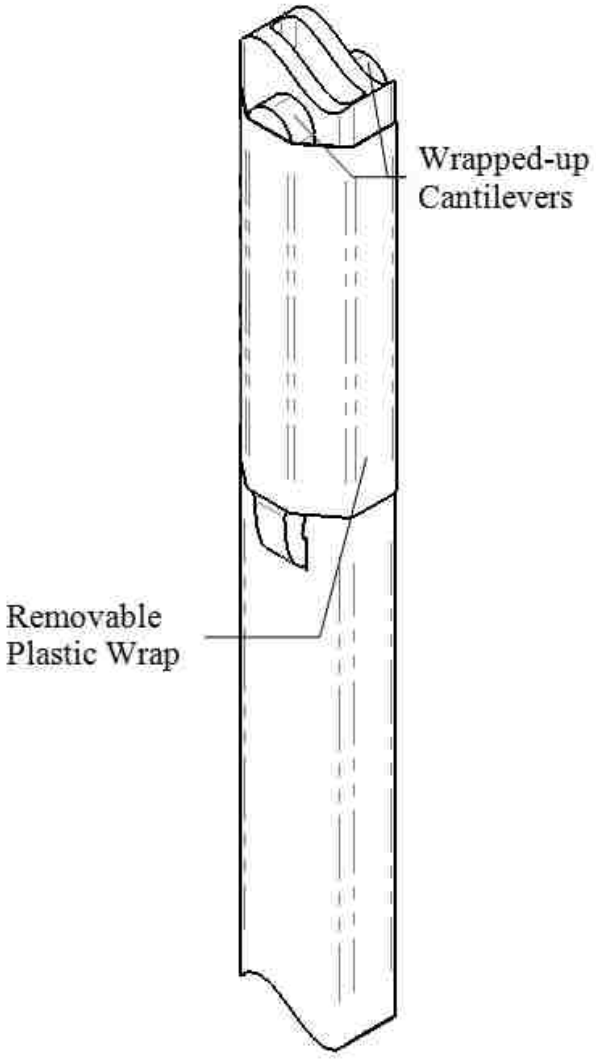

Figure 58: Isometric View. Packaging of the Bi-Cantilevered Drain/Cantilever composed of a Rectangular Drain and two Rectangular-shaped Cantilevers attached to the Base.

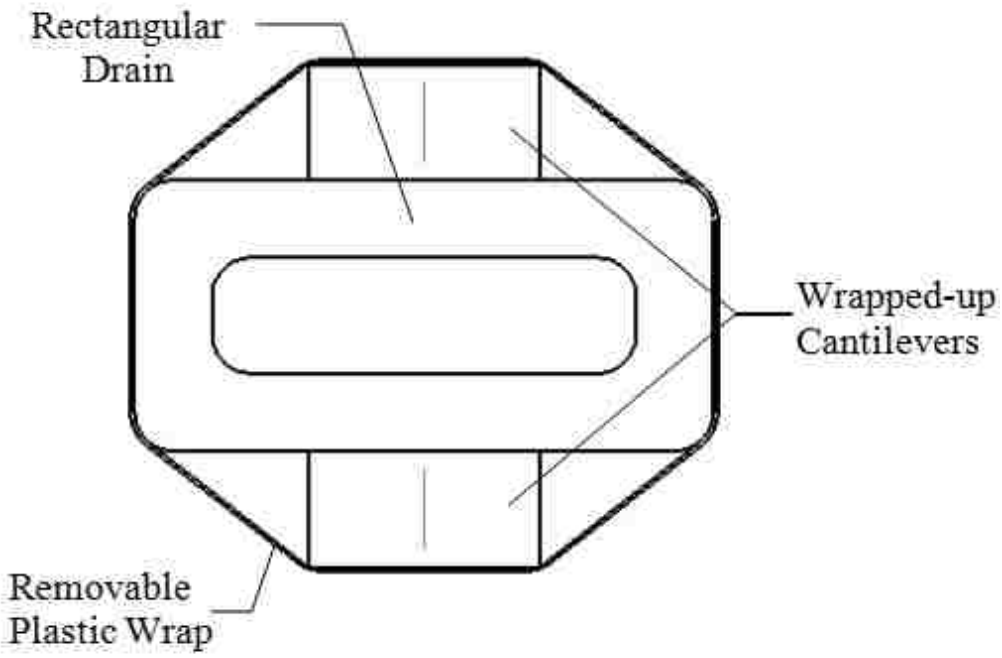

Figure 59: Enlarged Top View. Packaging of the Bi-Cantilevered Drain/Cantilever composed of a Rectangular Drain and two Rectangular-shaped Cantilevers attached to the Base.

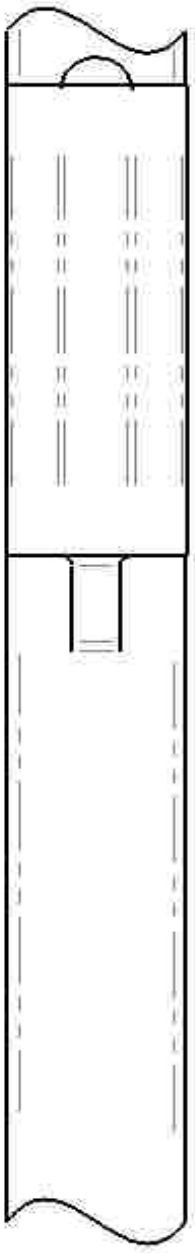

Figure 60: Side View. Packaging of the Bi-Cantilevered Drain/Cantilever composed of a Rectangular Drain and two Rectangular-shaped Cantilevers attached to the Base.

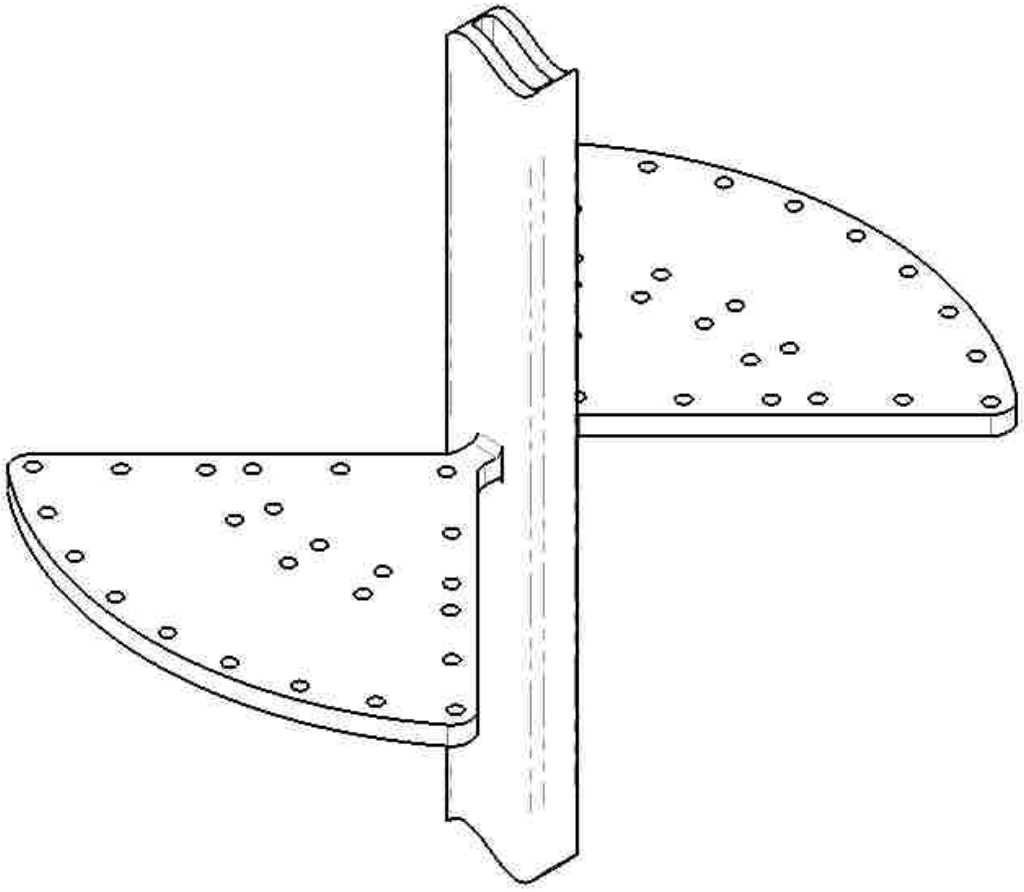

Figure 61: Isometric View. Bi-Cantilevered Drain/Cantilever composed of a Rectangular Drain and two Quarter-circular-shaped Cantilevers attached to the Base.

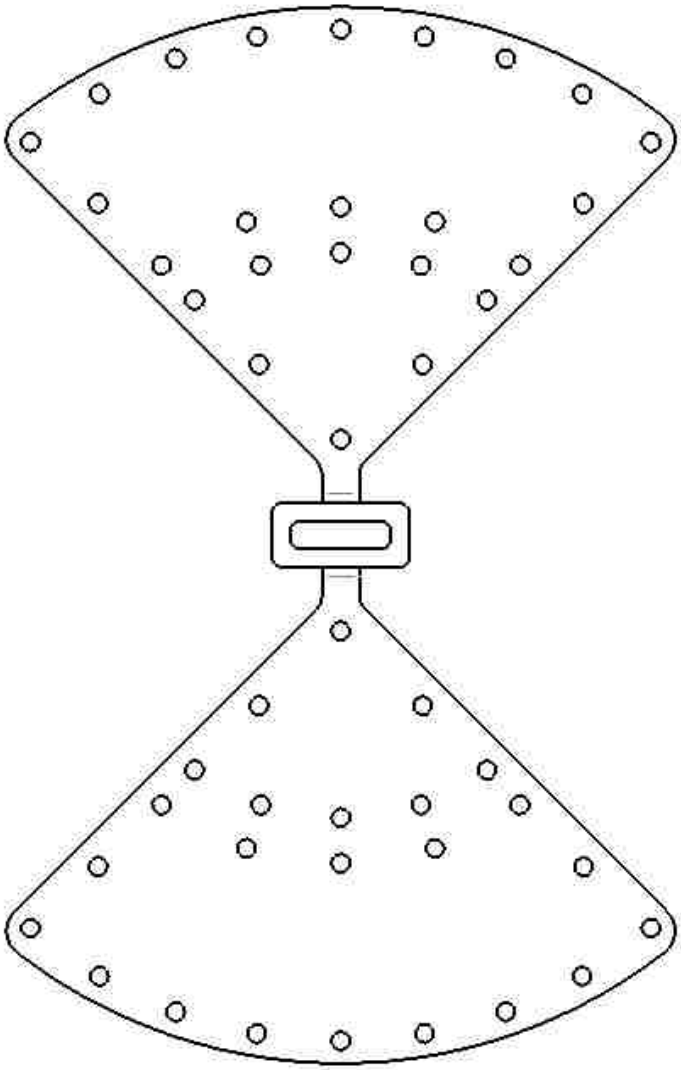

Figure 62: Top View. Bi-Cantilevered Drain/Cantilever composed of a Rectangular Drain and two Quarter-circular-shaped Cantilevers attached to the Base.

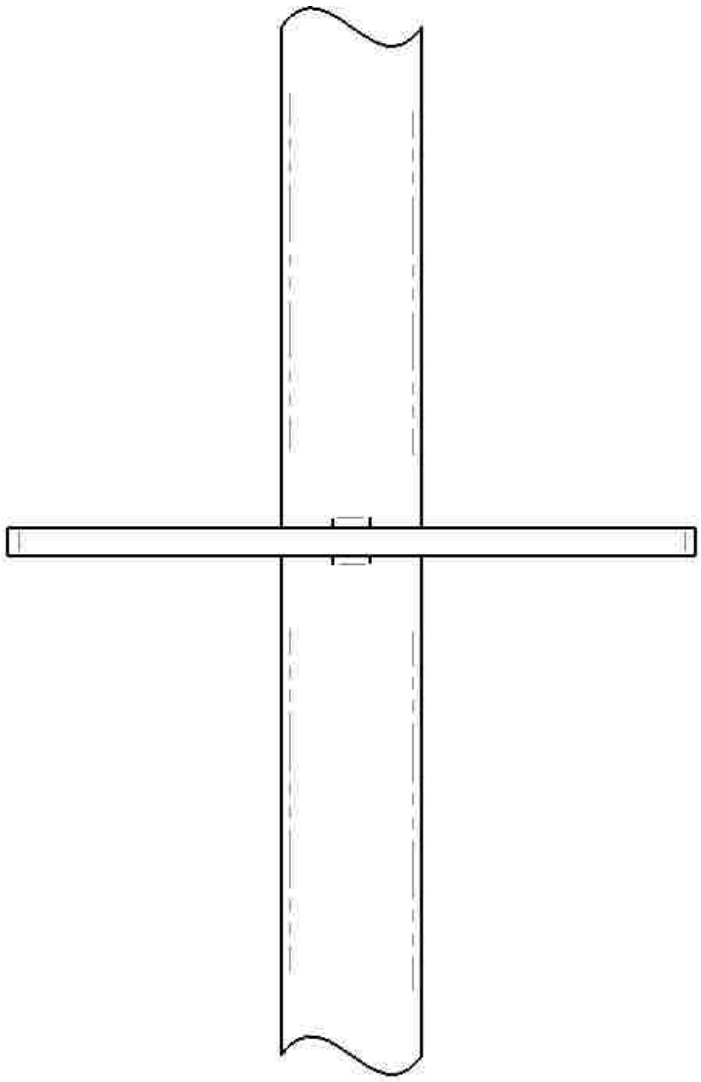

Figure 63: Side View. Bi-Cantilevered Drain/Cantilever composed of a Rectangular Drain and two Quarter-circular-shaped Cantilevers attached to the Base.

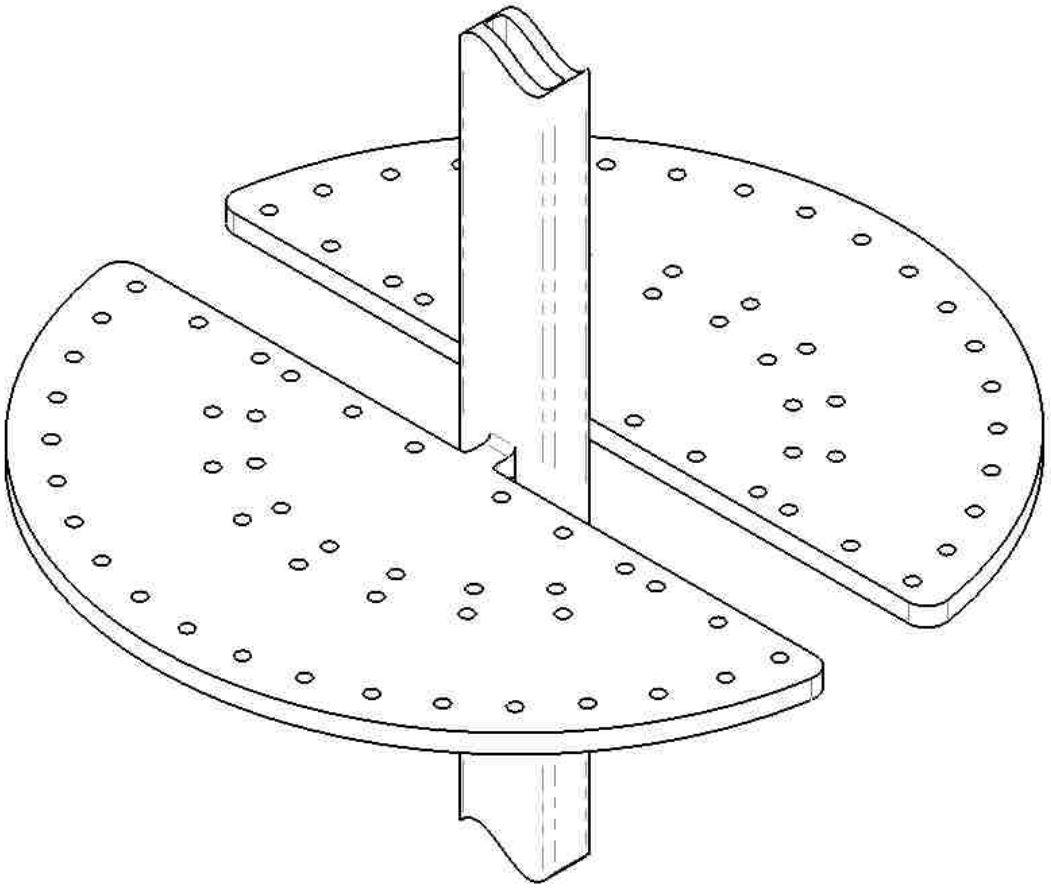

Figure 64: Isometric View. Bi-Cantilevered Drain/Cantilever composed of a Rectangular Drain and two Semicircular-shaped Cantilevers attached to the Base.

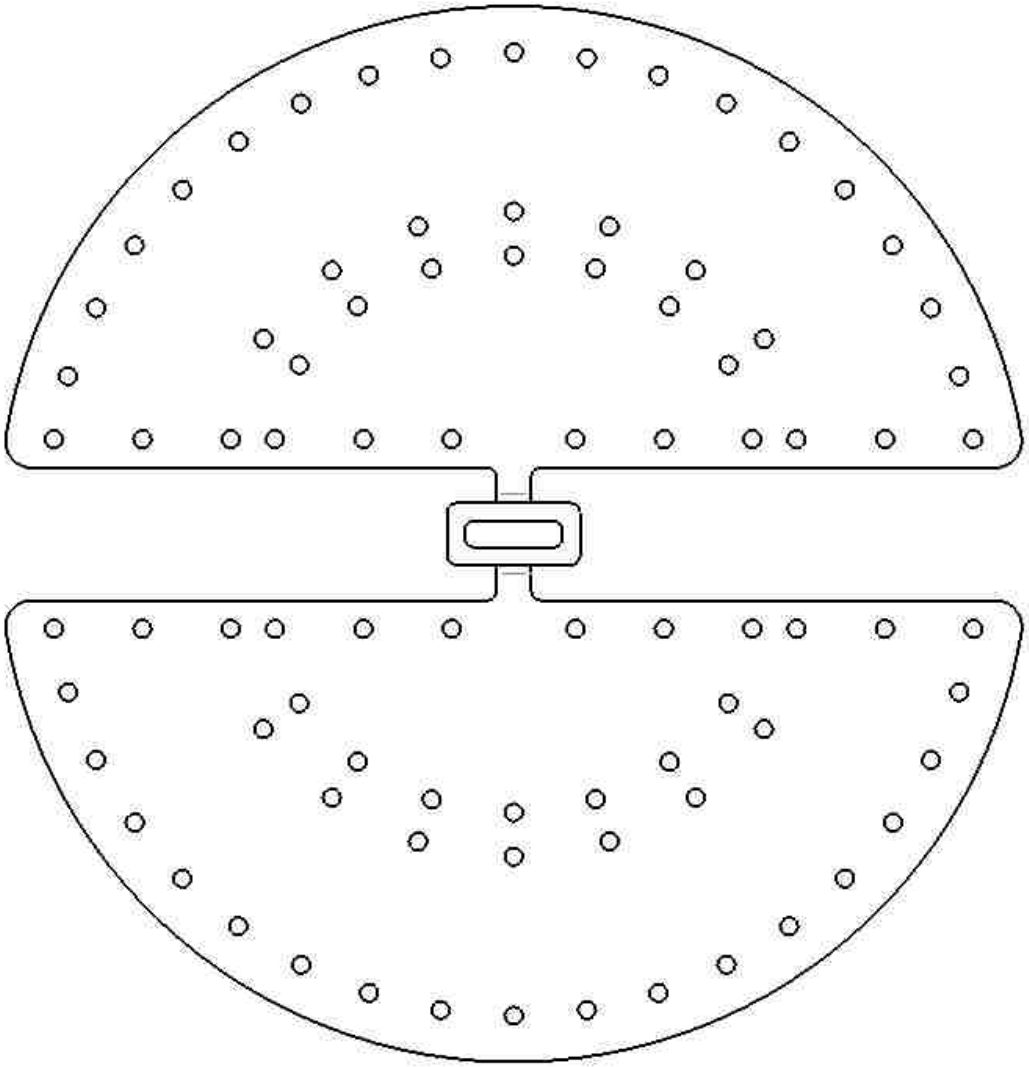

Figure 65: Top View. Bi-Cantilevered Drain/Cantilever composed of a Rectangular Drain and two Semicircular-shaped Cantilevers attached to the Base.

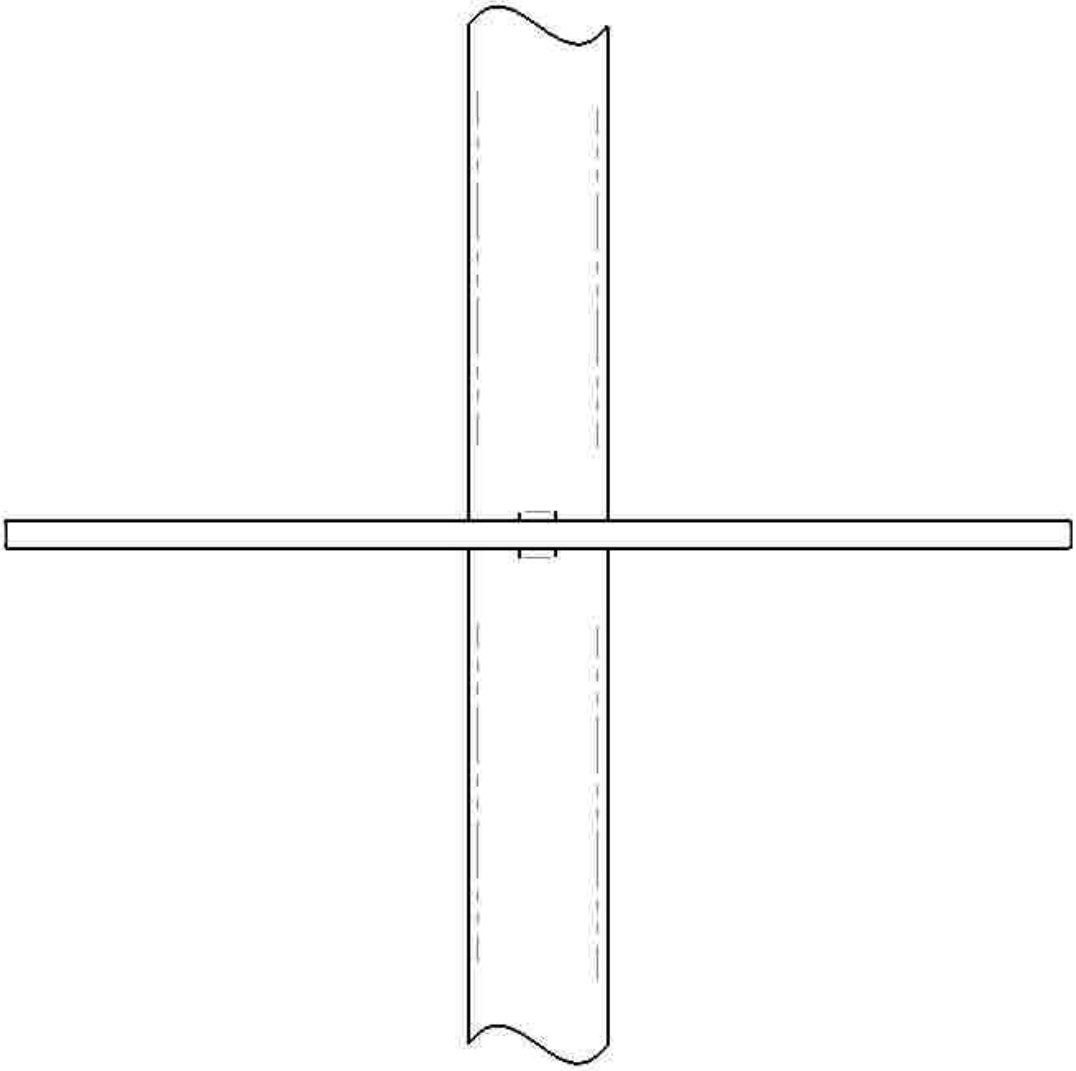

Figure 66: Side View. Bi-Cantilevered Drain/Cantilever composed of a Rectangular Drain and two Semicircular-shaped Cantilevers attached to the Base.

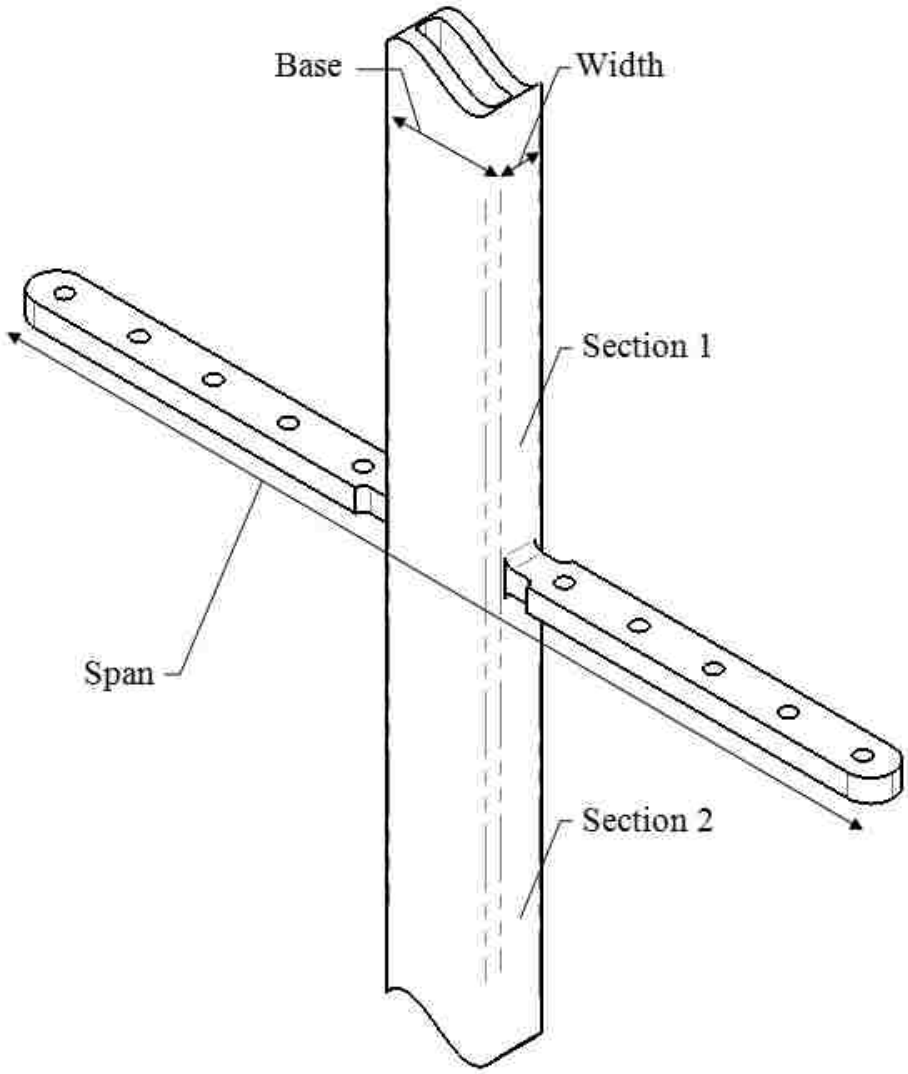

Figure 67: Isometric View. Bi-Cantilevered Drain/Cantilever composed of a Rectangular Drain and two Rectangular-shaped Cantilevers attached to the Width.

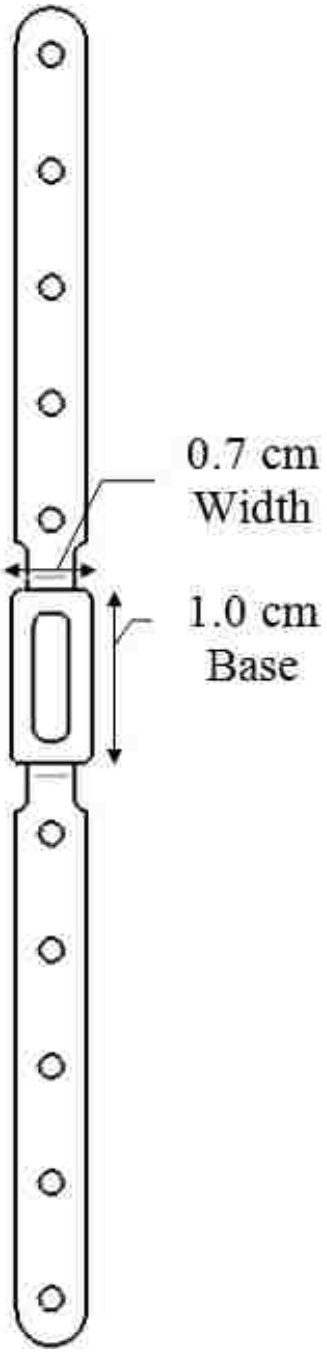

Figure 68: Top View. Bi-Cantilevered Drain/Cantilever composed of a Rectangular Drain and two Rectangular-shaped Cantilevers attached to the Width.

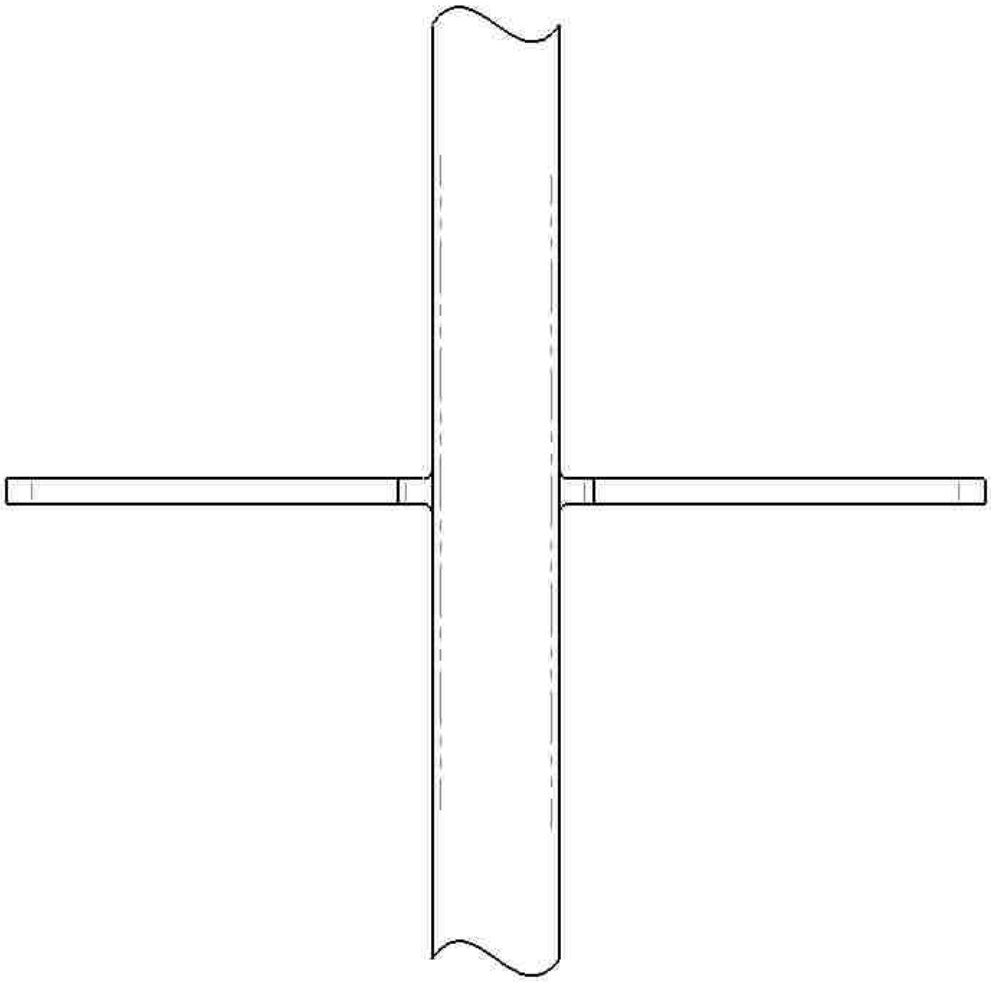

Figure 69: Side View. Bi-Cantilevered Drain/Cantilever composed of a Rectangular Drain and two Rectangular-shaped Cantilevers attached to the Width.

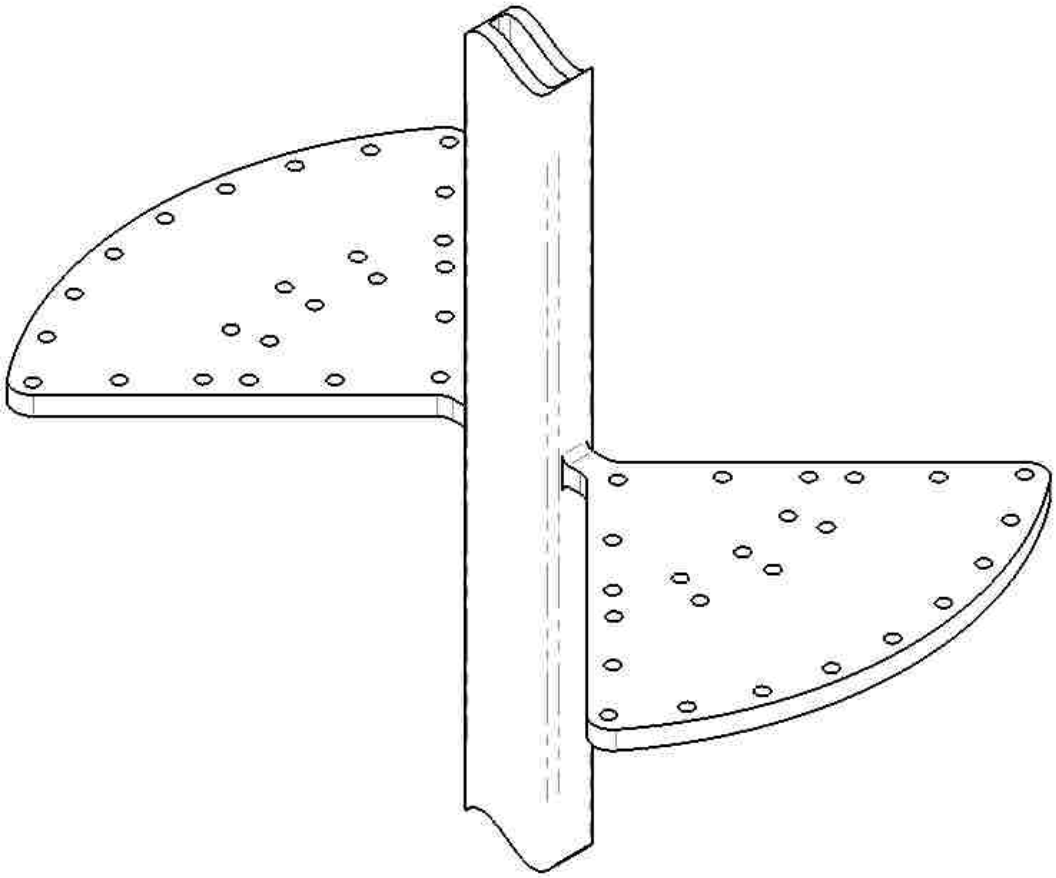

Figure 70: Isometric View. Bi-Cantilevered Drain/Cantilever composed of a Rectangular Drain and two Quarter-circular-shaped Cantilevers attached to the Width.

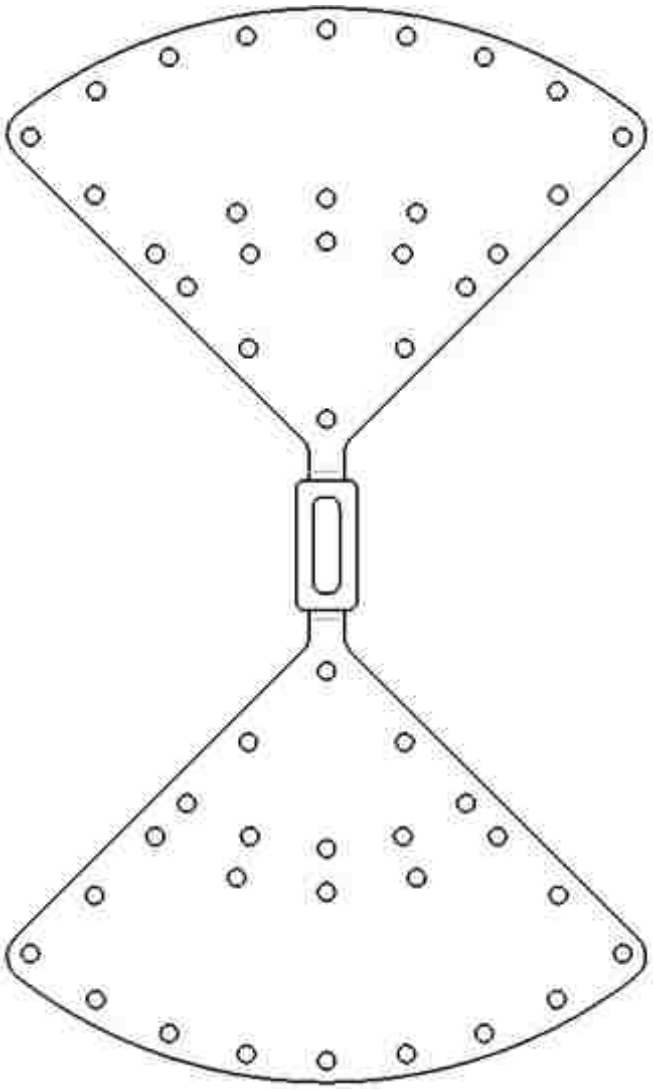

Figure 71: Top View. Bi-Cantilevered Drain/Cantilever composed of a Rectangular Drain and two Quarter-circular-shaped Cantilevers attached to the Width.

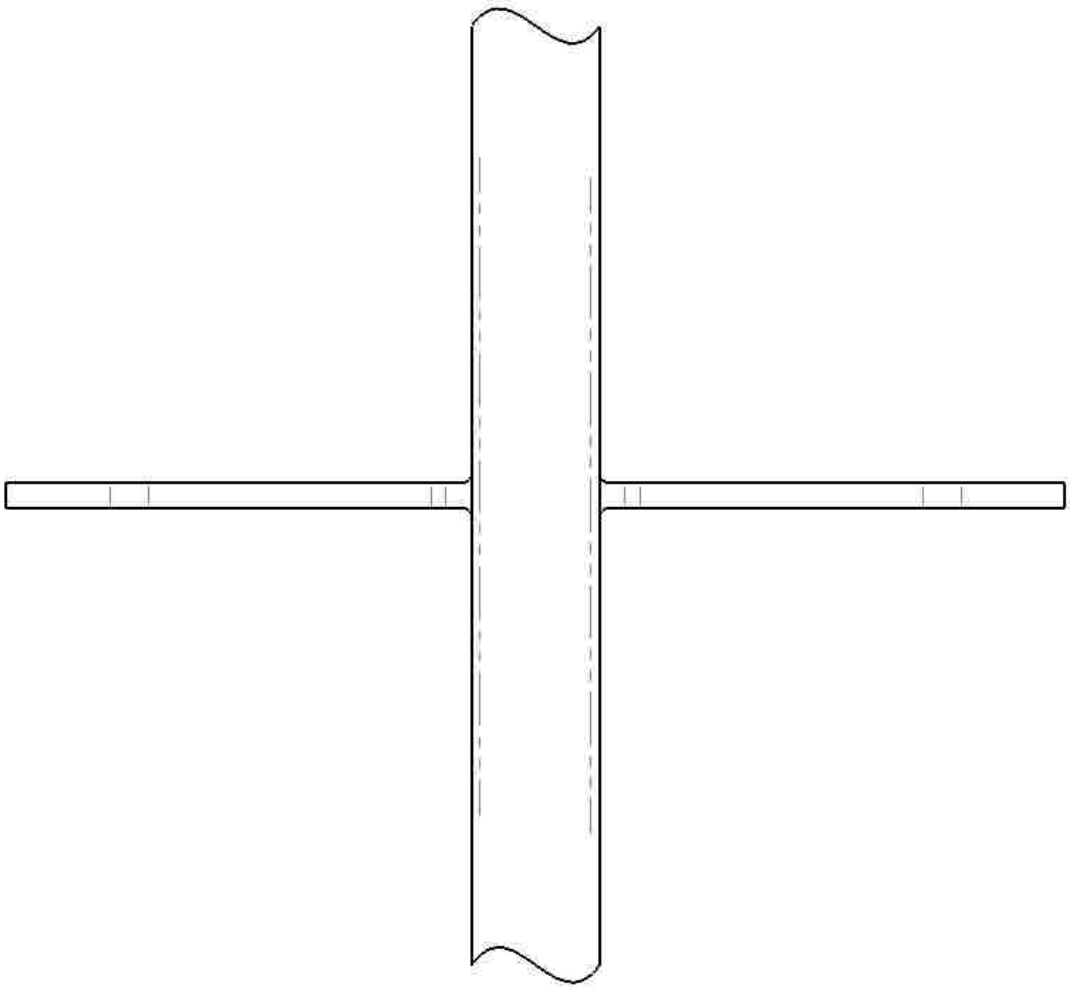

Figure 72: Side View. Bi-Cantilevered Drain/Cantilever composed of a Rectangular Drain and two Quarter-circular-shaped Cantilevers attached to the Width.

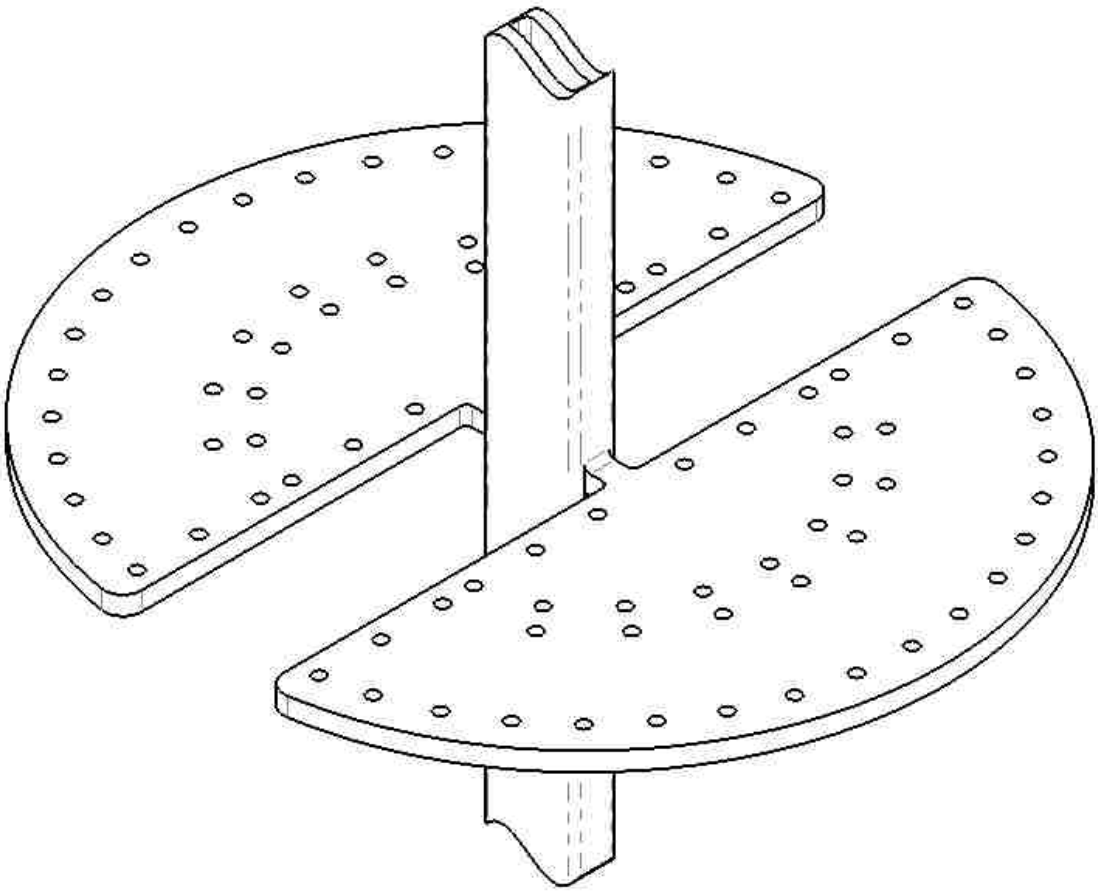

Figure 73: Isometric View. Bi-Cantilevered Drain/Cantilever composed of a Rectangular Drain and two Semicircular-shaped Cantilevers attached to the Width.

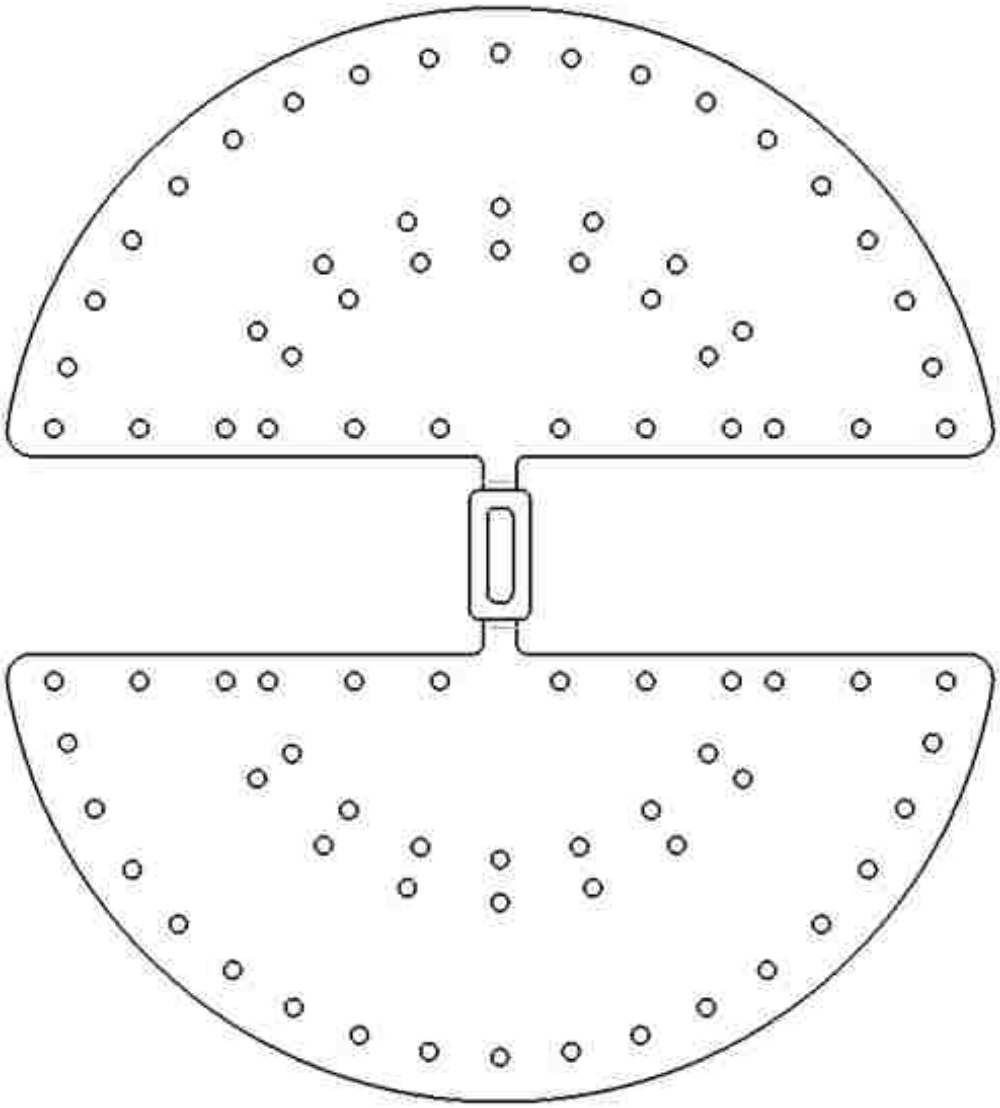

Figure 74: Top View. Bi-Cantilevered Drain/Cantilever composed of a Rectangular Drain and two Semicircular-shaped Cantilevers attached to the Width.

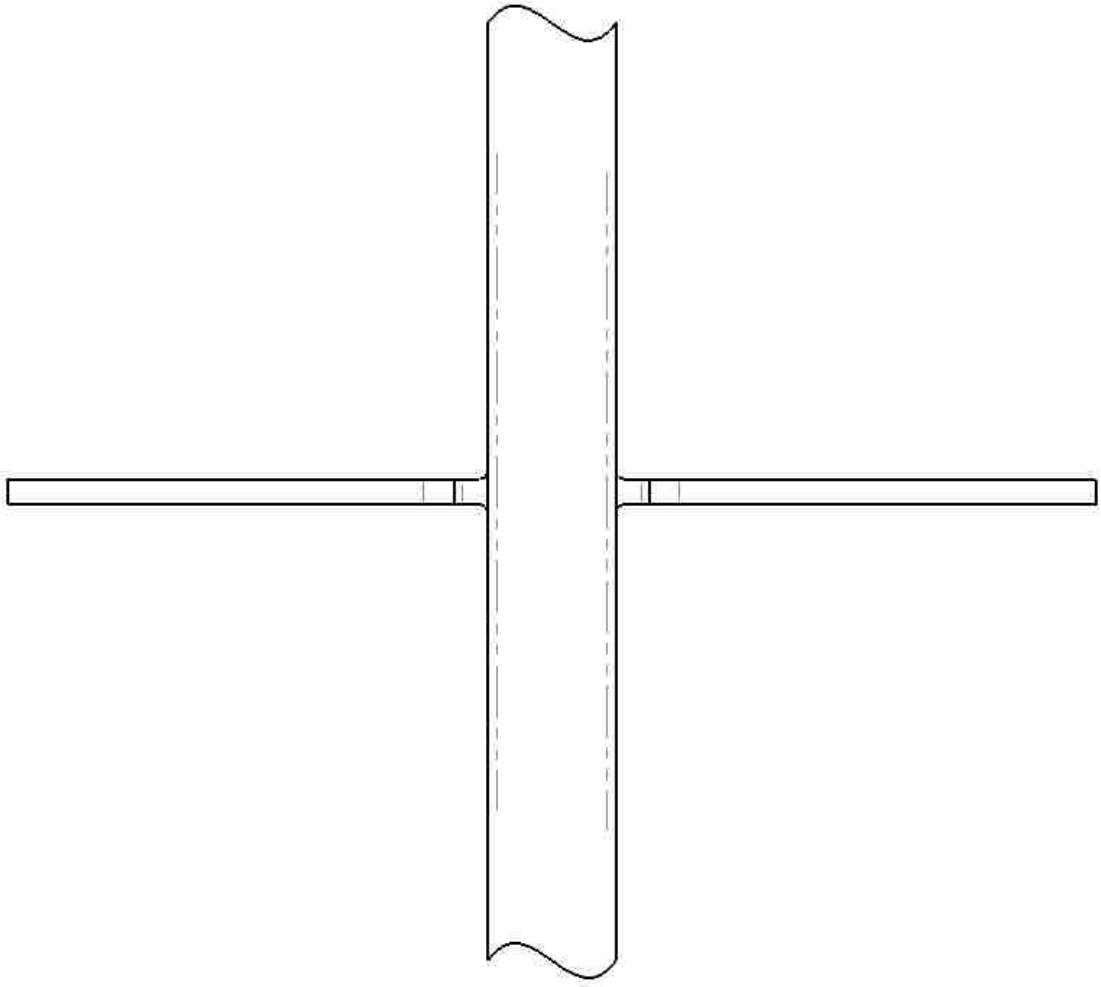

Figure 75: Side View. Bi-Cantilevered Drain/Cantilever composed of a Rectangular Drain and two Semicircular-shaped Cantilevers attached to the Width.

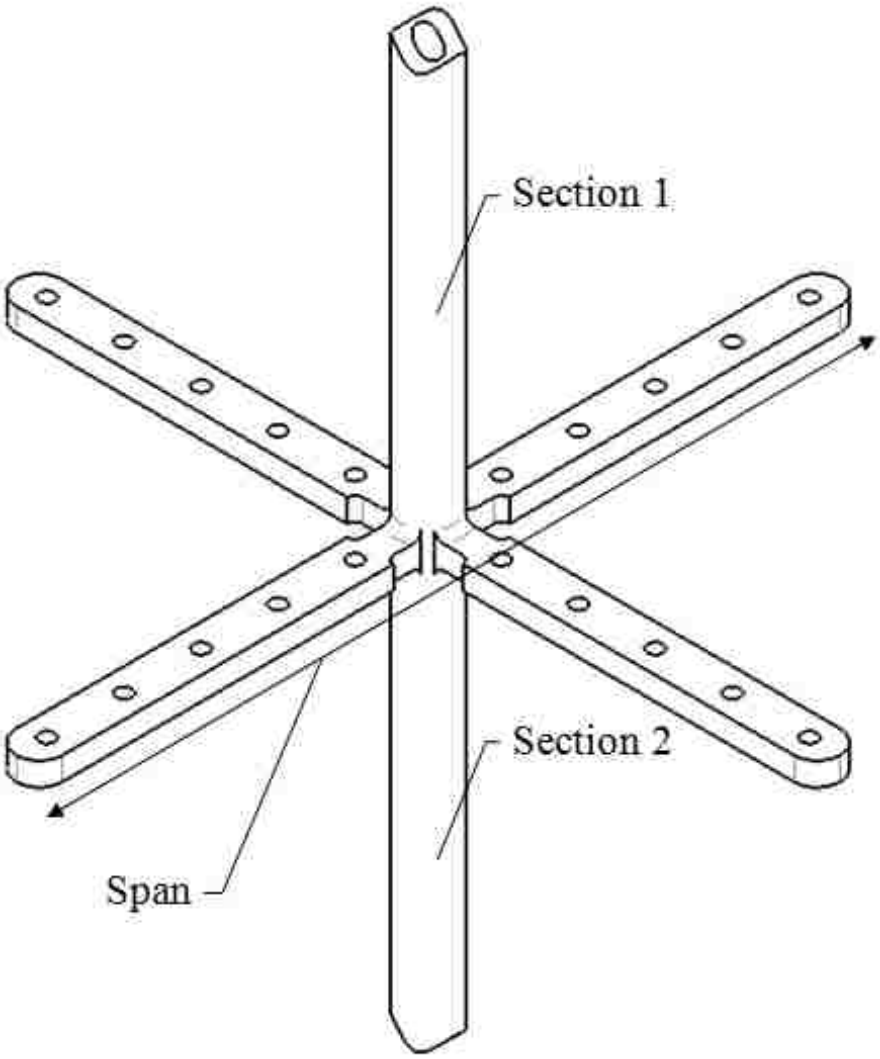

Figure 76: Isometric View. Quad-Cantilevered Drain/Cantilever System composed of a Circular Drain and four Rectangular-shaped Cantilevers. Identical to Fig. 40.

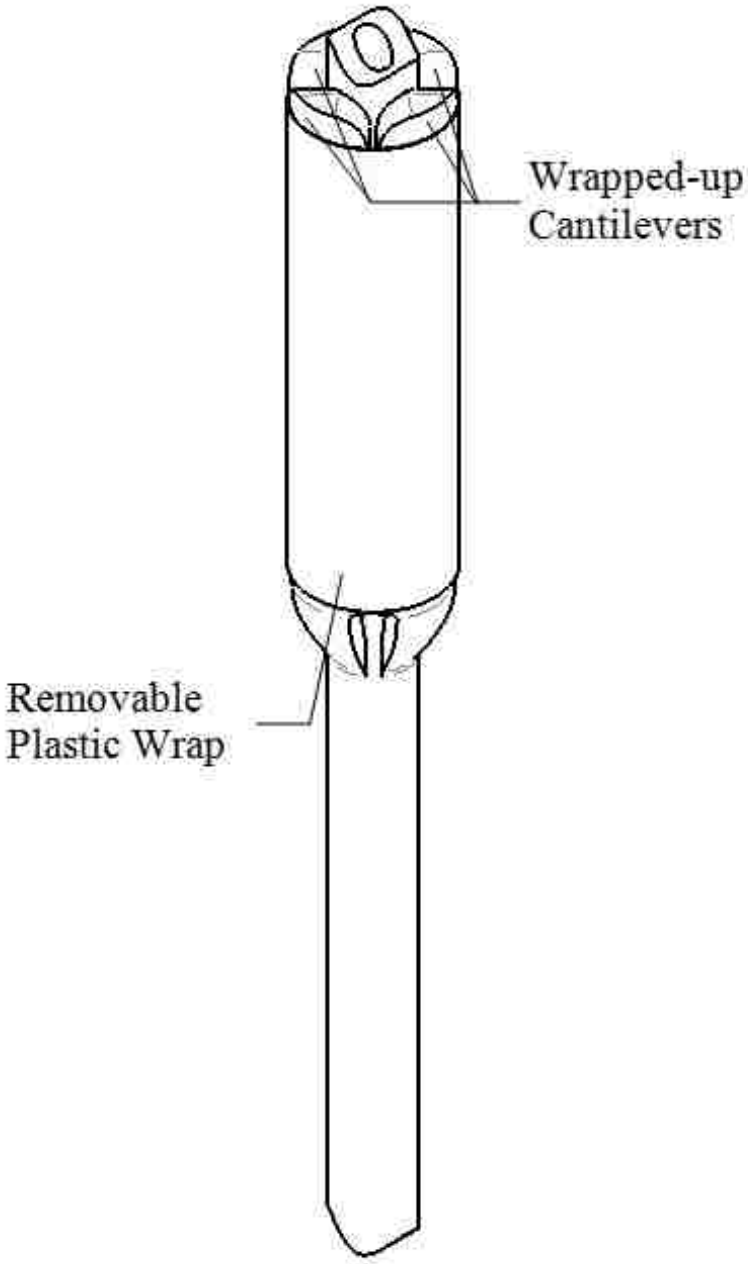

Figure 77: Isometric View. Packaging of the Quad-Cantilevered Drain/Cantilever System with a Circular Drain, via a Removable Plastic Wrap.

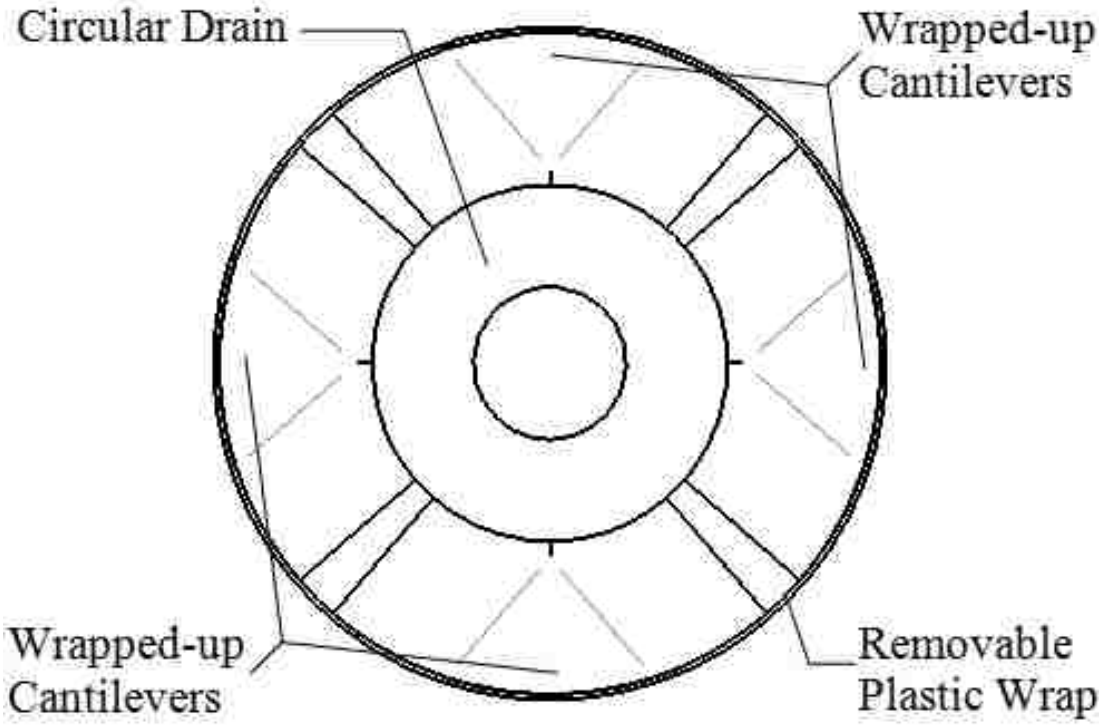

Figure 78: Enlarged Top View. Packaging of the Quad-Cantilevered Drain/Cantilever System with a Circular Drain, via a Removable Plastic Wrap.

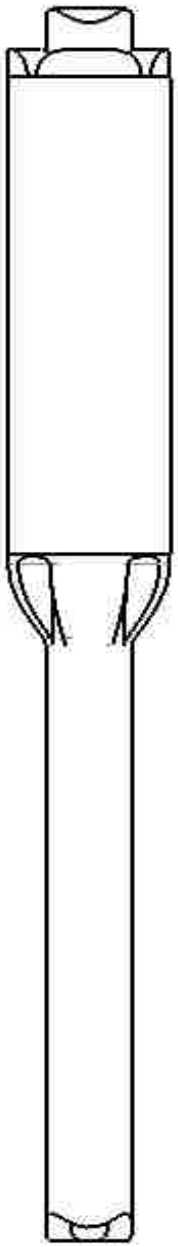

Figure 79: Side View. Packaging of the Quad-Cantilevered Drain/Cantilever System with a Circular Drain, via a Removable Plastic Wrap.

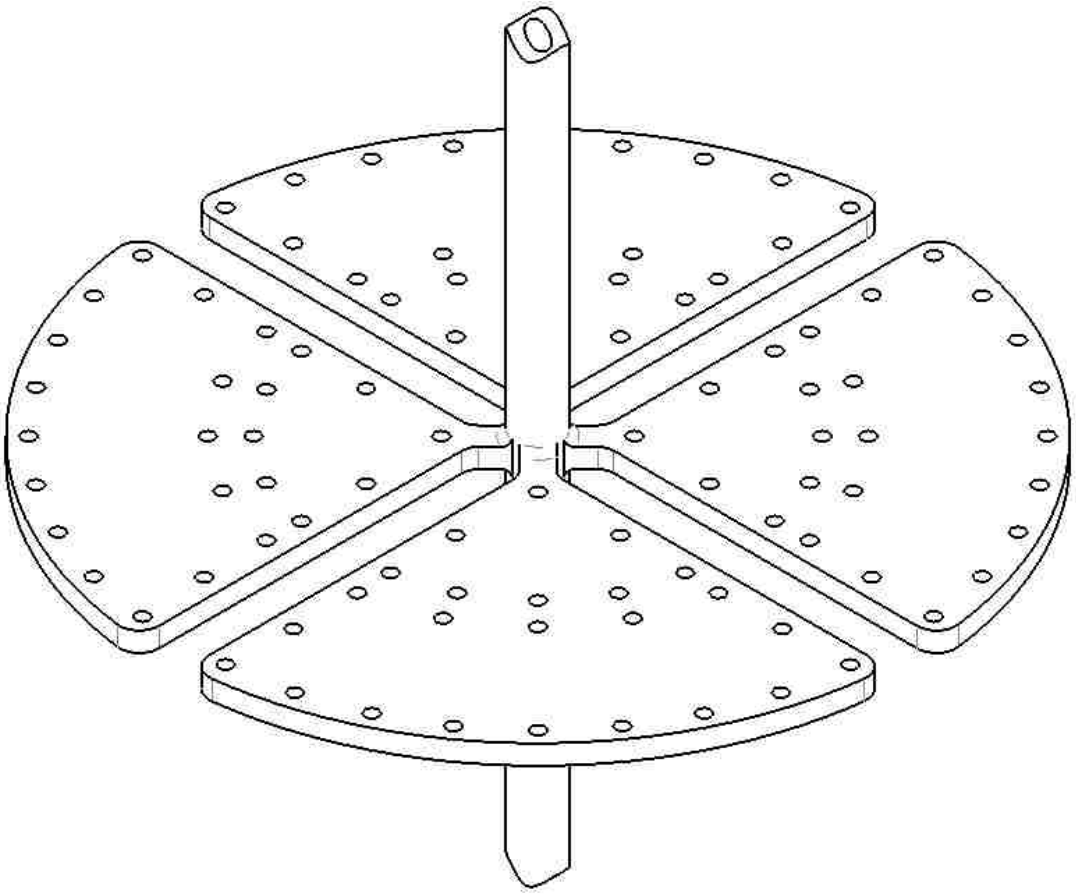

Figure 80: Isometric View. Quad-Cantilevered Drain/Cantilever System composed of a Circular Drain and four Semicircular-shaped Cantilevers.

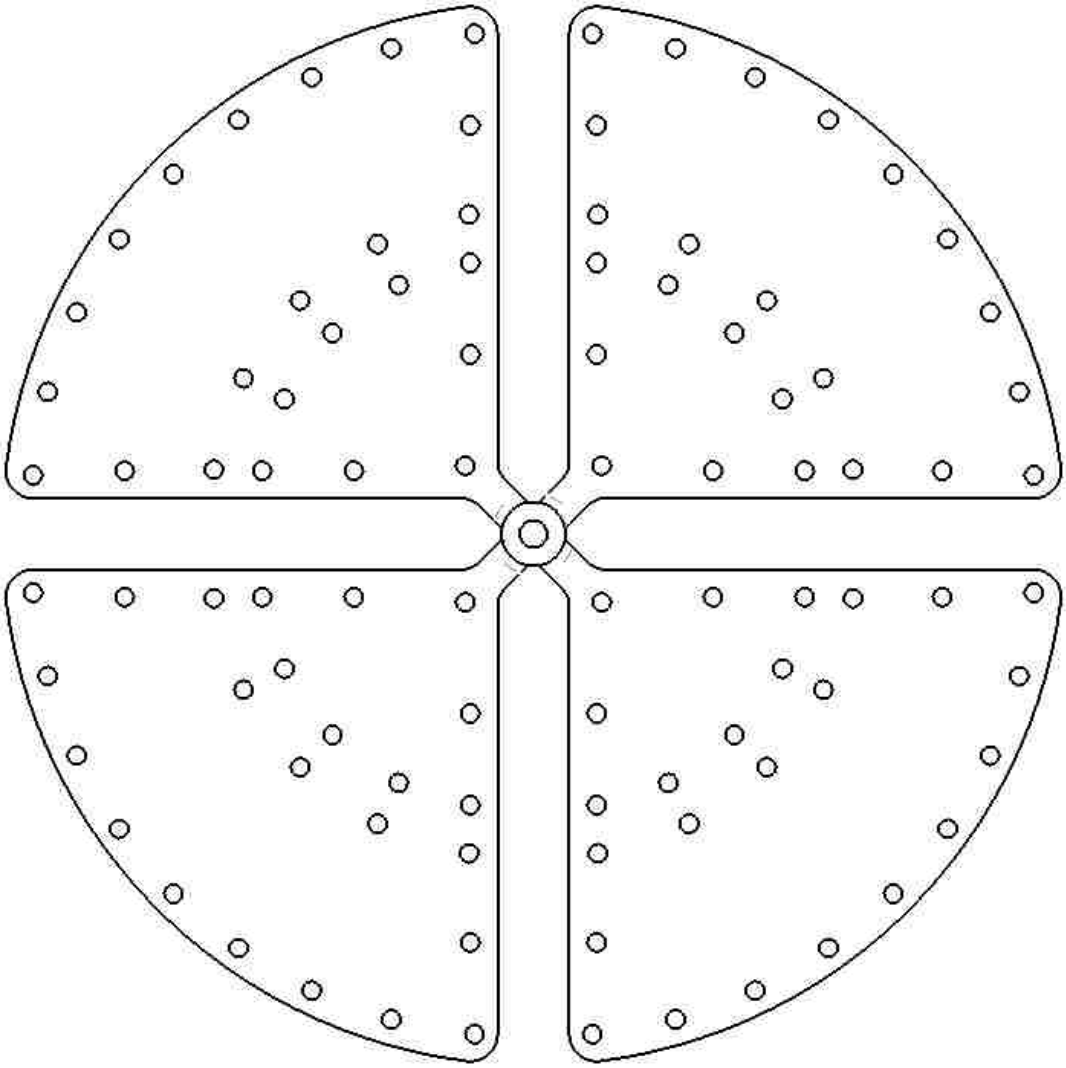

Figure 81: Top View. Quad-Cantilevered Drain/Cantilever System composed of a Circular Drain and four Semicircular-shaped Cantilevers.

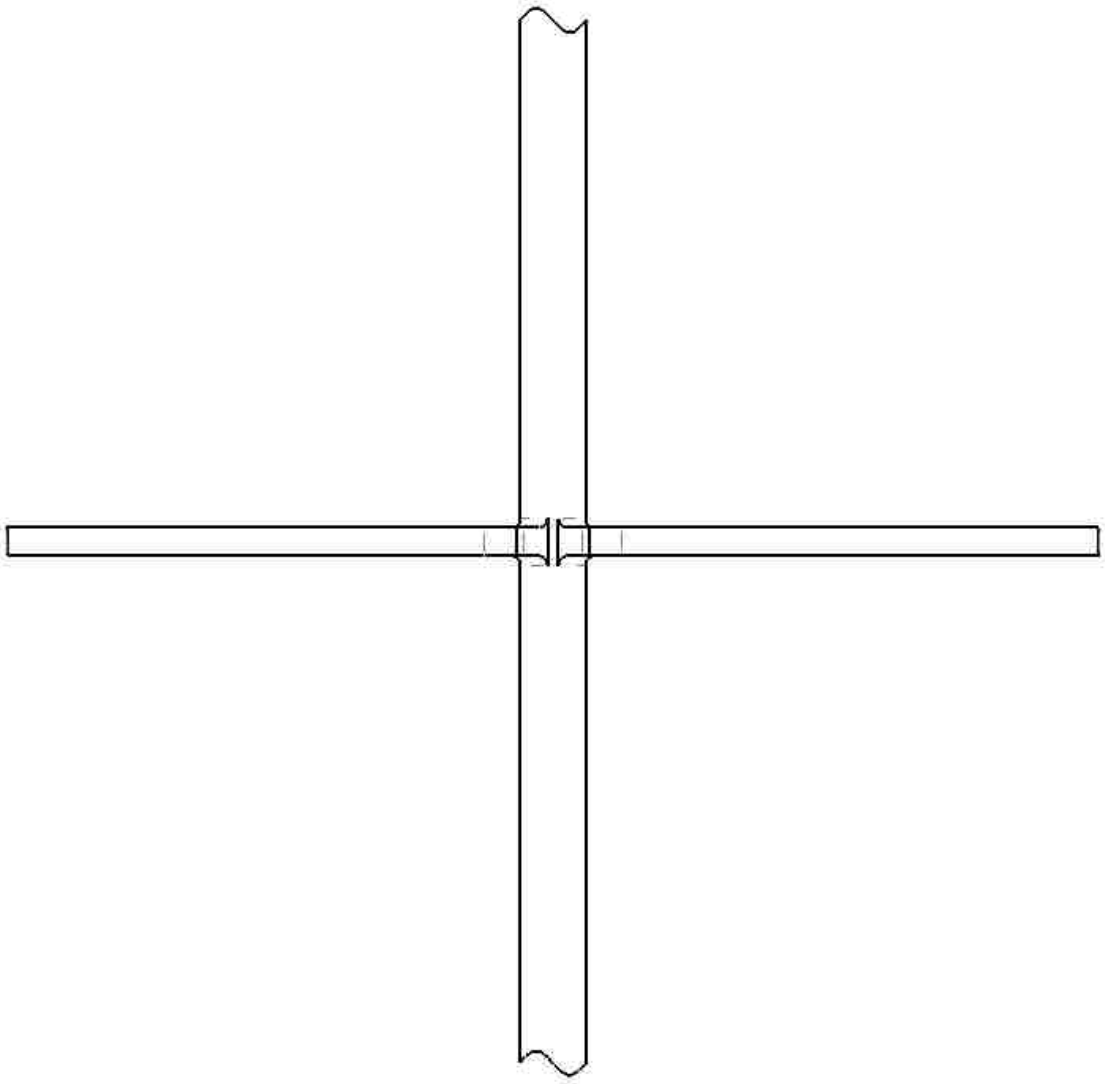

Figure 82: Side View. Quad-Cantilevered Drain/Cantilever System composed of a Circular Drain and four Semicircular-shaped Cantilevers.

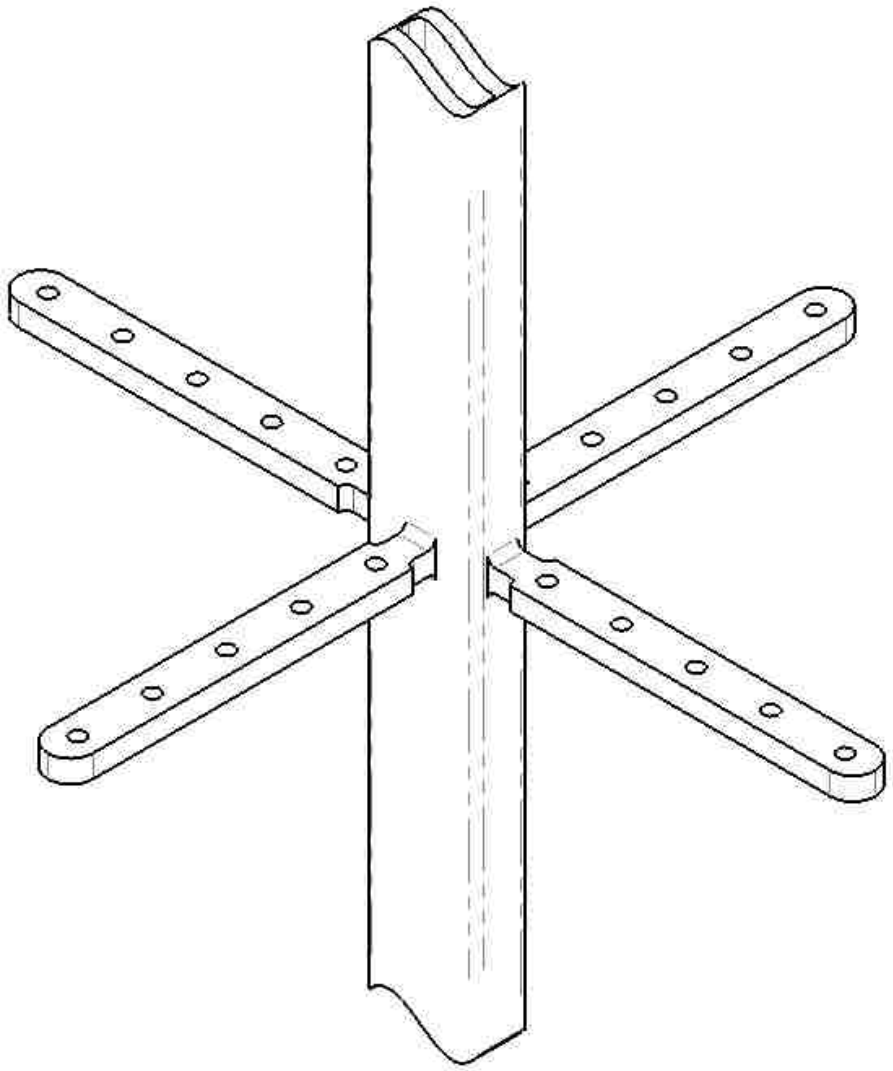

Figure 83: Isometric View. Quad-Cantilevered Drain/Cantilever System composed of a Rectangular Drain and four Rectangular-shaped Cantilevers.

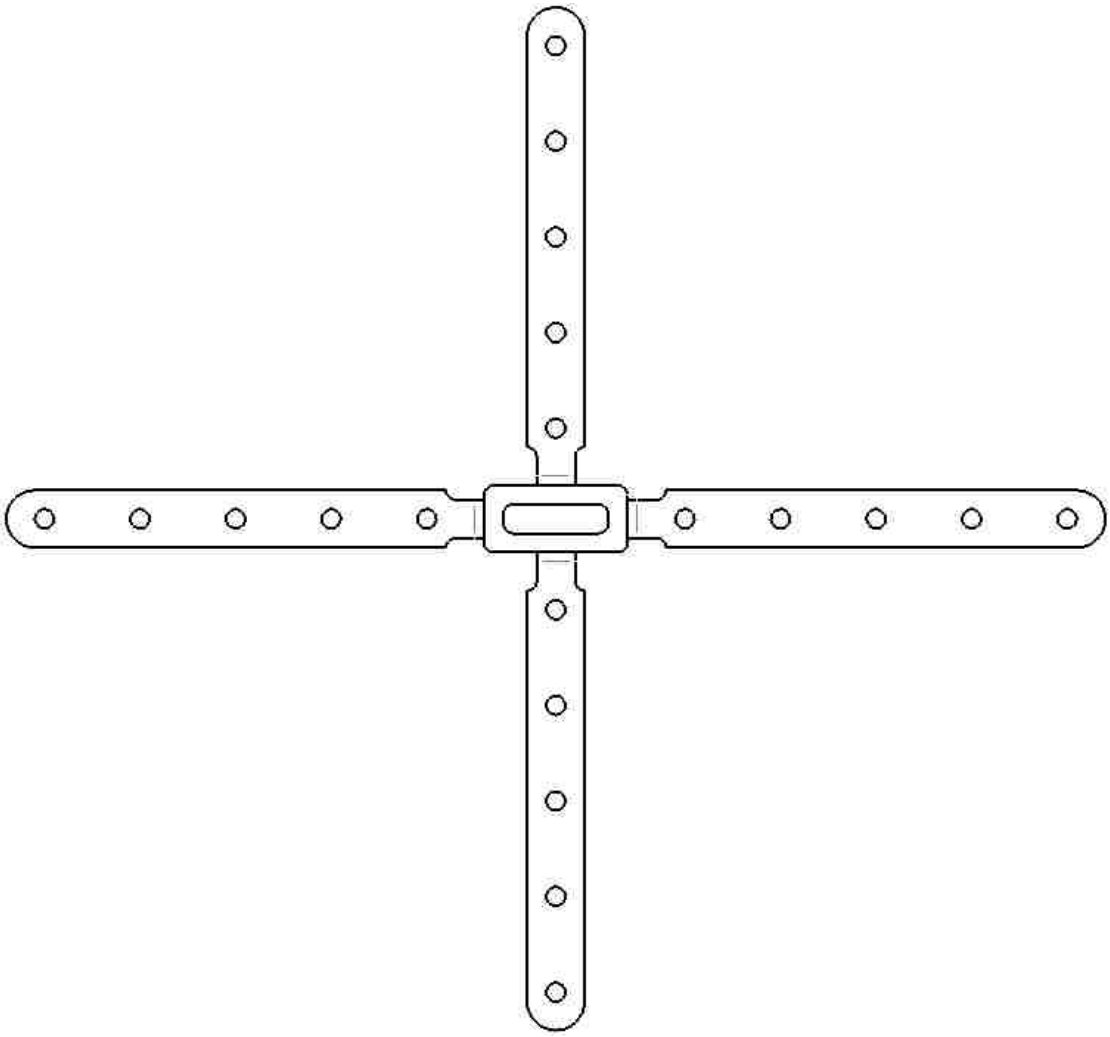

Figure 84: Isometric View. Quad-Cantilevered Drain/Cantilever System composed of a Rectangular Drain and four Rectangular-shaped Cantilevers.

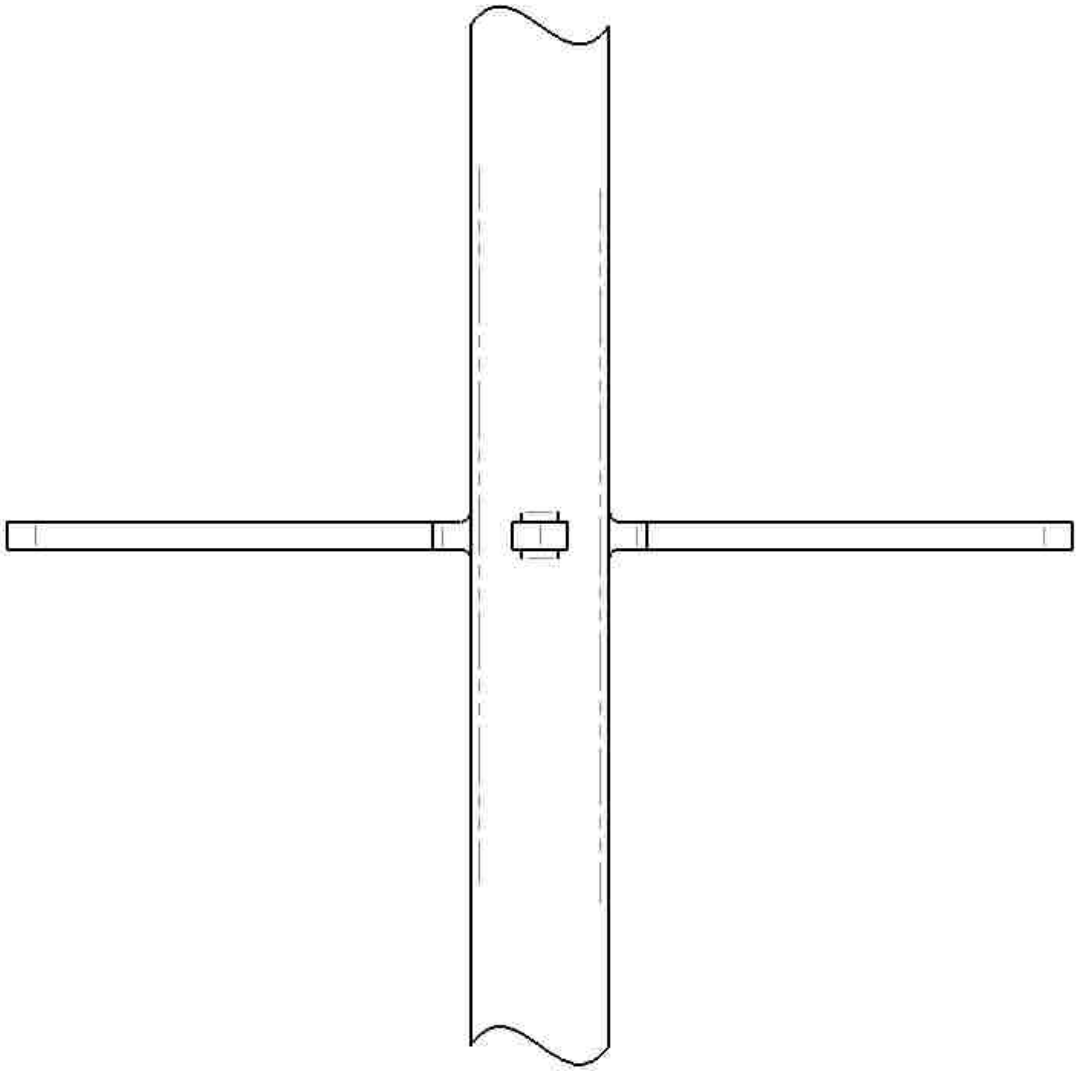

Figure 85: Side View. Quad-Cantilevered Drain/Cantilever System composed of a Rectangular Drain and four Rectangular-shaped Cantilevers.

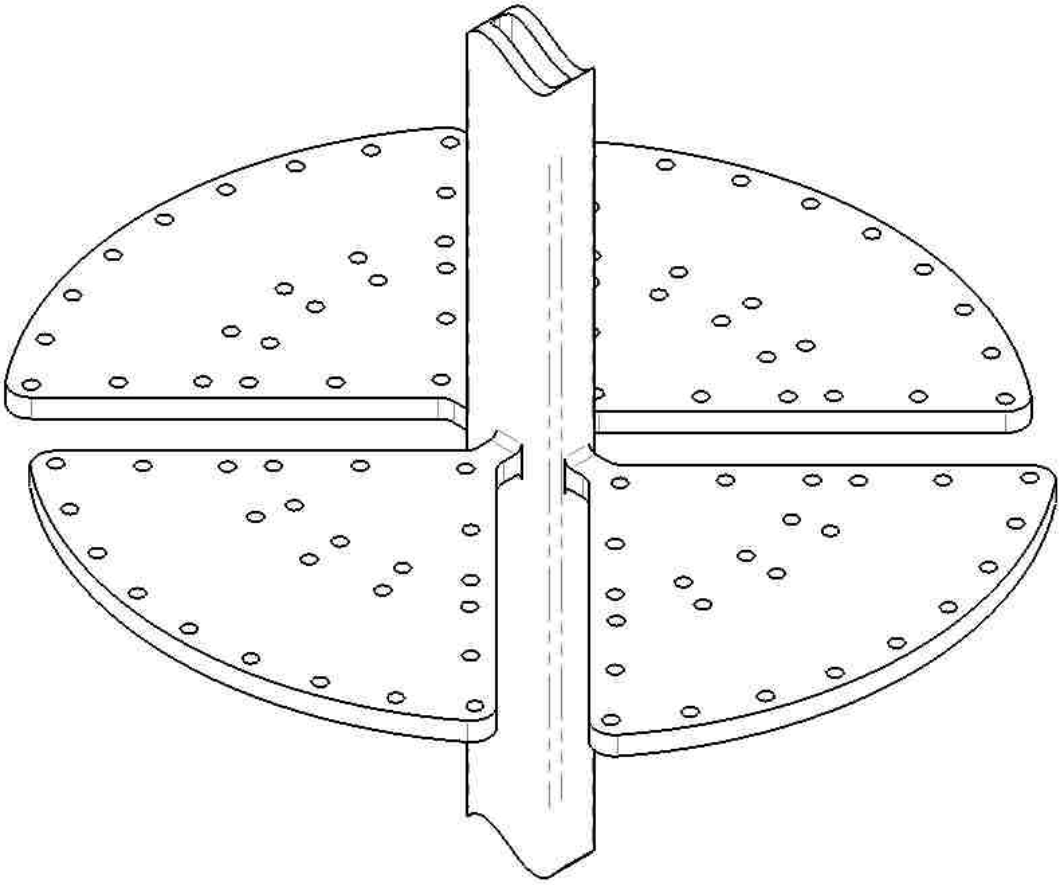

Figure 86: Isometric View. Quad-Cantilevered Drain/Cantilever System composed of a Rectangular Drain and four Quarter-Circular-shaped Cantilevers.

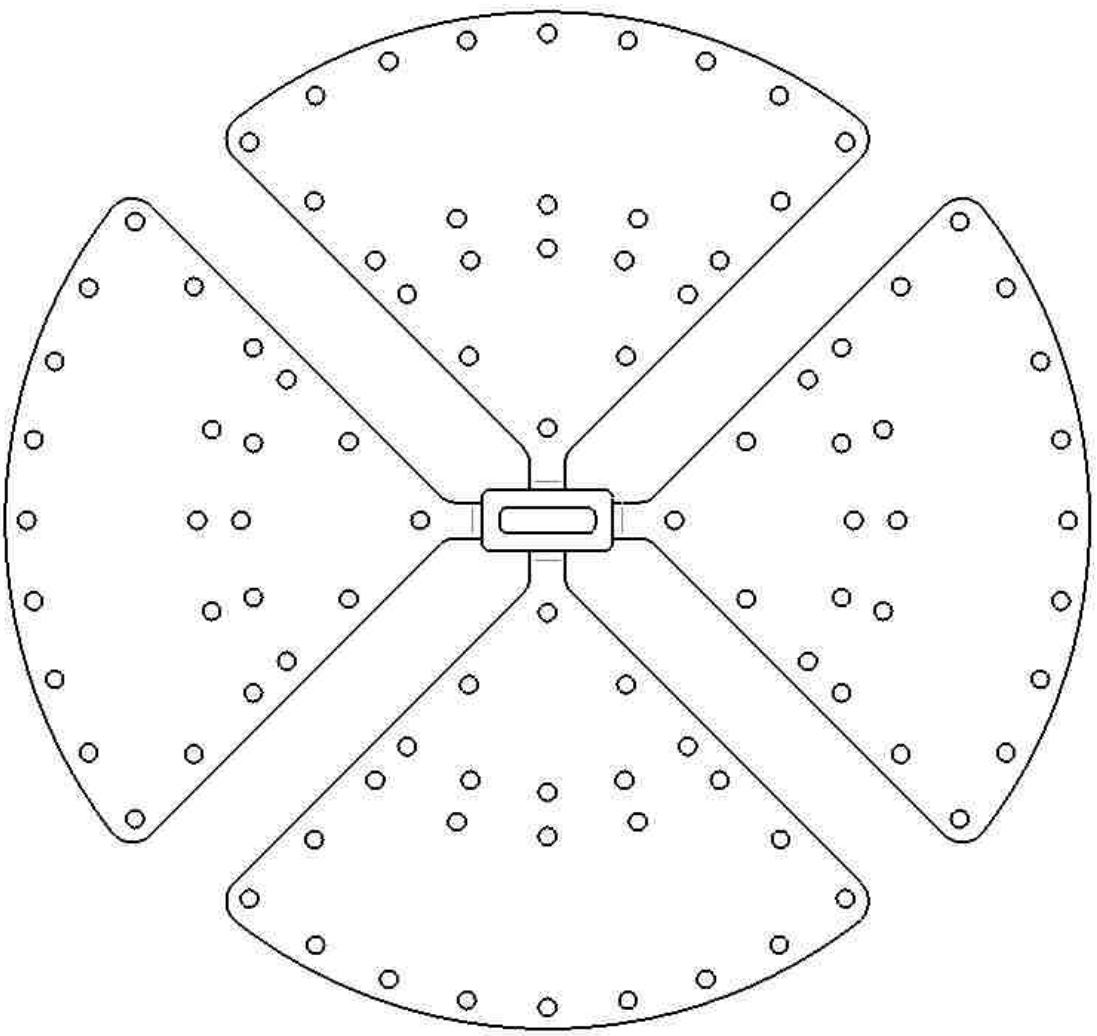

Figure 87: Top View. Quad-Cantilevered Drain/Cantilever System composed of a Rectangular Drain and four Quarter-Circular-shaped Cantilevers.

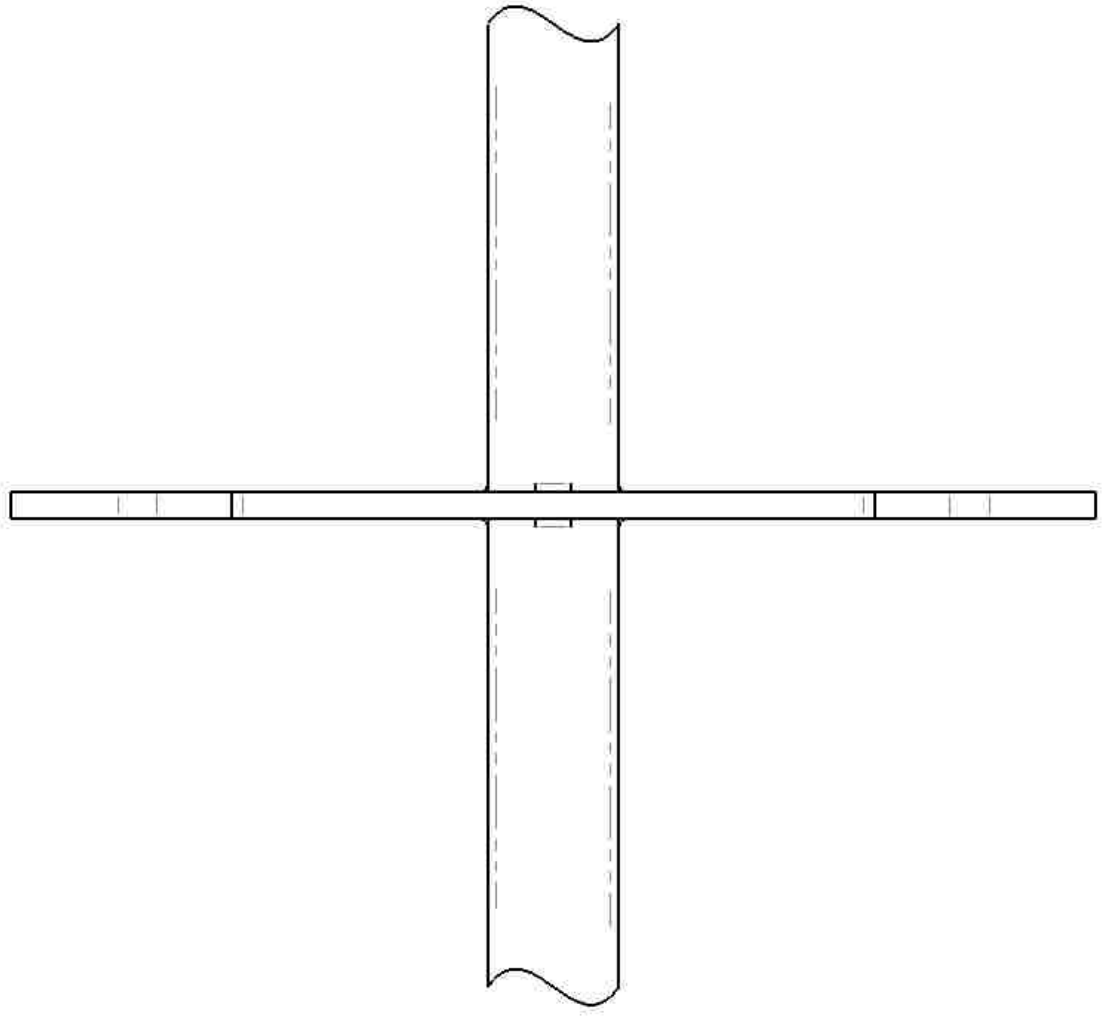

Figure 88: Side View. Quad-Cantilevered Drain/Cantilever System composed of a Rectangular Drain and four Quarter-Circular-shaped Cantilevers.

5-8 Distinction from the Related U.S. Patent Documents

U.S. Pat. No. 4,654,032 [RP1] is a drain/anchoring system that utilizes an extruded elliptical flange. Unlike to the herein described drain/cantilever systems, which consist of a bi- or quad-cantilever, the connection between the elliptical flange and the drain covers the full range of 360° and thus a different design.

CHAPTER 6

6-1 Inventors

1. Cyrus O. Abbasi B.S., University of New Mexico, Mechanical Engineering Department.
2. Tariq A. Khraishi PhD., University of New Mexico, Mechanical Engineering Department.
3. Bret Baack MD., University of New Mexico, Department of Plastic Surgery.

6-2 Title

"Flexi Drain/Catheter": A New & Ultra Flexible Surgical Drain/Catheter.

6-3 Abstract

A new flexible surgical drain/catheter system is developed. The flexible system encompasses a *Flexible Section* that can be incorporated in the design of surgical drains/catheters of any kind. By incorporating this flexible system, a surgical drain/catheter will possess three significant additional characteristics. These additional characteristics will make the herein designs superior to the existing designs [P21-P40]. The first characteristic is that the surgical drain/catheter can be bent without causing any fold/crease to its outer and inner surfaces. The second characteristic prevents internal occlusions while the drain/catheter is bent. The third characteristic is that *Flexible Section* can also be used as a reliable region of drain/catheter anchorage to the patient's body. The developed *Flexible Sections* are categorized in three different types: *Semicircular*, *Triangular* and *Rectangular*. Note that these three categories are used as examples only. Other geometries within the *Flexible Section* can be developed and are encompassed by this patent.

6-4 Background of the Invention

Surgical drains/catheters are efficient and reliable means to extract or relocate undesirable bodily fluids from or within the body of patient during and after a surgery. Surgical drains/catheters can be *Circular-bodied* or *Rectangular-bodied* as shown in Figs. 89 & 119 respectively. A Circular-bodied drain/catheter incorporates a drainage tube that has a circular cross-section as shown in Figs. 89 & 92. A Rectangular-bodied drain/catheter incorporates a drainage tube that has a rectangular cross-section as shown in Figs. 119 & 122. The shape of the surgical drain's/catheter's body is chosen by the surgeon according to the type of surgical procedure that he/she is conducting as well as the location of the drain's/catheter's placement inside or outside of a patient's body.

For instance, after the removal of an abdominal cancerous tumor the remaining cavity is usually filled with bodily fluids such as blood that can cause infections and delay the healing process of the affected area. Usually for an abdominal surgical procedure Circular-bodied drains/catheters are utilized. After employing the drains/catheters within or extending out of the body, they are connected to vacuum chambers, which extract the undesirable fluids via the suction forces induced by the vacuum chambers.

The drains/catheters are held in place by suture-threads that are knotted around the outer surface of the surgical drains/catheters and then sutured to the skin or the surrounding tissue. Then the remainder of the extruding drain is folded and taped flush against the skin of the patient. This is the most widely used drain/catheter-to-the-body attachment technique.

Several problems arise after using this mode of attachment. Upon constant respiration of the patient, the knots involved in the anchoring sutures might loosen up and the drain/catheter can move and be displaced from its intended position. In case of a drain/catheter attached to the skin of a patient, it has been reported that upon the natural respiratory motion of the patient's body the knots will loosen up within a period of 2 to 3 weeks. Furthermore, it has also been reported that upon accidental events (e.g. such as the drain/catheter getting stuck to a doorknob) the entire drain/catheter can be pulled out due to the rupture of the sutures or the anchoring skin/tissue. Hence, a second surgery will be needed to place a new drain/catheter.

Another problematic pattern is developed when the drain/catheter is folded and taped along the skin. The folding of the drain/catheter causes internal occlusion that leads to reduced fluid drainage. Moreover, the folding induces creases along the internal/external surfaces of the drain/catheter, which may lead to internal/external damages to the drain/catheter.

One more significant problem is faced in some cases of chest and abdominal trauma. When a patient has severe internal bleeding the utilization of large diameter drains (0.75 cm to 2.0 cm external diameter) is a routine procedure. The high diameter drain is usually run through the rips of the patient connecting the internal and external environments of the patient's body. The high diameter drains are highly inflexible and maintain an almost perpendicular position to the patient's skin. In other words after they exit the body through the rips, they just stick out of the body and cannot be made flush with the skin unless brute force is used. This forcing action not only induces severe internal drain occlusions but also causes restoring tensile and compressive forces in the skin/tissue,

which in turn cause severe pain to the patient. Moreover, the above-described conventional drain/catheter-to-the-body attachment becomes more and more unreliable as the diameter of the drain/catheter increases. This is because as the diameter of the drain increases more suture material is needed to be wrapped around the drain to hold it in place. The longer the sutures the higher is the probability of the suture's slippage and their tangling.

The herein developed new drain/catheter *Flexible Sections* are also intended to be utilized as reliable drain segments around which sutures can be securely wrapped. These rims and grooves of the *Flexible Sections* provide the perfect geometry within which sutures can securely fit without any subsequent slippage. The sutures can then be run through the skin or any other underlying tissue to ensure a secure mode of attachment. It should be noted that the herein-described drain/catheter *Flexible Sections* can be incorporated in most if not all of the conventional surgical drains/catheters, namely drains/catheters without the *Flexible Section*. In other words, a continuous drain/catheter composed of only Section 1 (see Figs. 97 & 127) & Section 2 (see Figs. 98 & 128) can be considered as a conventional drain/catheter.

6-5 Summary of the Invention

This document includes two types of the drain/catheter systems, namely drains/catheters with either a circular or a rectangular cross-sectioned body. Examples of these the *Circular-bodied* and the *Rectangular-bodied* drain/catheter types are shown in Figs. 89 & 119 respectively. The drain/catheter types are intended to be manufactured from biocompatible and flexible polymer material. Both drain/catheter types can be utilized completely within the patient's body or extending from the body's interior and passing through the skin into its exterior surroundings or vice versa.

In the case of extension from the interior to the exterior of the body, both types can be inserted through the skin into the body from the outside environment or pulled out through the skin after being placed within the interior of the patient's body. The drains usually can pass through the natural openings of the body or through the skin/tissue-incisions performed by the operating surgeon.

After the drain/catheter is placed in its intended position, the surgeon secures in its position via surgical sutures. The most widely-used mode of drain/catheter attachment to the skin or any other underlying tissue is by passing the surgical sutures through the skin/tissue, tightly wrapping them around the drain/catheter and finally knotting them.

The herein presented *Flexible Sections* of the drains/catheters possesses three additional features over any conventional drain/catheter, i.e. a drain/catheter without a *Flexible Section*. These three additional features are explained in what follows.

6-5-1 Increased Drain/Catheter Flexibility

6-5-1-1 Circular-Bodied Drain/Catheter

As seen in Fig. 89, the drain/catheter is composed of three segments: Section 1, the *Flexible Section* and Section 2. Let's assume that Section 2 is fixated in space. Then, Section 1, with respect to Section 2, can be bent anywhere from 0° to 180° within any plane that is parallel and passing through the longitudinal-axis of the drain/catheter, i.e. the *z*-axis. Fig. 93 illustrates a 90° bend relation between Sections 1 & 2 within the *z-y* plane.

6-5-1-2 Rectangular-Bodied Drain/Catheter

As seen in Fig. 119, the drain/catheter is composed of three segments: Section 1, the *Flexible Section* and Section 2. Let's assume that Section 2 is fixated in space. Then, Section 1, with respect to Section 2, can be bent anywhere from 0° to 180° within the *z-y* or *x-y* planes. The base and the width of the Rectangular-bodied drain/catheter are illustrated in Fig. 119. Fig. 123 illustrates a 90° bend relation between Sections 1 & 2 within the *z-y* plane. Additionally, at any already bent position, for instance the shown 90° bend, other bends can be made within the *z-y* or the *x-y* planes.

6-5-2 Flexibility without any Undesirable Consequences

The above-mentioned increased flexibility comes without any undesirable consequences. Specifically, the increased flexibility does not induce any internal or external transverse fold/crease to either the internal or the external surfaces of the drain/catheter. Without an internal or external fold/crease the internal drain/catheter passage does not close/collapse and maintains its initial diameter, i.e. the internal diameter of the straight drain/catheter. By doing so, the flow of fluids within the internal passage of a bent drain/catheter is not hindered and stays continuous at the same rate as within the straight portion of the drain/catheter.

Figs. 97 & 98 represent the two sections that are incorporated in the design of conventional Circular-bodied drains/catheters. More specifically, a continuous connection between these two sections without incorporating a *Flexible Section*, results in a conventional Circular-bodied drain/catheter, see Fig. 99. Figs. 127 & 128 represent the two sections that are incorporated in the design of conventional Rectangular-bodied drains/catheters. More specifically, a continuous connection between these two sections without incorporating a *Flexible Section*, results in a conventional Rectangular-bodied drain/catheter, see Fig. 129.

When a surgeon applies a sharp bend, i.e. a bend with a relative low radius of curvature to these conventional drains/catheters, a transverse fold/crease will be induced to the cross-section of that drain/catheter. This fold/crease occurs about the center of curvature of the bend and is parallel to the transverse direction of the drain/catheter. Note that the transverse direction can lie along either the *x*- or the *y*-axis as illustrated in Fig. 146.

Figs. 147 through 151 show the severity of the drain's/catheter's deformation induced by the fold/crease. Note that Figs. 146 through 151 illustrate a conventional drain/catheter, which experiences a 180° bend. Fig. 148 gives a better insight into both the internal and external deformations of the drain/catheter. 'I' signifies the internal diameter of a straight portion of the drain/catheter. 'II' signifies a reduced internal diameter of the drain/catheter. As illustrated in Fig. 148, it should be noted that as one moves closer and closer to the location of the transverse fold/crease the internal diameter almost vanishes. This means that the internal passage of the drain/catheter almost fully closes.

Fig. 149 is the best representative of how much a conventional drain/catheter can deform once a sharp bend is applied to the drain/catheter. It shows the expansion of the external drain/catheter diameters along the one of the two transverse directions. Here the expansion occurs along the *x*-axis. Note that albeit not being shown, the internal diameter also experiences an expansion along the *x*-axis. 'I' shows the cross-sectional transverse fold/crease that occurs at the cross-section of the drain/catheter. 'II' shows the expansion of the external diameter into the surrounding space. 'III' shows that original unexpanded external diameter of the drain/catheter. Note that 'II' has almost twice the length of 'III'.

Fig. 151 underlines the collapse of the internal/external drain/catheter diameters along the other transverse direction, namely along the *y*-axis. Note that the internal passage of the drain/catheter is almost closed. Figs. 146 through 151 represent the internal/external deformations that happen to the cross-section of a conventional Circular-bodied drain/catheter. Although not illustrated here, similar internal/external

deformations would happen to the cross-section of a conventional Rectangular-bodied drain/catheter as well. These types of deformation are dictated by the laws of Elasticity and cannot be avoided when the drain/catheter does not incorporate a *Flexible Section*.

The following undesirable consequences arise if a drain/catheter does not incorporate a *Flexible Section* in its design and undergoes a bend.

6-5-2-1 1st Undesirable Consequence

The internal passage of the drain/catheter can be closed and with that the flow of any fluids within the drain/catheter can be hindered.

6-5-2-2 2nd Undesirable Consequence

Depending on the degree of the bend as well as the stiffness of the drain's/catheter's material, internal and external cracks can initiate and propagate starting at or within the vicinity of the transverse fold/crease. Such cracks can disrupt the structural integrity of the drain/catheter and lead to leaks and with that to the failure or inefficiency of the drain/catheter.

6-5-2-3 3rd Undesirable Consequence

The expansion of the drain's/catheter's internal/external diameters along one transverse axis as well as their simultaneous collapse along the other transverse axis can induce unnecessary strains/stresses to the underlying or surrounding skin/tissue of the patient.

Usually the drains/catheters that extend from the interior of the body to its exterior are bent right where they exit the skin/tissue. If the surgeon had to insert an incision to make the opening through which the drain/catheter exits the body, the healing process of that incision can be prolonged if it experiences unnecessary strains/stresses. The anchoring sutures are also wrapped around the drain's/catheter's external surface right at or in the vicinity of the bend. Hence, such an expansion or collapse of the drain's/catheter's external diameter can

possibly lead to loosening of the anchoring sutures. Loosened sutures can then lead to instability and possible failure of the drain's/catheter's anchorage.

The *Flexible Sections* of both the Circular- and the Rectangular-bodied drains/catheters are able to be sharply bent without inducing any of the three undesirable consequences mentioned above. This is because the incorporated Rims and Grooves of the *Flexible Section* are specifically designed to stretch or compress once the *Flexible Section* is bent.

The stretchability or compressibility of the *Flexible Section's* Rims/Grooves are therefore able to embrace any external deformations induced by a sharp bend. By doing so, the internal and external diameters of the drain/catheter are maintained as they were before any bend. As seen in Figs. 95, 109 & 117, the shortest internal diameter within the *Flexible Sections* of all three different types of Circular-bodied drains/catheters, namely the distances illustrated by 'I', are equal to 'II', namely the internal diameters of the unbent Section 2. Also, as seen in Figs. 125, 136 & 144, the shortest internal diameter within the *Flexible Sections* of all three different types of Rectangular-bodied drains/catheters, namely the distances illustrated by 'I', are equal to 'II'. To better understand the ongoing deformations of a sharply bent drain/catheter please refer to Figs. 152 through 157.

When a surgeon applies a sharp bend, i.e. a bend with a relative low radius of curvature to a drain/catheter that incorporates a *Flexible Section*, no transverse fold/crease will be induced to the cross-section of that drain/catheter. Fig. 152 shows

a drain/catheter that incorporates a *Flexible Section*. Although, the drain/catheter undergoes a 180° bend, no transverse fold/crease can be seen.

Fig. 154 gives a better insight into both the internal and external deformations of the drain/catheter. 'I' signifies the internal diameter of a straight portion of the drain/catheter. 'II' signifies the internal diameter of the drain/catheter within the *Flexible Section* of the drain/catheter. Fig. 154 shows that 'I' and 'II' are equal in their lengths. This means that the internal passage of the drain/catheter remains fully open and no hindrance is introduced to any fluid flow within the drain/catheter.

Fig. 155 is the best representative of how the internal diameter of a drain/catheter that incorporates a *Flexible Section* remains unchanged once a sharp bend is applied to the drain/catheter. It shows that there is no expansion or collapse of the external drain/catheter diameters along any of the two transverse directions. 'I' hints to the fact that no cross-sectional transverse fold/crease occurs at the cross-section of the drain/catheter. 'II' shows the external Groove diameter of the drain's/catheter's *Flexible Section*. 'III' shows that original external Groove diameter of the drain/catheter. Note that 'II' and 'III' are equal in length. This means that the drain/catheter does not expand into its surrounding space once it is bent.

Fig. 157 further underlines the fact that the cross-section of a bent drain/catheter that incorporates a *Flexible Section* remains totally intact and undeformed. Note that the internal passage of the drain/catheter is fully open.

Figs. 152 through 157 show that no internal/external deformations happen to the cross-section of a Circular-bodied drain/catheter that incorporates a *Flexible Section*.

Although not illustrated here, similarly, no internal/external deformations would happen to the cross-section of a Rectangular-bodied drain/catheter that incorporates a *Flexible Section*.

6-5-3 *Flexible Section*: A Region/Area for Drain/Catheter Anchorage

The *Flexible Section* can also be utilized as a suitable and reliable point of drain/catheter anchorage to the underlying skin/tissue. Figs. 100 & 102 illustrate how a Circular-bodied drain/catheter can be securely attached to the underlying skin/tissue. The same kind of attachment can be applied to the Rectangular-bodied drain/catheter as well. As illustrated in Figs. 100 & 102, a major portion of Section 2 of the drain/catheter is within the body of the patient. The upper part of Section 2, namely its connecting part to the *Flexible Section* penetrates and is surrounded by the skin/tissue of the patient.

As seen in Figs. 100 & 102, the bend in the drain/catheter occurs within the *Flexible Section*. Specifically, the bend starts at the start of the *Flexible Section* and ends not far into the *Flexible Section*. Depending on the geometry of the underlying skin/tissue, the angle of the bend can vary from 0° to 180°. Note that in Figs. 100 & 102 the bend occurs within the *z*-*y* plane. However, the bend can be made within other planes that are parallel to the *z*-axis and also pass through it. Bends with an angle greater than 180° are also possible if the geometry/space of the underlying skin/tissue allows it. After the bend terminates, the remaining and straight portion of the *Flexible Section* can be used for additional bends and/or anchorage purposes.

A safe anchorage to the underlying skin/tissue is made by utilizing surgical sutures. As seen in Figs. 100 & 102, the suture pass through the underlying skin/tissue and then wrap around the drain/catheter by fitting within the external Grooves of the *Flexible Section*. Once the sutures are in place and tightened they can no longer slip along the drain's/catheter's surface. This is because the *Flexible*

Section's external Rims act as physical barriers, which do not allow any suture dislodgement along the surface of the drain/catheter. It should be noted that the length of the *Flexible Section* can vary by the manufacturer. A longer *Flexible Section* provides more flexibility to the drain/catheter as well as a longer anchoring zone. More sutures can be wrapped around a longer anchoring zone and by doing so the reliability of the anchoring increases.

6-6 Specific Design-Details

Specific design details regarding both types of drain/catheter systems, namely the Circular- and the Rectangular- bodied drain/catheter systems are explained as follows.

6-6-1 Circular-Bodied Drain/Catheters

Three different drain/catheter designs have been developed as examples for a Circular-bodied drain/catheter system. Each of the three Circular-bodied drains/catheters is composed of a different *Flexible Section*. The *Flexible Sections* are of the following types: Semicircular, Triangular and Rectangular. Each of these three different Circular-bodied drain/catheter designs is laid out in detail as follows.

6-6-1-1 'Circular-Bodied' Drain/Catheter, 'Semicircular' *Flexible Section*

Figs. 89 through 96 represent a Circular-bodied drain/catheter with a 'Semicircular' *Flexible Section*. As illustrated in Fig. 89, this design is composed of a three sections: Sections 1 & 2 as well as a 'Semicircular' *Flexible Section*. A 'Semicircular' *Flexible Section* means that this particular *Flexible Section* encompasses 'Semicircular' external/internal Rims/Grooves as clearly illustrated by Figs. 89 through 91. Sections 1 & 2 as well as the Grooves of the *Flexible Section*, have an external diameter of 7.0 mm and a uniform thickness of 2.0 mm.

Section 1 depicts the top-end (usually external to the body) of the drain/catheter which serves as an outlet for the extraction of any undesirable fluid. An illustrative representative Extension of Section 1 is shown in Fig 97. This Extension is connected to a vacuum chamber, which provides the suction force that extracts the undesirable fluids. Section 2 is the low-end (usually internal to the body) of the drain/catheter which serves as an inlet for the undesirable fluid that needs to be extracted from the internal of the patient's body. An illustrative representative extension of Section 2 is shown in Fig 98.

Fig. 38 shows an enlarged view of the external 'Semicircular' Rims/Grooves involved in the *Flexible Section* of this particular design. Fig. 91 gives a better insight into the internal and external design of the 'Semicircular' *Flexible Section*. Every semicircle has a diameter of 1.0 mm. Based on that the pitch-to-pitch distance between each Semicircular Rim/Groove is 2.0 mm. 'I' represents the shortest internal diameter within the *Flexible Section*, namely the distance between the internal Rims. 'II' represents the diameter of the internal passage of

the drain/catheter, i.e. the internal diameter of Sections 1 & 2. The length of both ‘I’ and ‘II’ is 3.0 mm.

Fig. 92 shows the design from the top. ‘I’ signifies three different distances that are equal in magnitude: the internal diameters of both Sections 1 & 2 as well as the shortest internal diameter of the *Flexible Section*. Moreover, it can be seen that the external ‘Semicircular’ Rims of the *Flexible Section* do not extend much into the surrounding space around the drain/catheter. Therefore, the drain/catheter can be placed through natural or incised openings with diameters that are very close to the external diameter of Sections 1 & 2.

Figs. 93 through 96 show different angles of a 90° bend drain/catheter. As seen in Figs. 94 & 95, the 90° bend begins at the start of the *Flexible Section*, i.e. Section 2 is not involved in the bend. The bend ends within the early portions of the *Flexible Section*. The remaining straight portion of the *Flexible Section* can then be used for additional bends if desired by the surgeon. Moreover, this straight portion of the *Flexible Section* can also serve as a location of drain/catheter anchorage to its underlying skin/tissue via the utilization of surgical sutures. Figs. 100 through 102 illustrate how a Circular-bodied drain/catheter with a ‘Semicircular’ *Flexible Section* is anchored to the underlying skin/tissue.

Fig. 95 illustrates the interior of a bent drain’s/catheter’s *Flexible Section*. ‘I’ denotes the shortest diameter within the bent *Flexible Section*. ‘II’ denotes the internal diameter of the drain’s/catheter’s Section 2, which is equal to the internal diameter of Section 1 as well. Note that ‘I’ and ‘II’ are equal in their lengths. This

means that the internal passage of the drain/catheter maintains the same diameter regardless whether the drain/catheter is in a straight or in a bent configuration. Therefore, no occlusions are introduced within the internal passage of the drain/catheter. Hence, the flow of fluids within a drain/catheter, which incorporates a *Flexible Section*, is not hindered by internal occlusions.

Fig. 96 shows a closer view of the bent drain/catheter from the top. Note that the external 'Semicircular' Rims/Grooves in the straight portion of the *Flexible Section* provide the perfect location, where surgical sutures can be wrapped around the drain/catheter. Figs. 100 through 102 illustrate how a secure drain/catheter anchorage is made possible by these Rims/Grooves.

By looking at Figs. 100 & 101, it can be seen that surgical sutures pass through the underlying skin/tissue of the patient and then wrap around the 'Semicircular' *Flexible Section* of the drain/catheter. Specifically, the surgical sutures fit within the external 'Semicircular' Grooves of the *Flexible Section*. Once the sutures are wrapped around the *Flexible Section*, the *Flexible Section's* 'Semicircular' Rims prevent any motion of the drain/catheter unit along the *y*-axis as illustrated in Fig. 100 and 101. Moreover, other movements of the drain/catheter unit are prevented as well. By looking at Fig. 100, it can be seen that locations, which are wrapped by sutures within the 'Semicircular' *Flexible Section*, cannot be moved/displaced within the *x*-*y* plane. Therefore, the drain/catheter is securely locked in space and not dislodgeable.

6-6-1-2 'Circular-Bodied' Drain/Catheter, 'Triangular' *Flexible Section*

Figs. 103 through 110 represent a Circular-bodied drain/catheter with a 'Triangular' *Flexible Section*. As illustrated in Fig. 103, this design is composed of a three sections: Sections 1 & 2 as well as a 'Triangular' *Flexible Section*. A 'Triangular' *Flexible Section* means that this particular *Flexible Section* encompasses 'Triangular' external/internal Rims/Grooves as clearly illustrated by Figs. 103 through 105. Sections 1 & 2 as well as the Grooves of the *Flexible Section*, have an external diameter of 7.0 mm and a uniform thickness of 2.0 mm.

Fig. 104 shows an enlarged view of the external 'Triangular' Rims/Grooves involved in the *Flexible Section* of this particular design. Fig. 105 gives a better insight into the internal and external design of the 'Triangular' *Flexible Section*. All the triangles are equilateral triangles. The sides of each triangle are 1.0 mm long. Based on that the pitch-to-pitch distance between each Triangular Rim/Groove is 1.0 mm. 'I' represents the shortest internal diameter within the *Flexible Section*, namely the distance between the internal Rims. 'II' represents the diameter of the internal passage of the drain/catheter, i.e. the internal diameter of Sections 1 & 2. The length of both 'I' and 'II' is 3.0 mm.

Fig. 106 shows the design from the top. 'I' signifies three different distances that are equal in magnitude: the internal diameters of both Sections 1 & 2 as well as the shortest internal diameter of the *Flexible Section*. Moreover, it can be seen that the external 'Triangular' Rims of the *Flexible Section* do not extend much into the surrounding space around the drain/catheter. Therefore, the drain/catheter

can be placed through natural or incised openings with diameters that are very close to the external diameter of Sections 1 & 2.

Figs. 107 through 110 show different angles of a 90° bend drain/catheter. As seen in Figs. 108 & 109, the 90° bend begins at the start of the *Flexible Section*, i.e. Section 2 is not involved in the bend. The bend ends within the early portions of the *Flexible Section*. The remaining straight portion of the *Flexible Section* can then be used for additional bends if desired by the surgeon. Moreover, this straight portion of the *Flexible Section* can also serve as a location of drain/catheter anchorage to its underlying skin/tissue via the utilization of surgical sutures. Figs. 100 through 102 illustrate how a Circular-bodied drain/catheter with a 'Semicircular' *Flexible Section* is anchored to the underlying skin/tissue. In a very similar manner, a Circular-bodied drain/catheter with a 'Triangular' *Flexible Section* can be anchored to its underlying skin/tissue.

Fig. 109 illustrates the interior of a bent drain's/catheter's *Flexible Section*. 'I' denotes the shortest diameter within the bent *Flexible Section*. 'II' denotes the internal diameter of the drain's/catheter's Section 2, which is equal to the internal diameter of Section 1 as well. Note that 'I' and 'II' are equal in their lengths. This means that the internal passage of the drain/catheter maintains the same diameter regardless whether the drain/catheter is in a straight or in a bent configuration. Therefore, no occlusions are introduced within the internal passage of the drain/catheter. Hence, the flow of fluids within a drain/catheter, which incorporates a *Flexible Section*, is not hindered by internal occlusions.

Fig. 110 shows a closer view of the bent drain/catheter from the top. Note that the external 'Triangular' Rims/Grooves in the straight portion of the *Flexible Section* provide the perfect location, where surgical sutures can be wrapped around the drain/catheter. Figs. 100 through 102 illustrate how a secure anchorage of a Circular-bodied drain/catheter with a 'Semicircular' *Flexible Section* is made possible by these external Rims/Grooves. The external Rims/Grooves of a Circular-bodied drain/catheter with a 'Triangular' *Flexible Section* act in a similar manner.

Analogous to the anchoring method illustrated by Figs. 100 through 102, surgical sutures pass through the underlying skin/tissue of the patient and then wrap around the 'Triangular' *Flexible Section* of the drain/catheter. Specifically, the surgical sutures fit within the external 'Triangular' Grooves of the *Flexible Section*. Once the sutures are wrapped around the *Flexible Section*, the *Flexible Section's* 'Triangular' Rims prevent any motion of the drain/catheter unit along the *y*-axis (similar to the anchorage shown in Figs. 100 & 101). Moreover, other movements of the drain/catheter unit are prevented as well. Similar to what is seen in Fig. 100, locations that are wrapped by sutures within the 'Triangular' *Flexible Section*, cannot be moved/displaced within the *x*-*y* plane. Therefore, the drain/catheter is securely locked in space and not dislodgeable.

6-6-1-3 'Circular-Bodied' Drain/Catheter, 'Rectangular' *Flexible Section*

Figs. 111 through 118 represent a Circular-bodied drain/catheter with a 'Rectangular' *Flexible Section*. As illustrated in Fig. 111, this design is composed of a three sections: Sections 1 & 2 as well as a 'Rectangular' *Flexible Section*. A 'Rectangular' *Flexible Section* means that this particular *Flexible Section* encompasses 'Rectangular' external/internal Rims/Grooves as clearly illustrated by Figs. 111 through 113. Sections 1 & 2 as well as the Grooves of the *Flexible Section*, have an external diameter of 7.0 mm and a uniform thickness of 2.0 mm.

Fig. 112 shows an enlarged view of the external 'Rectangular' Rims/Grooves involved in the *Flexible Section* of this particular design. Fig. 113 gives a better insight into the internal and external design of the 'Rectangular' *Flexible Section*. All rectangles are squares. The sides of each square are 1.0 mm long. Based on that the pitch-to-pitch distance between each Rectangular Rim/Groove is 2.0 mm. 'I' represents the shortest internal diameter within the *Flexible Section*, namely the distance between the internal Rims. 'II' represents the diameter of the internal passage of the drain/catheter, i.e. the internal diameter of Sections 1 & 2. The length of both 'I' and 'II' is 3.0 mm.

Fig. 114 shows the design from the top. 'I' signifies three different distances that are equal in magnitude: the internal diameters of both Sections 1 & 2 as well as the shortest internal diameter of the *Flexible Section*. Moreover, it can be seen that the external 'Rectangular' Rims of the *Flexible Section* do not extend much into the surrounding space around the drain/catheter.. Therefore, the drain/catheter

can be placed through natural or incised openings with diameters that are very close to the external diameter of Sections 1 & 2.

Figs. 115 through 118 show different angles of a 90° bend drain/catheter. As seen in Figs. 116 & 117, the 90° bend begins at the start of the *Flexible Section*, i.e. Section 2 is not involved in the bend. The bend ends within the early portions of the *Flexible Section*. The remaining straight portion of the *Flexible Section* can then be used for additional bends if desired by the surgeon. Moreover, this straight portion of the *Flexible Section* can also serve as a location of drain/catheter anchorage to its underlying skin/tissue via the utilization of surgical sutures. Figs. 100 through 102 illustrate how a Circular-bodied drain/catheter with a 'Semicircular' *Flexible Section* is anchored to the underlying skin/tissue. In a very similar manner, a Circular-bodied drain/catheter with a 'Rectangular' *Flexible Section* can be anchored to its underlying skin/tissue.

Fig. 117 illustrates the interior of a bent drain's/catheter's *Flexible Section*. 'I' denotes the shortest diameter within the bent *Flexible Section*. 'II' denotes the internal diameter of the drain's/catheter's Section 2, which is equal to the internal diameter of Section 1 as well. Note that 'I' and 'II' are equal in their lengths. This means that the internal passage of the drain/catheter maintains the same diameter regardless whether the drain/catheter is in a straight or in a bent configuration. Therefore, no occlusions are introduced within the internal passage of the drain/catheter. Hence, the flow of fluids within a drain/catheter, which incorporates a *Flexible Section*, is not hindered by internal occlusions.

Fig. 118 shows a closer view of the bent drain/catheter from the top. Note that the external 'Rectangular' Rims/Grooves in the straight portion of the *Flexible Section* provide the perfect location, where surgical sutures can be wrapped around the drain/catheter. Figs. 100 through 102 illustrate how a secure anchorage of a Circular-bodied drain/catheter with a 'Semicircular' *Flexible Section* is made possible by these external Rims/Grooves. The external Rims/Grooves of a Circular-bodied drain/catheter with a 'Rectangular' *Flexible Section* act in a similar manner.

Analogous to the anchoring method illustrated by Figs. 100 through 102, surgical sutures pass through the underlying skin/tissue of the patient and then wrap around the 'Rectangular' *Flexible Section* of the drain/catheter. Specifically, the surgical sutures fit within the external 'Rectangular' Grooves of the *Flexible Section*. Once the sutures are wrapped around the *Flexible Section*, the *Flexible Section's* 'Rectangular' Rims prevent any motion of the drain/catheter unit along the *y*-axis (similar to the anchorage shown in Figs. 100 & 101). Moreover, other movements of the drain/catheter unit are prevented as well. Similar to what is seen in Fig. 100, locations that are wrapped by sutures within the 'Rectangular' *Flexible Section*, cannot be moved/displaced within the *x*-*y* plane. Therefore, the drain/catheter is securely locked in space and not dislodgeable.

6-6-2 Rectangular-Bodied Drain/Catheters

Three different drain/catheter designs have been developed as examples for a Rectangular-bodied drain/catheter system. Each of the three Rectangular-bodied drains/catheters is composed of a different *Flexible Section*. The *Flexible Sections* are of the following types: Semicircular, Triangular and Rectangular. Each of these three different Rectangular-bodied drain/catheter designs is laid out in detail as follows.

6-6-2-1 'Rectangular-Bodied' Drain/Catheter, 'Semicircular' *Flexible Section*

Figs. 119 through 126 represent a Rectangular-bodied drain/catheter with a 'Semicircular' *Flexible Section*. As illustrated in Fig. 119, this design is composed of a three sections: Sections 1 & 2 as well as a 'Semicircular' *Flexible Section*. A 'Semicircular' *Flexible Section* means that this particular *Flexible Section* encompasses 'Semicircular' external/internal Rims/Grooves as clearly illustrated by Figs. 119 through 91. As seen in Fig. 119, the Rectangular body of a drain/catheter with a 'Semicircular' *Flexible Section,* is composed of a base and a width. The base and the width are 1.0 cm and 7.0 mm long respectively. Sections 1 & 2 as well as the *Flexible Section* have a uniform thickness of 2.0 mm. Therefore, the base of the drain's/catheter's internal passage is 6.0 mm long and its width is 3.0 mm long.

Section 1 depicts the top-end (usually external to the body) of the drain/catheter which serves as an outlet for the extraction of any undesirable fluid. A representative extension of Section 1 is shown in Fig 127. This extension is connected to a vacuum chamber, which provides the suction force that extracts the undesirable fluids. Section 2 is the low-end (usually internal to the body) of

the drain/catheter which serves as an inlet for the undesirable fluid that needs to be extracted from the inside of the patient's body. A representative extension of Section 2 is shown in Fig 128.

Fig. 120 shows an enlarged view of the external 'Semicircular' Rims/Grooves involved in the *Flexible Section* of this particular design. Fig. 121 gives a better insight into the internal and external design of the 'Semicircular' *Flexible Section*. Every semicircle has a diameter of 1.0 mm. Based on that the pitch-to-pitch distance between each Semicircular Rim/Groove is 2.0 mm. 'I' represents the shortest internal transverse dimension of the *Flexible Section* along the *x*-axis, namely the distance between the internal Rims that are parallel to the *x*-axis. 'II' represents the transverse dimension of the internal passage of the drain/catheter, i.e. the internal transverse dimensions of Sections 1 & 2 that are parallel to the *x*-axis. The length of both 'I' and 'II' is 6.0 mm.

Fig. 122 shows the design from the top. 'I' signifies three different distances along the *y*-axis, which are equal in magnitude: the internal transverse dimensions of both Sections 1 & 2 as well as the shortest internal transverse dimension of the *Flexible Section*. Moreover, it can be seen that the external 'Semicircular' Rims of the *Flexible Section* do not extend much into the surrounding space around the drain/catheter. Therefore, the drain/catheter can be placed through natural or incised openings with diameters that are very close to the external diameter of Sections 1 & 2.

Figs. 123 through 126 show different angles of a 90° bend drain/catheter. As seen in Figs. 124 & 125, the 90° bend begins at the start of the *Flexible Section*, i.e. Section 2 is not involved in the bend. The bend ends within the early portions of the *Flexible Section*. The remaining straight portion of the *Flexible Section* can then be used for additional bends if desired by the surgeon. Moreover, this straight portion of the *Flexible Section* can also serve as a location of drain/catheter anchorage to its underlying skin/tissue via the utilization of surgical sutures. Figs. 100 through 102 illustrate how a Circular-bodied drain/catheter with a 'Semicircular' *Flexible Section* is anchored to the underlying skin/tissue. In a very similar manner, a Rectangular-bodied drain/catheter with a 'Semicircular' *Flexible Section* can be anchored to its underlying skin/tissue.

Fig. 125 illustrates the interior of a bent drain's/catheter's *Flexible Section*. 'I' denotes the shortest diameter within the bent *Flexible Section*. 'II' denotes the internal diameter of the drain's/catheter's Section 2, which is equal to the internal diameter of Section 1 as well. Note that 'I' and 'II' are equal in their lengths. This means that the internal passage of the drain/catheter maintains the same diameter regardless whether the drain/catheter is in a straight or in a bent configuration. Therefore, no occlusions are introduced within the internal passage of the drain/catheter. Hence, the flow of fluids within a drain/catheter, which incorporates a *Flexible Section*, is not hindered by internal occlusions.

Fig. 126 shows a closer view of the bent drain/catheter from the top. Note that the external 'Semicircular' Rims/Grooves in the straight portion of the *Flexible Section* provide the perfect location, where surgical sutures can be wrapped

around the drain/catheter. Figs. 100 through 102 illustrate how a secure anchorage of a Circular-bodied drain/catheter with a 'Semicircular' *Flexible Section* is made possible by these external Rims/Grooves. The external Rims/Grooves of a Rectangular-bodied drain/catheter with a 'Semicircular' *Flexible Section* act in a similar manner.

Analogous to the anchoring method illustrated by Figs. 100 through 102, surgical sutures pass through the underlying skin/tissue of the patient and then wrap around the 'Semicircular' *Flexible Section* of the drain/catheter. Specifically, the surgical sutures fit within the external 'Semicircular' Grooves of the *Flexible Section*. Once the sutures are wrapped around the *Flexible Section*, the *Flexible Section's* 'Semicircular' Rims prevent any motion of the drain/catheter unit along the *y*-axis (similar to the anchorage shown in Figs. 100 & 101). Moreover, other movements of the drain/catheter unit are prevented as well. Similar to what is seen in Fig. 100, locations that are wrapped by sutures within the 'Semicircular' *Flexible Section*, cannot be moved/displaced within the *x-y* plane. Therefore, the drain/catheter is securely locked in space and not dislodgeable.

6-6-2-2 'Rectangular-Bodied' Drain/Catheter, 'Triangular' *Flexible Section*

Figs. 130 through 137 represent a Rectangular-bodied drain/catheter with a 'Triangular' *Flexible Section*. As illustrated in Fig. 130, this design is composed of a three sections: Sections 1 & 2 as well as a 'Triangular' *Flexible Section*. A 'Triangular' *Flexible Section* means that this particular *Flexible Section* encompasses 'Triangular' external/internal Rims/Grooves as clearly illustrated by Figs. 130 through 132. Similar to Fig. 119, the Rectangular body of a drain/catheter with a 'Triangular' *Flexible Section*, is composed of a base and a width. The base and the width are 1.0 cm and 7.0 mm long respectively. Sections 1 & 2 as well as the *Flexible Section* have a uniform thickness of 2.0 mm. Therefore, the base of the drain's/catheter's internal passage is 6.0 mm long and its width is 3.0 mm long.

Fig. 131 shows an enlarged view of the external 'Triangular' Rims/Grooves involved in the *Flexible Section* of this particular design. Fig. 132 gives a better insight into the internal and external design of the 'Triangular' *Flexible Section*. All the triangles are equilateral triangles. The sides of each triangle are 1.0 mm long. Based on that the pitch-to-pitch distance between each Triangular Rim/Groove is 1.0 mm. 'I' represents the shortest internal transverse dimension of the *Flexible Section* along the *x*-axis, namely the distance between the internal Rims that are parallel to the *x*-axis. 'II' represents the transverse dimension of the internal passage of the drain/catheter, i.e. the internal the internal transverse dimensions of Sections 1 & 2 that are parallel to the *x*-axis. The length of both 'I' and 'II' is 6.0 mm.

Fig. 133 shows the design from the top. ‘I’ signifies three different distances along the *y*-axis, which are equal in magnitude: the internal transverse dimensions of both Sections 1 & 2 as well as the shortest internal transverse dimension of the *Flexible Section*. Moreover, it can be seen that the external ‘Triangular’ Rims of the *Flexible Section* do not extend much into the surrounding space around the drain/catheter. Therefore, the drain/catheter can be placed through natural or incised openings with diameters that are very close to the external diameter of Sections 1 & 2.

Figs. 134 through 137 show different angles of a 90° bend drain/catheter. As seen in Figs. 135 & 136, the 90° bend begins at the start of the *Flexible Section*, i.e. Section 2 is not involved in the bend. The bend ends within the early portions of the *Flexible Section*. The remaining straight portion of the *Flexible Section* can then be used for additional bends if desired by the surgeon. Moreover, this straight portion of the *Flexible Section* can also serve as a location of drain/catheter anchorage to its underlying skin/tissue via the utilization of surgical sutures. Figs. 100 through 102 illustrate how a Circular-bodied drain/catheter with a ‘Semicircular’ *Flexible Section* is anchored to the underlying skin/tissue. In a very similar manner, a Rectangular-bodied drain/catheter with a ‘Triangular’ *Flexible Section* can be anchored to its underlying skin/tissue.

Fig. 136 illustrates the interior of a bent drain’s/catheter’s *Flexible Section*. ‘I’ denotes the shortest diameter within the bent *Flexible Section*. ‘II’ denotes the internal diameter of the drain’s/catheter’s Section 2, which is equal to the internal diameter of Section 1 as well. Note that ‘I’ and ‘II’ are equal in their lengths. This

means that the internal passage of the drain/catheter maintains the same diameter regardless whether the drain/catheter is in a straight or in a bent configuration. Therefore, no occlusions are introduced within the internal passage of the drain/catheter. Hence, the flow of fluids within a drain/catheter, which incorporates a *Flexible Section*, is not hindered by internal occlusions.

Fig. 137 shows a closer view of the bent drain/catheter from the top. Note that the external 'Triangular' Rims/Grooves in the straight portion of the *Flexible Section* provide the perfect location, where surgical sutures can be wrapped around the drain/catheter. Figs. 100 through 102 illustrate how a secure anchorage of a Circular-bodied drain/catheter with a 'Semicircular' *Flexible Section* is made possible by these external Rims/Grooves. The external Rims/Grooves of a Rectangular-bodied drain/catheter with a 'Triangular' *Flexible Section* act in a similar manner.

Analogous to the anchoring method illustrated by Figs. 100 through 102, surgical sutures pass through the underlying skin/tissue of the patient and then wrap around the 'Triangular' *Flexible Section* of the drain/catheter. Specifically, the surgical sutures fit within the external 'Triangular' Grooves of the *Flexible Section*. Once the sutures are wrapped around the *Flexible Section*, the *Flexible Section's* 'Triangular' Rims prevent any motion of the drain/catheter unit along the *y*-axis (similar to the anchorage shown in Figs. 100 & 101). Moreover, other movements of the drain/catheter unit are prevented as well. Similar to what is seen in Fig. 100, locations that are wrapped by sutures within the 'Triangular'

Flexible Section, cannot be moved/displaced within the *x-y* plane. Therefore, the drain/catheter is securely locked in space and not dislodgeable.

6-6-2-3 'Rectangular-Bodied' Drain/Catheter, 'Rectangular' *Flexible Section*

Figs. 138 through 145 represent a Rectangular-bodied drain/catheter with a 'Rectangular' *Flexible Section*. As illustrated in Fig. 138, this design is composed of a three sections: Sections 1 & 2 as well as a 'Rectangular' *Flexible Section*. A 'Rectangular' *Flexible Section* means that this particular *Flexible Section* encompasses 'Rectangular' external/internal Rims/Grooves as clearly illustrated by Figs. Similar to Fig. 119, the Rectangular body of a drain/catheter with a 'Rectangular' *Flexible Section*, is composed of a base and a width. The base and the width are 1.0 cm and 7.0 mm long respectively. Sections 1 & 2 as well as the *Flexible Section* have a uniform thickness of 2.0 mm. Therefore, the base of the drain's/catheter's internal passage is 6.0 mm long and its width is 3.0 mm long.

Fig. 139 shows an enlarged view of the external Rectangular Rims/Grooves involved in the *Flexible Section* of this particular design. Fig. 140 gives a better insight into the internal and external design of the 'Rectangular' *Flexible Section*. All rectangles are squares. The sides of each square are 1.0 mm long. Based on that the pitch-to-pitch distance between each Rectangular Rim/Groove is 2.0 mm. 'I' represents the shortest internal transverse dimension of the *Flexible Section* along the *x*-axis, namely the distance between the internal Rims that are parallel to the *x*-axis. 'II' represents the transverse dimension of the internal passage of the drain/catheter, i.e. the internal the internal transverse dimensions of Sections 1 & 2 that are parallel to the *x*-axis. The length of both 'I' and 'II' is 6.0 mm.

Fig. 141 shows the design from the top. 'I' signifies three different distances along the *y*-axis, which are equal in magnitude: the internal transverse dimensions

of both Sections 1 & 2 as well as the shortest internal transverse dimension of the *Flexible Section*. Moreover, it can be seen that the external 'Rectangular' Rims of the *Flexible Section* do not extend much into the surrounding space around the drain/catheter. Therefore, the drain/catheter can be placed through natural or incised openings with diameters that are very close to the external diameter of Sections 1 & 2.

Figs. 142 through 145 show different angles of a 90° bend drain/catheter. As seen in Figs. 143 & 144, the 90° bend begins at the start of the *Flexible Section*, i.e. Section 2 is not involved in the bend. The bend ends within the early portions of the *Flexible Section*. The remaining straight portion of the *Flexible Section* can then be used for additional bends if desired by the surgeon. Moreover, this straight portion of the *Flexible Section* can also serve as a location of drain/catheter anchorage to its underlying skin/tissue via the utilization of surgical sutures. Figs. 100 through 102 illustrate how a Circular-bodied drain/catheter with a 'Semicircular' *Flexible Section* is anchored to the underlying skin/tissue. In a very similar manner, a Rectangular-bodied drain/catheter with a 'Rectangular' *Flexible Section* can be anchored to its underlying skin/tissue.

Fig. 144 illustrates the interior of a bent drain's/catheter's *Flexible Section*. 'I' denotes the shortest diameter within the bent *Flexible Section*. 'II' denotes the internal diameter of the drain's/catheter's Section 2, which is equal to the internal diameter of Section 1 as well. Note that 'I' and 'II' are equal in their lengths. This means that the internal passage of the drain/catheter maintains the same diameter regardless whether the drain/catheter is in a straight or in a bent configuration.

Therefore, no occlusions are introduced within the internal passage of the drain/catheter. Hence, the flow of fluids within a drain/catheter, which incorporates a *Flexible Section*, is not hindered by internal occlusions.

Fig. 145 shows a closer view of the bent drain/catheter from the top. Note that the external 'Rectangular' Rims/Grooves in the straight portion of the *Flexible Section* provide the perfect location, where surgical sutures can be wrapped around the drain/catheter. Figs. 100 through 102 illustrate how a secure anchorage of a Circular-bodied drain/catheter with a 'Semicircular' *Flexible Section* is made possible by these external Rims/Grooves. The external Rims/Grooves of a Rectangular-bodied drain/catheter with a 'Rectangular' *Flexible Section* act in a similar manner.

Analogous to the anchoring method illustrated by Figs. 100 through 102, surgical sutures pass through the underlying skin/tissue of the patient and then wrap around the 'Rectangular' *Flexible Section* of the drain/catheter. Specifically, the surgical sutures fit within the external 'Rectangular' Grooves of the *Flexible Section*. Once the sutures are wrapped around the *Flexible Section*, the *Flexible Section's* 'Rectangular' Rims prevent any motion of the drain/catheter unit along the *y*-axis (similar to the anchorage shown in Figs. 100 & 101). Moreover, other movements of the drain/catheter unit are prevented as well. Similar to what is seen in Fig. 100, locations that are wrapped by sutures within the 'Rectangular' *Flexible Section*, cannot be moved/displaced within the *x-y* plane. Therefore, the drain/catheter is securely locked in space and not dislodgeable.

6-6-3 Additional Design Details

6-6-3-1 Fillets

As clearly seen in Figs. 122, 133 & 141, the drains/catheters with a Rectangular body are filleted around all four corners. Fig. 122 illustrates the dimensions of the fillets the best. The four internal corners have a fillet radius of 1.0 mm as depicted by 'II'. All four external corners have a fillet radius of 3.0 mm as depicted by 'III'. This means that the middle of the 2.0 mm thick drain-/catheter-body has a 2.0 mm radius bend at all the four corners of the Rectangular-bodied drain/catheter. This is shown by 'IV'.

6-6-3-2 Extensions of Section 2

Figs. 98 & 128 illustrate the Extensions of Sections 2 for both the Circular-bodied and the Rectangular-bodied drains/catheters. In both cases, the Extension of Section 2 contains a series of holes that are along the transverse directions of the drain, namely along the *x*- and the *y*-axis. Each hole is 1.0 cm apart from the hole directly above it. The holes along the *y*- axis are positioned 0.5 cm above the holes that lie along the *x*-axis.

6-6-3-3 *Flexible Section* Designs

Note that only three different *Flexible Section* designs are shown in this manuscript, namely the Semicircular, Triangular and the Rectangular *Flexible Sections*. Alternatively, the *Flexible Section* can be composed of a combination of any of these *Flexible Sections*. For example a *Flexible Section* can be composed of three segments: a Semicircular-, a Triangular- and a Rectangular segment. The actual composition of the *Flexible Section* is set by the manufacturer.

The examples that were shown in this manuscript focus on only one *Flexible Section* within the entire length of a surgical drain/catheter. However, multiple *Flexible Sections* can be incorporated at different locations along the length of a drain/catheter. Also, the entire length of a surgical drain/catheter can be composed of a continuous *Flexible Section*. Meaning, that the entire body of the drain/catheter can be one long *Flexible Section*, i.e. the *Flexible Section* can start from the starting point of Section 1's Extension (Figs. 97 & 127), continue all the way through Sections 1 & 2 and end at the end point of Section 2's Extension (Figs. 98 & 128). The frequency, length and location of *Flexible Section*(s) within the final design of a surgical drain/catheter are left to the manufacturer.

Although only three different *Flexible Section* examples were presented in this manuscript, other designs of *Flexible Section* are possible as well. All other *Flexible Section* designs are also covered under this Patent document.

Moreover, it should be noted that all the *Flexible Section* designs can be employed to conventional drain/catheter systems that are currently available in the market.

6-6-3-4 Dimensions of the Inventions

It should be noted that all the above-mentioned dimensions are for illustrative purposes only and can be changed according to the different utilizations of the drain/catheter systems, i.e. different types of surgeries, locations of attachment, drainage volume and the properties of its polymer material, etc. Moreover, this means that all three Sections, namely Sections 1 & 2 as well as the *Flexible Section* can also have any other arbitrary lengths. Based on the above discussion all final dimensions involved in the design of all the drain/catheter systems are left to the manufacturer.

6-7 Claims

As a result of incorporating a *Flexible Section* or a combination of different *Flexible Section* designs within the composition of a surgical drain/catheter, several benefits will arise. The following paragraphs outline these benefits.

6-7-1 Enhanced 3D Flexibility

A Circular- or Rectangular-bodied drain/catheter that incorporates one or many *Flexible Section*(s) will embrace a highly Enhanced Three Dimensional (3D) Flexibility. The benefits that result from this Enhanced 3D Flexibility are laid out as follows.

- The Enhanced 3D Flexibility enables the operating surgeon to bend the drain/catheter at its *Flexible Section*(s) with almost infinite degrees of rotational freedom.

- The Enhanced 3D Flexibility enables the drain/catheter to be bent at its *Flexible Section*(s). The bend(s) can happen without inducing any occlusion(s) or tightening(s) of the drain's/catheter's internal passage within the bent *Flexible Section*(s).

- The Enhanced 3D Flexibility enables the drain/catheter to be sharply bent at its *Flexible Section*(s). The sharp bend(s) can happen without inducing any transverse Fold(s)/Crease(s) at the drain's/catheter's sharply bent *Flexible Section*(s).

- The Enhanced 3D Flexibility enables the drain/catheter to be sharply bent at its *Flexible Section*(s). The sharp bend(s) can happen without inducing any expansion or

collapse of the drain's/catheter's cross-sections within the drain's/catheter's sharply bent *Flexible Section*(s).

- The Enhanced 3D Flexibility enables the drain/catheter to be sharply bent at its *Flexible Section*(s). The sharp bend(s) can happen without inducing any change in the external/internal diameter(s) of the drain's/catheter's sharply bent *Flexible Section*(s).

- The Enhanced 3D Flexibility enables the drain/catheter to be sharply bent at its *Flexible Section*(s). The sharp bend(s) can happen without inducing any strain/stress to the underlying/surrounding skin/tissue of the patient's body.

- The Enhanced 3D Flexibility enables the drain/catheter to be sharply bent at its *Flexible Section*(s). The sharp bend(s) can happen without inducing any unnecessary pain to patient caused by the bending of the drain's/catheter's bend(s) within its *Flexible Section*(s).

- The Enhanced 3D Flexibility enables the drain/catheter to be somewhat longitudinally (along the *z*-axis) stretched at its *Flexible Section*(s).

- The Enhanced 3D Flexibility, and with that the longitudinal (along the *z*-axis) stretching ability of the drain/catheter at its *Flexible Section*(s), dampen the longitudinal forces involved in any natural or accidental pulling action(s) on the drain/catheter. The pulling action(s) can be internal or external to a patient's body.

- The Enhanced 3D Flexibility, and with that the longitudinal (along the *z*-axis) dampening ability of the drain/catheter at its *Flexible Section*(s), reduce the risk of

drain's/catheter's accidental dislodgment from its intended placement within or external to a patient's body.

- The Enhanced 3D Flexibility, and with that the longitudinal (along the *z*-axis) dampening ability of the drain/catheter at its *Flexible Section*(s), reduce the risk of a drain/catheter to be accidentally pulled out of the patient's body in case of a drain/catheter that connects the internal and external environments of a patient's body.

- The Enhanced 3D Flexibility, and with that the longitudinal (along the *z*-axis) dampening ability of the drain/catheter at its *Flexible Section*(s), reduce the risk of a drain's/catheter's accidental slippage and with that the need of a secondary operation to replace the drain/catheter at its intended position.

6-7-2 Enhanced Anchorage Capability

A Circular- or Rectangular-bodied drain/catheter that incorporates one or many *Flexible Section*(s) will embrace a highly Enhanced Anchorage Ability. The benefits that result from this Enhanced Anchorage Ability are laid out as follows.

- The Enhanced Anchorage Ability enables a drain/catheter to be securely attached to its underlying/surrounding skin/tissue.

- The Enhanced Anchorage Ability is enabled by the utilization of surgical sutures that wrap around the drain's/catheter's *Flexible Section*(s).

- The Enhanced Anchorage Ability is enabled by the *Flexible Section's* external Rims/Grooves. Specifically, the surgical sutures perfectly fit within the external Grooves of the *Flexible Section*(s). The *Flexible Section*(s) external Rims act as physical barriers that restrict the slippage of the surgical sutures along the external surface of the drain's/catheter's *Flexible Section*(s).

- The Enhanced Anchorage Ability is applicable to surgical drains/catheters independent of the magnitude of their external diameters. Both large diameter and low diameter drains/catheters can be securely anchored to their underlying/surrounding skin/tissue.

- The Enhanced Anchorage Ability is achieved independent of the length or frequency of a drain's/catheter's *Flexible Section*(s).

6-8 Figures

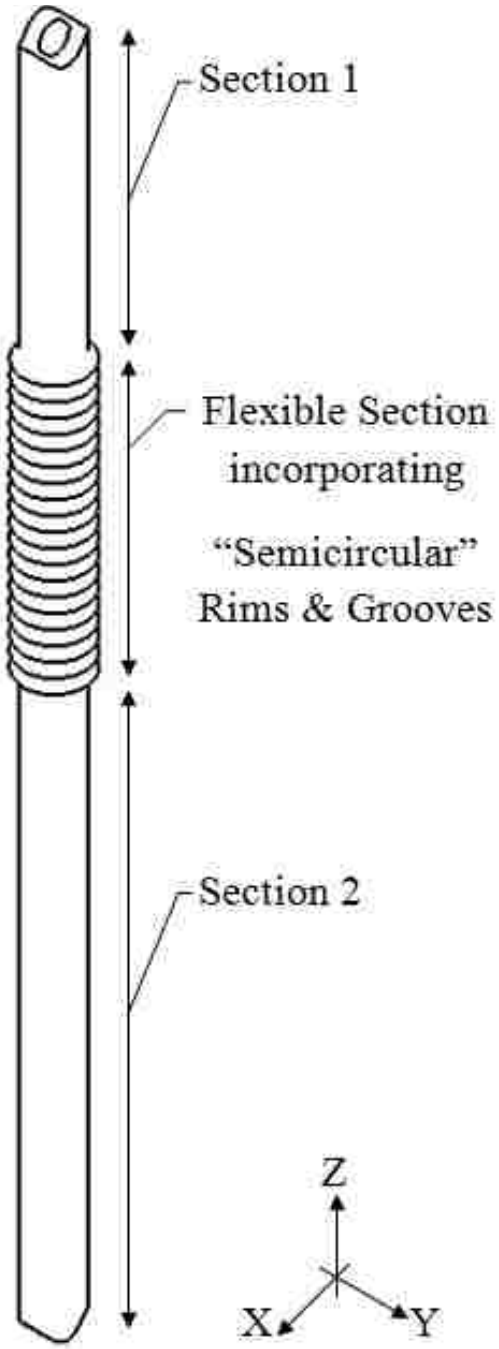

Figure 89: Isometric View. Straight Circular-bodied Flexi-Drain with a Flexible Section composed of "Semicircular" Rims and Grooves. Section 1 and Section 2, which respectively connect to the Upper and the Lower extensions of the Flexi-Drain are shown as well.

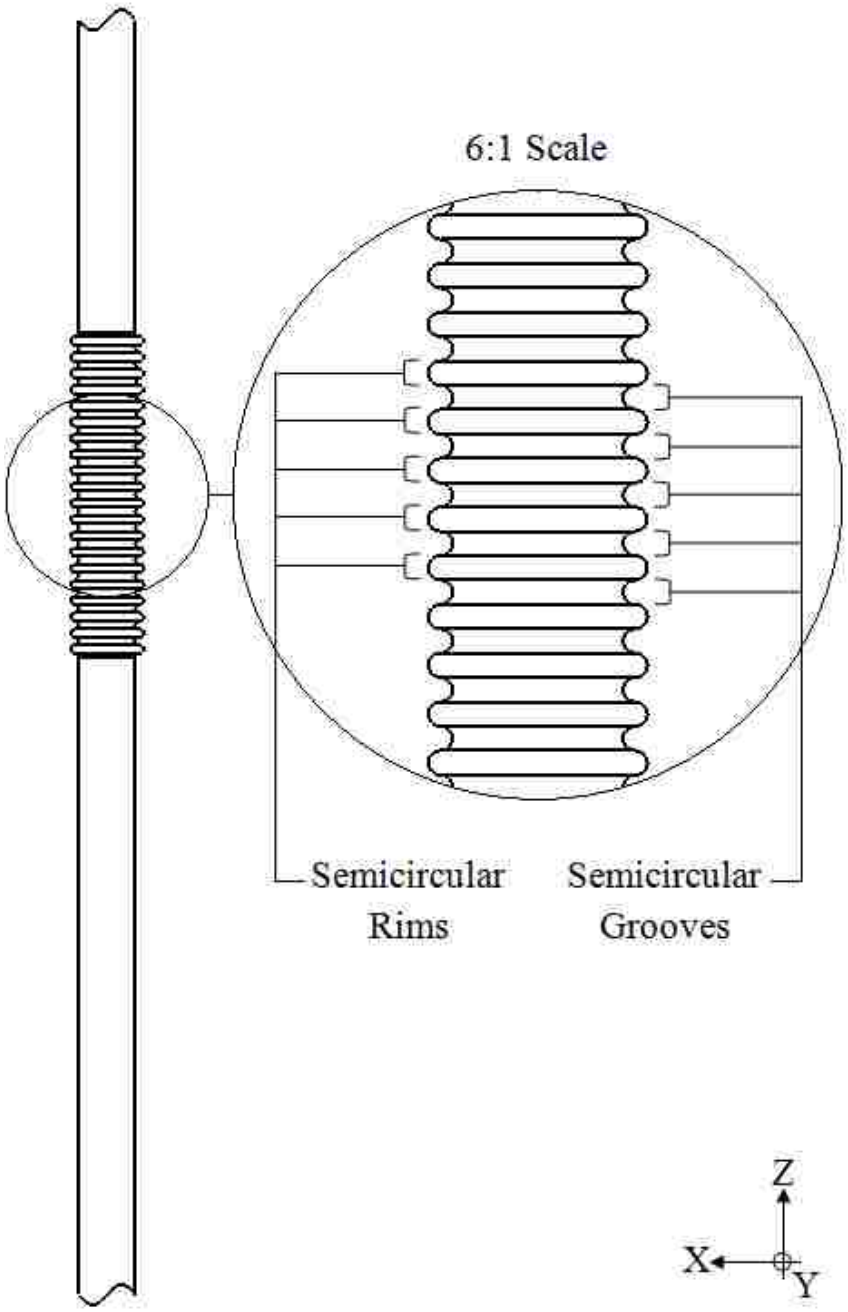

Figure 90: Right View. Straight Circular-bodied Flexi-Drain with a Flexible Section composed of "Semicircular" Rims and Grooves. A six times larger view of the "Semicircular" Rims and Grooves are shown in the circle.

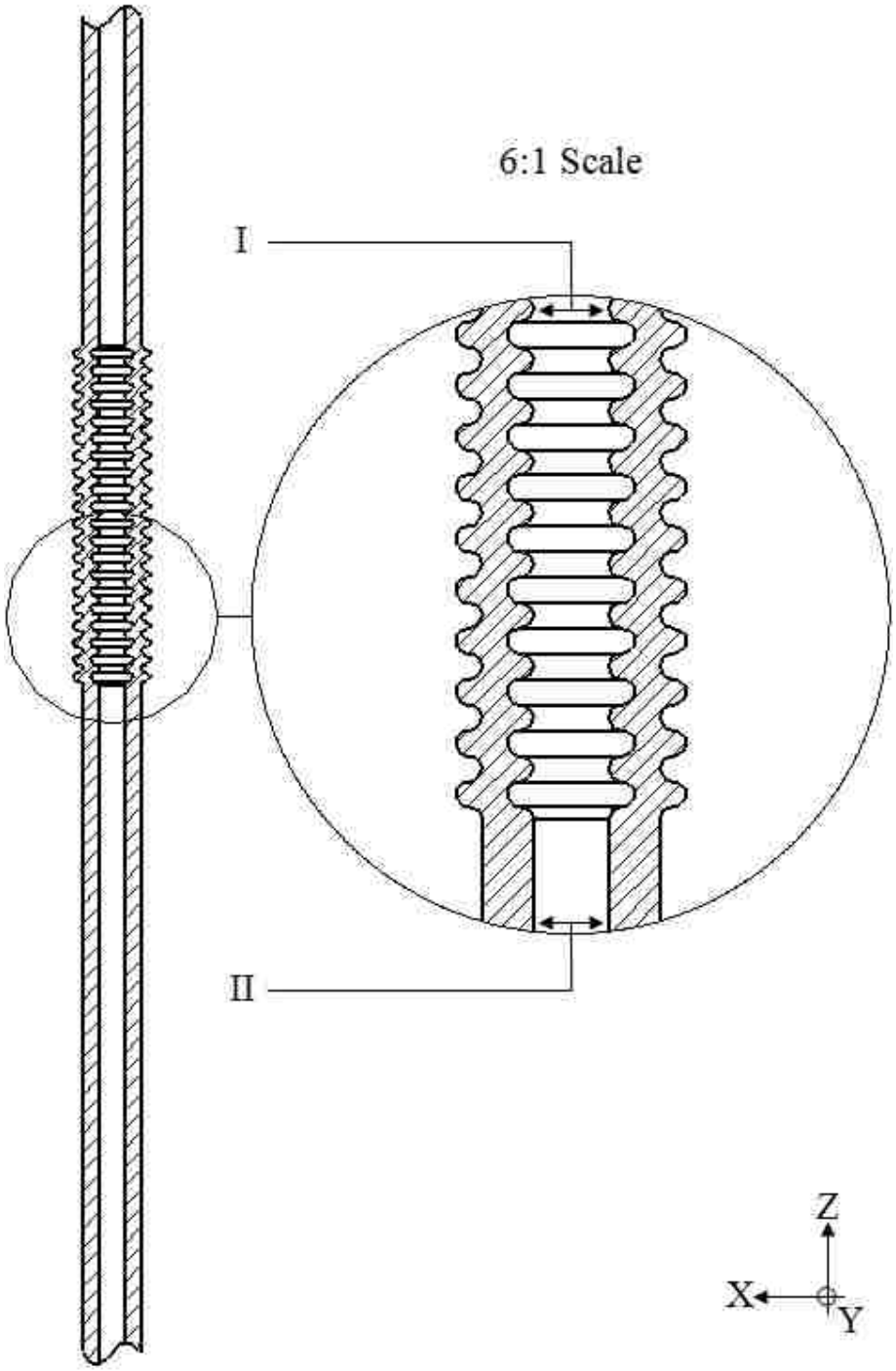

Figure 91: Cross-sectional Right View. Straight Circular-bodied Flexi-Drain with a Flexible Section composed of "Semicircular" Rims and Grooves. A Six times larger view of the "Semicircular" Rims and Grooves are shown within the circle. 'I' indicates the diameter of the inner Rims. 'II' indicates the inner diameter of the Drain. Note that lengths represented by 'I' and 'II' are almost identical.

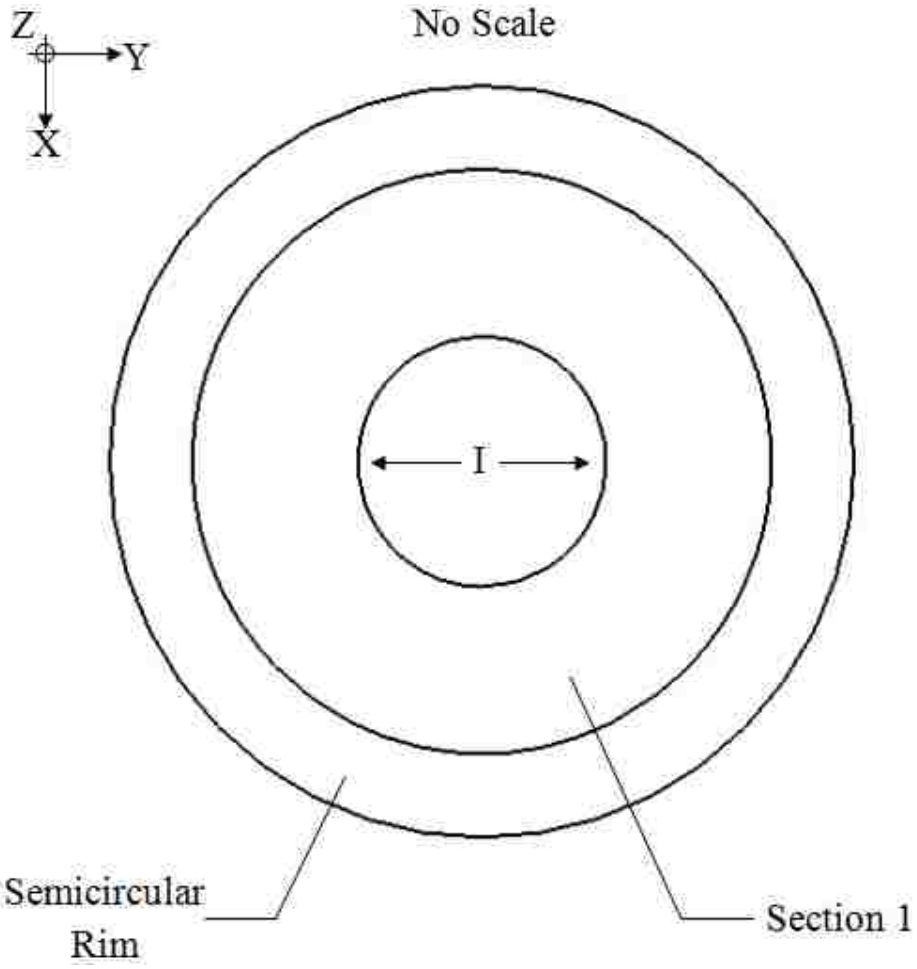

Figure 92: Enlarged Top View. No Scale. Straight Circular-bodied Flexi-Drain with a Flexible Section composed of "Semicircular" Rims and Grooves. 'I' indicates the diameter of the inner Rims as well as the inner diameter of the Drain.

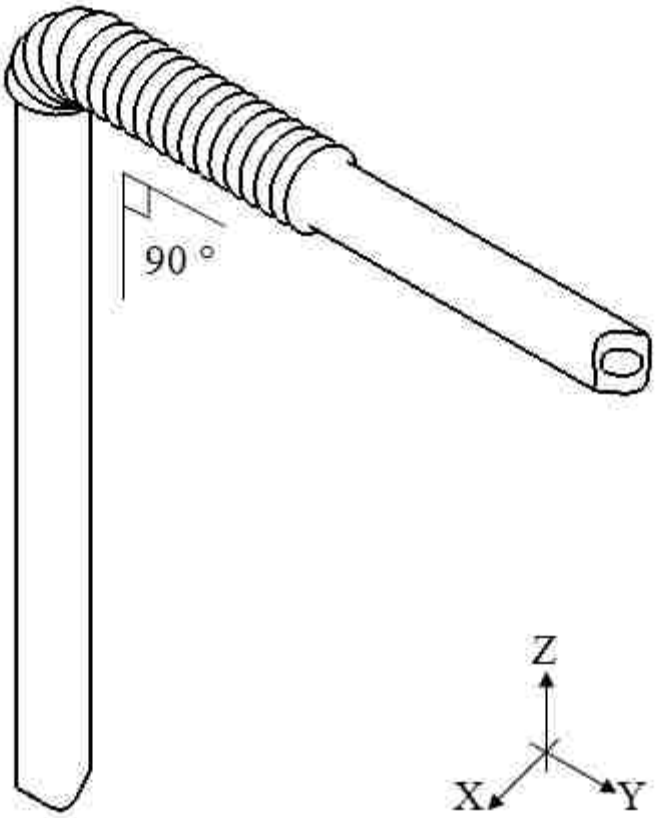

Figure 93: Isometric View. 90° bent Circular-bodied Flexi-Drain with a Flexible Section composed of “Semicircular” Rims and Grooves.

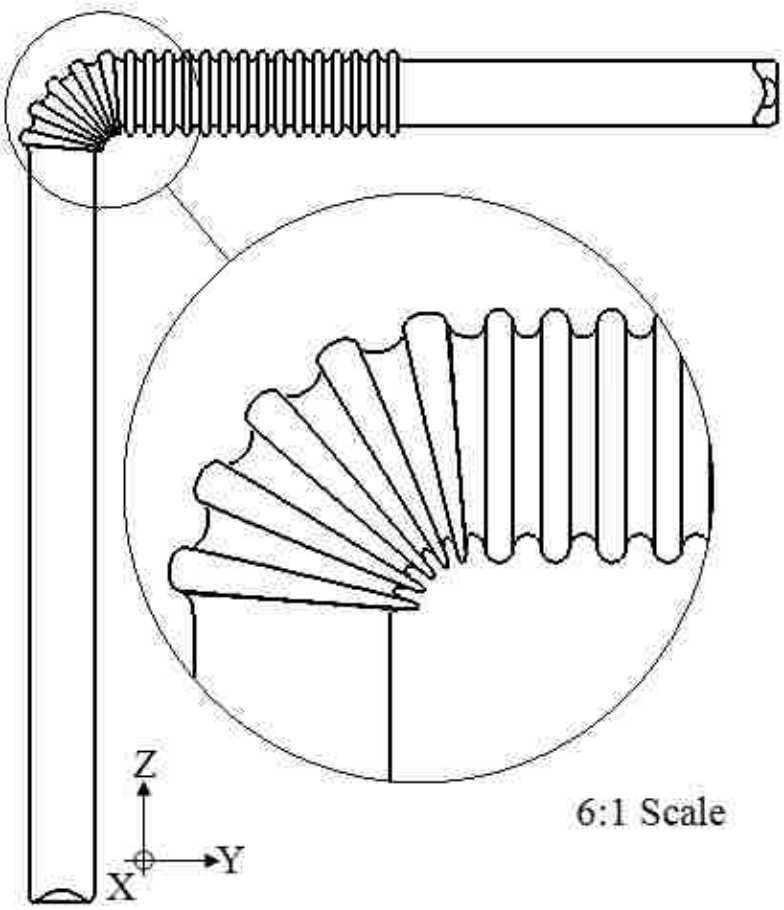

Figure 94: Front View. 90° bent Circular-bodied Flexi-Drain with a Flexible Section composed of “Semicircular” Rims and Grooves. A six times larger view of the bent Flexible Section is shown in the circle.

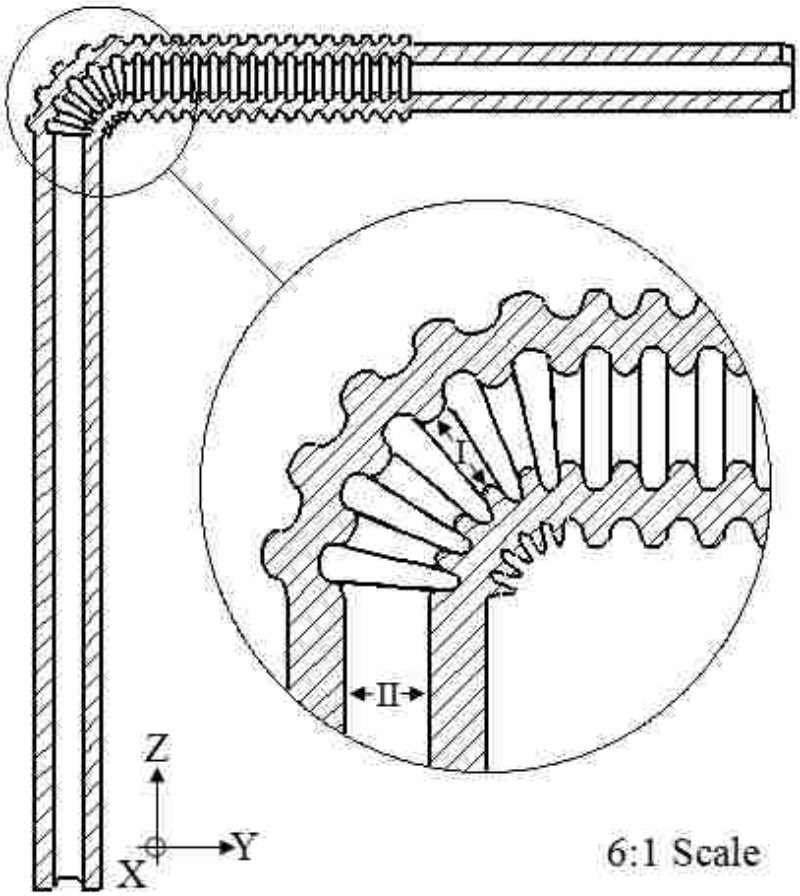

Figure 95: Cross-sectional Front View. 90° bent Circular-bodied Flexi-Drain with a Flexible Section composed of "Semicircular" Rims and Grooves. A six times larger view of the bent Flexible Section is shown in the circle. 'I' indicates the diameter of the inner Rims in their bent position. 'II' indicates the inner diameter of the Drain. Note that lengths represented by 'I' and 'II' are almost identical.

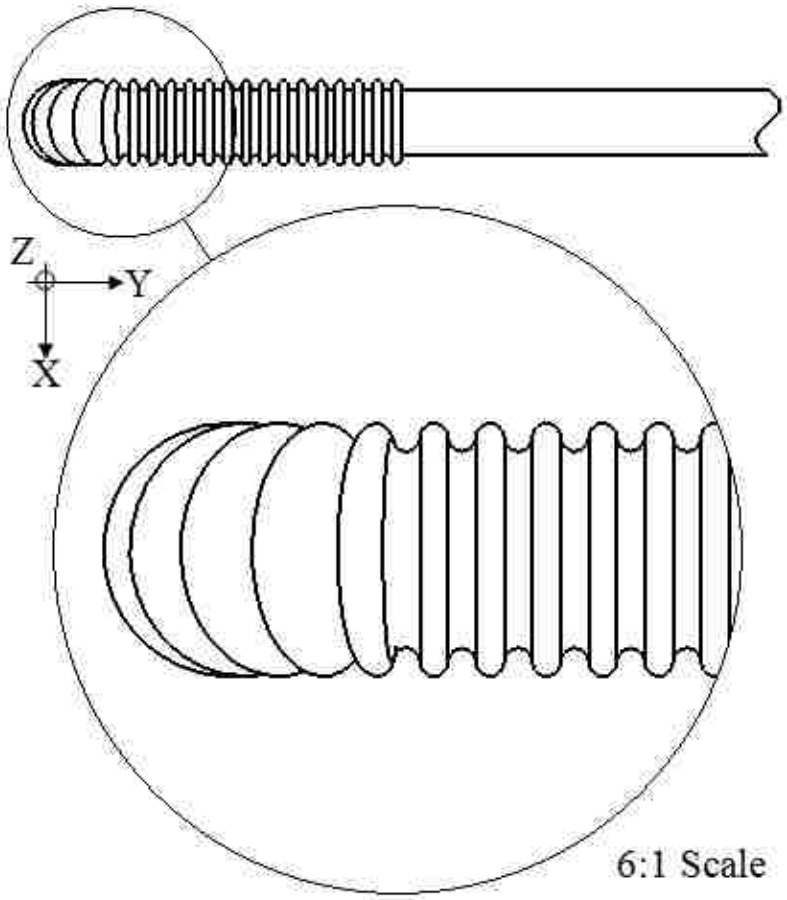

Figure 96: Top View. 90° bent Circular-bodied Flexi-Drain with a Flexible Section composed of “Semicircular” Rims and Grooves. A six times larger view of the bent Flexible Section is shown in the circle.

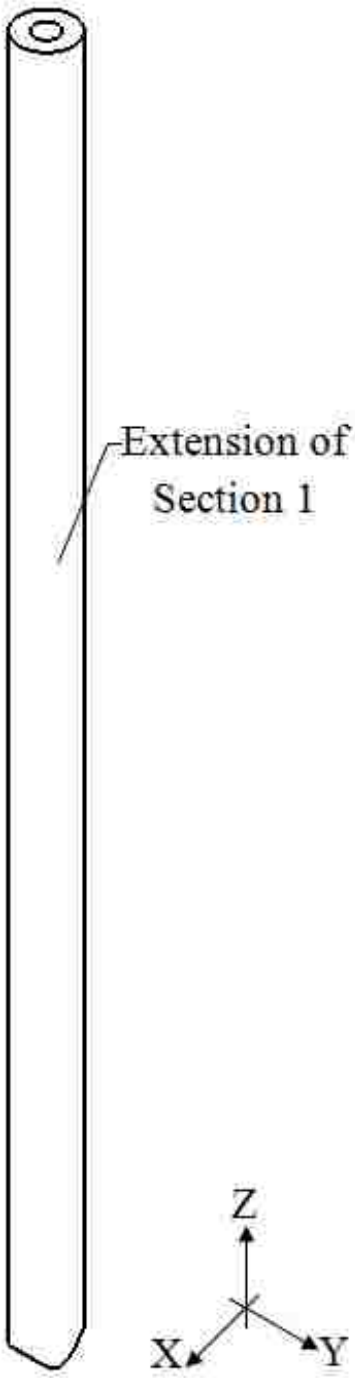

Figure 97: Isometric View. Extension of Section 1. It presents the Upper extension of the Circular Flexi-Drain. Section 1 is shown in Figure 1a.

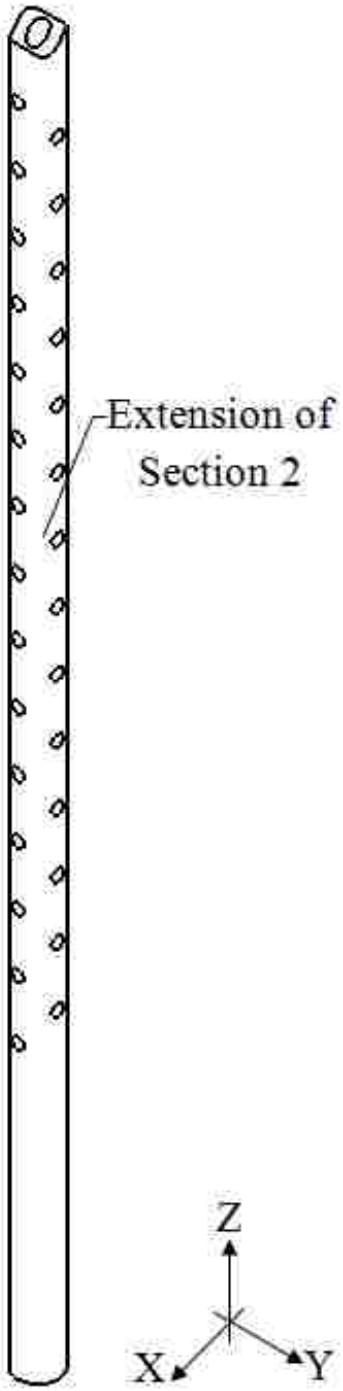

Figure 98: Isometric View. Extension of Section 2. It presents the Lower extension of the Circular Flexi-Drain. Section 2 is shown in Figure 1a.

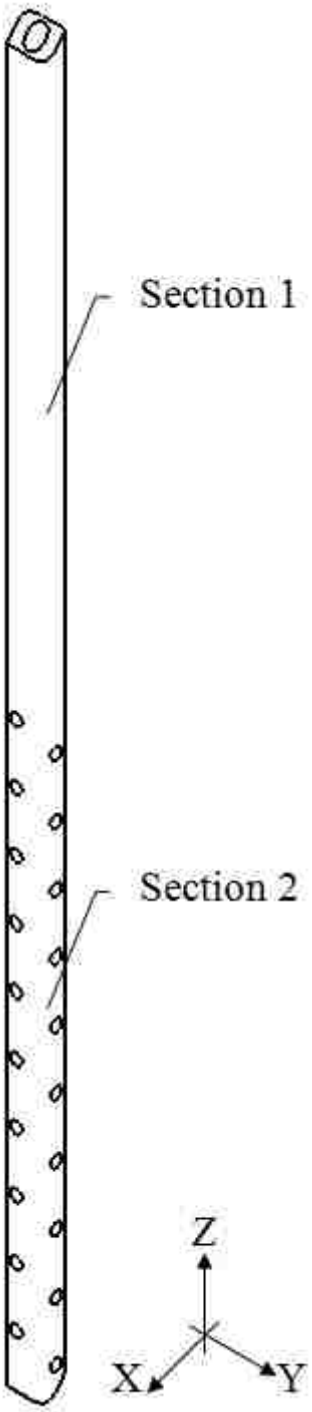

Figure 99: Isometric View. A conventional Circular-bodied drain/catheter composed of a continuous connection between Extension of Section1 and Extension of Section 2 without incorporating a Flexible Section.

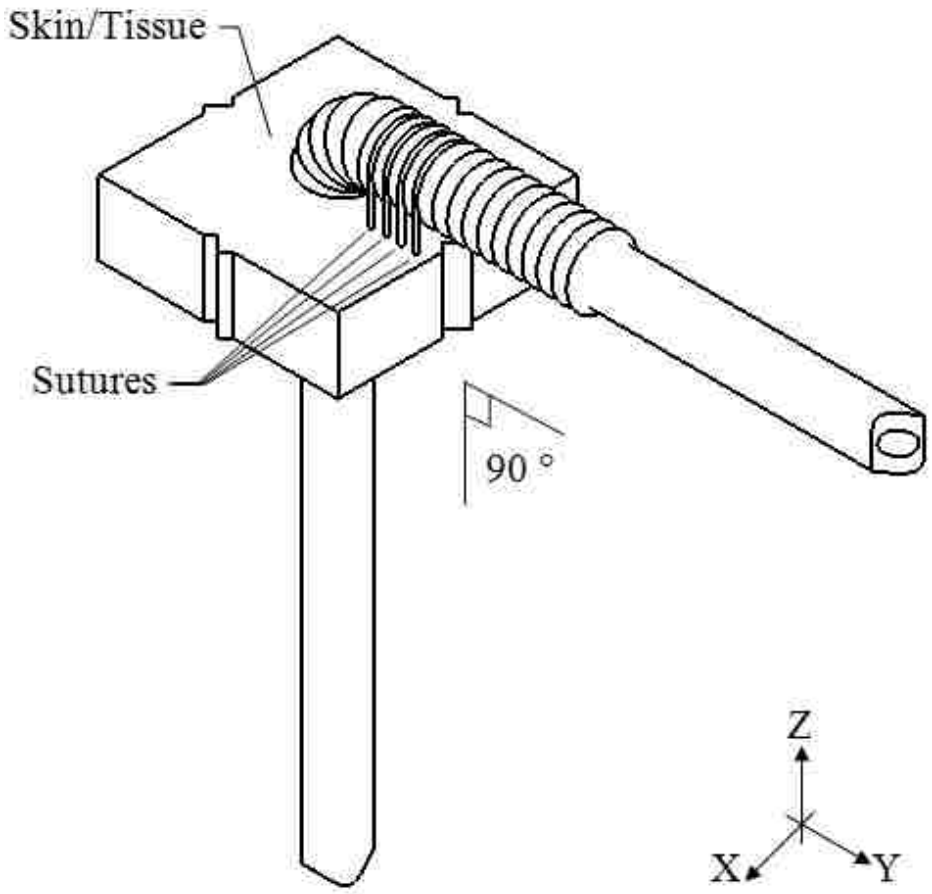

Figure 100: Isometric View. 90° bent Circular-bodied Flexi-Drain with a Flexible Section composed of "Semicircular" Rims and Grooves. The Flexi-Drain is passed through the skin/tissue. Sutures are also passed through the skin/tissue and secure the Flexi-Drain in place by fitting in the grooves of the Flexible Section.

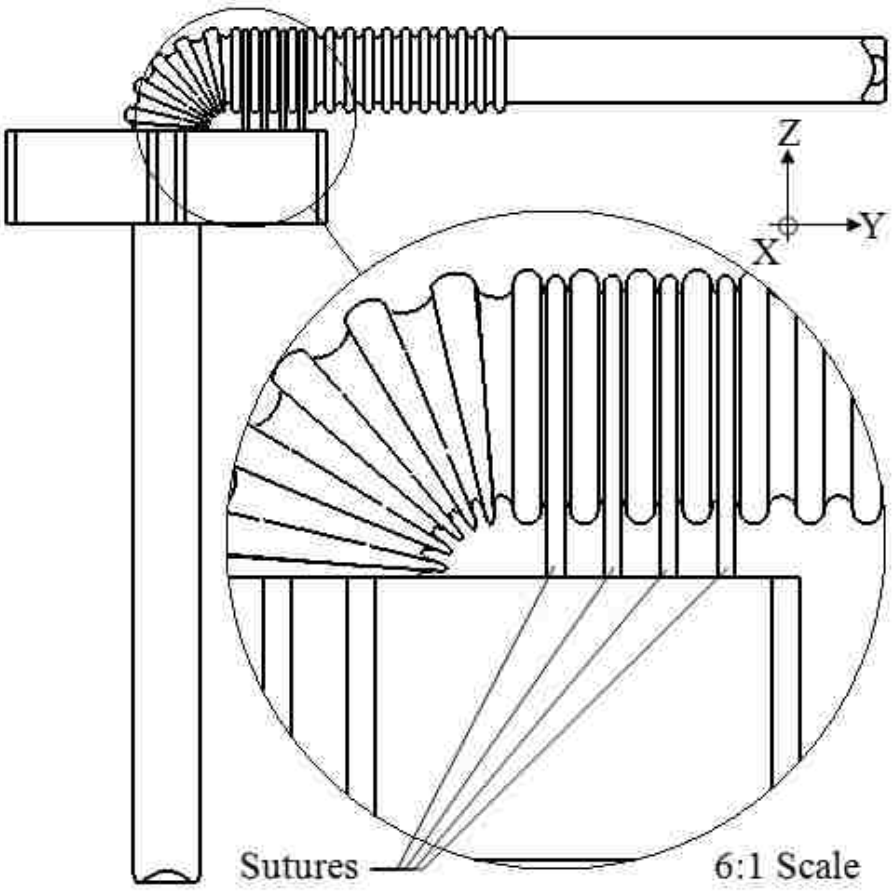

Figure 101: Front View. 90° bent Circular-bodied Flexi-Drain with a Flexible Section composed of "Semicircular" Rims and Grooves. A Six times larger view of the bent Flexible Section, the sutures as well as the skin/tissue are shown within the circle. The Flexi-Drain is passed through the skin/tissue. Sutures are also passed through the skin/tissue and secure the Flexi-Drain in place by fitting in the grooves of the Flexible Section.

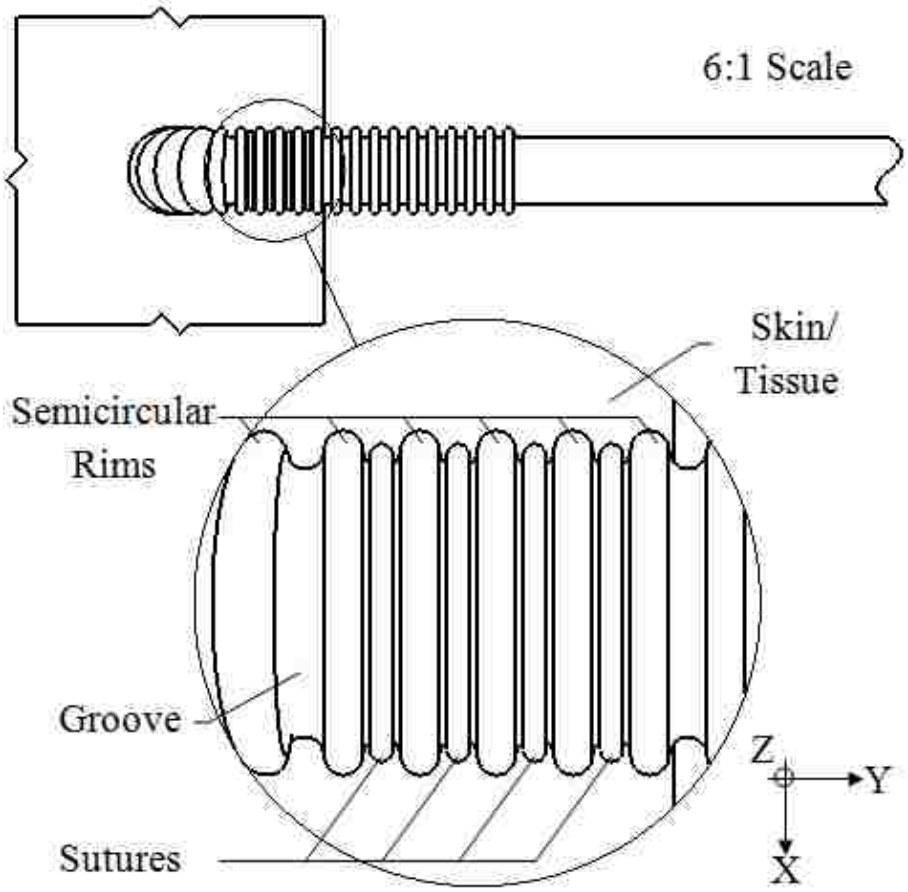

Figure 102: Top View. 90° bent Circular-bodied Flexi-Drain with a Flexible Section composed of "Semicircular" Rims and Grooves. A Six times larger view of the bent Flexible Section, the sutures as well as the skin/tissue are shown within the circle. The Flexi-Drain is passed through the skin/tissue. Sutures are also passed through the skin/tissue and secure the Flexi-Drain in place by fitting in the grooves of the Flexible Section.

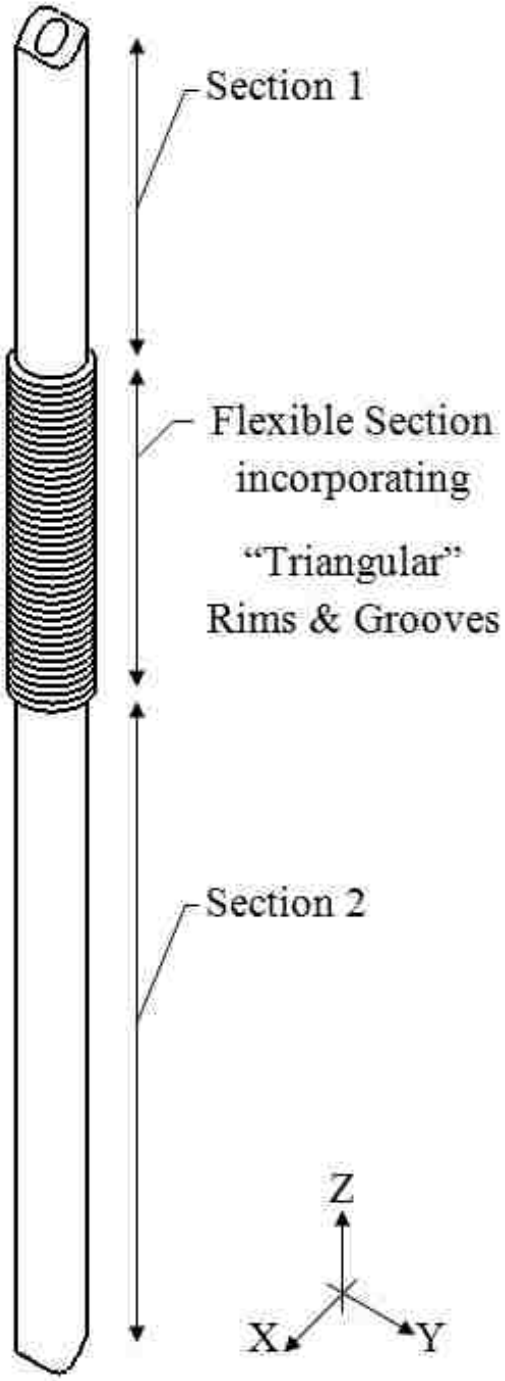

Figure 103: Isometric View. Straight Circular-bodied Flexi-Drain with a Flexible Section composed of "Triangular" Rims and Grooves. Section 1 and Section 2, which respectively connect to the Upper and the Lower extensions of the Flexi-Drain are shown as well.

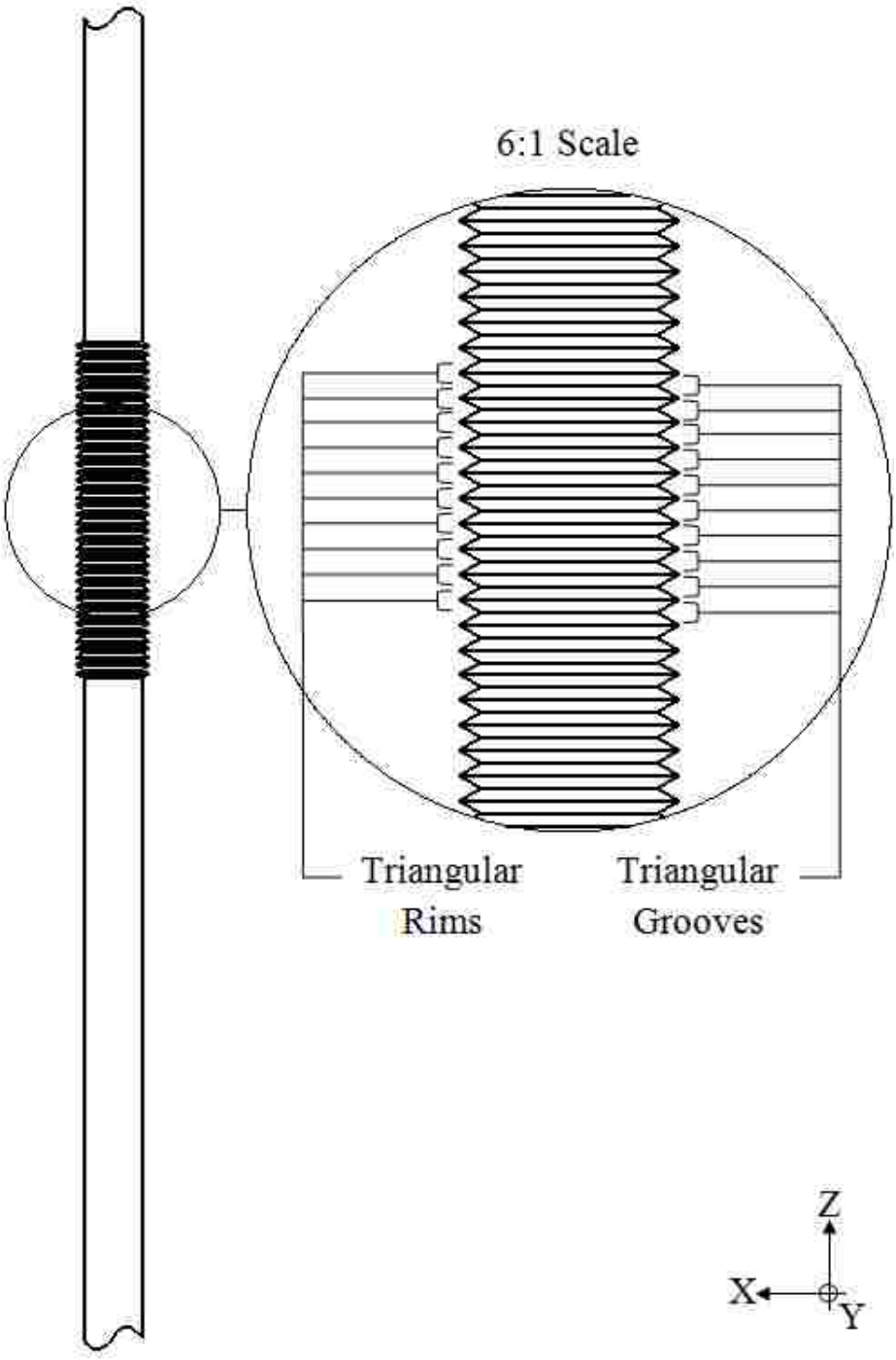

Figure 104: Right View. Straight Circular-bodied Flexi-Drain with a Flexible Section composed of "Triangular" Rims and Grooves. A six times larger view of the "Triangular" Rims and Grooves are shown in the circle.

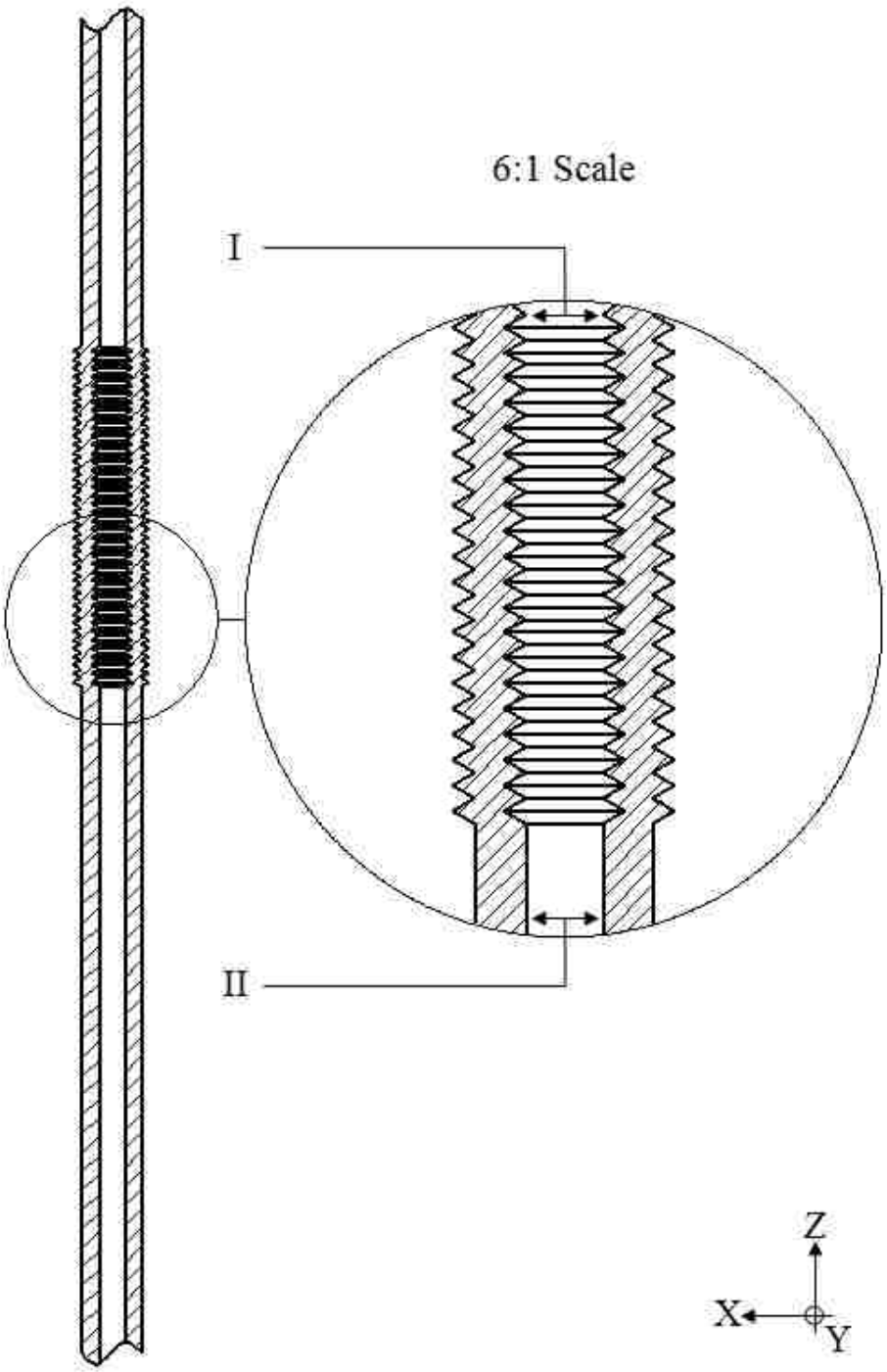

Figure 105: Cross-sectional Right View. Straight Circular-bodied Flexi-Drain with a Flexible Section composed of "Triangular" Rims and Grooves. A Six times larger view of the "Triangular" Rims and Grooves are shown within the circle. 'I' indicates the distance between the inner Rims. 'II' indicates the inner diameter of the Drain. Note that lengths represented by 'I' and 'II' are almost identical.

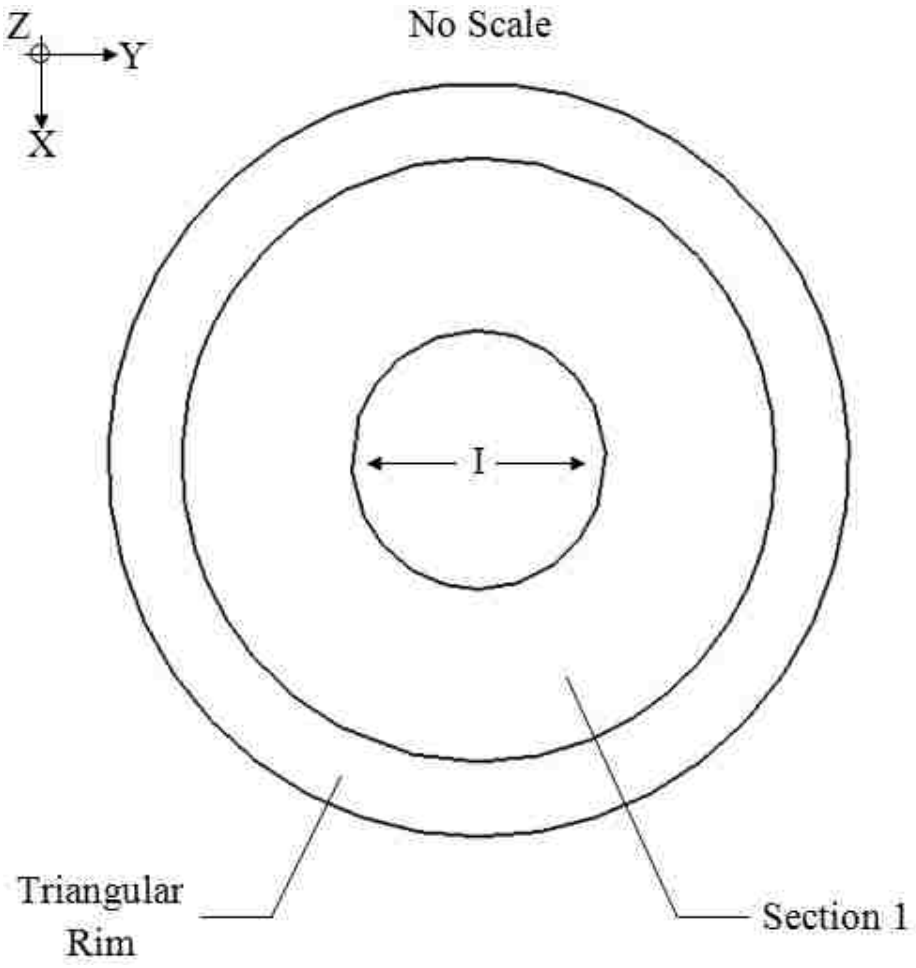

Figure 106: Enlarged Top View. No Scale. Straight Circular-bodied Flexi-Drain with a Flexible Section composed of "Triangular" Rims and Grooves. 'I' indicates the diameter of the inner Rims as well as the inner diameter of the Drain.

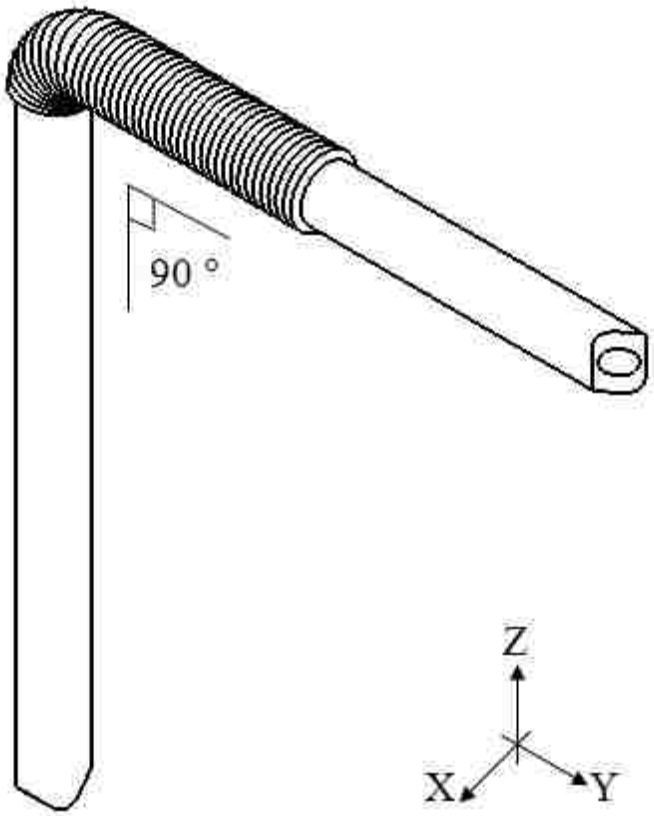

Figure 107: Isometric View. 90° bent Circular-bodied Flexi-Drain with a Flexible Section composed of “Triangular” Rims and Grooves.

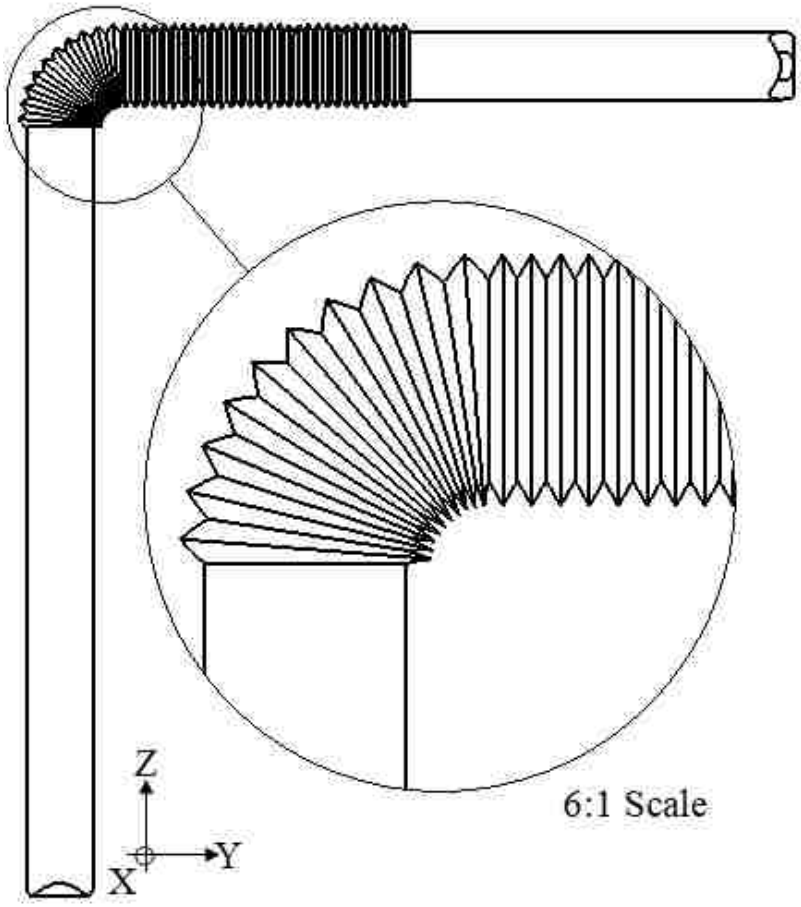

Figure 108: Front View. 90° bent Circular-bodied Flexi-Drain with a Flexible Section composed of “Triangular” Rims and Grooves. A six times larger view of the bent Flexible Section is shown in the circle.

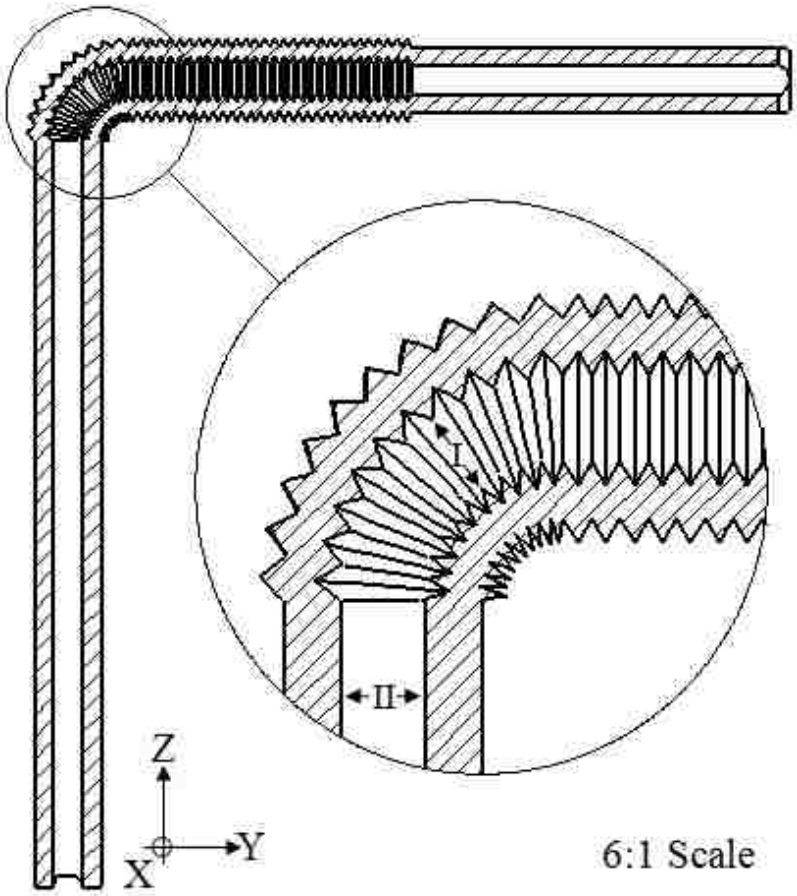

Figure 109: Cross-sectional Front View. 90° bent Circular-bodied Flexi-Drain with a Flexible Section composed of "Triangular" Rims and Grooves. A six times larger view of the bent Flexible Section is shown in the circle. 'I' indicates the diameter of the inner Rims in their bent position. 'II' indicates the inner diameter of the Drain. Note that lengths represented by 'I' and 'II' are almost identical.

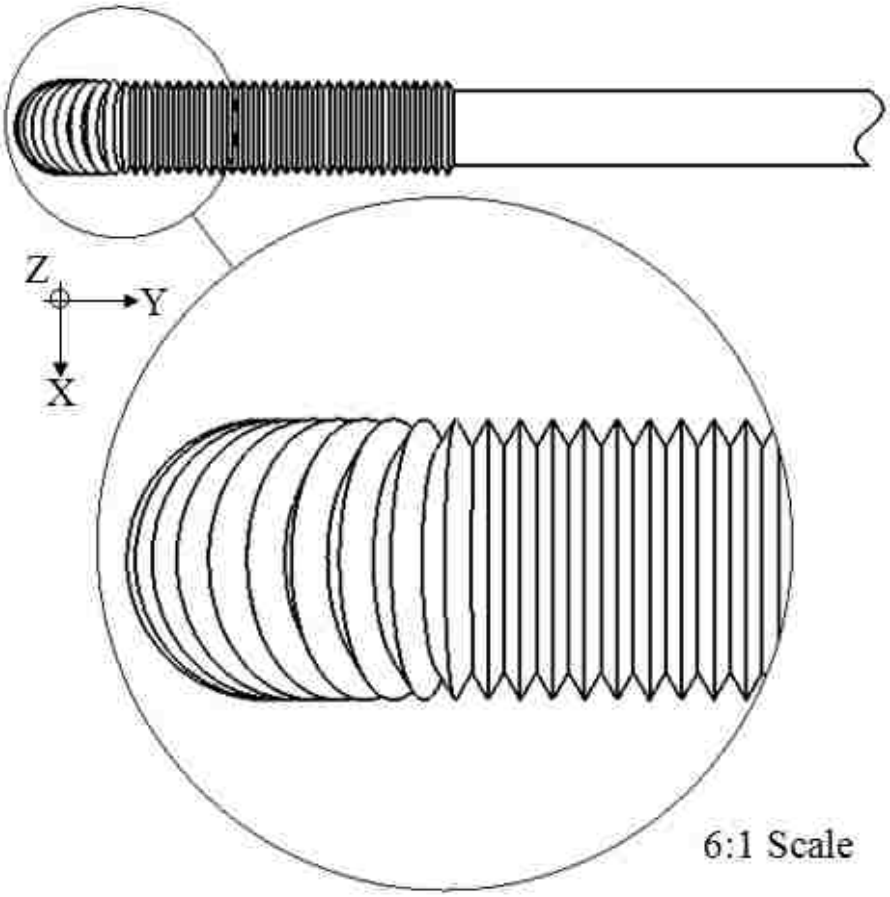

Figure 110: Top View. 90° bent Circular-bodied Flexi-Drain with a Flexible Section composed of “Triangular” Rims and Grooves. A six times larger view of the bent Flexible Section is shown in the circle.

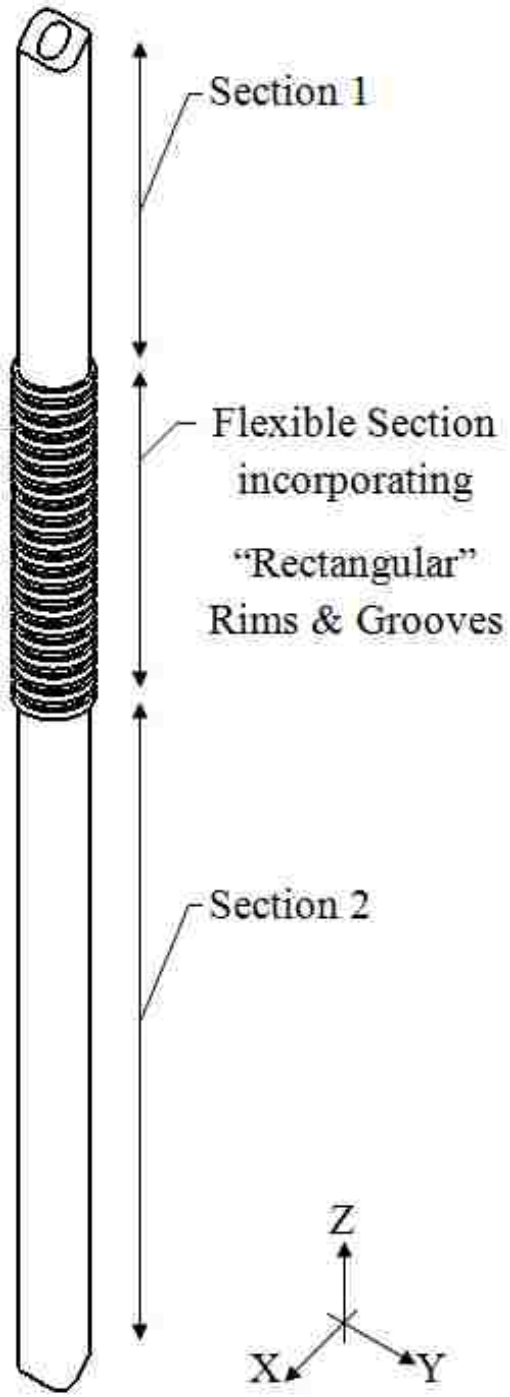

Figure 111: Isometric View. Straight Circular-bodied Flexi-Drain with a Flexible Section composed of "Rectangular" Rims and Grooves. Section 1 and Section 2, which respectively connect to the Upper and the Lower extensions of the Flexi-Drain are shown as well.

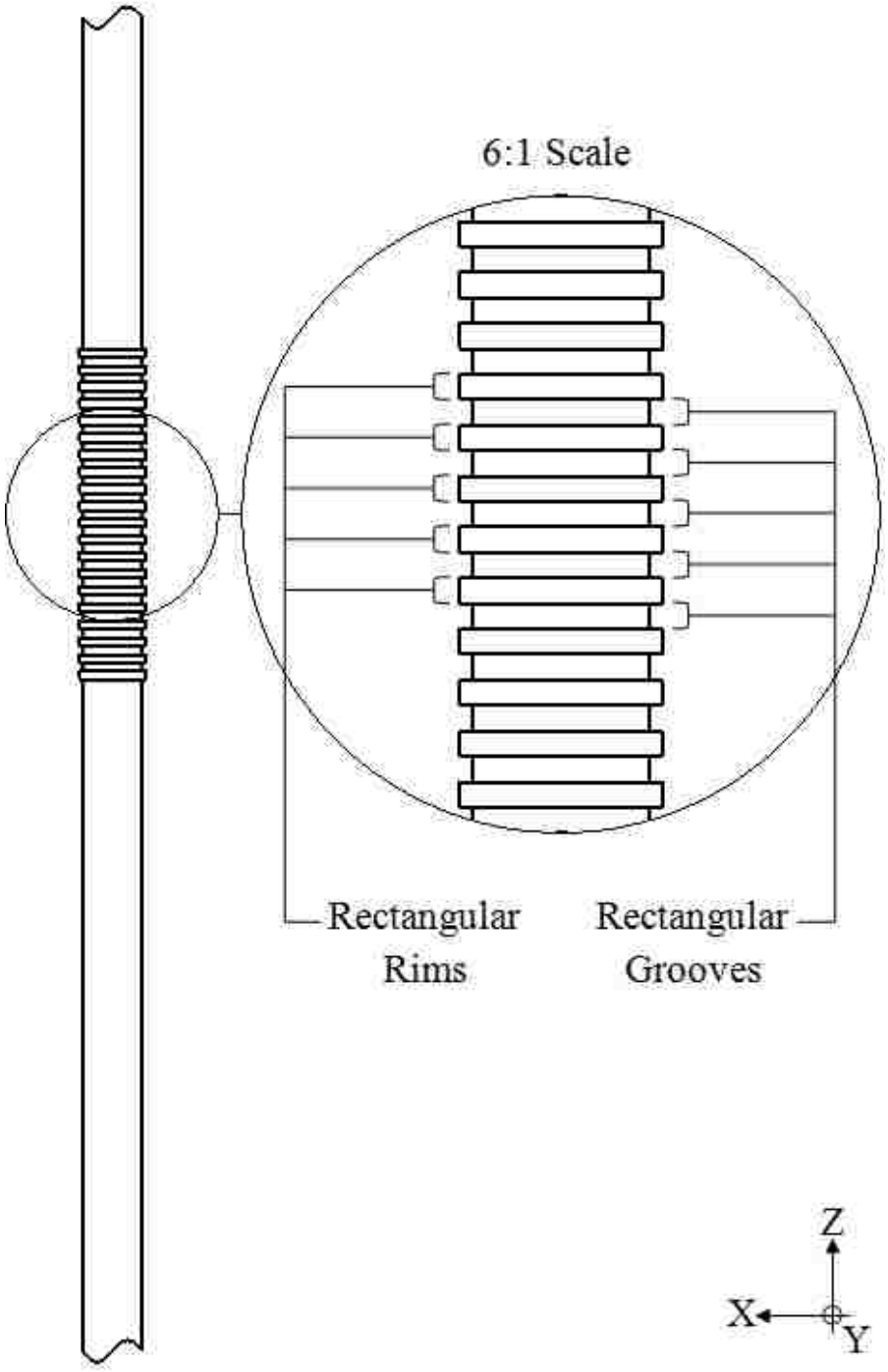

Figure 112: Right View. Straight Circular-bodied Flexi-Drain with a Flexible Section composed of "Rectangular" Rims and Grooves. A six times larger view of the "Rectangular" Rims and Grooves are shown in the circle.

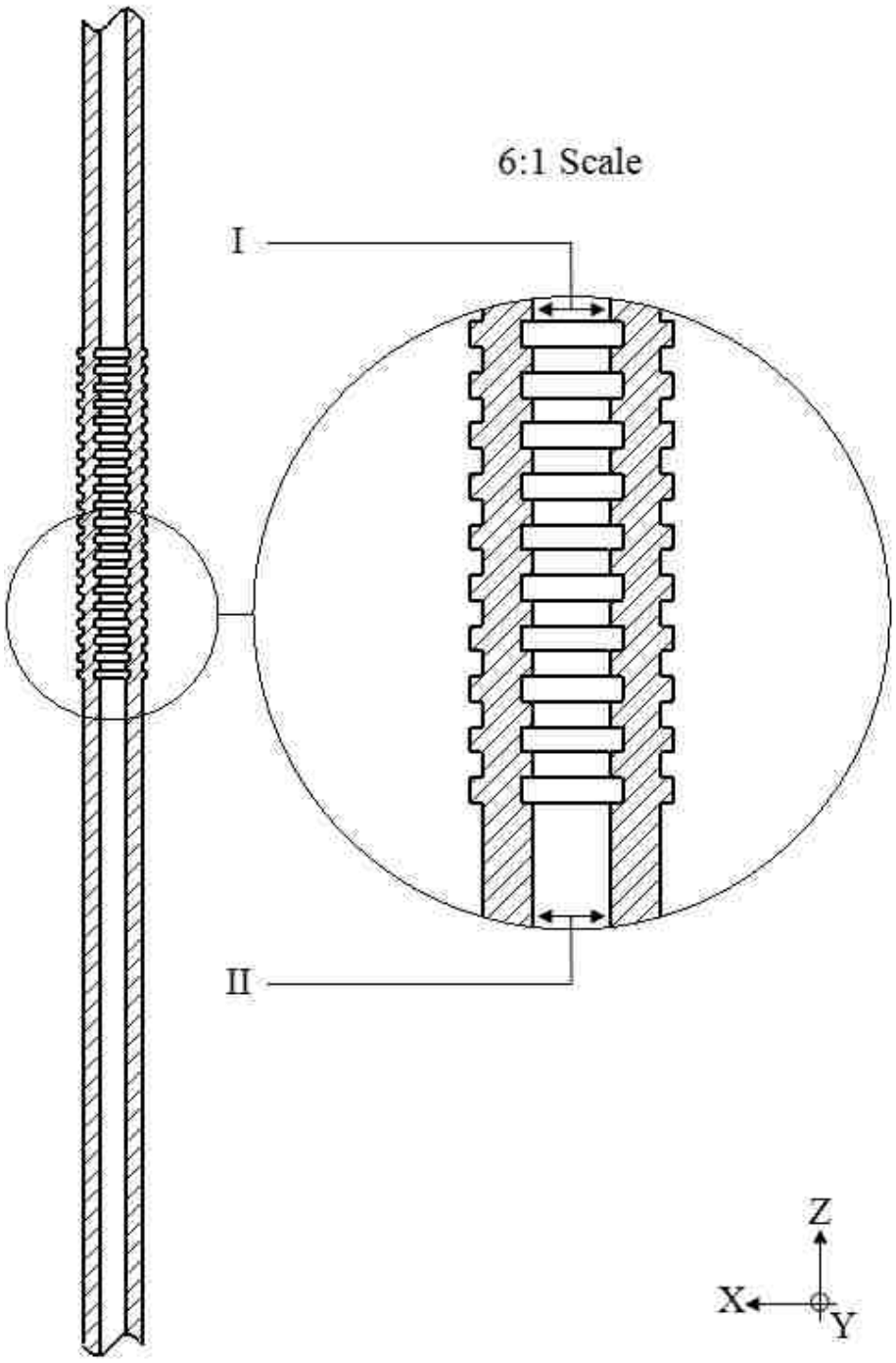

Figure 113: Cross-sectional Right View. Straight Circular-bodied Flexi-Drain with a Flexible Section composed of “Rectangular” Rims and Grooves. A Six times larger view of the “Rectangular” Rims and Grooves are shown within the circle. ‘I’ indicates the distance between the inner Rims. ‘II’ indicates the inner diameter of the Drain. Note that lengths represented by ‘I’ and ‘II’ are almost identical.

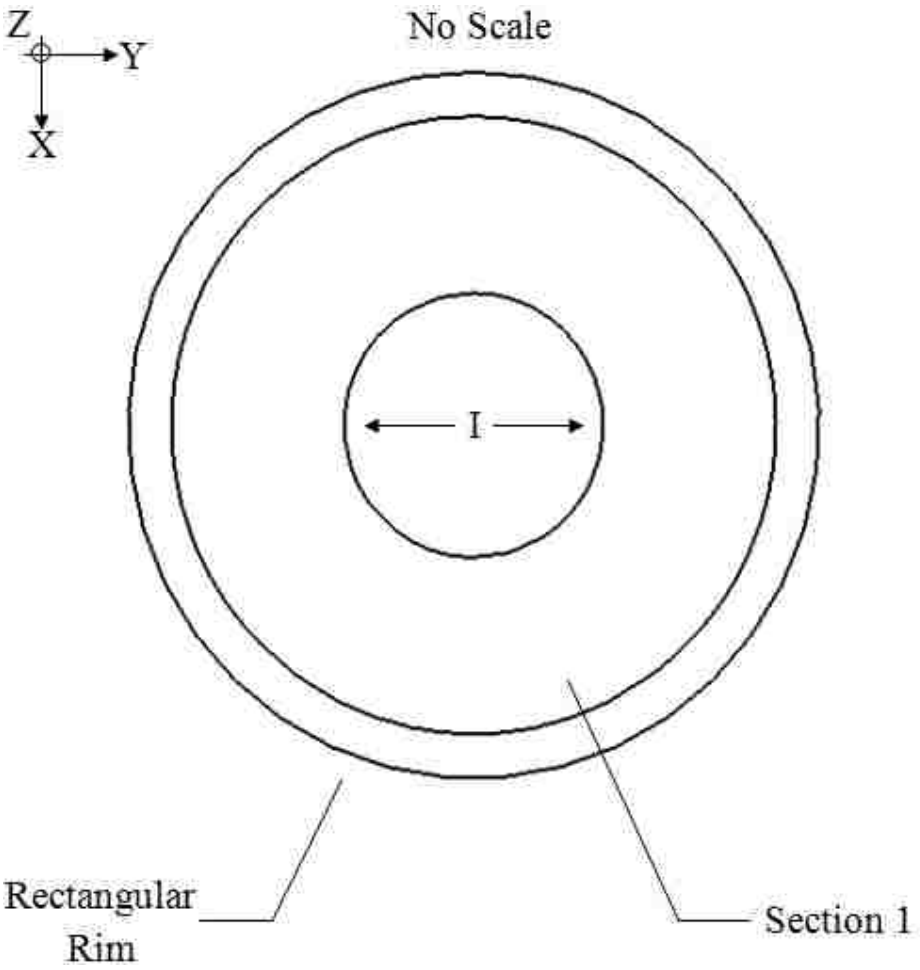

Figure 114: Enlarged Top View. No Scale. Straight Circular-bodied Flexi-Drain with a Flexible Section composed of "Rectangular" Rims and Grooves. 'I' indicates the diameter of the inner Rims as well as the inner diameter of the Drain.

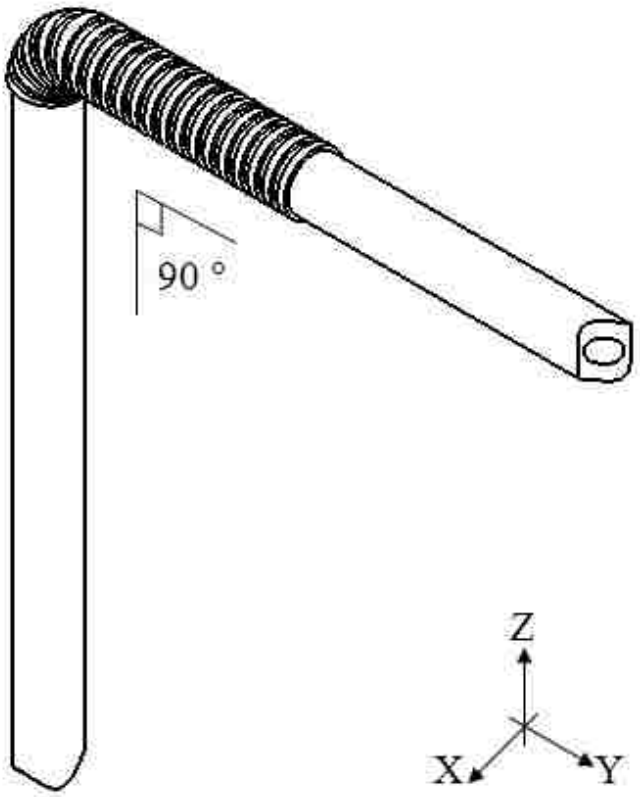

Figure 115: Isometric View. 90° bent Circular-bodied Flexi-Drain with a Flexible Section composed of “Rectangular” Rims and Grooves.

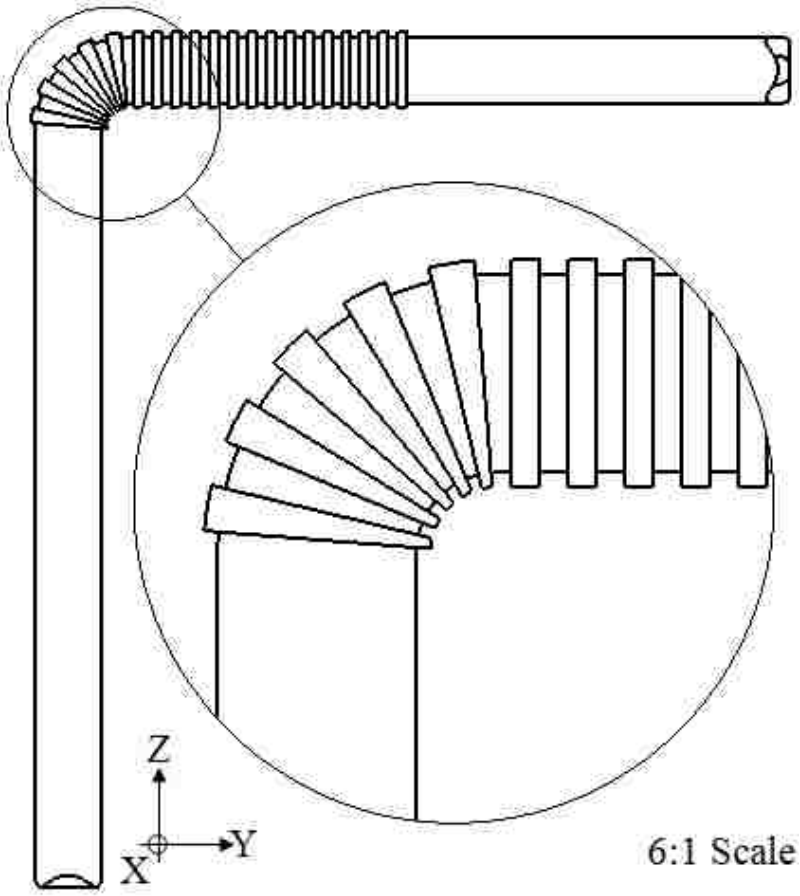

Figure 116: Front View. 90° bent Circular-bodied Flexi-Drain with a Flexible Section composed of "Rectangular" Rims and Grooves. A six times larger view of the bent Flexible Section is shown in the circle.

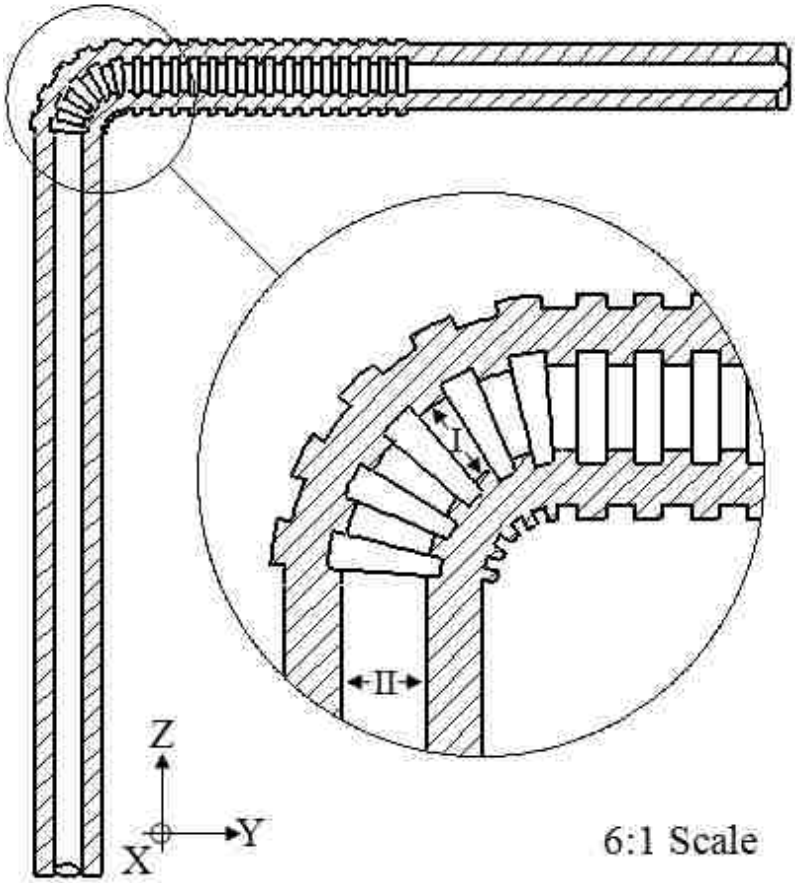

Figure 117: Cross-sectional Front View. 90° bent Circular-bodied Flexi-Drain with a Flexible Section composed of "Rectangular" Rims and Grooves. A six times larger view of the bent Flexible Section is shown in the circle. 'I' indicates the diameter of the inner Rims in their bent position. 'II' indicates the inner diameter of the Drain. Note that lengths represented by 'I' and 'II' are almost identical.

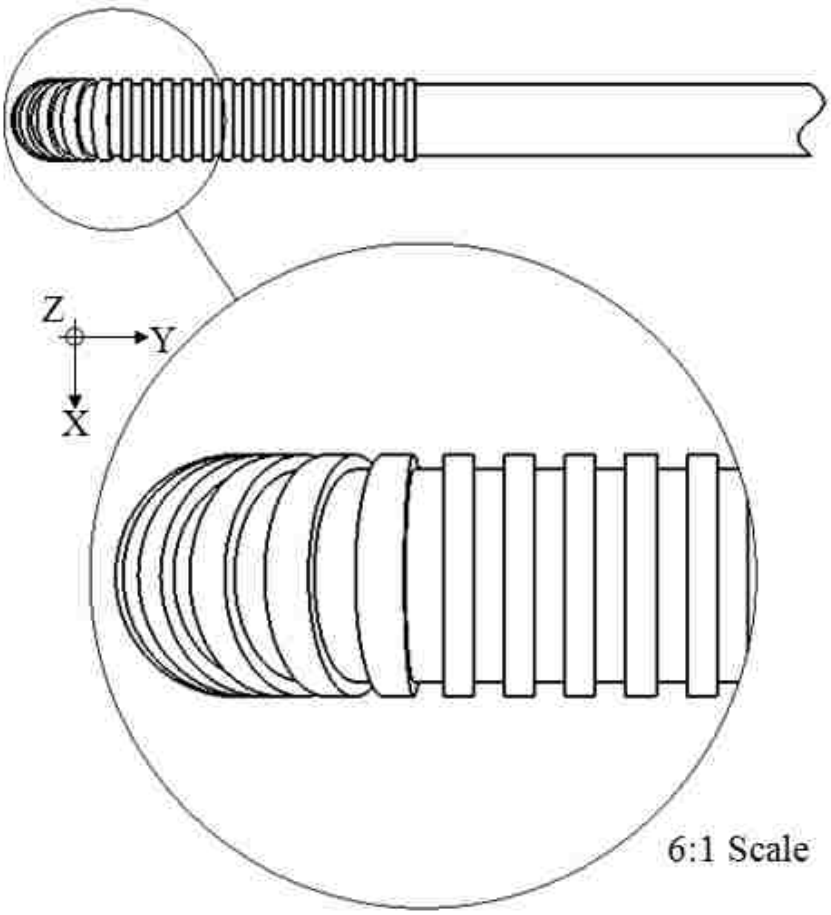

Figure 118: Top View. 90° bent Circular-bodied Flexi-Drain with a Flexible Section composed of “Rectangular” Rims and Grooves. A six times larger view of the bent Flexible Section is shown in the circle.

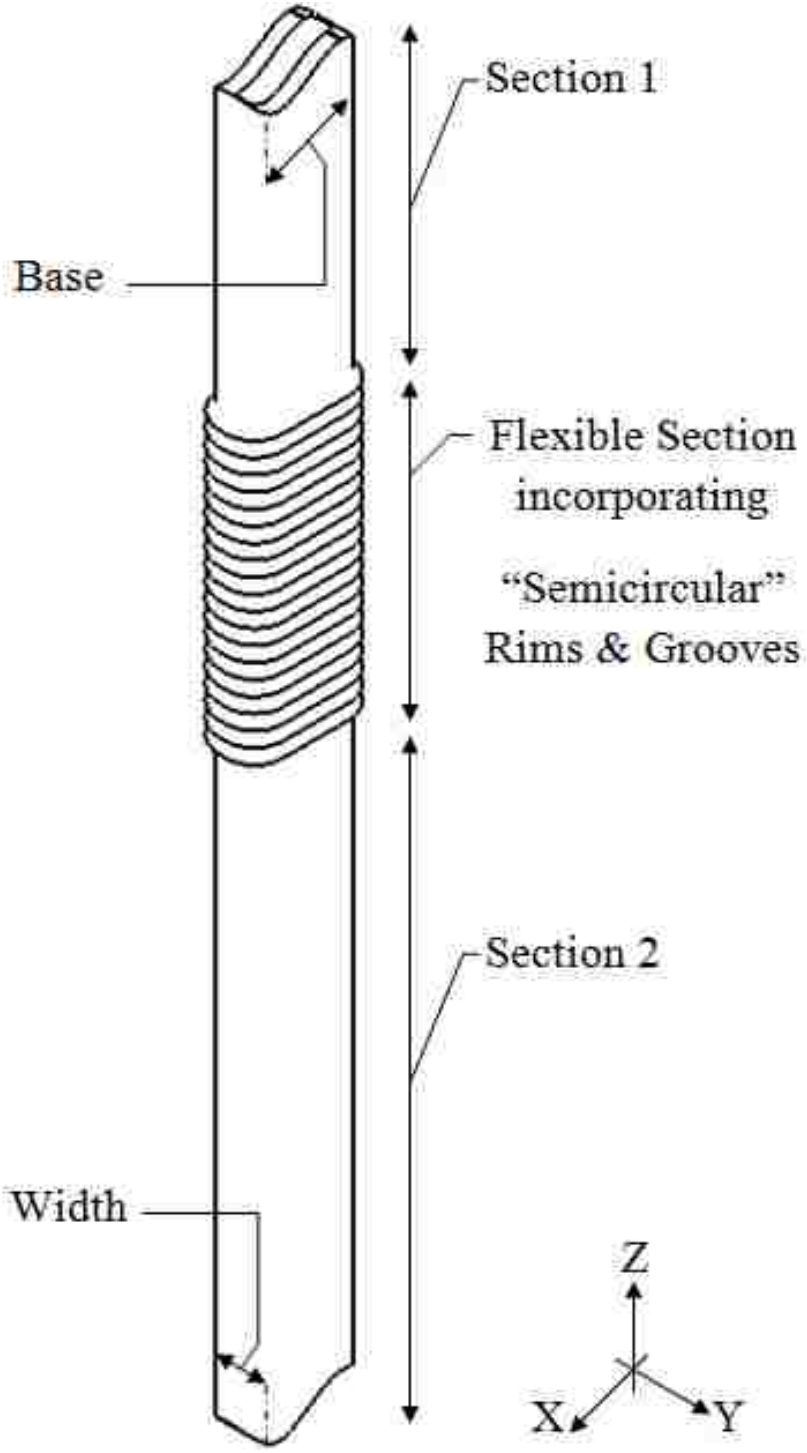

Figure 119: Isometric View. Straight Rectangular-bodied Flexi-Drain with a Flexible Section composed of "Semicircular" Rims and Grooves. Section 1 and Section 2, which respectively connect to the Upper and the Lower extensions of the Flexi-Drain are shown as well.

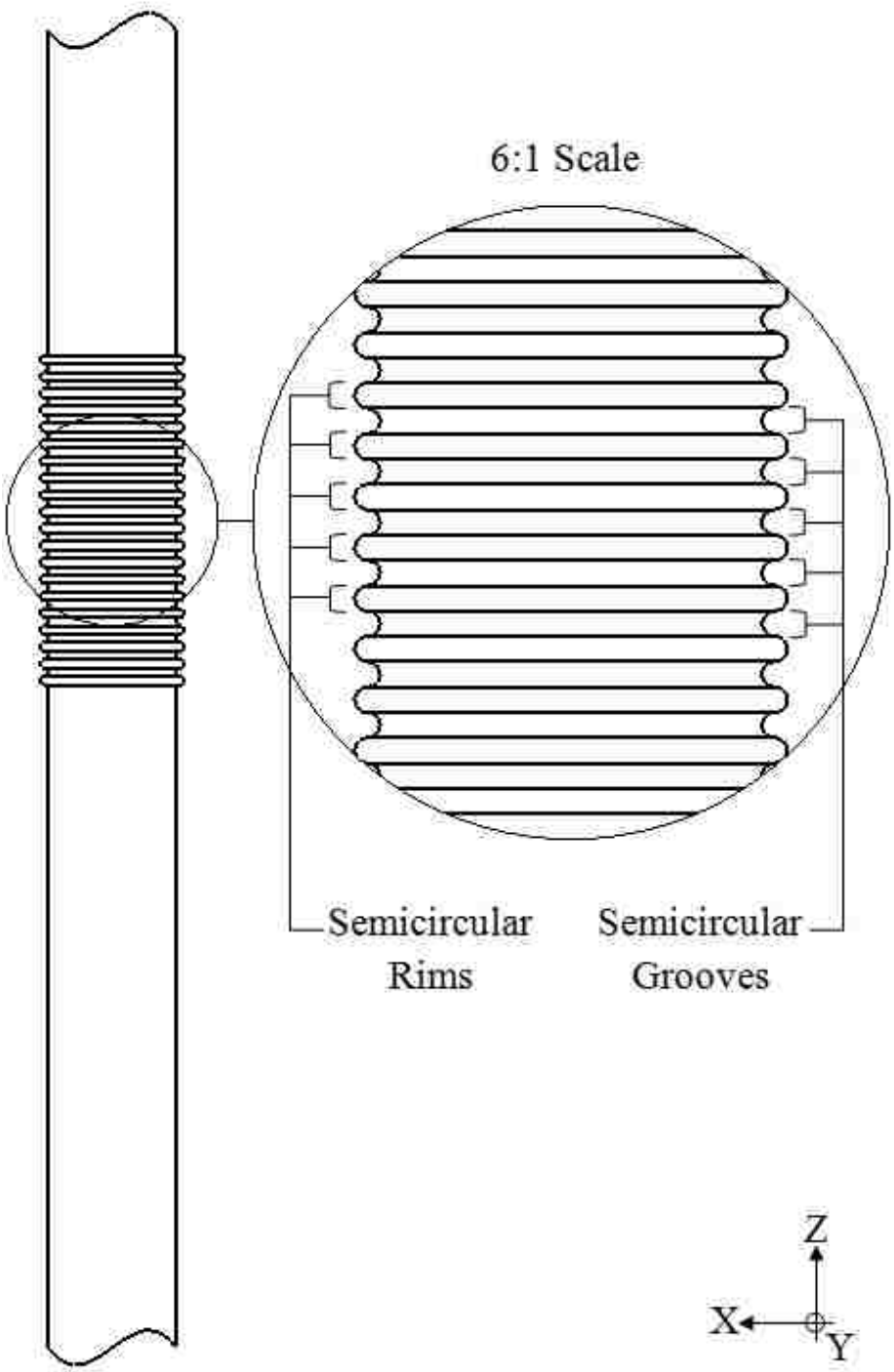

Figure 120: Right View. Straight Rectangular-bodied Flexi-Drain with a Flexible Section composed of "Semicircular" Rims and Grooves. A six times larger view of the "Semicircular" Rims and Grooves are shown in the circle.

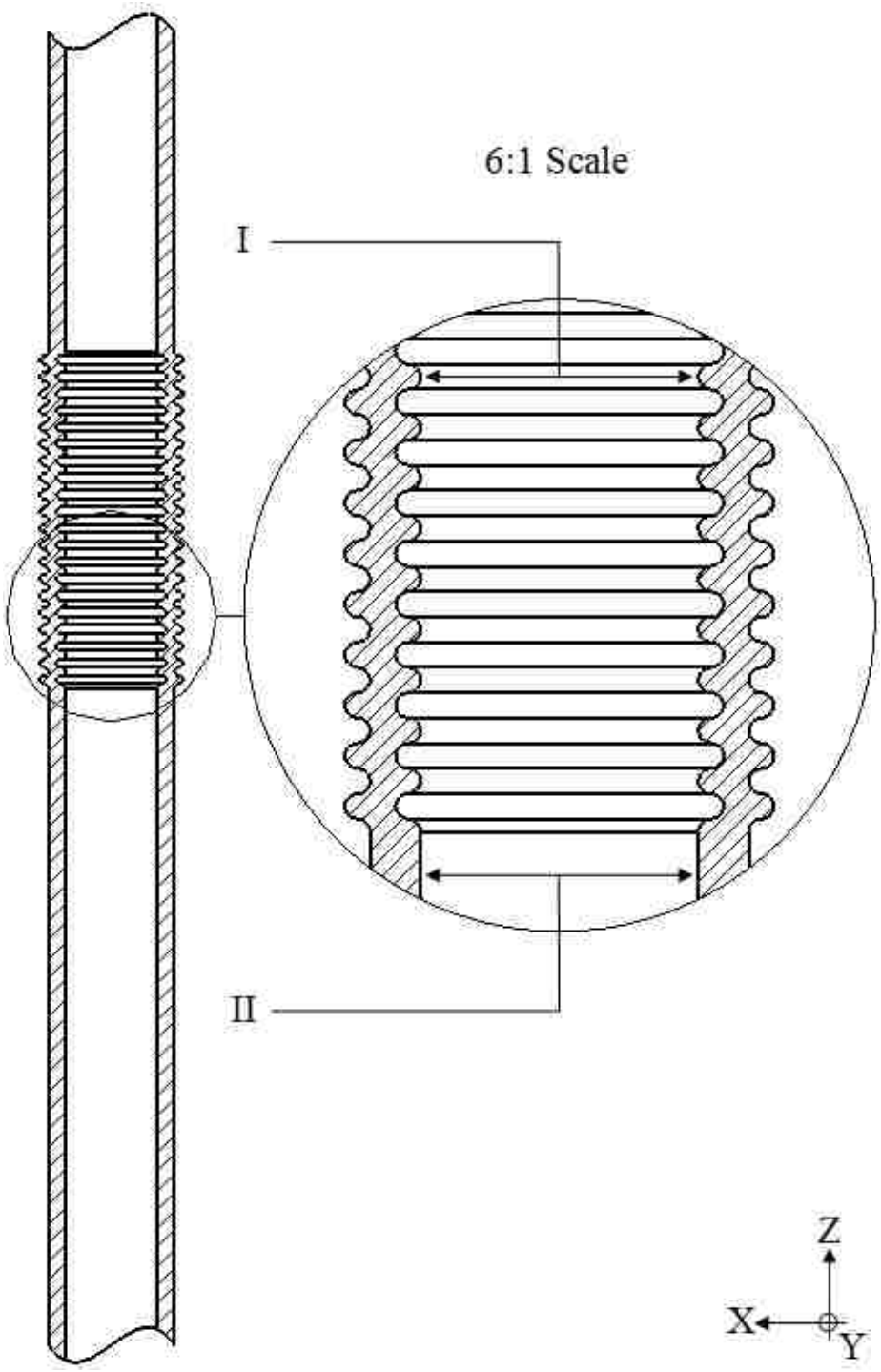

Figure 121: Cross-sectional Right View. Straight Rectangular-bodied Flexi-Drain with a Flexible Section composed of “Semicircular” Rims and Grooves. A six times larger view of the “Semicircular” Rims and Grooves are shown within the circle. ‘I’ indicates the distance between the inner Rims. ‘II’ indicates the inner diameter of the Drain. Note that lengths represented by ‘I’ and ‘II’ are almost identical.

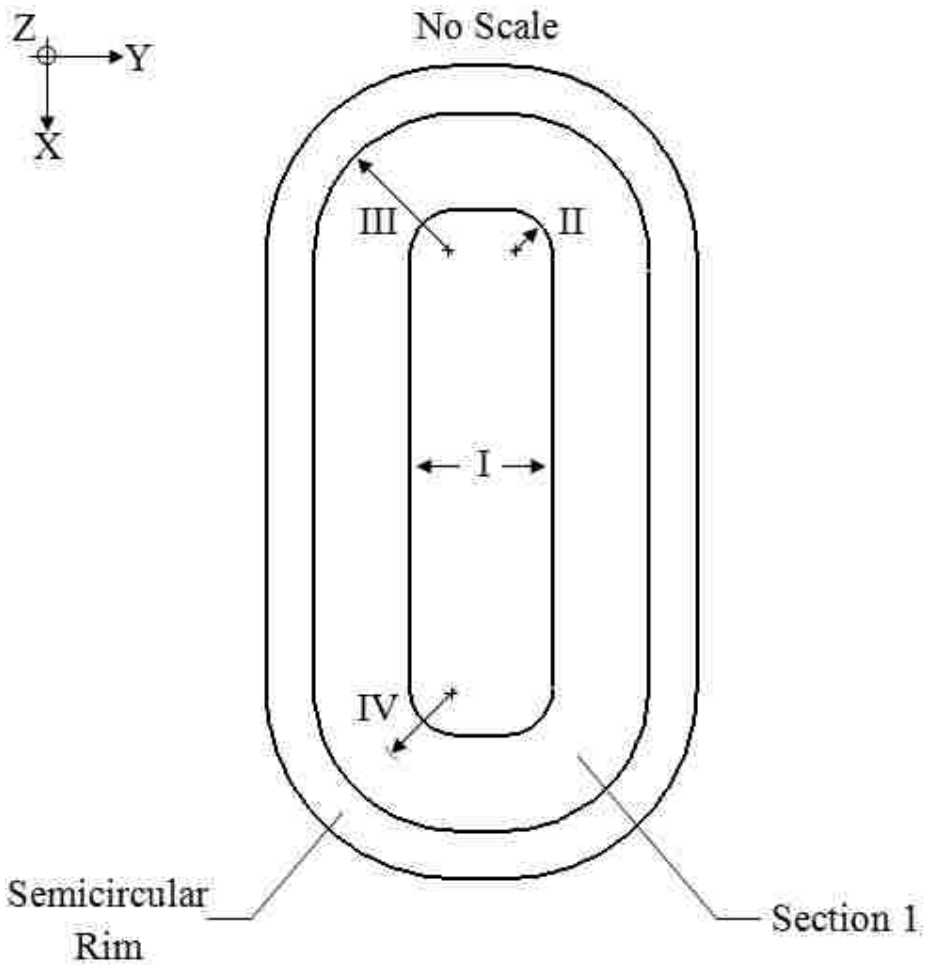

Figure 122: Enlarged Top View. No Scale. Straight Rectangular-bodied Flexi-Drain with a Flexible Section composed of “Semicircular” Rims and Grooves. ‘I’ indicates the diameter of the inner Rims as well as the inner diameter of the Drain.

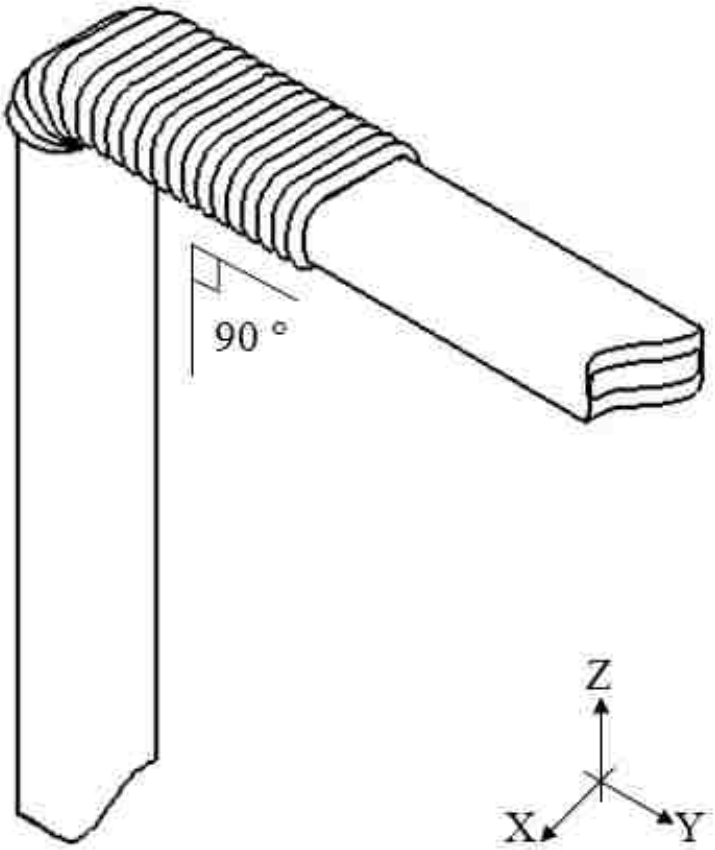

Figure 123: Isometric View. 90° bent Rectangular-bodied Flexi-Drain with a Flexible Section composed of “Semicircular” Rims and Grooves.

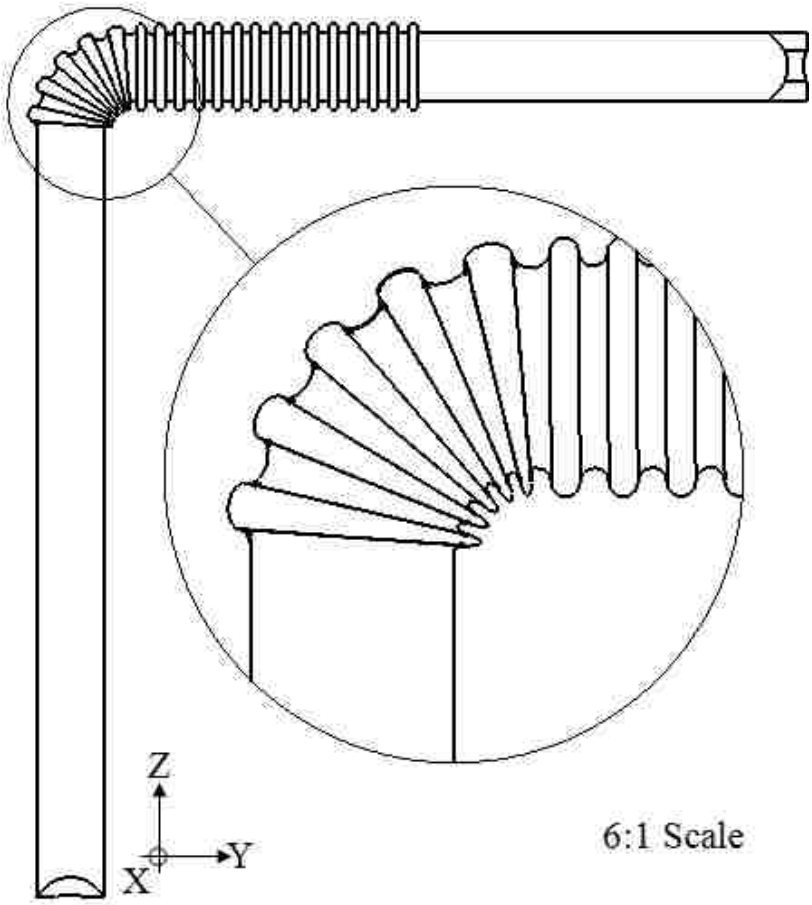

Figure 124: Front View. 90° bent Rectangular-bodied Flexi-Drain with a Flexible Section composed of “Semicircular” Rims and Grooves. A six times larger view of the bent Flexible Section is shown in the circle.

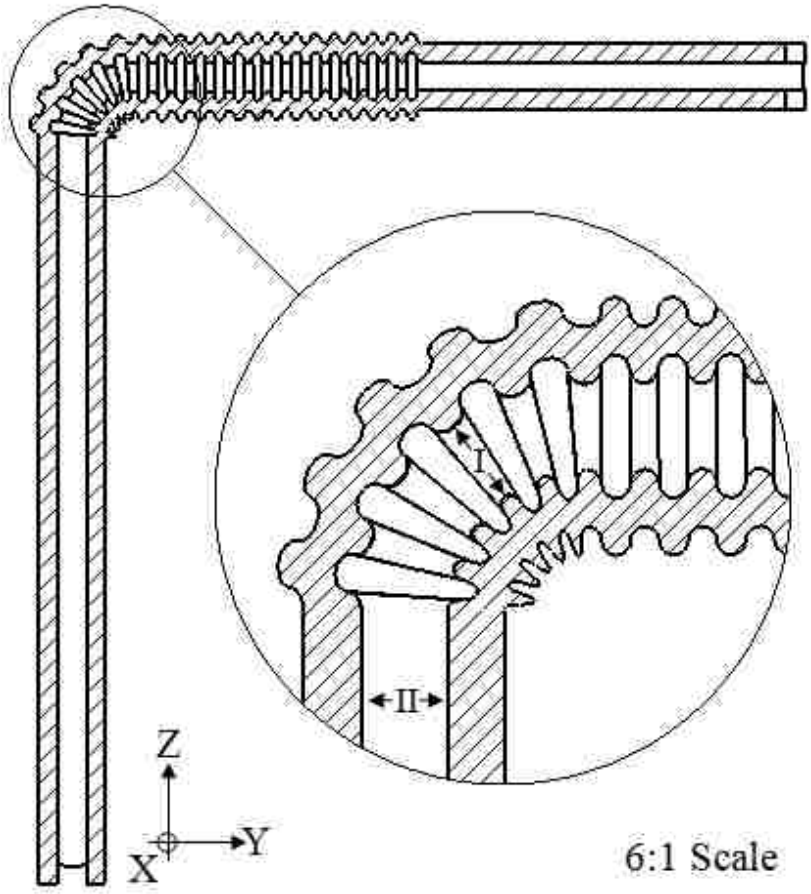

Figure 125: Cross-sectional Front View. 90° bent Rectangular-bodied Flexi-Drain with a Flexible Section composed of "Semicircular" Rims and Grooves. A six times larger view of the bent Flexible Section is shown in the circle. 'I' indicates the diameter of the inner Rims in their bent position. 'II' indicates the inner diameter of the Drain. Note that lengths represented by 'I' and 'II' are almost identical.

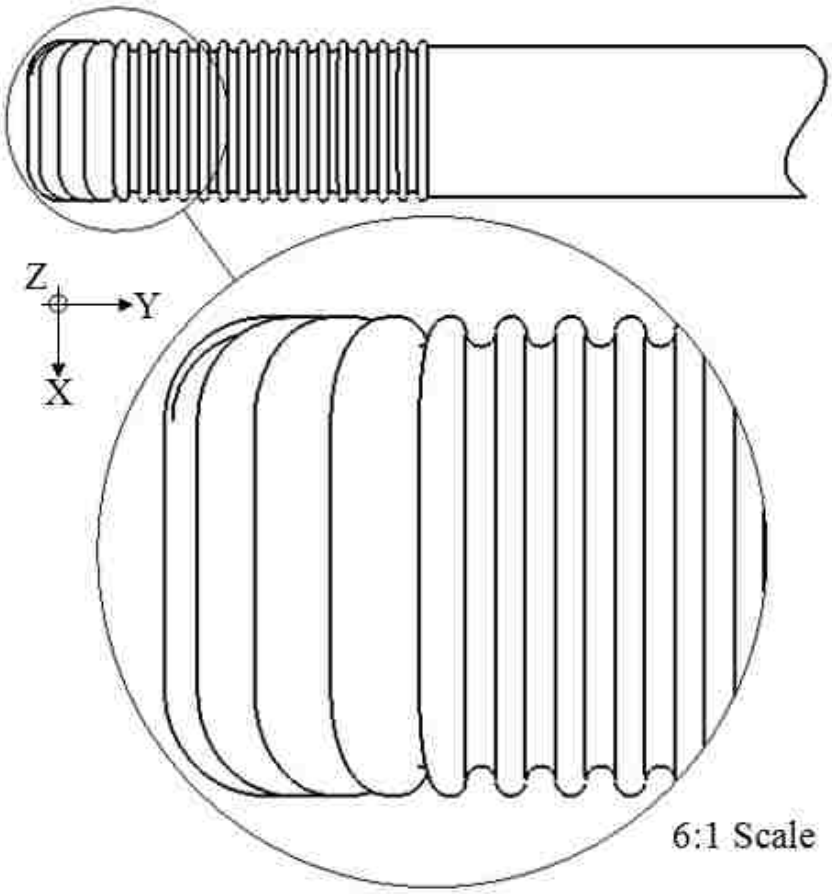

Figure 126: Top View. 90° bent Rectangular-bodied Flexi-Drain with a Flexible Section composed of “Semicircular” Rims and Grooves. A six times larger view of the bent Flexible Section is shown in the circle.

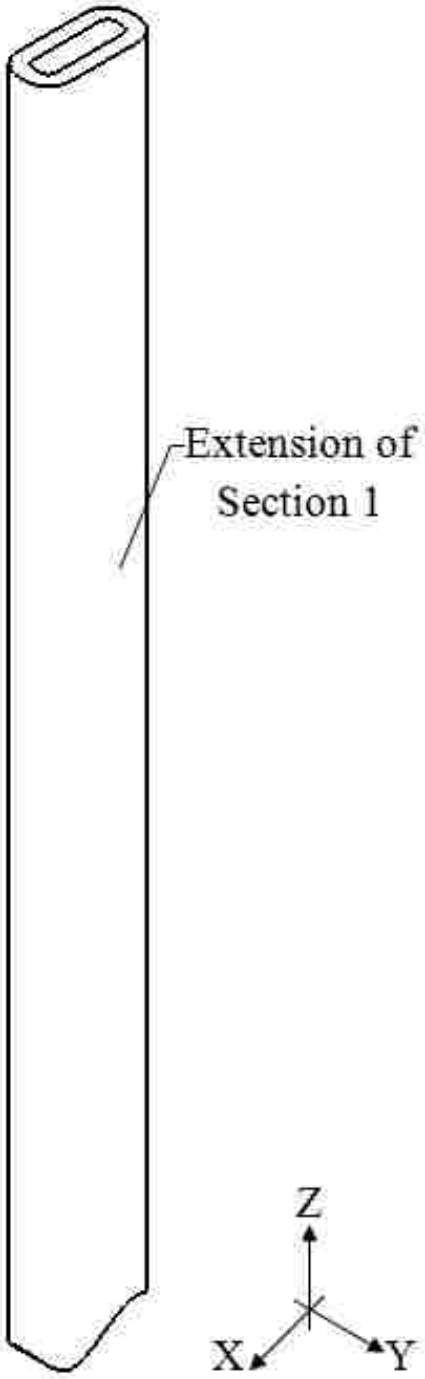

Figure 127: Isometric View. Extension of Section 1. It presents the Upper extension of the Rectangular Flexi-Drain. Section 1 is shown in Figure 6a.

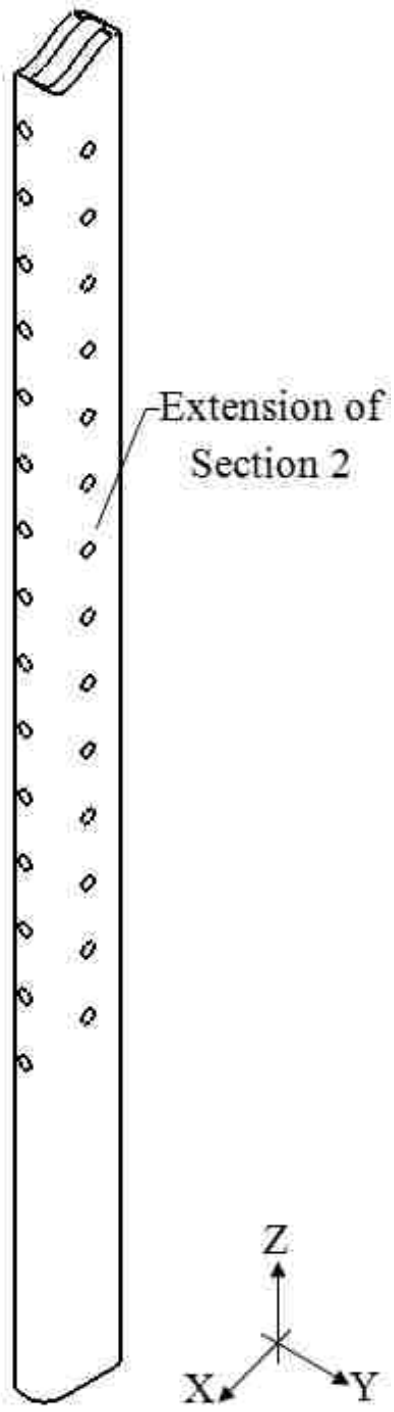

Figure 128: Isometric View. Extension of Section 2. It presents the Lower extension of the Rectangular Flexi-Drain. Section 2 is shown in Figure 6b.

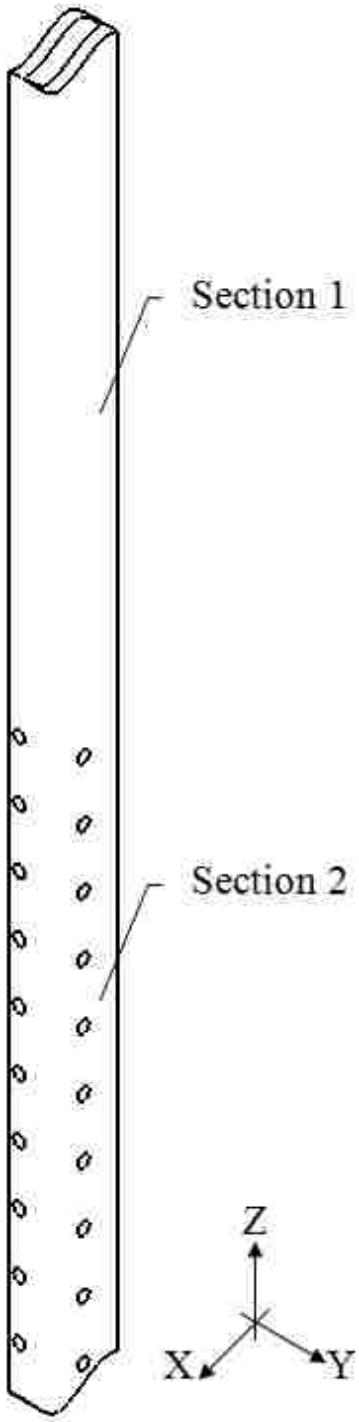

Figure 129: Isometric View. A conventional Rectangular-bodied drain/catheter composed of a continuous connection between Extension of Section1 and Extension of Section 2 without incorporating a Flexible Section.

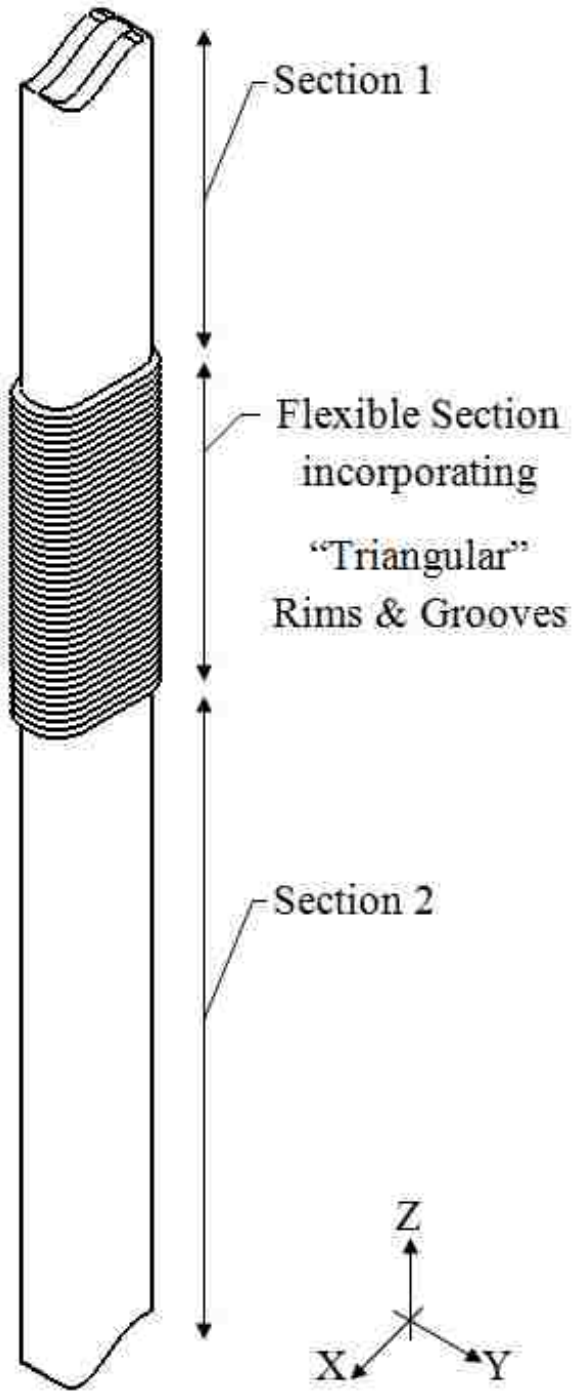

Figure 130: Isometric View. Straight Rectangular-bodied Flexi-Drain with a Flexible Section composed of "Triangular" Rims and Grooves. Section 1 and Section 2, which respectively connect to the Upper and the Lower extensions of the Flexi-Drain are shown as well.

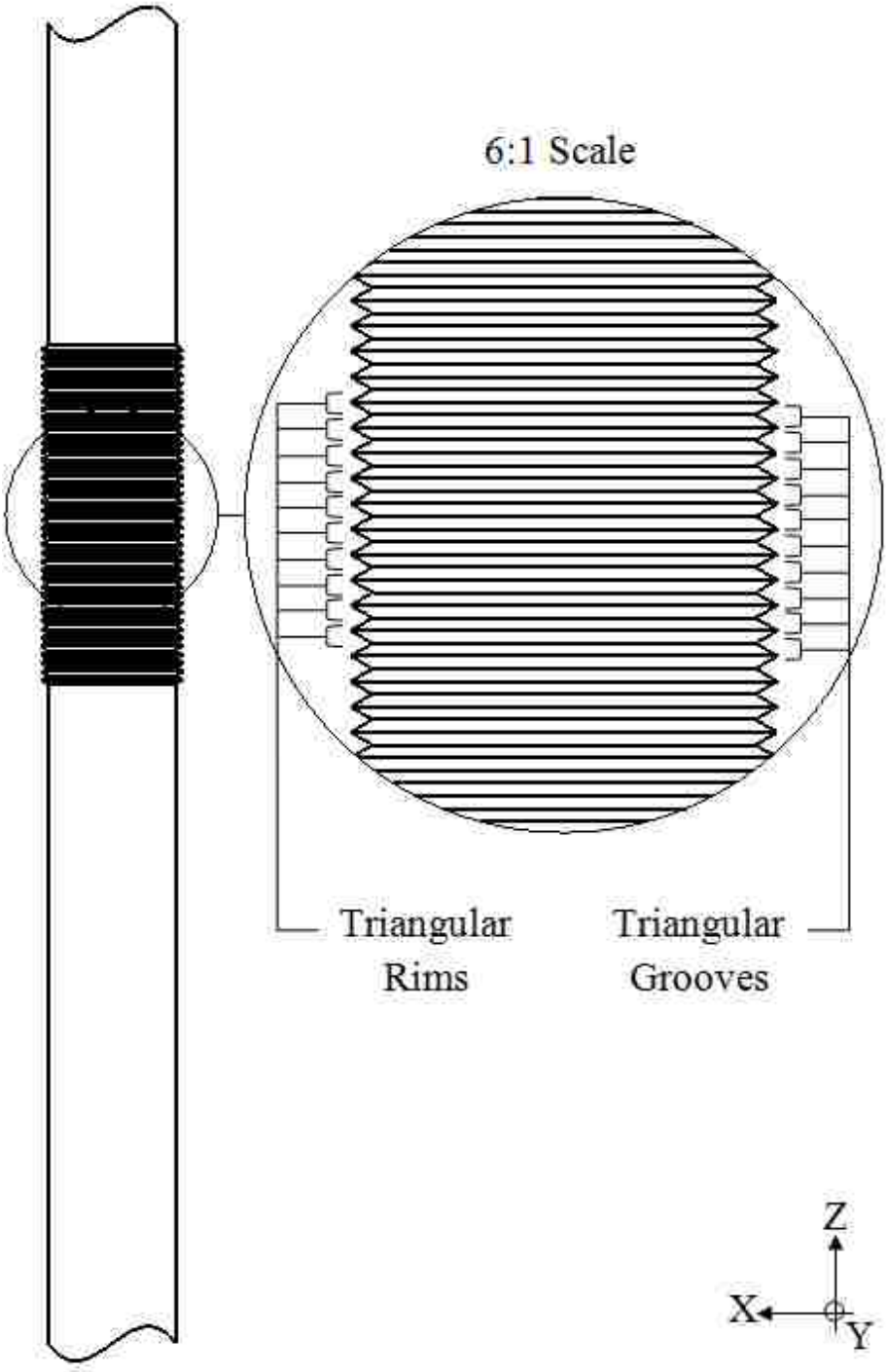

Figure 131: Right View. Straight Rectangular-bodied Flexi-Drain with a Flexible Section composed of "Triangular" Rims and Grooves. A six times larger view of the "Triangular" Rims and Grooves are shown in the circle.

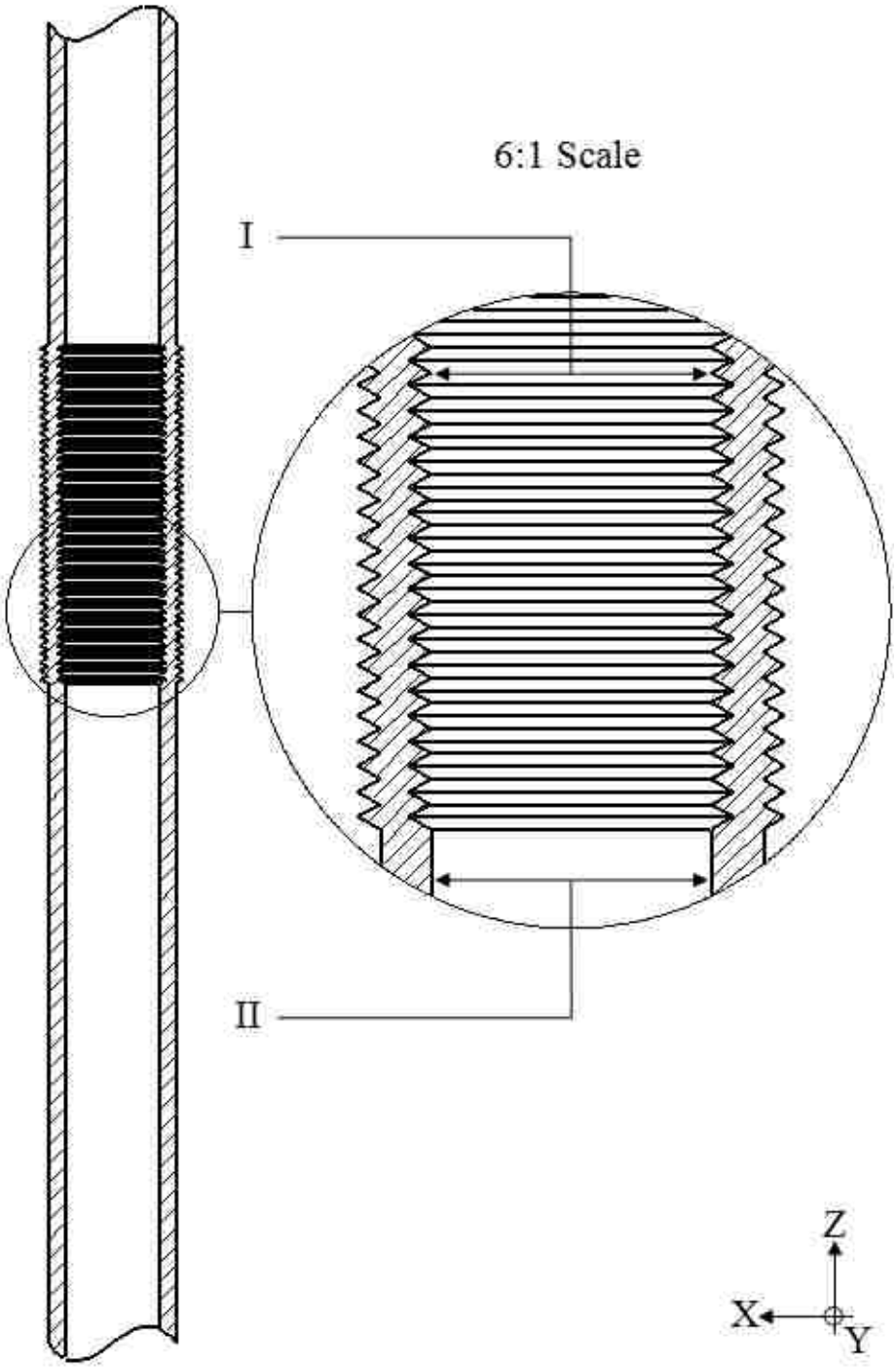

Figure 132: Cross-sectional Right View. Straight Rectangular-bodied Flexi-Drain with a Flexible Section composed of "Triangular" Rims and Grooves. A Six times larger view of the "Triangular" Rims and Grooves are shown within the circle. 'I' indicates the distance between the inner Rims. 'II' indicates the inner diameter of the Drain. Note that lengths represented by 'I' and 'II' are almost identical.

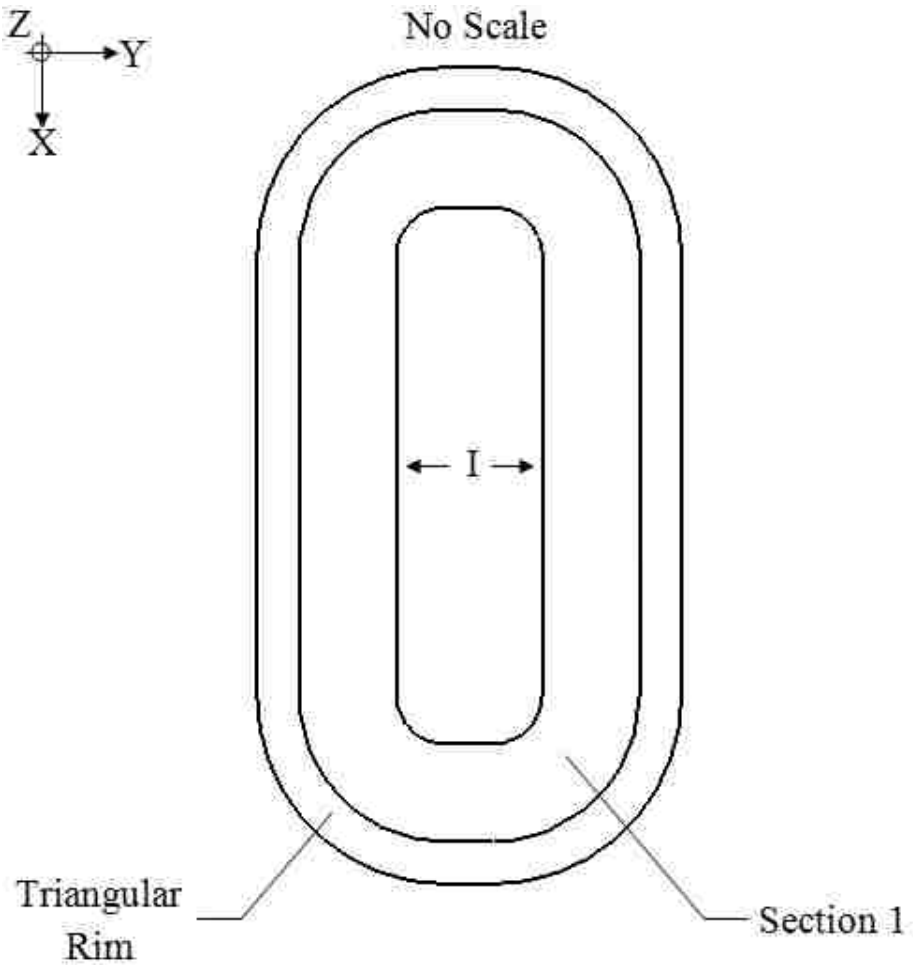

Figure 133: Enlarged Top View. No Scale. Straight Rectangular-bodied Flexi-Drain with a Flexible Section composed of "Triangular" Rims and Grooves. 'I' indicates the diameter of the inner Rims as well as the inner diameter of the Drain.

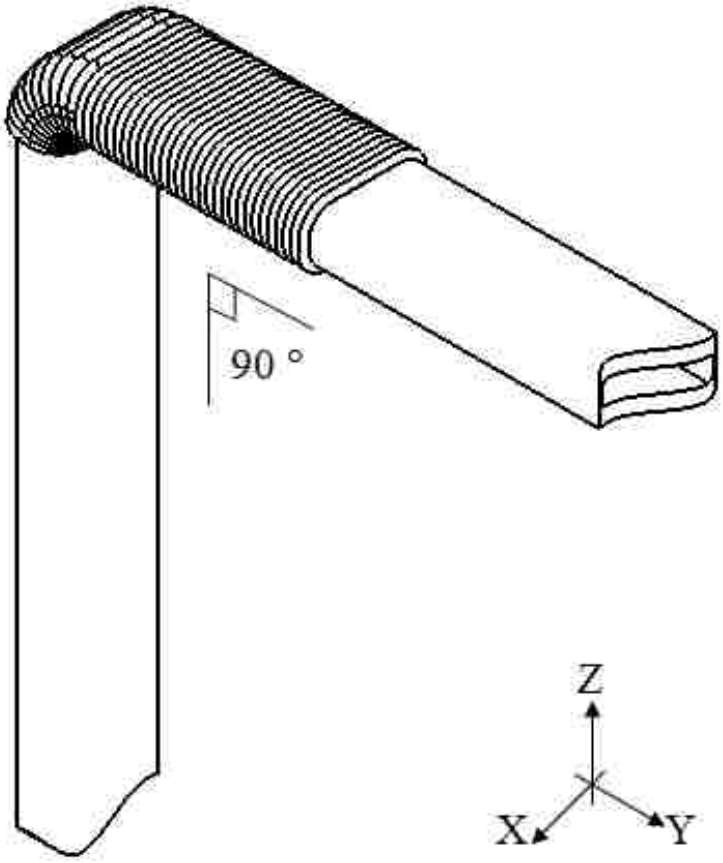

Figure 134: Isometric View. 90° bent Rectangular-bodied Flexi-Drain with a Flexible Section composed of “Triangular” Rims and Grooves.

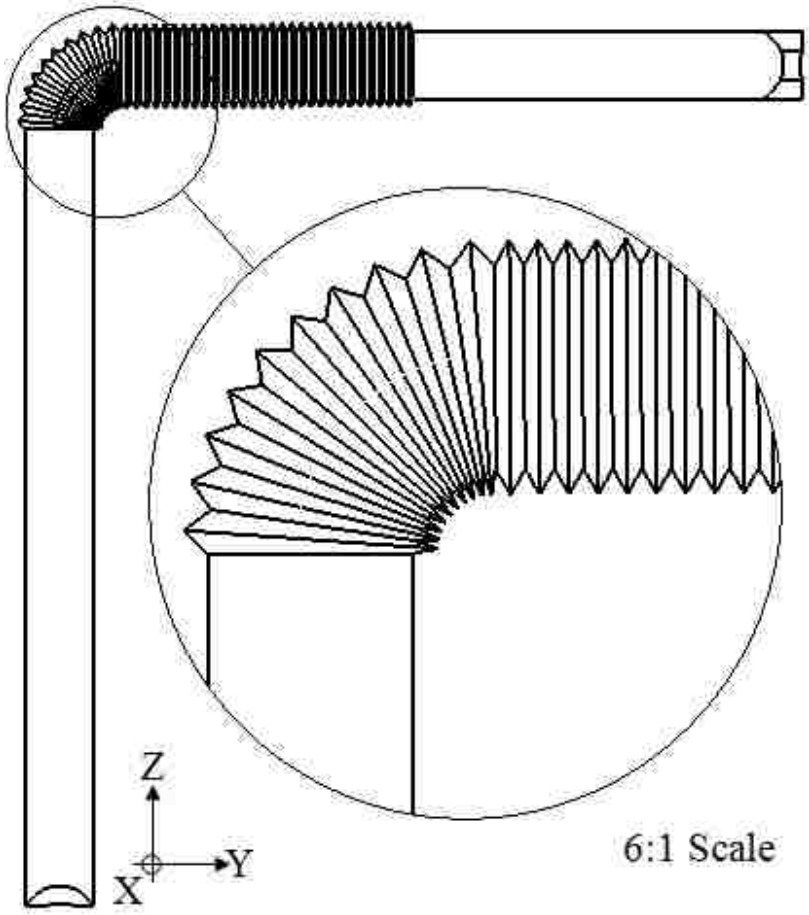

Figure 135: Front View. 90° bent Rectangular-bodied Flexi-Drain with a Flexible Section composed of “Triangular” Rims and Grooves. A six times larger view of the bent Flexible Section is shown in the circle.

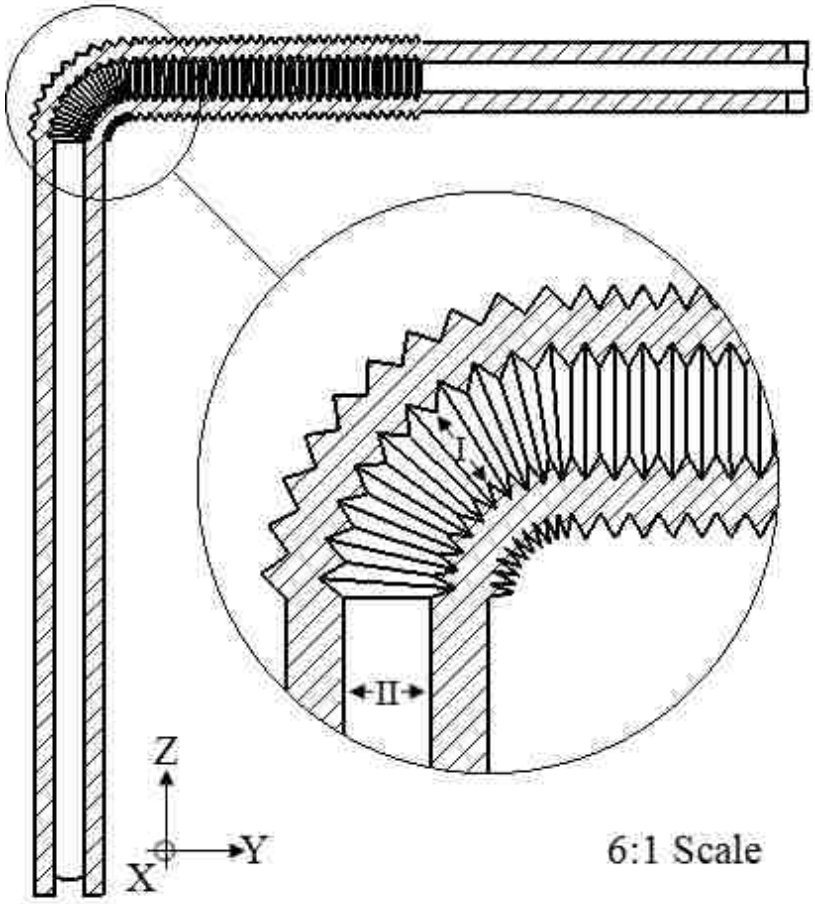

Figure 136: Cross-sectional Front View. 90° bent Rectangular-bodied Flexi-Drain with a Flexible Section composed of "Triangular" Rims and Grooves. A six times larger view of the bent Flexible Section is shown in the circle. 'I' indicates the diameter of the inner Rims in their bent position. 'II' indicates the inner diameter of the Drain. Note that lengths represented by 'I' and 'II' are almost identical.

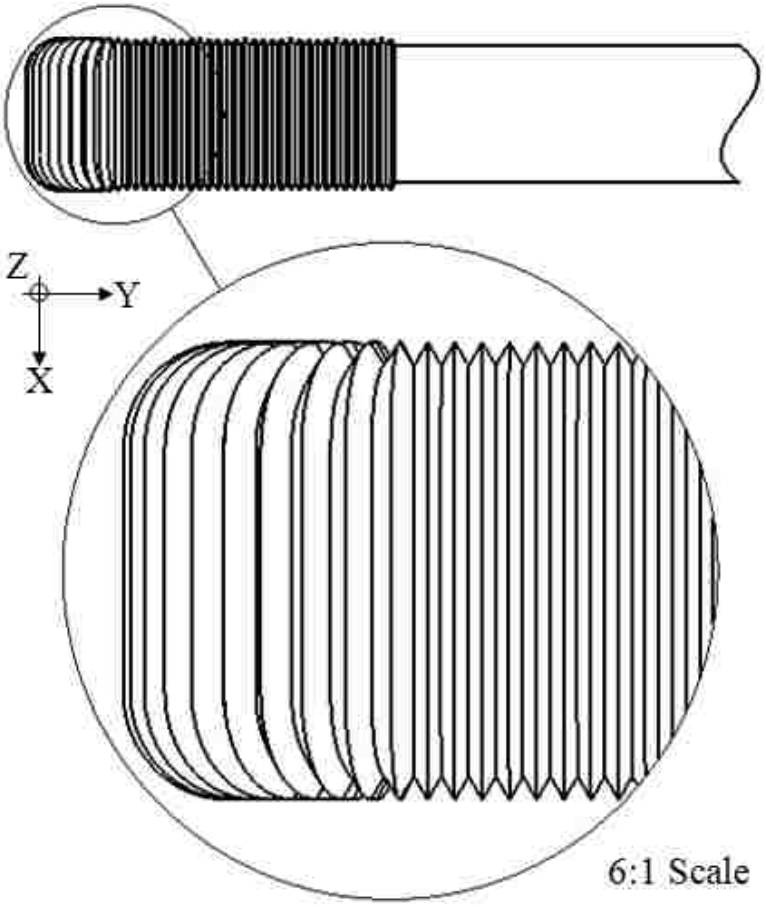

Figure 137: Top View. 90° bent Rectangular-bodied Flexi-Drain with a Flexible Section composed of “Triangular” Rims and Grooves. A six times larger view of the bent Flexible Section is shown in the circle.

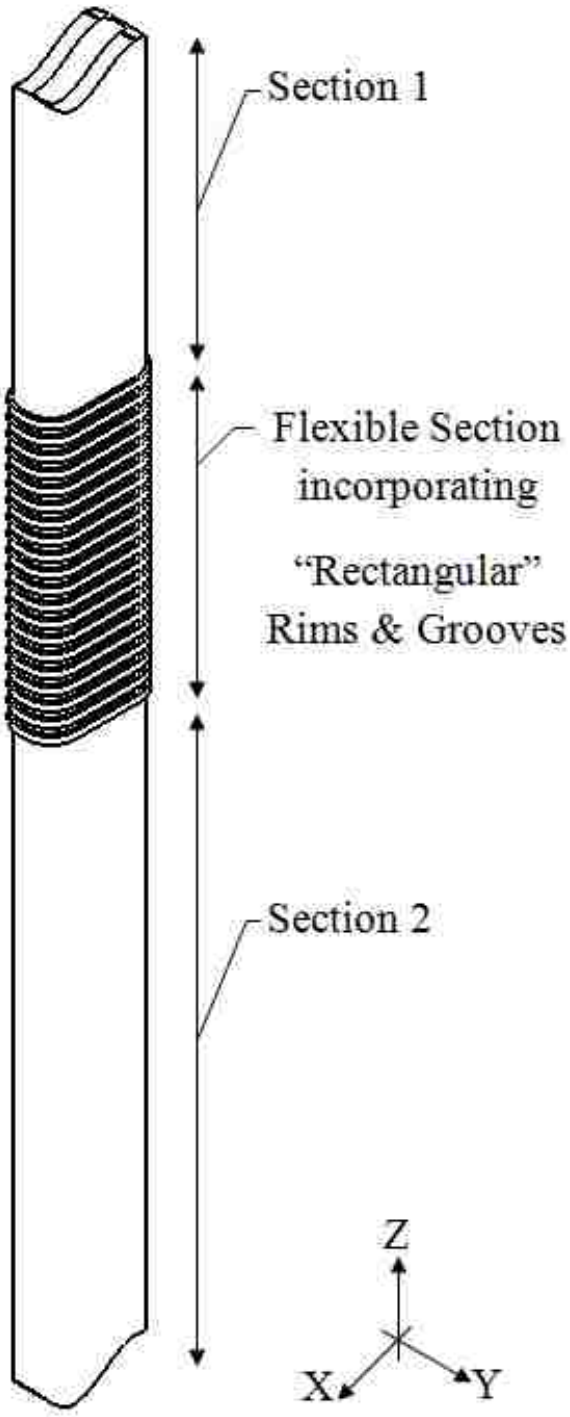

Figure 138: Isometric View. Straight Rectangular-bodied Flexi-Drain with a Flexible Section composed of "Rectangular" Rims and Grooves. Section 1 and Section 2, which respectively connect to the Upper and the Lower extensions of the Flexi-Drain are shown as well.

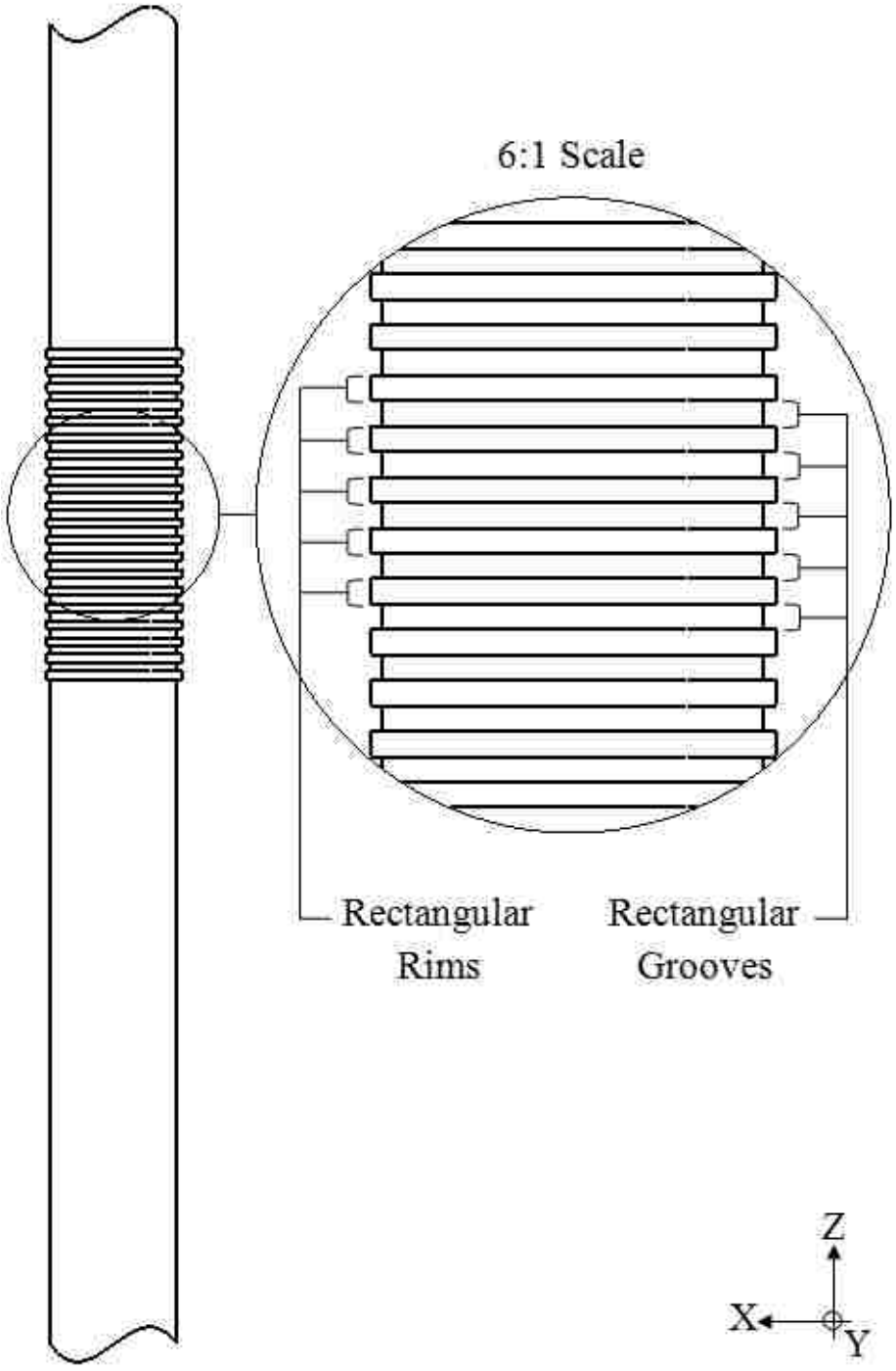

Figure 139: Right View. Straight Rectangular-bodied Flexi-Drain with a Flexible Section composed of "Rectangular" Rims and Grooves. A six times larger view of the "Rectangular" Rims and Grooves are shown in the circle.

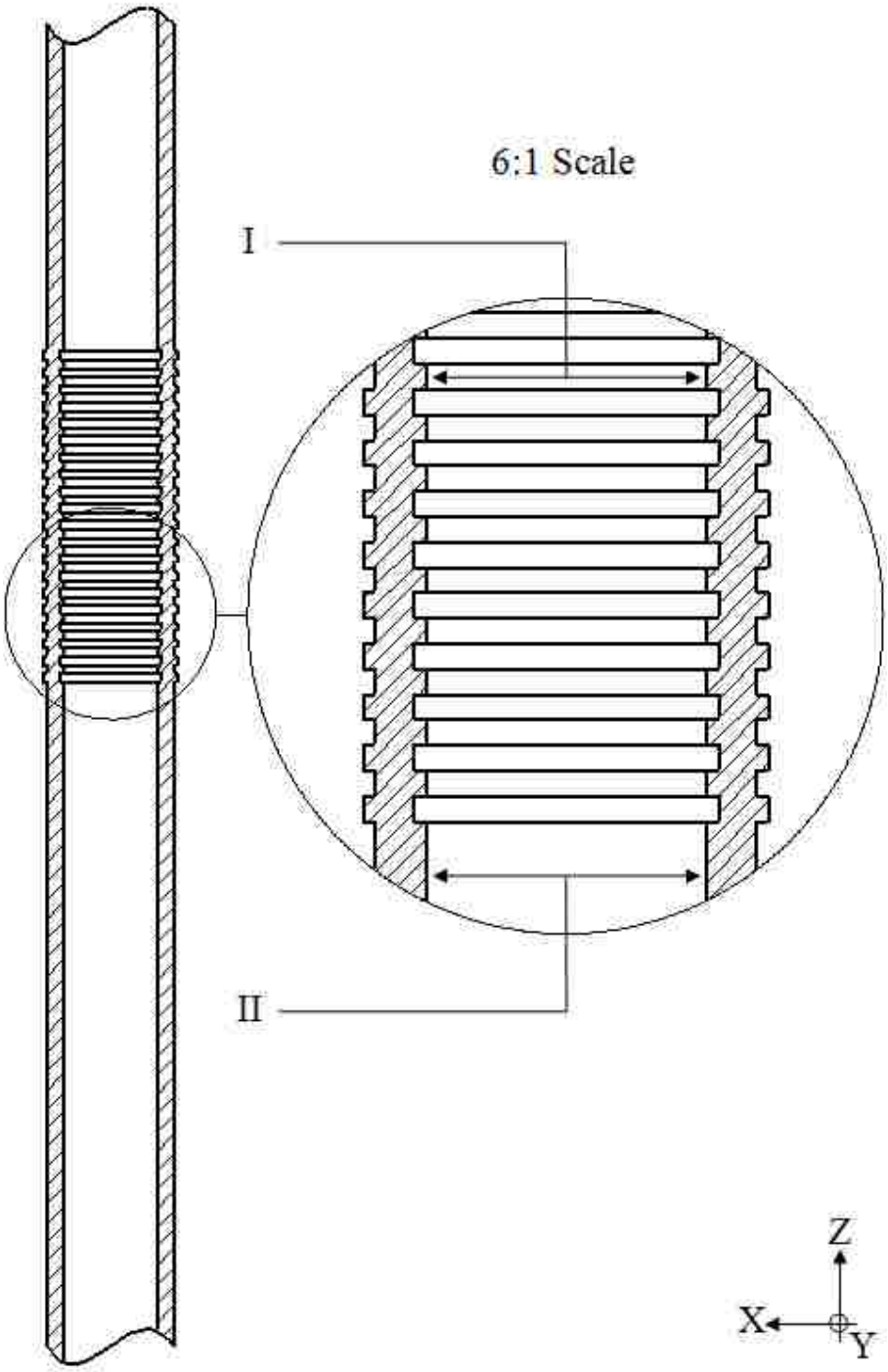

Figure 140: Cross-sectional Right View. Straight Rectangular-bodied Flexi-Drain with a Flexible Section composed of "Rectangular" Rims and Grooves. A Six times larger view of the "Rectangular" Rims and Grooves are shown within the circle. 'I' indicates the distance between the inner Rims. 'II' indicates the inner diameter of the Drain. Note that lengths represented by 'I' and 'II' are almost identical.

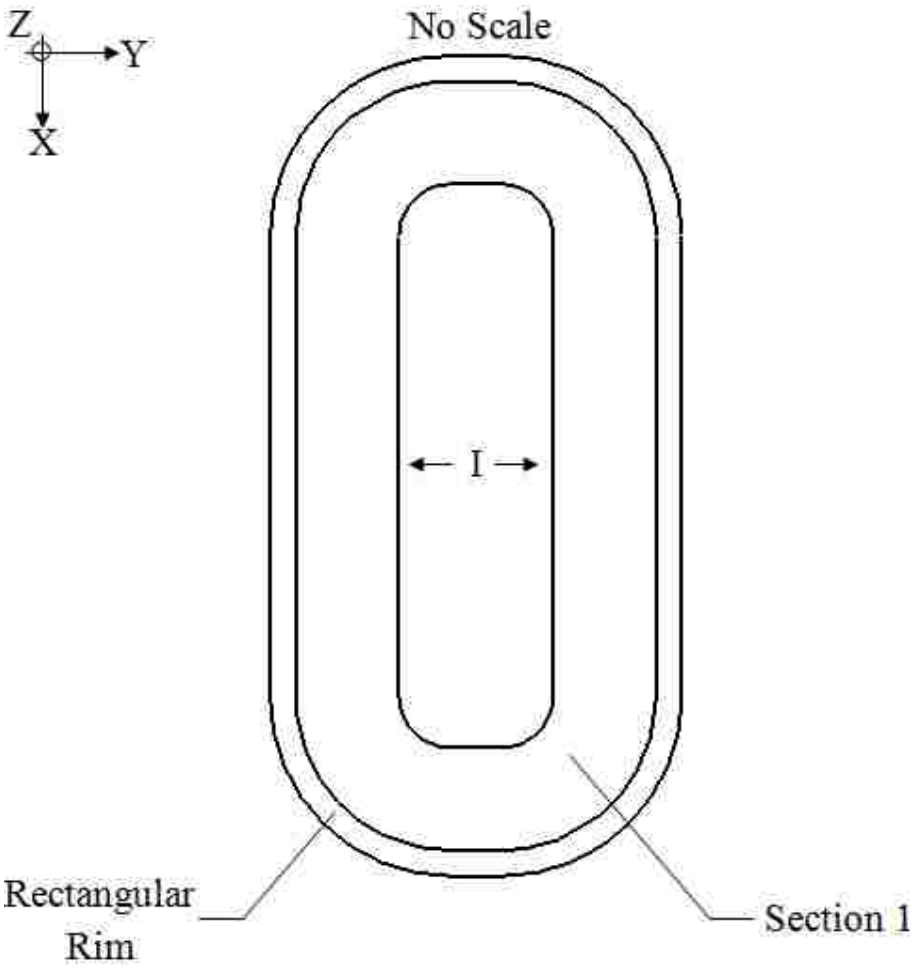

Figure 141: Enlarged Top View. No Scale. Straight Rectangular-bodied Flexi-Drain with a Flexible Section composed of "Rectangular" Rims and Grooves. 'I' indicates the diameter of the inner Rims as well as the inner diameter of the Drain.

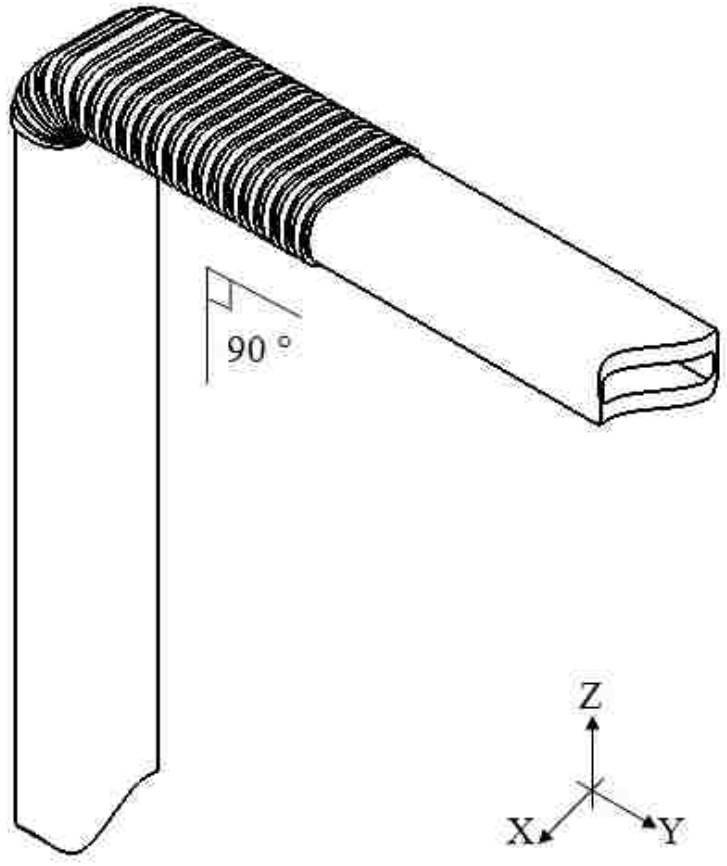

Figure 142: Isometric View. 90° bent Rectangular-bodied Flexi-Drain with a Flexible Section composed of “Rectangular” Rims and Grooves.

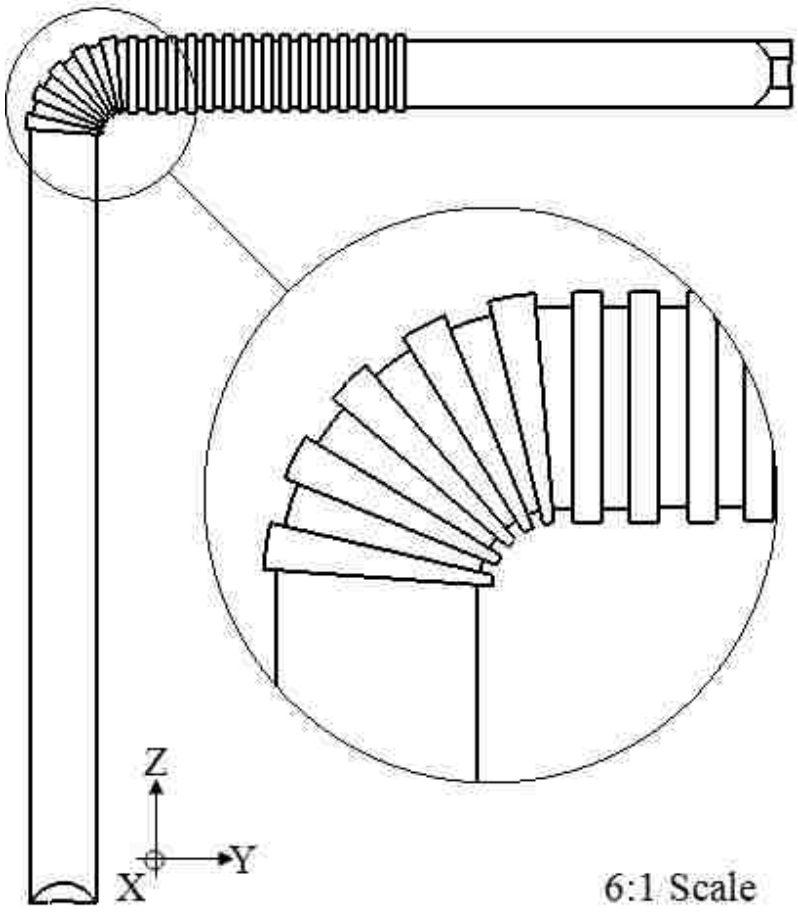

Figure 143: Front View. 90° bent Rectangular-bodied Flexi-Drain with a Flexible Section composed of "Rectangular" Rims and Grooves. A six times larger view of the bent Flexible Section is shown in the circle.

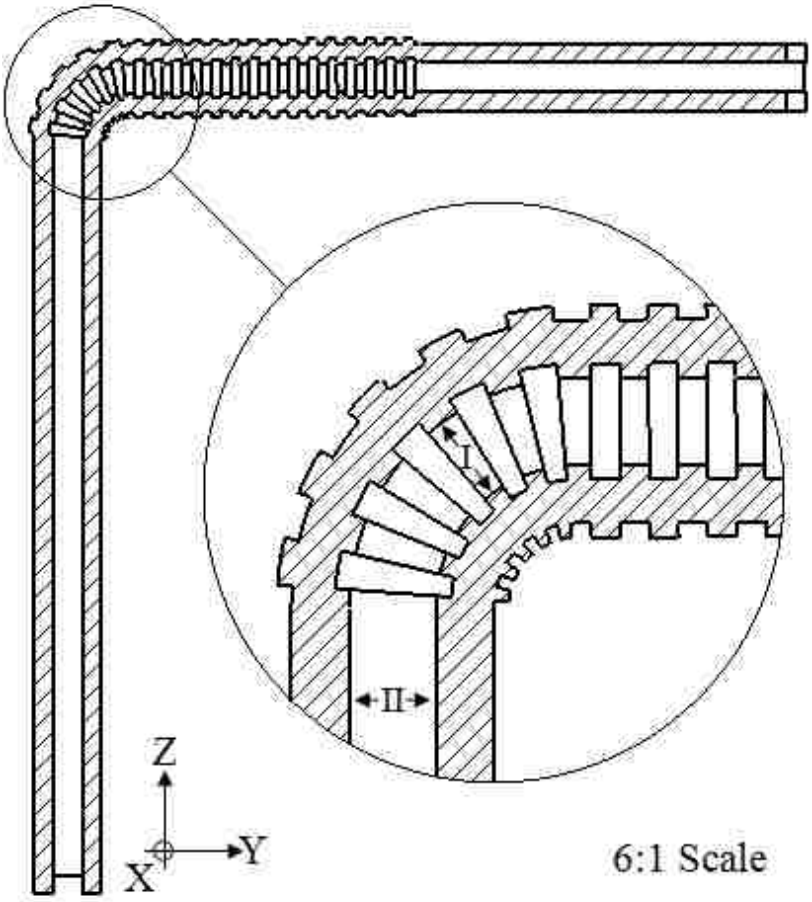

Figure 144: Cross-sectional Front View. 90° bent Rectangular-bodied Flexi-Drain with a Flexible Section composed of "Rectangular" Rims and Grooves. A six times larger view of the bent Flexible Section is shown in the circle. 'I' indicates the diameter of the inner Rims in their bent position. 'II' indicates the inner diameter of the Drain. Note that lengths represented by 'I' and 'II' are almost identical.

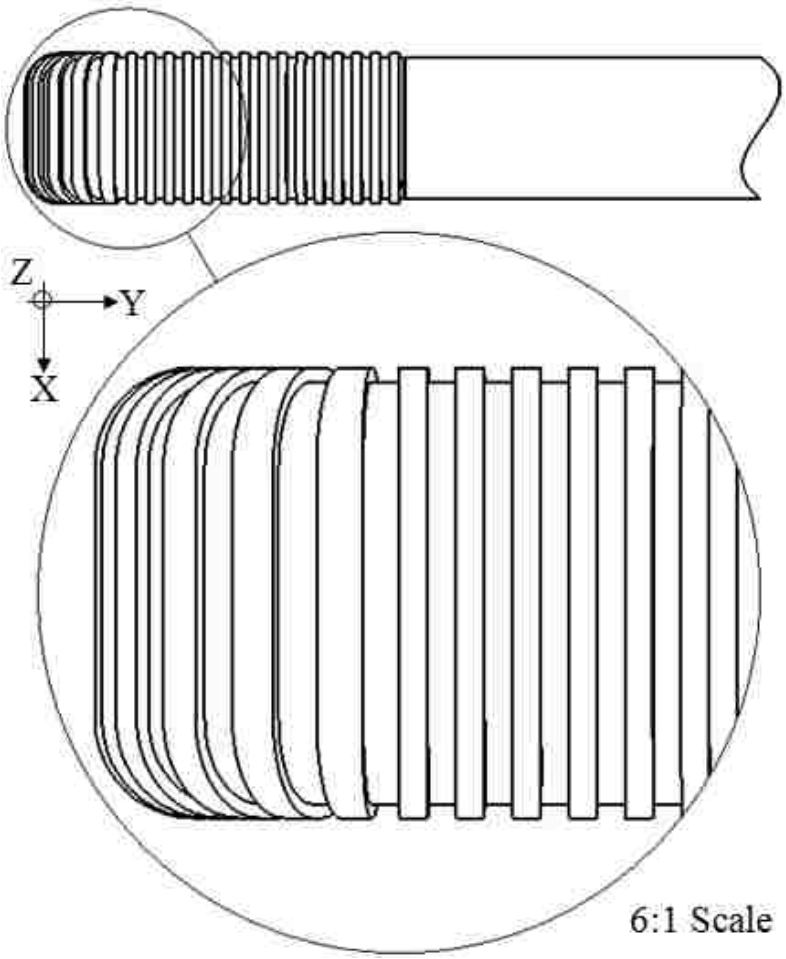

Figure 145: Top View. 90° bent Rectangular-bodied Flexi-Drain with a Flexible Section composed of “Rectangular” Rims and Grooves. A six times larger view of the bent Flexible Section is shown in the circle.

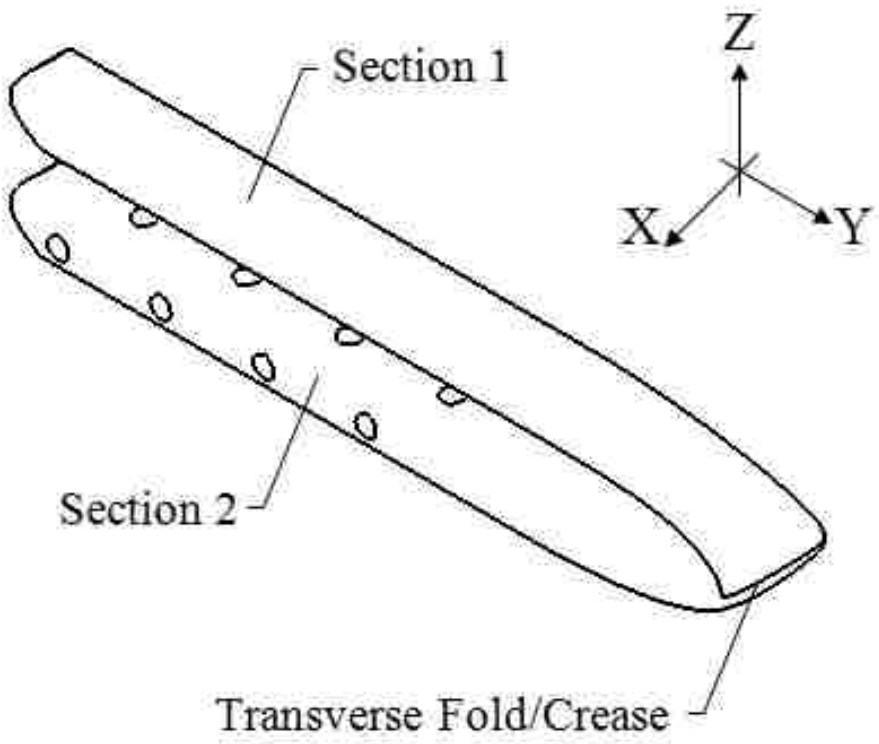

Figure 146: Isometric View. 180° bent conventional Circular-bodied Flexi-Drain. As Section 1 is bent over Section 2, a clear Transverse Fold/Crease occurs as shown.

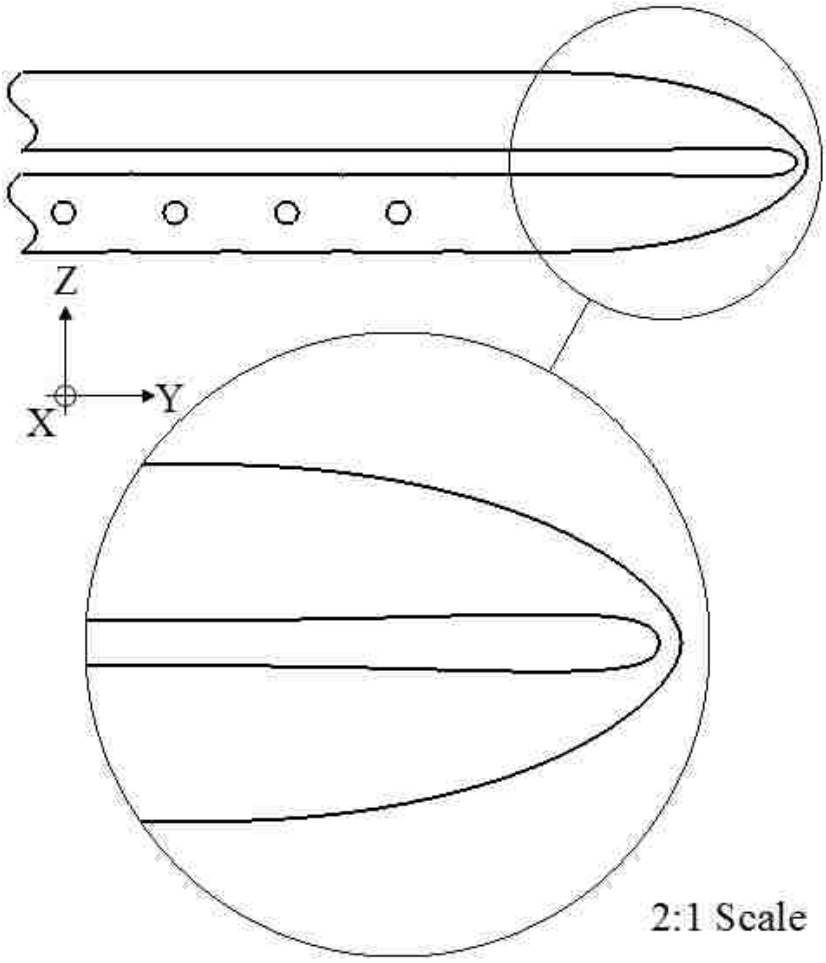

Figure 147: Front View. 180° bent conventional Circular-bodied Flexi-Drain. Severe external deformations at and around the Transverse Fold/Crease are illustrated.

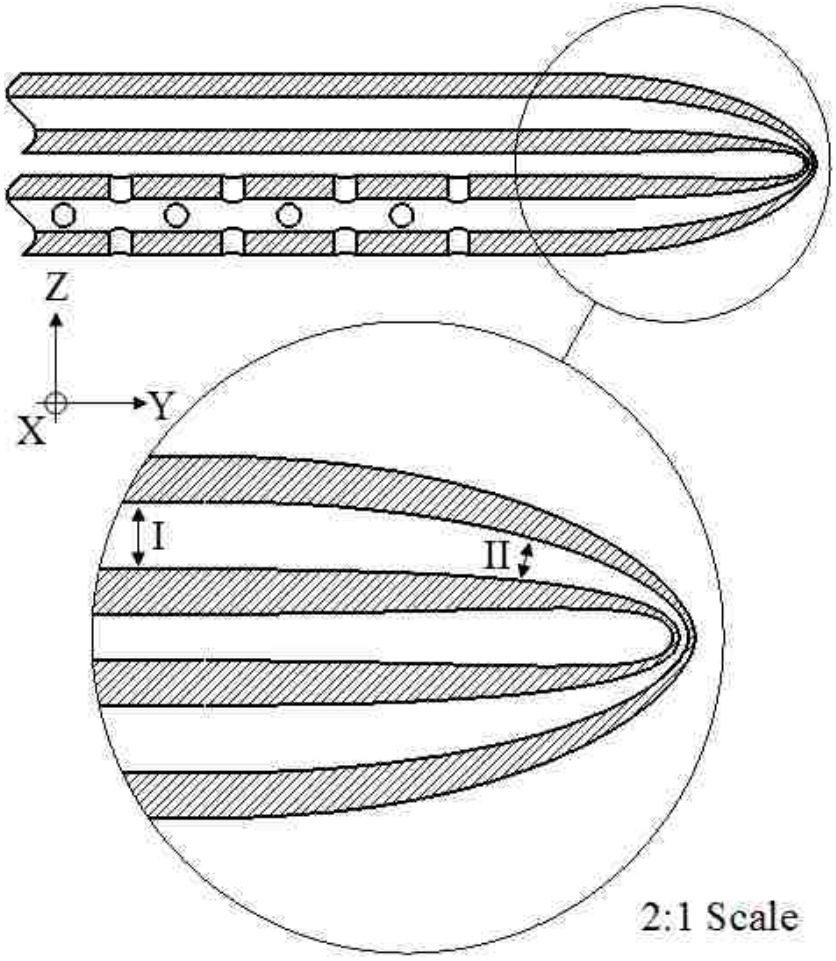

Figure 148: Cross-sectional Front View. 180° bent conventional Circular-bodied Flexi-Drain. Severe external and internal deformations at and around the Transverse Fold/Crease are illustrated. ‘I’ denotes the diameter of the drain/catheter in a straight region. ‘II’ denoted that diameter of the drain/catheter in a bent region. ‘II’ reduces in its length as one moves to the right, i.e. to the Transverse Fold/Crease. At the Transverse Fold/Crease, the internal passage of the conventional drain is almost closed.

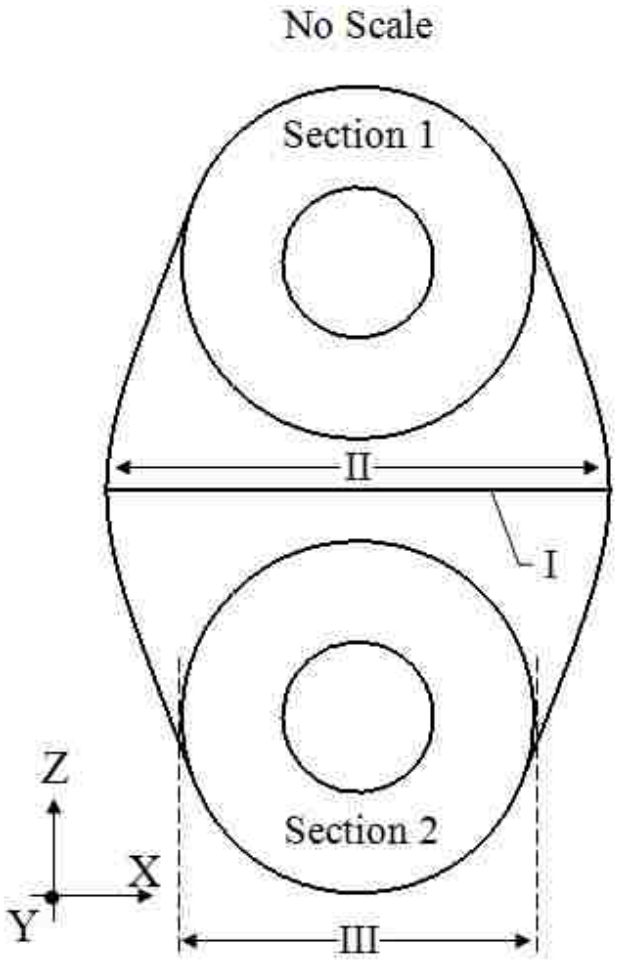

Figure 149: Left View. 180° bent conventional Circular-bodied Flexi-Drain. Severe external and deformations at and around the Transverse Fold/Crease are illustrated. ‘I’ denotes the Transverse Fold/Crease. ‘II’ denotes the length of the drain’s/catheter’s expanded external diameter at the Transverse Fold/Crease. ‘III’ denotes the external diameter of the drain’s/catheter’s unbent Section 2 or equivalently unbent Section 1. Note that ‘II’ is much longer than ‘III’. This emphasizes the severity of drain’s/catheter’s cross-sectional transverse expansion along the x-axis.

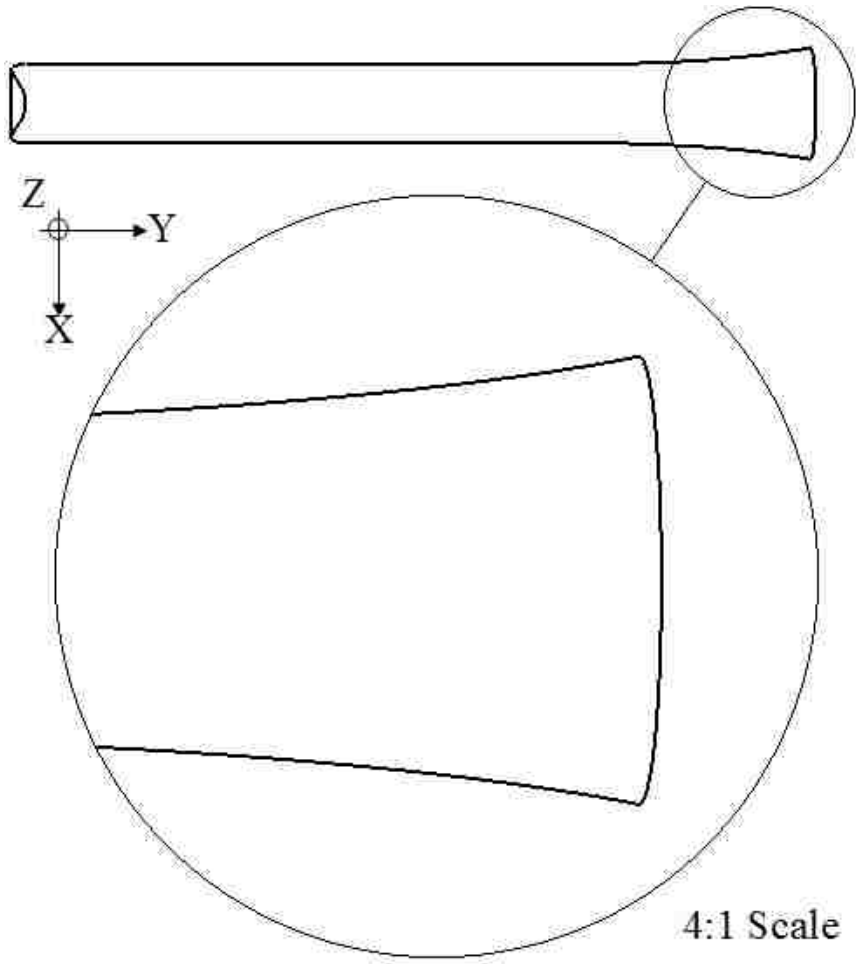

Figure 150: Top View. 180° bent conventional Circular-bodied Flexi-Drain. Severe external and deformations at and around the Transverse Fold/Crease are illustrated. Here, the severity of drain's/catheter's cross-sectional transverse expansion along the x-axis, is shown from the Top View.

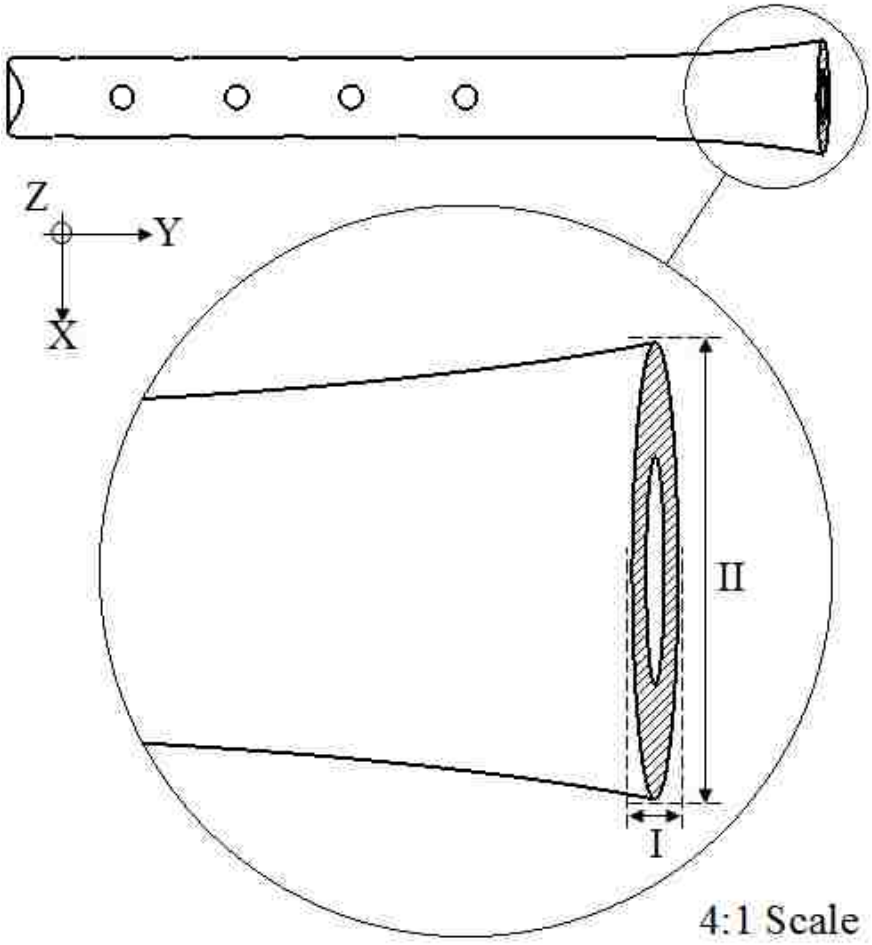

Figure 151: Cross-sectional Top View. 180° bent conventional Circular-bodied Flexi-Drain. Severe external and deformations at and around the Transverse Fold/Crease are illustrated. 'I' denotes the external transverse collapse of the cross-section along the y-axis. Note that the drain's/catheter's internal diameter along the same direction, namely the y-axis, is also collapsed. 'II' denotes the external transverse expansion of the cross-section along the x-axis. Note that the drain's/catheter's internal diameter along the same direction, namely the x-axis, is also expanded. Here, the severity of drain's/catheter's cross-sectional transverse expansion along the x-axis, is shown from the Top cross-sectional view.

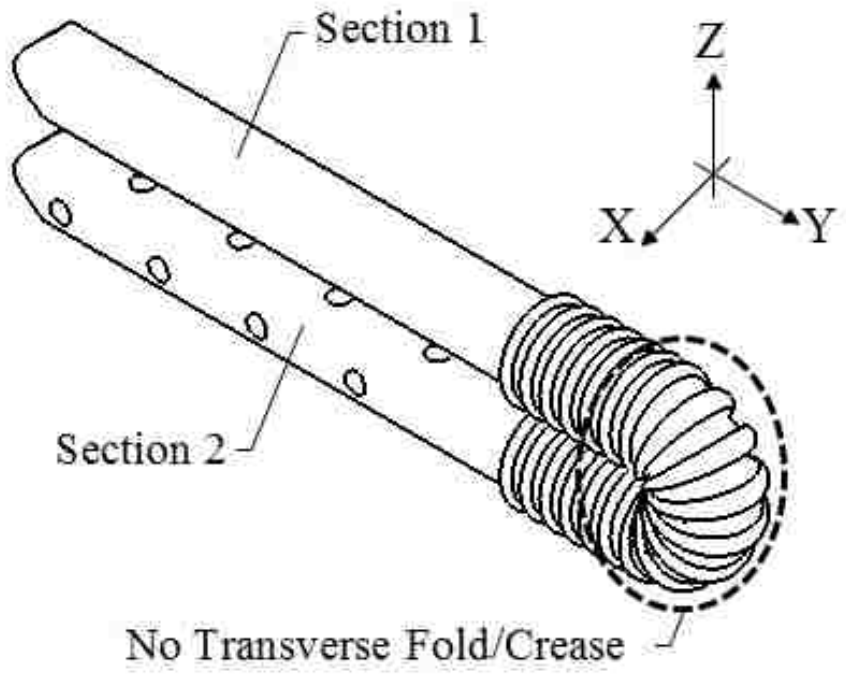

Figure 152: Isometric View. 180° bent Circular-bodied Flexi-Drain with a ‘Semicircular’ Flexible Section. As Section 1 is bent over Section 2, no Transverse Fold/Crease occurs at or around the location of maximum bend within the Flexible Section.

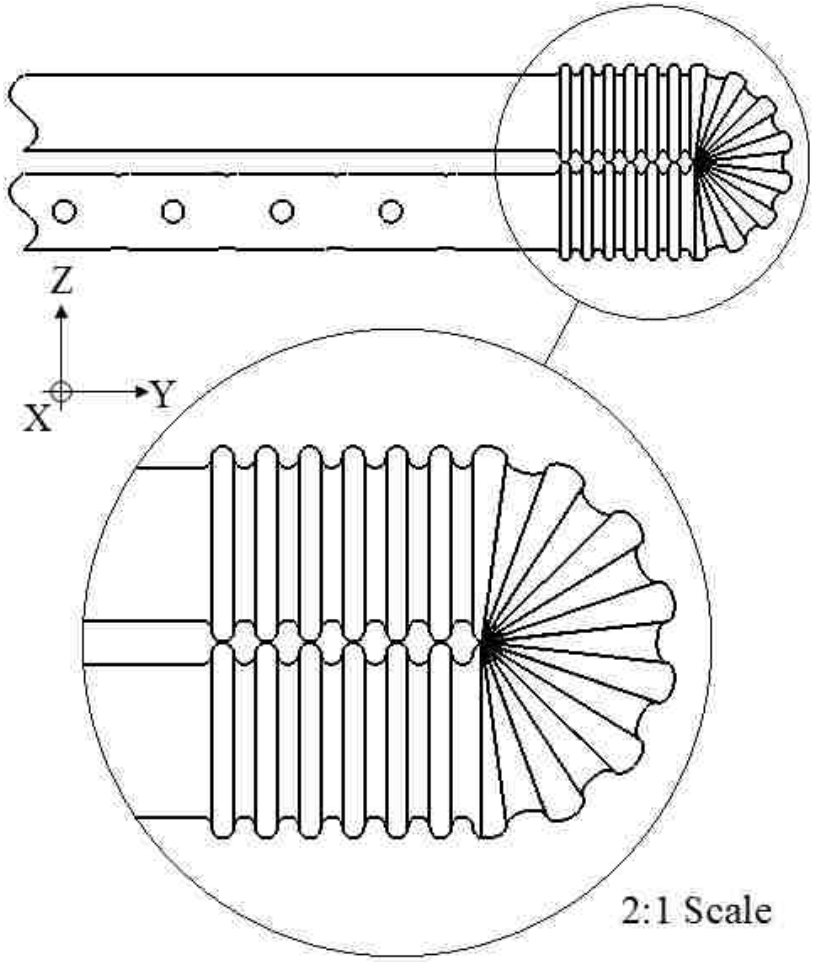

Figure 153: Front View. 180° bent Circular-bodied Flexi-Drain with a ‘Semicircular’ Flexible Section. No external deformations occur at or around the location of maximum bend within the Flexible Section.

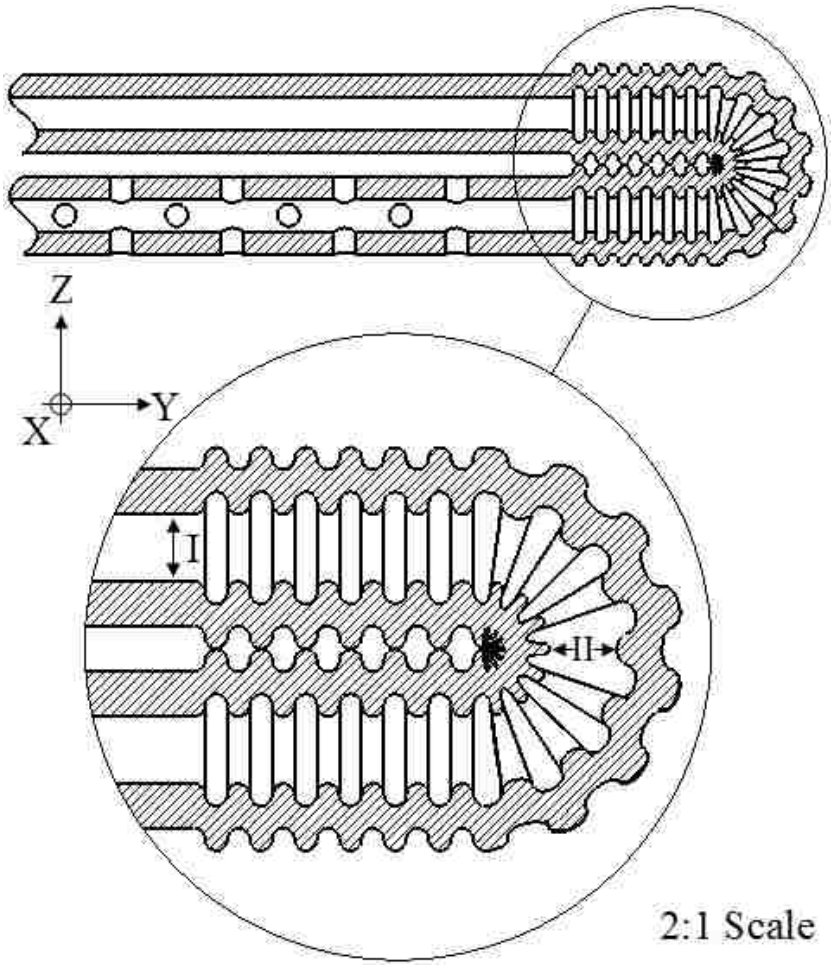

Figure 154: Cross-sectional Front View. 180° bent Circular-bodied Flexi-Drain with a ‘Semicircular’ Flexible Section. No external and internal deformations occur at or around the location of maximum bend within the Flexible Section. ‘I’ denotes the diameter of the drain/catheter in a straight region. ‘II’ denoted that diameter of the drain/catheter at the location of maximum bend within the Flexible Section. ‘I’ equals ‘II’ in its length.

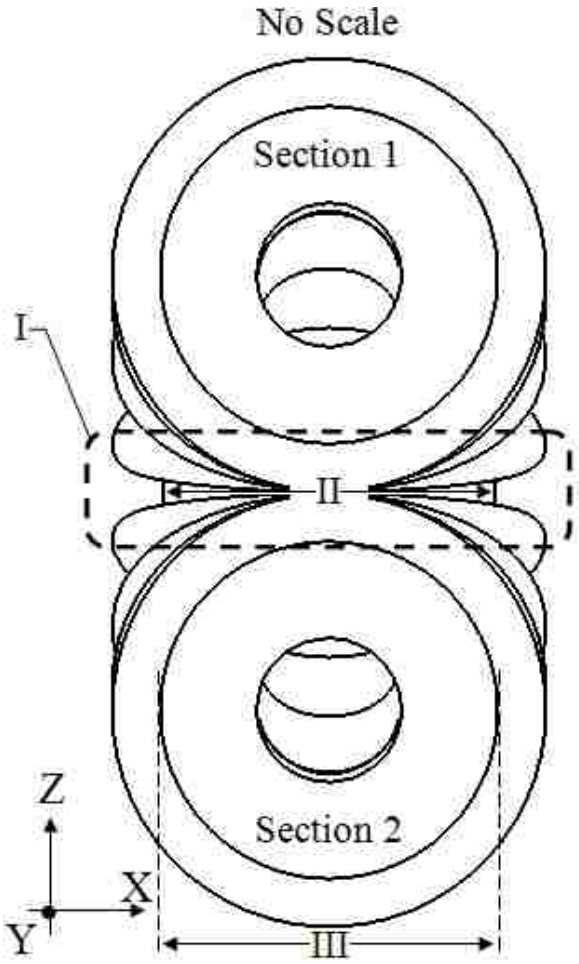

Figure 155: Left View. 180° bent Circular-bodied Flexi-Drain with a ‘Semicircular’ Flexible Section. No external and deformations at and around the bend occur. ‘I’ emphasizes that there is no Transverse Fold/Crease. ‘II’ denotes the length of the drain’s/catheter’s external diameter at the location of maximum bend within the Flexible Section. ‘III’ denotes the external diameter of the drain’s/catheter’s unbent Section 2 or equivalently unbent Section 1. Note that ‘II’ equals ‘III’ in its length. This emphasizes that there is no transverse external expansion of the drain’s/catheter’s cross-section along the x-axis.

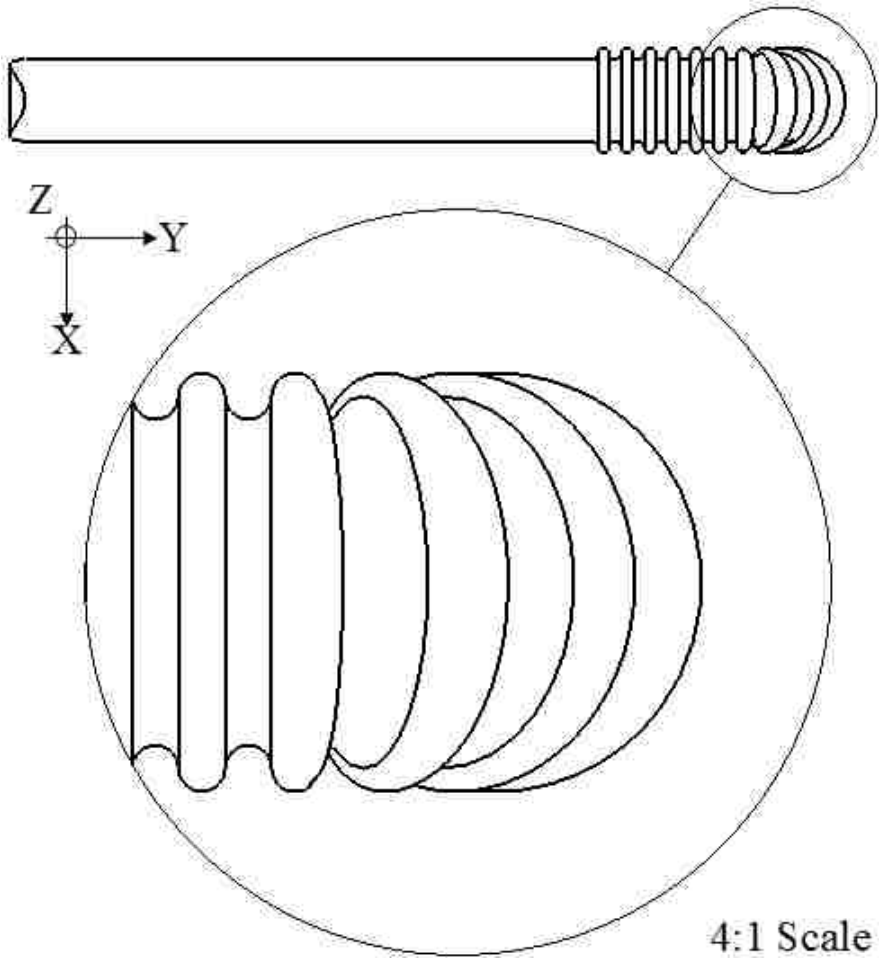

Figure 156: Top View. 180° bent Circular-bodied Flexi-Drain with a ‘Semicircular’ Flexible Section. No external and deformations occur at or around the location of maximum bend within the Flexible Section.

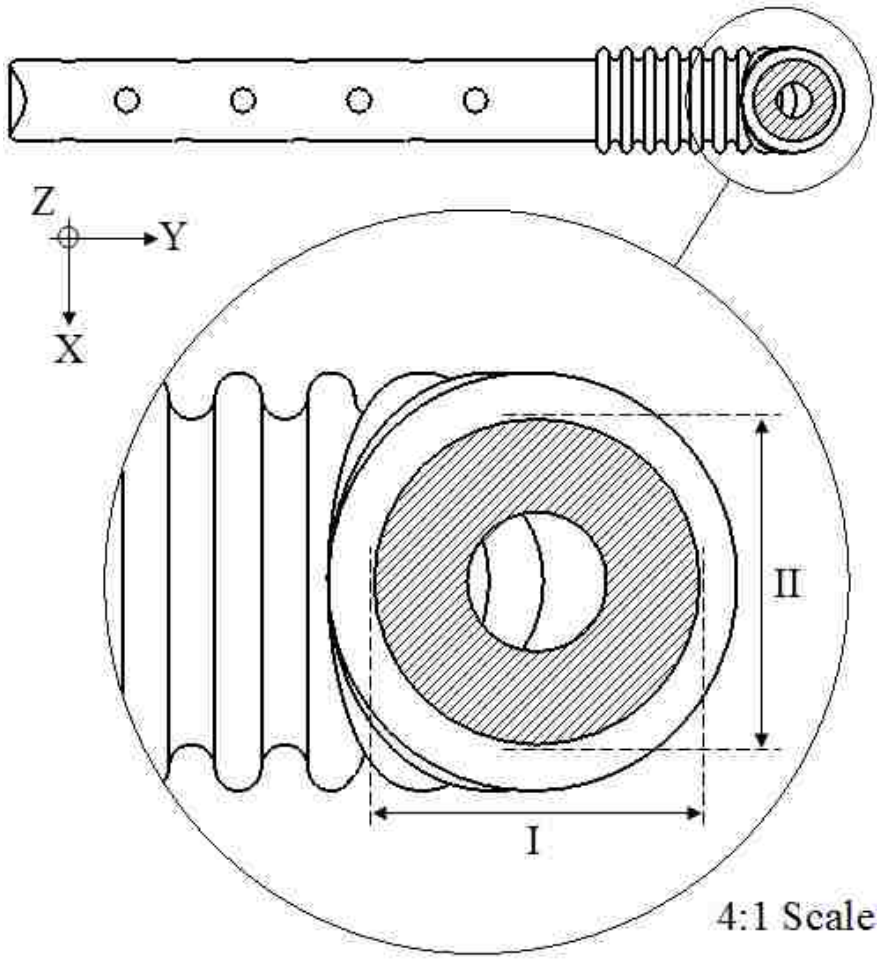

Figure 157: Cross-sectional Top View. 180° bent Circular-bodied Flexi-Drain with a 'Semicircular' Flexible Section. No external and deformations occur at or around the location of maximum bend within the Flexible Section. 'I' denotes the external diameter of the drain's/catheter's Flexible Section along the y-axis. 'II' denotes the external diameter of the drain's/catheter's Flexible Section along the x-axis. 'I' equals 'II' in its length. This emphasizes that the cross-section of the drain/catheter within its bent Flexible Section maintains its original unbent external and equivalently internal dimensions.

6-9 Distinction from other Related designs

U.S. Pat. No. 4,653,542 [RP2] is a drain/tube system that uses a tube section and a *Flexible Section*. The tubing and the *Flexible Sections* are two different segments of this invention, which snap to each other creating a continuous drain/tube system. The herein-described drain/catheter system consists of three different segments: two straight drain/catheter segments and one flexible drain/catheter segment. Moreover, the invention herein-described, does not incorporate a snapping system in order to create a continuous surgical drain/catheter. Rather, all the segments are physically and continuously connected to each other.

CHAPTER 7

7-1 Authors

1. Cyrus O. Abbasi B.S., University of New Mexico, Mechanical Engineering Department.
2. Tariq A. Khraishi PhD., University of New Mexico, Mechanical Engineering Department.

7-2 Title

Biomechanical Behavior Involved in the Shortfall *of a 6 Months Old Child.*

7-3 Abstract

This research project explores the biomechanical forces/accelerations involved in the shortfall of a 6 months old child. Specifically, this research project studies the impact accelerations in *numbers of 'g's* that are experienced by the child's skull during a *head-first ground collision*. The main goal of this research project is to address the existing controversy whether the impact accelerations involved in shortfalls can cause serious damage to the head of a child or not. Magnitudes of the impact accelerations involved in twelve different computer-simulated shortfalls are obtained in 'g's. The simulations are divided in two six-membered groups. The simulations within the first group run at a horizontal velocity of $\mathbf{V}_x$ = -1.0 m/s and the simulations within the second group run at a horizontal velocity of $\mathbf{V}_x$ = -3.0 m/s. Every shortfall simulation initiates from a different initial shortfall height. The results showed that very high impact accelerations can result during these shortfalls, which can lead to serious and/or fatal head injuries. Moreover, this work paves the way for additional future research simulations. Future research simulations can utilize the results obtained from this work to investigate the biomechanical movement-patterns of the unfused bones that constitute the skull of a 6 months old child's.

7-4 Introduction

7-4-1 Definition of "Shortfall"

The terminology shortfall refers to the *fall* of a human from an object with a height ranging anywhere from few inches to a height, close or a bit higher than the height of the falling individual. In the case of newborns, toddlers and children, shortfalls typically occur from home furniture or from playground equipment. Examples of such objects are beds/changing-beds, countertops, desks, slides, monkey bars, swings etc.

7-4-2 Current Shortfall Controversy and the Need of Additional Research

Park et al. consider shortfalls to be the leading mechanism of injuries as well as cause of morbidity and mortality among young children [63]. In addition to young children, other researchers such as Saywer et al., consider shortfalls to be the leading cause of morbidity and mortality among young adults as well [64]. Other researcher such as Johnson et al. believe that only shortfalls from objects of 1.0 m or higher heights can lead to serious injuries such as skull fracture amongst young children [65]. As one can see, there is a controversy amongst the medical/professional community whether a shortfall can cause a serious or even fatal injury to a young child. Several research endeavors have been conducted by some other professionals to address this controversy.

Cory et al. laid out a thorough and methodical set of equations that explain the parameters involved in the shortfall of young children [66]. However, their work does not include shortfall simulations that can clearly clarify whether shortfalls involve high impact accelerations that can lead to serious head injuries. The work of Nimityongskul et al. report that a direct fall of a child's head from 1.0 ft onto a concrete surface can lead to an impact acceleration of 160.0 g, which could be fatal [67]. However, a fall from a 1.0 ft object seldom results in a 'direct' head and ground impact. During such very low shortfalls, usually the sides of the head as well as the shoulders are involved. Moreover, the floor material within an average household as well as on the playground field is not concrete. The controversy mentioned above as well as the absence of a clear explanation addressing this controversy, lead to the need for deeper research. The work presented here tries to provide a clear pattern of

impact accelerations involved in twelve different shortfall scenarios involving a young child.

When it comes to the shortfalls of children, another controversy might exist between the scientific community and the general population, i.e. people who are not engaged in scientific research. Sometimes an average adult would automatically think that a child's shortfall is harmless and totally safe. This is because relative to his/her height, he/she would think that the child does not fall from a significant height. For instance, he/she would think that a 1.5 ft shortfall, initiates from a height that is not much higher than his/her knees. Therefore, the average adult would automatically think that a 1.5 ft shortfall is harmless. He/She might not realize that a child involved in a 1.5 ft shortfall, might not even be 1.5 ft tall. Therefore, regarding the consequent physical damages after a shortfall, the opinions of the general population and the scientific community might be different. This work tries to address this difference and prove that shortfalls of young children, can indeed lead to very serious physical damages.

7-5 Methods

This research study investigates the shortfall of an average six month old child. For ethical purposes, this study does not involve any human or animal subjects. Rather, shortfalls are simulated within a computerized Multibody Dynamics Code, called Working Model 2D (Design Simulation Technologies, Inc., 43311 Joy Road, #237 Canton, MI 48187, USA).

7-5-1 'Working Model 2D' and the Definition of Rigid Body Dynamics

Working Model 2D utilizes the principals of *Rigid Body Dynamics* [68]. Rigid Body Dynamics studies the motion of one or a set of rigid bodies that either move dependent or independent of each other. The term *dynamics* refers to the study of forces and/or moments that are subjected on a body. Dynamics also studies the effects of these forces and/or moments on the body, i.e. static equilibrium, motion or rotation of that body.

Dynamics can deal with *linear* and/or *angular* motion of a body. *Linear dynamics* deals with the linear motion of bodies, i.e. when bodies move along a line. In the case of linear dynamics the involved positions (s), velocities (v), accelerations (a) and moments of inertia (I) are also linear. A body involved in linear dynamics posses a mass (m). The mass of a body is actually a measure of that body's resistance to motion. *Angular dynamics* deals with the non-linear motion of bodies, i.e. when bodies move along a line that is not linear, e.g. a curved line. In the case of angular dynamics the involved positions (θ), velocities (ω) and accelerations (α) are also angular. A body involved in angular dynamics posses a mass (m) as well, however,

instead of its mass, its moment of inertia ($I = \int_m r^2\, dm$) are of importance. The moment of inertia of a body is actually a measure of that body's resistance to angular motion and/or rotation.

As the name says, rigid body dynamics is dynamics that is applied to rigid bodies. The dynamical motion of these rigid bodies is governed by Newton's second law of motion. Newton's second law of motion applies to one or many rigid bodies to which external forces and/or moments are applied as shown in Fig. 158 through Fig. 159. In a two dimensional setting Newton's second law of motion is illustrated by Fig. 158 through Fig. 159 as well as Eqn. 3 through Eqn. 9 [68 & 69].

$$\boldsymbol{v}_G = \frac{d(S_G)}{dt} \quad \text{(Eqn. 3)}$$

$$\boldsymbol{a}_G = \frac{d(\boldsymbol{v}_G)}{dt} \quad \text{(Eqn. 4)}$$

$$\boldsymbol{\omega} = \frac{d(\theta_G)}{dt} \quad \text{(Eqn. 5)}$$

$$\boldsymbol{\alpha} = \frac{d\omega}{dt} \quad \text{(Eqn. 6)}$$

$$\sum \boldsymbol{F}_x = m * (\boldsymbol{a}_G)_x \quad \text{(Eqn. 7)}$$

$$\sum \boldsymbol{F}_y = m * (\boldsymbol{a}_G)_y \quad \text{(Eqn. 8)}$$

$$\sum \boldsymbol{M}_G = I_G * \boldsymbol{\alpha} \quad \text{(Eqn. 9)}$$

- S_G: Linear position vector of a rigid body's center of gravity. Linear position vector can be along the *x*-axis or the *y*-axis.

- $\boldsymbol{v}_G$: Linear velocity vector of a rigid body's center of gravity. Linear velocity vector can be along the *x*-axis or the *y*-axis.

- $\boldsymbol{a}_G$: Linear acceleration vector of a rigid body's center of gravity. Linear acceleration vector can be along the *x*-axis or the *y*-axis.

- θ: Angular position of a rigid body. Angular velocity vector is directed into or out of the page in a perpendicular relation to the 2D surface of the rigid body.

- $\boldsymbol{\omega}$: Angular velocity vector of a rigid body. Angular velocity vector is directed into or out of the page in a perpendicular relation to the 2D surface of the rigid body.

- $\boldsymbol{\alpha}$: Angular acceleration vector of a rigid body. Angular acceleration vector is directed into or out of the page in a perpendicular relation to the 2D surface of the rigid body.

- $\sum \boldsymbol{F}_x$: Sum of all the external forces acting on the rigid body along the *x*-axis as illustrated in Fig. 158 [69]

- $\sum \boldsymbol{F}_y$: Sum of all the external forces acting on the rigid body along the *y*-axis as illustrated in Fig. 158 [69]

- $(\boldsymbol{a}_G)_x$: Rigid body's center of mass acceleration vector along the *x*-axis as illustrated in Fig. 159 [69]

- $(\boldsymbol{a}_G)_y$: Rigid body's center of mass acceleration vector along the *y*-axis as illustrated in Fig. 159 [69]

- $\sum \boldsymbol{M}_G$: Sum of the external moment vectors acting on the rigid body about its center of mass as illustrated in Fig. 159 [69]

- I_G: Moment of Inertia of the rigid body about an imaginary axis coming out of the page through the center of mass of the rigid body. This axis is in a perpendicular relation to the page as illustrated in Fig. 159 [69]

As mentioned above Eqn. 3 through Eqn. 9 equations describe the dynamics of a rigid body [68 & 69]. They are the governing equations that Working Model 2D utilizes during any simulation conducted with it. Once a simulation is initiated Working Model 2D starts to solve these equations by considering the initial conditions (e.g. initial velocity of a rigid body) and different parameters (e.g. gravitational acceleration in the surrounding of the rigid body) to continuously simulate the proper dynamics of the rigid body at every instant [68]. Instead of solving Eqn. 3 through Eqn. 9 via the conventional *analytical methods*, Working Model 2D relies on *numerical methods* to solve them [68]. Unlike analytical methods, numerical methods can very accurately trace the dynamics of a body.

To solve Eqn. 3 through Eqn. 9 *numerically*, both sides of the equations are integrated [68]. Then the '*dt*' terms are replaced by 'Δt' [68]. Δt represents a so called *time-step* during which each equation is solved once by considering the initial conditions for that time step. The results (linear and/or angular positions, velocities and accelerations) obtained during a time-step are utilized as the initial conditions for the calculations conducted during the next time-step [68]. To improve accuracy of the calculation the time-step Δt is minimized to almost an infinitesimal measure, i.e. very

close to 0.0 sec. The calculations then are continued from one time-step to the next. This process is referred to as *numerical integration* [68].

Working Model 2D can utilize one of two different *numerical integration* methods for conducting its numerical calculations. The first numerical integration method is called the '*Euler*' numerical integration, which is one of the simplest amongst the many integration methods [68]. Euler integration method solves Eqn. 3 through Eqn. 9 in a single step [68]. This means that a single very long Δt is used for conducting all the calculations. Working Model 2D chooses the length of the single Δt and does not offer a variable time-step option to the user. Meaning, the user cannot set the length of Δt. This makes the Euler integration method a very fast but not very accurate [68].

The second integration method is called the "Kutta-Merson" also known as the "5^{th}-order Runge-Kutta" or the "Runge-Kutta 5" method [68]. The Kutta-Merson integration method is a complex mathematical process that constantly recalculates Eqn. 3 through Eqn. 9. Unlike the Euler integration method, the Kutta-Merson integration method does not solve Eqn. 3 through Eqn. 9 during one time-step. Rather many time-steps are used [68]. Moreover, Working Model 2D enables the researcher to set the length of Δt. The calculations are repeated at the beginning of each subsequent time-step. By doing so Working Model 2D can accurately track/calculate the rigid body's instantaneous acceleration, instantaneous velocity and instantaneous position [68]. By putting all the instantaneous results next to each other continuous acceleration, velocity and position patterns are represented by Working Model 2D.

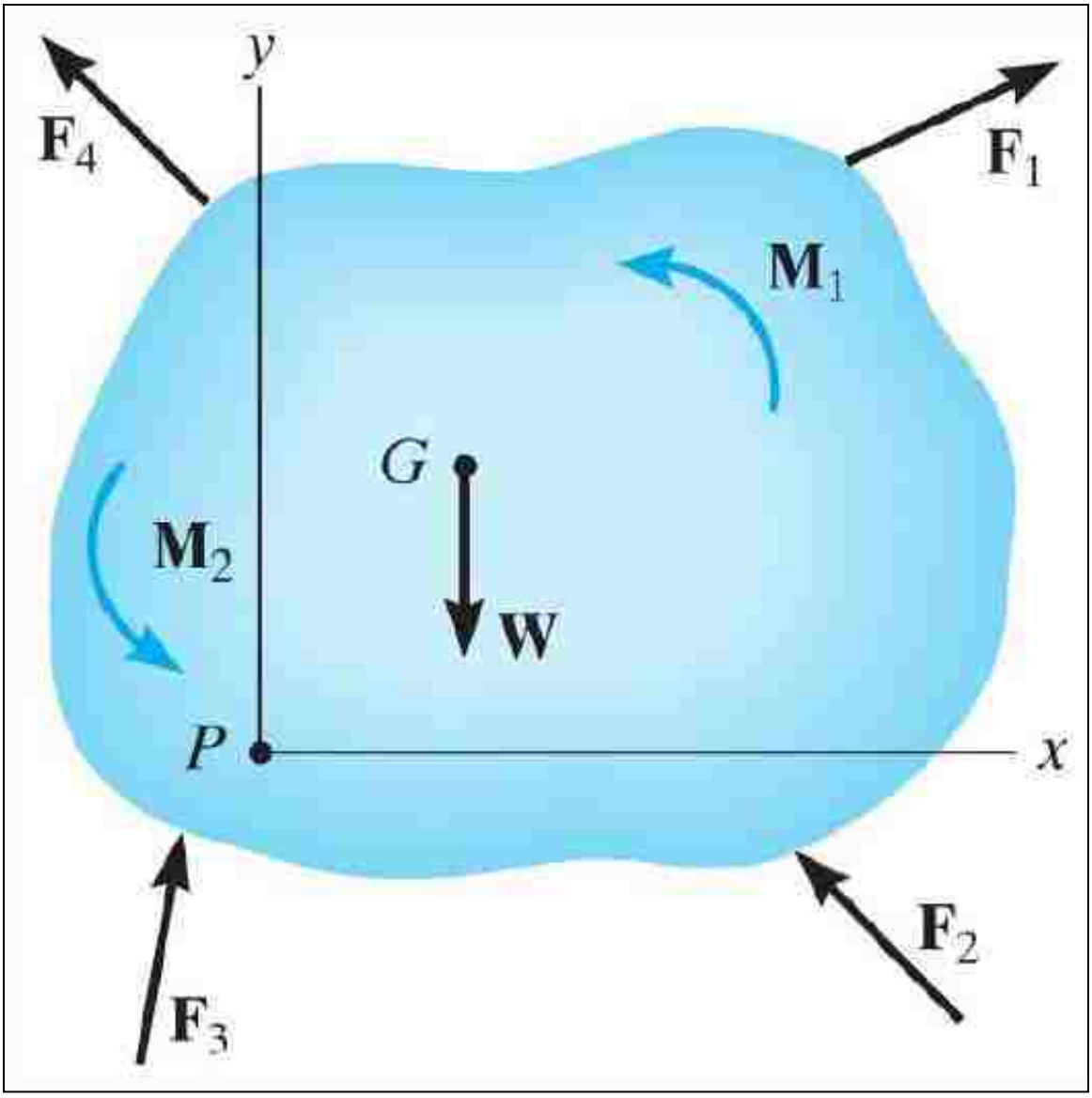

Figure 158: A rigid body with the weight 'W' and the center of gravity 'G'. External forces F_1, F_2, F_3 & F_4 as well as external moments M_1 & M_2 are applied to the rigid body. Point 'P' is an arbitrary point at which the coordinate axis is positioned.

Fig. 158 shows all the external forces and moments that are applied to the rigid body. Every external force can be decomposed in two force-components. The first force-component is the so called *x*-force-component, which lies parallel to the *x*-axis. The second force-component is the so called *y*-force-component, which lies parallel to the *y*-axis. The moments cannot be decomposed in any moment-component. The

moments can be substituted by a force applied by a lever-arm. To do so either the magnitude of the lever-arm or the magnitude of the force needs to be set. Note that a lever-arm has to initiate from the same point on the rigid body about which the moment takes place. Once the moment has been substituted by force applied by a lever-arm, the involved force can also be decomposed in its *x*-force-component and y-force-component. At this point the rigid body can either be in static equilibrium, i.e. not move at all or undergo dynamic motion.

To be in static equilibrium three conditions must be satisfied. These conditions are presented by Eqn. 10 through Eqn. 12.

$$\sum \boldsymbol{F}_x = 0 \qquad \text{(Eqn. 10)}$$

$$\sum \boldsymbol{F}_y = 0 \qquad \text{(Eqn. 11)}$$

$$\sum \boldsymbol{M}_G = 0 \qquad \text{(Eqn. 12)}$$

The condition described by Eqn. 10 comes about if all the *x*-force-components would cancel each other. The condition described by Eqn. 11 comes about if all the *y*-force-components would cancel each other. The condition described by Eqn. 12 comes about if all the moments would cancel each other. As described above, the external moments can also be replaced by forces applied by lever-arms. Equivalently, the condition described by Eqn. 12 can also come about if all the forces that substituted the moments would be equal in magnitude and oppose each other. For this to be valid, all the lever-arms should be of equal magnitude as well. However, the same condition described by Eqn. 12 can also come about regardless of the magnitude

of the opposing forces. For instance a weaker force applied by a longer lever-arm might cancel an opposing stronger force, which is applied by a shorter lever-arm.

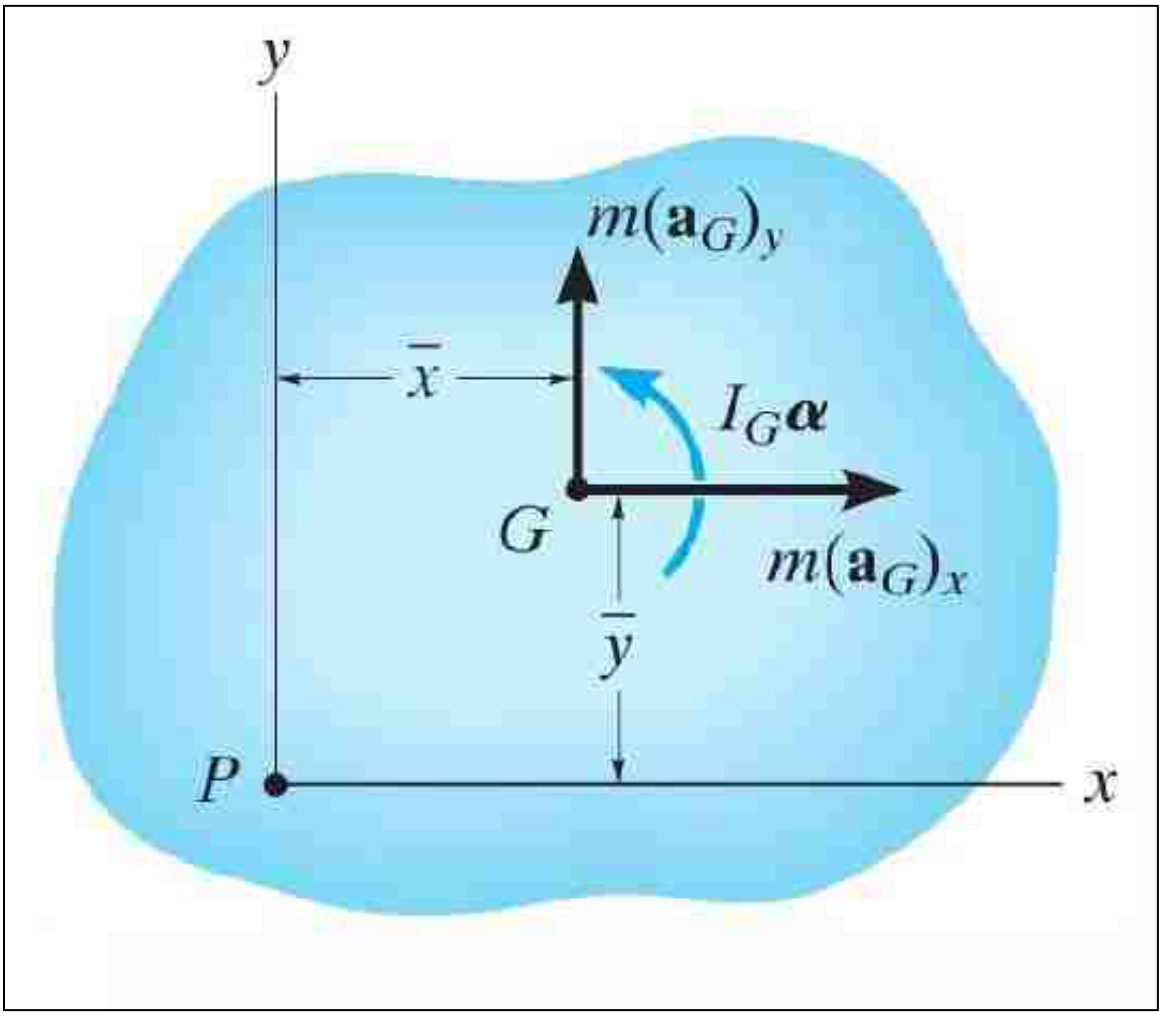

Figure 159: A rigid body with the center of gravity 'G'. $\bar{x}$ and $\bar{y}$ signify the location of the center of gravity with respect to point 'P'.Point 'P' is an arbitrary point at which the coordinate axis is positioned.

Fig. 159 shows a rigid body that is in dynamic motion. This is because *x* & *y* components of the linear acceleration as well as the angular acceleration are visible on the illustrated rigid body. Dynamic motion results when even the conditions described by Eqn. 10 through Eqn. 12 are not satisfied. This leads to conditions described by Eqn. 13 through 15.

$$\sum \boldsymbol{F}_x \neq 0 \qquad \text{(Eqn. 13)}$$

$$\sum \boldsymbol{F}_y \neq 0 \qquad \text{(Eqn. 14)}$$

$$\sum \boldsymbol{M}_G \neq 0 \qquad \text{(Eqn. 15)}$$

Eqn. 12 implies that the resulting *x*-force-components of the externally applied forces do not cancel each other. Eqn. 14 implies that the resulting *y*-force-components of the externally applied forces do not cancel each other. Eqn. 14 implies that the externally applied moments do not cancel each other. Note that it takes only one of the conditions described by Eqn. 12 through Eqn. 15 to bring the rigid body in dynamic motion. For instance a moving rigid body can experience conditions described by Eqn. 11 through Eqn. 13.

Most researchers who investigate the shortfall of young children and adults prefer to use Multibody Dynamics codes to conduct their research [70-73]. This proves the reliability of Multibody Dynamics codes in simulating shortfall scenarios. Therefore, Working Model 2D is utilized to conduct the necessary simulations for this work.

7-5-2 Six Months Old Child's Body Characteristics

In order to simulate the shortfall of the six months old child, first a 2D model of the child's body was created within the Working Model 2D code. To do so, proper dimensions and characteristics of the child's body were obtained. Table 4 through Table 7 summarize different measurements and characteristics of a six months old child. Note that some of the child's body characteristics were directly obtained from a reference source whereas other characteristics were calculated based on the obtained body characteristics or simplifying assumptions.

Table 4: Body Size Measurements of a "6" Months Old Child				
Description	**Size**	**Units**	**Reference/ Source**	**Remarks**
Age	6	Months	[11]	
Total Body Mass	9	kg	[11]	90th Percentile.
Total Body Weight	88.29	N	Calculated using "Total Body Mass"	Weight (N) = Mass*g, where g = 9.81 m/s^2
"Average" Human Body Mass Density	1	kg/m^3	Several Online Source	Similar to "Water's" density, since a Human can more or less float on Water.
Body Length	67	cm	[11]	> 95th Percentile.
Chest Circumference	43.25	cm	[11]	
Chest width	21.625	cm	Calculated using "Chest Circumference"	"Chest Circumference" is assumed to be Twice the "Chest Width". "Chest Width" is actually 15.3 cm [1].
Abdominal Circumference	46	cm	[11]	

Table 4: Body size measurements and characteristics of a six months old child obtained and/or calculated from referenced material.

Table 5: Body Size Measurements of a "6" Months Old Child				
Description	**Size**	**Units**	**Reference/ Source**	**Remarks**
Head Circumference	45.5	cm	[11]	90th - 95th Percentile.
Head Diameter	14.48	cm	Calculated from "Head Circumference"	Head is assumed to be a Sphere. The diameter (i.e. Head Breadth) is more like 13.0 cm [1].
Head & Neck %-Mass	8.4		[12]	For a Male 6 Months Old Child.
Head & Neck Mass	0.76	kg		Head & Neck Mass = "Head & Neck %-Mass" * "Total Body Mass"
Head %-Mass	73.8		[12]	For a Male 6 Months Old Child.
Head Mass	0.56	kg	[12]	Head Mass = "Head %-Mass" * "Head & Neck Mass"
Neck %-Mass	26.2		[12]	For a Male 6 Months Old Child.
Neck Mass	0.20	kg	[12]	Neck Mass = "Head %-Mass" * "Head & Neck Mass"
"I": Neck Circumference / Head Circumference	0.49		[11]	For a Male 6 Months Old Child. Also, for 25-30 Months of Age.
Neck Circumference	22.36	cm	Calculated from "I"	
Neck Diameter	7.12	cm	Calculated from "Neck Circumference"	Neck is assumed to be a Sphere. Neck's dimension is not used in model. Practically NO neck length at this age.

Table 5: Body size measurements and characteristics of a six months old child obtained and/or calculated from referenced material.

Table 6: Body Size Measurements of a "6" Months Old Child				
Description	**Size**	**Units**	**Reference/ Source**	**Remarks**
Arm %-Mass	5.1		[12]	For a Male 6 Months Old Child.
Arm Mass	0.46	kg		Arm Mass = "Arm %-Mass" * "Total Body Mass"
Upper Arm Circumference	15	cm	[11]	Upper Arm is assumed to be a Cylinder.
Upper Arm Width	4.77	cm	Calculated from "Upper Arm Circumference"	
Upper Arm Length	19.10	cm	[11]	
Lower Arm Length	14.10	cm	[11]	
Total Arm Length	33.20	cm	[11]	For a Male 6 Months Old Child.
"II": Total Arm Length / Body Length	0.50		[13]	95th Percentile.
Total Arm Length	33.8	cm	Calculated from "II"	Almost the same as the "Total Arm Length" obtained from [1].
Hand Width	4.7	cm	[11]	Hand Width is approximately Equal to Arm Width.

Table 6: Body size measurements and characteristics of a six months old child obtained and/or calculated from referenced material.

Table 7: Body Size Measurements of a "6" Months Old Child				
Description	**Size**	**Units**	**Reference/ Source**	**Remarks**
Leg %-Mass	15.7		[12]	For a Male 6 Months Old Child.
Leg Mass	1.41	kg		Leg Mass = "Leg %-Mass" * "Total Body Mass"
Leg Length	31.4	cm	[11]	95th Percentile.
Upper Leg Breadth	8	cm	Calculated using "Torso Breadth"	Approximately Equal to Half of the "Torso Breadth".
Torso Breadth	16	cm	[11]	Approximately Equal to Twice the "Upper Leg Breadth"
Mass of Torso	4.5	kg	Calculated using All Masses obtained above	Mass of Torso = Total Body Mass - Head & Neck Mass - 2*(Arm Mass + Leg Mass)
Length of Torso	21.1	kg	Calculated using All Lengths obtained above	Length of Torso = Body Length - Head Radius - Leg Length Note: Neck Length is Negligible.

Table 7: Body size measurements and characteristics of a six months old child obtained and/or calculated from referenced material.

7-5-3 Shortfall Simulation Models

A total of twelve different simulation models were developed for this work. Each simulation model incorporated a 2D model of the six months old child, a piece of furniture from which the child falls as well as a solid ground on which the piece of furniture rests as shown in Fig. 160.

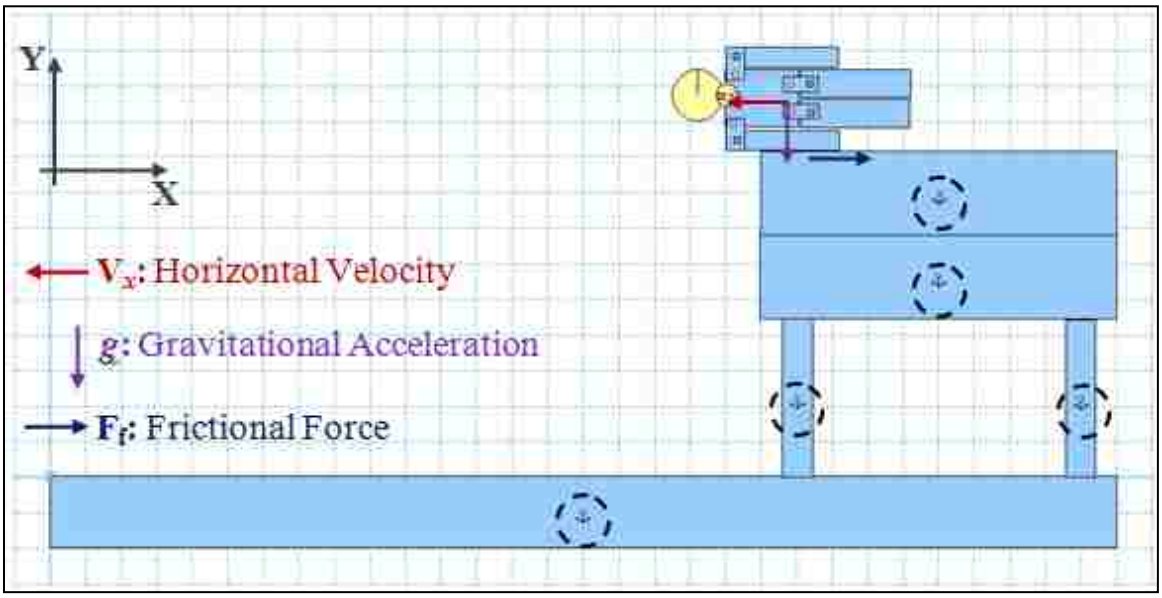

Figure 160: A typical simulation model created within Working Model 2D code.

The anchor signs within the dashed black circles (see Fig. 160) fix the ground as well as the home furniture in space. The home furniture illustrated in Fig. 160 is a 3.0 ft tall bed/changing-bed. By doing so, it is ensured that the fixed items do not move as the simulation is running.

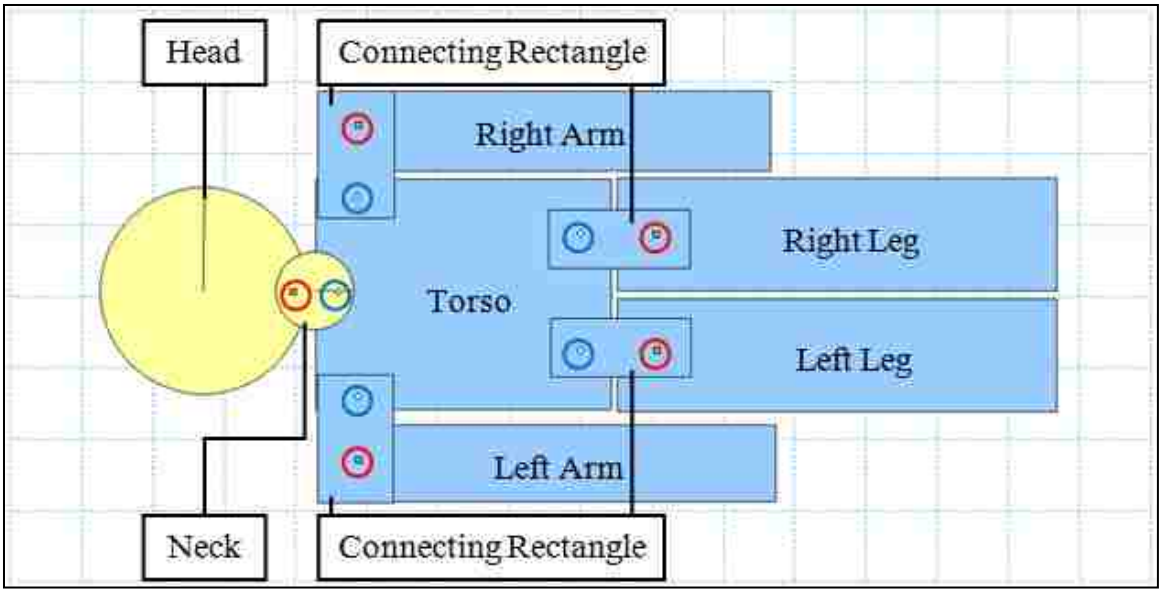

Figure 161: A close-up view of the six months old child's model

The highlighted body dimensions and masses within Table 4 through Table 7 were used to create the proper model of the six months old child as illustrated in Fig. 161. To connect the child's extremities to its torso, four connecting rectangles were used. Each of the four connecting rectangles overlaps the torso as well as one extremity as shown in Fig. 161. All extremities connect to the connecting rectangles via fixed joints. The fixed joints are shown within the red circles in Fig. 161. Fixed joints are joints which fix the movement of two connected members. Meaning, the motions of one member is the same as the motions of the second members. For instance, a *weld* that connects two rod irons with each other, can be thought of as a fixed joint.

The connecting rectangles are connected to the torso via pin joints. The pin joints are shown within the blue circles in Fig. 161. Pin joints are joints that allow the free movement of one member with respect to another member as they are connected to

each other. For instance, the two handles of most *pliers* are connected to each other via a pin joint. Although they are connected to each other, they can move/rotate with respect to each other.

Note that the head is fix-connected to the neck and the neck is pin-connected to the torso. Also note that neck really extends into the torso region of the child. This is because at this young age the neck has practically no length. Meaning, as one looks at a child, one can only see a big head sitting on top of the shoulders. The neck is not really visible.

Every model utilizes the "Kutta-Merson" integration method in order to obtain results that are as accurate as possible. Δt is chosen to be 0.0001 sec. This means that Working Model 2D solves Eqn. 3 through Eqn. 9 every 0.0001 sec.

The twelve simulations were categorized in two different groups of six simulations each. The characteristics of the first six-member group are laid out in Table 8. The characteristics of the second six-member group are laid out in Table 9.

Table 8: Parameters and Initial Conditions Incorporated in Each Simulation Model of the *First* Group (V_x = -1.0 m/s)		
Earth's vertical Gravitational Acceleration	-9.81	m/s^2
Integration time-step, Δt	0.0001	s
Body's horizontal velocity, $\mathbf{V}_x$	-1.0	m/s
Coefficient of Restitution, e	0.5	NA
Coefficient of Static Friction, μ_s (Between all bodies)	0.3	NA
Coefficient of Kinetic Friction, μ_k (Between bodies)	0.3	NA

Table 8: Applied parameters and initial conditions within each simulation of the first group.

Table 9: Parameters and Initial Conditions Incorporated in Each Simulation Model of the *Second* Group (V_x = -3.0 m/s)		
Earth's vertical Gravitational Acceleration	-9.81	m/s^2
Integration time-step, Δt	0.0001	s
Body's horizontal velocity, $\mathbf{V}_x$	-3.0	m/s
Coefficient of Restitution, e	0.5	NA
Coefficient of Static Friction, μ_s (Between all bodies)	0.3	NA
Coefficient of Kinetic Friction, μ_k (Between bodies)	0.3	NA

Table 9: Applied parameters and initial conditions within each simulation of the second group.

As highlighted in Table 8 and Table 9, the only difference between the first group and the second group is the horizontal velocity $\mathbf{V_x}$, which is applied to each simulation. The six simulation models in the first group have a body-velocity of $\mathbf{V_x}$ = -1.0 m/s. The six simulation models in the second group have a body-velocity of $\mathbf{V_x}$ = -3.0 m/s. The purpose of this difference is to see how different the impact accelerations differ when only the horizontal velocity of the child is altered. Moreover, in many shortfall cases, the child is assumed to be abused [91-93]. If a child is abused, it is usually thrown to the ground. The throwing occurs at higher horizontal velocities compared to the slower horizontal velocities involved during a

natural shortfall. This is another reason why a higher horizontal body-velocity of $\mathbf{V_x}$ = -3.0 m/s was chosen.

Note that the horizontal velocity $\mathbf{V_x}$, is not only an initial velocity. From the starting of each simulation at t = 0.00 sec until the end of each simulation at t = 2.5 sec, $\mathbf{V_x}$ is continuously applied to the child's model. This horizontal velocity is the only "driving force" that will pull/push the child's model towards the negative regime of the *x*-axis until the opposing frictional forces stop the child's model sometime during the simulation. If the $\mathbf{V_x}$ would only be an initial velocity and not applied the entire time to the child's model the opposing frictional forces would immediately bring the model to a halt on the piece of furniture. Therefore, it is necessary to continuously apply the horizontal velocity $\mathbf{V_x}$, to the child's model for it to attain the required horizontal displacement.

For these simulations a Coefficient of Restitution of 0.5 was chosen. Therefore, the rigid bodies involved in the simulations are actually deformable and not actually rigid bodies. Let's elaborate on the Coefficient of Restitution's definition.

The Coefficient of Restitution '*e*', is the ratio of the relative velocities of two bodies, e.g. body *A* and body *B*, shortly after and shortly before a collision [68 & 69]. $e = [(V_A)_f - (V_B)_f]/[(V_B)_i - (V_A)_i]$. In the above equation the subscript 'f' represents a *final* velocity whereas the subscript 'i' represents the *initial* velocity of bodies *A* and *B*. Coefficient of Restitution ranges between the following two limits: $0 \leq e \leq 1$.

A Coefficient of Restitution equal to *zero* corresponds to a *perfectly plastic* impact. A *perfectly plastic* impact occurs when $\left[(V_A)_f - (V_B)_f\right] = 0$. This means that the difference between the finial velocities of bodies *A* and *B* is zero. This means that bodies A and B fused to each other after the collision and move with the same velocity.

A Coefficient of Restitution equal to *unity* corresponds to a *perfectly elastic* impact. A *perfectly elastic* impact occurs when $\left[(V_A)_f - (V_B)_f\right] = [(V_B)_i - (V_A)_i]$. This leads to the two following conditions:

- $(V_A)_f = -(V_A)_i$
- $(V_B)_f = -(V_B)_i$

The two conditions above indicate that each body has maintained its magnitude of velocity regardless of colliding with the other body. However, after the collision, each body moves in the opposite direction to its initial direction of movement before the collision.

None of the conditions above, i.e. *perfectly elastic* or *perfectly plastic*, can be perfectly applied to the collision between a child's head and the ground. Therefore, a middle-ground between these two extreme conditions is chosen for all shortfall simulations, namely a Coefficient of Restitution equal to 0.5.

7-6 Results

All the twelve shortfall simulations resulted in different impact acceleration patterns. Since the collision of the head with the ground was the main investigative point within this work, impact acceleration patterns of the head were measured. Working Model 2D outputted the total force |**F**| that the head experienced during the entire simulation. The total force is a resultant force of the two external x-force-component and y-force-component that were exerted on the head during each simulation. Definitions of the x-force-component and the y-force-component are presented by Eqn. 7 and Eqn. 8 respectively. The definition of |**F**| is presented by Eqn. 16.

$$|\boldsymbol{F}| = \sqrt{(\boldsymbol{F}_x)^2 + (\boldsymbol{F}_y)^2} \qquad \text{(Eqn. 16)}$$

Knowing the mass of the child and by utilizing the |**F**| pattern outputted by Working Model 2D, the *total-acceleration* |**a**|, of the head can be obtained. This is shown by Eqn. 17 [68].

$$|\boldsymbol{a}| = \frac{|\boldsymbol{F}|}{m} \qquad \text{(Eqn. 17)}$$

Once |**a**| is determined, it is divided by earth's gravity, namely -9.81 m/s^2 to determine the *number of 'g's*. The *number of 'g's* is defined by Eqn. 18.

$$Number\ of\ 'g's\ (NGS) = \frac{|\boldsymbol{a}|}{-9.81} \qquad \text{(Eqn. 18)}$$

The duration of all shortfall simulations is set to be 2.5 sec. This specific duration time ensures that each simulation has enough time for its full completion, i.e. from t = 0.00 sec to the total still stand of the child on the ground sometime after the collision.

Figures/snapshots of several significant stages within each simulation are represented as follows. These stages include the *Initial Stage* at time 0.0 sec, *Head and Ground impact(s)*, *Significant Head and Shoulder Impact(s)* & *Final Stage* at time 2.5 sec. Note that the *Moment of Collision(s)* stage(s) include(s) the moment(s) that the child's head collides with the ground as well as the moment(s) that the child's head collides with its shoulders.

7-6-1 Shortfall Simulation from '0.5 ft' at V_x = '-1.0 m/s'

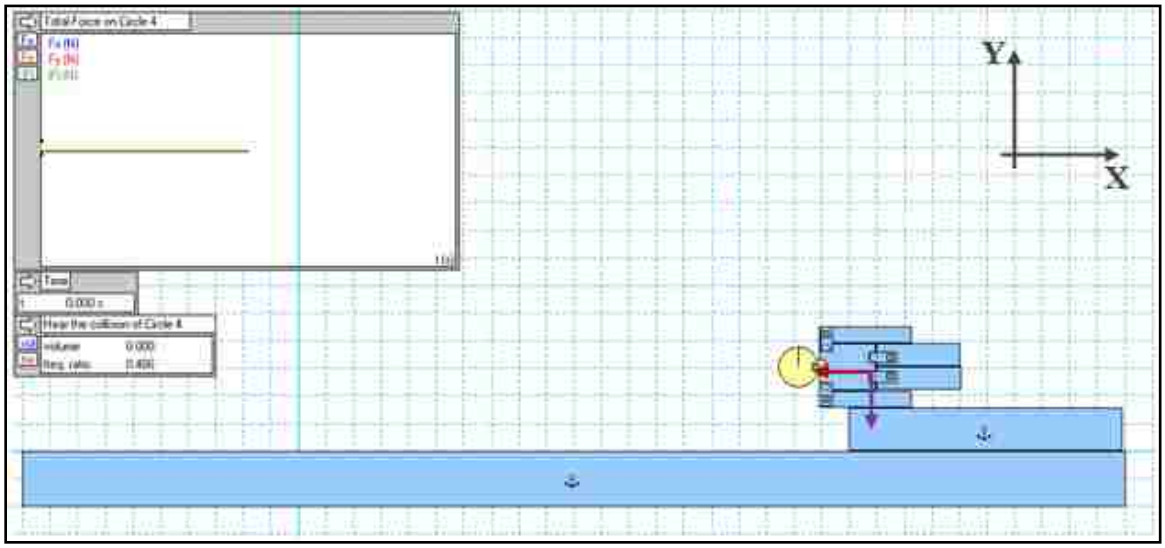

Figure 162: 0.5 ft shortfall at V_x = -1.0 m/s. Initial State.

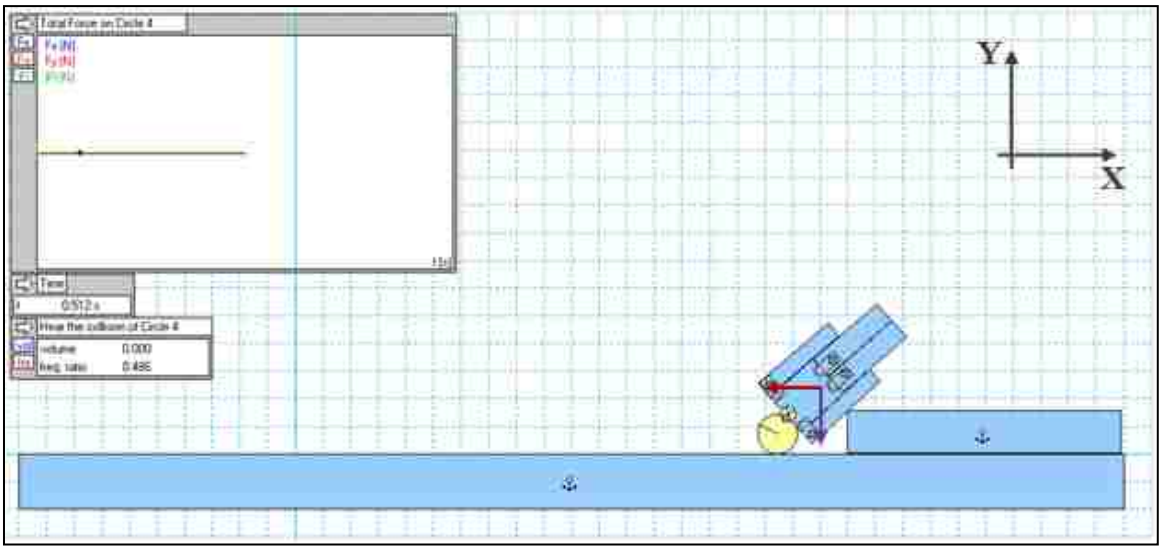

Figure 163: 0.5 ft shortfall at V_x = -1.0 m/s. Head and Ground Impact.

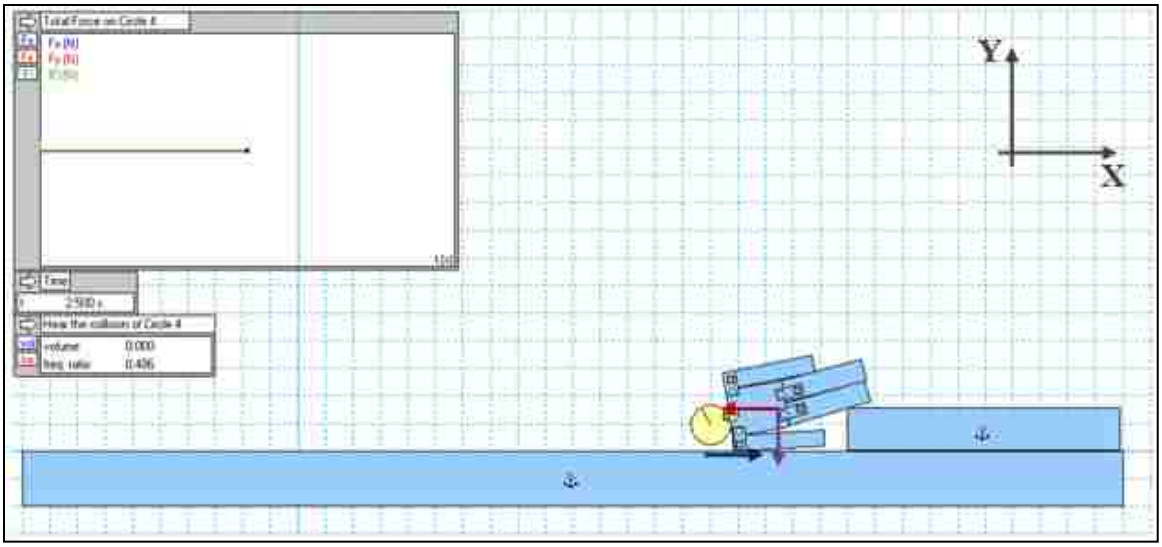

Figure 164: 0.5 ft shortfall at V_x = -1.0 m/s. Final State.

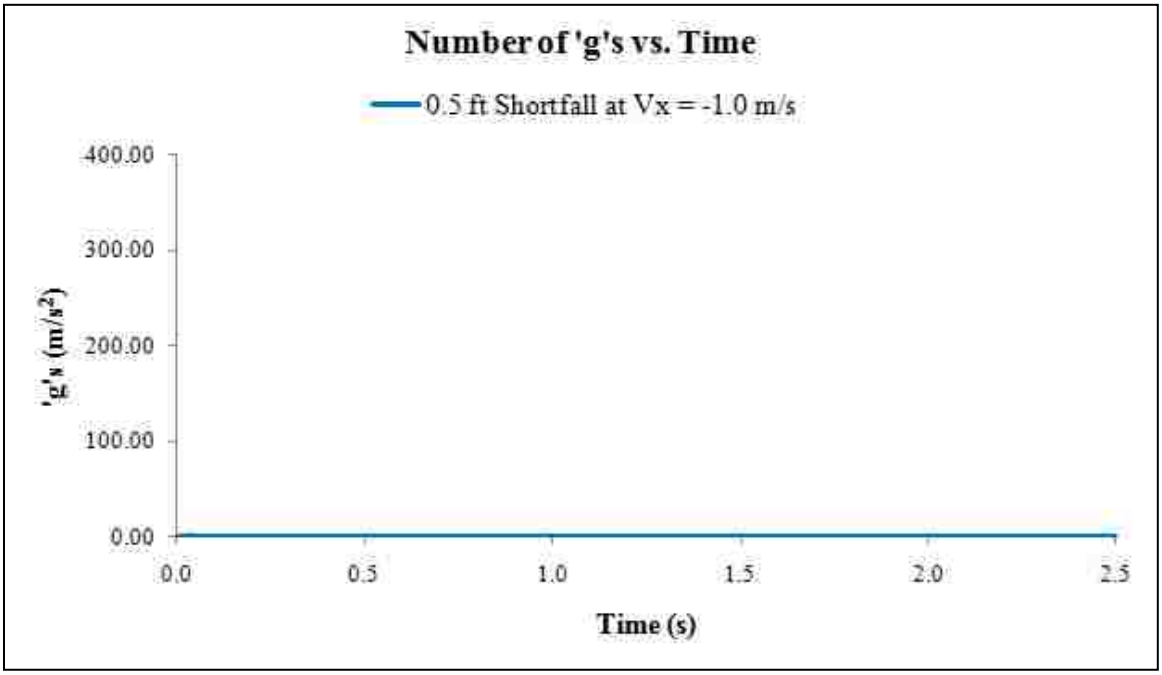

Chart 17: 0.5 ft shortfall at V_x = -1.0 m/s. Number of 'g's vs. Time.

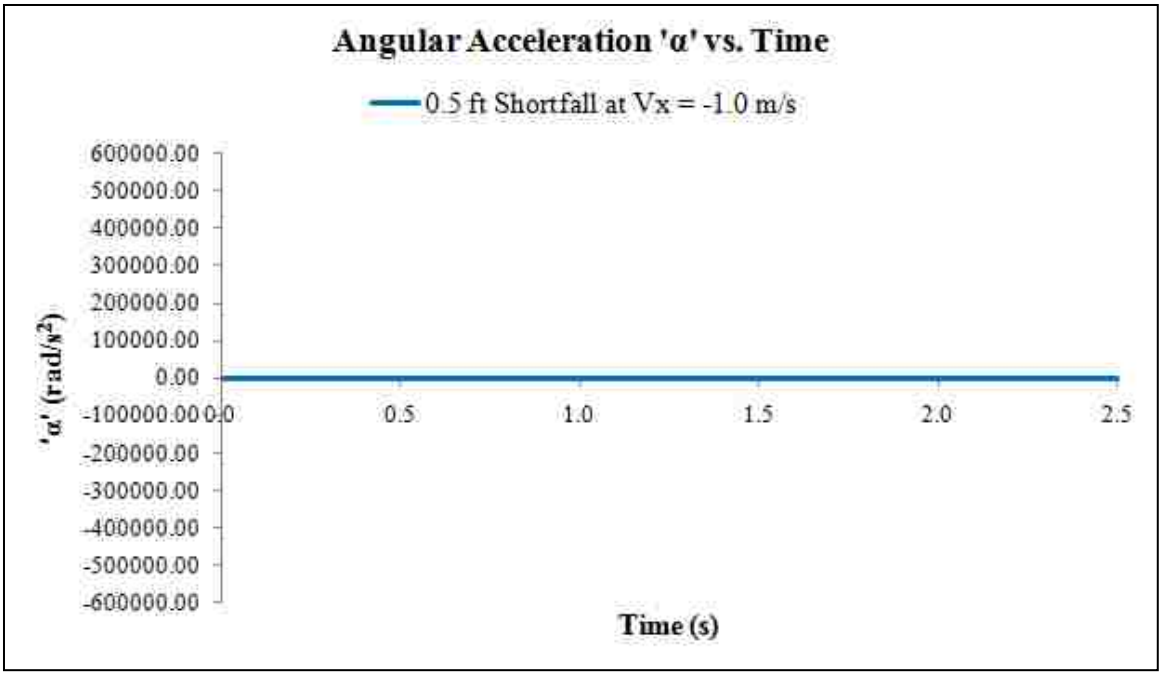

Chart 18: 0.5 ft shortfall at V_x = -1.0 m/s. Angular Acceleration ‘α’ vs. Time.

7-6-2 Shortfall Simulation from '1.0 ft' at V_x = '-1.0 m/s'

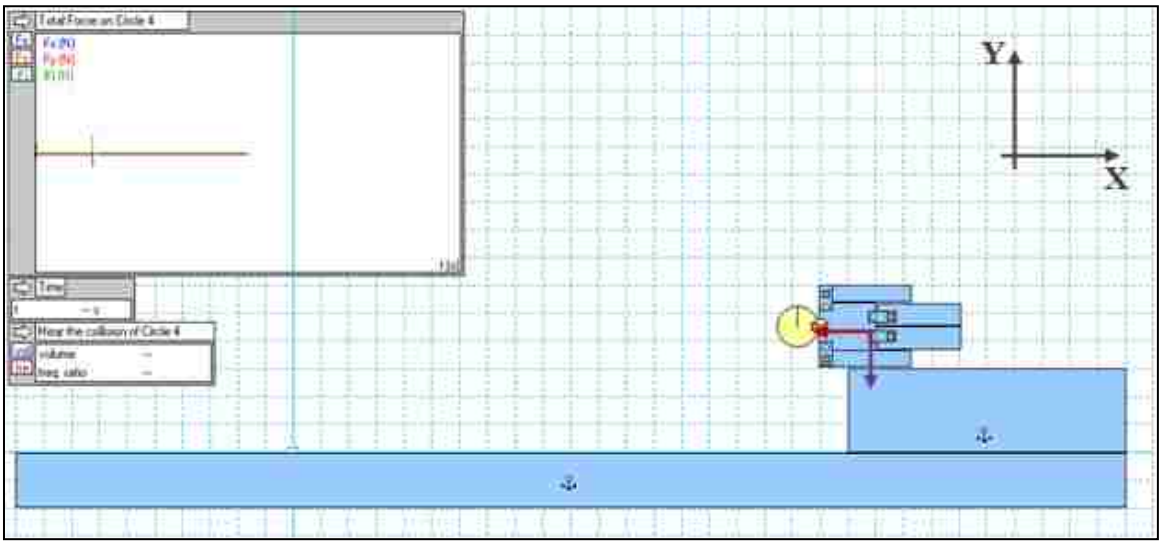

Figure 165: 1.0 ft shortfall at V_x = -1.0 m/s. Initial State.

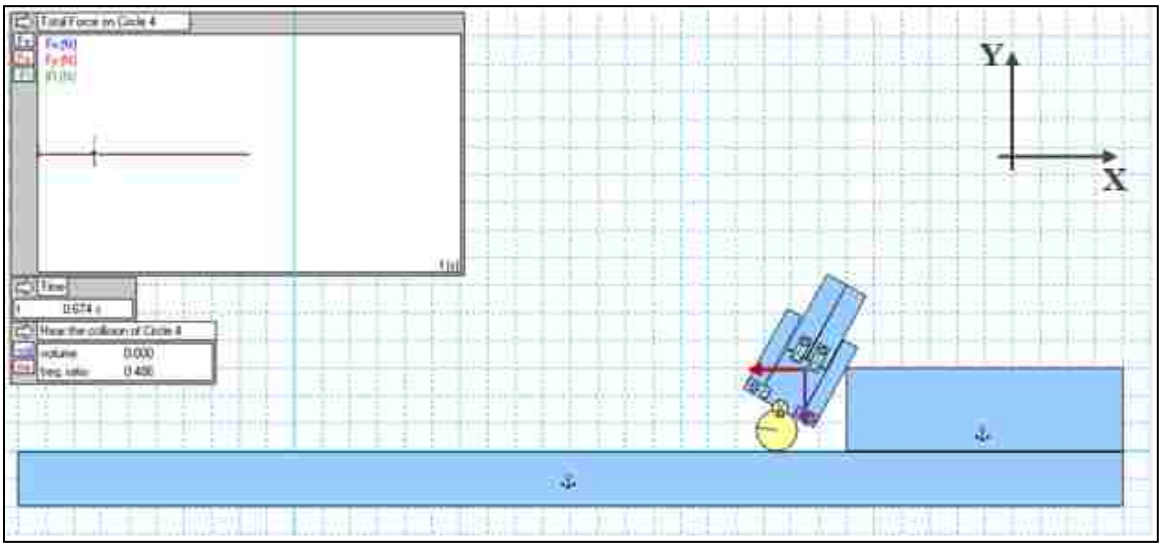

Figure 166: 1.0 ft shortfall at V_x = -1.0 m/s. 1st Head and Ground Impact.

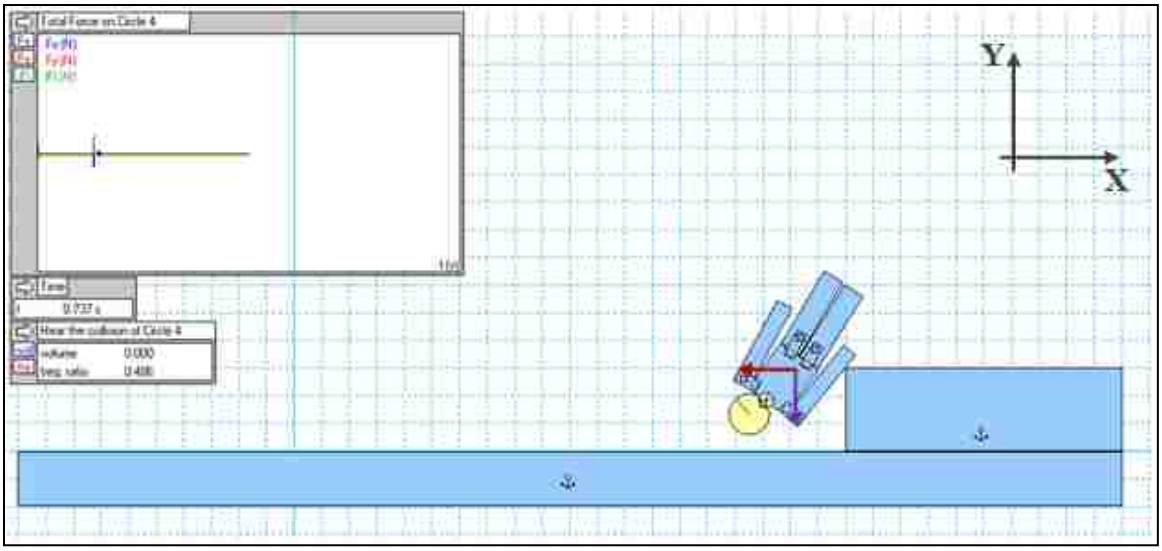

Figure 167: 1.0 ft shortfall at V_x = -1.0 m/s. Head and Left-shoulder Impact.

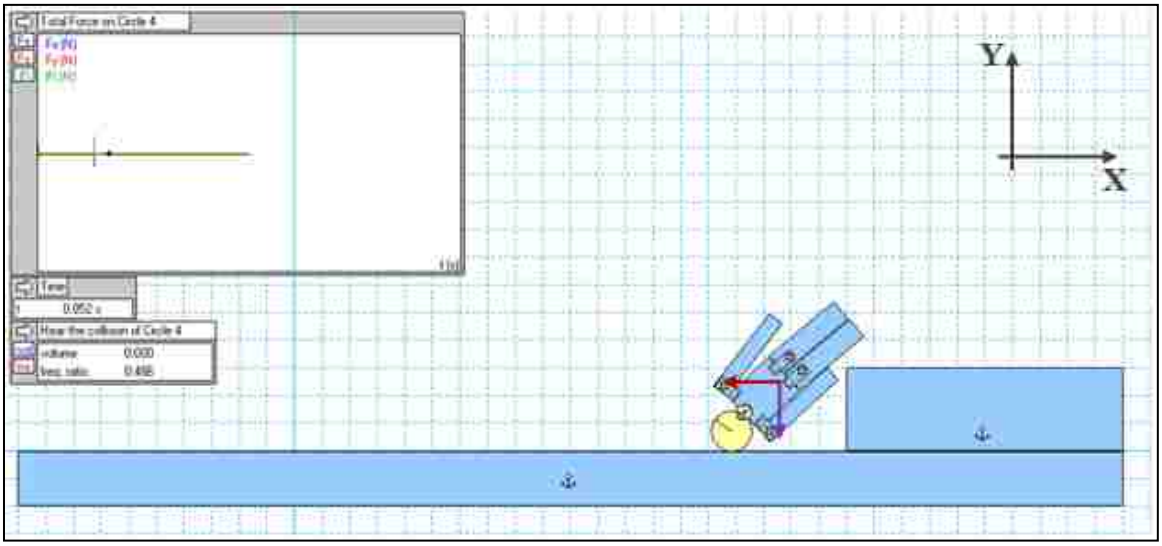

Figure 168: 1.0 ft shortfall at V_x = -1.0 m/s. 2nd Head and Ground Impact.

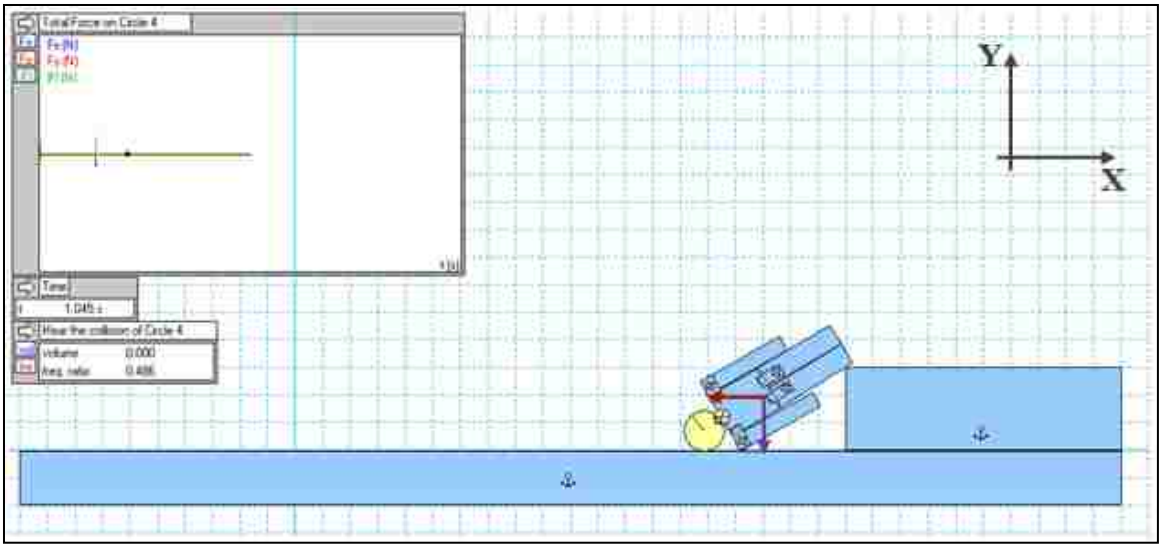

Figure 169: 1.0 ft shortfall at V_x = -1.0 m/s. 3rd Head and Ground Impact.

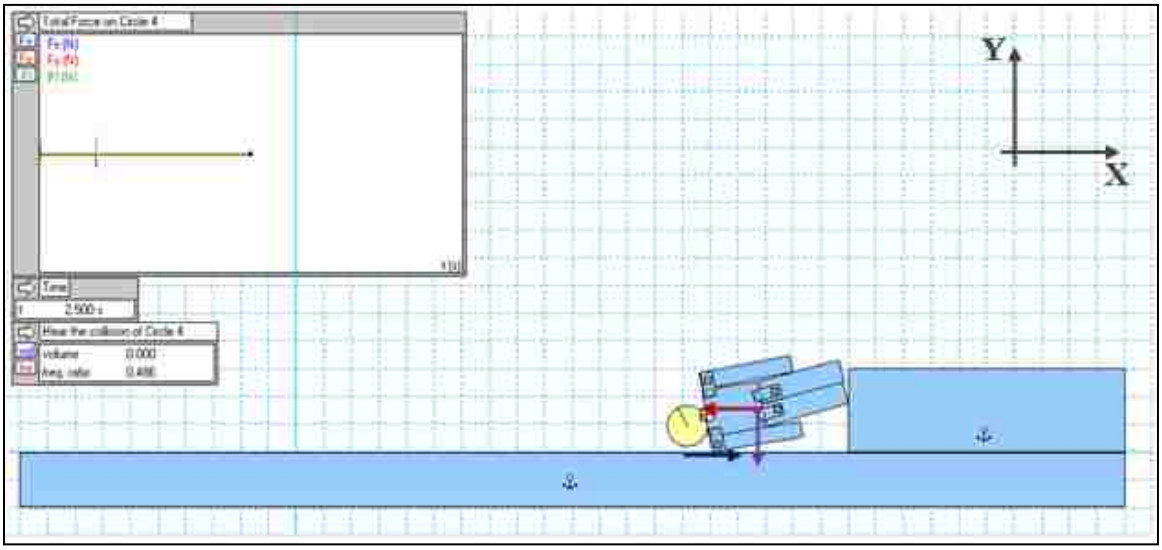

Figure 170: 1.0 ft shortfall at V_x = -1.0 m/s. Final State.

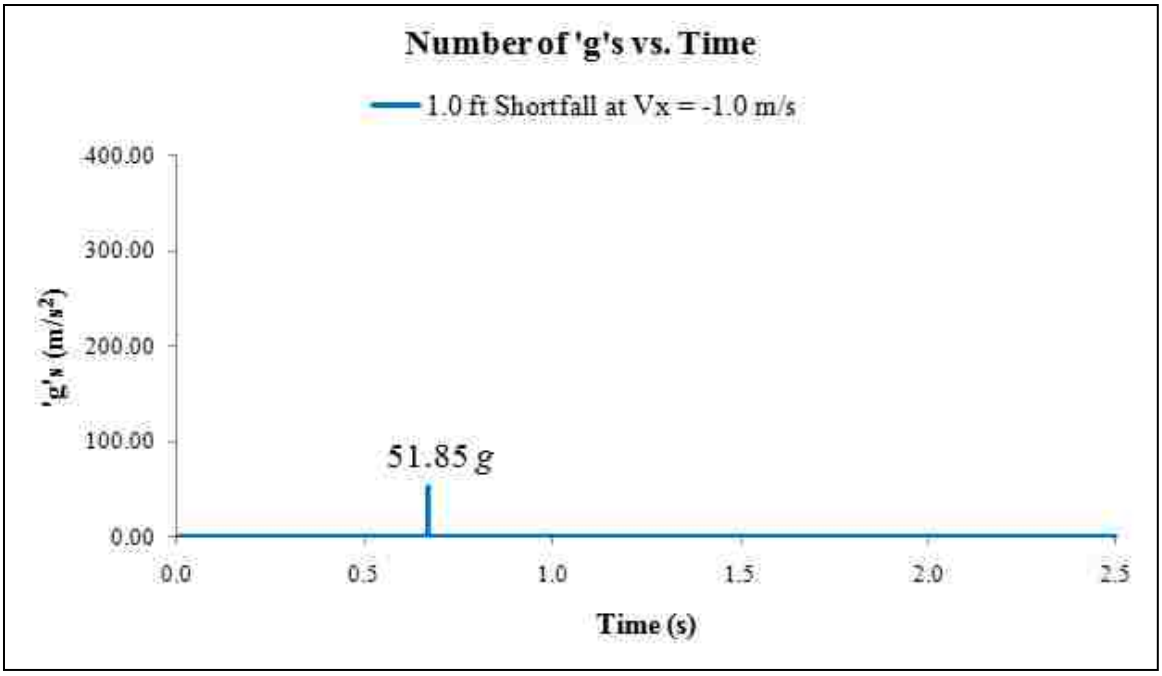

Chart 19: 1.0 ft shortfall at V_x = -1.0 m/s. Number of 'g's vs. Time.

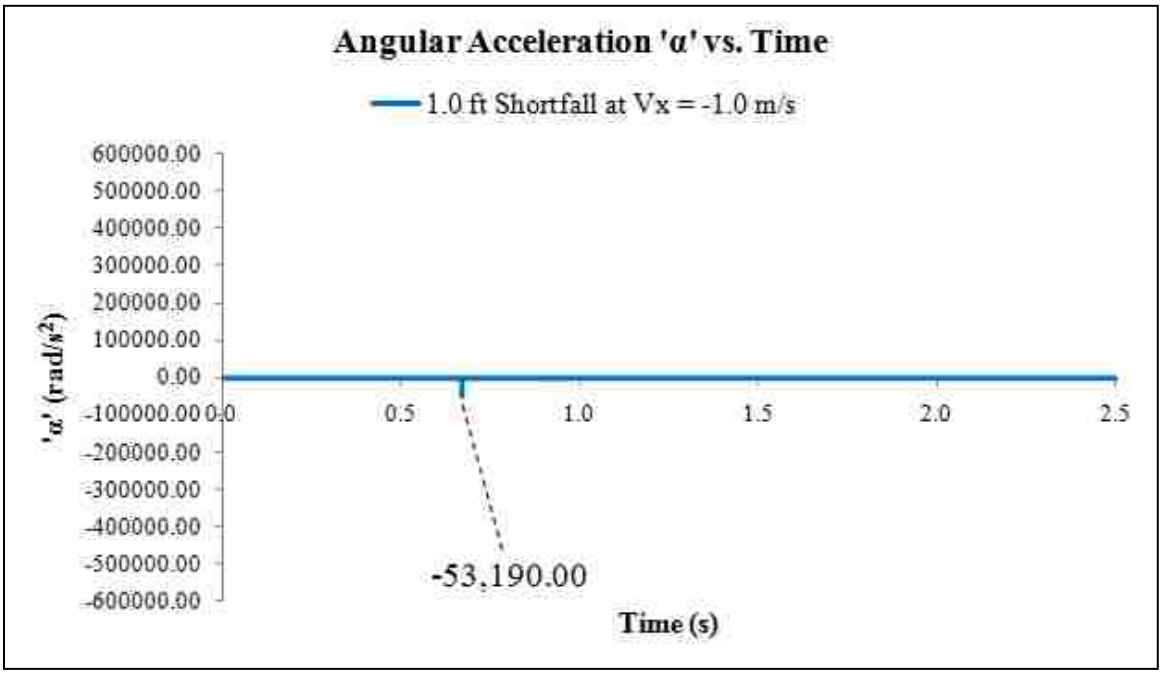

Chart 20: 1.0 ft shortfall at V_x = -1.0 m/s. Angular Acceleration 'α' vs. Time.

7-6-3 Shortfall Simulation from '1.5 ft' at V_x = '-1.0 m/s'

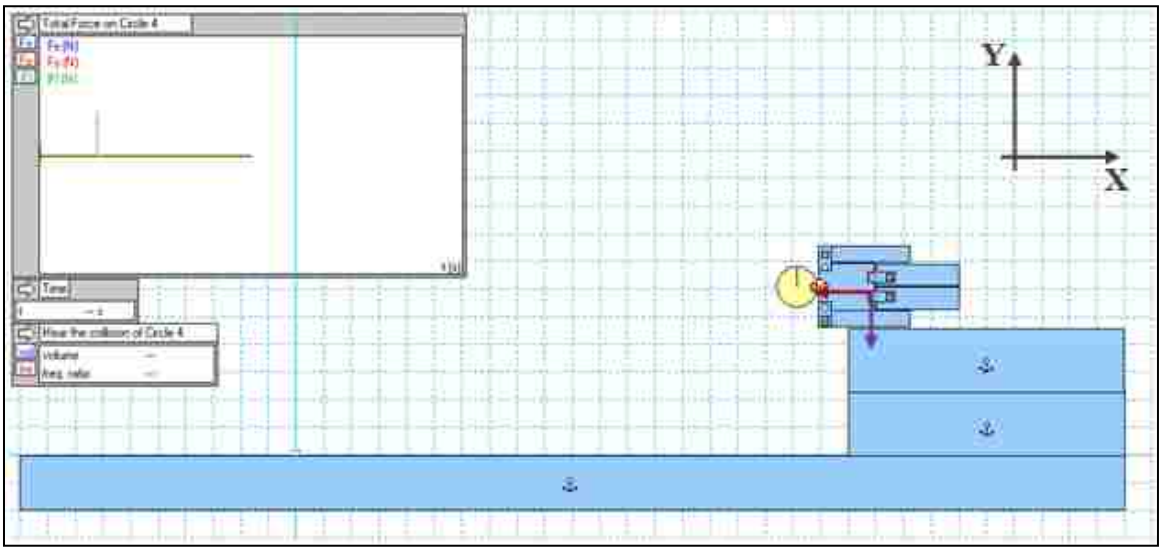

Figure 171: 1.5 ft shortfall at V_x = -1.0 m/s. Initial State.

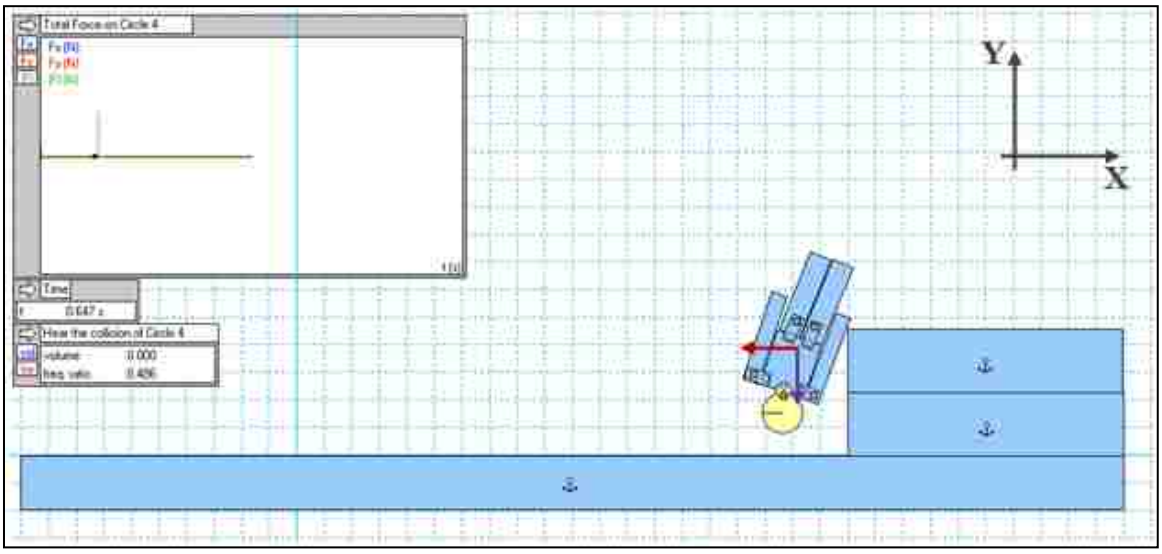

Figure 172: 1.5 ft shortfall at V_x = -1.0 m/s. Moment of Body's Separation from Furniture.

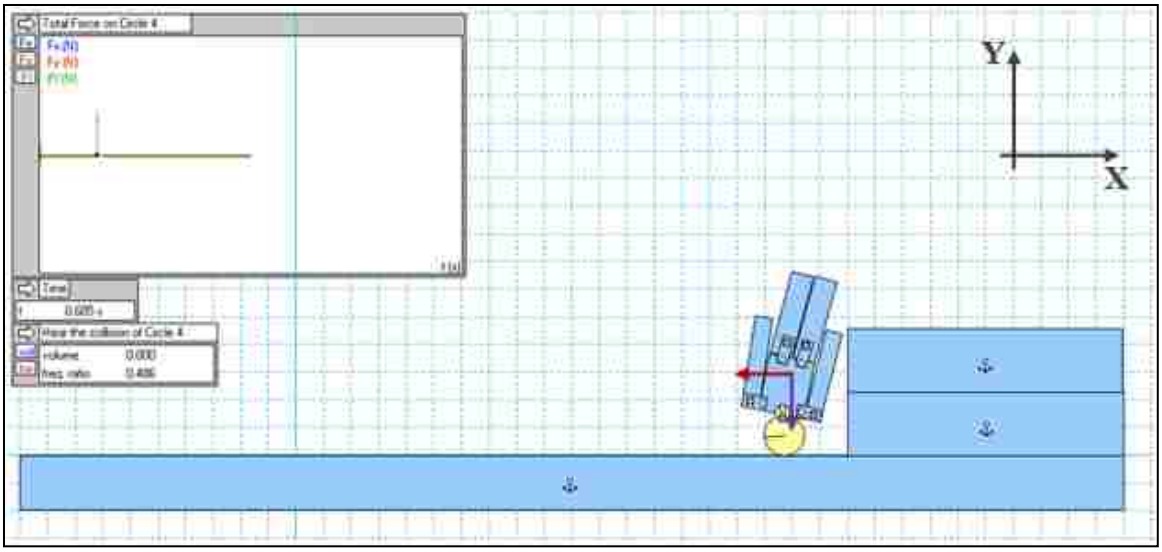

Figure 173: 1.5 ft shortfall at V_x = -1.0 m/s. 1st Head and Ground Impact.

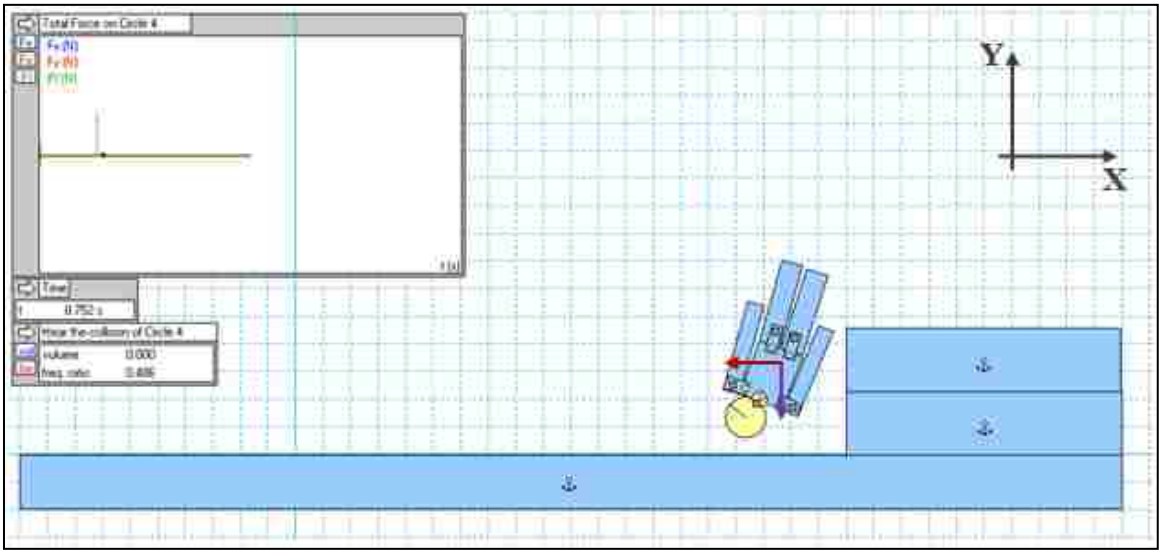

Figure 174: 1.5 ft shortfall at V_x = -1.0 m/s. Head and Left-Shoulder Impact.

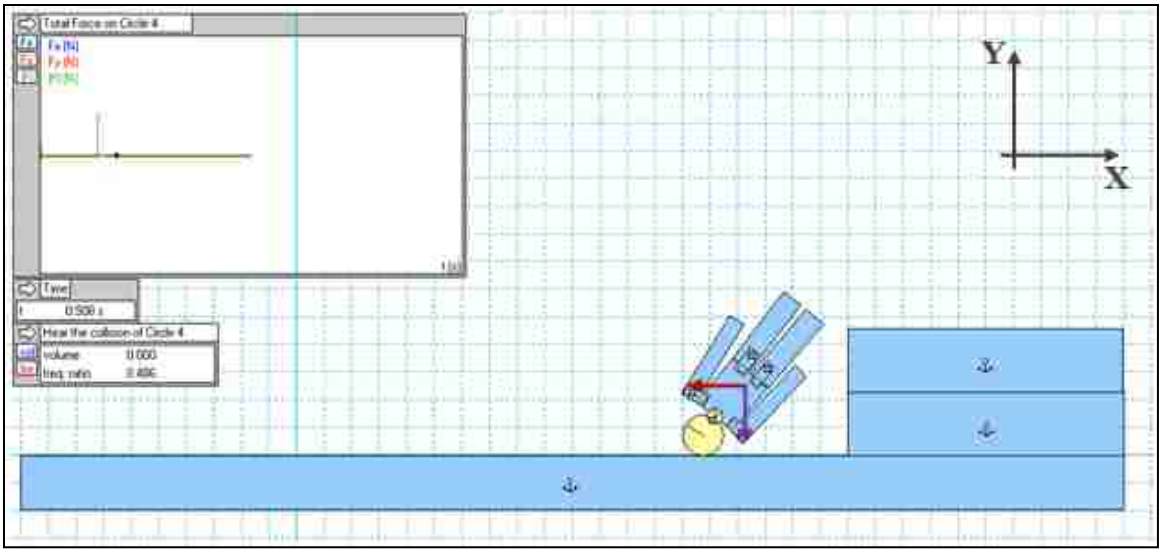

Figure 175: 1.5 ft shortfall at V_x = -1.0 m/s. 2nd Head and Ground Impact.

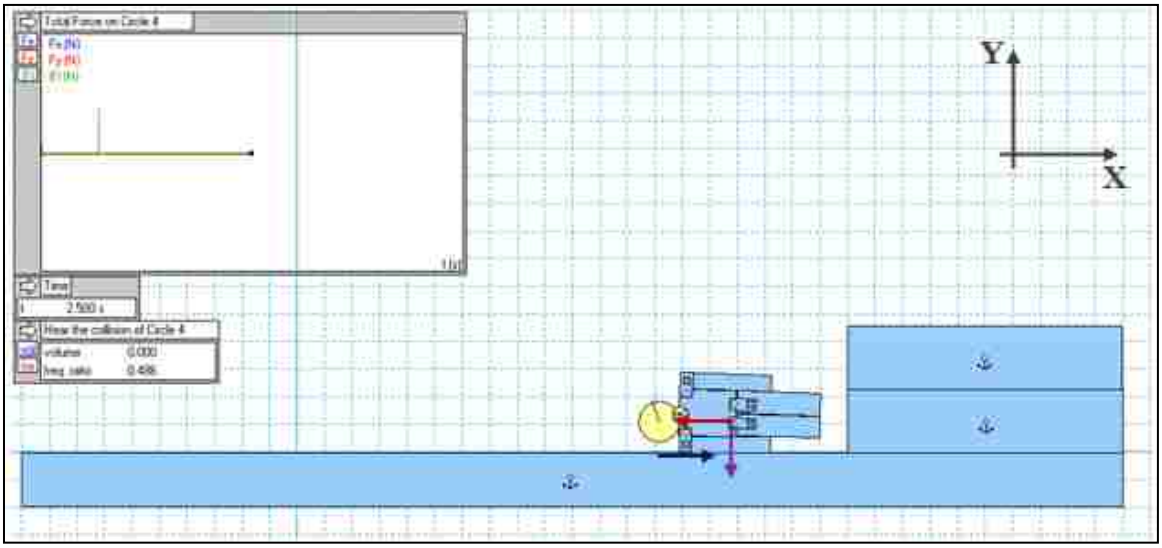

Figure 176: 1.5 ft shortfall at V_x = -1.0 m/s. Final State.

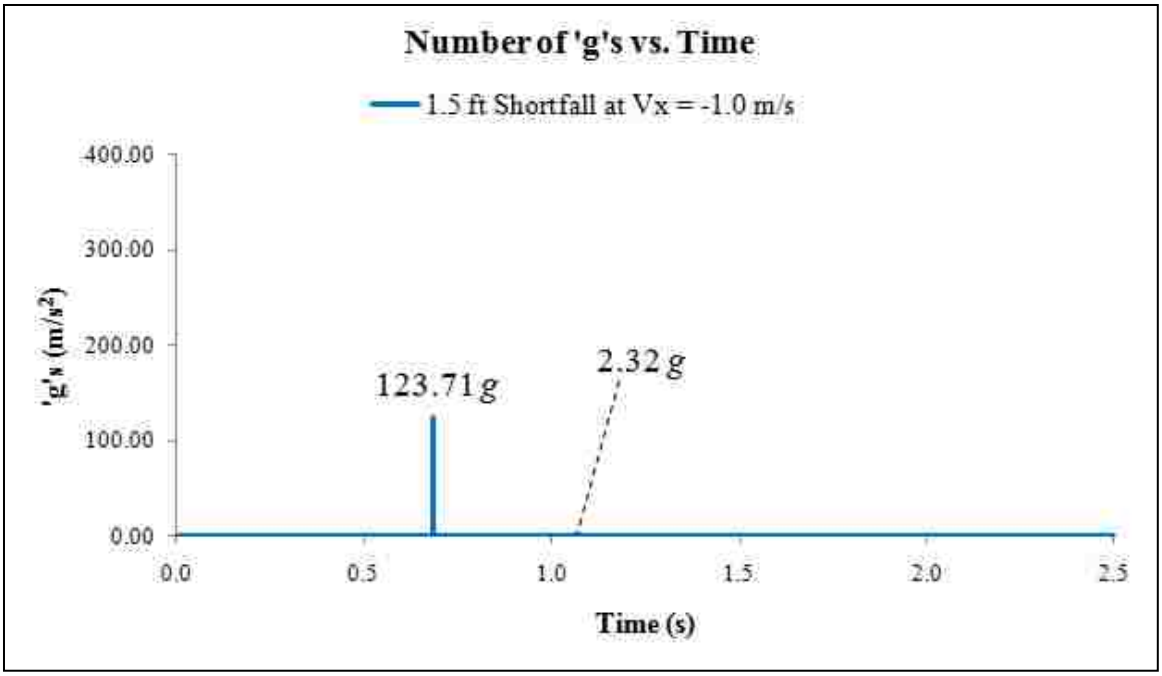

Chart 21: 1.5 ft shortfall at V_x = -1.0 m/s. Number of 'g's vs. Time.

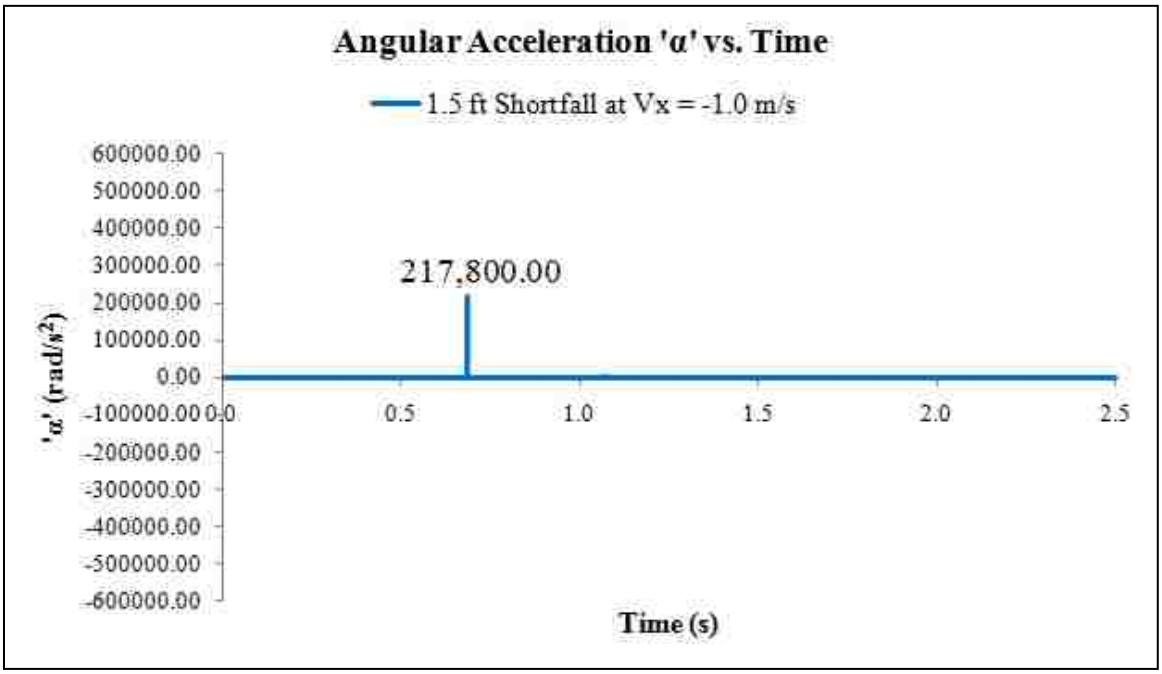

Chart 22: 1.5 ft shortfall at V_x = -1.0 m/s. Angular Acceleration 'α' vs. Time.

7-6-4 Shortfall Simulation from '2.0 ft' at V_x = '-1.0 m/s'

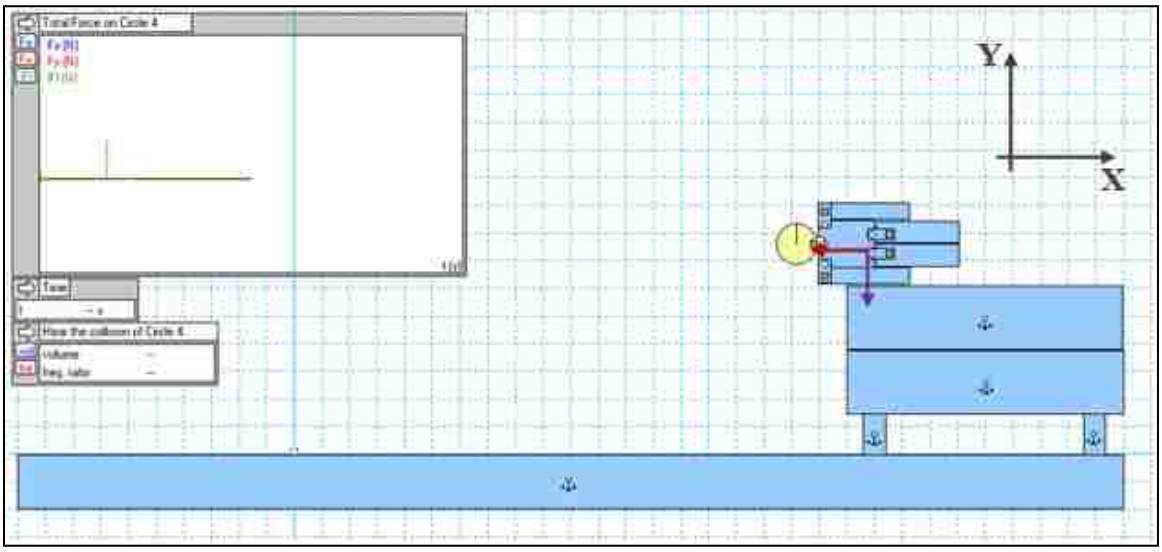

Figure 177: 2.0 ft shortfall at V_x = -1.0 m/s. Initial State.

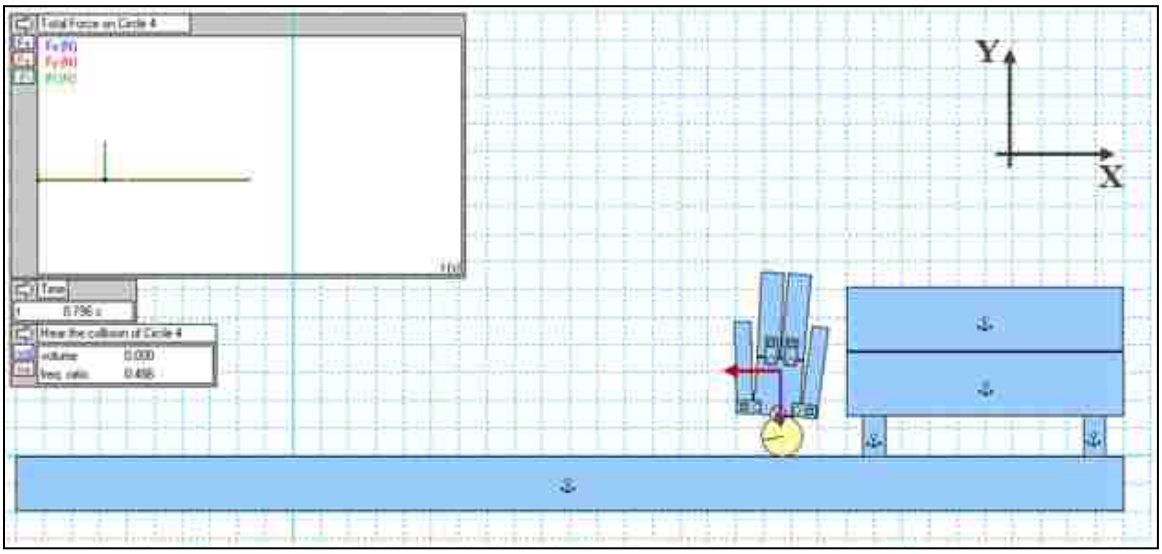

Figure 178: 2.0 ft shortfall at V_x = -1.0 m/s. 1st Head and Ground Impact.

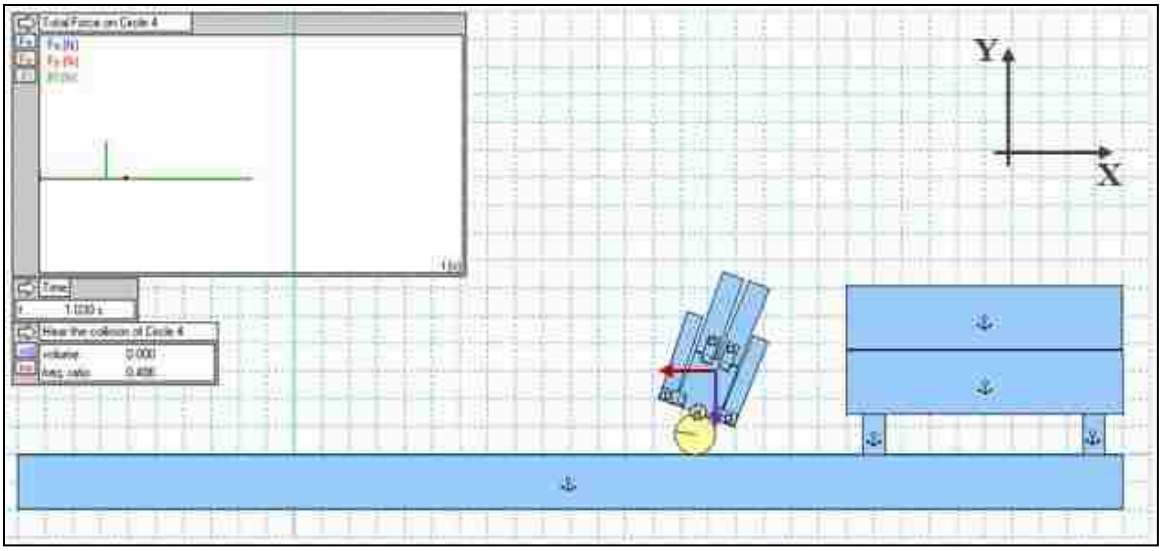

Figure 179: 2.0 ft shortfall at V_x = -1.0 m/s. 2nd Head and Ground Impact.

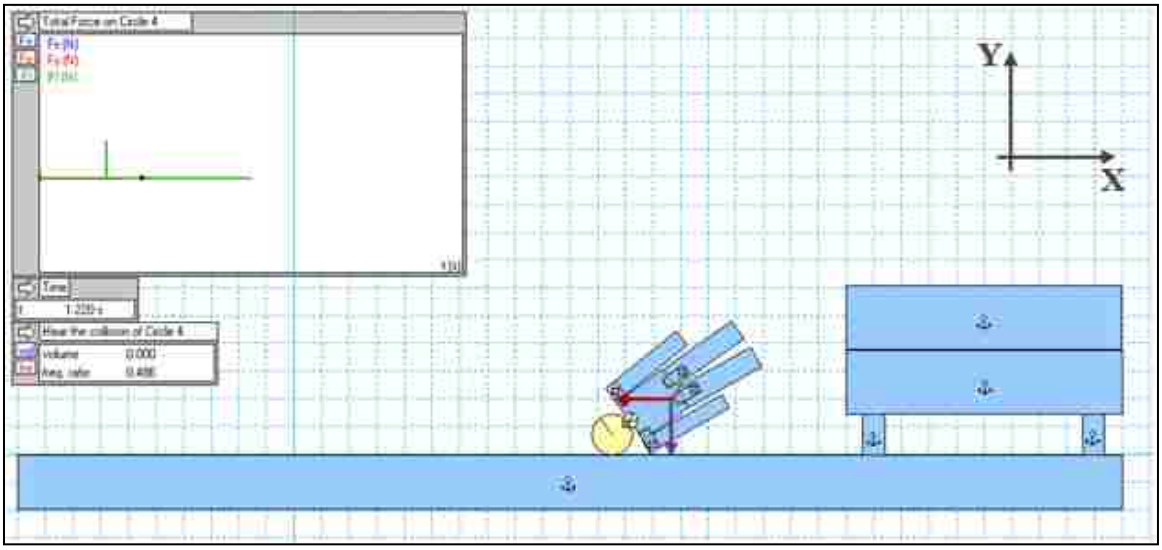

Figure 180: 2.0 ft shortfall at V_x = -1.0 m/s. 3rd Head and Ground Impact.

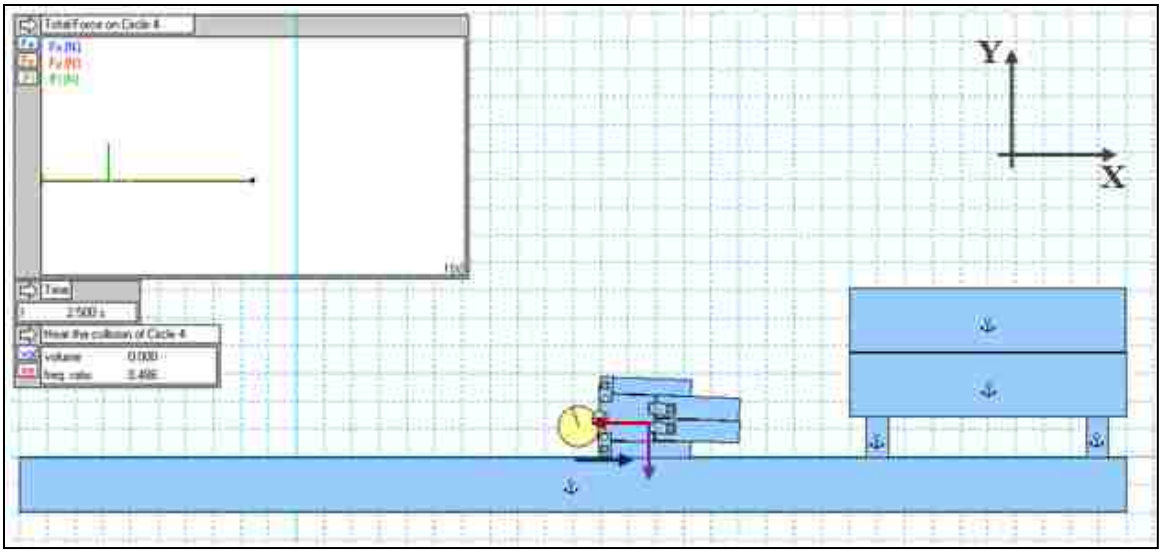

Figure 181: 2.0 ft shortfall at V_x = -1.0 m/s. Final State.

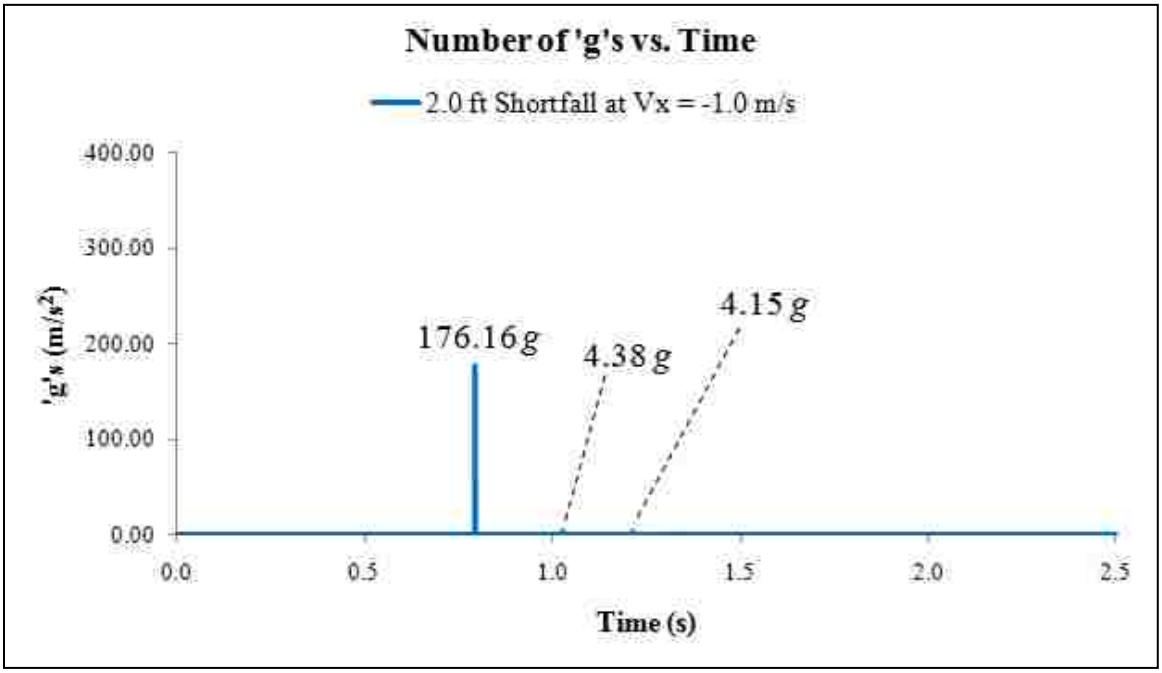

Chart 23: 2.0 ft shortfall at V_x = -1.0 m/s. Number of 'g's vs. Time.

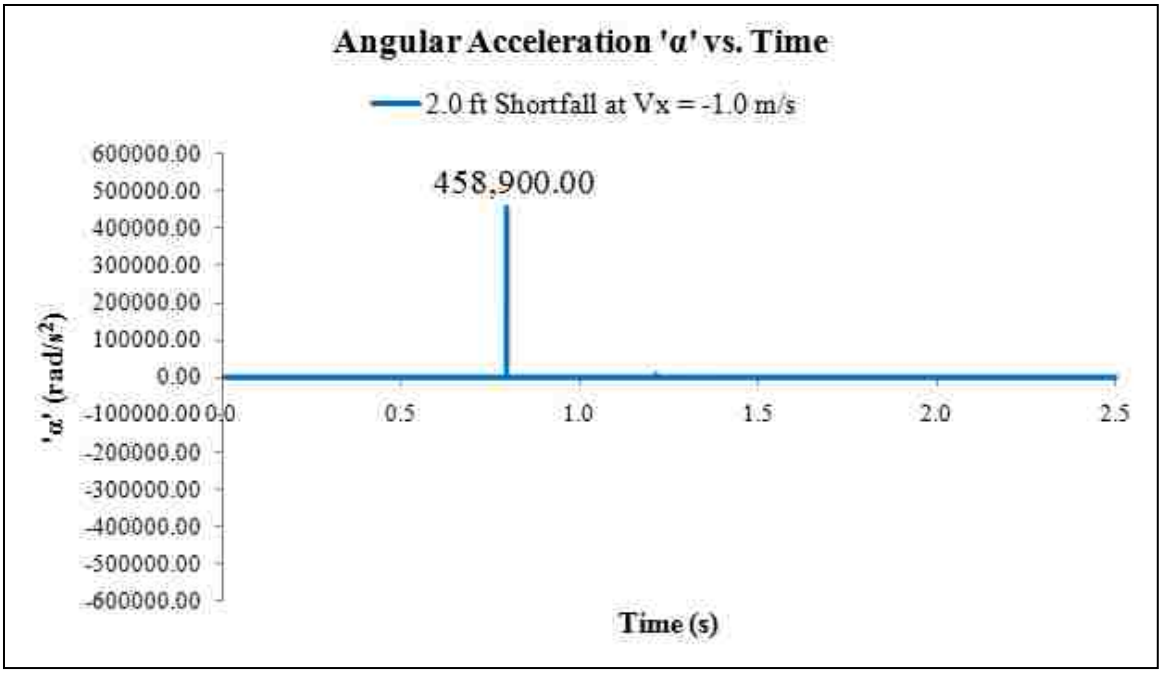

Chart 24: 2.0 ft shortfall at V_x = -1.0 m/s. Angular Acceleration ‘α’ vs. Time.

7-6-5 Shortfall Simulation from '2.5 ft' at V_x = '-1.0 m/s'

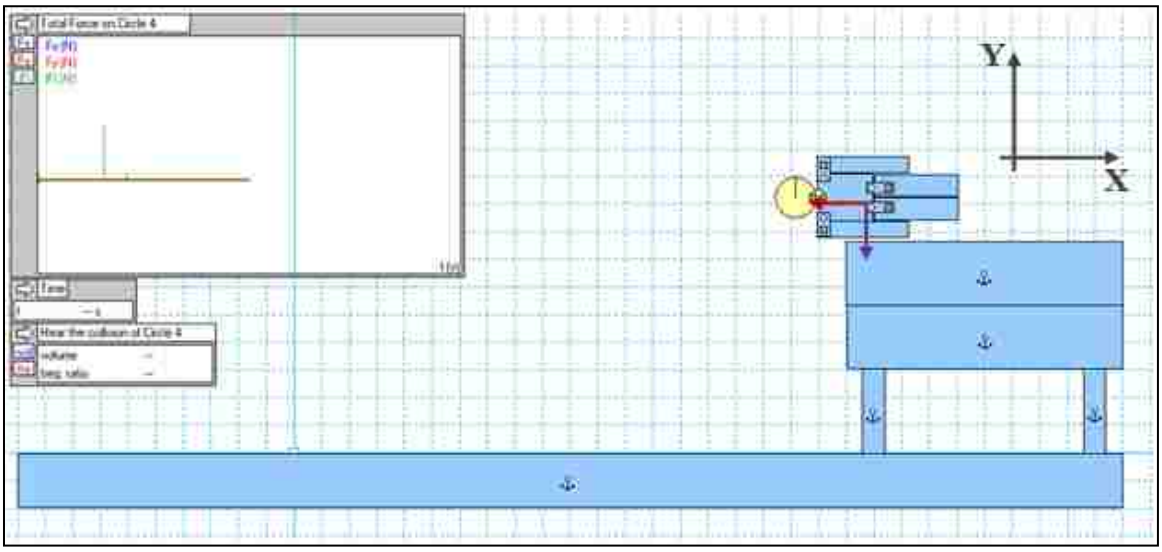

Figure 182: 2.5 ft shortfall at V_x = -1.0 m/s. Initial State.

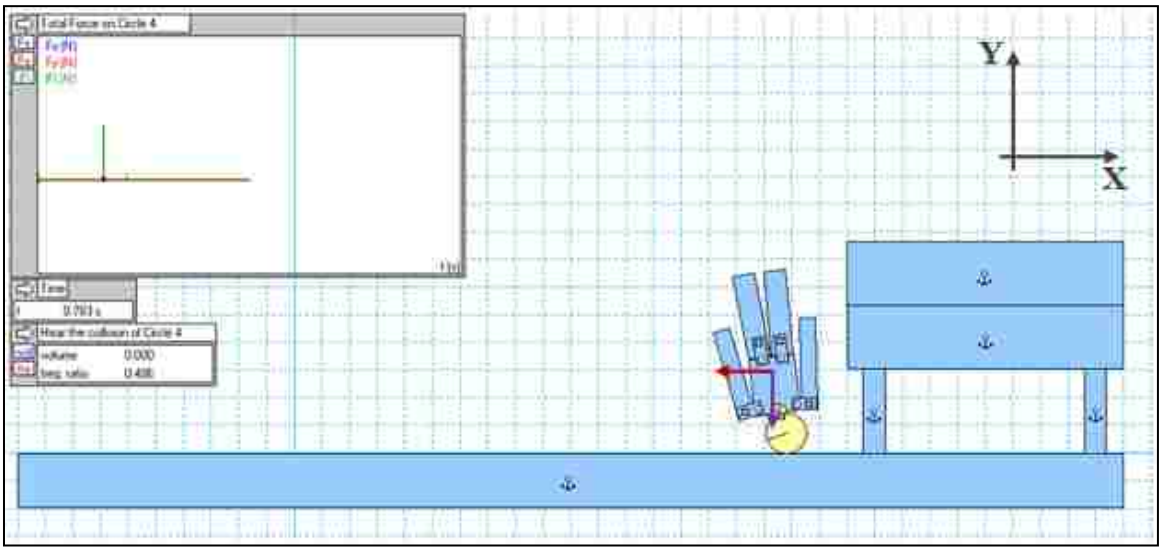

Figure 183: 2.5 ft shortfall at V_x = -1.0 m/s. 1st Head and Ground Impact.

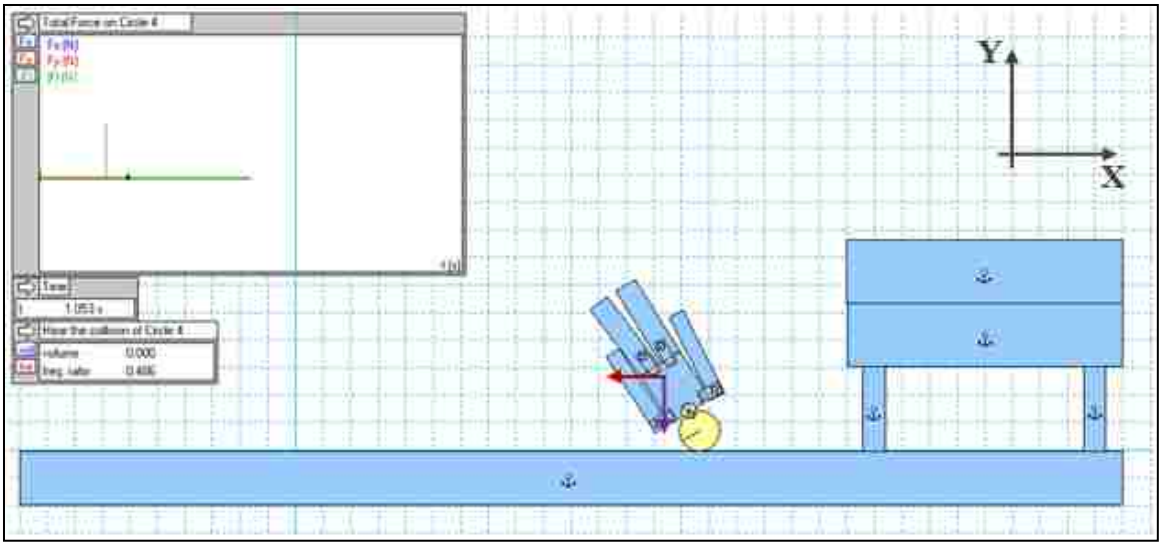

Figure 184: 2.5 ft shortfall at V_x = -1.0 m/s. 2nd Head and Ground Impact.

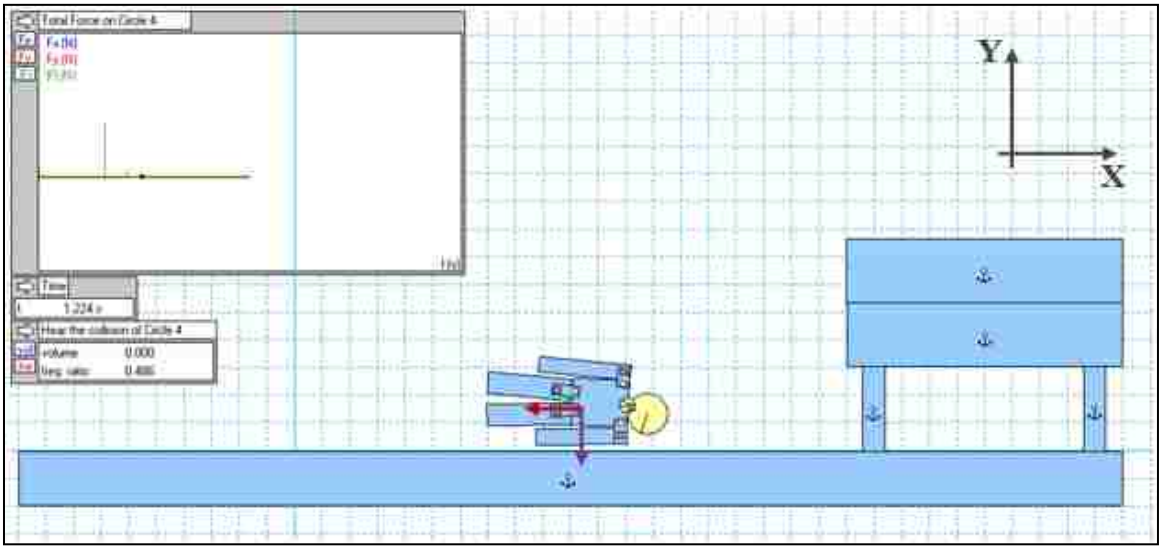

Figure 185: 2.5 ft shortfall at V_x = -1.0 m/s. Head and Right-Shoulder Impact.

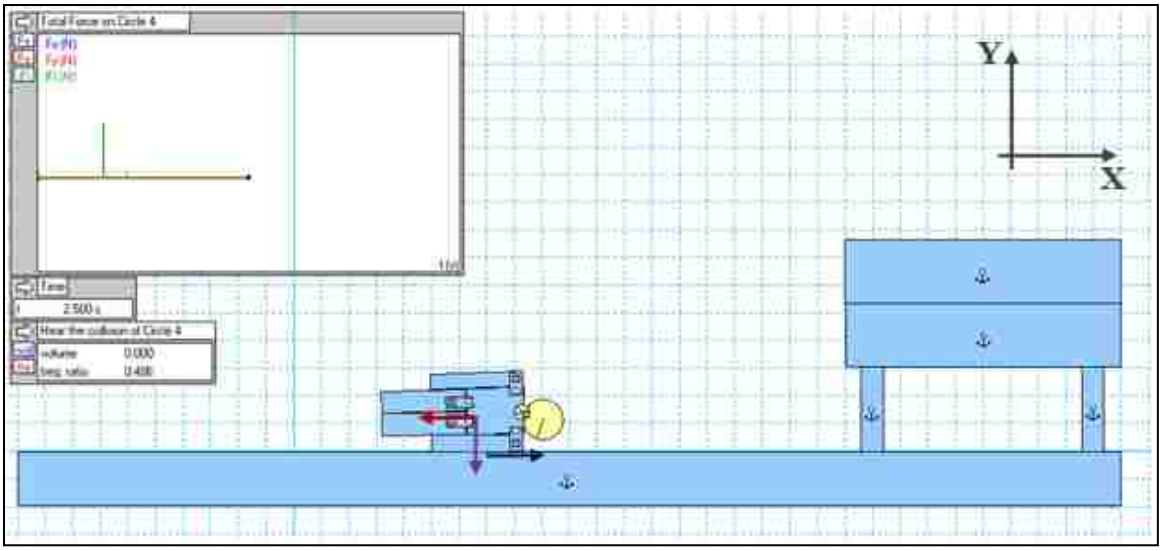

Figure 186: 2.5 ft shortfall at V_x = -1.0 m/s. Final State.

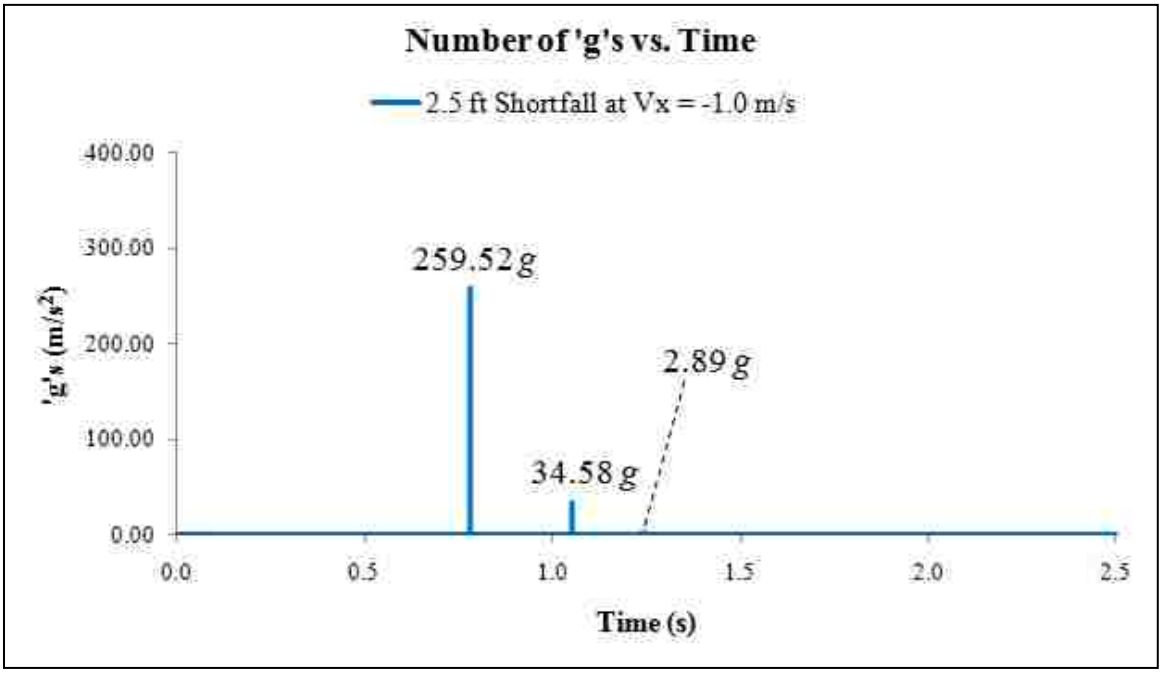

Chart 25: 2.5 ft shortfall at V_x = -1.0 m/s. Number of 'g's vs. Time.

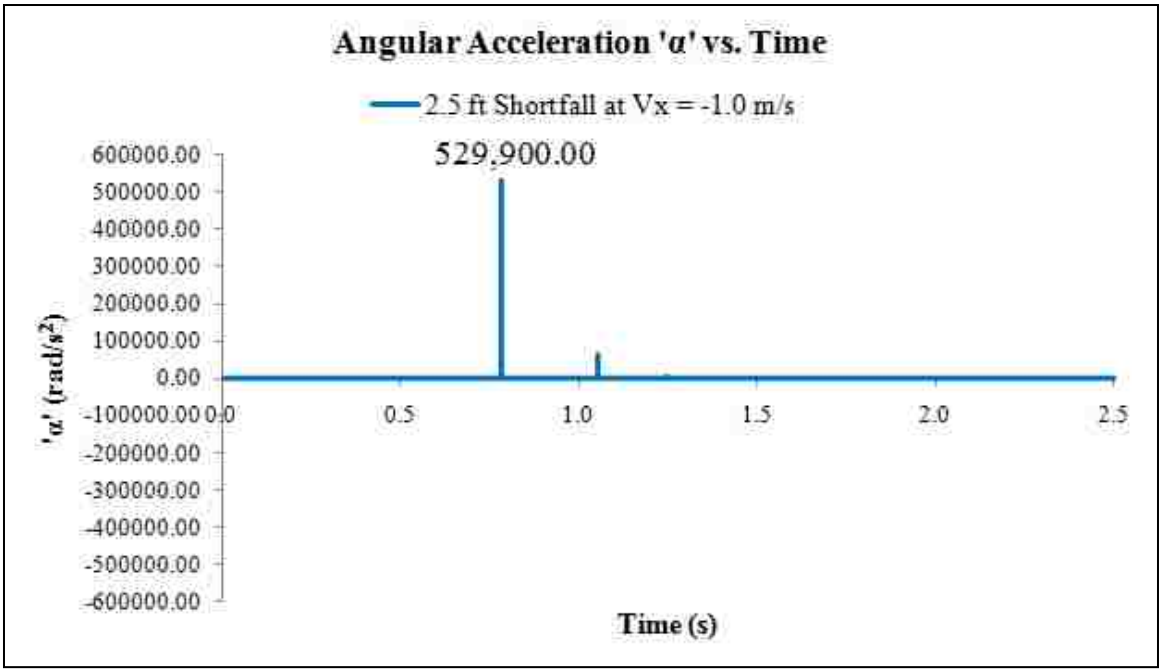

Chart 26: 2.5 ft shortfall at V_x = -1.0 m/s. Angular Acceleration ‘α’ vs. Time.

7-6-6 Shortfall Simulation from '3.0 ft' at V_x = '-1.0 m/s'

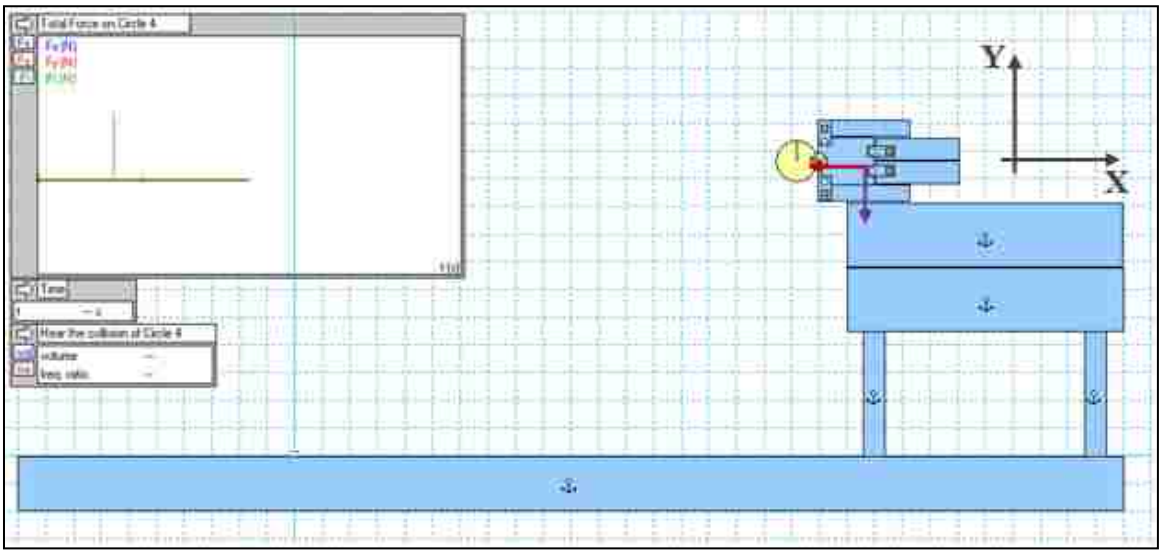

Figure 187: 3.0 ft shortfall at V_x = -1.0 m/s. Initial State.

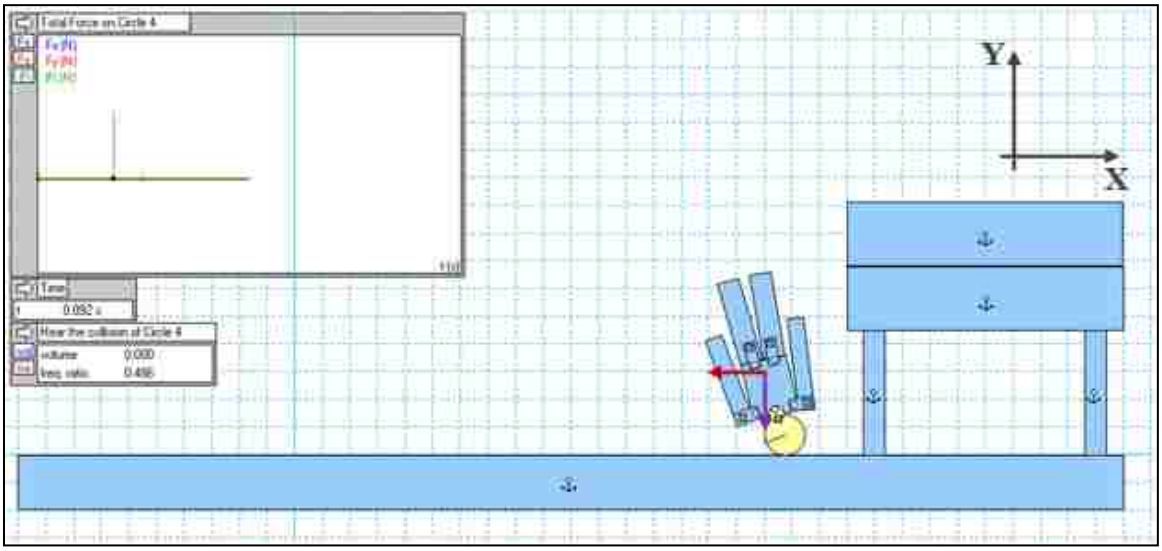

Figure 188: 3.0 ft shortfall at V_x = -1.0 m/s. Head and Ground Impact.

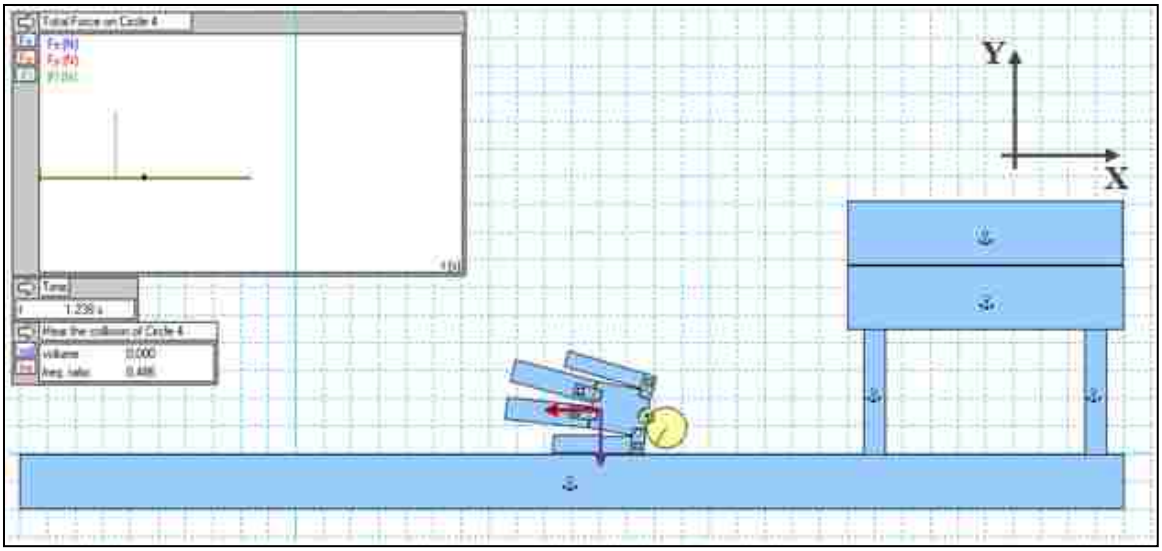

Figure 189: 3.0 ft shortfall at V_x = -1.0 m/s. Right-Shoulder/Arm and Ground Impact.

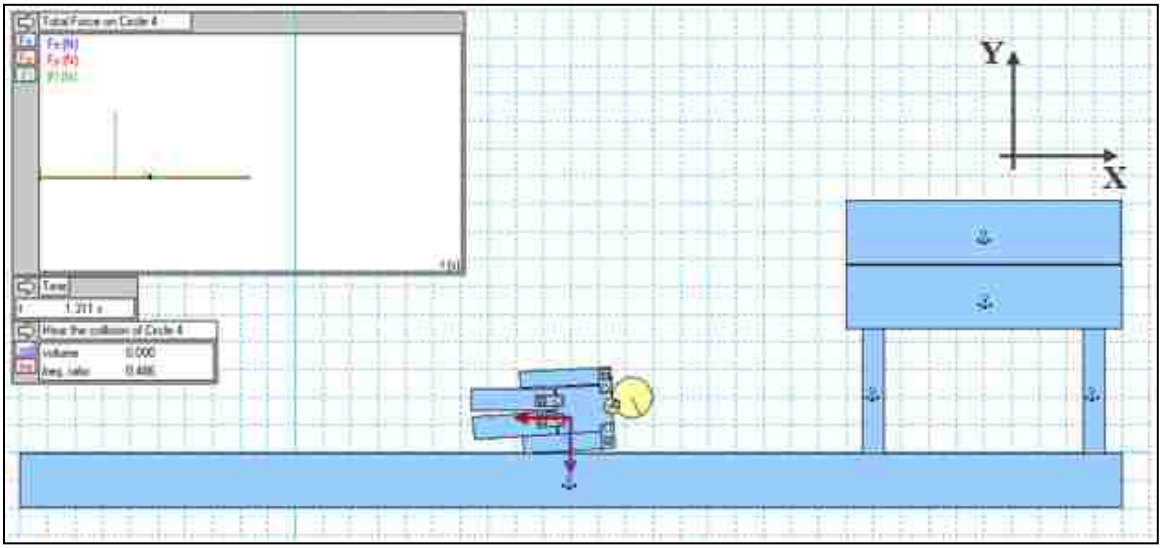

Figure 190: 3.0 ft shortfall at V_x = -1.0 m/s. Head and Left-Shoulder Impact.

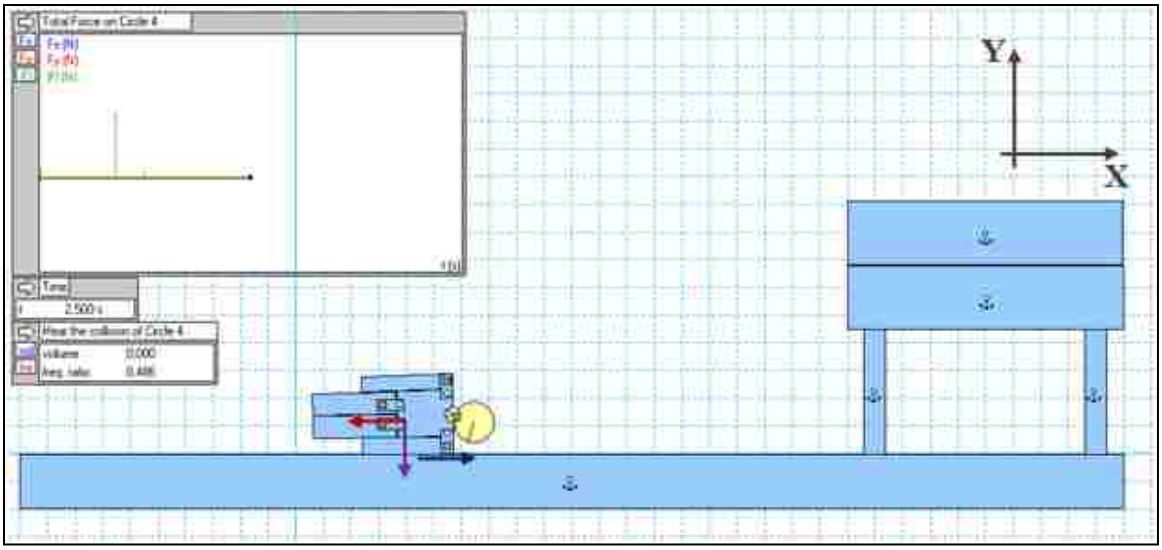

Figure 191: 3.0 ft shortfall at V_x = -1.0 m/s. Final State.

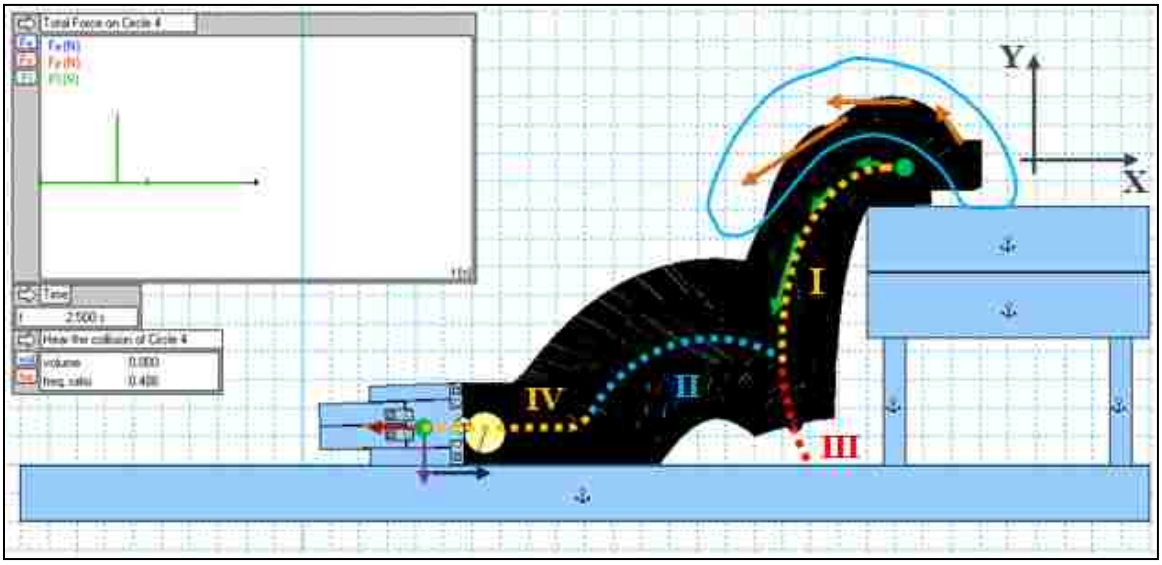

Figure 192: 3.0 ft shortfall at V_x = -1.0 m/s. Path of Shortfall.

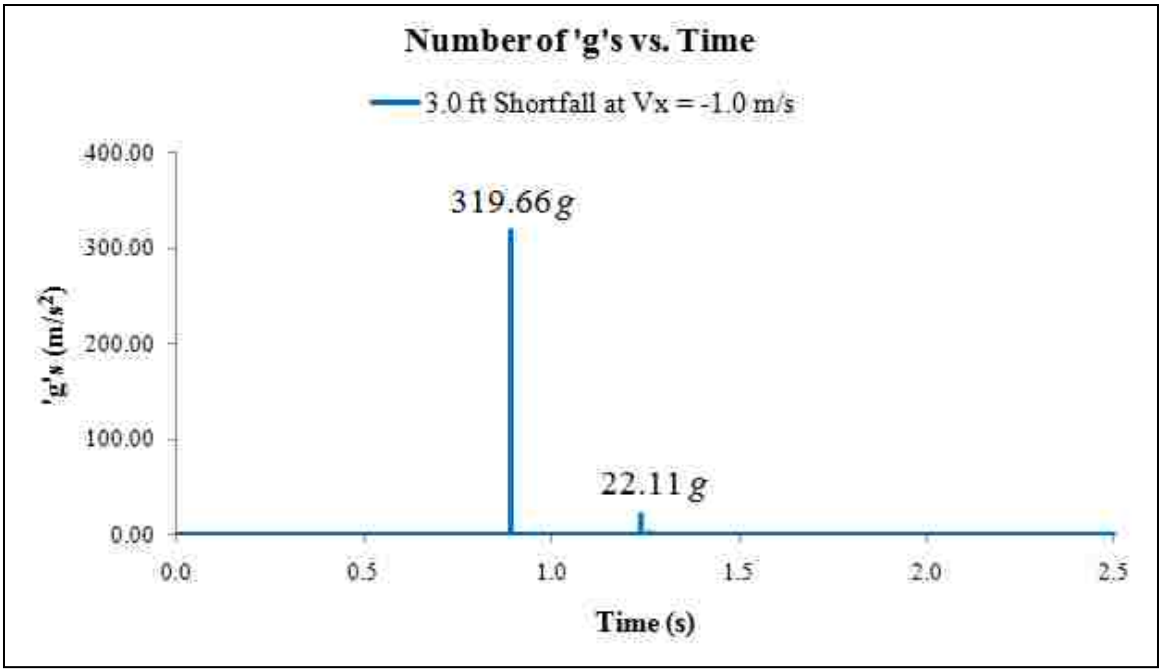

Chart 27: 3.0 ft shortfall at V_x = -1.0 m/s. Number of 'g's vs. Time.

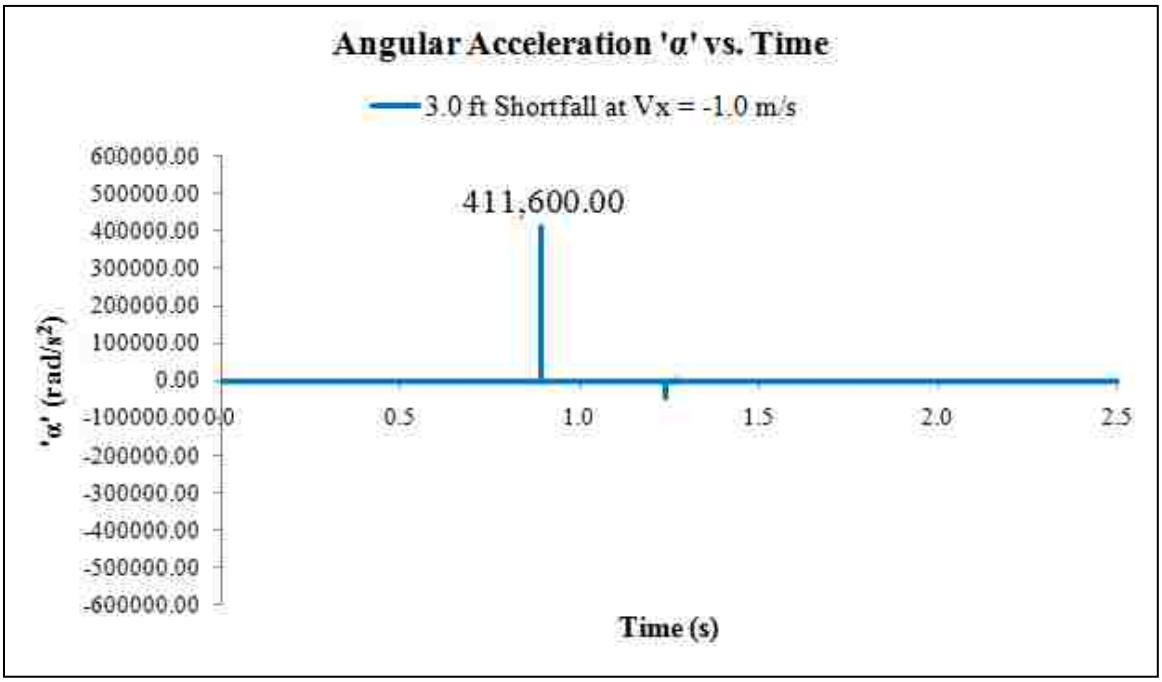

Chart 28: 3.0 ft shortfall at V_x = -1.0 m/s. Angular Acceleration 'α' vs. Time.

7-6-7 Shortfall Simulation from '0.5 ft' at V_x = '-3.0 m/s'

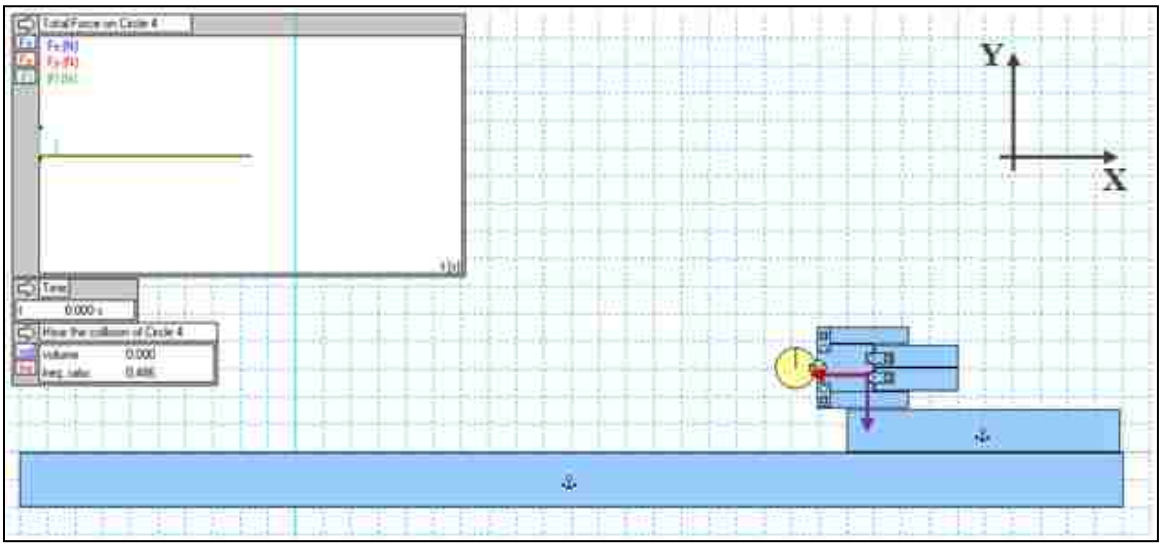

Figure 193: 0.5 ft shortfall at V_x = -3.0 m/s. Initial State.

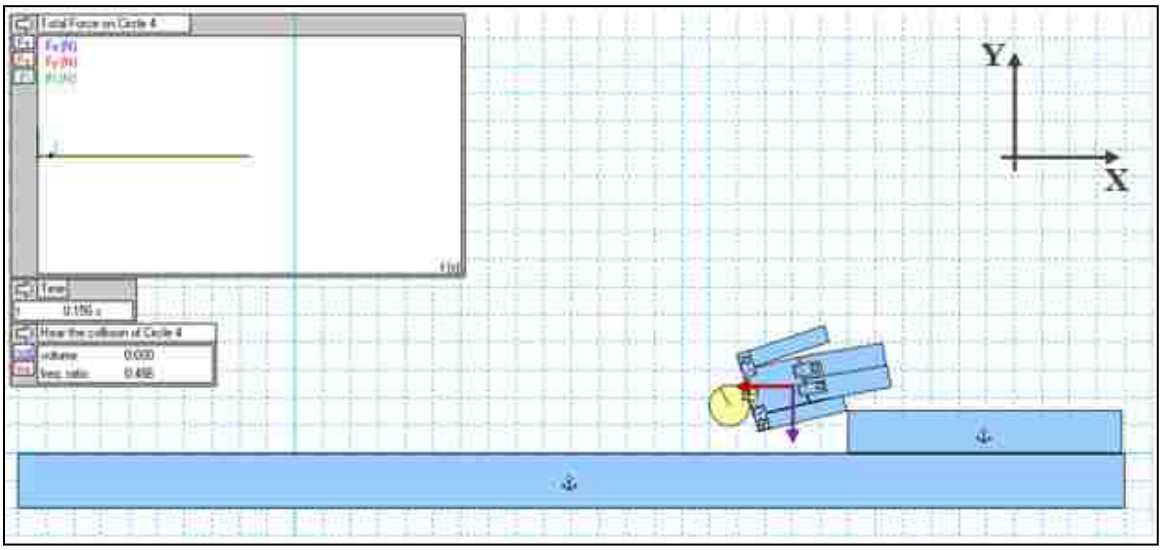

Figure 194: 0.5 ft shortfall at V_x = -3.0 m/s. Moment of Body's Separation from Furniture.

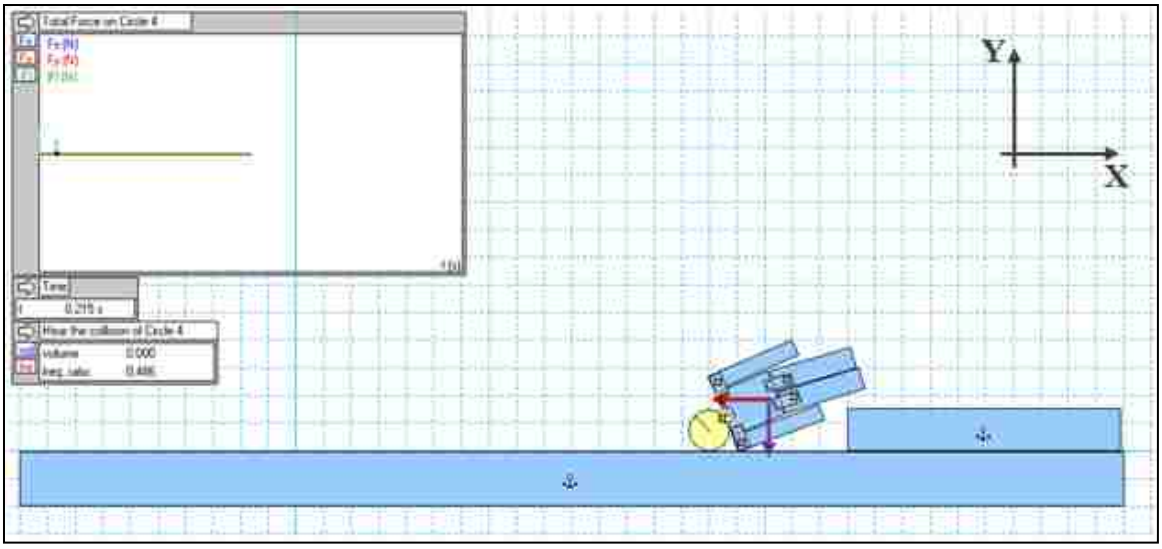

Figure 195: 0.5 ft shortfall at V_x = -3.0 m/s. Head and Ground Impact.

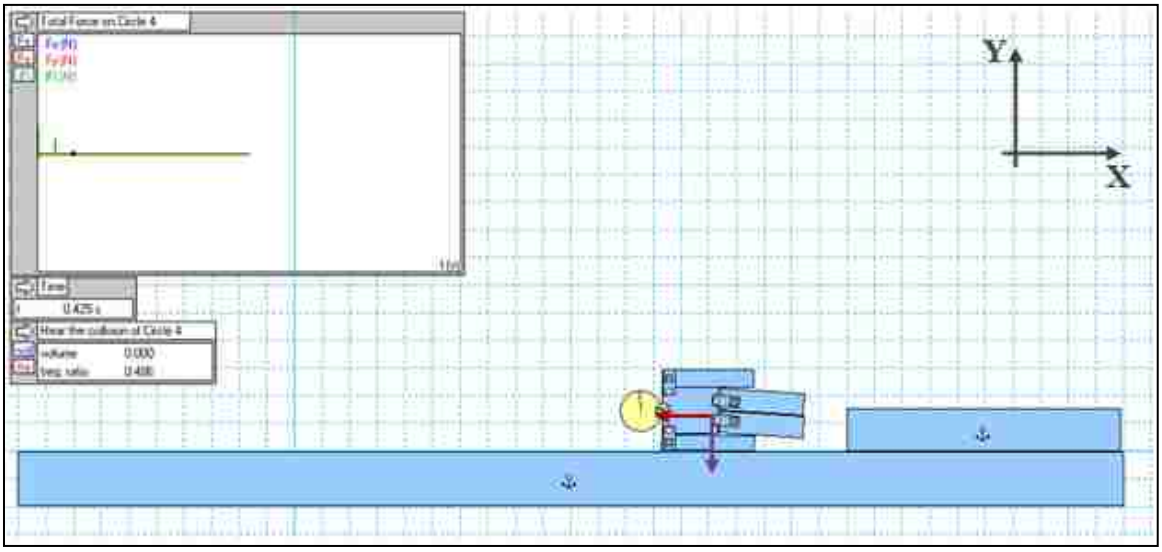

Figure 196: 0.5 ft shortfall at V_x = -3.0 m/s. Lower-Left-Arm and Ground Impact.

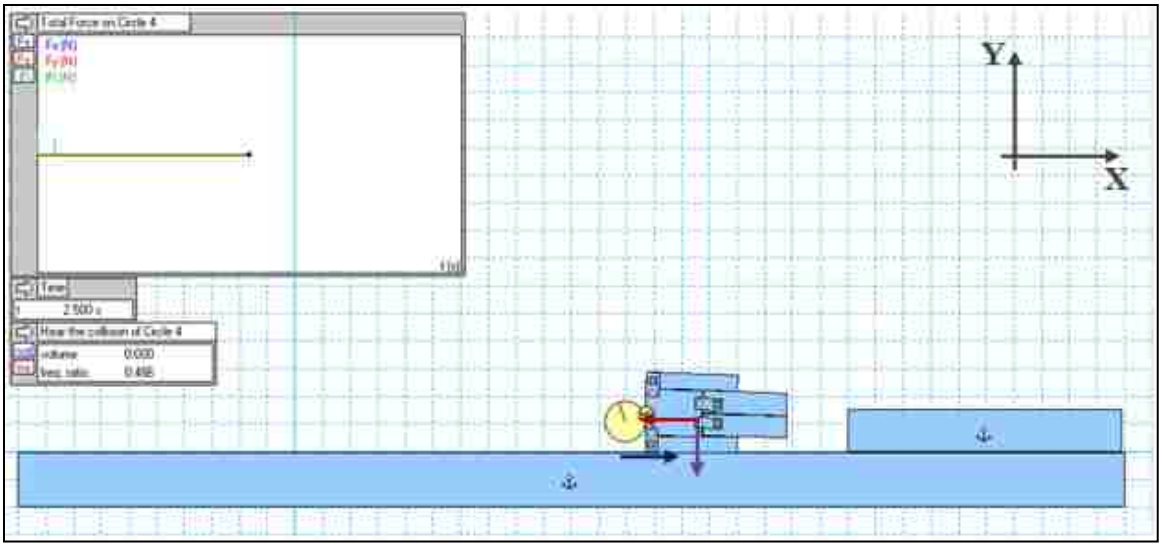

Figure 197: 0.5 ft shortfall at V_x = -3.0 m/s. Final State.

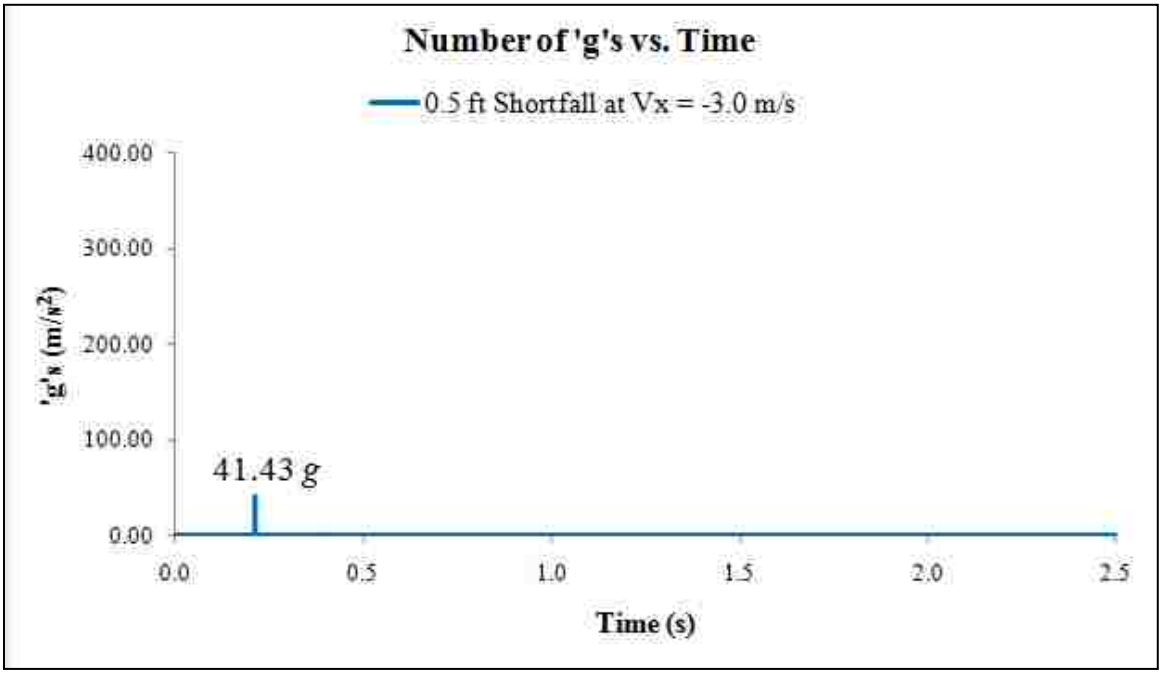

Chart 29: 0.5 ft shortfall at V_x = -3.0 m/s. Number of ‘g’s vs. Time.

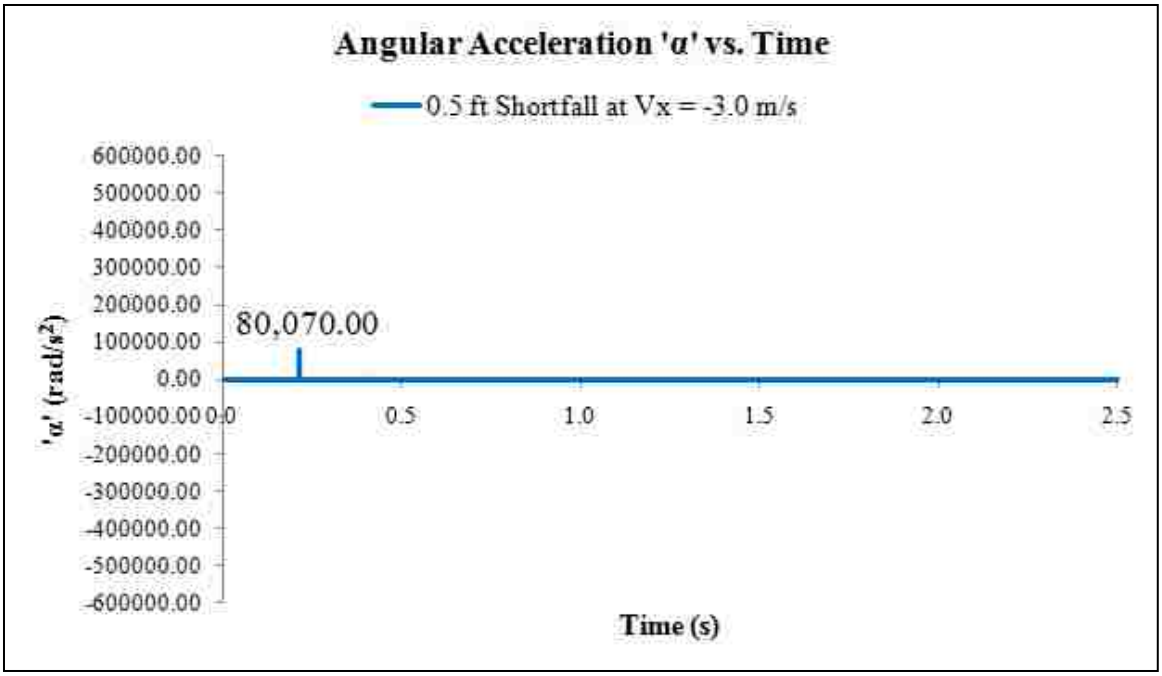

Chart 30: 0.5 ft shortfall at V_x = -3.0 m/s. Angular Acceleration ‘α’ vs. Time.

7-6-8 Shortfall Simulation from '1.0 ft' at V_x = '-3.0 m/s'

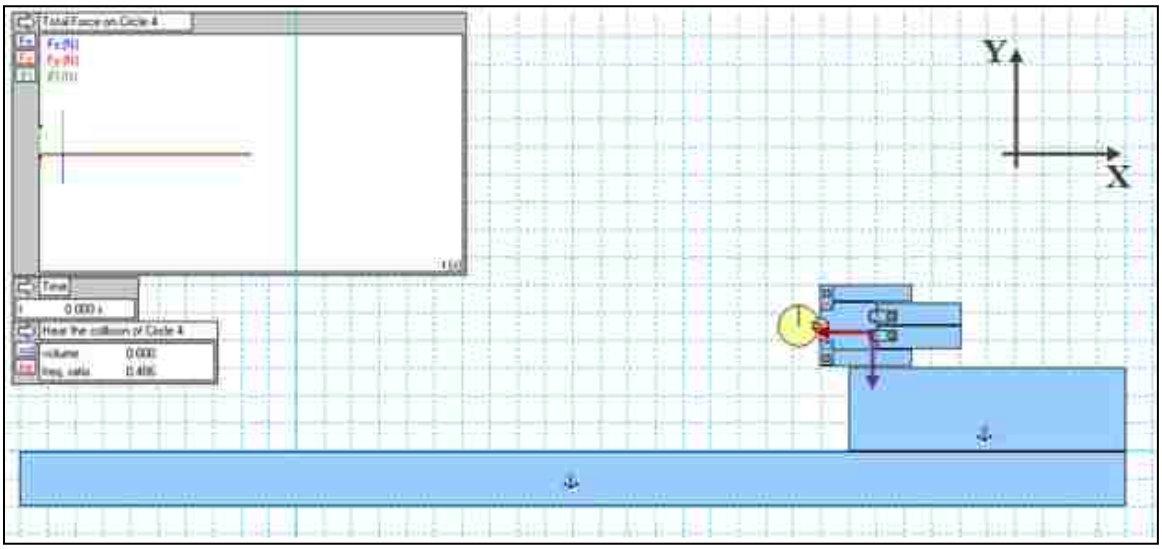

Figure 198: 1.0 ft shortfall at V_x = -3.0 m/s. Initial State.

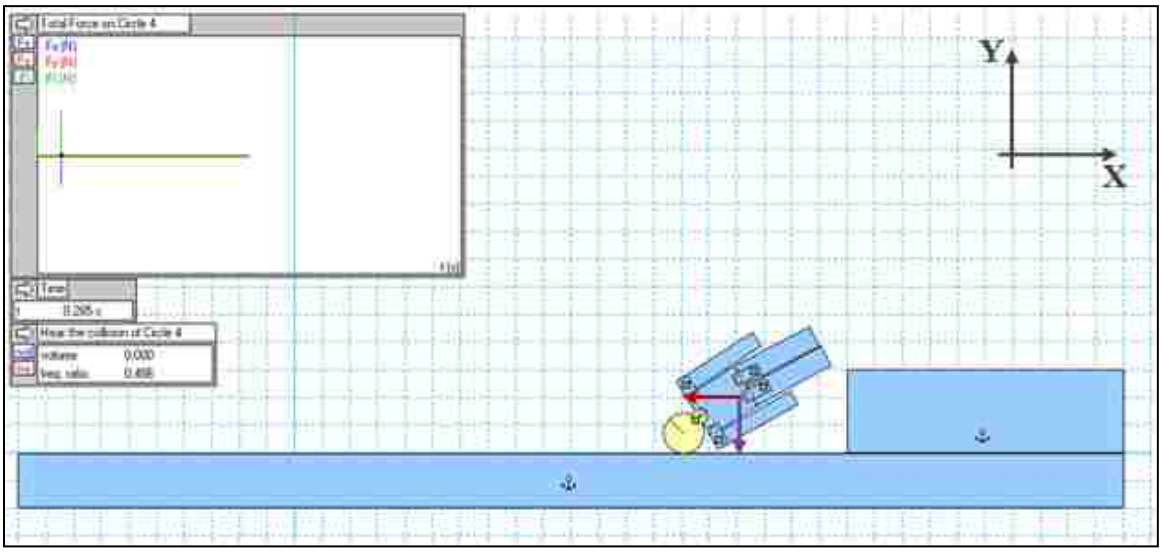

Figure 199: 1.0 ft shortfall at V_x = -3.0 m/s. Head and Ground Impact.

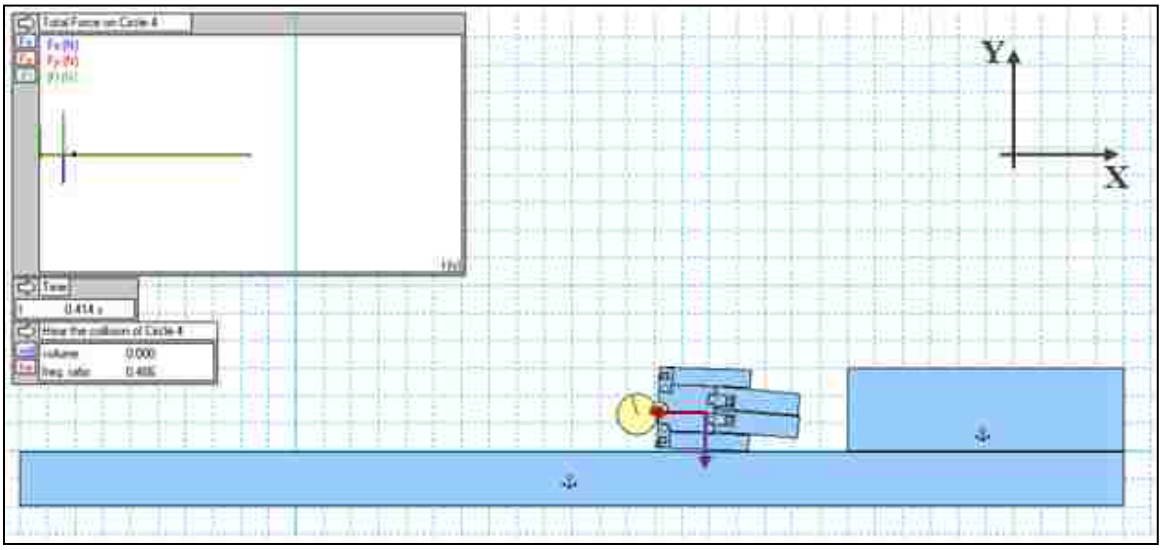

Figure 200: 1.0 ft shortfall at V_x = -3.0 m/s. Lower-Left-Arm and Ground Impact.

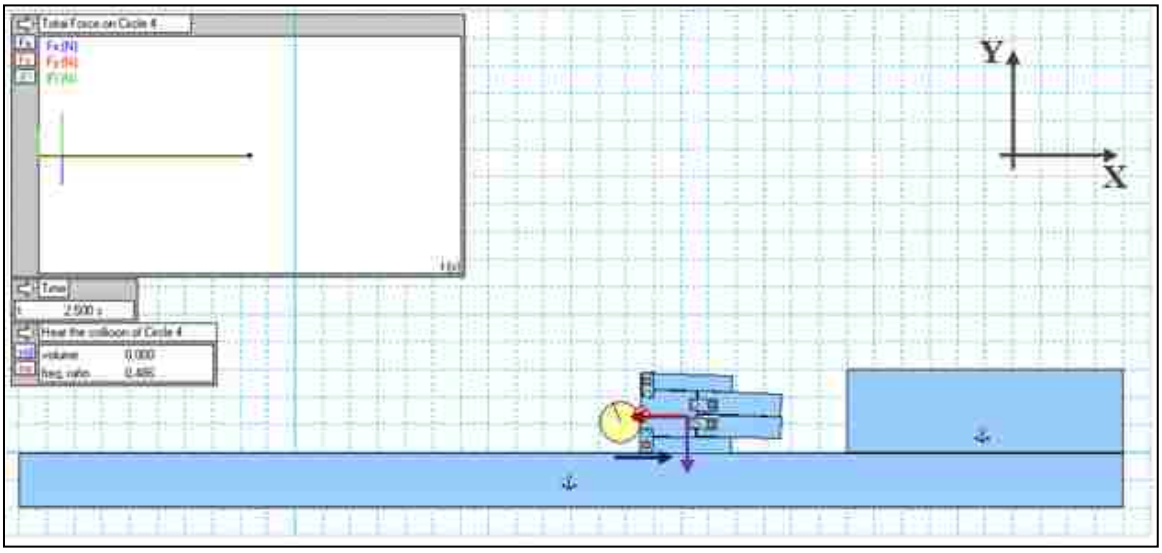

Figure 201: 1.0 ft shortfall at V_x = -3.0 m/s. Final State.

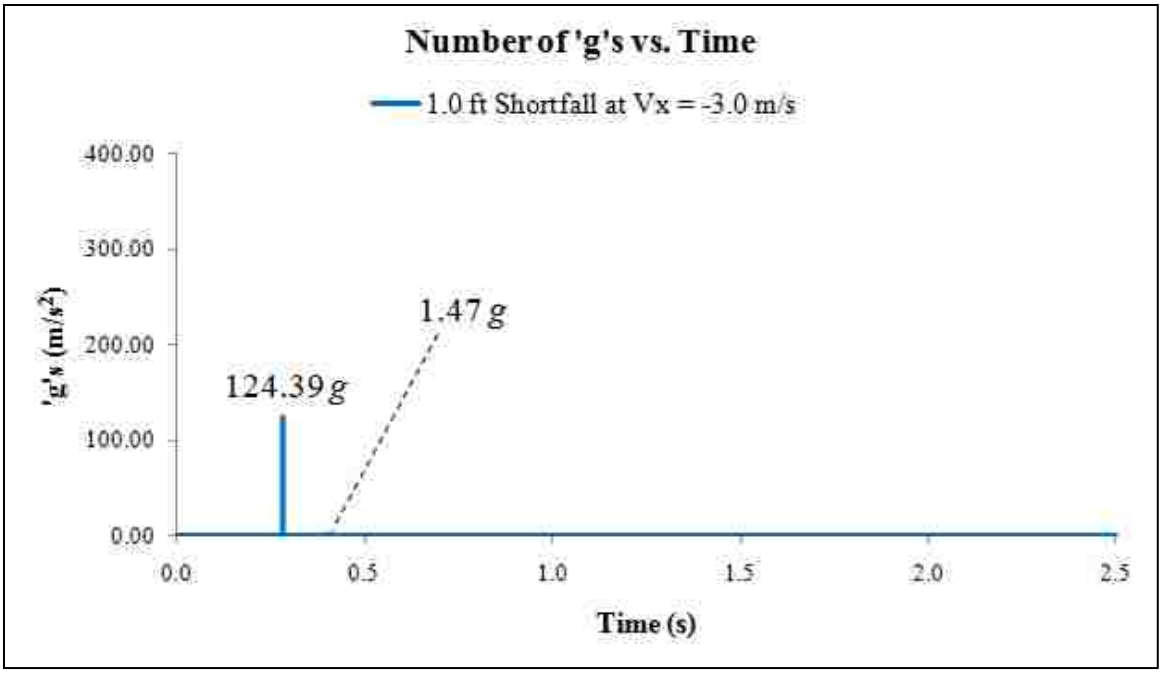

Chart 31: 1.0 ft shortfall at V_x = -3.0 m/s. Number of 'g's vs. Time.

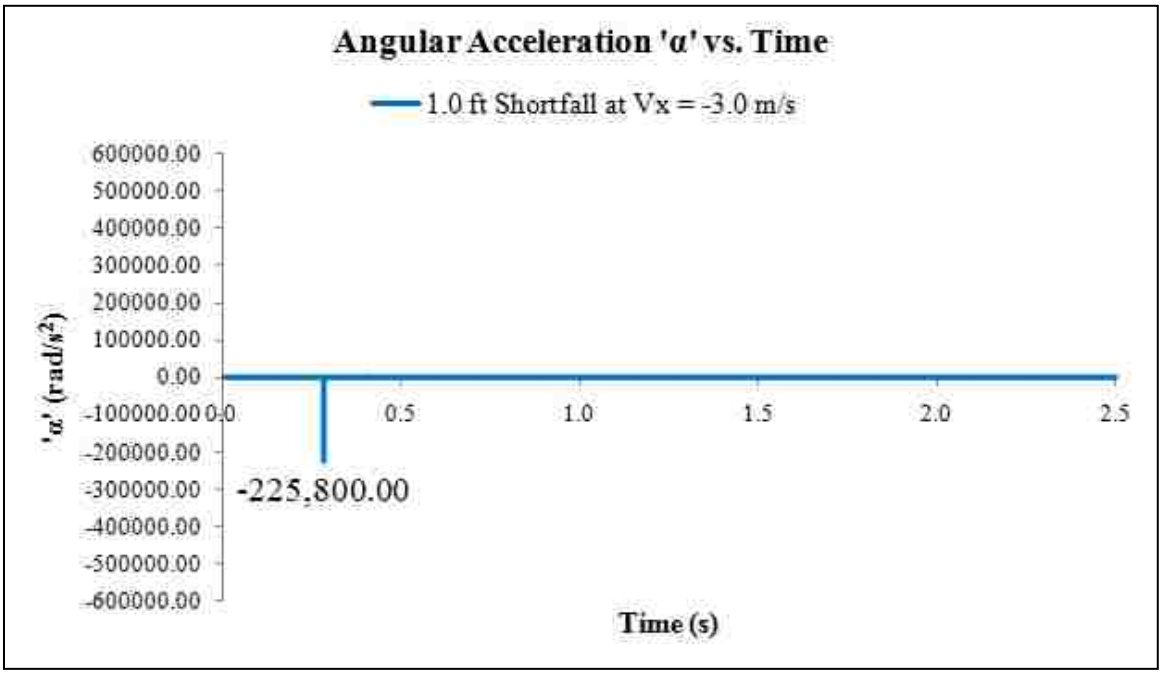

Chart 32: 1.0 ft shortfall at V_x = -3.0 m/s. Angular Acceleration 'α' vs. Time.

7-6-9 Shortfall Simulation from '1.5 ft' at V_x = '-3.0 m/s'

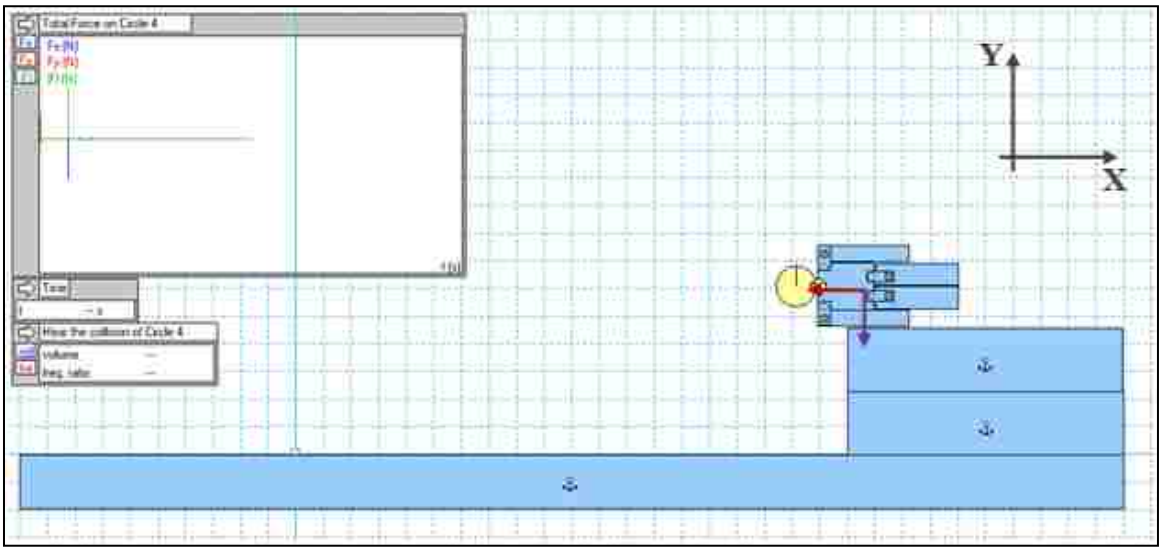

Figure 202: 1.5 ft shortfall at V_x = -3.0 m/s. Initial State.

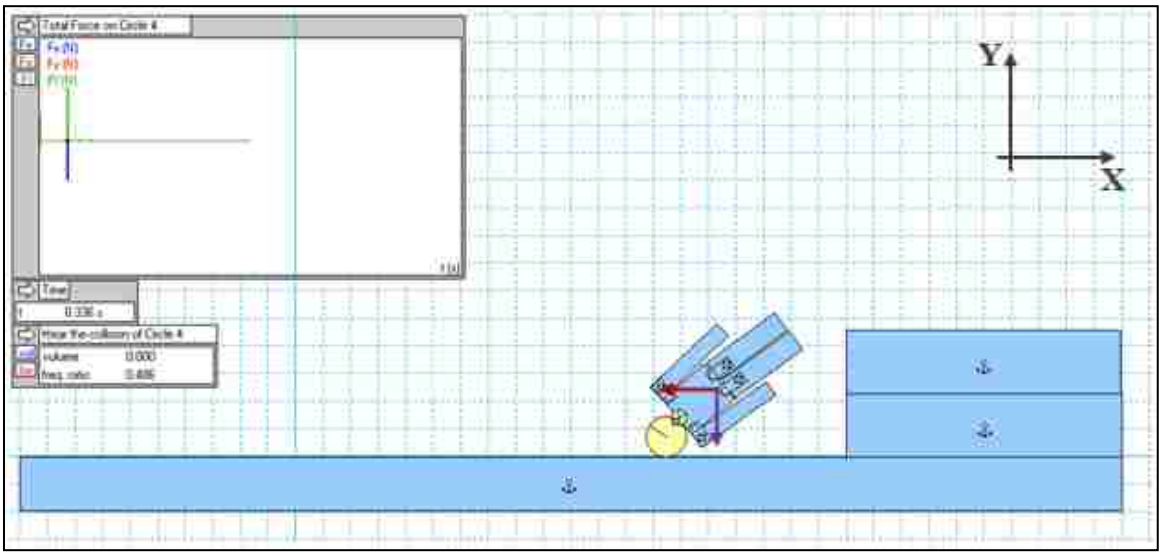

Figure 203: 1.5 ft shortfall at V_x = -3.0 m/s. Head and Ground Impact.

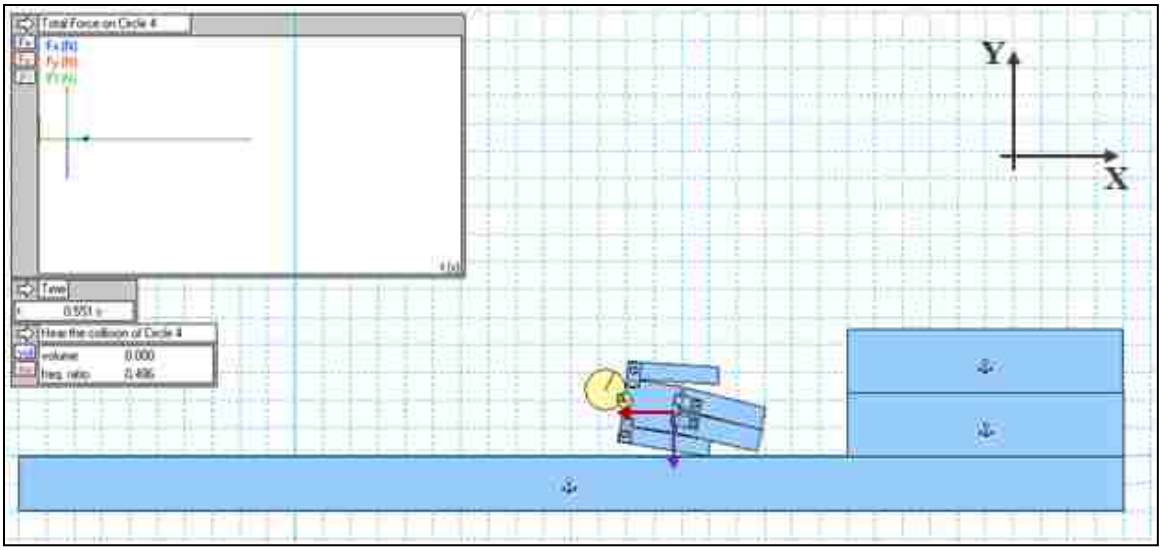

Figure 204: 1.5 ft shortfall at V_x = -3.0 m/s. Lower-Left-Arm and Ground Impact.

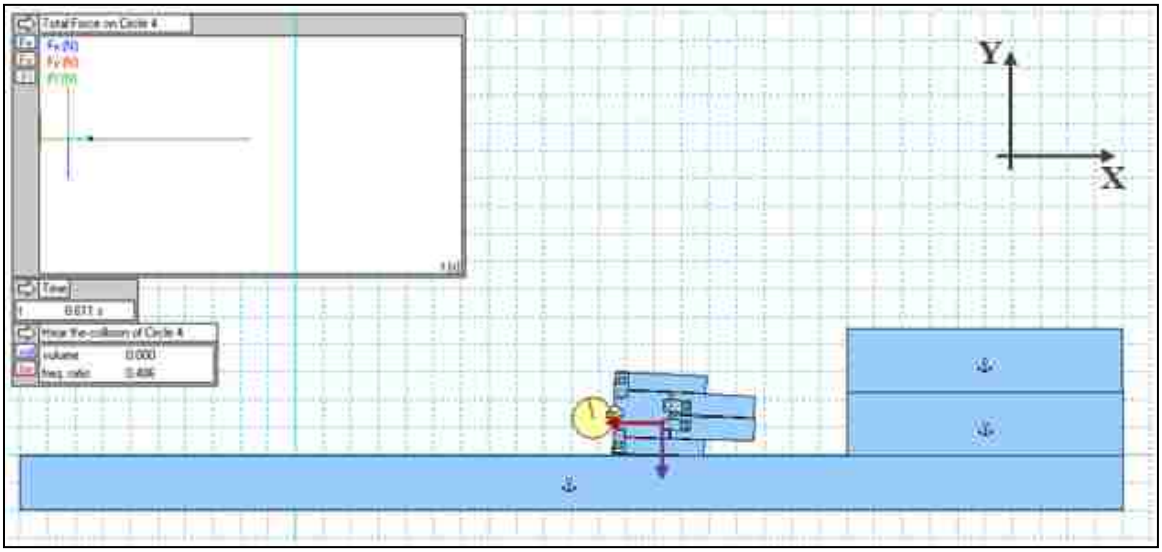

Figure 205: 1.5 ft shortfall at V_x = -3.0 m/s. Landing on the Left-Shoulder/Arm.

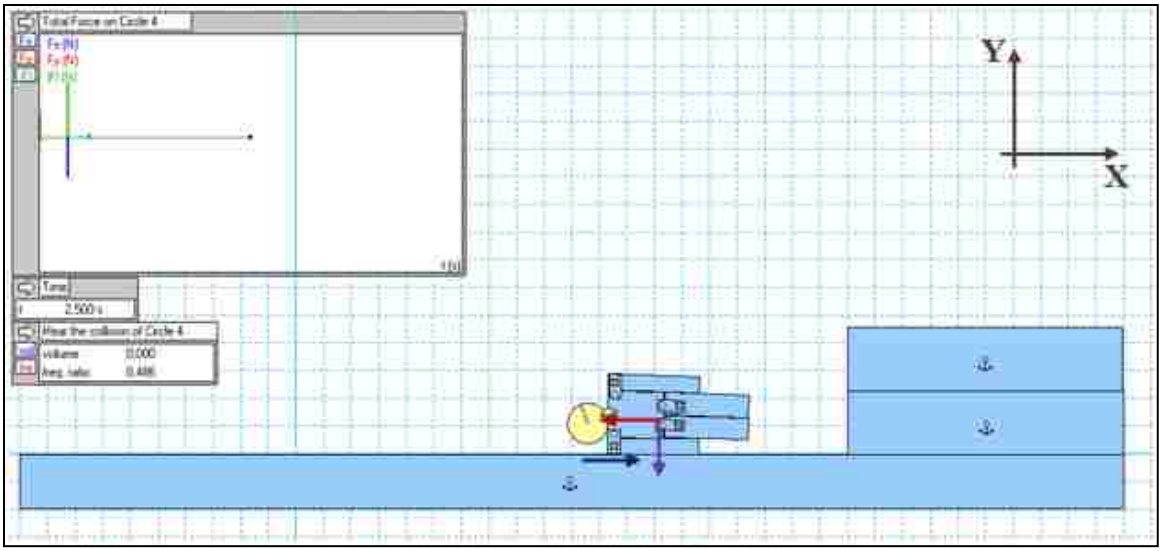

Figure 206: 1.5 ft shortfall at V_x = -3.0 m/s. Final State.

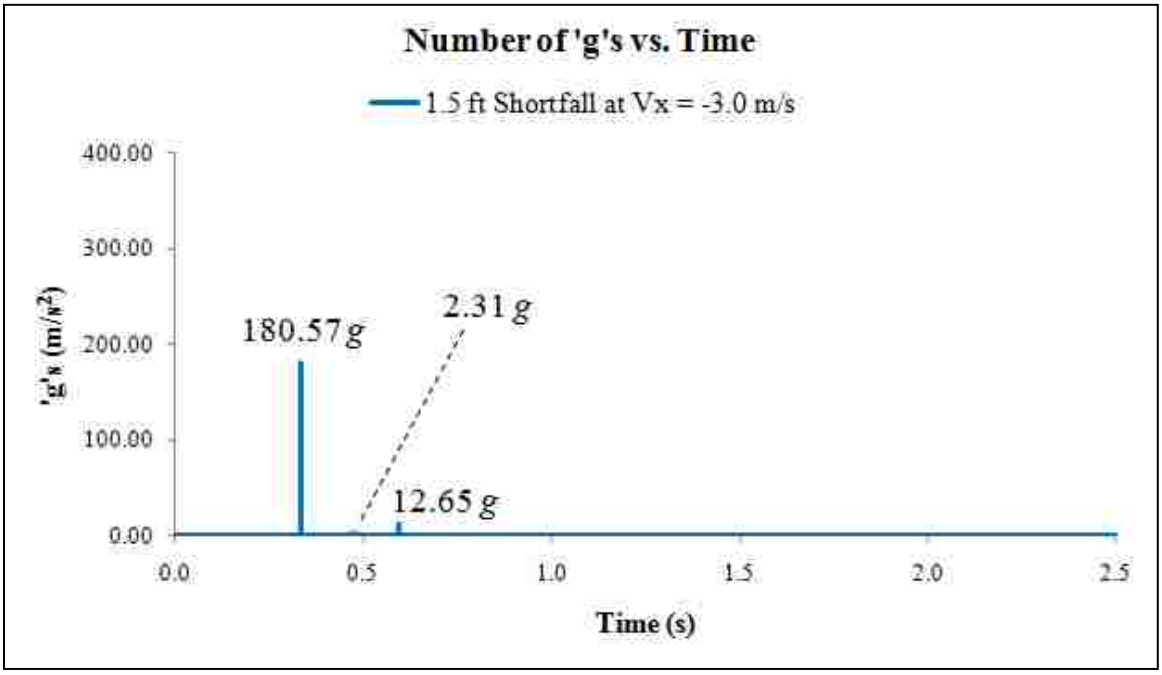

Chart 33: 1.5 ft shortfall at V_x = -3.0 m/s. Number of 'g's vs. Time.

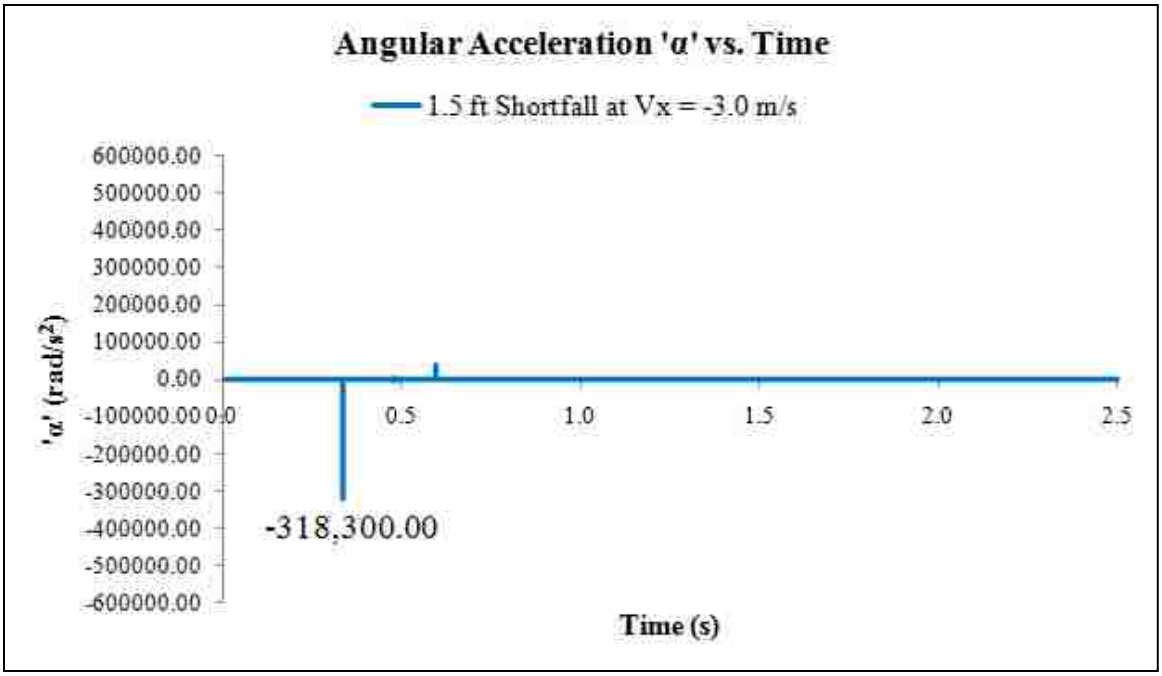

Chart 34: 1.5 ft shortfall at V_x = -3.0 m/s. Angular Acceleration ‘α’ vs. Time.

7-6-10 Shortfall Simulation from '2.0 ft' at V_x = '-3.0 m/s'

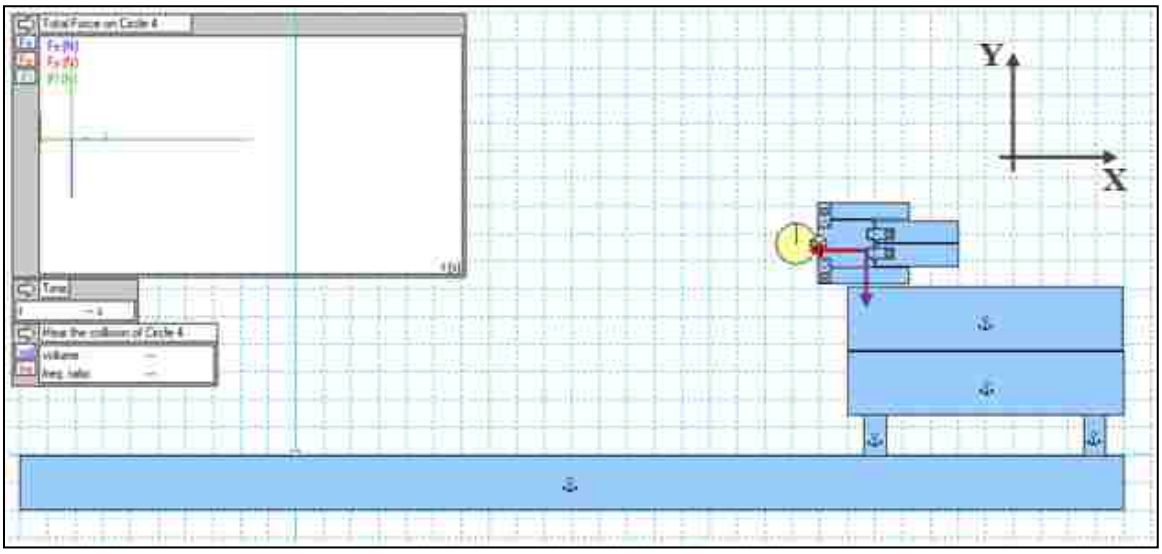

Figure 207: 2.0 ft shortfall at V_x = -3.0 m/s. Initial State.

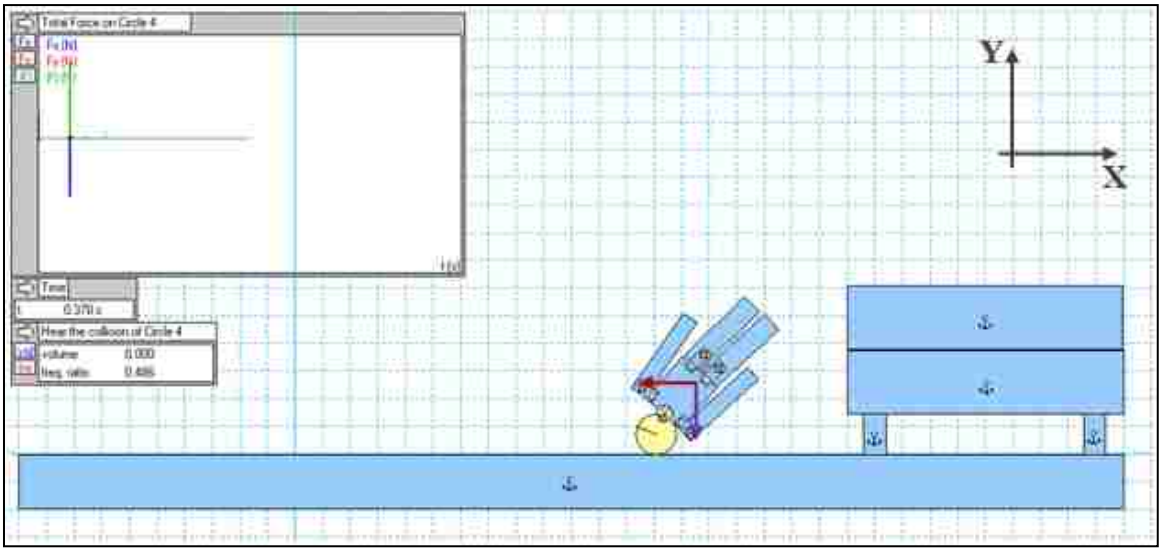

Figure 208: 2.0 ft shortfall at V_x = -3.0 m/s. Head and Ground Impact.

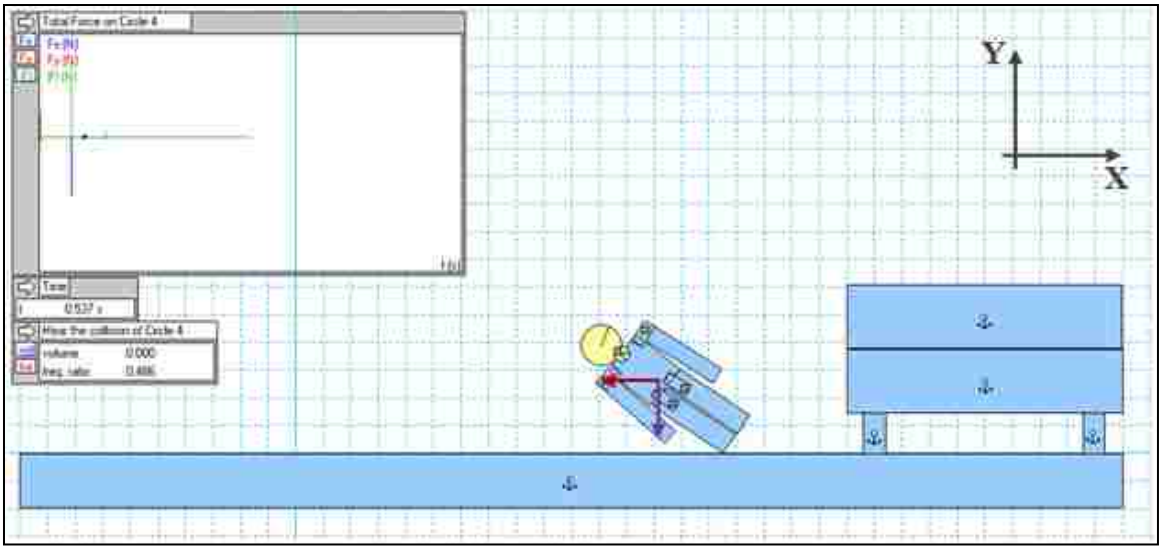

Figure 209: 2.0 ft shortfall at V_x = -3.0 m/s. Lower-Left-Arm/Leg and Ground Impact.

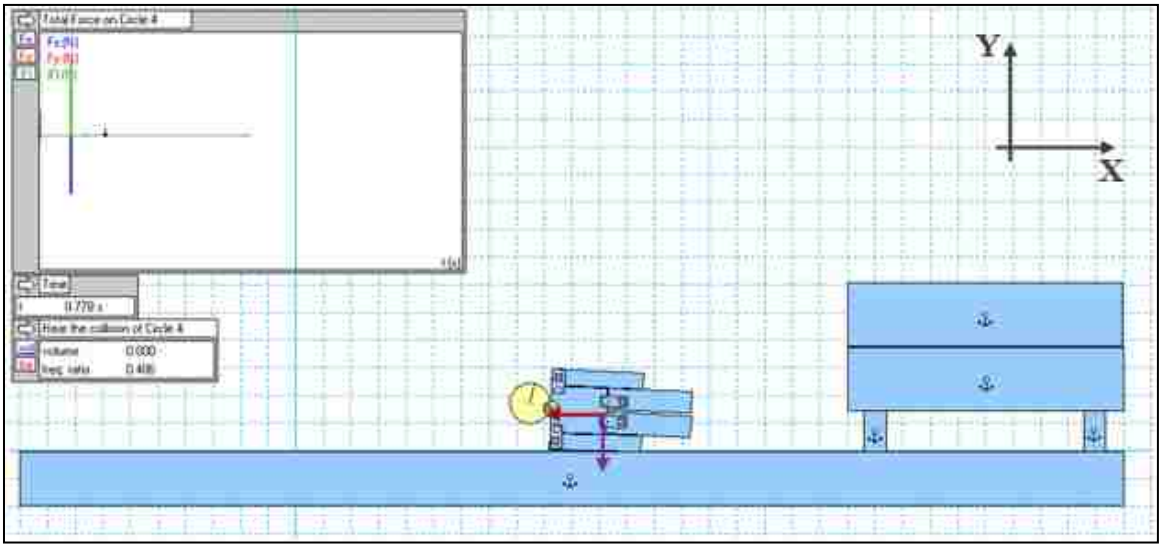

Figure 210: 2.0 ft shortfall at V_x = -3.0 m/s. Landing on the Left-Shoulder/Arm.

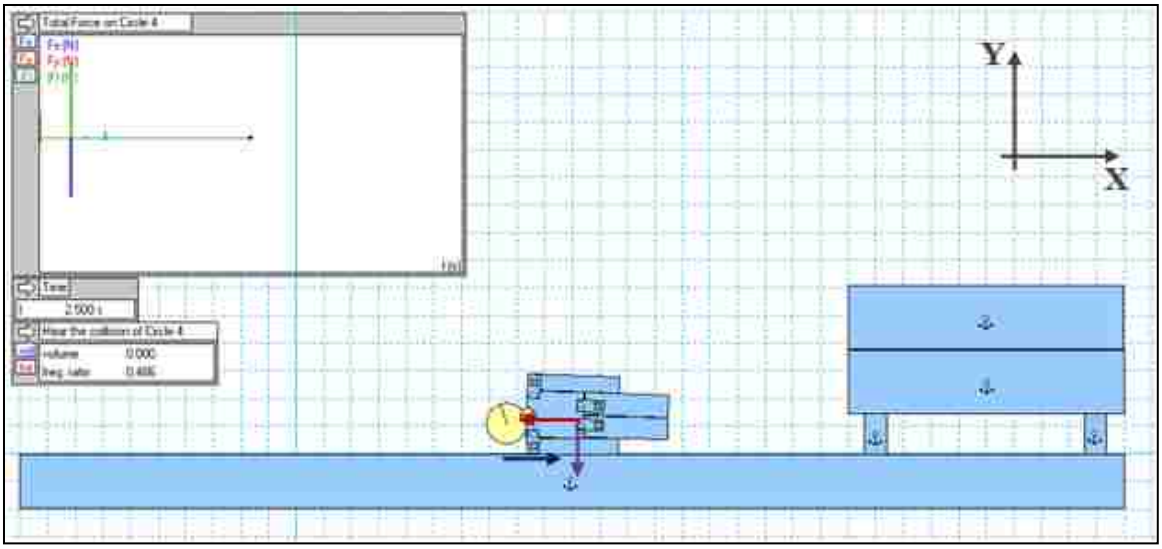

Figure 211: 2.0 ft shortfall at V_x = -3.0 m/s. Final State.

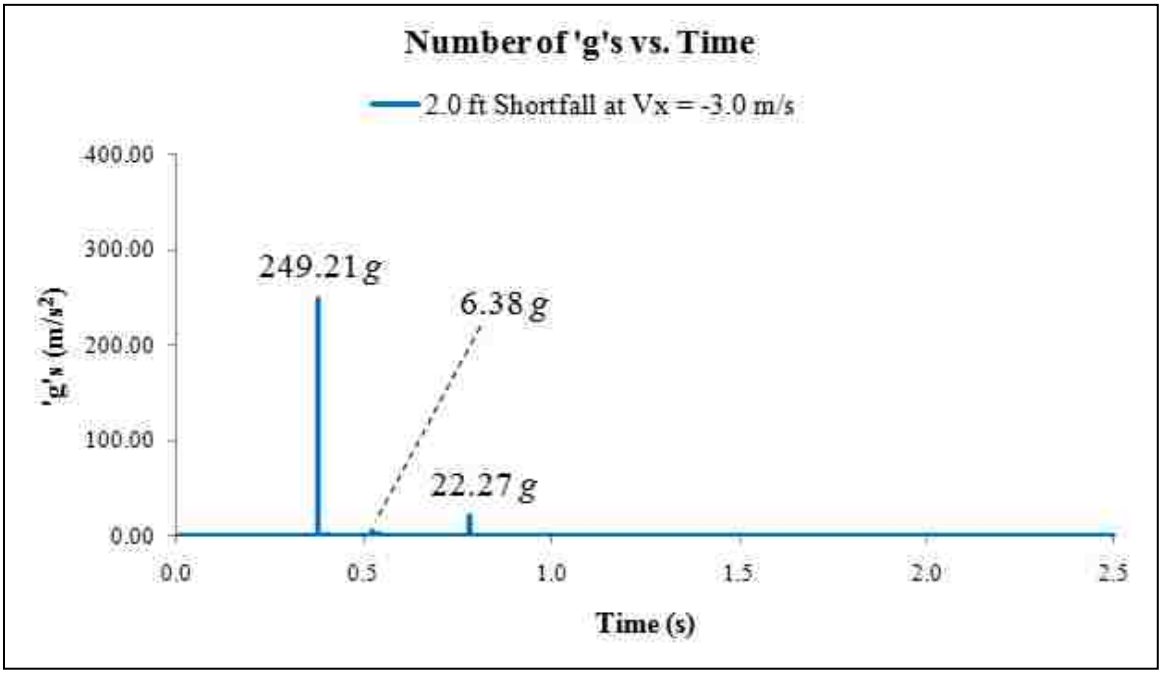

Chart 35: 2.0 ft shortfall at V_x = -3.0 m/s. Number of 'g's vs. Time.

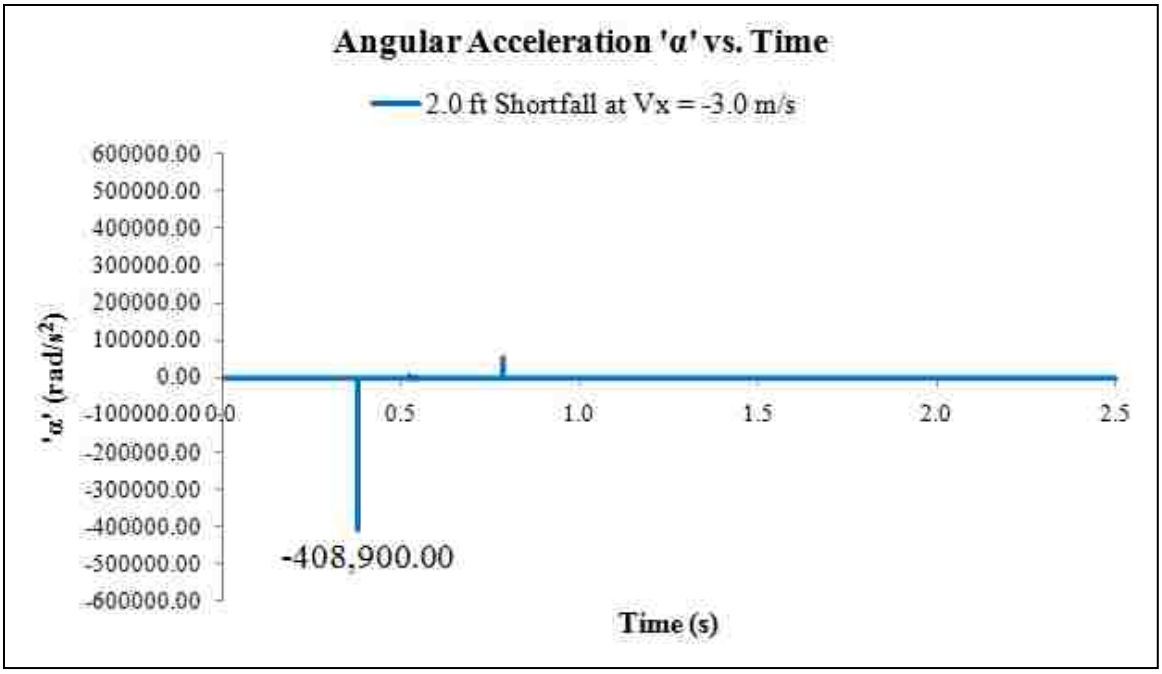

Chart 36: 2.0 ft shortfall at V_x = -3.0 m/s. Angular Acceleration ‘α’ vs. Time.

7-6-11 Shortfall Simulation from '2.5 ft' at V_x = '-3.0 m/s'

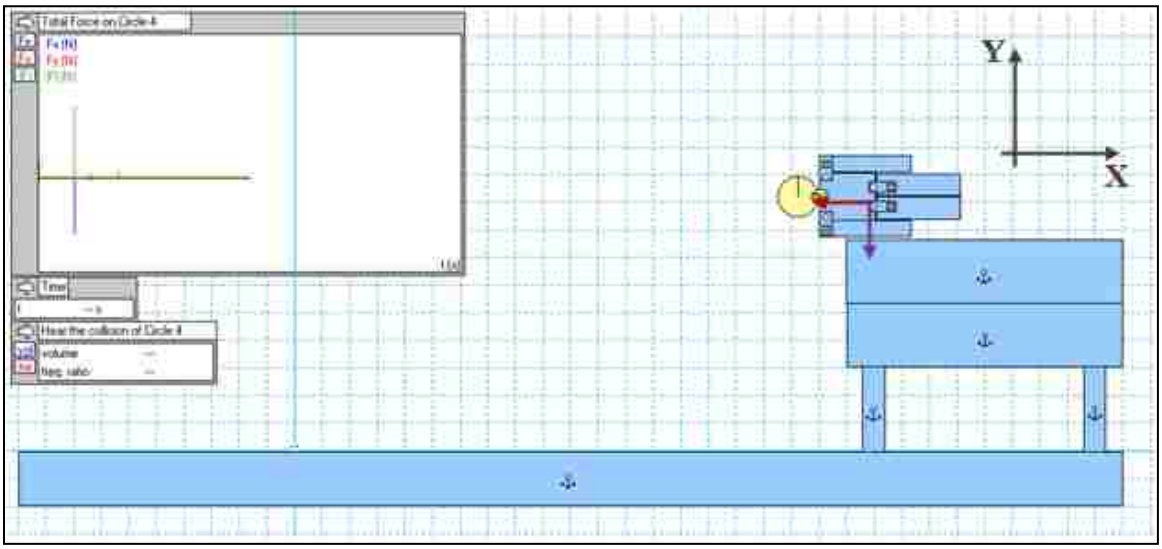

Figure 212: 2.5 ft shortfall at V_x = -3.0 m/s. Initial State.

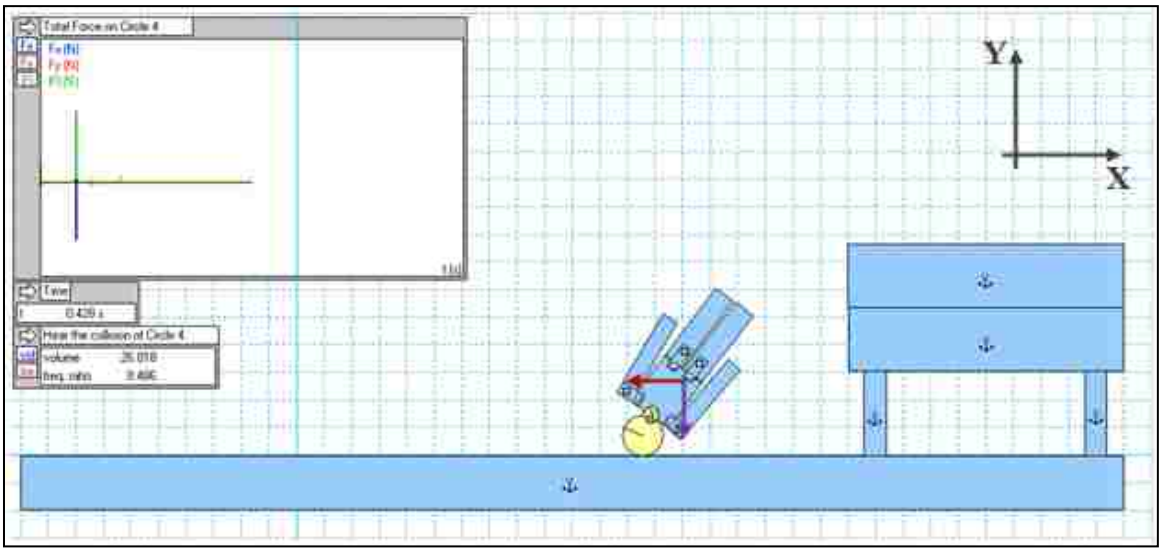

Figure 213: 2.5 ft shortfall at V_x = -3.0 m/s. Head and Ground Impact.

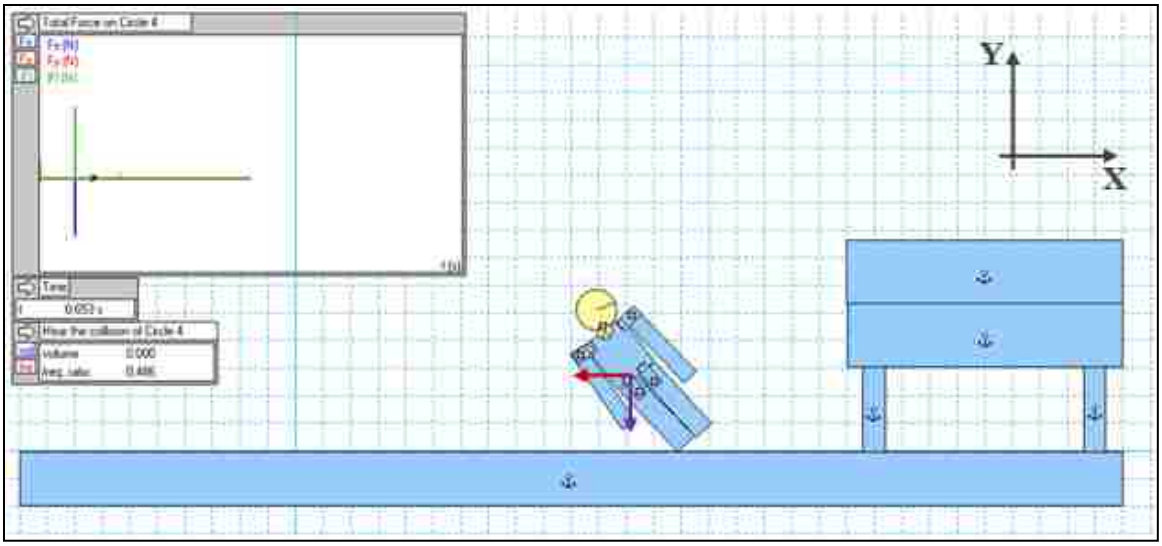

Figure 214: 2.5 ft shortfall at V_x = -3.0 m/s. Lower-Left-Leg and Ground Impact.

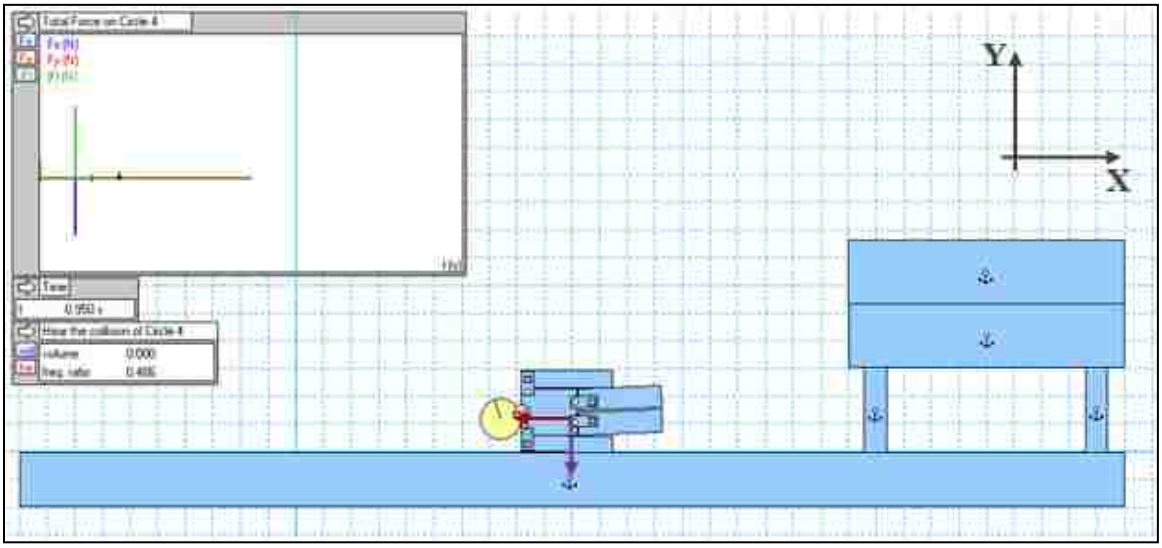

Figure 215: 2.5 ft shortfall at V_x = -3.0 m/s. Landing on the Left-Shoulder/Arm.

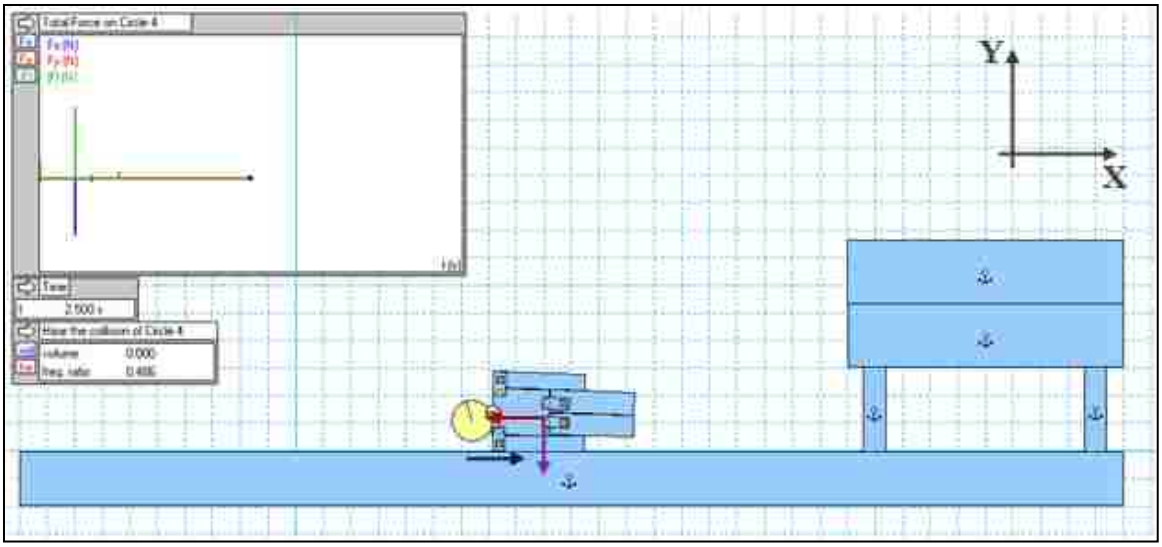

Figure 216: 2.5 ft shortfall at V_x = -3.0 m/s. Final State.

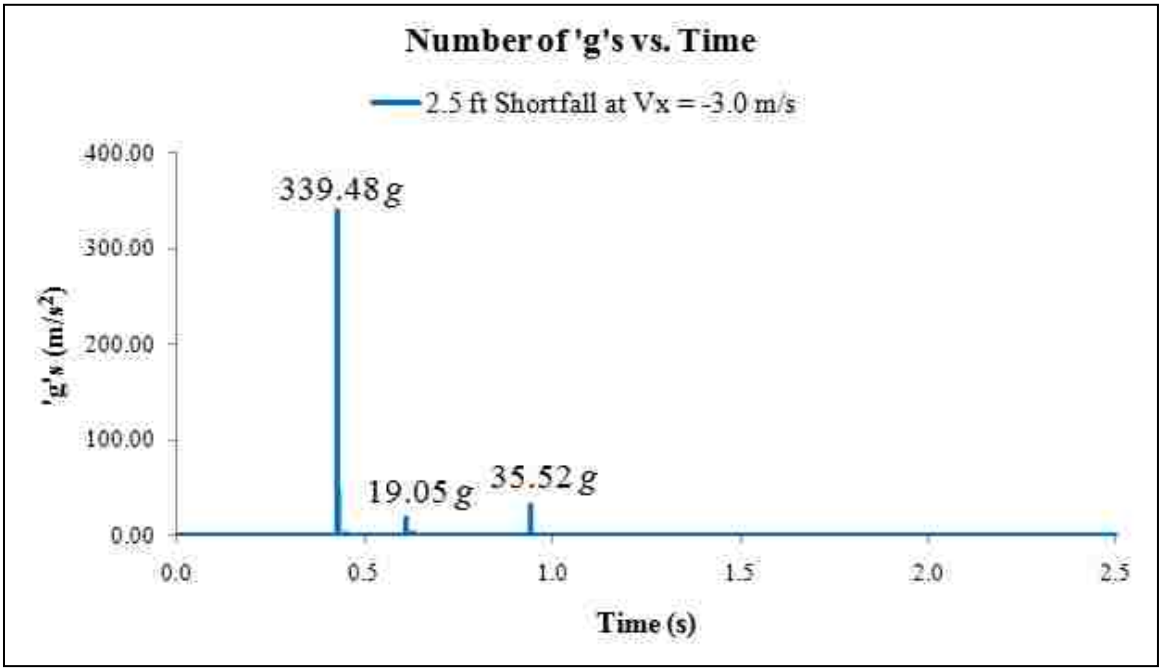

Chart 37: 2.5 ft shortfall at V_x = -3.0 m/s. Number of 'g's vs. Time.

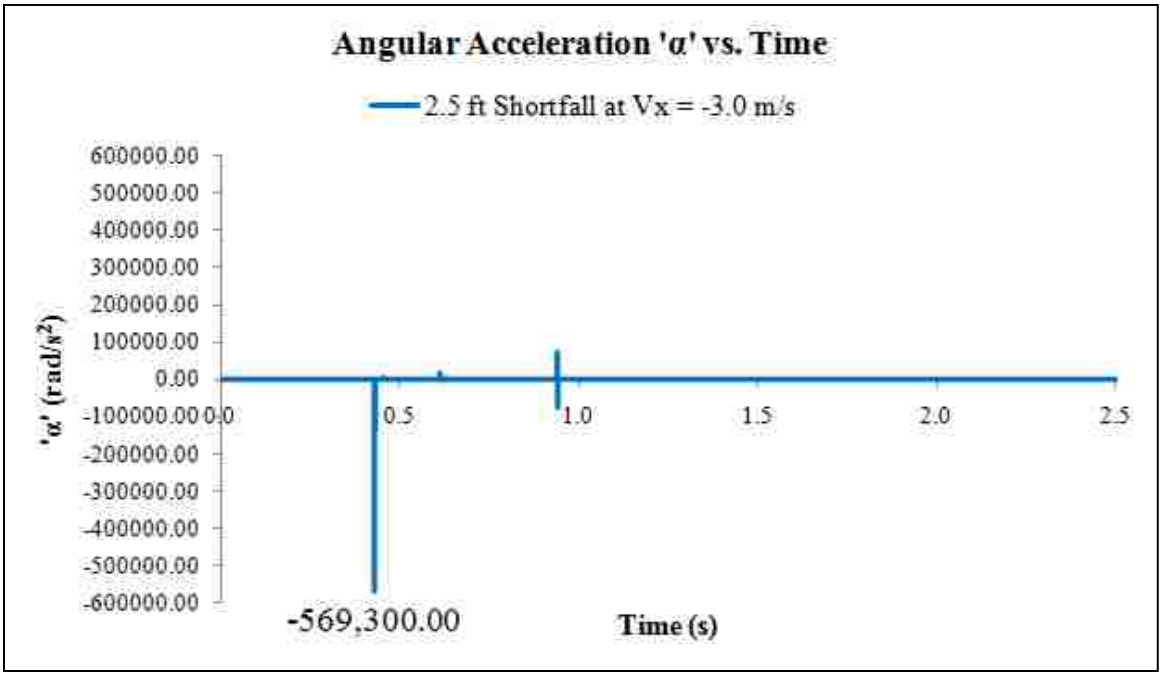

Chart 38: 2.5 ft shortfall at V_x = -3.0 m/s. Angular Acceleration ‘α’ vs. Time.

7-6-12 Shortfall Simulation from '3.0 ft' at V_x = '-3.0 m/s'

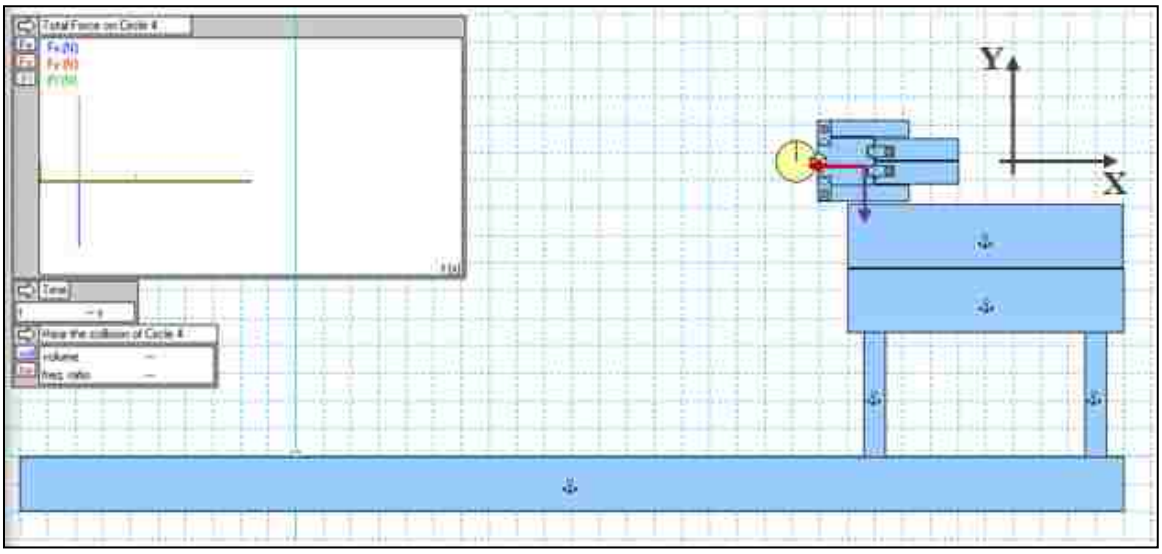

Figure 217: 3.0 ft shortfall at V_x = -3.0 m/s. Initial State.

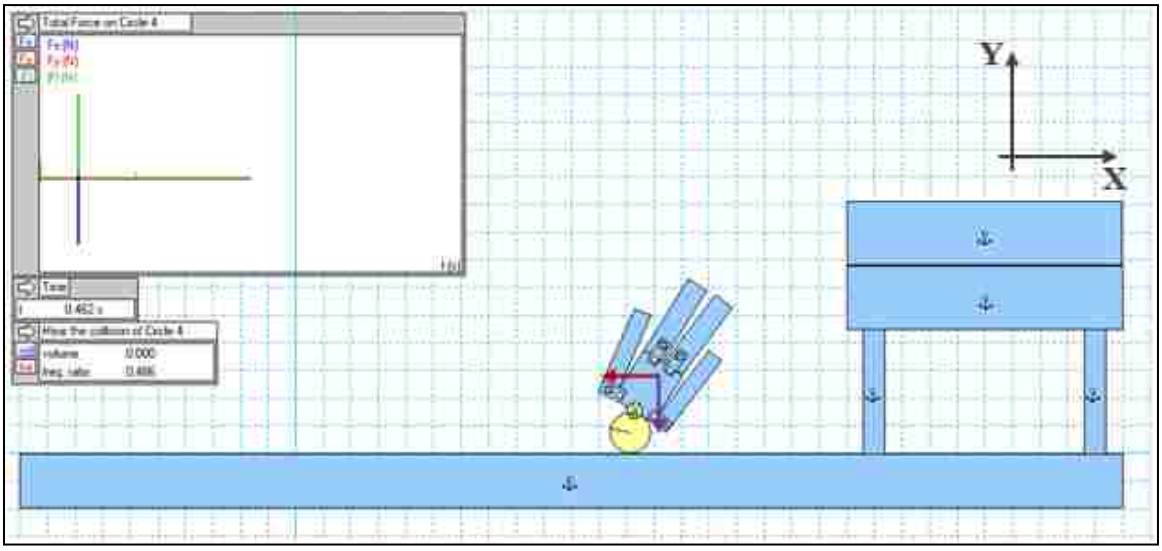

Figure 218: 3.0 ft shortfall at V_x = -3.0 m/s. Head and Ground Impact.

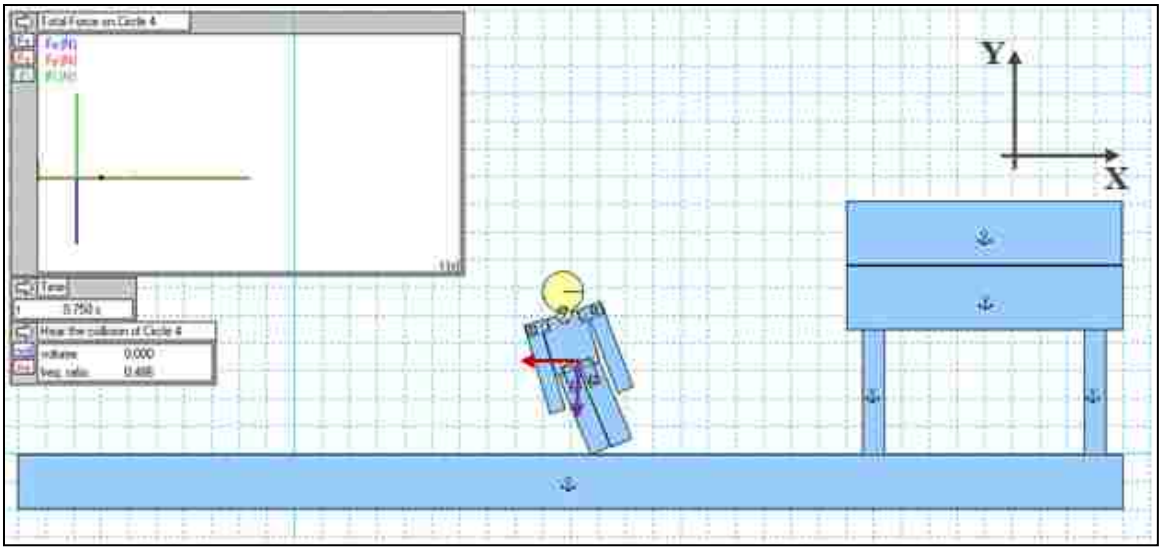

Figure 219: 3.0 ft shortfall at V_x = -3.0 m/s. Lower-Left-Leg and Ground Impact.

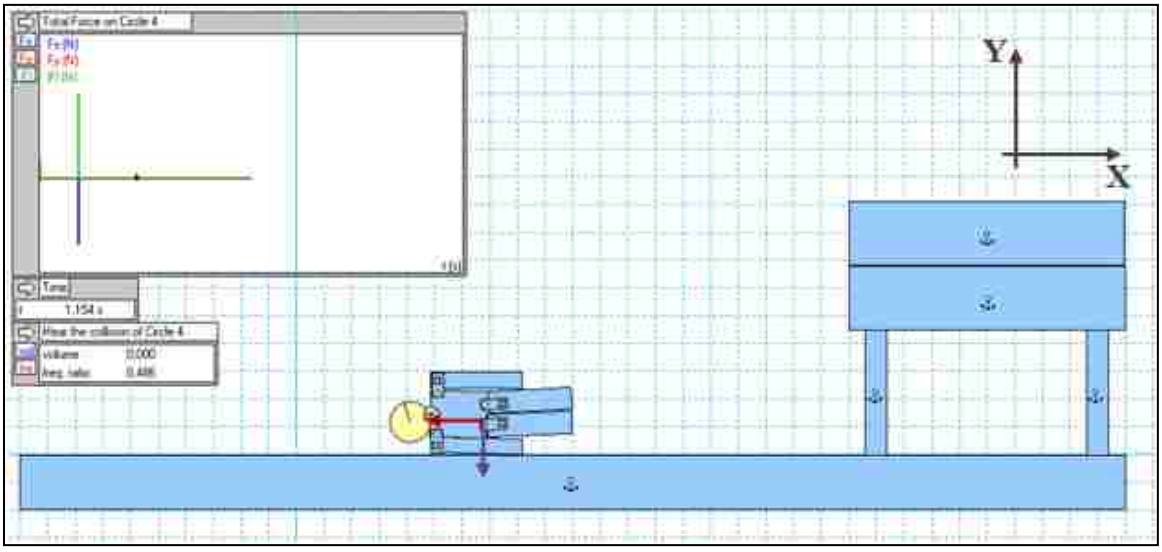

Figure 220: 3.0 ft shortfall at V_x = -3.0 m/s. Landing on the Left-Shoulder/Arm.

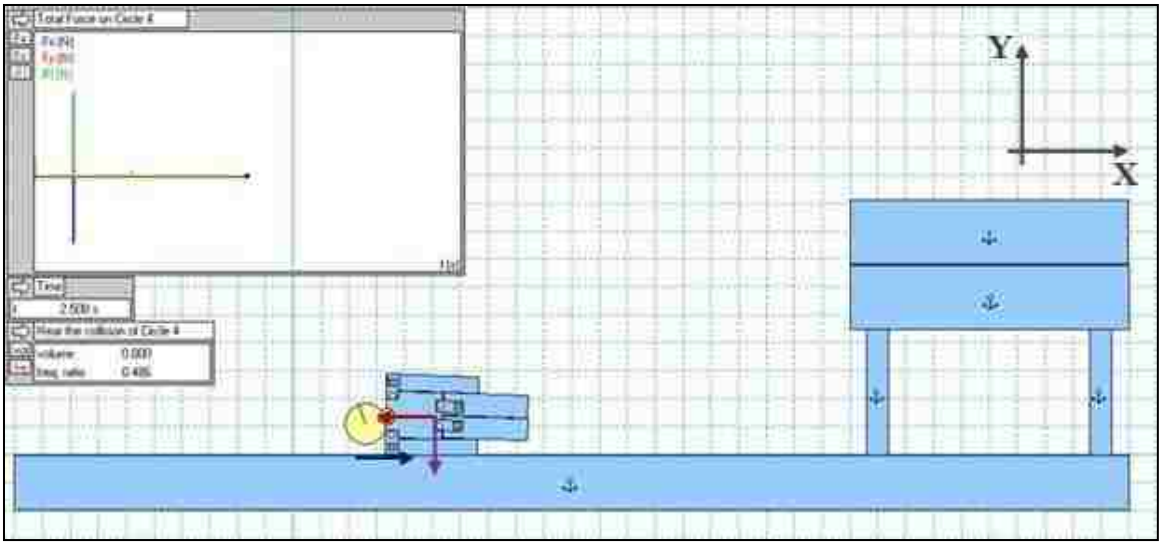

Figure 221: 3.0 ft shortfall at V_x = -3.0 m/s. Final State.

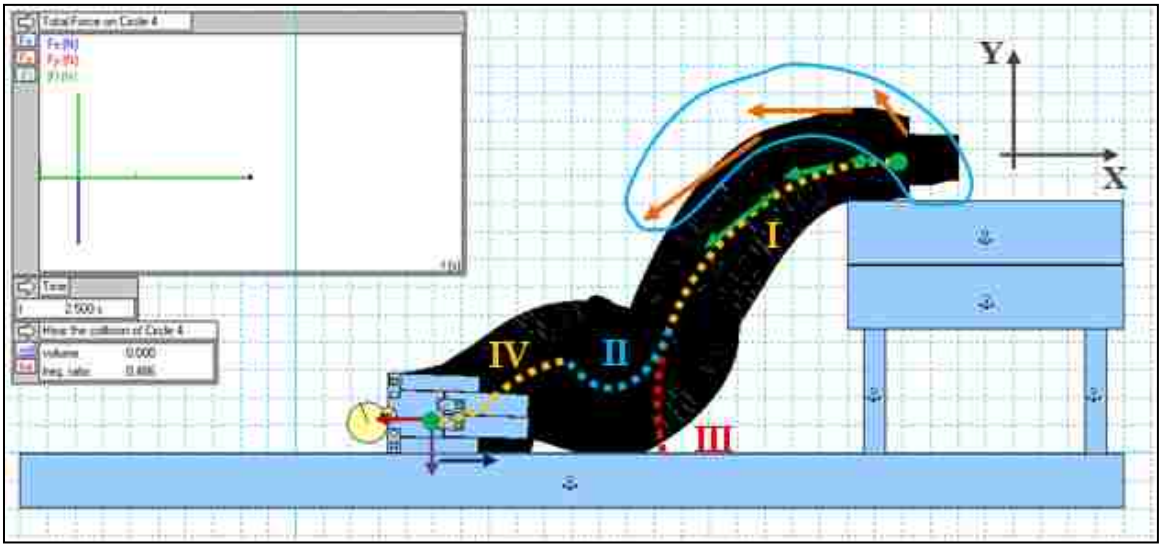

Figure 222: 3.0 ft shortfall at V_x = -3.0 m/s. Path of Movement.

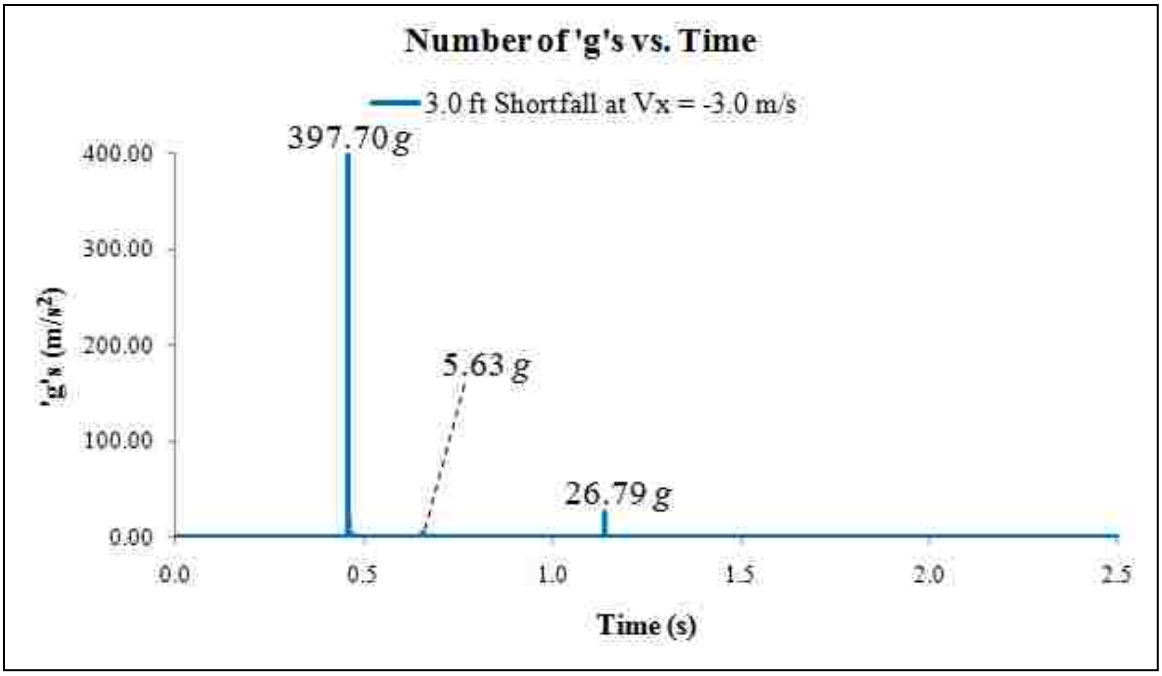

Chart 39: 3.0 ft shortfall at V_x = -3.0 m/s. Number of 'g's vs. Time.

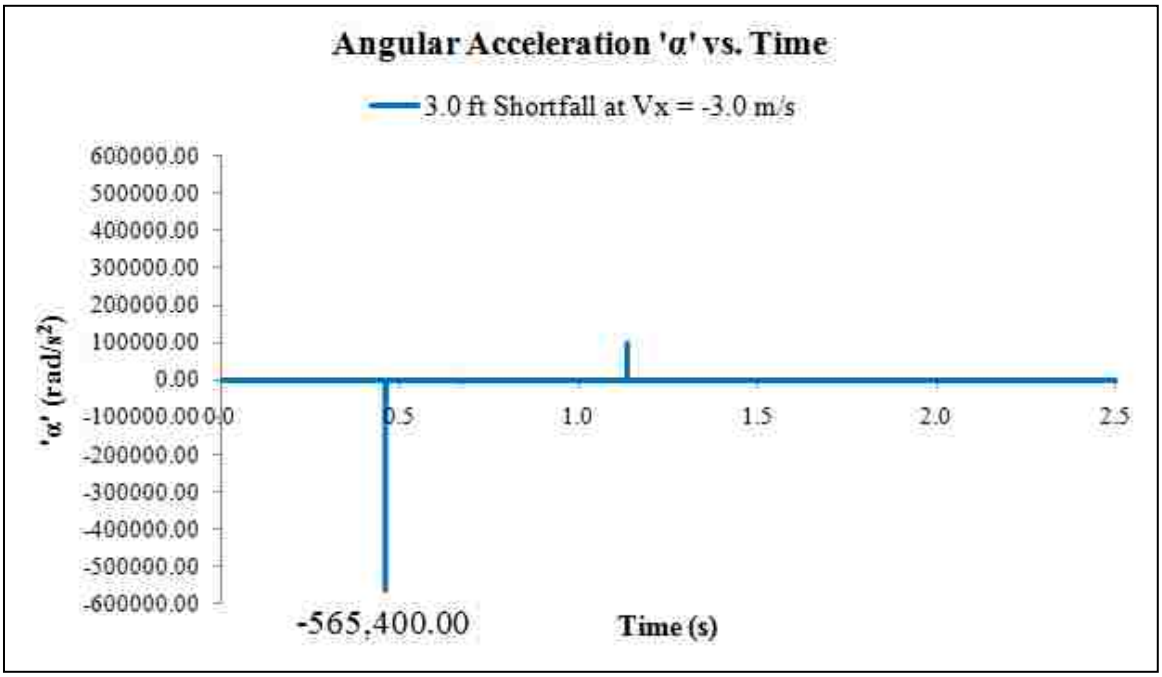

Chart 40: 3.0 ft shortfall at V_x = -3.0 m/s. Angular Acceleration 'α' vs. Time.

7-7 Discussions

7-7-1 General Movement Dynamics Involved in each shortfall Simulation

The following six subsections discuss the results obtained from each individual shortfall simulation that were categorized

The discussions regarding all the results presented above will be presented in three main categories. The first discussion-category will discuss the results regarding the first simulation group consisting of six simulations conducted at $\mathbf{V_x}$ = -1.0 m/s. The second discussion-category will discuss the results regarding the first simulation group consisting of six simulations conducted at $\mathbf{V_x}$ = -3.0 m/s. The third discussion-category will compare the obtained results regarding both simulation groups.

Before discussing the results, it is better to first discuss the dynamical movements present in each shortfall simulation. Let's reiterate that the horizontal velocity $\mathbf{V_x}$, involved in each shortfall simulation is a *continuously* applied horizontal velocity. Therefore, the movement of the child's model cannot be categorized as *Projectile Motion*. However, the involved dynamics in each model are very similar to the dynamics involved in *Projectile Motion*.

The horizontal pulling/pushing forces induced by the horizontal velocity $\mathbf{V_x}$, the vertical pulling forces induced by the gravitational acceleration g = -9.81 m/s^2 as well as the frictional forces between the child's body members and the surfaces of the furniture and the ground, all dictate the child's movement-pattern in each simulation (see Fig. 160).

To be more precise, the applied horizontal velocity $\mathbf{V_x}$ as well as the gravitational acceleration, g = -9.81 m/s^2 are the driving forces that cause the child's body to move/fall. The frictional forces on the other hand are the stopping forces. The horizontal velocity pulls/pushes the child's body to the left. At the same time gravity pulls the body towards the ground. Similar to the dynamics seen during a *Projectile Motion* scenario, regardless of the forces induced by the horizontal velocity $\mathbf{V_x}$, the gravitational force will always have the same effect on the child's body. Therefore, the extent of the child's advancement into the negative regime solely depends on the magnitude of the horizontal velocity $\mathbf{V_x}$. At a low horizontal velocity the gravitational forces will outweigh the induced horizontal pulling/pushing forces of $\mathbf{V_x}$. Hence, under a low $\mathbf{V_x}$ circumstance, naturally the child's body will end up landing in close vicinity of the furniture. However, at a high horizontal velocity the horizontal forces will have a higher contribution in the overall motion of the child's body. Hence, under a high $\mathbf{V_x}$ circumstance, naturally the child's body will end up landing further away from the furniture.

Based on the arguments made in the above paragraph, at a low horizontal velocity, for instance $\mathbf{V_x}$ = -1.0 m/s, the child's body will not really advance far towards the negative horizontal regime of the *x*-axis. However, if the child would have a very high horizontal velocity, for instance $\mathbf{V_x}$ = -100.00 m/s, it would relatively advance far into the negative horizontal regime of the *x*-axis.

The short furniture height also plays big role regarding the child's landing location. The taller the furniture, the more time will be available to the horizontal velocity $\mathbf{V_x}$, to pull/push the child's body to the left. Hence, it will land further to left

of the furniture. The shorter the furniture, the less time will be available to the horizontal velocity $\mathbf{V_x}$, to pull/push the child's body to the left. Hence, it will land closer to left of the furniture.

7-7-2 Simulations Conducted at V_x = '-1.0 m/s'

The following six subsections discuss the results obtained from each individual shortfall simulation that were categorized within the first simulation group, namely shortfall simulations incorporating a horizontal velocity of $\mathbf{V_x}$ = -1.0 m/s.

7-7-2-1 Shortfall Simulation from '0.5 ft' at V_x = '-1.0 m/s'

Fig. 162 through Fig. 164 represent the main dynamical stages during a shortfall simulation of a six months old child from a furniture with a height of 0.5 ft. Fig. 162 shows the child at the beginning of the simulation. Once the simulation starts both driving forces, namely the red horizontal force induced by $\mathbf{V_x}$ as well as the purple gravitational force move the child's body to the left and downwards respectively. The combination of both of these applied forces makes the body to rotate in a *counter clock wise* (CCW) fashion around the upper left corner of the furniture. This CCW leftwards and downwards/falling motion continuous until the child experiences a *head-first* impact as shown in Fig. 163. During this impact the child is still leaning on the 0.5 ft furniture. As explained in Sec. 7-7-1, this occurs because of the short furniture's height as well as the low magnitude horizontal velocity of $\mathbf{V_x}$ = -1.0 m/s.

A head and left-shoulder impact shortly follows after the head and ground impact as seen in Fig. 163. Then the body slides to the left with the head and the left shoulder continuously touching the ground. As the body slides more and more towards the left, more and more weight is transferred to the ground. This causes the increase in the magnitude of the normal forces that the ground exerts to the

body. The blue frictional force is directly related to the magnitude of the normal force. Eqn. 19 and Eqn. 20 as well as Fig. 223 define the force of friction and its relation to the normal force.

$$(\boldsymbol{F}_f)_s = \mu_s * \boldsymbol{N} \quad \text{(Eqn. 19)}$$

$$(\boldsymbol{F}_f)_k = \mu_k * \boldsymbol{N} \quad \text{(Eqn. 20)}$$

- $(\boldsymbol{F}_f)_s$: *Static Force of Friction* directed parallel to the ground's surface and opposite to the direction of the rigid body's movement. The *Static Force of Friction* appears at the beginning (t= 0.0 sec) and end (t= 2.5 sec) of the simulation, where the body is not moving.

- $(\boldsymbol{F}_f)_k$: *Kinetic Force of Friction* directed parallel to the ground's surface and opposite to the direction of the rigid body's movement. The *Kinetic Force of Friction* appears during the motion of the body, i.e. when the body slides/moves on the furniture and/or the ground.

- μ_s: *Static* Friction Coefficient.

- μ_k: *Kinetic* Friction Coefficient.

- $\boldsymbol{N}$: Normal Force exerted on the rigid body by the ground. It is always directed perpendicular to the ground's surface. If gravitational force is the only vertical force experienced by the rigid body, $\boldsymbol{N}$'s magnitude is equal to the rigid body's mass multiplied by the earth's acceleration, i.e. the *weigh*t of the rigid body.

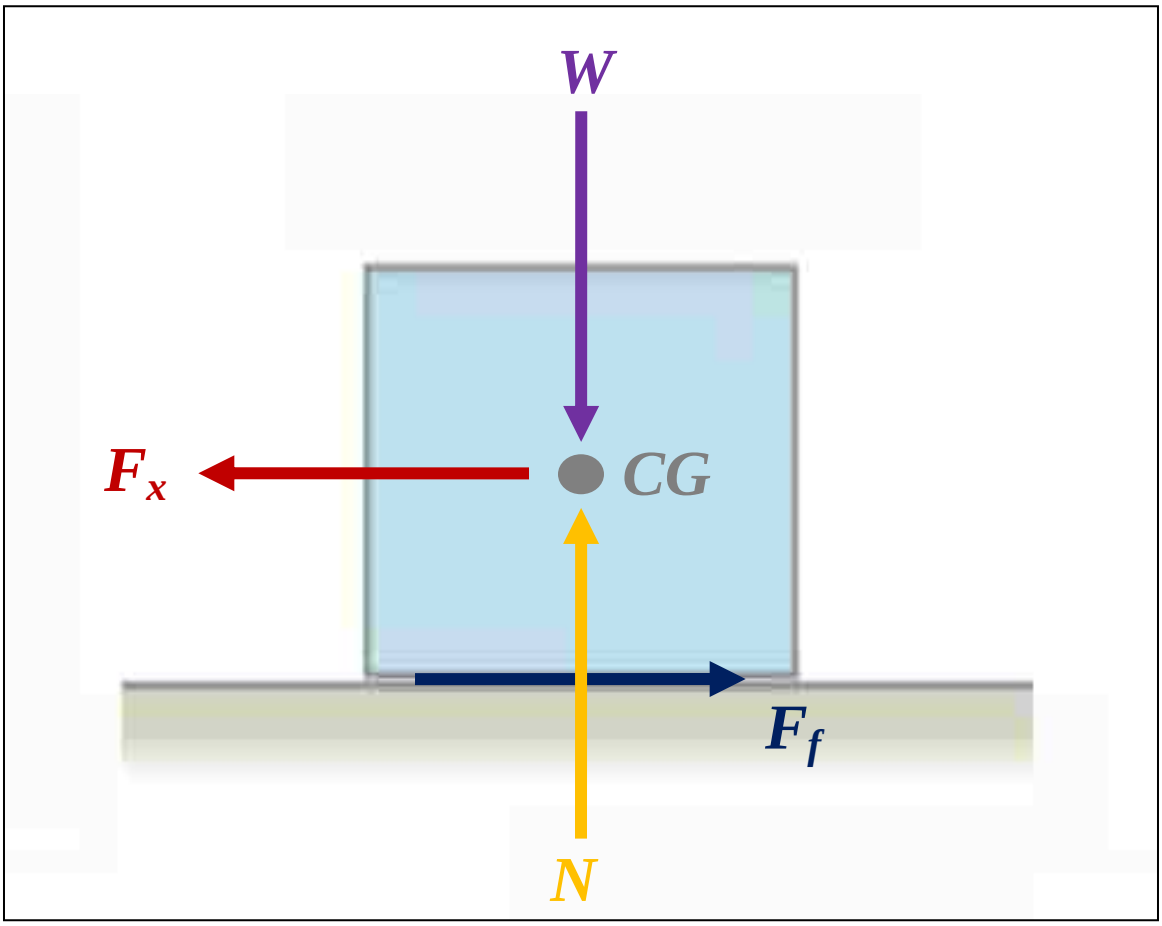

Figure 223: A towards the left moving rigid body exposed to horizontal and vertical forces. CG: Center of Gravity, W: Weight, F_x: Driving horizontal external force, F_f: Frictional Force & N: Normal force.

Eqn. 19 shows a direct relation between the static frictional force and the normal force. This equation applies to rigid bodies that are at *Static Equilibrium*. Eqn. 20 shows a direct relation between the kinetic frictional force and the normal force. This equation applies to rigid bodies that are not at *Static Equilibrium*, i.e. they are moving. Fig. 223 shows a moving rigid body. The externally applied force $\mathbf{F}_x$, drives the rigid body to the left. For the simulations conducted in this work, $\mathbf{F}_x$ is induced by the horizontal velocity $\mathbf{V}_x$. The normal force N, is exerted

by the ground to the rigid body. It will always have a 90° relation to the ground's surface. If weight W, is the only applied vertical force, the magnitude of N equals the W. This only applies if the ground's surface is perfectly horizontal and not tilted with respect to the horizon. $\mathbf{F}_f$ is the frictional force and will always lie parallel to the ground's surface in a direction opposing the direction of motion. The line-of-action of all forces, except the normal force N, pass through the rigid body's center of gravity (CG). The line-of-action of the frictional force, $\mathbf{F}_x$ is located between the rigid body and the ground's surface.

Going back to the discussion regarding the shortfall simulation of this subsection, as the body slides more and more towards the left, the kinetic frictional force continues to grow. The sliding continues until the magnitude of the kinetic frictional force equals the magnitude of the horizontal driving force. At this instance, the motion of the child's body stops and the child does not move anymore. Fig. 164 demonstrates the final position and configuration of the child. Note that the child's legs are still leaning on the furniture.

Chart 17 graphs the *NGS* (see Eqn. 18) experienced by the child's head as the simulation time progresses. As illustrated in this chart, throughout the simulation, on average, the child's head continues to experience a NGS equal to 1.0. This means that the child's head experiences a total-acceleration $|\mathbf{a}|$ (see Eqn. 17), equal to the earth's gravitational acceleration. Note that the NGS during the child's head and ground impact is equal to 1.288. This means that during the child's head and ground impact, the head experiences a total-acceleration $|\mathbf{a}|$ (see Eqn. 17), 1.288 times the earth's gravitational acceleration.

As mentioned in Sec. 7-6, throughout the simulation, Working Model 2D outputted the total-force **|F|** (see Eqn. 16). The NGS (see Eqn. 17) and the subsequent total-acceleration **|a|** (see Eqn. 17), were calculated from the outputted **|F|** values. The NGS of 1.288 g corresponds to a **|F|** of 113.76 N. According to Eqn. 8, when the child's mass (9.00 kg) is applied by the earth's gravitational acceleration (|-9.81| m/s), the child's *weight* can be obtained. By doing so, the child's weight equals 88.29 N. The division of the obtained **|F|** of 113.76 N by 88.29 N (child's weight) equals to 1.288. In other words, during the head and ground impact, the child's head experiences a force 1.288 times the entire weight of the child's body. Therefore, a shortfall from 0.5 ft at a horizontal velocity of $\mathbf{V_x}$ = -1.0 m/s results in a relatively soft head and ground impact.

Chart 18 graphs the *angular acceleration* α, experienced by the child's head as the simulation time progresses. It can be seen that during the first head and ground impact, the child's head experiences an angular acceleration equal to 0.00 rad/s^2. According to Cory et al., once the *magnitude* of angular acceleration experienced by a child's head equals or exceeds 10,000.00 rad/s^2, the child can experience serious to fatal cranial damages [97]. Therefore, an angular acceleration of 0.00 rad/s^2 does not lead to serious cranial damages.

For this simulation, the highest-magnitude *angular velocity* ω, was also retrieved from Working Model 2D. This angular velocity was equal to 0.00 rad/s. According to Cory et al., the threshold for serious to fatal cranial damages is: $\omega \geq$ 43.00 rad/s [97]. Therefore, during this simulation, the angular velocity experienced by the child's head does not lead to serious or fatal damages.

Summarizing the discussion for this subsection at a shortfall height of 0.5 ft and with a $\mathbf{V_x}$ = -1.0 m/s the child's head experiences almost the same amount of acceleration as the gravitational acceleration. During the head and ground impact, the child's head only experiences a total-acceleration 1.288 times higher than the earth's gravitational acceleration of 9.81 m/s^2. Moreover, throughout the simulation, the child's head experiences an angular acceleration equal to 0.00 rad/s^2 as well as an angular velocity equal to 0.00 rad/s.

7-7-2-2 Shortfall Simulation from '1.0 ft' at V_x = '-1.0 m/s'

Fig. 165 through Fig. 170 represent the main dynamical stages during a shortfall simulation of a six months old child from a furniture with a height of 1.0 ft. Fig. 165 shows the child at the beginning of the simulation. Once the simulation starts both driving forces, namely the red horizontal force induced by $\mathbf{V_x}$ as well as the purple gravitational force move the child's body to the left and downwards respectively. The combination of both of these applied forces makes the body to rotate in a CCW fashion around the upper left corner of the furniture. This CCW leftwards and downwards/falling motion continuous until the child experiences the first head and ground impact as shown in Fig. 166. During this impact the child is still leaning on the 1.0 ft furniture. As explained in Sec. 7-7-1, this occurs because of the short furniture's height as well as the low magnitude horizontal velocity of $\mathbf{V_x}$ = -1.0 m/s.

Upon the first head and ground impact, the body bounces back to the air and starts a *clock wise* (CW) rotation as it advances leftwards. This CW uplift continues until the child's head hits the left shoulder as shown in Fig. 167. This impact stops the body from the upwards advancement. Then, the body falls back and undergoes another CCW rotation until the second head and ground impact is experienced by the child as illustrated by Fig. 168. A second short rebound occurs followed by a second minute CCW uplift. Then the body falls back in a CW fashion and the third head and ground impact occurs as shown in Fig. 169. Then the body slides to the left. While doing so, the head lifts from the ground and leans against the right shoulder. This occurs because the torso and the left

shoulder become more and more parallel to the ground. As the body slides more and more towards the left, the kinetic frictional force continues to grow. The sliding continues until the magnitude of the kinetic frictional force equals the magnitude of the horizontal driving force. At this instance, the motion of the child's body stops and the child does not move anymore. Fig. 170 demonstrates the final position and configuration of the child. Note that the child's legs are still leaning on the furniture. However, the child has advanced more to the left regime of the *x*-axis compared to the child involved in a 0.5 ft shortfall. The reason for this further leftwards advancement is the higher elevation of the furniture. With a higher elevation, the horizontal driving force had more time to pull/push the body towards the left before landing.

Chart 19 graphs the *NGS* experienced by the child's head as the simulation time progresses. As illustrated in this chart, throughout the simulation, on average, the child's head continues to experience a NGS equal to 1.0. This means that the child's head experiences a total-acceleration $|\mathbf{a}|$, equal to the earth's gravitational acceleration. However, at the following instant the child's head experiences a higher acceleration compared to the earth's gravitational acceleration:

1. The First Head and Ground Impact. NGS = 51.85 g.

During the child's first head and ground impact, the child's head experiences a total-acceleration $|\mathbf{a}|$, 51.88 times higher than the earth's gravitational acceleration. The NGS of 51.85 g was calculated from a outputted $|\mathbf{F}|$ = 4,577.73

N. Similar to the calculations made in Sec. 7-7-2-1, the child, the division of the obtained |**F**| of 4,577.73 N by 88.29 N (child's weight) equals to 51.85. In other words, during the first head and ground impact, the child's head experiences a force 51.85 times the entire weight of the child's body. Therefore, a shortfall from 0.5 ft at a horizontal velocity of $\mathbf{V_x}$ = -1.0 m/s results in a relatively soft head and ground impact.

This shows that the first head and ground impact absorbed the majority of the energy potential and kinetic energy involved during the shortfall. Hence, it is imaginable that the consequent damages to the child's head, neck and spine originate from the first head and ground impact. However, the constant left and right movement of the head during the upward rebounds from the ground as well as the downward falls could result in the stretching of the neck's muscles and arteries. This stretching action can also cause damages to the child's head, neck and spine similar to the damages reported for "The Shaken Baby Syndrome" [94-96].

Chart 20 graphs the *angular acceleration* α, experienced by the child's head as the simulation time progresses. It can be seen that during the first head and ground impact, the child's head experiences a fatal angular acceleration equal to -53,190.00 rad/s^2.

For this simulation, the highest-magnitude *angular velocity* ω, was also retrieved from Working Model 2D. This angular velocity was equal to -14.989 rad/s and occurred during the first head and ground impact. Based on the reason

stated in Sec. 7-7-2-1, during this simulation, the angular velocity experienced by the child's head does not lead to serious or fatal damages.

Summarizing the discussion for this subsection at a shortfall height of 1.0 ft and with a $\mathbf{V_x}$ = -1.0 m/s the child's head experiences a severe NGS of 51.85 g. This translates to a dangerous total-acceleration 51.85 times higher than the earth's gravitational acceleration of 9.81 m/s^2. Moreover, during the first head and ground impact, the child's head experiences a fatal angular acceleration of -53,190.00 rad/s^2 as well as a maximum nonfatal angular velocity equal to -14.989 rad/s.

7-7-2-3 Shortfall Simulation from '1.5 ft' at V_x = '-1.0 m/s'

Fig. 171 through Fig. 175 represent the main dynamical stages during a shortfall simulation of a six months old child from a furniture with a height of 1.5 ft. Fig. 171 shows the child at the beginning of the simulation. Once the simulation starts both driving forces, namely the red horizontal force induced by $\mathbf{V_x}$ as well as the purple gravitational force move the child's body to the left and downwards respectively. The combination of both of these applied forces makes the body to rotate in a CCW fashion around the upper left corner of the furniture. As the CCW rotation and leftward translation of the child's body continues, the body separates itself from the furniture as shown in Fig. 172. Here an interesting phenomenon that needs a deeper discussion.

Fig. 172 shows the movement of the child's separation from the body. As shown on this figure, the body separates from the furniture while the child's right arm has not entirely dragged along the upper left corner of the furniture. There is still some its length remaining above the corner. Hence, for the child to separate from the furniture and experience the consequent *freefall*, not all of its entire length has to drag at the furniture's upper left corner. The child's legs do not even touch the corner while the body separates from the furniture. This further underlines the statement that not all the body's length has to touch the upper left corner of the furniture before the body separates itself from the furniture. To better understand the undergoing dynamics during the separation, a typical path of motion of a falling child with $\mathbf{V_x}$ = -1.0 m/s is shown in Fig. 192.

Fig. 192 depicts the *Path of shortfall* of a child, who undergoes a 3.0 ft shortfall at a $\mathbf{V_x}$ = -1.0 m/s. The black area in Fig. 192 represents the tracking of the body's position and configuration as it falls during the simulation. As mentioned previously, after the start of the simulation, the horizontal driving force and the existing gravitational force move the body leftwards and downwards. This action causes the body to attain a CCW motion. The yellow path 'I', illustrates the path along which the child's CG, shown as a green dot, will move as the child undergoes a CCW motion/fall. The green arrows depict the approximate velocity of the CG as the body falls. Note that they are tangent to path 'I'. At the beginning of path 'I', the child's CG has a slow velocity. As the child moves leftwards and downwards, more and more of the child's weight is displaced into the free air and taken away from the furniture's surface. This causes the gravity to pull more and more on the body and cause a faster and faster fall of the child. The gain in the velocity of the child's CG is illustrated by the growing (in magnitude) green arrows.

As the CG attain more and more speed, the child's remaining body, i.e. the arms and the legs, have to go around the upper left corner of the furniture as well. The left arm is positioned beneath the torso and the left leg and therefore drags at that upper left corner of the furniture. However, both legs as well as the right arm swing into the space in a CCW fashion. This swinging action is shown in the area enclosed by the blue loop.

Note that during this CCW motion, all body members experience the same instantaneous angular velocity. This is because that the body as a whole,

experiences only one instantaneous angular velocity. Compare to the body's CG, which is very close to the furniture's left corner, the individual centers of gravity of all swinging extremities are further away from that corner. This results in relatively higher tangential velocities at the CGs of every individual swinging extremity and a relatively lower tangential velocity at the body's CG. The brown arrows depict the approximate tangential velocities of the swinging extremities. Note that they are longer than the green arrows.

Similar to the more and more increasing velocity of the body's CG, as the child's weight displaces more and more into the free air, the tangential velocities of every the swinging extremity also gain in magnitude. With higher tangential velocities of the swinging extremities and lower tangential velocities of the body's CG, the CCW motion of the body will follow the curved path 'I'. Therefore, the body separates off from the furniture before the entire right arm is dragged upper left corner of the furniture. Notice that path 'I' applies to all the simulations conducted at $\mathbf{V_x}$ = -1.0 m/s. However, at lower furniture elevations, path 'I' intersects with the ground.

After the child separates it will continue its CCW rotation and falling along paths 'I' and 'III'. Path 'III' is a continuation of path 'I'. The body will continue its motion along path 'III' only if the furniture's height is high enough. In none of the simulations conducted at $\mathbf{V_x}$ = -1.0 m/s herein, the child's body followed path 'III'. Rather, depending on the shortfall's initial height path 'II' or a similar path like it was followed.

As the child falls in a CCW fashion along path ‘I’, at some point its head will collide with the ground. For shortfalls from an initial height of 1.5 ft and 2.0 ft, after the head and ground impact, the child’s body continues a CW motion along a path that is not illustrated here. Then the body rotates and falls on the left arm before sliding leftwards on the ground. For shortfalls from an initial height of 2.5 ft and 3.0 ft, after the head and ground impact, the child’s body continues a second CCW motion along path ‘II’ (for 3.0 ft, shown in Fig. 192) or a similar path (for 2.5 ft, not shown). The CCW motion along path ‘II’ is an upwards and leftwards motion followed by a downwards and leftwards motion. Hence, the body rises and falls along path ‘II’ as it moves leftwards. This motion occurs as the body rotates more than 90° CCW causing it to land on the right arm or shoulder depending on the initial height of the shortfall. After the landing the body slides on the ground along the yellow path ‘IV’.

Let’s go back to where the original discussion regarding the simulation of this subchapter was left off. After the child’s body separates from the furniture, the CCW leftwards and downwards/falling motion continuous until the child experiences the first head and ground impact as shown in Fig. 173. Note that this CCW follows the same path shown for a 3.0 ft shortfall, namely path ‘I’ (see Fig. 192). At the instant of first head and ground impact, the child’s head and neck are almost perfectly vertical. However, the torso and the rest of the body are still tilted compared to the *y*-axis. This kind of configuration can be extremely dangerous since the head and neck are not aligned with the remainder of the body

above. As the upper body pushes on the head and neck, the neck could brake due to the existing non-alignment.

Upon the first head and ground impact, the body bounces back to the air and starts CW uplift as it advances leftwards. This CW uplift continues until the child's head hits the left shoulder as shown in Fig. 174. This impact stops the body from the upwards advancement. Then, the body advances leftwards and falls back as it continues its CW rotation until the second head and ground impact occurs as illustrated by Fig. 175. Then the head slightly lifts from the ground and the body undergoes an almost 45° rotation landing on the left arm. The body slightly slides to the left and stops. Fig. 176 demonstrates the final position and configuration of the child. Note that the child has advanced more to the left regime of the *x*-axis compared to the child involved in a 1.0 ft shortfall. The reason for this further leftwards advancement is the higher elevation of the furniture. With a higher elevation, the horizontal driving force had more time to pull/push the body towards the left before landing.

Chart 21 graphs the *NGS* experienced by the child's head as the simulation time progresses. As illustrated in this chart, throughout the simulation, on average, the child's head continues to experience a NGS equal to 1.0. This means that the child's head experiences a total-acceleration $|\mathbf{a}|$, equal to the earth's gravitational acceleration. However, at the following instant the child's head experiences a higher acceleration compared to the earth's gravitational acceleration:

1. The First Head and Ground Impact. NGS = 123.71 g.
2. The Second Head and Ground Impact. NGS = 2.32 g.

During the child's first head and ground impact, the child's head experiences a total-acceleration **|a|**, 123.71 times higher than the earth's gravitational acceleration. The NGS of 123.71 g was calculated from a outputted **|F|** = 10,922.77 N. Similar to the calculations made in Sec. 7-7-2-1, the child, the division of the obtained **|F|** of 10,922.77 N by 88.29 N (child's weight) equals to 123.71. In other words, during the first head and ground impact, the child's head experiences a force 123.71 times the entire weight of the child's body. Therefore, a shortfall from 1.5 ft at a horizontal velocity of $\mathbf{V_x}$ = -1.0 m/s results in a very severe head and ground impact, leading to possible damages to the head, neck and spine of the child. Moreover, as mentioned previously, the non-aligned configuration of the head and neck compared to the rest of the child's body could lead to neck breakage during the first head and ground impact. The second head and ground impacts produced a total-acceleration **|a|**, 2.32 times higher than the earth's gravitational acceleration. The second head and ground impact results in a relatively soft landing. The head and left-shoulder collision did not result in accelerations higher than the earth's gravity.

This shows that the first head and ground impact absorbed the majority of the energy potential and kinetic energy involved during the shortfall. Hence, it is imaginable that the majority of the consequent damages to the child's head, neck and spine originate from the first head and ground impact. However, the constant left and right movement of the head during the upward rebounds from the ground

as well as the downward falls could result in the stretching of the neck's muscles and arteries. This stretching action can also cause damages to the child's head, neck and spine similar to the damages reported for "The Shaken Baby Syndrome" [94-96].

Chart 22 graphs the *angular acceleration* α, experienced by the child's head as the simulation time progresses. It can be seen that during the first head and ground impact, the child's head experiences a fatal angular acceleration equal to 217,800.00 rad/s^2.

For this simulation, the highest-magnitude *angular velocity* ω, was also retrieved from Working Model 2D. This angular velocity was equal to -14.119 rad/s and occurred during the first head and ground impact. Based on the reason stated in Sec. 7-7-2-1, during this simulation, the angular velocity experienced by the child's head does not lead to serious or fatal damages.

Summarizing the discussion for this subsection at a shortfall height of 1.5 ft and with a $\mathbf{V_x}$ = -1.0 m/s the child's head experiences a severe NGS of 123.71g. This translates to a dangerous total-acceleration 123.71 times higher than the earth's gravitational acceleration of 9.81 m/s^2. Moreover, during the first head and ground impact, the child's head experiences a fatal angular acceleration of 217,800.00 rad/s^2 as well as a maximum nonfatal angular velocity equal to -14.119 rad/s.

7-7-2-4 Shortfall Simulation from '2.0 ft' at V_x = '-1.0 m/s'

Fig. 177 through Fig. 181 represent the main dynamical stages during a shortfall simulation of a six months old child from a furniture with a height of 2.0 ft. Fig. 177 shows the child at the beginning of the simulation. Once the simulation starts both driving forces, namely the red horizontal force induced by $\mathbf{V_x}$ as well as the purple gravitational force move the child's body to the left and downwards respectively. The combination of both of these applied forces makes the body to rotate in a CCW fashion around the upper left corner of the furniture. As the CCW rotation and leftward translation of the child's body continues, the body separates itself from the furniture. The separation of the body is almost identical to that of a 1.0 ft shortfall as illustrated in Fig. 172.

After the child's body separates from the furniture, a CCW leftwards and downwards/falling motion continuous until the child experiences the first head and ground impact as shown in Fig. 178. Note that this CCW follows the same path shown for a 3.0 ft shortfall, namely path 'I' (see Fig. 192). At the instant of first head and ground impact, the child's head and neck align themselves slightly to the left of the *y*-axis. However, the torso and the rest of the body align themselves slightly to the right of the *y*-axis. This kind of configuration can be extremely dangerous since the head and neck are not aligned with the remainder of the body above. As the upper body pushes on the head and neck, the neck could brake due to the existing non-alignment.

Upon the first head and ground impact, the body bounces back to the air and starts a slight CW and almost towards the left translating uplift. Shortly after, the uplift stops and the child falls back towards the ground until a second head and ground impact occurs as illustrated by Fig. 179. Also at this instant the head and neck are non-aligned with the rest of the body. Upon the second head and ground impact the head slightly lifts from the ground and the body undergoes an almost 20° rotation while it still translates leftwards. A third head and ground impact occurs (see Fig. 180) followed by a 30° body rotation before the child lands on its left arm. The body slightly slides to the left and stops. Fig. 181 demonstrates the final position and configuration of the child. Note that the child has advanced more to the left regime of the *x*-axis compared to the child involved in a 1.5 ft shortfall. The reason for this further leftwards advancement is the higher elevation of the furniture. With a higher elevation, the horizontal driving force had more time to pull/push the body towards the left before landing.

Chart 23 graphs the *NGS* experienced by the child's head as the simulation time progresses. As illustrated in this chart, throughout the simulation, on average, the child's head continues to experience a NGS equal to 1.0. This means that the child's head experiences a total-acceleration $|\mathbf{a}|$, equal to the earth's gravitational acceleration. However, at the following instant the child's head experiences a higher acceleration compared to the earth's gravitational acceleration:

1. The First Head and Ground Impact. NGS = 176.16 g.
2. The Second Head and Ground Impact. NGS = 4.38 g.

3. The Third Head and Ground Impact. NGS = 4.15 g.

During the child's first head and ground impact, the child's head experiences a total-acceleration $|\mathbf{a}|$, 176.16 times higher than the earth's gravitational acceleration. The NGS of 176.16 g was calculated from a outputted $|\mathbf{F}|$ = 15,552.77 N. Similar to the calculations made in Sec. 7-7-2-1, the child, the division of the obtained $|\mathbf{F}|$ of 15,552.77 N by 88.29 N (child's weight) equals to 176.16. In other words, during the first head and ground impact, the child's head experiences a force 176.16 times the entire weight of the child's body. Therefore, a shortfall from 2.0 ft at a horizontal velocity of $\mathbf{V_x}$ = -1.0 m/s results in a very severe head and ground impact, leading to possible fatal damages to the head, neck and spine of the child. As reported by Nimityongskul et al., a total-acceleration $|\mathbf{a}| \geq 160.0$ g results in fatal damages [67]. Moreover, as mentioned previously, the non-aligned configuration of the head and neck compared to the rest of the child's body could lead to neck breakage during the first head and ground impact. The second and third head and ground impacts produced total-accelerations $|\mathbf{a}|$, 4.38 and 4.15 times higher than the earth's gravitational acceleration, respectively. The last two head and ground impacts result in relatively less severe landings. This shows that the first head and ground impact absorbed the majority of the energy potential and kinetic energy involved during the shortfall. Hence, it is imaginable that the majority of the consequent damages to the child's head, neck and spine originate from the first head and ground impact. However, the effects of the total-accelerations achieved during the second and third head and ground impacts combined with the non-linear head and neck

alignment with the rest of the child's body, could easily result in the neck-breakage of the child. Also, the constant left and right movement of the head during the upward rebounds from the ground as well as the downward falls could result in the stretching of the neck's muscles and arteries. This stretching action can also cause damages to the child's head, neck and spine similar to the damages reported for "The Shaken Baby Syndrome" [94-96].

Chart 24 graphs the *angular acceleration* α, experienced by the child's head as the simulation time progresses. It can be seen that during the first head and ground impact, the child's head experiences a fatal angular acceleration equal to 458,900.00 rad/s^2.

For this simulation, the highest-magnitude *angular velocity* ω, was also retrieved from Working Model 2D. This angular velocity was equal to -14.002 rad/s and occurred during the first head and ground impact. Based on the reason stated in Sec. 7-7-2-1, during this simulation, the angular velocity experienced by the child's head does not lead to serious or fatal damages.

Summarizing the discussion for this subsection at a shortfall height of 2.0 ft and with a $\mathbf{V_x}$ = -1.0 m/s the child's head experiences a severe NGS of 176.16 g followed by two less severe NGSs of 4.38 and 4.15. This translates to dangerous total-accelerations 176.16, 4.38 and 4.15 times higher than the earth's gravitational acceleration of 9.81 m/s^2. Moreover, during the first head and ground impact, the child's head experiences a fatal angular acceleration of

458,900.00 rad/s^2 as well as a maximum nonfatal angular velocity equal to -14.002 rad/s.

7-7-2-5 Shortfall Simulation from '2.5 ft' at V_x = '-1.0 m/s'

Fig. 182 through Fig. 186 represent the main dynamical stages during a shortfall simulation of a six months old child from a furniture with a height of 2.5 ft. Fig. 182 shows the child at the beginning of the simulation. Once the simulation starts both driving forces, namely the red horizontal force induced by $\mathbf{V_x}$ as well as the purple gravitational force move the child's body to the left and downwards respectively. The combination of both of these applied forces makes the body to rotate in a CCW fashion around the upper left corner of the furniture. As the CCW rotation and leftward translation of the child's body continues, the body separates itself from the furniture. The separation of the body is almost identical to that of a 1.0 ft shortfall as illustrated in Fig. 172.

After the child's body separates from the furniture, a CCW leftwards and downwards/falling motion continuous until the child experiences the first head and ground impact as shown in Fig. 183. Note that this CCW follows the same path shown for a 3.0 ft shortfall, namely path 'I' (see Fig. 192). At the instant of first head and ground impact, the child's head and neck align themselves to the left of the *y*-axis. The torso and the rest of the body also align themselves to the left of the *y*-axis. However, the head and neck are more tilted towards the left compared to the rest of the body. This kind of configuration can be extremely dangerous since the head and neck are not aligned with the remainder of the body above. As the upper body pushes on the head and neck, the neck could brake due to the existing non-alignment.

Upon the first head and ground impact, the body bounces back to the air and starts a second CCW motion. This motion occurs along a path similar to path 'II' illustrated in Fig. 192. The CCW motion involves and uplift and leftwards translation. Shortly after, the uplift stops and the child falls back towards the ground until a second head and ground impact occurs as illustrated by Fig. 184. Also at this instant the head and neck are slightly non-aligned with the rest of the body. Upon the second head and ground impact the head slightly lifts from the ground and the body undergoes an almost 45° rotation while it still translates leftwards before leading to a horizontal configuration (see Fig. 185). At this instance the child's head collides with its right shoulder before landing on its right arm. The body slightly slides to the left and stops. Fig. 186 demonstrates the final position and configuration of the child. Note that the child has advanced more to the left regime of the *x*-axis compared to the child involved in a 2.0 ft shortfall. The reason for this further leftwards advancement is the higher elevation of the furniture. With a higher elevation, the horizontal driving force had more time to pull/push the body towards the left before landing.

Chart 25 graphs the *NGS* experienced by the child's head as the simulation time progresses. As illustrated in this chart, throughout the simulation, on average, the child's head continues to experience a NGS equal to 1.0. This means that the child's head experiences a total-acceleration $|\mathbf{a}|$, equal to the earth's gravitational acceleration. However, at the following instant the child's head experiences a higher acceleration compared to the earth's gravitational acceleration:

1. The First Head and Ground Impact. NGS = 259.52 g.
2. The Second Head and Ground Impact. NGS = 34.58 g.
3. The Head and Right-Shoulder Impact. NGS = 2.89 g.

During the child's first head and ground impact, the child's head experiences a total-acceleration $|\mathbf{a}|$, 259.52 times higher than the earth's gravitational acceleration. The NGS of 259.52 g was calculated from a outputted $|\mathbf{F}|$ = 22,912.77 N. Similar to the calculations made in Sec. 7-7-2-1, the child, the division of the obtained $|\mathbf{F}|$ of 22,912.77 N by 88.29 N (child's weight) equals to 259.52. In other words, during the first head and ground impact, the child's head experiences a force 259.52 times the entire weight of the child's body. Therefore, a shortfall from 2.5 ft at a horizontal velocity of $\mathbf{V}_x$ = -1.0 m/s results in a very severe head and ground impact, leading to possible fatal damages to the head, neck and spine of the child. As reported by Nimityongskul et al., a total-acceleration $|\mathbf{a}| \geq 160.0$ g results in fatal damages [67]. Moreover, as mentioned previously, the non-aligned configuration of the head and neck compared to the rest of the child's body could lead to neck breakage during the first head and ground impact. The second head and ground impact as well as the head and right-shoulder impact produced total-accelerations $|\mathbf{a}|$, 34.58 and 2.89 times higher than the earth's gravitational acceleration, respectively. The second ground impact will also cause severe damages to the head, neck and spine of the child. The head and right-shoulder impact results in relatively less severe landing.

This shows that the first and the second head and ground impacts absorbed the majority of the energy potential and kinetic energy involved during the shortfall.

Hence, it is imaginable that the majority of the consequent damages to the child's head, neck and spine originate from the first and the second head and ground impacts. However, the effects of the total-accelerations achieved during the head and right-shoulder impact combined with the non-linear head and neck alignment with the rest of the child's body, could easily result in the neck-breakage of the child. Also, the constant left and right movement of the head during the upward rebounds from the ground as well as the downward falls could result in the stretching of the neck's muscles and arteries. This stretching action can also cause damages to the child's head, neck and spine similar to the damages reported for "The Shaken Baby Syndrome" [94-96].

Chart 26 graphs the *angular acceleration* α, experienced by the child's head as the simulation time progresses. It can be seen that during the first head and ground impact, the child's head experiences a fatal angular acceleration equal to 529,900.00 rad/s^2.

For this simulation, the highest-magnitude *angular velocity* ω, was also retrieved from Working Model 2D. This angular velocity was equal to -13.645 rad/s and occurred during the first head and ground impact. Based on the reason stated in Sec. 7-7-2-1, during this simulation, the angular velocity experienced by the child's head does not lead to serious or fatal damages.

Summarizing the discussion for this subsection at a shortfall height of 2.5 ft and with a $\mathbf{V_x}$ = -1.0 m/s the child's head experiences two severe NGSs of 259.52 g and 34.58 g followed by one less severe NGS of 2.89. This translates to

dangerous total-accelerations 259.52, 34.58 and 2.89 times higher than the earth's gravitational acceleration of 9.81 m/s^2. Moreover, during the first head and ground impact, the child's head experiences a fatal angular acceleration of 529,900.00 rad/s^2 as well as a maximum nonfatal angular velocity equal to -13.645 rad/s.

7-7-2-6 Shortfall Simulation from '3.0 ft' at V_x = '-1.0 m/s'

Fig. 187 through Fig. 192 represent the main dynamical stages during a shortfall simulation of a six months old child from a furniture with a height of 3.0 ft. Fig. 187 shows the child at the beginning of the simulation. Once the simulation starts both driving forces, namely the red horizontal force induced by $\mathbf{V_x}$ as well as the purple gravitational force move the child's body to the left and downwards respectively. The combination of both of these applied forces makes the body to rotate in a CCW fashion around the upper left corner of the furniture. As the CCW rotation and leftward translation of the child's body continues, the body separates itself from the furniture. The separation of the body is almost identical to that of a 1.0 ft shortfall as illustrated in Fig. 172.

After the child's body separates from the furniture, a CCW leftwards and downwards/falling motion continuous until the child experiences the head and ground impact as shown in Fig. 188. Note that this CCW follows path 'I' as illustrated in Fig. 192. At the instant of head and ground impact, the child's head and neck align themselves to the left of the *y*-axis. The torso and the rest of the body also align themselves to the left of the *y*-axis. However, the head and neck are slightly more tilted towards the left compared to the rest of the body. This kind of configuration can be extremely dangerous since the head and neck are not aligned with the remainder of the body above. As the upper body pushes on the head and neck, the neck could brake due to the existing non-alignment.

Upon the head and ground impact, the body bounces back to the air and starts a second CCW motion. This motion occurs along path 'II' illustrated in Fig. 192. The CCW motion involves an almost 90° rotation, an uplift and leftwards translation. Shortly after, the uplift stops and the child falls back towards the ground until its right shoulder/arm collide with the ground as illustrated by Fig. 189. Note that the right shoulder/arm and ground impact occurs as the body is an almost horizontal configuration. After this impact the head slightly lifts from the ground until it hits the left shoulder as shown in Fig. 190. Then the child lands on its right arm. The body slightly slides to the left and stops. Fig. 191 demonstrates the final position and configuration of the child. Note that the child has advanced more to the left regime of the *x*-axis compared to the child involved in a 2.5 ft shortfall. The reason for this further leftwards advancement is the higher elevation of the furniture. With a higher elevation, the horizontal driving force had more time to pull/push the body towards the left before landing.

Chart 27 graphs the *NGS* experienced by the child's head as the simulation time progresses. As illustrated in this chart, throughout the simulation, on average, the child's head continues to experience a NGS equal to 1.0. This means that the child's head experiences a total-acceleration $|\mathbf{a}|$, equal to the earth's gravitational acceleration. However, at the following instant the child's head experiences a higher acceleration compared to the earth's gravitational acceleration:

1. The Head and Ground Impact. NGS = 319.66 g.
2. The Right-Shoulder/Arm and Ground Impact. NGS = 22.11 g.

During the child's head and ground impact, the child's head experiences a total-acceleration $|\mathbf{a}|$, 319.66 times higher than the earth's gravitational acceleration. The NGS of 319.66 g was calculated from a outputted $|\mathbf{F}|$ = 28,222.77 N. Similar to the calculations made in Sec. 7-7-2-1, the child, the division of the obtained $|\mathbf{F}|$ of 28,222.77 N by 88.29 N (child's weight) equals to 319.66. In other words, during the head and ground impact, the child's head experiences a force 319.66 times the entire weight of the child's body. Therefore, a shortfall from 3.0 ft at a horizontal velocity of $\mathbf{V_x}$ = -1.0 m/s results in a very severe head and ground impact, leading to possible fatal damages to the head, neck and spine of the child. As reported by Nimityongskul et al., a total-acceleration $|\mathbf{a}| \geq 160.0$ g results in fatal damages [67]. Moreover, as mentioned previously, the non-aligned configuration of the head and neck compared to the rest of the child's body could lead to neck breakage during the head and ground impact. The right shoulder/arm and ground impact produced a total-acceleration $|\mathbf{a}|$, 22.11 times higher than the earth's gravitational acceleration. The right shoulder/arm and ground impact will also cause severe damages to the head, neck and spine of the child.

Based on the results seen on Chart 27, the head and ground impact absorbed the majority of the energy potential and kinetic energy involved during the shortfall. Hence, it is imaginable that the majority of the consequent damages to the child's head, neck and spine originate from the head and ground impacts. However, the effects of the total-accelerations achieved during the right shoulder/arm and ground impact combined with the non-linear head and neck

alignment with the rest of the child's body, could easily result in the neck-breakage of the child. Also, the constant left and right movement of the head during the upward rebounds from the ground as well as the downward falls could result in the stretching of the neck's muscles and arteries. This stretching action can also cause damages to the child's head, neck and spine similar to the damages reported for "The Shaken Baby Syndrome" [94-96].

Chart 28 graphs the *angular acceleration* α, experienced by the child's head as the simulation time progresses. It can be seen that during the head and ground impact, the child's head experiences a fatal angular acceleration equal to 411,600.00 rad/s^2.

For this simulation, the highest-magnitude *angular velocity* ω, was also retrieved from Working Model 2D. This angular velocity was equal to 17.535 rad/s and occurred during the head and ground impact. Based on the reason stated in Sec. 7-7-2-1, during this simulation, the angular velocity experienced by the child's head does not lead to serious or fatal damages.

Summarizing the discussion for this subsection at a shortfall height of 3.0 ft and with a $\mathbf{V_x}$ = -1.0 m/s the child's head experiences two severe NGSs of 319.66 g and 22.11 g. This translates to dangerous total-accelerations 319.66 and 22.11 times higher than the earth's gravitational acceleration of 9.81 m/s^2. Moreover, during the head and ground impact, the child's head experiences a fatal angular acceleration of 411,600.00 rad/s^2 as well as a maximum nonfatal angular velocity equal to 17.535 rad/s.

7-7-3 Simulations Conducted at V_x = '-3.0 m/s'

The following six subsections discuss the results obtained from each individual shortfall simulation that were categorized within the second simulation group, namely shortfall simulations incorporating a horizontal velocity of $\mathbf{V_x}$ = -3.0 m/s.

7-7-3-1 Shortfall Simulation from '0.5 ft' at V_x = '-3.0 m/s'

Fig. 193 through Fig. 197 represent the main dynamical stages during a shortfall simulation of a six months old child from a furniture with a height of 0.5 ft. Fig. 193 shows the child at the beginning of the simulation. Once the simulation starts both driving forces, namely the red horizontal force induced by $\mathbf{V_x}$ as well as the purple gravitational force move the child's body to the left and downwards respectively. The combination of both of these applied forces makes the body to rotate in a CCW fashion around the upper left corner of the furniture. Shortly after, the child separates itself from the upper left corner of the furniture as illustrated in Fig. 194. The CCW leftwards and downwards/falling motion continuous until the child experiences a *head-first* impact as shown in Fig. 195. Unlike to the 0.5 ft shortfall simulation conducted at $\mathbf{V_x}$ = -1.0 m/s, during this impact the child is not leaning on the 0.5 ft furniture. Based on the statements made in Sec. 7-7-1, albeit both shortfalls initiated form the same furniture height, the child does not lean on the furniture during its head and ground impact. This is because the body separates itself from the furniture prior to the head and ground impact as illustrated in Fig. 194. The dynamics involved during the separation of the body from the furniture requires a deeper discussion.

To better understand the undergoing dynamics during the separation, a typical path of motion of a falling child with $\mathbf{V_x}$ = -3.0 m/s is shown in Fig. 222. Fig. 222 depicts the *Path of shortfall* of a child, who undergoes a 3.0 ft shortfall at a $\mathbf{V_x}$ = -3.0 m/s. The black area in Fig. 222 represents the tracking of the body's position and configuration as it falls during the simulation. As mentioned previously, after the start of the simulation, the horizontal driving force and the existing gravitational force move the body leftwards and downwards. This action causes the body to attain a CCW motion. The yellow path 'I', illustrates the path along which the child's CG, shown as a green dot, will move as the child undergoes a CCW motion/fall. It should be noted that path 'I' in Fig. 222 has a larger radius of curvature compared to the path 'I' illustrated in Fig. 192. This is because the higher magnitude $\mathbf{V_x}$ = -3.0 m/s. As the magnitude of the horizontal velocity increases, the radius of curvature of path 'I' increases as well.

The green arrows depict the approximate velocity of the CG as the body falls. Note that they are tangent to path 'I'. At the beginning of path 'I', the child's CG has a slow velocity. As the child moves leftwards and downwards, more and more of the child's weight is displaced into the free air and taken away from the furniture's surface. This causes the gravity to pull more and more on the body and cause a faster and faster fall of the child. The gain in the velocity of the child's CG is illustrated by the growing (in magnitude) green arrows.

As the CG attain more and more speed, the child's remaining body, i.e. the arms and the legs, have to go around the upper left corner of the furniture as well. The left arm is positioned beneath the torso and the left leg and therefore drags at

that upper left corner of the furniture. However, both legs as well as the right arm swing into the space in a CCW fashion. This swinging action is shown in the area enclosed by the blue loop.

Note that during this CCW motion, all body members experience the same instantaneous angular velocity. This is because that the body as a whole, experiences only one instantaneous angular velocity. Compare to the body's CG, which is very close to the furniture's left corner, the individual centers of gravity of all swinging extremities are further away from that corner. This results in relatively higher tangential velocities at the CGs of every individual swinging extremity and a relatively lower tangential velocity at the body's CG. The brown arrows depict the approximate tangential velocities of the swinging extremities. Note that they are longer than the green arrows.

Similar to the more and more increasing velocity of the body's CG, as the child's weight displaces more and more into the free air, the tangential velocities of every the swinging extremity also gain in magnitude. With higher tangential velocities of the swinging extremities and lower tangential velocities of the body's CG, the CCW motion of the body will follow the curved path 'I'. Therefore, the body separates off from the furniture before the entire right arm is dragged upper left corner of the furniture. Notice that path 'I' applies to all the simulations conducted at $\mathbf{V_x}$ = -3.0 m/s. However, at lower furniture elevations, path 'I' intersects with the ground.

After the child separates it will continue its CCW rotation and falling along paths ‘I’ and ‘III’. Path ‘III’ is a continuation of path ‘I’. The body will continue its motion along path ’III’ only if the furniture’s height is high enough. In none of the simulations conducted at $\mathbf{V_x}$ = -3.0 m/s herein, the child’s body followed path ‘III’. Rather, depending on the shortfall’s initial height path ‘II’ or a similar path like it was followed.

As the child falls in a CCW fashion along path ‘I’, at some point its head will collide with the ground. For all shortfalls from initial height of 0.5 ft and 3.0 ft, after the head and ground impact, the child’s body continues a CW motion along path ‘II’ or a similar but shorter path depending on the initial shortfall’s height. This CW motion involves a rotation and the uplift of the head, shoulders and the torso. The rotation seems to occur about an out-of-the-paper-extruding axis that is situated between the lower-legs of the child. The CW motion continues until the lower-legs touch the ground and the head touches the right shoulder. Then another CCW motion along path ‘III’ or a similar path depending on depending on the initial shortfall’s height follows (see Fig. 222). After the landing the body slides on the ground along the yellow path ‘IV’.

Let’s go back to where the original discussion regarding the simulation of this subchapter was left off. After the head and ground impact the head and the shoulders experience an upwards lift while the entire body undergoes a CW rotation. This CW motion follows a similar but shorter version of path ‘II’ as illustrated in Fig. 222. The upwards lift continues until the lower left arm attains an almost horizontal configuration and touches the ground as shown in Fig. 196.

At this point the body undergoes a CCW fall along a similar but shorter version of path 'IV' (see Fig. 222). At the end of this CCW fall, the body lands on the left arm and slides leftwards until it is stopped by the blue horizontal frictional forces. Fig. 197 shows the final configuration of the child's body.

Chart 29 graphs the *NGS* experienced by the child's head as the simulation time progresses. As illustrated in this chart, throughout the simulation, on average, the child's head continues to experience a NGS equal to 1.0. This means that the child's head experiences a total-acceleration $|\mathbf{a}|$, equal to the earth's gravitational acceleration. However, at the following instant the child's head experiences a higher acceleration compared to the earth's gravitational acceleration:

1. The Head and Ground Impact. NGS = 41.43 g.

During the child's head and ground impact, the child's head experiences a total-acceleration $|\mathbf{a}|$, 41.43 times higher than the earth's gravitational acceleration. The NGS of 41.43 g was calculated from a outputted $|\mathbf{F}|$ = 3,657.83 N. Similar to the calculations made in Sec. 7-7-2-1, the child, the division of the obtained $|\mathbf{F}|$ of 3,657.83 N by 88.29 N (child's weight) equals to 41.43. In other words, during the head and ground impact, the child's head experiences a force 41.43 times the entire weight of the child's body. Therefore, a shortfall from 0.5 ft at a horizontal velocity of $\mathbf{V_x}$ = -3.0 m/s results in a relatively severe head and ground impact, leading to possible damages to the head, neck and spine of the child. The right-arm and ground impact did not result in a total-acceleration $|\mathbf{a}|$,

higher than the earth's gravitational acceleration. However, the constant left and right movement of the head during the upward rebounds from the ground as well as the downward falls could result in the stretching of the neck's muscles and arteries. This stretching action can also cause damages to the child's head, neck and spine similar to the damages reported for "The Shaken Baby Syndrome" [94-96].

Chart 30 graphs the *angular acceleration* α, experienced by the child's head as the simulation time progresses. It can be seen that during the head and ground impact, the child's head experiences a fatal angular acceleration equal to 80,070.00 rad/s^2.

For this simulation, the highest-magnitude *angular velocity* ω, was also retrieved from Working Model 2D. This angular velocity was equal to 17.770 rad/s and occurred during the head and ground impact. Based on the reason stated in Sec. 7-7-2-1, during this simulation, the angular velocity experienced by the child's head does not lead to serious or fatal damages.

Summarizing the discussion for this subsection at a shortfall height of 0.5 ft and with a $\mathbf{V_x}$ = -3.0 m/s the child's head experiences a relatively severe NGS of 41.43 g. This translates to a total-acceleration 41.43 times higher than the earth's gravitational acceleration of 9.81 m/s^2. Moreover, during the head and ground impact, the child's head experiences a fatal angular acceleration of 80,070.00 rad/s^2 as well as a maximum nonfatal angular velocity equal to 17.770 rad/s.

7-7-3-2 Shortfall Simulation from '1.0 ft' at V_x = '-3.0 m/s'

Fig. 198 through Fig. 201 represent the main dynamical stages during a shortfall simulation of a six months old child from a furniture with a height of 1.0 ft. Fig. 198 shows the child at the beginning of the simulation. Once the simulation starts both driving forces, namely the red horizontal force induced by $\mathbf{V_x}$ as well as the purple gravitational force move the child's body to the left and downwards respectively. The combination of both of these applied forces makes the body to rotate in a CCW fashion around the upper left corner of the furniture. This CCW leftwards and downwards/falling motion continuous until the child experiences a *head-first* impact as shown in Fig. 199. Unlike to the 0.5 ft shortfall simulation conducted at $\mathbf{V_x}$ = -1.0 m/s, during this impact the child is totally separated from the furniture. As explained in Sec. 7-7-1 and Sec. 7-7-3-1, the higher initial shortfall height and the faster horizontal velocity are the reasons why the child separates from the furniture prior the head and ground impact. The separation of the child's body from the furniture is almost identical to the same separation pattern described in Sec. 7-7-3-1 (see Fig. 194).

After the head and ground impact the head and the shoulders experience an upwards lift while the entire body undergoes a CW rotation. This CW motion follows a similar but shorter version of path 'II' as illustrated in Fig. 222. The upwards lift continues until the lower left arm attains an almost horizontal configuration and touches the ground as shown in Fig. 200. At this point the body undergoes a CCW fall along a similar but shorter version of path 'IV' (see Fig. 222). At the end of this CCW fall, the body lands on the left arm and slides

leftwards until it is stopped by the blue horizontal frictional forces. Fig. 201 shows the final configuration of the child's body. Note that the body landed further to the left compared to final position of the child involved in a 0.5 ft shortfall conducted at $\mathbf{V_x}$ = -3.0 m/s (see Fig. 197). This is because of the 0.5 ft higher initial shortfall height.

Chart 31 graphs the *NGS* experienced by the child's head as the simulation time progresses. As illustrated in this chart, throughout the simulation, on average, the child's head continues to experience a NGS equal to 1.0. This means that the child's head experiences a total-acceleration **|a|**, equal to the earth's gravitational acceleration. However, at the following instant the child's head experiences a higher acceleration compared to the earth's gravitational acceleration:

1. The Head and Ground Impact. NGS = 124.39 g.
2. The Lower Left-Arm and Ground Impact. NGS = 1.47 g.

During the child's head and ground impact, the child's head experiences a total-acceleration **|a|**, 41.43 times higher than the earth's gravitational acceleration. The NGS of 124.39 g was calculated from a outputted **|F|** = 10,982.75 N. Similar to the calculations made in Sec. 7-7-2-1, the child, the division of the obtained **|F|** of 10,982.75 N by 88.29 N (child's weight) equals to 124.39. In other words, during the head and ground impact, the child's head experiences a force 124.39 times the entire weight of the child's body. Therefore, a shortfall from 1.0 ft at a horizontal velocity of $\mathbf{V_x}$ = -3.0 m/s results in a

relatively severe head and ground impact, leading to possible damages to the head, neck and spine of the child. The lower left-arm and ground impact did not result in a total-acceleration **|a|**, significantly higher than the earth's gravitational acceleration. However, the constant left and right movement of the head during the upward rebounds from the ground as well as the downward falls could result in the stretching of the neck's muscles and arteries. This stretching action can also cause damages to the child's head, neck and spine similar to the damages reported for "The Shaken Baby Syndrome" [94-96].

Chart 32 graphs the *angular acceleration* α, experienced by the child's head as the simulation time progresses. It can be seen that during the head and ground impact, the child's head experiences a fatal angular acceleration equal to -225,800.00 rad/s^2.

For this simulation, the highest-magnitude *angular velocity* ω, was also retrieved from Working Model 2D. This angular velocity was equal to -22.822 rad/s and occurred during the head and ground impact. Based on the reason stated in Sec. 7-7-2-1, during this simulation, the angular velocity experienced by the child's head does not lead to serious or fatal damages.

Summarizing the discussion for this subsection at a shortfall height of 1.0 ft and with a $\mathbf{V_x}$ = -3.0 m/s the child's head experiences a relatively severe NGS of 124.39 g. This translates to a total-acceleration 124.39 times higher than the earth's gravitational acceleration of 9.81 m/s^2. Moreover, during the head and ground impact, the child's head experiences a fatal angular acceleration of -

225,800.00 rad/s^2 as well as a maximum nonfatal angular velocity equal to -22.822 rad/s.

7-7-3-3 Shortfall Simulation from '1.5 ft' at V_x = '-3.0 m/s'

Fig. 202 through Fig. 206 represent the main dynamical stages during a shortfall simulation of a six months old child from a furniture with a height of 1.5 ft. Fig. 202 shows the child at the beginning of the simulation. Once the simulation starts both driving forces, namely the red horizontal force induced by $\mathbf{V_x}$ as well as the purple gravitational force move the child's body to the left and downwards respectively. The combination of both of these applied forces makes the body to rotate in a CCW fashion around the upper left corner of the furniture. This CCW leftwards and downwards/falling motion continuous until the child experiences a *head-first* impact as shown in Fig. 203. Unlike to the 0.5 ft shortfall simulation conducted at $\mathbf{V_x}$ = -1.0 m/s, during this impact the child is totally separated from the furniture. As explained in Sec. 7-7-1 and Sec. 7-7-3-1, the higher initial shortfall height and the faster horizontal velocity are the reasons why the child separates from the furniture prior the head and ground impact. The separation of the child's body from the furniture is almost identical to the same separation pattern described in Sec. 7-7-3-1 (see Fig. 194).

After the head and ground impact the head and the shoulders experience an upwards lift while the entire body undergoes a CW rotation. This CW motion follows a similar but shorter version of path 'II' as illustrated in Fig. 222. The upwards lift continues until the lower left arm touches the ground as shown in Fig. 204. At this point the head collides with the left shoulder and the body undergoes a CCW fall along a similar but shorter version of path 'IV' (see Fig. 222). At the end of this CCW fall, the body lands on the left shoulder/arm as seen

in Fig. 205. Then, the body slides leftwards until it is stopped by the blue horizontal frictional forces. Fig. 206 shows the final configuration of the child's body. Note that the body landed further to the left compared to final position of the child involved in a 1.0 ft shortfall conducted at $\mathbf{V_x}$ = -3.0 m/s (see Fig. 201). This is because of the 0.5 ft higher initial shortfall height.

Chart 33 graphs the *NGS* experienced by the child's head as the simulation time progresses. As illustrated in this chart, throughout the simulation, on average, the child's head continues to experience a NGS equal to 1.0. This means that the child's head experiences a total-acceleration **|a|**, equal to the earth's gravitational acceleration. However, at the following instant the child's head experiences a higher acceleration compared to the earth's gravitational acceleration:

1. The Head and Ground Impact. NGS = 180.57 g.
2. The Lower-Left-Arm and Ground Impact. NGS = 2.31 g.
3. The Left-Shoulder/Arm and Ground Impact. NGS = 12.65 g.

During the child's head and ground impact, the child's head experiences a total-acceleration **|a|**, 180.57 times higher than the earth's gravitational acceleration. The NGS of 180.57 g was calculated from a outputted **|F|** = 15,942.75 N. Similar to the calculations made in Sec. 7-7-2-1, the child, the division of the obtained **|F|** of 15,942.75 N by 88.29 N (child's weight) equals to 180.57. In other words, during the head and ground impact, the child's head experiences a force 180.57 times the entire weight of the child's body. Therefore,

a shortfall from 1.5 ft at a horizontal velocity of $\mathbf{V_x}$ = -3.0 m/s results in a very severe head and ground impact, leading to possible fatal damages to the head, neck and spine of the child. As reported by Nimityongskul et al., a total-acceleration $|\mathbf{a}| \geq 160.0$ g results in fatal damages [67]. The lower-left-arm and ground impact produced a total-acceleration $|\mathbf{a}|$, 2.31 times higher than the earth's gravitational acceleration. This impact results in a relatively soft landing. The left-shoulder/arm and ground impact results in total-acceleration $|\mathbf{a}|$, 12.56 times higher than the gravitational acceleration.

This shows that the first and last impacts, specially the first impact, absorbed the majority of the energy potential and kinetic energy involved during the shortfall. Hence, it is imaginable that the majority of the consequent damages to the child's head, neck and spine originate from the head and ground impact as well as the left-shoulder/arm and ground impact. However, the constant left and right movement of the head that followed after each upwards rebound and downwards falling could result in the stretching of the neck's muscles and arteries. This stretching action can also cause damages to the child's head, neck and spine similar to the damages reported for "The Shaken Baby Syndrome" [94-96].

Chart 34 graphs the *angular acceleration* α, experienced by the child's head as the simulation time progresses. It can be seen that during the head and ground impact, the child's head experiences a fatal angular acceleration equal to -318,300.00 rad/s^2.

For this simulation, the highest-magnitude *angular velocity* ω, was also retrieved from Working Model 2D. This angular velocity was equal to -28.224 rad/s and occurred during the head and ground impact. Based on the reason stated in Sec. 7-7-2-1, during this simulation, the angular velocity experienced by the child's head does not lead to serious or fatal damages.

Summarizing the discussion for this subsection at a shortfall height of 1.5 ft and with a $\mathbf{V_x}$ = -3.0 m/s the child's head experiences two severe NGSs of 180.57 g and 12.65 g. This translates to dangerous total-accelerations 180.57 and 12.65 times higher than the earth's gravitational acceleration of 9.81 m/s^2. Moreover, during the head and ground impact, the child's head experiences a fatal angular acceleration of -318,300.00 rad/s^2 as well as a maximum nonfatal angular velocity equal to -28.224 rad/s.

7-7-3-4 Shortfall Simulation from '2.0 ft' at V_x = '-3.0 m/s'

Fig. 207 through Fig. 211 represent the main dynamical stages during a shortfall simulation of a six months old child from a furniture with a height of 2.0 ft. Fig. 207 shows the child at the beginning of the simulation. Once the simulation starts both driving forces, namely the red horizontal force induced by $\mathbf{V_x}$ as well as the purple gravitational force move the child's body to the left and downwards respectively. The combination of both of these applied forces makes the body to rotate in a CCW fashion around the upper left corner of the furniture. This CCW leftwards and downwards/falling motion continuous until the child experiences a *head-first* impact as shown in Fig. 208. Unlike to the 0.5 ft shortfall simulation conducted at $\mathbf{V_x}$ = -1.0 m/s, during this impact the child is totally separated from the furniture. As explained in Sec. 7-7-1 and Sec. 7-7-3-1, the higher initial shortfall height and the faster horizontal velocity are the reasons why the child separates from the furniture prior the head and ground impact. The separation of the child's body from the furniture is almost identical to the same separation pattern described in Sec. 7-7-3-1 (see Fig. 194).

After the head and ground impact the head and the shoulders experience an upwards lift while the entire body undergoes a CW rotation. This CW motion follows a similar but shorter version of path 'II' as illustrated in Fig. 222. The upwards lift continues until the lower left arm and leg touch the ground as shown in Fig. 209. At this point the head collides with the left shoulder and the body undergoes a CCW fall along a similar but shorter version of path 'IV' (see Fig. 222). At the end of this CCW fall, the body lands on the left shoulder/arm as seen

in Fig. 210. Then, the body slides leftwards until it is stopped by the blue horizontal frictional forces. Fig. 211 shows the final configuration of the child's body. Note that the body landed further to the left compared to final position of the child involved in a 1.5 ft shortfall conducted at $\mathbf{V_x}$ = -3.0 m/s (see Fig. 206). This is because of the 0.5 ft higher initial shortfall height.

Chart 35 graphs the *NGS* experienced by the child's head as the simulation time progresses. As illustrated in this chart, throughout the simulation, on average, the child's head continues to experience a NGS equal to 1.0. This means that the child's head experiences a total-acceleration **|a|**, equal to the earth's gravitational acceleration. However, at the following instant the child's head experiences a higher acceleration compared to the earth's gravitational acceleration:

1. The Head and Ground Impact. NGS = 249.21 g.
2. The Lower-Left-Arm and Ground Impact. NGS = 6.38 g.
3. The Left-Shoulder/Arm and Ground Impact. NGS = 22.27 g.

During the child's head and ground impact, the child's head experiences a total-acceleration **|a|**, 249.21 times higher than the earth's gravitational acceleration. The NGS of 249.21 g was calculated from a outputted **|F|** = 22,002.75 N. Similar to the calculations made in Sec. 7-7-2-1, the child, the division of the obtained **|F|** of 22,002.75 N by 88.29 N (child's weight) equals to 249.21. In other words, during the head and ground impact, the child's head experiences a force 249.21 times the entire weight of the child's body. Therefore,

a shortfall from 2.0 ft at a horizontal velocity of $\mathbf{V_x}$ = -3.0 m/s results in a very severe head and ground impact, leading to possible fatal damages to the head, neck and spine of the child. As reported by Nimityongskul et al., a total-acceleration $|\mathbf{a}| \geq 160.0$ g results in fatal damages [67]. The lower-left-arm and ground impact produced a total-acceleration $|\mathbf{a}|$, 6.38 times higher than the earth's gravitational acceleration. This impact results in a relatively soft landing. The left-shoulder/arm and ground impact results in total-acceleration $|\mathbf{a}|$, 22.27 times higher than the gravitational acceleration.

This shows that the first and last impacts, specially the first impact, absorbed the majority of the energy potential and kinetic energy involved during the shortfall. Hence, it is imaginable that the majority of the consequent damages to the child's head, neck and spine originate from the head and ground impact as well as the left-shoulder/arm and ground impact. However, the constant left and right movement of the head that followed after each upwards rebound and downwards falling could result in the stretching of the neck's muscles and arteries. This stretching action can also cause damages to the child's head, neck and spine similar to the damages reported for "The Shaken Baby Syndrome" [94-96].

Chart 36 graphs the *angular acceleration* α, experienced by the child's head as the simulation time progresses. It can be seen that during the head and ground impact, the child's head experiences a fatal angular acceleration equal to -408,900.00 rad/s^2.

For this simulation, the highest-magnitude *angular velocity* ω, was also retrieved from Working Model 2D. This angular velocity was equal to -36.875 rad/s and occurred during the head and ground impact. Based on the reason stated in Sec. 7-7-2-1, during this simulation, the angular velocity experienced by the child's head does not lead to serious or fatal damages.

Summarizing the discussion for this subsection at a shortfall height of 2.0 ft and with a $\mathbf{V_x}$ = -3.0 m/s the child's head experiences two severe NGSs of 249.21 g and 22.27 g. This translates to dangerous total-accelerations 249.21 and 22.27 times higher than the earth's gravitational acceleration of 9.81 m/s^2. Moreover, during the head and ground impact, the child's head experiences a fatal angular acceleration of -408,900.00 rad/s^2 as well as a maximum nonfatal angular velocity equal to -36.875 rad/s.

7-7-3-5 Shortfall Simulation from '2.5 ft' at V_x = '-3.0 m/s'

Fig. 212 through Fig. 216 represent the main dynamical stages during a shortfall simulation of a six months old child from a furniture with a height of 2.5 ft. Fig. 212 shows the child at the beginning of the simulation. Once the simulation starts both driving forces, namely the red horizontal force induced by $\mathbf{V_x}$ as well as the purple gravitational force move the child's body to the left and downwards respectively. The combination of both of these applied forces makes the body to rotate in a CCW fashion around the upper left corner of the furniture. This CCW leftwards and downwards/falling motion continuous until the child experiences a *head-first* impact as shown in Fig. 213. Unlike to the 0.5 ft shortfall simulation conducted at $\mathbf{V_x}$ = -1.0 m/s, during this impact the child is totally separated from the furniture. As explained in Sec. 7-7-1 and Sec. 7-7-3-1, the higher initial shortfall height and the faster horizontal velocity are the reasons why the child separates from the furniture prior the head and ground impact. The separation of the child's body from the furniture is almost identical to the same separation pattern described in Sec. 7-7-3-1 (see Fig. 194).

After the head and ground impact the head and the shoulders experience an upwards lift while the entire body undergoes a CW rotation. This CW motion follows a similar but shorter version of path 'II' as illustrated in Fig. 222. The upwards lift continues until the lower left leg touches the ground as shown in Fig. 214. At this point the head collides with the left shoulder and the body undergoes a CCW fall along a similar but shorter version of path 'IV' (see Fig. 222). At the end of this CCW fall, the body lands on the left shoulder/arm as seen in Fig. 215.

Then, the body slides leftwards until it is stopped by the blue horizontal frictional forces. Fig. 216 shows the final configuration of the child's body. Note that the body landed further to the left compared to final position of the child involved in a 2.0 ft shortfall conducted at $\mathbf{V_x}$ = -3.0 m/s (see Fig. 211). This is because of the 0.5 ft higher initial shortfall height.

Chart 37 graphs the *NGS* experienced by the child's head as the simulation time progresses. As illustrated in this chart, throughout the simulation, on average, the child's head continues to experience a NGS equal to 1.0. This means that the child's head experiences a total-acceleration **|a|**, equal to the earth's gravitational acceleration. However, at the following instant the child's head experiences a higher acceleration compared to the earth's gravitational acceleration:

1. The Head and Ground Impact. NGS = 339.48 g.
2. The Lower-Left-Arm and Ground Impact. NGS = 19.05 g.
3. The Left-Shoulder/Arm and Ground Impact. NGS = 35.52 g.

During the child's head and ground impact, the child's head experiences a total-acceleration **|a|**, 339.48 times higher than the earth's gravitational acceleration. The NGS of 339.48 g was calculated from a outputted **|F|** = 29,972.75 N. Similar to the calculations made in Sec. 7-7-2-1, the child, the division of the obtained **|F|** of 29,972.75 N by 88.29 N (child's weight) equals to 339.48. In other words, during the head and ground impact, the child's head experiences a force 339.48 times the entire weight of the child's body. Therefore,

a shortfall from 2.5 ft at a horizontal velocity of $\mathbf{V_x}$ = -3.0 m/s results in a very severe head and ground impact, leading to possible fatal damages to the head, neck and spine of the child. As reported by Nimityongskul et al., a total-acceleration $|\mathbf{a}| \geq 160.0$ g results in fatal damages [67]. The lower-left-arm and ground impact produced a total-acceleration $|\mathbf{a}|$, 19.05 times higher than the earth's gravitational acceleration. This impact results in a relatively severe landing. The left-shoulder/arm and ground impact results in total-acceleration $|\mathbf{a}|$, 35.52 times higher than the gravitational acceleration.

This shows that the first and last impacts, specially the first impact, absorbed the majority of the energy potential and kinetic energy involved during the shortfall. Hence, it is imaginable that the majority of the consequent damages to the child's head, neck and spine originate from the head and ground impact as well as the left-shoulder/arm and ground impact. However, the second impact could also lead to some severe head, neck and spine damages. Moreover, the constant left and right movement of the head that followed after each upwards rebound and downwards falling could result in the stretching of the neck's muscles and arteries. This stretching action can also cause damages to the child's head, neck and spine similar to the damages reported for "The Shaken Baby Syndrome" [94-96].

Chart 38 graphs the *angular acceleration* α, experienced by the child's head as the simulation time progresses. It can be seen that during the head and ground impact, the child's head experiences a fatal angular acceleration equal to -569,300.00 rad/s^2.

For this simulation, the highest-magnitude *angular velocity* ω, was also retrieved from Working Model 2D. This angular velocity was equal to -38.573 rad/s and occurred during the head and ground impact. Based on the reason stated in Sec. 7-7-2-1, during this simulation, the angular velocity experienced by the child's head does not lead to serious or fatal damages.

Summarizing the discussion for this subsection at a shortfall height of 2.5 ft and with a $\mathbf{V_x}$ = -3.0 m/s the child's head experiences three severe NGSs of 339.48 g, 19.05 g and 35.52 g. This translates to dangerous total-accelerations 339.48, 19.05 and 35.52 times higher than the earth's gravitational acceleration of 9.81 m/s^2. Moreover, during the head and ground impact, the child's head experiences a fatal angular acceleration of -569,300.00 rad/s^2 as well as a maximum nonfatal angular velocity equal to -38.573 rad/s.

7-7-3-6 Shortfall Simulation from '3.0 ft' at V_x = '-3.0 m/s'

Fig. 217 through Fig. 221 represent the main dynamical stages during a shortfall simulation of a six months old child from a furniture with a height of 3.0 ft. Fig. 217 shows the child at the beginning of the simulation. Once the simulation starts both driving forces, namely the red horizontal force induced by $\mathbf{V_x}$ as well as the purple gravitational force move the child's body to the left and downwards respectively. The combination of both of these applied forces makes the body to rotate in a CCW fashion around the upper left corner of the furniture. This CCW leftwards and downwards/falling motion continuous until the child experiences a *head-first* impact as shown in Fig. 218. Unlike to the 0.5 ft shortfall simulation conducted at $\mathbf{V_x}$ = -1.0 m/s, during this impact the child is totally separated from the furniture. As explained in Sec. 7-7-1 and Sec. 7-7-3-1, the higher initial shortfall height and the faster horizontal velocity are the reasons why the child separates from the furniture prior the head and ground impact. The separation of the child's body from the furniture is almost identical to the same separation pattern described in Sec. 7-7-3-1 (see Fig. 194).

After the head and ground impact the head and the shoulders experience an upwards lift while the entire body undergoes a CW rotation. This CW motion follows a similar but shorter version of path 'II' as illustrated in Fig. 222. The upwards lift continues until the lower left leg touches the ground as shown in Fig. 219. At this point the head collides with the left shoulder and the body undergoes a CCW fall along a similar but shorter version of path 'IV' (see Fig. 222). At the end of this CCW fall, the body lands on the left shoulder/arm as seen in Fig. 220.

Then, the body slides leftwards until it is stopped by the blue horizontal frictional forces. Fig. 221 shows the final configuration of the child's body. Note that the body landed further to the left compared to final position of the child involved in a 2.5 ft shortfall conducted at $\mathbf{V_x}$ = -3.0 m/s (see Fig. 216). This is because of the 0.5 ft higher initial shortfall height.

Chart 39 graphs the *NGS* experienced by the child's head as the simulation time progresses. As illustrated in this chart, throughout the simulation, on average, the child's head continues to experience a NGS equal to 1.0. This means that the child's head experiences a total-acceleration **|a|**, equal to the earth's gravitational acceleration. However, at the following instant the child's head experiences a higher acceleration compared to the earth's gravitational acceleration:

1. The Head and Ground Impact. NGS = 397.70 g.
2. The Lower-Left-Arm and Ground Impact. NGS = 5.63 g.
3. The Left-Shoulder/Arm and Ground Impact. NGS = 26.79 g.

During the child's head and ground impact, the child's head experiences a total-acceleration **|a|**, 397.70 times higher than the earth's gravitational acceleration. The NGS of 397.70 g was calculated from a outputted **|F|** = 35,112.75 N. Similar to the calculations made in Sec. 7-7-2-1, the child, the division of the obtained **|F|** of 35,112.75 N by 88.29 N (child's weight) equals to 397.70. In other words, during the head and ground impact, the child's head experiences a force 397.70 times the entire weight of the child's body. Therefore,

a shortfall from 3.0 ft at a horizontal velocity of $\mathbf{V_x}$ = -3.0 m/s results in a very severe head and ground impact, leading to possible fatal damages to the head, neck and spine of the child. As reported by Nimityongskul et al., a total-acceleration $|\mathbf{a}| \geq 160.0$ g results in fatal damages [67]. The lower-left-arm and ground impact produced a total-acceleration $|\mathbf{a}|$, 5.63 times higher than the earth's gravitational acceleration. This impact results in a relatively severe landing. The left-shoulder/arm and ground impact results in total-acceleration $|\mathbf{a}|$, 26.79 times higher than the gravitational acceleration.

This shows that the first and last impacts, specially the first impact, absorbed the majority of the energy potential and kinetic energy involved during the shortfall. Hence, it is imaginable that the majority of the consequent damages to the child's head, neck and spine originate from the head and ground impact as well as the left-shoulder/arm and ground impact. However, the constant left and right movement of the head that followed after each upwards rebound and downwards falling could result in the stretching of the neck's muscles and arteries. This stretching action can also cause damages to the child's head, neck and spine similar to the damages reported for "The Shaken Baby Syndrome" [94-96].

Chart 40 graphs the *angular acceleration* α, experienced by the child's head as the simulation time progresses. It can be seen that during the head and ground impact, the child's head experiences a fatal angular acceleration equal to -565,400.00 rad/s^2.

For this simulation, the highest-magnitude *angular velocity ω*, was also retrieved from Working Model 2D. This angular velocity was equal to 36.902 rad/s and occurred during the head and ground impact. Based on the reason stated in Sec. 7-7-2-1, during this simulation, the angular velocity experienced by the child's head does not lead to serious or fatal damages.

Summarizing the discussion for this subsection at a shortfall height of 3.0 ft and with a $\mathbf{V_x}$ = -3.0 m/s the child's head experiences three severe NGSs of 397.70 g, 5.63 g and 26.79 g. This translates to dangerous total-accelerations 339.48, 19.05 and 35.52 times higher than the earth's gravitational acceleration of 9.81 m/s^2. Moreover, during the head and ground impact, the child's head experiences a fatal angular acceleration of -565,400.00 rad/s^2 as well as a maximum nonfatal angular velocity equal to 36.902 rad/s.

7-7-4 Comparison of All Results

The following three subsections compare all the obtained results with each other. The first subsection compares the results obtained for all individual shortfall simulations that were categorized within the first simulation group, namely shortfall simulations incorporating a horizontal velocity of $\mathbf{V_x}$ = -1.0 m/s. The second subsection compares the results obtained for all individual shortfall simulations that were categorized within the second simulation group, namely shortfall simulations incorporating a horizontal velocity of $\mathbf{V_x}$ = -3.0 m/s. The third subsection compares the results obtained from both simulation groups with each other.

7-7-4-1 Comparison of Results within the First Group (V_x = *-1.0 m/s)*

Fig. 162 through Fig. 191 as well as Chart 17 through Chart 28 represent the main dynamical stages during all the shortfall simulations of a six months old child. The initial shortfall heights of all shortfall simulations range from 0.5 ft to 3.0 ft. Fig. 192 represents a typical *Path of shortfall* for a shortfall simulation conducted at $\mathbf{V_x}$ = -1.0 m/s.

The obtained results regarding the 0.5 ft and the 1.0 ft shortfall simulations (see Fig. 162 through Fig. 170) show that these shortfalls follow a very similar *Path of shortfall* before the head and ground impact. The child models within both of these simulations experience a CCW leftward and downward motion along the initial portions of path 'I' as illustrated in Fig. 192. Then, the child's heads of both simulations hit the ground while the body still leans on the furniture. After the head and ground impact, both models bounce of the ground for a very short distance and then fall back on their head and left shoulder. Consequently, they slide leftwards on the ground until they are stopped by the frictional forces existing between them and the ground. Although the child within the 1.0 ft shortfall simulation stops further left compared to the within the 0.5 ft shortfall simulation, no major difference between the *Fall-Pattern* of these two simulations can be seen. Clearly, a higher NGS of 51.85 g is reached by the 1.0 ft shortfall simulation compared to the lower NGS of 1.00 g, reached during in the 0.5 ft shortfall simulation.

shortfall simulations starting from an initial shortfall-height ≥ 1.5 ft result in the separation of the child's body from the furniture prior the first head and ground impact. Clearly, this results in total-accelerations of higher magnitudes, since unlike the previous cases, the furniture does not continuously drag on the child's body until the occurrence of the first head and ground impact. However, shortfalls with an initial shortfall height ≥ 1.5 ft follow different *Paths of* shortfall and therefore possess different *Fall-Patterns*.

The obtained results regarding the 1.5 ft and the 2.0 ft shortfall simulations (see Fig. 171 through Fig. 181) show that these shortfalls follow a very similar *Path of shortfall* throughout their entire simulations. Both child models experience a switch in their rotation once they experience the first head and ground impact. Their rotation changes from a CCW rotation to a CW rotation. This behavior only applies to the child models involved in the 1.5 ft and 2.0 ft shortfall simulations. After the first head and ground impact, both models experience additional head and ground impacts. The model within the 1.5 ft shortfall simulation experiences a second head and ground impact before it finally lands on the ground. The model within the 2.0 ft shortfall simulation experiences a second and third head and ground impact before it finally lands on the ground. After the last head and ground impact, both models land on their left arms. Then, they slightly slide leftwards and stop moving. Due to the 0.5 ft higher initial shortfall height, the final position of the child involved in the 2.0 ft shortfall simulation is further to the left compared to the final position of the child involved in a 1.5 ft shortfall simulation. Additionally, a higher NGS is reached by the child

involved in the 2.0 ft shortfall simulation. The first head and ground impact of the 1.5 ft shortfall simulation results in a maximum NGS of 123.71 g. The first head and ground impact of the 2.0 ft shortfall simulation results in a maximum NGS of 176.16 g.

The obtained results regarding the 2.5 ft and the 3.0 ft shortfall simulations (see Fig. 182 through Fig. 192) show that these shortfalls follow a very similar *Path of shortfall* throughout their entire simulations. At first, all child models experience a CCW leftward and downward motion along path 'I' as illustrated in Fig. 192. It should be noted that only the child in the 3.0 ft simulation follows the entire length of path 'I'. The 2.0 ft and 2.5 ft models collide with the ground before reaching the end of path 'I'. After the first head and ground impact, in both simulations, the child does not experience a switch in its CCW rotation. The CCW rotation continues all the way to end.

After experiencing the first head and ground impact, both models within the 2.5 ft and 3.0 ft simulations experience additional ground impacts before they finally land on the ground. The model within the 2.5 ft shortfall simulation experiences a second head and ground impact before it finally lands on the ground. The model within the 3.0 ft shortfall simulation experiences an additional right-shoulder/arm and ground impact before it finally lands on the ground. Consequently after landing, both models slide leftwards on the ground until they are stop moving. Due to the 0.5 ft higher initial shortfall height, the final position of the child involved in the 3.0 ft shortfall simulation is further to the left compared to the final position of the child involved in a 2.5 ft shortfall simulation.

Additionally, a higher NGS is reached by the child involved in the 3.0 ft shortfall simulation. The first head and ground impact of the 2.5 ft shortfall simulation results in a maximum NGS of 259.52 g. The first head and ground impact of the 2.0 ft shortfall simulation results in a maximum NGS of 319.66 g.

By comparing the results of all the shortfall simulations conducted at $\mathbf{V_x}$ = -1.0 m/s, it is clear that the initial shortfall height plays a big roll. As this low horizontal velocity, if the initial shortfall height is equal or shorter than 1.0 ft, the body drags along the furniture's corner until is collides with the ground. Since the body drags along the furniture's corner, the child experiences a relatively soft landing.

With an initial shortfall height of 1.5 ft or higher, the child separates itself from the furniture prior the first head and ground impact. By doing so, it experiences a severe head and ground impact. If the initial height is 1.5 ft or 2.0 ft, the child switches from an original CCW rotation to a CW rotation once it experiences the first head to ground impact. This sudden change in rotation direction can result in severe neck and spine damages. In all simulations with an initial shortfall height of 2.0 ft or less the child lands on its left arm.

With an initial shortfall height of 2.5 ft and 3.0 ft the child does not undergo a switch in its CCW rotation. The CCW rotation continues throughout all head/body and ground impacts. Therefore, after finally landing on the ground the child has rotated 180° compared to its original position at t = 0.00 sec. This drastic rotation can also severely damage the neck and spine of the child.

For all simulations, the first head and ground impact resulted in the maximum NGS. As the initial shortfall height gradually increased, the maximum NGSs reached higher and higher magnitudes. Moreover, the increase in the initial shortfall height caused the child's body to lend further and further away from the furniture.

7-7-4-2 Comparison of Results within the Second Group (V_x = -3.0 m/s)

Fig. 193 through Fig. 221 as well as Chart 29 through Chart 40 represent the main dynamical stages during all the shortfall simulations of a six months old child. The initial shortfall heights of all shortfall simulations range from 0.5 ft to 3.0 ft. Fig. 222 represents a typical *Path of shortfall* for a shortfall simulation conducted at $\mathbf{V_x}$ = -3.0 m/s.

Unlike the first two shortfalls conducted at $\mathbf{V_x}$ = -1.0 m/s, the child's body within all the shortfalls conducted at $\mathbf{V_x}$ = -3.0 m/s separates itself from the furniture before experiencing the first head and ground impact. This results in the fact that all shortfalls conducted at $\mathbf{V_x}$ = -3.0 m/s follow a very similar *Path of shortfall* before the head and ground impact. The child models within all of these simulations experience a CCW leftward and downward motion along path 'I' as illustrated in Fig. 222. However, depending on the initial shortfall height, every model reaches a certain length of path 'I' before it collides with the ground. Only the model involved in a 3.0 ft shortfall follows the entire length of path 'I'.

After the first head and ground impact all models switch their rotation from a CCW rotation to a CW rotation. With a CW rotation their head and shoulders lifts from the ground while their bodies follow a path similar to path 'II' as shown in Fig. 222. The extent of this uplift depends on the initial shortfall height. Only the child involved in the 3.0 ft shortfall simulation follows the entire length of path 'II'. Other models reach a lower elevation depending on their initial shortfall height.

Depending on the initial shortfall height, this CW uplift continues until either the lower-left-arm or lower-left-leg touches the ground. At this instant, the child's rotation changes again, namely, form a CW rotation back to a CCW rotation. The CCW rotation is continued along a path similar to path 'IV'. Only the child involved in the 3.0 ft shortfall simulation follows the entire length of path 'IV'. Other models follow a similar path depending on their initial shortfall height.

By comparing the results of all the shortfall simulations conducted at $\mathbf{V_x}$ = -3.0 m/s with the shortfall simulations conducted at $\mathbf{V_x}$ = -1.0 m/s, it is clear that higher NGS are reached with the higher horizontal velocity $\mathbf{V_x}$ = -3.0 m/s. Even with an initial shortfall length of 0.5 ft a NGS of 41.43 g is achieved. When comparing this high magnitude NGS with the NGS of 1.00 g achieved from the same height but a lower horizontal velocity $\mathbf{V_x}$ = -1.0 m/s, it is clear that a higher horizontal velocity results in more devastating landings.

It is very interesting that only one head and ground impact was seen throughout all the simulations conducted at $\mathbf{V_x}$ = -3.0 m/s. As explained in Sec. 7-7-2-3 and Sec. 7-7-3-1, this is because that a higher horizontal velocity $\mathbf{V_x}$ results in a falling path, i.e. path 'I' with a higher radius of curvature. With a higher radius curvature, the child requires a higher initial shortfall length to get close to extension of path 'I', namely path 'III' (see Fig. 192 and Fig. 222). If the initial shortfall height is high enough, the child's falling pattern will follow path 'I' and then continue along path 'III'. In none of the simulations conducted herein, path 'III' was followed. This is because the initial shortfall height was not high enough. The closer the body gets to path 'III' the more it rotates in a CCW

fashion as it falls. The degree of this CCW rotation dictates the consequent *Fall-Patterns*. The reason why all the shortfall simulations conducted at $\mathbf{V_x}$ = -3.0 m/s resulted in similar *Fall-Patterns* is the fact that they experienced more or less similar amounts of CCW rotations while they are approaching the ground.

For all simulations, the first head and ground impact resulted in the maximum NGS. As the initial shortfall height gradually increased, the maximum NGSs reached higher and higher magnitudes. An overall maximum NGS = 397.70 g was achieved during the head to ground impact of 3.0 ft simulation conducted at $\mathbf{V_x}$ = -3.0 m/s. Moreover, the increase in the initial shortfall height caused the child's body to lend further and further away from the furniture.

7-7-4-3 Comparison of All Results obtained for Both Groups

Table 10 represents the maximum NGSs achieved during the first head and ground impact of all twelve shortfall simulations.

Table 10:
Maximum Number of 'g's (NGS)

Initial Shortfall Height (ft)	*NGS* (m/s^2) for Vx = -1.0 m/s Simulations	*NGS* (m/s^2) for Vx = -3.0 m/s Simulations
0.0	0.00	0.00
0.5	1.29	41.43
1.0	51.85	124.39
1.5	123.71	180.57
2.0	176.16	249.21
2.5	259.52	339.48
3.0	319.66	397.70
Fatal NGS $\geq$ 160.00 g [Nimityongskul et al, 5]		

Table 10: Ground impact NGSs involved in shortfalls at V_x = -1.0 m/s & V_x = -3.0 m/s.

As seen in Table 10, it is clear that at the same initial shortfall height, a higher NGS is achieved at a higher horizontal velocity of $\mathbf{V_x}$ = -3.0 m/s. Note that at both horizontal velocities, no simulations at 0.0 ft were conducted. It is assumed that shortfalls from an initial shortfall height of 0.0 ft do not occur in real life. Therefore, it is assumed that the resulting NGSs are 0.00 g. Moreover, Table 10

illustrates that at the same horizontal velocity $\mathbf{V_x}$, higher NGSs are achieved as the initial shortfall height is increased.

By utilizing the values within Table 10, three additional charts are constructed. The first chart, namely Chart 41, represents the first and by far the most severe *ground impact 'g's* obtained from the first group of simulation ($\mathbf{V_x}$ = -1.0 m/s). The second chart, namely Chart 42, represents the first and by far the most severe *ground impact 'g's* obtained from the second group of simulations ($\mathbf{V_x}$ = -3.0 m/s). The third chart, namely Chart 43, represents and compares the *ground impact 'g's* of all twelve simulations with each other.

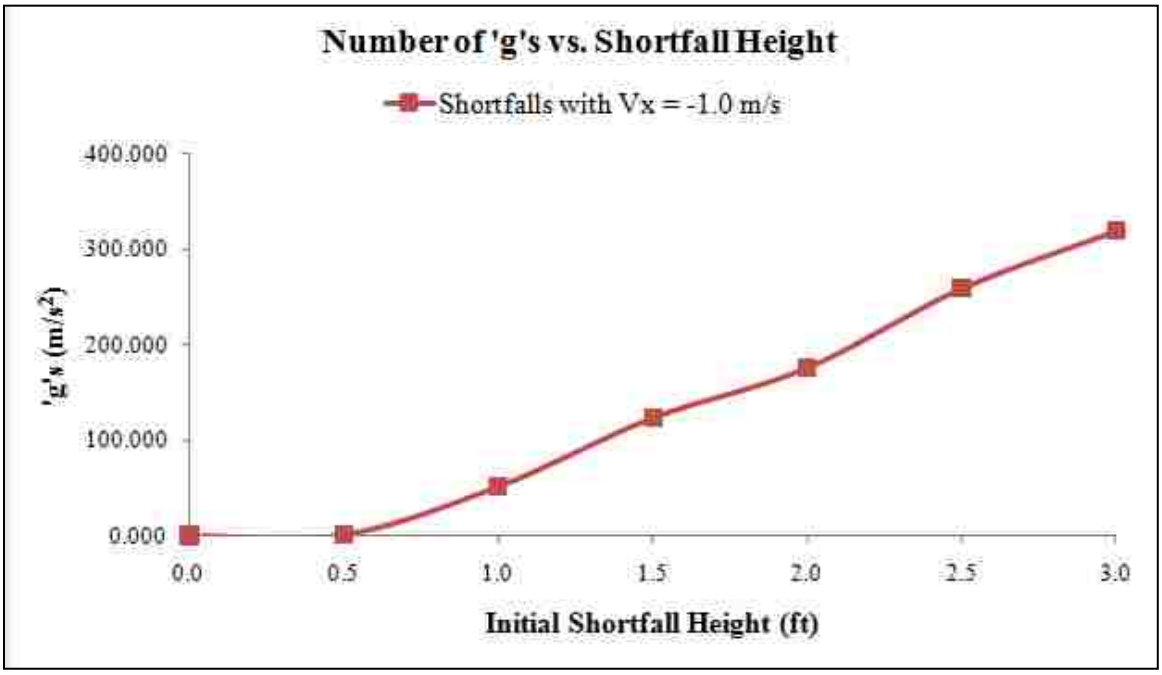

Chart 41: Ground impact 'g's involved in shortfalls at V_x = -1.0 m/s.

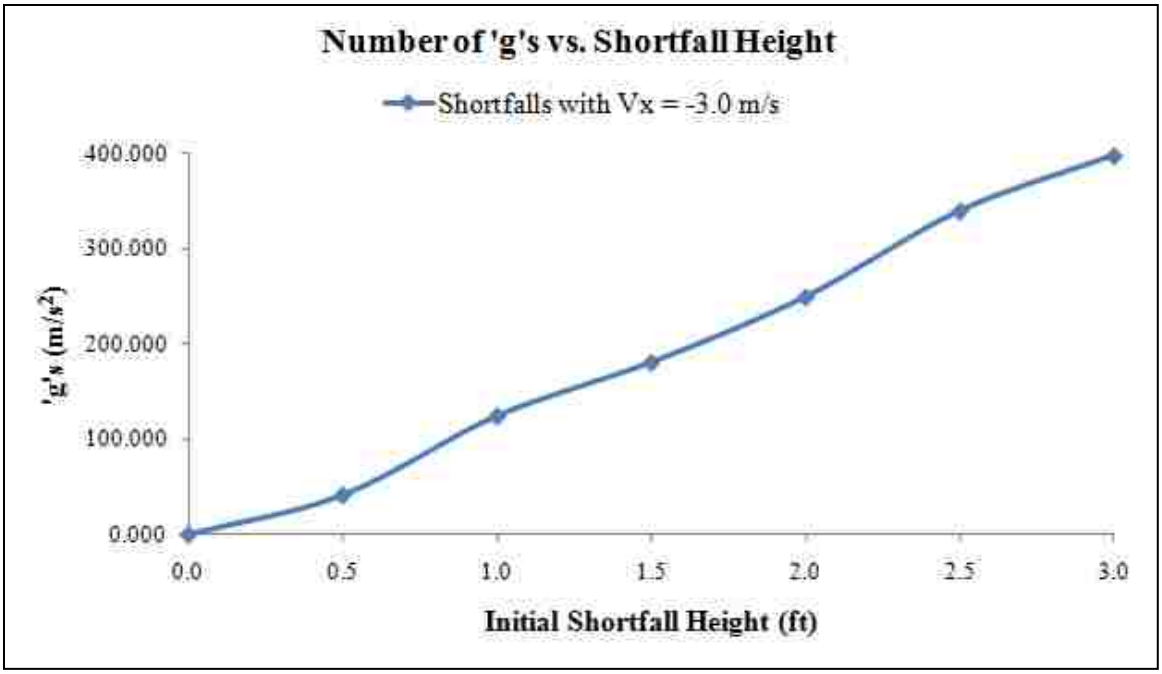

Chart 42: Ground impact 'g's involved in shortfalls at V_x = -3.0 m/s.

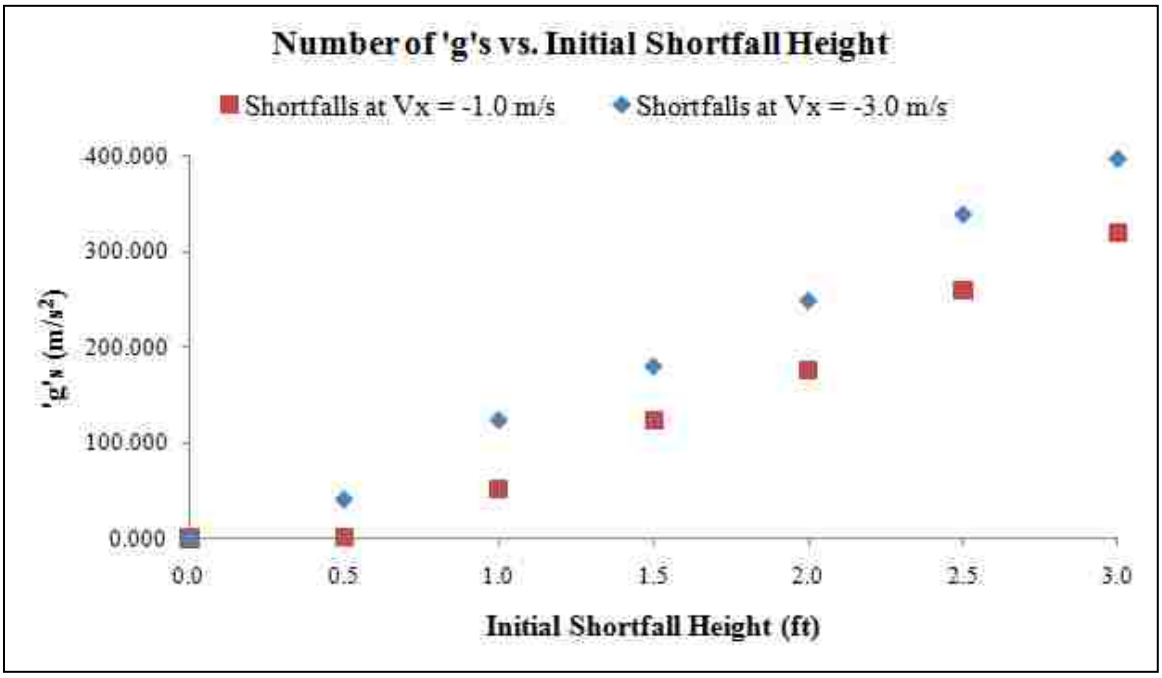

Chart 43: Ground impact 'g's involved in shortfalls at V_x = -1.0 m/s & V_x = -3.0 m/s.

As seen on Chart 41 and Chart 42, the NGSs in either chart approximately increase in a linear fashion as the initial shortfall height is changed in a linear

fashion. This shows that at both horizontal velocities a linear 0.5 ft increase in initial shortfall height leads to a linear increase in the resulting NGS. Chart 43 directly compares the maximum NGSs of the first simulation group ($\mathbf{V_x}$ = -1.0 m/s) and the second simulation group ($\mathbf{V_x}$ = -3.0 m/s). The second group follows a very similar pattern as the first group's pattern. However, the pattern of the second group is shifted upwards as it should be due to a difference in horizontal velocity of -2.0 m/s.

Table 11 represents the highest-magnitude *angular accelerations 'α's* achieved during the first head and ground impact of all twelve shortfall simulations.

Table 11: Highest Magnitude of Angular Acceleration 'α'		
Shortfall Height (ft)	**α (rad/s^2) for Vx = -1.0 m/s Simulations**	**α (rad/s^2) for Vx = -3.0 m/s Simulations**
0.0	0.000	0.000
0.5	0.000	80070.000
1.0	-53190.000	-225800.000
1.5	217800.000	-318300.000
2.0	458900.000	-408900.000
2.5	529900.000	-569300.000
3.0	411600.000	-565400.000
Serious and/or Fatal $\alpha \geq 10{,}000.00$ rad/s^2 [Cory et al., 35]		

Table 11: Highest-magnitude 'α's involved in shortfalls at V_x = -1.0 m/s & V_x = -3.0 m/s.

As seen in Table 11, except the 0.5 ft shortfall at $\mathbf{V_x}$ = -1.0 m/s, all other shortfalls result in serious or fatal cranial injuries. Note that the positive or negative signs of the 'α's only underline the CW or CCW direction of the 'α's. A positive sign means that the child's head was accelerated towards its left shoulder. A negative sign means that the child's head was accelerated towards its right

shoulder. Only the magnitude of an angular acceleration indicates the severity/danger of that angular acceleration.

Table 12 represents the highest-magnitude *angular velocities 'ω's* achieved during the first head and ground impact of all twelve shortfall simulations.

Table 12: Highest Magnitude of Angular Velocity 'ω'		
Shortfall Height (ft)	**ω (rad/s) for Vx = -1.0 m/s Simulations**	**ω (rad/s) for Vx = -3.0 m/s Simulations**
0.0	0.000	0.000
0.5	0.000	17.770
1.0	-14.989	-22.822
1.5	-14.119	-28.224
2.0	-14.002	-36.875
2.5	-13.645	-38.573
3.0	17.535	36.902
Serious and/or Fatal $\omega \geq 45.00$ rad/s [Cory et al., 35]		

Table 12: Highest-magnitude 'ω's involved in shortfalls at V_x = -1.0 m/s & V_x = -3.0 m/s.

As seen in Table 12, all shortfalls result in no injuries. However, during the 2.0 ft, 2.5 ft and 3.0 ft shortfalls of the second group, 'ω's close to 45.00 rad/s are achieved. Although these 'ω's could result in cranial injuries, the cranial injuries would be non-serious or nonfatal. Note that the positive or negative signs of the ''ω's only underline the CW or CCW direction of the 'ω's. A positive sign means that the child's head was moved towards its left shoulder. A negative sign means

that the child's head was moved towards its right shoulder. Only the magnitude of an angular velocity indicates the severity/danger of that angular velocity.

7-8 Additional Research, Results and Discussions

7-8-1 3.0 ft *Vertical* Free-Fall

The shortfall simulations conducted in Sec. 7-6 all involve a continuous horizontal velocity $\mathbf{V_x}$. It is also interesting to conduct a simulation where the child experiences just a *free-fall*, i.e., a shortfall that does not incorporate a horizontal velocity $\mathbf{V_x}$.

To investigate the *free-fall* of a six months old child a 3.0 ft simulation incorporating a horizontal velocity $\mathbf{V_x}$ = 0.0 m/s is conducted. For this simulation the child's body is aligned along the vertical axis, namely the *y*-axis. Moreover, the child is not in contact with any piece of furniture. Rather, the child's body is released from 3.0 ft straight down towards the ground.

For this vertical *free-fall* simulation, the forces as well as the angular velocities and accelerations experienced by the child's head were tracked. From the obtained forces, linear accelerations were calculated.

Fig. 224 through Fig. 232 as well as Chart 44 through Chart 45 represent the results obtained for the 3.0 ft shortfall simulation incorporating a horizontal velocity $\mathbf{V_x}$ = 0.0 m/s.

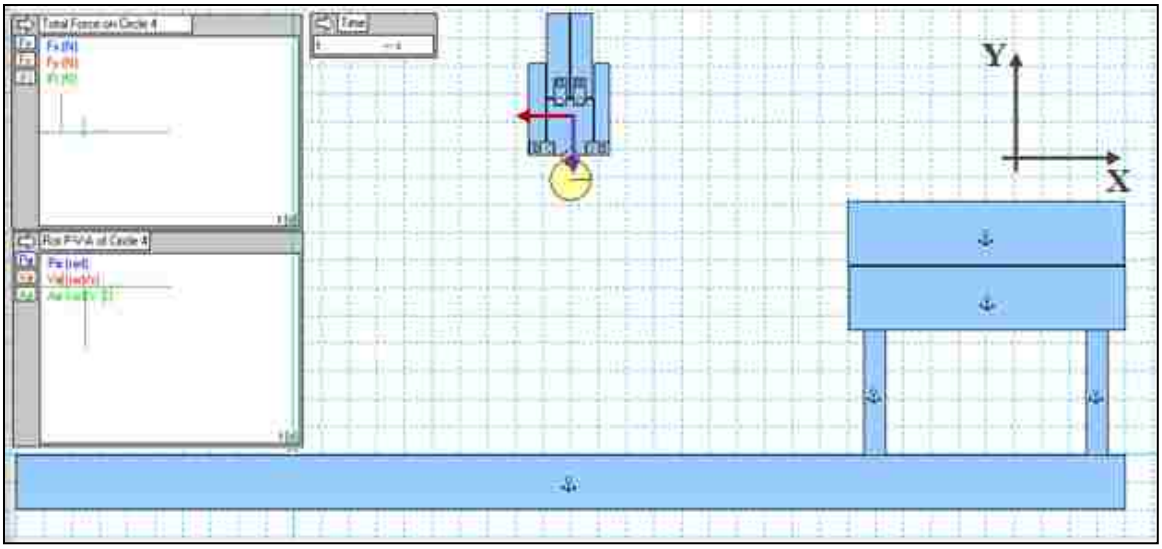

Figure 224: 3.0 ft shortfall at V_x = 0.0 m/s. Initial State.

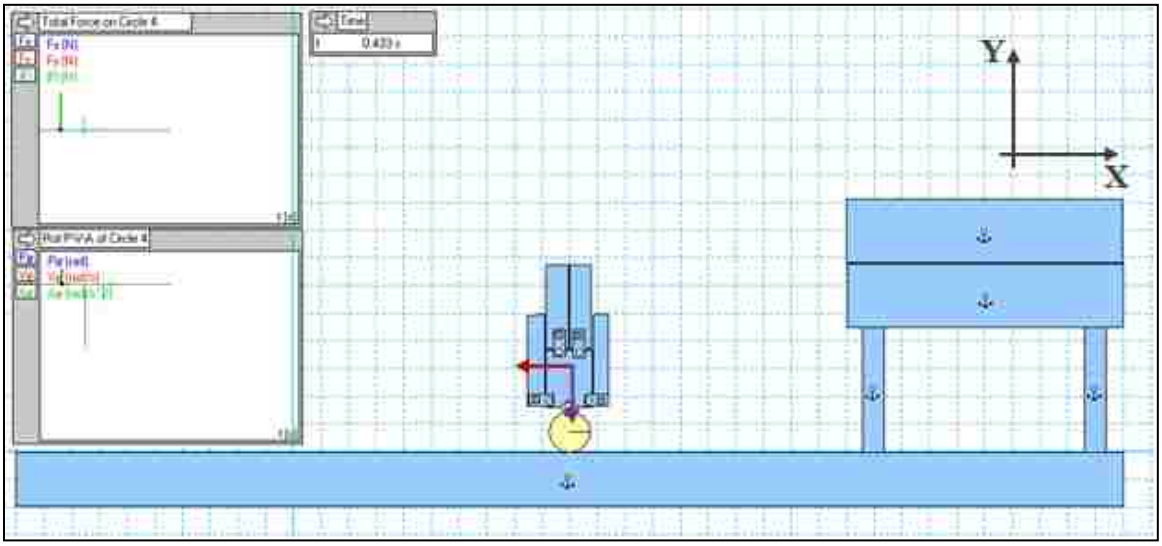

Figure 225: 3.0 ft shortfall at V_x = 0.0 m/s. 1st Head and Ground Impact.

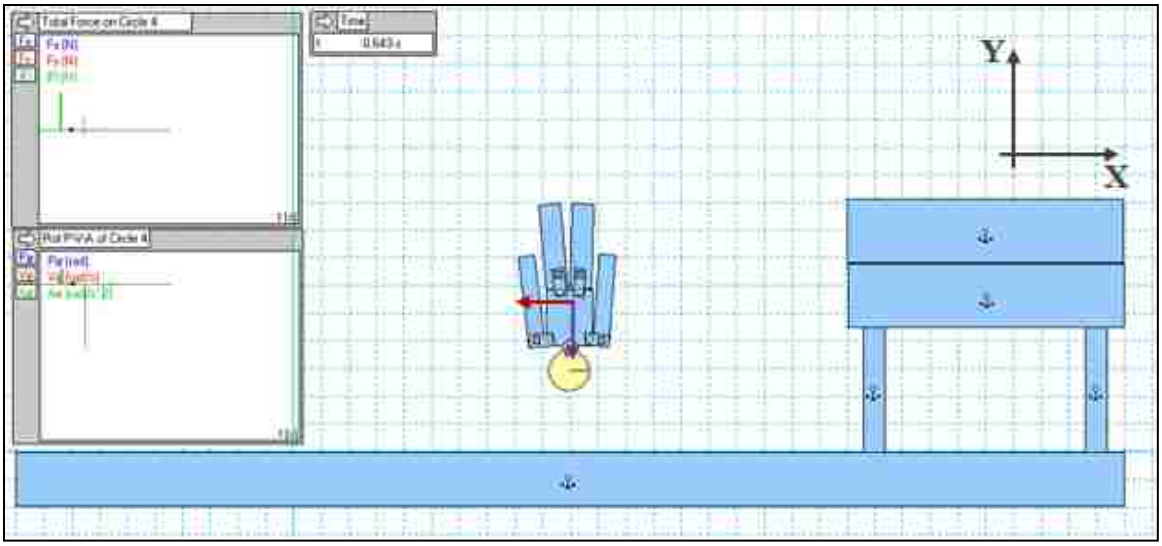

Figure 226: 3.0 ft shortfall at V_x = 0.0 m/s. Body's Configuration at the End of 1st Rebound.

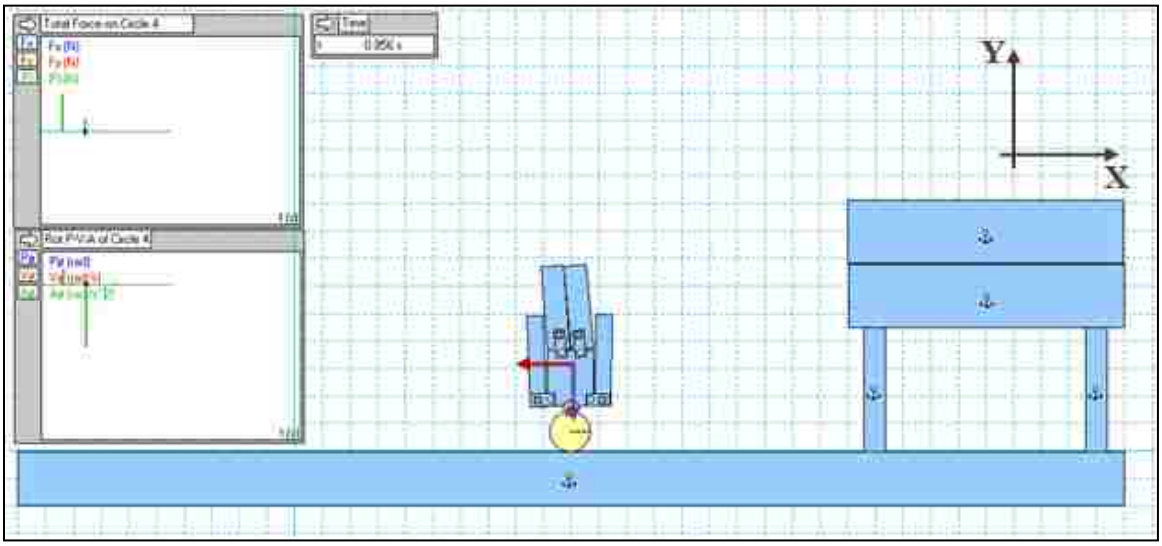

Figure 227: 3.0 ft shortfall at V_x = 0.0 m/s. 2nd Head and Ground Impact.

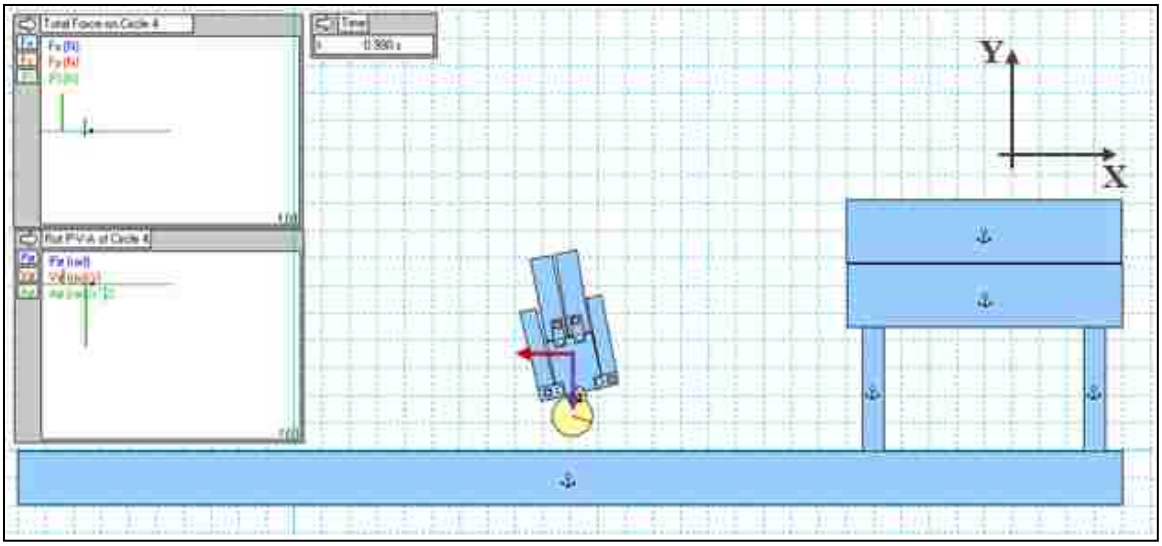

Figure 228: 3.0 ft shortfall at V_x = 0.0 m/s. Body's Configuration at the End of 2nd Rebound.

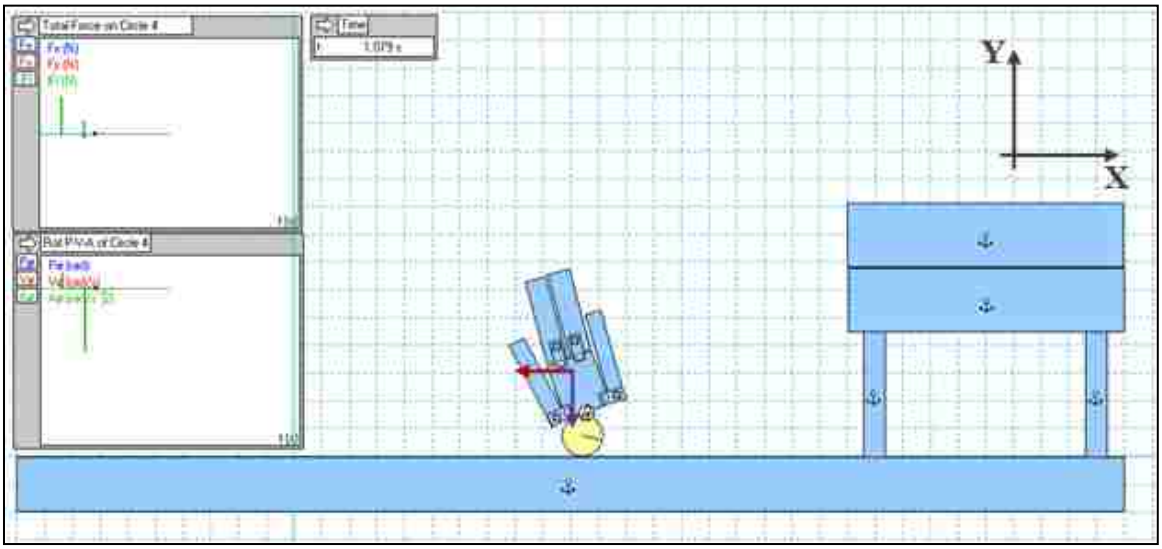

Figure 229: 3.0 ft shortfall at V_x = 0.0 m/s. 3rd Head and Ground Impact.

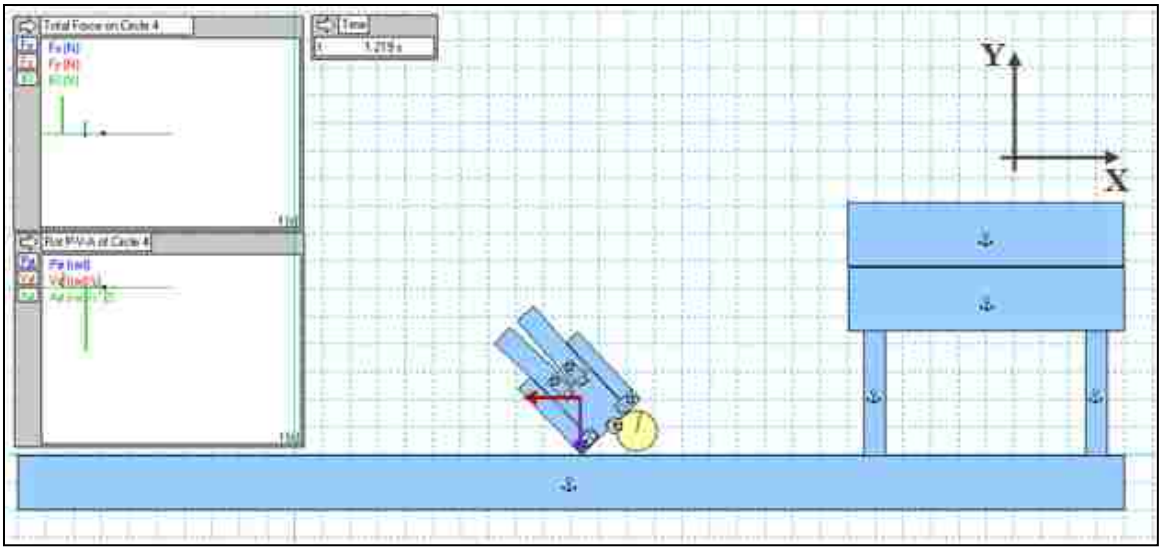

Figure 230: 3.0 ft shortfall at V_x = 0.0 m/s. Right-Shoulder and Ground Impact.

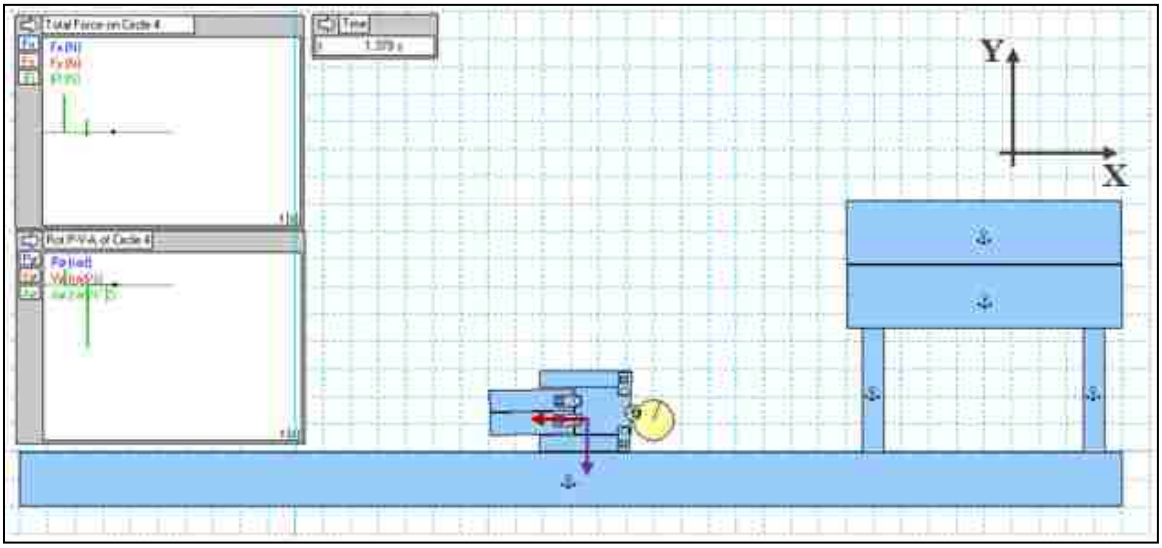

Figure 231: 3.0 ft shortfall at V_x = 0.0 m/s. Landing on the Right-Shoulder/Arm.

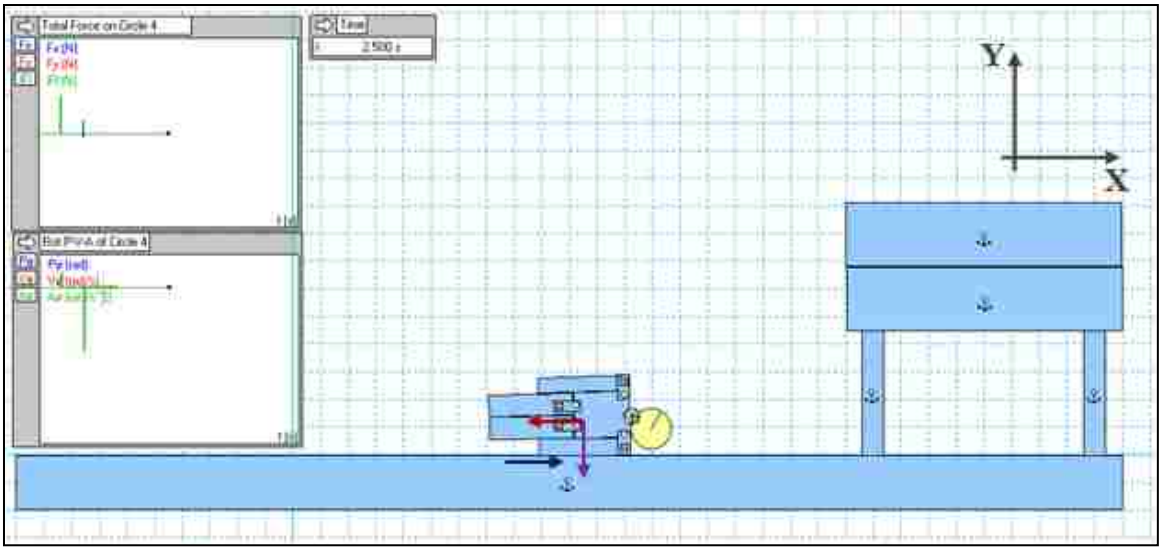

Figure 232: 3.0 ft shortfall at V_x = 0.0 m/s. Final State.

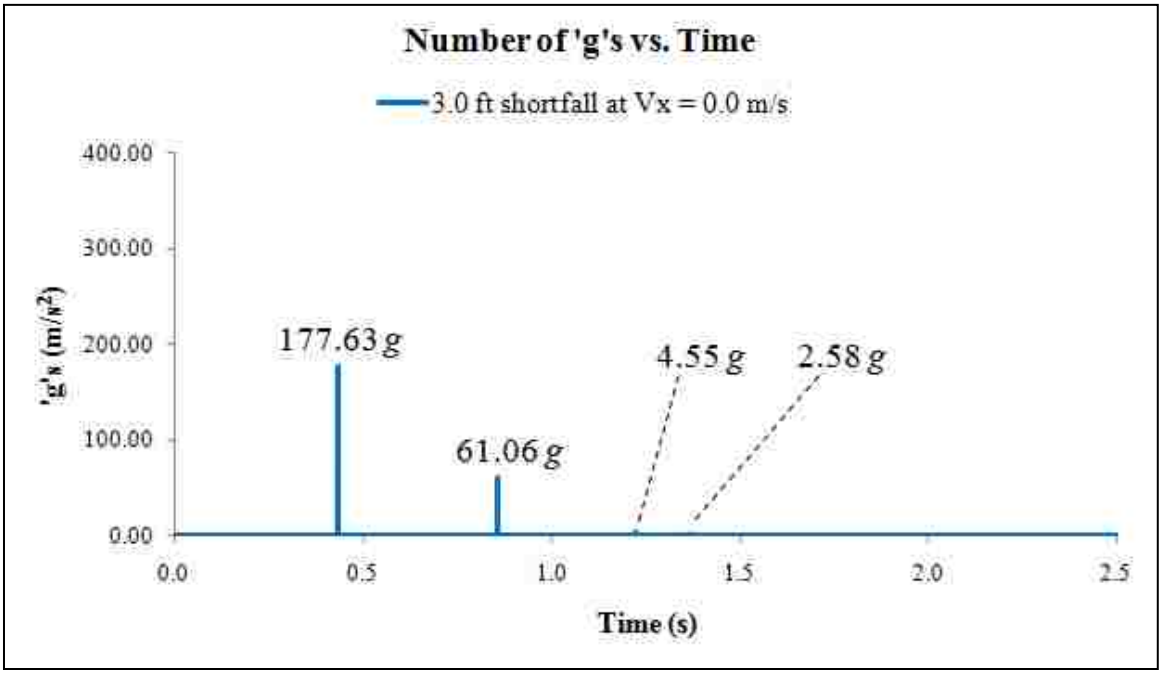

Chart 44: 3.0 ft shortfall at V_x = 0.0 m/s. Number of 'g's vs. Time.

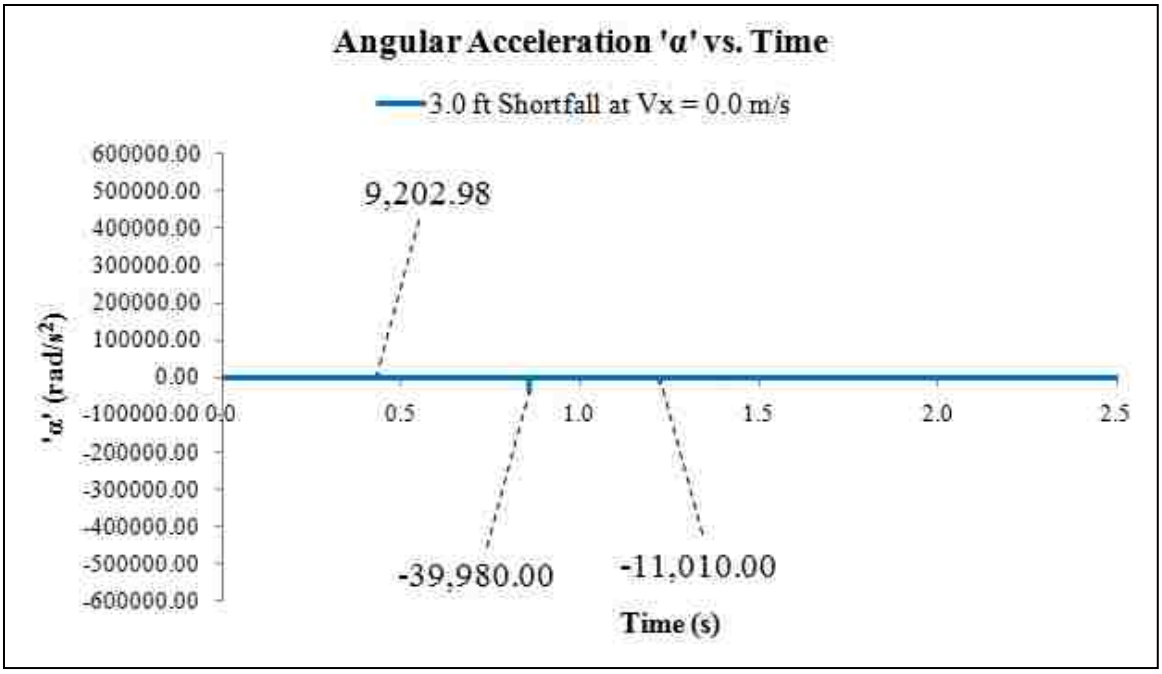

Chart 45: 3.0 ft shortfall at V_x = 0.0 m/s. Angular Acceleration ‘α’ vs. Time.

Fig. 224 through Fig. 232 represent the main dynamical stages during a shortfall simulation of a six months old child from a furniture with a height of 3.0 ft conducted at a horizontal velocity $\mathbf{V_x}$ = 0.0 m/s. Fig. 224 shows the child at the beginning of the simulation. Once the simulation starts both driving force, namely the purple gravitational force moves the child's body downwards. Note that the red force, namely the force induced by the horizontal velocity is zero. This is because no horizontal velocity was applied to the child's body during this simulation.

With only the gravitational acceleration applied to the child's body, it experiences *free-fall*. The *free-fall* continuous until the child experiences a first *head-first* impact as shown in Fig. 225. Note that during the 1st head and ground impact the child's body possesses an almost perfect vertical configuration.

After the first head and ground impact the entire body experience an upwards lift without experiencing a CW or CCW rotation. Fig. 226 shows the body at the end of the first uplift/rebound. Following the configuration shown in Fig. 226, the body experiences a second *free-fall*. Fig. 227 illustrates the child's configuration during the second head and ground impact. Note that the legs are slightly tilted towards the left of the *y*-axis. With this slight tilt, as the body undergoes the second rebound, it experiences a slight CCW rotation as well. Fig. 228 shows the body's configuration at the end of the second rebound. Note that the child's body is entirely tilted to the left of the *y*-axis.

With this total-body tilt, the body's CCW increases as the body undergoes a third *free-fall*. Fig. 229 shows the third head and ground impact. Then a third rebound

occurs followed by a right-shoulder and ground impact as illustrated in Fig. 230. Fig. 231 shows the landing of the child on its right-shoulder/arm. Fig. 232 shows the final configuration of the child's body at the end of the 2.5 sec shortfall simulation.

Chart 44 graphs the *NGS* experienced by the child's head as the simulation time progresses. As illustrated in this chart, throughout the simulation, on average, the child's head continues to experience a NGS equal to 1.0. This means that the child's head experiences a total-acceleration $|\mathbf{a}|$, equal to the earth's gravitational acceleration. However, at the following instant the child's head experiences a higher acceleration compared to the earth's gravitational acceleration:

1. The 1st Head and Ground Impact. NGS = 177.63 g.
2. The 2nd Head and Ground Impact. NGS = 61.06 g.
3. The 3rd Head and Ground Impact. NGS = 4.55 g.
4. The Right-Shoulder and Ground Impact. NGS = 2.58 g.

During the child's first head and ground impact, the child's head experiences a total-acceleration $|\mathbf{a}|$, 177.63 times higher than the earth's gravitational acceleration. The NGS of 177.63 g was calculated from a outputted $|\mathbf{F}|$ = 15,600.00 N. Similar to the calculations made in Sec. 7-7-2-1, the child, the division of the obtained $|\mathbf{F}|$ of 15,600.00 N by 88.29 N (child's weight) equals to 177.63. In other words, during the head and ground impact, the child's head experiences a force 177.63 times the entire weight of the child's body. Therefore, a shortfall from 3.0 ft at a horizontal velocity of $\mathbf{V_x}$ = 0.0 m/s results in a very severe head and ground impact, leading to possible

fatal damages to the head, neck and spine of the child. As reported by Nimityongskul et al., a total-acceleration $|\mathbf{a}| \geq 160.0$ g results in fatal damages [67].

The second head and ground impact resulted in a total-acceleration $|\mathbf{a}|$, 61.06 times higher than the earth's gravitational acceleration. In other words, during the second head and ground impact, the child's head experiences a force 61.06 times the child's weight. The third head and ground impact and the right-arm and ground impact respectively produced total-accelerations, 4.55 and 2.58 times higher than the earth's gravitational acceleration. Therefore, the last two impacts with the ground do not result in serious or fatal damages.

By looking at Table 10, it can be seen that the obtained NGSs involved in this simulation do not exceed the NGSs of the 3.0 ft simulations conducted at $\mathbf{V_x}$ = -1.0 m/s and $\mathbf{V_x}$ = -3.0 m/s. This is based on the fact that there is no applied horizontal velocity $\mathbf{V_x}$ during the *free-fall* simulation. Without a horizontal velocity $\mathbf{V_x}$, no horizontal force $\mathbf{F}_x$, is applied to the child's body. Therefore, according to Eqn. 16, the total force $|\mathbf{F}|$ will have a smaller magnitude compared to the shortfall simulations where a horizontal force exists, namely simulations conducted at $\mathbf{V_x}$ = -1.0 m/s and $\mathbf{V_x}$ = -3.0 m/s. With a reduced total applied force $|\mathbf{F}|$, the consequent total applied acceleration $|\mathbf{a}|$, will also have a smaller magnitude (see Eqn. 17). Therefore, as expected the NGSs obtained during the free-fall shortfall simulation have a smaller magnitude compared the NGSs obtained during the shortfall simulations conducted at $\mathbf{V_x}$ = -1.0 m/s and $\mathbf{V_x}$ = -3.0 m/s.

This shows that the first and second head and ground impacts, specially the first impact, absorbed the majority of the energy potential and kinetic energy involved during the shortfall. Hence, it is imaginable that the majority of the consequent damages to the child's head, neck and spine originate from the first and second head and ground impacts. However, the constant left and right movement of the head that followed after each upwards rebound and downwards falling could result in the stretching of the neck's muscles and arteries. This stretching action can also cause damages to the child's head, neck and spine similar to the damages reported for "The Shaken Baby Syndrome" [94-96].

Chart 45 graphs the *angular acceleration α*, experienced by the child's head as the simulation time progresses. It can be seen that during the second and third head and ground impacts, respectively, the child's head experiences fatal angular accelerations equal to -39,980.00 rad/s^2 and -11,010.00 rad/s^2. The first head ground impact also resulted in a nearly fatal angular acceleration of 9,202.00 rad/s^2. The right-shoulder and ground impact resulted in relatively harmless angular acceleration of 732.11 rad/s^2.

By comparing these angular accelerations with the angular accelerations obtained for the 3.0 ft shortfall simulations conducted at $\mathbf{V_x}$ = -1.0 m/s and $\mathbf{V_x}$ = -3.0 m/s (see Table 11), it can be determined that they have a smaller magnitude. This is because of the perfect vertical configuration of the child's body during the free-fall. To be more precise, the child's vertical configuration prior the first head and ground impact.

A perfectly vertical impact should not result in any angular accelerations. However, during such collision, the child's neck undergoes *buckling*. In fact, it is the *buckling* that causes the (lower magnitude) angular accelerations. As the body's configuration deviates from the vertical axis, the subsequent head and ground impacts, naturally, do result in higher magnitude angular accelerations. Therefore, the angular acceleration obtained during the second head and ground impact has a higher magnitude compared to the angular acceleration obtained during the first head and ground impact.

For this simulation, the highest-magnitude *angular velocity* ω, was also retrieved from Working Model 2D. This angular velocity was equal to -13.18 rad/s and occurred during the second head and ground impact. Based on the reason stated in Sec. 7-7-2-1, during this simulation, the angular velocity experienced by the child's head does not lead to serious or fatal damages.

By comparing this angular velocity with the angular velocities obtained for the 3.0 ft shortfall simulations conducted at $\mathbf{V_x}$ = -1.0 m/s and $\mathbf{V_x}$ = -3.0 m/s (see Table 12), it can be determined that it has a smaller magnitude. This is because of the perfect vertical configuration of the child's body during the free-fall. To be more precise, the child's vertical configuration prior the first head and ground impact.

A perfectly vertical impact should not result in any angular velocities. However, during such collision, the child's neck undergoes *buckling*. In fact, it is the *buckling* that causes the (lower magnitude) angular velocities.

Summarizing the discussion for this subsection at a shortfall height of 3.0 ft and with a $\mathbf{V_x}$ = 0.0 m/s the child's head experiences three severe NGSs of 177.63 g, 61.06 g and 4.55 g. This translates to dangerous total-accelerations 177.63, 61.06 and 4.55 times higher than the earth's gravitational acceleration of 9.81 m/s^2. Moreover, during the first three head and ground impacts, the child's head experiences fatal or nearly fatal angular accelerations of 9,202.98 rad/s^2, -39,980.00 rad/s^2 and -11,010.00 rad/s^2 as well as a maximum nonfatal angular velocity equal to -13.18 rad/s.

7-8-2 Variation of the Coefficient of Restitution, *'e'*

For the shortfall simulations in Sec. 7-1, a *Coefficient of Restitution* of 0.5 was chosen. This is because of the simple fact that a precise and definitive '*e*' cannot be set for the shortfalls of a child. The value of 'e' depends on the hardness, elastic and plastic values of the child's head and the floor. Since, these characteristics values can change from one shortfall case to another shortfall case, it is better to use the average of both extreme coefficients of restitution, namely $e = 0.0$ and $e = 1.0$ is $e = 0.5$. This is the reason that a value of e = 0.5 was chosen for all simulations so far. However, it is interesting to investigate whether the use of $e = 0.5$ was a valid choice or not. This can be done by conducting several additional shortfall simulations that incorporate different values of '*e*'s and comparing the results obtained from them.

Ten additional 3.0 ft shortfall simulations at $\mathbf{V_x} = -3.0$ m/s were conducted. Every simulation incorporated a different coefficient of restitution. Table 13 summarizes the results that were obtained from these ten shortfall simulations. Note that a shortfall simulation incorporating $e = 0.5$ was not repeated.

Table 13: Maximum & Average Values of Number of 'g's (NGS), ω & α for 3.0 ft Shortfall Simulations @ Vx = -3.0 m/s as 'e' is varied gradually			
Coefficient of Restitution, 'e'	**Maximum**		
	NGS **(m/s^2)**	**ω (rad/s)**	**α (rad/s^2)**
0.0	386.4	15.5	-493800.0
0.1	383.8	17.1	-490000.0
0.2	389.5	17.8	-508800.0
0.3	279.8	29.1	-432800.0
0.4	274.1	32.6	-374600.0
0.5	397.7	36.9	-565400.0
0.6	343.6	36.8	-498300.0
0.7	273.8	32.6	-404300.0
0.8	396.5	32.2	-596100.0
0.9	323.9	31.8	-494700.0
1.0	414.6	31.6	-643000.0
Averaged e = 0.0 & e = 1.0 Values →	400.5	23.5	-568400.0

Table 13: Results obtained for Ten additional 3.0 ft shortfall simulations at V_x = -3.0 m/s. Each shortfall simulation incorporates a different Coefficient of Restitution 'e'.

Table 14:
***'%-Difference'* between the**
'Maximum Values'* & the *'Averaged e = 0.00 & e = 1.00 Values'
as seen in Table 13

Coefficient of Restitution, *'e'*	***NGS* (m/s^2)**	***ω* (rad/s)**	***α* (rad/s^2)**
0.0	3.6	52.1	15.1
0.1	4.4	37.5	16.0
0.2	2.8	32.1	11.7
0.3	43.1	19.1	31.3
0.4	46.1	27.9	51.7
0.5	0.7	36.2	0.5
0.6	16.6	36.1	14.1
0.7	46.3	27.8	40.6
0.8	1.0	27.0	4.6
0.9	23.7	26.0	14.9
1.0	3.4	25.5	11.6
Averaged e = 0.0 & *e* = 1.0 Values →	0.0	0.0	0.0

Table 14: %-Differences between the results of simulations with varying Coefficients of Restitution as tabulated in Table 13.

As seen on Table 13, the '*e*' values are linearly increased by 0.1 increments. However, no particular pattern can be seen between the obtained results. As one follows the results shown on the *NGS*-, ω- and α-*columns*, neither a linear nor a nonlinear development can be traced. The results are very random. Therefore, it is necessary to choose one coefficient of restitution and apply it to all simulations.

In order to determine whether the utilized $e = 0.5$ was a good choice or not, the average of the results obtained for the $e = 0.0$ and $e = 1.0$ are taken as shown in the last row of Table 13. Then, the %-difference between the average values and every individual value is taken as illustrated in Table 14. As shown on Table 14, the lowest possible %-differences are obtained when a coefficient of restitution of 0.5 is used. Therefore, the choice of $e = 0.5$ is a good choice.

7-8-3 Duration of the time-step, Δt

One of the most important parameters involved during *numerical analysis* is the proper 'time-step', Δt. As mentioned in Sec. 7-5-1, the shorter the Δt, the more accurate are the numerical calculations and the subsequent results. However, how small should the time-step be? According to Cory et al., a very short time-step results in a more devastating head and ground impact [66]. In their study, Cory et al., report that 'Δt's involved in the collisions between a child's head and a hard floor, possess magnitudes of the order of milliseconds.

In this study, the main goal was to generate the worst shortfall scenarios that a six months old child could possibly face. Namely, a child who experiences a *head-first* ground collision where the floor is not cushioned, i.e., concrete or hardwood floor. As reported by Cory et al., the harder the ground the shorter is the *Impact-Duration* between the child's head and the ground [66]. Impact-Duration is equivalent to the time-step, Δt that is utilized during numerical analysis.

Based on the statements made above, a $\Delta t = 0.1$ ms was chosen to ensure that all head and ground collisions involve a very hard floor.

7-9 Future Work

The study of shortfalls has been of great interest to the scientific/professional community [76-89]. In particular, most of these researchers have focused on determining a shortfall-height from which a shortfall could result in a serious head injuries or death amongst young children. However, no research has been conducted on the actual movement mechanics of the unfused cranial bones during shortfall impacts.

The skull of newborns is not completely fused [76-86]. Rather, the skull is composed of several bone-plates that are connected to each other via suture materials as shown in Fig. 233 and Fig. 234 [90]. Fig. 232 represents the lateral view of a newborn's head. It can clearly be seen that the Frontal bone, the Parietal bone, the Occipital bone and the Temporal bone are not fused with each other. They are outlined by sutures and fontanelles, which act at the connection between them.

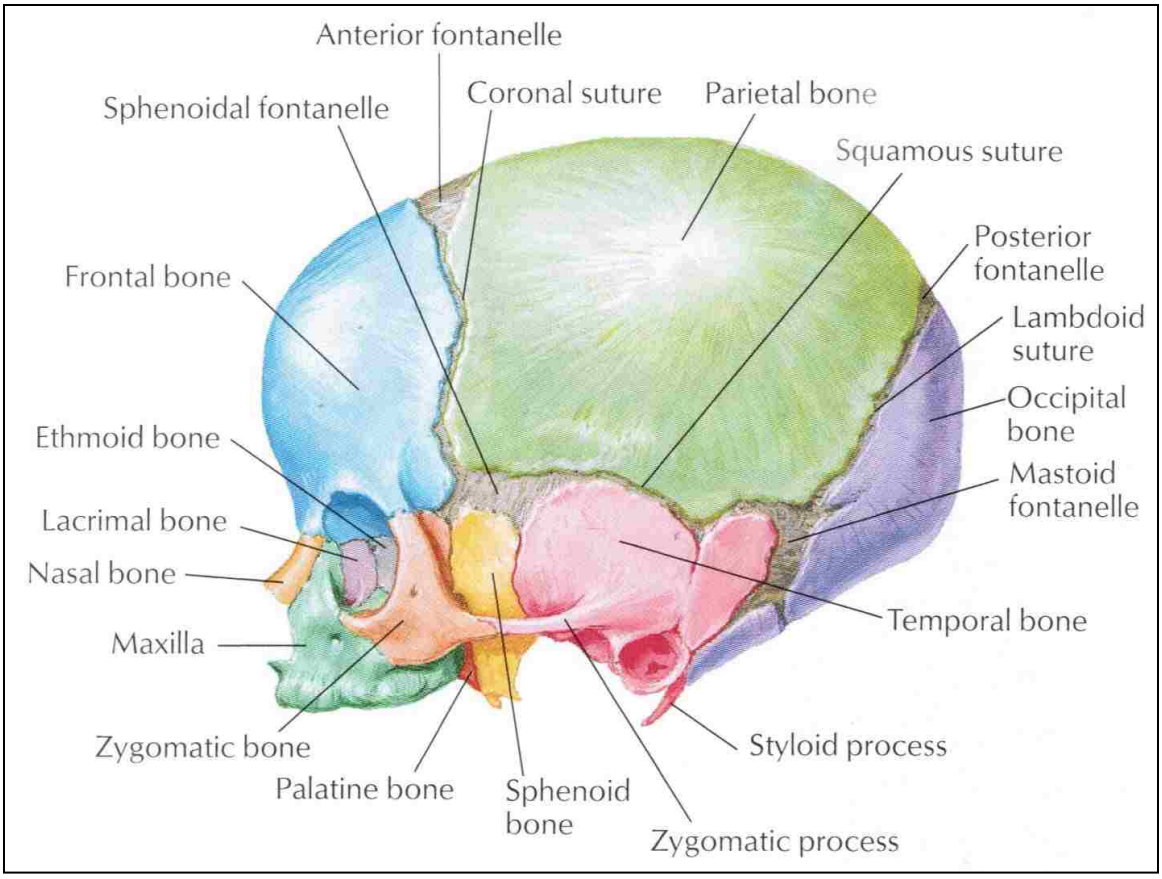

Figure 233: Lateral view of a newborn's skull and suture patterns.

Fig. 234 provides a superior view of the newborn's head. The extent of the sutures, specifically the anterior fontanelle as well as the posterior fontanelle is clearly visible.

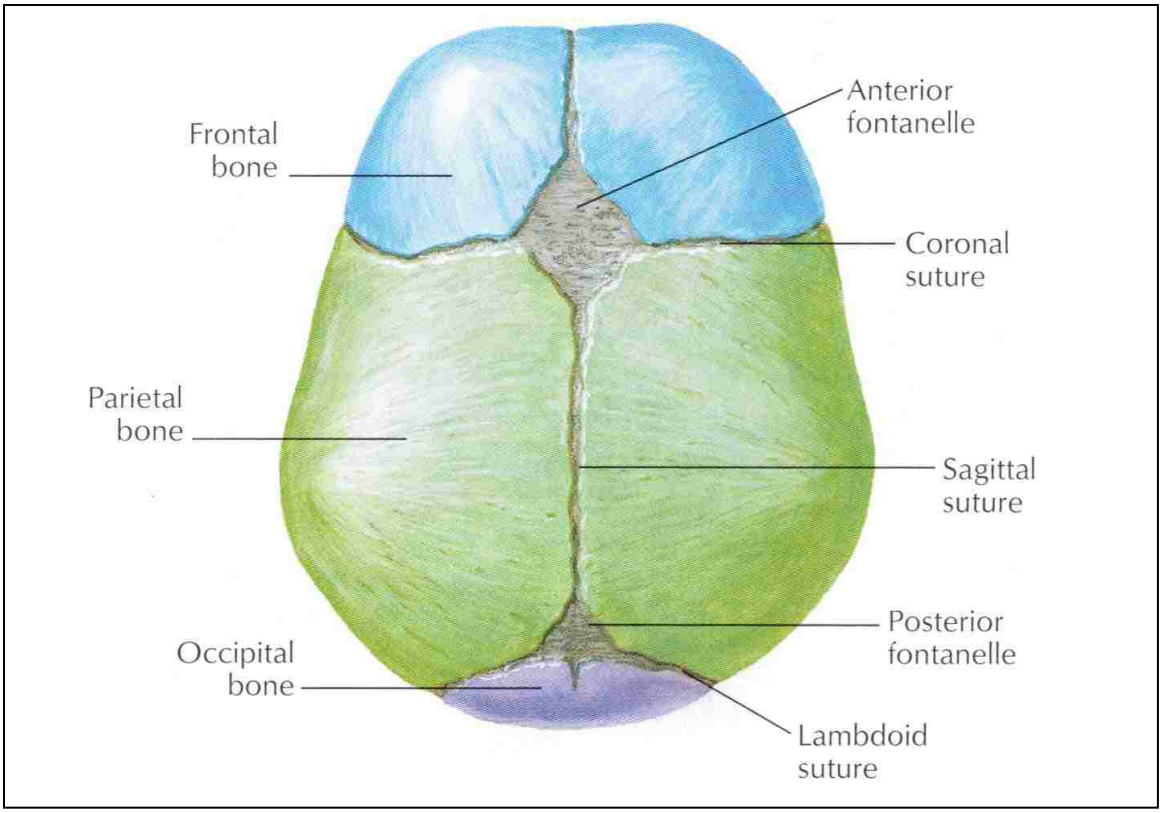

Figure 234: Superior view of a newborn's skull and suture patterns.

The existence of these sutures and fontanelles is essential during labor [84-86]. The sutures and the fontanelles allow the newborn's head to be deformed during labor. A newborn's head has the largest circumference compared to any other members of its body [73]. The sutures and the fontanelles of a newborn's head allow the Frontal bones, the Parietal bones, the Occipital bones and the Temporal bones to move with respect each other as the newborn's head squeezes through the mother's relatively narrower opening [84-86]. Only with the help of these super flexible sutures and fontanelles, a newborn's head can exit the mother's body without utilizing any externally applied incision to the mother's body [84-86].

As the child grows, the sutures and the fontanelles ossify. This will lead to a fused skull. Roth et al., have reported that the ossification of the sutures continues until the age of three [83]. However, in the meantime, the unfused skull might not be able to provide the same brain protection that a fused skull would provide. Coats et al. have reported that the pediatric cranial bones are 35 times stiffer than the pediatric cranial sutures [76]. Moreover, they have reported that the pediatric cranial suture deforms 30 times more than the pediatric cranial bone before its failure. This shows the high flexibility of the pediatric cranial sutures and hints to their relatively low resistivity against any externally applied forces.

Based on these reported characteristics of a young child's sutures and bones, it can be imagined that during a shortfall *head-first* impact, the sutures and specifically the fontanelles (based on their larger suture area) do not provide any significant resistance. Therefore, due to the impact forces involved in a shortfall, the unfused bones can leave there original position and directly push/press on the underlying brain. Moreover, via the application of an impact force, it is hypothesized that each individual unfused bone can almost move independently without causing the other unfused bones to move. The unfused bones can be imagined as islands of bones that are surrounded by very flexible sutures. Therefore, every bone-island can have a more or less independent *relative-motion* with respect to the other bone-island. This independent relative-motion of a bone-island can be thought of as a normal/perpendicular bone movement with respect to the surface of the brain. This means that each bone-island can push/press on the surface of the brain.

Based on the laws of mechanics and the partially spherical geometry of the cranial bones, it can be imagined that a *perfectly perpendicular* bone-movement can only occur via external forces, which are applied only within a small region of the bone. The location of this small region can be away from the perimeters of the bone and more towards the bone's center of gravity. Moreover, it could be imagined that these forces must possess a certain direction, i.e. angle with respect to the bone's surface. For instance, a force that is nearly tangential to the bone's surface might not cause a drastic penetration of the bone into the child's brain as a force that is more normal to the bone's surface. Most importantly, the magnitude of the externally applied forces can play a big role. Naturally, the higher a force's magnitude, the more it can cause the unfused bone to penetrate into the brain.

The penetration of the cranial bone into the underlying brain can cause severe shearing forces acting on the brain tissue [87-89]. Vowles et al. reported that the subdural veins are highly sensitive to shearing forces, which can lead to acute subdural hemorrhage [87]. Additionally, Nicolle et al., have reported that shearing is the most common cause of brain damage [89].

All of the above mentioned biomechanical behavior of the cranial bones, sutures as well as the information reported by other researchers call for a deeper investigation of the response/movement of an unfused pediatric cranial bone once it experiences external forces that are involved in a shortfall. The results obtained in this work pave the way for the in-depth future study of any possible cranial bone movements that occur during a shortfall *head-first* collision with the ground.

To conduct an in-depth pediatric skull study several steps must be taken.

1. Due to ethical reasons, it must be noted that any shortfall research involving children must be conducted in a computerized world. Meaning, only computerized shortfall simulations should be conducted. However, shortfall simulation using children-dummies can be conducted as well. However, the consistency, accuracy and repeatability of computerized models is on average higher than real world experiments with dummies. Specifically, the skull biomechanics of a six months old child's head with the ground. Specifically, the absorption of the impact energy by the cranial bones and the transfer of this energy to the underlying brain issue need to be studied. Additionally, the mechanical movement of the unfused skull bones with respect to each other as well as to the underlying brain tissue can be studied.

2. In a Rigid Body Dynamics software such as Working Model 2D, a model of the child's body with its proper dimensions needs to be constructed. Then under the earth's gravitational acceleration, shortfall simulations form different heights need to be conducted. The impact forces involved in each simulation need to be recorded.

3. A 3D computerized digital model of a child's skull and brain of is needed. To create a 3D digital model, it is suggested to use MRI images of a child. The MRI images must originate from a child without any damages to its skull, skull sutures and the underlying brain. The age and gender of the child must be recorded for publication purposes. Via a MRI-to-3D-digital-model converting code such as

MIMICS (Materialise International, 4650 Helm Court Plymouth, MI 48170, USA), the MRI images can be converted to an actual 3D digital model. The model should be separated into several connected volumes. These different volumes can be the bone-volume, the suture-volume and the brain-volume. Note other volumes can also be incorporated in the model. For instance the volumes such as the Cerebrospinal Fluid (CSF), etc.

4. The 3D digital model is then imported into a Finite Element Method (FEM) Code such as ANSYS (ANSYS, Inc., Southpointe, 275 Technology Drive, Canonsburg, PA 15317, USA). Then within the FEM code every volume of the 3D model is meshed. Fig. 235 represents an example of a meshed skull and sutures of a three years old child as reported by Roth et al. [83].

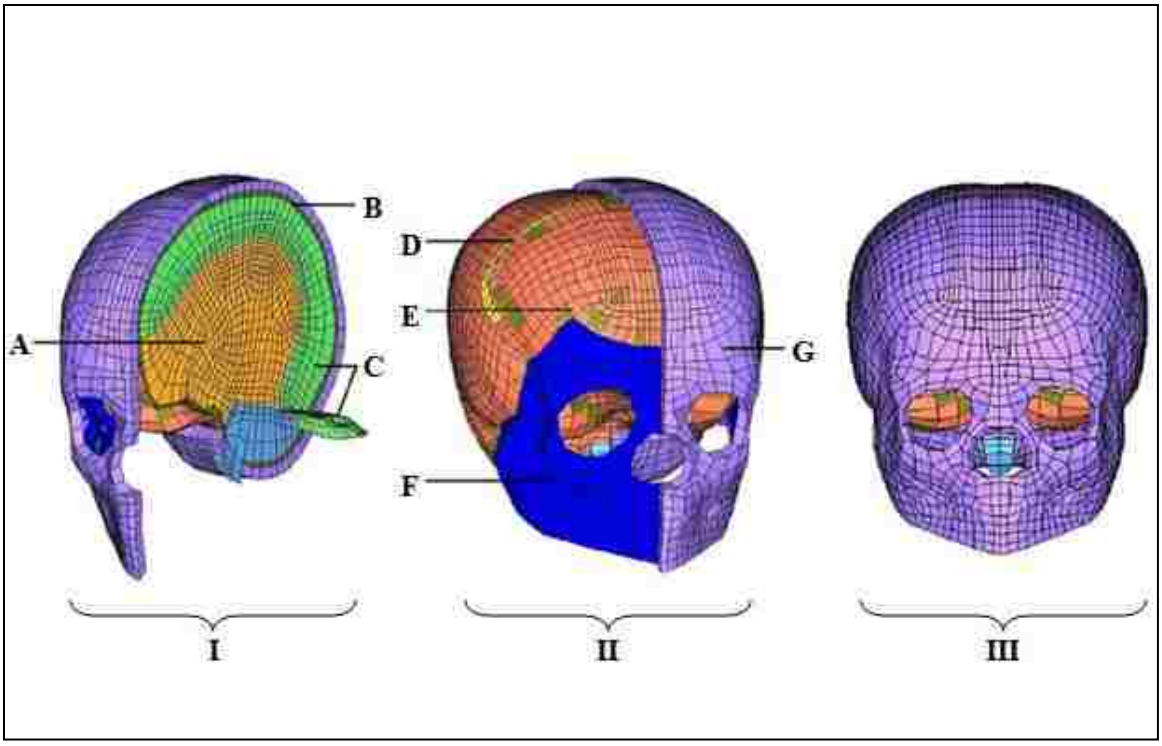

Figure 235: Meshed Skull, Suture and Fontanelle Volumes as well as a precise differentiation of a three years old child's various cranial members [83]. A: Meshed Brain Volume. B: Meshed CSF Volume. C: Meshed Membranes Volume. D: Meshed Sutures Volume. E: Skull Volume. F: Meshed Face Volume. G: Meshed Scalp Volume. I: Cross-sectional view of the meshed CSF, Membranes and Brain tissues. II: Cross-sectional view of the Scalp overlapping the meshed Suture, Skull and Face tissues. III: Front view of the Scalp overlapping the meshed Suture, Skull and Face tissues.

5. The obtained impact forces can then be applied to the 3D head model of the child within the FEM code. The forces can be applied at different locations of the skull. Moreover, the obtained forces can be applied to the child's head from different angles as well. By doing so, impacts to the head at different locations and from different angles can be taken into account. Fig. 236 represents an example of several load applications on different skull regions of a three years old child as reported by Roth et al. [83].

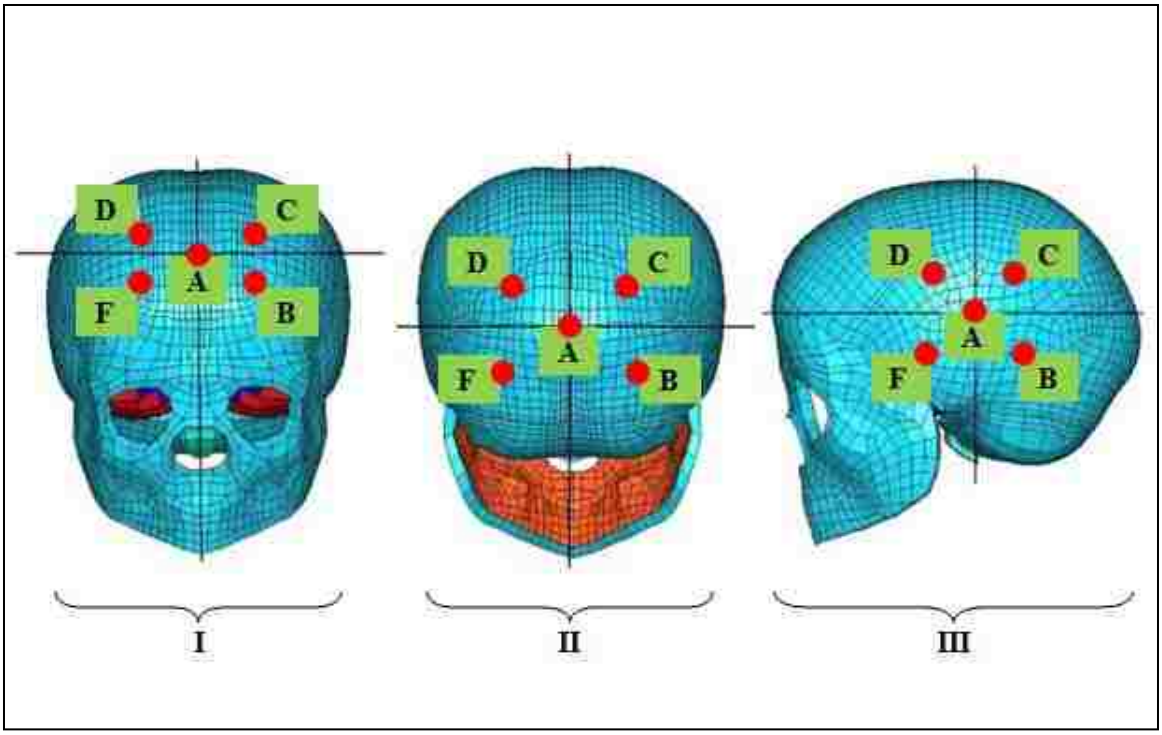

Figure 236: Application of external forces on different skull regions of a three years old child. Points A, B, C, D and F represent the center of regions where external loads where applied to the child's head by Roth et al. [83].

After conducting the five steps above, different biomechanical behavior of the skull, the sutures and the brain can then be obtained from the FEM code. In particular, biomechanical behaviors of the skull, sutures, fontanelles and the brain such as their displacement, normal and shearing strains as well as normal and shearing stresses are acquirable from the FEM code. The FEM code will also the extent of skull/bone penetration into or pressing onto the brain. It can also reveal how the skull and sutures behave/move while being exposed to externally applied loads involved in a shortfall.

From the interaction between the skull and the brain under different load applications and/or from different angles, *patterns of skull pressing onto the brain* can be developed. For future investigative work, these patterns could relate the location of brain injury to

the location, magnitude and angle of the applied force on the child's skull. The production of these patterns is highly desirable amongst the medical and the law professionals.

Many young children who are admitted into a hospital setting because of having a head trauma are domestically abused [91-93]. The *skull pressing onto the brain patterns* developed from the proposed future work above, can help the physicians in determining a fast and reliable treatment option. The physicians might be able to look at the characteristics and location of force application and utilize the developed patterns and quickly find potential locations of brain damage. The investigative law professionals can also utilize the developed patterns. The patterns can be used to conclude whether the child was thrown onto to the ground or not.

To develop a reliable archive of *skull pressing onto the brain patterns* that could relate the location, magnitude and direction of the applied force on the skull to the location and magnitude of underlying brain damage(s), many shortfall simulations are necessary. These simulations must include a range of pediatric shortfalls that cover different ages and genders of children. However, the work within this chapter is related to a six months old child. Therefore, the cranial material properties of a six months old child are provided within this chapter. These material properties can be utilized when constructing a 3D digital model of a six months old child. External sources are needed to obtain the material properties and the body dimensions of children from other age groups.

Table 15 summarizes the material properties of a six months old child (gender is not specified) as reported by Roth et al.

Table 15: Mechanical Properties of a 6 month old child's CSF, Scalp, Skull, Membranes, Sutures, Fontenelles & Brain [20]			
	E (MPa)	Poisson's Ratio	Density (kg/m^3)
CSF	0.012	0.49	1040.0
Scalp	16.7	0.42	1200.0
Skull	2500.0	0.22	2150.0
Membranes	31.5	0.45	1140.0
Sutures & Fontanelles	1500.0	0.22	2150.0
Brain's time-dependent Shear Modulus, G(t)	$G(t)= G_\infty + (G_0 - G_\infty) e^{-\beta t}$ G_∞ = 2.32 E-3 MPa G_0 = 5.99 E-3 MPa β = 0.09248 sec^{-1} 't' is in seconds		

Table 15: Various mechanical properties of a six months old child's cranial members [82].

The brain's shear modulus G(t) represented in Table 15, is a theoretical and time-dependent expression obtained by Roth et al. [82].

Looking at the five steps laid out above, the herein work has completed the first two steps. The remaining three steps can be completed with the suggested directions and material properties provided above. By incorporating MRI images of male and female children from different age groups a vast archive of *skull pressing onto the brain patterns* can be developed, which can enhance and accelerate the performance of the medical and law professionals.

7-10 Conclusion

This research project explored the biomechanical forces/accelerations involved in the shortfall of a 6 months old child. Specifically, the herein work studied the impact accelerations in *numbers of 'g's* (NGS) that are experienced by the child's skull during a *head-first ground collision*. Magnitudes of the impact accelerations involved in twelve different computer-simulated shortfalls were obtained in 'g's. The simulations were divided in two six-membered groups. The simulations within the first group ran at a horizontal velocity of $\mathbf{V}_x$ = -1.0 m/s and the simulations within the second group ran at a horizontal velocity of $\mathbf{V}_x$ = -3.0 m/s. Every shortfalls simulation initiated from a different initial shortfall height. The results showed that very high impact accelerations can result during these shortfalls, which can lead to serious and/or fatal head injuries. Moreover, it was determined that NGSs grow non-linearly as the initial shortfall height is increased linearly. The herein obtained results pave the way for additional future research simulations. Future research simulations can utilize the results obtained within this work to investigate the biomechanical movement-patterns of the unfused bones that constitute the skull of a 6 months old child's. bones.

REFERENCES

[1] Hall, S.J., “Basic Biomechanics,” Mc Graw Hill, 2011, 6th Edition, pp. 3-4.

[2] Khraishi, T.A., and Shen, Y.L., “Introductory Continuum Mechanics with Applications to Elasticity,” Cognella, 2012, first Edition, pp. 1.

[3] Nelson, R.C., ”Biomechanics: Past and Present,” 1980 Proceedings of the Biomechanics 1980 Symposium, Bloomington, Indiana.

[4] Hatze, H., "The Meaning of the Term Biomechanics," Journal of Biomechanics, 1974, Vol. 7, pp. 189-190.

[5] Rasch, P. J., “Kinesiology and Applied Anatomy,” Lea & Febiger, 1989, 7th Edition, pp. 2.

[6] Purtscher O. Noch unbekannte Befunde nach Schaedel-trauma. Ber. dtsch. Ophthal. Gesl. 1910;36:294-301.

[7] Tietze A. Arch. Klin. Chir. 1911;95:369.

[8] Noren D, Palmer HJ, Frame MD. Predicted wall shear rate gradients in t-type arteriolar bifurcations. Biorh. 2000;37:325-340.

[9] Frame MD, Sarelius IH. Endothelial cell dilatory pathways link flow and WSS in an intact arteriolar network. J Appl Physiol. 1996;81:2105-14.

[10] Steinman DA. Image-based computational fluid dynamics modeling in realistic arterial geometries. Ann. Biomed. Engrg. 2002;30:483–497.

[11] Leuprecht A, Kozerke S, Boesiger P, et al. Blood flow in the human ascending aorta: a combined MRI and CFD study, J. Engrg. Math. 2003;47:387–404.

[12] Siggers J, Waters S. Steady flows in pipes with finite curvature. Physics of Fluids. 2005;17(077102)

[13] Siggers J, Waters S. Unsteady flows in pipes with finite curvature. J Fluid Mech. 2008;600:133–165

[14] Frame MDS, Chapman GB, Markino Y, et al;. Shear stress gradient over endothelial cells in

a curved microchannel system. Biorh. 1998;35:245e61.

[15] Egelhoff CJ, Budwig RS, Elger DF, et al. Model Studies of the Flow in Abdominal Aortic neurysms During Resting and Exercise Conditions. J Biomech. 1999; 32(12):1319-1329.

[16] Lovald S, Yonas H, Heinrich J, et al. The Role of Fluid Dynamics in Plaque Excavation and Rupture in the Human Carotid Bifurcation: A Computational Study. Int J Experimental and computational Biomechanics. 2009;1:76-95.

[17] Nagaoka T, Sato E, Takahashi A, et al. New System to evaluate wall shear stress on retinal vessel using a retinal laser Doppler velocimetry system. IOVS. 2003;44 E-Abstract 340 (ARVO].

[18] Steele BN, Olufsen MS, Taylor CA. Fractal network model for simulating abdominal and lower extremity blood flow during resting and exercise conditions. Computer Methods in Biomechanics and Biomedical Engineering. 2007;10:39-51

[19] Feke GT, Tagawa H, Deupree DM, et al. Blood flow in the normal human retina. IOVS. 1989;30:58-65.

[20] Cutnell J, Johnson K. Physics, 4th Ed. Wiley. Hoboken, New Jersey. 1998:308.

[21] Nagaoka T, Yoshida A. Noninvasive evaluation of wall shear stress on retinal microcirculation in humans. IOVS. 2000;47:1113-1119.

[22] Elert G. The Physics Hypertextbook, http://physics.info/viscosity.

[23] White FM. Fluid Mechanics, 4th Edition, Mc Graw Hill, Boston, Massachusetts, Chapter 1, Eq.1.24:24

[24] White FM. Fluid Mechanics, 4th Edition, Mc Graw Hill, Boston, Massachusetts, Chapter 6, Eq.6.6:331.

[25] Behrens-Baumann W, Scheurer G. Purtscher disease; range of variation of clinical manifestation in Morbus Purtscher. Klin Monatsbl Augenhulkd. 1991:198:99-107.

[26] Behrens-Baumann W, Scheurer G, Schroer H. Pathogensis of Purtscher-like retinopathy. An experimental study. Graefes Arch Klin Exp Ophthalmol.1992;230:286-91.

[27] Scheurer G, Praetorius G, Damerau B, et al. Vascular occlusion of the retina: an experimental model. !. Leukocyte aggregates. Graefe's Arch Clin Exp Ophthalmol. 1992;230:275-80.

[28] Schroer H, Scheurer G, Behrens-Baumann W. Vascular occlusion of the retina: an experimental model. II Platelet aggregates. Graefe Archives Ophthalmology 1992;230:281-5.

[29] Qiu Y, Tarbell JM. Interaction between wall shear stress and circumferential strain affects endothelial cell biochemical production. J Vas Research. 1999;37:1-11.

[30] DePaola N, Gimbrone MA, Davies PF, et al. Vascular endothelium responds to fluid shear stress gradients. Arterioscler Thromb.1992;12:1254-7.

[31] Klabunde RE. Cardiovascular Physiology Concepts. Supplemental Content. Philadelphia, PA:Lippincott Williams & Wilkins;2005:2-28.

[32] Chandran KB, Yoganathan AP, Rittgers SE. Biofluid Mechanics: The Human Circulation. Taylor & Francis, Boca, London and New York.2007.

[33] Fry DL. Acute vascular endothelial changes associated with increased blood velocity gradients. Circulation Research.1968;22:165-97.

[34] Chaum E. Retinopathy, Purtscher. Emedicine Specialties, Ophthalmology, Retina. Updated:Feb 26, 2010.

[35] Wise GN, Dollery CT, Henkind P. Pattern and location of Retinal Vessels.The Retinal

Circulation.first ed. New York: Department, Harper & Row, Publishers. 1971:21-31.

[36] Frame MD and Sarelius IH. Arteriolar bifurcation angles vary with position and when flow is changed. Microvas Res. 1993;46:190-205.

[37] Apple DJ & Rabb MF. Fundus.Ocular Pathology Clinical Applications & Self Assessment. 3rd ed. St Louis: CV Mosby Company. 1985:261.

[38] Gibson CM, Diaz L, Kandarpa K, et al. Relation of vessel wall shear stress to atherosclerosis progression in human coronary arteries. Arteriosclerosis and Thrombosis. 1993;13:310-5.

[39] Katritsis DG, Efstathopulos EP, Pantos J, et al. Anatomic characteristics of culprit sites in acute coronary syndromes. J Intery Cardiol. 2008;21:140-50.

[40] Hassan R, Timofeev EV, Saito T, et al. A proposed parent vessel geometry based categorization of saccular intracranial aneurysms: computational flow dynamics analysis of the risk factors for lesion rupture. J Neurosurgery. 2005;104:662-80.

[41] Egelhoff CJ, Budwig RS, Elger DF, et al. Model studies of he flow in abdominal aortic aneurysms during resting and exercise conditions. J Biomech. 1999;32:1319-29.

[42] Malek AM, Alper SL, Izumo S. Hemodynamic shear stress and its role in atherosclerosis. JAMA. 1999;282:2035-42.

[43] Stoumbos VD, Klein ML, Goodman S. Purtscher's retinopathy in chronic renal failure. Ophthalmol. 1992;99:1833-9.

[44] Stewart MW, Brazis PW, Guier CP, et al. Purtscher-like retinopathy in a patient with HELLP syndrome. Am J Ophthalmol. 2007;143:886-7.

[45] Liu FC, Chiang SY, Chang DM, et al. Purtscher's-like retinopathy as an initial presentation of adult onset Still's disease: a case report and review of the literature. Clin Rheumatol. 2007;26:1204-6.

[46] Hayreh SS. Inter-individual variation in blood supply of the optic nerve head. Documentation Ophthalmologica.1985;59:217-46.

[47] Oku H, Sugiyama T, Kojima S, Watanabe T, et al. Experimental optic cup enlargement caused by endothelin-1 induced chronic optic nerve head ischemia. Surv Ophthalmol. 1999;44 Suppl1s:74-84.

[48] Flammer J, Mozaffarieh M. What is the present pathogenetic concept of glaucomatous optic neuropathy? Surv Ophthalmol. 2007;a52.Supple 2:162-73.H.

[49] Emre M, Orgul S, Gugleta K, et al. Ocular blood flow alteration in glaucoma is related to systemic vascular dysregulation. Br J Ophthalmol. 2004;88:662-6.

[50] Gomez-Ulla F, Fente B, Torreiro MG, et al. Choroidal vascular abnormality in Purtscher's retinopathy shown by indocyanine green angiography. Am J Ophthalmol.1991;2:261-3.

[51] Lucas, P. W., Prinz, J. F., Agrawal, K. R., and Bruce, I. C., "Food physics and oral physiology," Food Quality and Preference, 2002, Vol. 13-4, pp. 203-213.

[52] Yven, C., Guessasma, S., Chaunier, L., Della Valle, G., and Salles, C., "The role of mechanical properties of brittle airy foods on the masticatory performance," Journal of Food Engineering, 2010, Vol. 101-1, pp. 85-91.

[53] Sandoval, A. J., Chaunier, L., Courcoux, P., and Della Valle, G., "Bulk mechanical behavior of commercial particle food foams," Journal of Texture Studies, 2008, Vol. 39-4, pp. 405-425.

[54] Guessasma, S., Chaunier, L., and Lourdin, D., “Finite element modelling of the mechanical behaviour of vitreous starch/protein composite,” Journal of Food Engineering, 2010, Vol. 98-2, pp. 150-158.

[55] Dini, G.M., De Castillo, H.T., Ferreira, L.M., “A Simple Technique to Ensure Drain Fixation.” Journal of Plastic Reconstructive Surgery, 2003, Vol. 112(3), pp. 923-924.

[56] O'Flynn, P., and Akhtar, S., “Effective securing of a drain.” Annals of the Royal College of Surgeons of England, 1999, Vol. 81, pp. 418–419.

[57] Hormbrey, E., Pandya, A., and Humzah, D., “Drain fixation made foolproof.” Annals of the Royal College of Surgeons of England, 2000, Vol. 82, p. 219.

[58] Scardillo, J., “Postoperative Care of Patients with Surgical Drains. Perspectives: Recovery Strategies from the OR to Home.” Vol. 4, n.4.

[59] Scandola, M., Gasperotti, L., Vicentini, M., and Fiorini, P., “The role of visual-haptic discrepancy in virtual reality environments.” 2012 IEEE Haptics Symposium (HAPTICS). Conference Publication. pp. 289-295.

[60] Kirk, R.K., “Basic Surgical Techniques.” Elsevier Health Sciences, 2002, 5th Edition, Chapter 11.

[61] Sherwood, L., “Fundamentals of Physiology: A Human Perspective.” Thomson Brooks/Cole, 2006, 3rd Edition, p. 380.

[62] Hibbeler, R., C., “Engineering Mechanics, Statics” Pearson, 10th Edition, pp. 414-415.

[63] Park, S., Cho, B., and Oh, S., “Head injuries from falls in preschool children,” Yonsei Medical Journal, 2004, Vol. 45, No. 2, pp. 229-232.

[64] Sawyer, J.R., Flynn, J.M, Dormans, J.P., Catalano, J., and Drummond, D.S., “Fracture patterns in children and young adults who fall from significant heights,” Journal of Pediatric Orthopeics, 2000, Vol. 20, pp. 197-202.

[65] Johnson, K., Fischer, T., Chapman, S., and Wilson, B., “Accidental head injuries in children under 5 years of age,” Journal of Clinical Radiology, 2005, Vol. 60, pp. 464-468.

[66] Cory, C.Z., Jones, M.D., James, D.S., Leadbeatter, S., and Nokes, L.D.M., “The potential and limitations of utilizing head impact injury models to assess the likelihood of significant head injury in infants after a fall,” Journal of Forensic Science International, 2001, Vol. 123, pp. 89-106.

[67] Nimityongskul, P., and Anderson, L.D., “The likelihood of injuries when children fall out of bed,” Journal of Pediatric Orthopedics, 1987, Vol. 7, pp. 184-186.

[68] Knowledge Revolution, “Working Model 2D User’s Manual,” 1992-1996 Summit Software Company, 1989-1999, pp. A1-A28.

[69] Hibbeler, R.C., “Engineering Mechanics: Dynamics,” Pearson Prentice Hall, 2010, Edition 12, pp. 440.

[70] O’Riordian, K., Thomas, P.M., Phillips, J.P., and Gilchrist, M.D., “Reconstruction of real world head injury accidents resulting from falls using Multibody Dynamics,” Journal of Clinicla Biomechanics, 2003, Vol. 18, pp. 590-600.

[71] Schultz, B.W., William, E.L., and Lloyd, J.D., “Estimation, Simulation, and Experimentation of a fall from bed,” Journal of Rehabilitation Research and Development, 2008, Vol. 45, No. 8, pp. 1227-1236.

[72] Doorly, M.C., and Gilchrist, M.D., “The use of Accident Reconstruction for the Analysis of Traumatic brain Injury due to head impacts arising from falls,” Journal of Computer Models in Biomechanics and Biomedical Engineering, 2006, Vol. 9, No. 6, pp. 371-377.

[73] Raul, J.S., Baumgartner, D., Willinger, R., and Ludes, B., “Finite element modeling of human head injuries caused by a fall,” International Journal of Legal Medicine, 2006, Vol. 120, pp. 212-218.

[74] Snyder, R.G., Spencer, M. L., Clyde, L.O., and Schneider, L.W., “Anthropometry of US Infants and Children,” SP-394, Proceedings of the 1975 SAE Automotive Engineering Congress and Exposition, Detroit, Michigan, 1975, Paper No. 750423, SP-394.

[75] NASA, "Anthropometric Source Book, Volume 1: Anthropometry for Designers,” NASA Reference Publication 1024, 07/1978, Table 15.

[76] NASA, "Anthropometric Source Book, Volume 2: A Handbook of Anthropometric Data,” NASA Reference Publication 1024, 07/1978, Definitions 32 and 805.

[77] Coats, B., and Margulies, S.S., “Material properties of human infant skull and suture at high rates,” Journal of Neurotrauma, 2006, Vol. 23, No. 8, pp. 1222-1232.

[78] Margulies, S.S., and Thibault, K.L., “Infant skull and suture properties: Measurements and implications for mechanisms of pediatric brain injury,” Transition of the ASME, 2000, Vol. 122, pp. 364-371.

[79] Kriewall, T.J., McPherson, G.K., and Tsai, A.C., “Bending properties and ash content of fetal cranial bone,” Journal of Biomechanics, 1981, Vol. 14, pp. 73-79.

[80] McPherson, G.K., and Kriewall, T.J., “The elastic modulus of fetal cranial bone: A first step towards an understanding of the biomechanics of fetal head molding,” Journal of Biomechanics, 1980, Vol. 14, pp. 9-16.

[81] Klinich, K.DeS., Hulbert, G.M., and Schneider, L.W., “Estimating infant head injury criteria and impact response using crash reconstruction and finite element modeling,” Stapp Car Crash Journal, 2002, Vol. 46, pp. 165-194.

[82] Roth, S., Raul, J.S., Ludes, B., and Willinger, R., “Finite element analysis of impact and shaking inflicted to a child,” International Journal of Legal Medicine, 2007, Vol. 121, pp. 223-228.

[83] Roth, S., Vappou, J., Raul, J.S., and Willinger, R., “Child head injury criteria investigation through numerical simulation of real world trauma,” Journal of Computer Methods and Programs in Biomedicine, 2009, Vol. 93, pp. 32-45.

[84] Lapeer, R.J., and Prager, R.W., “Fetal head moulding: Finite element analysis of a fetal skull subjected to uterine pressures during the first stage of labour,” Journal of Biomechanics, 2001, Vol. 34, pp. 1125-1133.

[85] Lapeer, R.J., and Prager, R.W., “Finite element model of a fetal skull subjected to labour forces,” Springer Verlag, 1999, Taylor, C., Colchester, A. (Eds.),, MICCAI’99, Lecture Notes in Computer Science, Vol. 1679, pp. 1143-1155.

[86] McPherson, G.K., and Kriewall, T.J., “Fetal head molding: An investigation utilizing a finite element model of the fetal parietal bone,” Journal of Biomechanics, 1980, Vol. 13, pp. 17-26.

[87] Vowles, G.H., Scholtz, C.L., and Cameron, J.M., “Diffuse axonal injury in early infancy,” Journal of Clinical Pathol, 1987, Vol. 40, pp. 185-189.

[88] Donnelly, B.R., and Medige, J., “Shear properties of human brain tissue,” Journal of Biomechanical Engineering, 1997, Vol. 119, pp. 423-432.

[89] Nicolle, S., Lounis, M., Willinger, R., Palierne, J.F., “Shear properties of human brain tissue,” Journal of Bioheology, 2005, Vol. 42, pp. 209-223.

[90] Netter, F., “Atlas of the human body,” Barron’s, Published by Icon Learning Systems LLC., 2006, pp. 10.

[91] Oehmichen, M., Meissner, C., and Saternus, K.S., “Fall or shaken: Traumatic brain injury in children caused by falls or abuse at home-a review on biomechanics and diagnosis,” Journal of Neuropediatrics, 2005, Vol. 36, pp. 240-245.

[92] Hennrikus, W.L., Shaw, B.A., and Gerardi, J.A., “Injuries when children reportedly fall from a bed or couch,” Journal of Clinical Orthopedics and Related Research, 2003, No. 47, pp. 148-151.

[93] Billmire, M.E., and Meyers, P.A., “Serious head injury in infants: Accident or abuse?,” Journal of Pediatrics, 2003, Vol. 75, No. 2, pp. 340-342.

[94] Duhaime, A.C, Gennarelli, T.A., Thibault, L.E., Bruce, D.A., Margulies, S.S., and Wiser, R., “The shaken baby syndrome,” Journal of Neurosurgery, 1987, Vol. 66, pp. 409-415.

[95] Duhaime, A.C, Christian, C.W., Rorke, L.B., and Zimmerman, R.A., “Nonaccidental head injury in infants — The “Shaken-baby syndrome”,” The New England Journal of Medicine, 1998, Vol. 338, No. 25, pp. 1822-1829.

[96] Blumenthal, I., “Shaken baby syndrome,” Postgrad Medical Journal, 2002, Vol. 78, pp. 732-735.

[97] Cory, C.Z., and Jones, M.D., “Can Shaking Alone Cause Fatal Brain Injury?” Journal of Medical Science Law, 2003, Vol. 43, No. 4, pp. 317-333.

RELATED U.S. PATENT DOCUMENTS

[RP1] Drainage T tube used for abdominal surgery. U.S. Pat. No. 4,654,032. 03/1987. Inventor: Morales-George.

[RP2] Medical tubing and connector. U.S. Pat. No.: 4,653,542. 03/1987. Inventor: Edward R. Tascher.

REFERENCED U.S. PATENT DOCUMENTS

[P1] Surgical Retaining Device. U.S. Pat. No.: 2,898,917. 04/1958. Inventor: Wallace.

[P2] Bacteria-Resistant Percutaneous Conduit. U.S. Pat. No.: 3,663,965. 05/1972. Inventor: Lee, Jr. et al.

[P3] Anchoring plate for medical tubes. U.S. Pat. No.: 4,029,103. 06/1977. Inventor: McConnell.

[P4] Post hysterectomy fluid drainage tube. U.S. Pat. No.: 4,072,153. 02/1978. Inventor: Swartz.

[P5] Post-Operative Combination Dressing And Internal Drain Tube With External Shield And Tube Connector. U.S. Pat. No.: 4,080,970. 03/1978. Inventor: Miller.

[P6] Retention clips for body fluid drains. U.S. Pat. No.: 4,261,363. 04/1981. Inventor: Russo.

[P7] Brain lead anchoring system. U.S. Pat. No.: 4,328,813. 05/1982. Inventor: Ray.

[P8] Skin mounted drainage catheter retention disc. U.S. Pat. No.: 4,533,349. 08/1985. Inventor: Bark.

[P9] Surgical tube anchoring device and method for using same. U.S. Pat. No.: 4,717,385. 01/1988. Inventor: Cameron et al.

[P10] Abdominal wall pathway. U.S. Pat. No.: 4,781,694. 11/1988. Inventor: Branemark et al.

[P11] Retainer for a percutaneous tube. U.S. Pat. No.: 4,959,055. 09/1990. Inventor: Hillyer.

[P12] Device for attaching a flexible tube to a patient's skin. U.S. Pat. No.: 5,470,321. 11/1995. Inventor: Forster et al.

[P13] Catheter and feeding tube retention device and method of use. U.S. Pat. No.: 6,471,676 B1. 10/2002. Inventor: DeLegge et al.

[P14] Feeding tube skin guard. U.S. Pat. No.: 6,765,122 B1. 07/2004. Inventor: Stout.

[P15] Antibacterial chest tube, surgical drain, port or access line securing device. U.S. Pub. No.: US 2006/0225723 A1. 02/2006. Inventor: Ballarini.

[P16] Moveable Inflatable Anchor For Medical Devices. U.S. Pub. No.: US 2006/0079845 A1. 04/2006. Inventor: Howard. et al.

[P17] Stent. U.S. Pat. No.: 7,338,530 B2. 03/2008. Inventor: Carter et al.

[P18] Drain Tube Assembly for Draining a Body Cavity. U.S. Pub. No.: US 2008/0228174 A1. 09/2008. Inventor. Ibrahim et al.

[P19] System for surgical drain fixation. U.S. Pub. No.: US 2008/0243082 A1. 10/2008. Inventor: Goodman.

[P20] Trocar Anchor. U.S. Pub. No.: US 2009/0182279 A1. 07/2009. Inventor: Wenchell et al.

[P21] Universal Endotracheal Tube Coupling or Adaptor. U.S. Pat. No. 3,388,705. 04/1968. Inventor: Stanley L. Grosshandler.

[P22] Endotracheal intubation device. U.S. Pat. No.: 4,275,724. 06/1981. Inventor: Barry Behrstock.

[P23] Jet controlled catheter. U.S. Pat. No.: 4,403,985. 09/1983. Inventor: John W. Boretos.

[P24] Endotracheal tubes with improved proximal end connector units. U.S. Pat. No.: 4,593,690. 06/1986. Inventor: David S. Sheridan et al.

[P25] Vascular shunt. U.S. Pat. No.: 4,712,551. 02/1987. Inventor: Simon B. Rayhanabad.

[P26] Catheter and method of inserting catheter. U.S. Pat. No.: 4,784,639. 11/1988. Inventor: Piyush V. Patel.

[P27] Flexible connectors for medico-surgical tubes. U.S. Pat. No.: 4,852,564. 08/1989. Inventor: David S. Sheridan et al.

[P28] Flexible and extendible pipe section. U.S. Pat. No.: 5,058,934. 10/1991. Inventor: Duane A. Brannon.

[P29] Flexible tubular channel with external supporting ridges. U.S. Pat. No.: 5,125,909. 06/1992. Inventor: Rudolf Heimberger.

[P30] Drain hose for washing machine and which includes a corrugated intermediate Portion. U.S. Pat. No.: 5,311,753. 05/1994. Inventor: Shiro Kanao.

[P31] Bendable shape-retaining Cannula. U.S. Pat. No.: 6,440,120. 09/1998. Inventor: Tracy D. Maahs.

[P32] Breathing circuit. U.S. Pat. No.: 5,823,184. 10/1998. Inventor: James R. Gross.

[P33] Corrugated pipe. U.S. Pat. No.: 6,021,816. 02/2000. Inventor: Thomas Jeltsch et al.

[P34] Breathing tube for conveying oxygen or anesthesia gas to lungs and conveying exhaled gas away from lungs of patient. U.S. Pat. No.: D424,687. 05/2000. Inventor: Richard Hoenig et al.

[P35] Flexible connector. U.S. Pat. No.: D466,607. 03/2002. Inventor: David M. Cise et al.

[P36] Adjustable length breathing circuit. U.S. Pat. No.: 7,178,521. 02/2007. Inventor: Kevin D. Burrow et al.

[P37] Central Nervous System Ultrasonic Drain. U.S. Pub. No.: US 2008/0154181 A1. 01/2008. Inventor: Rohit K. Khanna.

[P38] Portable flexible and extendable drain pipe. U.S. Pat. No.: 7,677,271. 03/2010. Inventor: E. Michael Boettner et al.

[P39] Catheter and medical tube. U.S. Pat. No.: 8,043,279. 10/2011. Inventor: Takatomo Hisamatsu et al.

[P40] Tube joint. U.S. Pat. No.: 6,764,102. 07/2004. Inventor: Takumi Ezura.